

# **Spectroscopic investigations of detachment on TCV**

*Investigating the role of atomic physics on the ion  
current roll-over and the dynamics of detachment in  
TCV*

Kevin Henricus Annemarie Verhaegh, MSc. MSc.

PhD

University of York

Physics

September 2018

# Abstract

The process of divertor detachment, whereby heat and particle fluxes to divertor surfaces are strongly reduced, is required to reduce heat loading and erosion in a magnetic fusion reactor. In this thesis the physics leading to the decrease of the divertor ion current ( $I_t$ ), or ‘roll-over’, is experimentally explored on the TCV tokamak through characterization of the location, magnitude and role of the various divertor ion sinks and sources including a complete measure of particle and power balance. These first measurements of the profiles of divertor ionisation and hydrogenic radiation along the divertor leg are enabled through the development of a TCV divertor spectrometer, together with careful Stark broadening analysis and novel Balmer line spectroscopic techniques.

Over a range in core plasma conditions (plasma current, impurity-seeding, density) the  $I_t$  roll-over is caused by a drop in the divertor ion source; recombination remains either small or negligible until later in the detachment process. In agreement with simple analytical predictions, this ion source is limited by a reduction in the power available for ionisation,  $P_{recl}$ , sometimes characterised as ‘power starvation’. Concurrent increases in the energy required per ionisation,  $E_{ion}$ , further reduce the number of ionizations. The detachment threshold is found experimentally (in agreement with analytic model predictions) to be  $P_{recl}/I_t E_{ion} < 2$ , corresponding to the target electron temperature,  $T_t \sim E_{ion}/\gamma$  where  $\gamma$  is the sheath transmission coefficient. Target pressure loss, required for target ion current loss, is observed to be delivered by both volumetric momentum loss, as typically assumed, and by a drop of the upstream pressure.

The evolution of measured divertor profiles through detachment of the various ion sources/- sinks as well as power losses and charge exchange are quantitatively reproduced through full 2D SOLPS modelling of a ramp of core plasma density through the detachment process.

# Contents

<b>Abstract</b>	<b>2</b>
<b>Contents</b>	<b>3</b>
<b>List of Figures</b>	<b>8</b>
<b>List of Tables</b>	<b>18</b>
<b>Acknowledgements</b>	<b>19</b>
<b>Author's Declaration</b>	<b>21</b>
<b>Preface</b>	<b>22</b>
<b>Executive summary</b>	<b>23</b>
<b>1 Introduction</b>	<b>25</b>
1.1 Energy sources and its future . . . . .	25
1.2 Nuclear Fusion: a possible solution for the energy problem . . . . .	29
1.3 Confining the plasma: tokamaks . . . . .	31
1.4 The power exhaust challenge: divertors . . . . .	32
1.5 Taming the power exhaust: detachment . . . . .	35
1.6 Detachment: an in-depth overview, its gaps in knowledge and the relevance of this work . . . . .	35
1.7 Goals and objectives of this thesis . . . . .	38
1.8 Merit of this work . . . . .	41
1.8.1 Diagnostic interpretation, analysis and development . . . . .	41
1.8.2 Detachment interpretation . . . . .	42
<b>2 Literature and theory of detachment</b>	<b>44</b>
2.1 Divertor physics fundamentals and its processes . . . . .	45
2.2 Understanding different divertor operational regimes through simplified modelling: Two Point Model . . . . .	48
2.2.1 Derivation of the 'basic' two point model . . . . .	49
2.2.2 Including 'missing' physics by implementing correction terms . . . . .	51
2.3 Detachment . . . . .	53
2.3.1 Observing and characterising detachment . . . . .	56
2.4 Atomic physics and its role in divertor physics . . . . .	61

2.4.1	Atomic databases and collisional radiative models . . . . .	61
2.4.2	Hydrogen Ionisation, recombination and charge exchange rates . . . . .	62
2.4.3	Momentum losses due to atomic and molecular reactions . . . . .	64
2.4.4	Hydrogen Balmer Line emissivities . . . . .	66
2.4.5	Hydrogen radiative losses . . . . .	67
2.4.6	Impurity radiation —carbon . . . . .	68
2.4.7	Molecular reactions . . . . .	70
2.5	Alternative geometries and divertor performance . . . . .	70
2.6	Advanced modelling of divertor plasmas and detachment: SOLPS-ITER . . . . .	72
<b>3</b>	<b>Analytical divertor models</b>	<b>73</b>
3.1	Power and particle balance . . . . .	74
3.2	Modelling the ion source from power/particle balance . . . . .	79
3.2.1	Physical expectations of power/particle balance and scalings . . . . .	82
3.3	Including recycling energy cost in the Two Point Model: the 2PMR . . . . .	83
3.3.1	Derivation and key points . . . . .	84
3.4	2PMR with explicit conductivity . . . . .	90
3.5	Exceeding the 2PMR critical limits . . . . .	93
3.5.1	Exceeding the 2PMR critical limits: upstream density loss . . . . .	97
3.6	Reduced analytical models in comparison with experiments . . . . .	98
3.7	Summary and discussion . . . . .	101
<b>4</b>	<b>TCV: Tokamak à Configuration Variable</b>	<b>102</b>
4.1	TCV overview and capabilities . . . . .	102
4.2	TCV diagnostic capabilities . . . . .	103
4.2.1	Measuring radiative losses: bolometry . . . . .	103
4.2.2	Measuring target heat fluxes: infrared thermography . . . . .	106
4.2.3	Langmuir probes . . . . .	106
4.2.4	Reciprocating probe . . . . .	107
4.2.5	Measuring core and upstream temperatures/densities: Thomson scattering	107
4.2.6	Measuring neutral pressures: baratrons . . . . .	108
4.2.7	Spectroscopy for boundary physics studies . . . . .	108
4.2.8	TCV Diagnostic Control Systems . . . . .	110
4.3	Evaluating and using this experimental data for verification with SOLPS-ITER: synthetic diagnostics . . . . .	111
4.3.1	Synthetic bolometry . . . . .	111
4.3.2	Synthetic baratrons . . . . .	112
4.4	Discharge reproducibility . . . . .	114
<b>5</b>	<b>Divertor Spectroscopy System (DSS) on TCV</b>	<b>115</b>
5.1	Divertor spectroscopy on TCV . . . . .	115
5.1.1	Overview and capabilities of the Divertor Spectroscopy System on TCV	115
5.2	General details, alignment and track selection . . . . .	119
5.3	Hardware and control details of the DSS . . . . .	124
5.3.1	Spectrometer . . . . .	124

5.3.2	Camera	126
5.4	Camera smearing and post-shot corrections	130
5.5	Spectrometer absolute intensity calibration	134
5.5.1	Stray light and the absolute intensity calibration	135
5.6	Spectrometer instrumental function characterisation and calibration	140
5.6.1	Assessing the uncertainty in the instrumental function	141
5.7	Spectrometer characterisation	145
5.8	Synthetic diagnostic implementation in SOLPS-ITER	148
<b>6</b>	<b>Application of Stark broadening measurements on TCV</b>	<b>149</b>
6.1	Stark broadening introduction and fundamentals	149
6.1.1	An introduction to Stark fitting on TCV	151
6.2	Stark broadening compared to other line broadening effects	152
6.2.1	Stark broadening under the presence of a magnetic field —Zeeman splitting	154
6.2.2	$T_e$ dependence of Stark broadening	154
6.2.3	Stark broadening and Doppler broadening	155
6.3	TCV's Stark fitting techniques	158
6.4	TCV Stark broadening uncertainty and sensitivity analysis	162
6.4.1	Uncertainties induced due to signal-to-noise ratio and the instrumental function	162
6.4.2	Deviations between different Stark models	166
6.4.3	Uncertainties induced due to uncertainties in $T_e$ , $B$ and $T_i$ effects	167
6.4.4	Putting it all together: general uncertainty	169
6.5	Stark broadening and line integration effects	172
6.6	TCV Stark broadening results and verifications	173
6.6.1	Comparison of Stark inferred density with respect to different Balmer lines	174
6.7	Summary and applicability of Stark broadening on TCV	177
<b>7</b>	<b>Quantitative analysis of Balmer line spectra</b>	<b>178</b>
7.1	Introduction of Balmer line analysis	179
7.1.1	Output parameters of the analysis chain	179
7.1.2	Input parameters and their uncertainties	181
7.2	Separating recombination and excitation contributions to the Balmer line emission	187
7.2.1	Determining $F_{rec}(n)$ in the $F_{rec}(n)$ limits	193
7.2.2	$F_{rec}(n)$ and the recombination to ionisation fraction	195
7.3	Inferring recombination and ionisation rates	196
7.3.1	The excitation and recombination temperatures	197
7.4	Estimating hydrogenic radiative losses	200
7.5	Estimating charge exchange rates and charge exchange to ionisation ratios	202
7.6	Monte-Carlo probabilistic analysis methodology	203
7.7	Applying a synthetic diagnostic to SOLPS simulations and investigating line integration effects	208

<b>8 The physics of detachment and its dynamics on TCV</b>	<b>212</b>
8.1 General detachment characteristics on TCV . . . . .	212
8.1.1 Experimentally observed TCV detachment dynamics with a comparison to SOLPS results . . . . .	214
8.1.2 Evolution of electron density near the target . . . . .	217
8.2 Characterisation of the loss of source and its effect on the ion target flux . . . . .	218
8.2.1 Characterisation of ion sinks and sources in density ramp discharges .	218
8.2.2 Characterisation of ion sinks and sources in $N_2$ seeded discharges . .	219
8.2.3 Estimating the flow of ions from upstream into the divertor . . . . .	222
8.3 Power balance in the divertor and its relationship to ionisation . . . . .	223
8.4 Evidence for molecular reactions during TCV detachment . . . . .	226
8.5 Summary . . . . .	229
<b>9 Discussion</b>	<b>230</b>
9.1 Investigating detachment in the framework of power and particle balance . .	231
9.1.1 The variation of $E_{ion}$ during detachment . . . . .	231
9.1.2 Target temperature predictions . . . . .	234
9.1.3 Comparing the measured and predicted ion target current . . . . .	234
9.1.4 Power dynamics in the TCV recycling region . . . . .	236
9.2 Investigating detachment in the framework of power, particle and momentum balance . . . . .	237
9.2.1 Modelling total target ion current behaviour with both power and momentum balance . . . . .	238
9.2.2 Detachment thresholds and implications for momentum/pressure losses along a flux tube (separatrix) . . . . .	240
9.2.3 The 2PMR and momentum losses . . . . .	243
9.2.4 The case for divertor processes reducing the upstream pressure and density . . . . .	245
9.2.5 The role of momentum loss and upstream pressure loss in target ion current loss . . . . .	246
9.3 $N_2$ seeded detachment on TCV . . . . .	247
9.4 Applicability of TCV results to other existing and planned tokamaks . . . . .	249
<b>10 Conclusion</b>	<b>251</b>
<b>Appendices</b>	<b>252</b>
<b>A Technical details DSS: <i>Correction algorithms, Hardware and Software</i></b>	<b>253</b>
A.1 Advanced smearing correction algorithms . . . . .	253
A.1.1 Application of advanced smearing correction - example $N_2$ seeded discharge	255
A.2 Stray light detection and correction during absolute calibration . . . . .	257
A.3 Mechanical and 3D printed assemblies . . . . .	261
A.4 Analysing pick-up and choice of ROI . . . . .	263
A.5 Software systems and hardware control . . . . .	266

<b>B Statistical investigation of Balmer line analysis sensitivities</b>	<b>270</b>
B.1 Investigating the influence of uncertainties in atomic rate coefficient . . . . .	270
B.2 Investigating the robustness against various neutral fraction PDFs . . . . .	271
B.3 Investigating the different sensitivities of output parameters to input uncertainties	273
<b>Bibliography</b>	<b>276</b>

# List of Figures

1.1	Power consumption per person versus population density, in 2005. Point size is proportional to land area. Both axes are logarithmic. The straight lines with slope -1 are contours of equal power consumption per unit area and as a reference, the energy densities generated using renewable technologies are shown. Adopted from [11, 23, 24]. . . . .	27
1.2	Schematic overview of a tokamak a) and a stellarator b) adopted from [32]. . . . .	31
1.3	Overview of ITER and its various components. Courtesy of the ITER organisation, file obtained from <a href="https://www.iter.org/album/Media/7%20-%20Technical">https://www.iter.org/album/Media/7%20-%20Technical</a> . With manually added labels. . . . .	32
1.4	Overview of the limiter and divertor configuration on TCV, together with the planned baffle upgrade [34]. The equilibria have been taken from an experiment performed on TCV. . . . .	33
2.1	A schematic picture of straightening out the poloidal SOL geometry in a 1D model, implemented from [81] and the JET image database. . . . .	48
2.2	A schematic overview of the various detachment processes in the divertor adopted from [1] and [2]. a) Schematic overview of TCV detachment processes as function of increasing upstream density or seeding level. b) More detailed schematic overview of a detached TCV divertor. c) A schematic overview of the different processes in the divertor and their influences on power, particle and momentum balance. . . . .	55
2.3	Various divertor spectra measured by the DSS on TCV obtained during repeat discharges. They are shown for both an attached (red) and detached (blue) case. . . . .	56
2.4	Overview of TCV detachment adopted from [101]. a) Ion target current (integrated) evolution during a core density ramp $\langle n_e \rangle$ . b) Evolution of the degree of detachment during a core density ramp. c) Profiles of the ion target flux compared between an attached/detached phase. d) Profiles of the heat flux at the target compared between the attached/detached phase. e-g) Comparison between upstream (reciprocating probe) and target (Langmuir probe) density profiles during attached/detached conditions. h-j) Comparison between upstream (reciprocating probe) and target (Langmuir probe) temperature profiles during attached/detached conditions. k-m) Comparison between upstream (reciprocating probe) and target (Langmuir probe) pressure profiles during attached/detached conditions. . . . .	60
2.5	Hydrogen effective recombination, ionisation and charge exchange rates as function of electron temperature for three different electron densities. . . . .	62
2.6	2D maps of effective recombination, ionisation and charge exchange rates as function of electron temperature and electron density with a linear colour map. Contour lines are shown which correspond to cases where the charge exchange rate is 1, 2, 10 times the ionisation rate and where the recombination reaction rate is $10^{-1}, 10^{-2}, 10^{-3}$ times the ionisation rate (which would correspond to a case where the recombination volume rate and ionisation volume rate equal each other assuming a neutral fraction of $10^{-1}, 10^{-2}, 10^{-3}$ ). . . . .	63
2.7	a) 2D evaluation of $f_{mom}$ through the Self-Ewald model as function of $n_e, T_e$ using ADAS and equation 2.9 with contour lines. b) $f_{mom}$ as function of $T_e$ (for $n_e = 5 \times 10^{19} \text{ m}^{-3}$ ), together with several scaling laws obtained from [4, 49]. . . . .	65
2.8	Photon emission coefficients (PEC) for the hydrogen Balmer lines of $n = 3 - 8$ as function of $T_e$ for three different electron densities. Both the excitation and recombination PECs are shown. . . . .	67
2.9	2D maps of the PLT and (corrected) PRB coefficients as function of electron temperature and electron density with a linear colour map. . . . .	67

2.10	Charge resolved carbon PLT coefficients as function of temperature. An effective PLT —which is determined assuming ionisation balance determined through ionisation and recombination coefficients and assuming no transport is shown. An 'effective' PLT curve which includes TCV simulated transport is shown for a SOLPS modelled discharge # 106278 where the effective PLT is determined by determining the individual PLTs for each charge state in the grid cell using $n_e, T_e$ and multiplying those with the simulated fractional abundances obtained from the SOLPS simulation. All PLT values for all grid cell are shown where one data point represents one grid cell. . . . .	69
2.11	Designed TCV magnetic geometry configurations, corresponding to single-null, snowflake, super-X divertor geometries. . . . .	71
3.1	Schematic overview of power and particle balance in the outer divertor. The blue shaded region represents the divertor. The various parameters are defined in the text. . . . .	75
3.2	$E_{ion}/\gamma$ as function of $T_e$ including the $T_e = E_{ion}/\gamma$ curve for a range of $n_e$ and $\gamma$ . . . . .	76
3.3	Evaluation of different models for $E_{CX}$ compared to $E_{ion}$ as function of temperature. . . . .	77
3.4	$E_{rec}$ as function of $T_e, n_e$ with a contour line at zero. . . . .	78
3.5	a) $f_{ion}$ as function of $T_t$ , b) $f_{target}, f_{pot}, f_{kin}$ as function of $T_t$ c) $\Gamma_t/q_{recl} = \frac{f_{ion}(T_t^*)}{E_{ion}}$ as function of $T_t$ , d) $p_t/q_{recl}$ as function of $T_t$ . All of this is shown for both a fixed $E_{ion}$ and for $E_{ion} = f(T_t, n_t)$ . . . . .	82
3.6	2PMR solutions for $T_t$ for a given $q_{recl} = 15 \text{ MW m}^{-2}$ compared with the standard two point model solution (equation 2.4) . . . . .	86
3.7	2PMR solutions for $T_t$ as function of $p_u$ (same as figure 3.6), $q_{recl}$ and $p_u/q_{recl}$ . For the $E_{ion}(T_t)$ function (which has a negligible $n_t$ dependence as well), $p_u = 80 \text{ Pa}$ is assumed in C. . . . .	87
3.8	2PMR solutions for $\Gamma_t$ (stable branch) as function of $p_t$ and $q_{recl}$ compared with the standard two point model solution (equation 3.19b). . . . .	89
3.9	Solutions of $T_u$ and $T_t$ from the 2PMR, which accounts for ionisation energy losses during recycling ( $E_{ion} = 30 \text{ eV}$ ), and the 2PM, which does not account for ionisation energy losses; both while taking conductivity into account. A) $T_t$ and $T_u$ as function of $n_u$ for a case with no impurity radiation. B) $T_t$ and $T_u$ as function of $f_{rad}^{imp}$ (e.g. the fraction of $q_{  }$ radiated before reaching the recycling region). The 2PMR solutions are obtained until $T_t = E_{ion}/\gamma$ and show lower temperatures/a larger temperature gradient due to the power lost during recycling. . . . .	91
3.10	2PMR and 2PM solutions $\Gamma_t$ as function of $n_u$ (A: fixed $L, \kappa, q_{  }, f_{rad}^{imp} = 0$ ) and $f_{rad}^{imp}$ (B: fixed $L, \kappa, q_{  }, n_u = 5 \times 10^{18} \text{ m}^{-3}$ ) taking conductivity into account to determine $T_u$ . $E_{ion} = 30 \text{ eV}$ has been assumed. Dotted lines have been provided to compare the scaling of the obtained trend with power scaling dependencies. . . . .	92
3.11	Graphical solution to the implicit equation 3.16a for the target temperature where both sides of this equation are plotted against each other. The intersection between the shown curves and the dashed line represents solution points where both sides equal. This graphical solution is shown for two values of $p_t$ and for using a <i>fixed</i> $p_t$ or using a <i>temperature dependent</i> $p_t$ (equation 3.23 with $n = 1$ ). . . . .	95
3.12	2PMR results of $T_t, p_t, \Gamma_t$ as function of $q_{recl}$ for $E_{ion} = 30 \text{ eV}$ ; $p_{t,0} = 75 \text{ Pa}$ . Five different relations of $p_t$ are shown: 1) $p_t = p_{t,0}$ ; 2) $p_t = 1/2 p_{t,0}$ , 3) $p_t = p_{t,0}$ until $p_t > p_{t,max}$ , where $p_t$ is kept at $p_{t,max}$ ; 4) equation 3.23 with $n = 1/2$ ; 5) equation 3.23 with $n = 1$ . As a reference, the $p_{t,max}$ trend is shown as $q_{recl}$ varies. . . . .	96
3.13	2PMR results with explicit conductivity and $n_u(T_t)$ dependency (similar to equation 3.23 with $n = 1$ and $p_t \rightarrow n_u$ of $T_t, p_u, \Gamma_t$ as function of $f_{rad}^{imp}$ ). The fixed parameters are: $E_{ion} = 30 \text{ eV}$ ; $n_{u,0} = 1 \times 10^{19} \text{ m}^{-3}$ ; $q_{  } = 20 \text{ MW m}^{-2}$ ; $L = 10 \text{ m}$ ; $\kappa = 2000$ . . . . .	98
4.1	Picture of the interior of TCV with graphite tiles installed. Courtesy of SPC, EPFL, Lausanne, Switzerland . . . . .	103
4.2	a): Lines of sight of the horizontal and vertical DSS systems. Divertor geometries for #56567 (red), #54868 (green), #52158 (blue) are shown. b) Lines of sight and locations of other diagnostics (Thomson/Langmuir probes/Vertical IR/Reciprocating probe/Bolometry together with the divertor geometry of #56567. Adopted from [2]. . . . .	104
4.3	a): Radiative power as function of time for # 52065 determined through the default analysis and through the inversion-less routine. b) Example of the inversion result [2] . . . . .	105

4.4	a): Langmuir probe coverage adopted from [117]. For illustration a typical plasma geometry (single null) is plotted (shot #52062). b) Thomson scattering coverage before upgrade adopted from [170]. c) Thomson scattering coverage after upgrade adopted from [170]. . . . .	106
4.5	Example of inverted (non-calibrated) emissivities from the MultiCam system on #52065 in attached (0.6 s) and detached (1.0 s) conditions. Adopted from [79]. . . . .	109
4.6	Comparison between a radiation map of a SOLPS discharge and the estimated radiation map by bolometry using a synthetic bolometer diagnostic with an inversion algorithm on the same colour axis. The SOLPS grid is over-plotted . . . . .	112
4.7	Comparison of the neutral pressure measured by baratrons (divertor and mid-plane) with the neutral pressure obtained in modelling through a synthetic baratron as function of the upstream density. The mid-plane neutral pressure has been multiplied by 10. . . . .	113
4.8	a) $9 \rightarrow 2$ Balmer line brightness and b) inferred Stark density from the $9 \rightarrow 2$ Balmer line obtained from the vertical system using the line of sight closest to the strike point location. Each colour indicates a different discharge. Characteristic uncertainties are shown in the figure.	114
5.1	DSS lines of sight, showing the three different horizontal orientations (blue, red, green) and the vertical lines of sight (magenta) together with the equilibrium of # 56567 at 1.0 s. . . . .	117
5.2	Pictures of DSS (Horizontal) system. a) Machine side. b) Tokamak side. . . . .	118
5.3	Image of the full-frame observation while monitoring a spectral lamp using the horizontal system with indicators of the spectral and spatial direction and the used ROIs. The spectral lamp used is Mercury-Cadmium at 365 nm central wavelength using a 600 l/mm grating. . . . .	120
5.4	Spectra (full-framed) with tracks. Multiple spectra are appended. The colour bar corresponds to counts where yellow corresponds to the highest signal and blue corresponds to the lowest signal	121
5.5	Modelled instrumental functions (convolution between a block function and a Lorentzian) as function of 'slit width', shown by the colour bar. The instrumental functions given a slit width of 25 and 35 micron are highlighted a) Lorentzian Full-Width-Half-Maximum is 35 micron (indicative of central fibres). b) Lorentzian Full-Width-Half-Maximum is 80 micron (indicative of edge fibres) . . . . .	122
5.6	Parameters obtained from slit model highlighted in figure 5.5 as function of slit width in micron. a) Full-Width-Half-Maximum obtained for two different Lorentzian FWHMs shown together with the 1:1 trend to which the result will converge if the instrumental function is dominated by the slit function. b) Obtained peak intensity normalised such that 1 would be obtained if the slit function would no longer be smeared out. . . . .	123
5.7	Pictures from the CCD output using a Hg spectral lamp with the spectrometer central wavelength being set at 546.1 nm (corresponding to a Hg spectral line) for three different slit widths. This shows greater deviation between central and edge pixels and lower peak intensity for the smallest slit width. . . . .	124
5.8	Overview of the Princeton Instruments Isoplane SCT 320 spectrometer adopted from its patent by [185]. The light input and camera sensor locations are marked. . . . .	125
5.9	Integrated counts (not background corrected) for a single ROI as function of acquisition frame at 200 Hz acquisition for two different camera timing settings: fastest vertical shift with voltage overclock ('VSS 0 VSA 3') and second-fastest vertical shift without voltage overclock ('VSS 1 VSA 0') a) Time-stabilised source. b) LED flashing at 10 Hz. . . . .	128
5.10	Measured EM gain calibration for Pre-Amp gain 0, 1 (1 is the default value and the highest, 0 can be used for highly sensitive studies requiring maximum dynamic range); Horizontal shift speed 30 MHz (HSS 0), Vertical shift speed 1.33 $\mu$ s per row (VSS 1), no vertical shift voltage overclock (VSA 0). a) Set EM gain versus the measured EM gain shown relative to no EM gain and Pre-Amp gain 1. b) Set EM gain versus the ratio between the measured EM gain and the expected EM gain assuming a 1:1 trend between the EM gain set and the EM gain measured. . .	129
5.11	Measured signal on all ROIs when a range of ROI is illuminated for a series of exposure times ( $[t_{exp} = 5\text{ ms to }20\text{ ms}]$ ) and vertical shift speeds ( $t_{VSS} = 1.1\text{ ms to }4.3\text{ ms per row}$ ). The predicted smearing roughly scales as $\frac{t_{VSS}}{t_{exp}}$ , giving rise to the horizontal dotted lines. The lit ROIs (and partially lit ROIs) are shaded. Note that this measurement was done without fibres and thus the tracks have been set-up equidistant in 20 segments. . . . .	129

5.12 Overview of smearing correction on a measured $6 \rightarrow 2$ Balmer line at 200 Hz acquisition frequency (# 52065). a) Profile of $6 \rightarrow 2$ intensity as function of ROI at $t = 1.25$ s together with highlights of the ROI of which the spectra are shown. b) Profile of $6 \rightarrow 2$ intensity for LoS 3 (near target —brightest) as function of time, together with windows corresponding to the different acquisition phases. c-g) Spectra of $6 \rightarrow 2$ both measured (non-smearing correction) and smearing corrected for five different lines of sight. Also the deviation between the spectra and the smearing-corrected spectra (plusses) is shown, which indicates the amount of smearing contributing to the measured signal. . . . .	133
5.13 Measured spectra of a Xe spectral lamp (the input optics are illuminated through using an integrating sphere) using the horizontal spectrometer with a 1800 l/mm grating centred at 465 nm central wavelength (spectral coverage: 456 nm to 474 nm), shown both with the older (NA 0.22) fibres and the newer (NA 0.10) fibres. . . . .	136
5.14 Spectra shown using a Xe lamp in the 465 nm region (central wavelength) with a 1800 l/mm grating where either the collection optics are illuminated directly by the spectral Pen-Ray lamp or illuminated through using an integrating sphere. a) Full spectra normalised such that an integral over the brightest spectral line would yield 1. b) Zoom-in on brightest spectral line. . . . .	136
5.15 Illustration of the influence of stray light ( $1 \times 10^{-4}$ stray light (with respect to intensity) is assumed) on an absolute intensity calibration. a) Pre-calibrated lamp spectra (intensity on a log scale) where the influence of stray light has been modelled. The different lamp curves have been normalised with respect to their integral. b) Relative difference in the spectra due to stray light ((Stray light spectra —lamp spectra) / stray light spectra). . . . .	138
5.16 Absolute calibration curves showing the absolute calibration factors (e.g. calibrated signal = measured signal (counts / s) / calibration factor) as function of wavelength (corresponding to a single acquisition of central wavelength 369 nm —lowest calibrated wavelength) shown for three ROIs using the signal uncorrected for stray light, the stray light corrected signal and using a 424 nm short-pass filter (while taking that filter curve into account in the absolute calibration.). . . . .	139
5.17 Examples of extracted instrumental functions for the horizontal DSS system using a 1800 l/mm grating around the 460 nm to 470 nm wavelength region. a-c) Different instrumental functions (different colours) shown for three different lines of sight corresponding to a 467.81 nm line from a mercury-cadmium spectral lamp, positioned between horizontal (wavelength direction) pixel number 100 and 700. d-f) Different instrumental functions (different colours) shown for three different lines of sight (16 —centre; 4 edge; 27 edge), corresponding to 458.28, 462.43, 467.12, 469.7, 473.42 nm spectral lines obtained from a Xe spectral lamp obtained during a single acquisition (single grating angle), with and without integrating sphere. Note that the situation shown in a-c is from a different calibration run than the one shown in d-f. . . . .	142
5.18 2D PDF of the Bayesian fit (of instrumentals measured using a 1800 l/mm grating, 465 nm central wavelength and using a Xe lamp) of the $a, c$ using equation 5.3 (the result is marginalised along the $b$ direction), shown for two different errors. Each colour map shows the results of three separate PDFs (corresponding to three separate instrumental functions obtained during a single acquisition of the Xe lamp at different wavelengths) using red, green, blue colours. When all instrumentals overlap, a grey map would be obtained. When none of the instrumentals overlap, separate red, green, blue maps are obtained. . . . .	143
5.19 Extracted (median of distribution obtained through a Xe lamp) and a) simulated asymmetric Lorentzians obtained from the Bayesian asymmetric Lorentzian fit using the described Monte Carlo algorithm, b) simulated instrumental functions obtained by point-wise shifting the instrumental functions such that the median of the distribution of instrumental functions aligns with the input instrumental function. The data has been taken from the edge of the CCD (LoS 2) using a 1800 l/mm grating at 404 nm central wavelength, which deviates more strongly from the asymmetric Lorentzian fit than central chords, using a Mercury-Cadmium spectral lamp. Of the Monte Carlo generated instrumentals, 100 different instrumental functions are shown. . . . .	144
5.20 Extracted and simulated (100) instrumental functions (normalised with respect to intensity) using the described Monte Carlo algorithm for three different lines of sight. All shown correspond to spectral lines at 458.28, 462.43, 467.12, 469.7, 473.42 nm obtained from a Xe spectral lamp during a single acquisition (1800 l/mm grating), both with/without using an integrating sphere. . . . .	145

5.21	Instrumental function characterisation for the 1800 1/mm grating (a,c,e) and the 600 1/mm grating (b,d,f). Colour maps as function of ROI and wavelength are shown for the width (FWHM in pixels (a,b) and width at 10 % of the maximum intensity (c,d)) and for the asymmetry in pixels (e,f). . . . .	146
5.22	DSS 'efficiency', where the measured signal (in $\text{counts m}^{-2} \text{s}^{-1} \text{sr}^{-1} \text{nm}^{-1}$ ) equals the calibrated signal (in $\text{ph m}^{-2} \text{s}^{-1} \text{sr}^{-1} \text{nm}^{-1}$ ) times the shown efficiency coefficient (which is in counts per photon). The calibration coefficient is shown as function of wavelength for several calibration runs, the 1800 and 600 1/mm gratings and at several ROIs. b) Example of 2D calibration map obtained during a single acquisition corresponding to three curves highlighted in a). . . . .	148
6.1	Various line shapes on a a) linear scale and b) logarithmic scale of Stark/Doppler/Instrumental broadening for the $n = 7$ deuterium Balmer line (397 nm). All line profiles are normalised with respect to their integral. . . . .	152
6.2	Various fractional widths of the Stark lineshape using the Rosato Stark model for two different $n_e$ as function of $B$ for two different observational angles. . . . .	155
6.3	Various fraction widths of the Stark lineshape for two different $n_e$ as function of $T_e$ for both the parametrised Stehle model and the Rosato Stark model, which assumes $T_e = T_i$ and accounts for ion dynamics (only the Stark shape is shown —not the Doppler shape) . . . . .	156
6.4	Example of a Stark fit on a synthetically simulated spectra with multiple Doppler components denoted by their ion temperature and relative strength $f$ . The fit parameters are noted in the figure. Due to the multiple Doppler components, going to high temperatures (100 eV), wide Doppler wings are obtained (similar to Stark) and the Stark/Doppler broadening can no longer be distinguished. . . . .	157
6.5	Comparison between the electron density set in the synthetic spectrum with a $T_i = 15 \text{ eV}$ to the electron density inferred in the fit assuming a $T_i = 5 \text{ eV}$ for different weighting functions used in the fit. Uncertainties in the instrumental function and due to the signal to noise level of the synthetic spectra are accounted for using a Monte Carlo approach. . . . .	158
6.6	Example of a Stark fit using experimental TCV data on a linear scale (a) and a logarithmic scale (b). The shown instrumental function, Doppler line shape, Stark line shape are convolved and a polynomial background is added to form the fitting function. The shown spectral line corresponds to the $7 \rightarrow 2$ Balmer line. All line profiles are normalised with respect to their integral. . . . .	161
6.7	Probability density functions (PDFs) for the Monte Carlo inferred Stark density where the random noise and the instrumental function (according to its error) is varied for a case where the electron density corresponding to the synthetic spectra is fixed at $2 \times 10^{19} \text{ m}^{-3}$ . Different PDFs are shown for different lines of sight and different signal to noise level. . . . .	163
6.8	Comparison between the electron density set in the synthetic spectrum to the electron density inferred in the fit as function of S/N for two LoS at a) $n_e = 2 \times 10^{19} \text{ m}^{-3}$ density, b) $n_e = 1.1 \times 10^{20} \text{ m}^{-3}$ with 68 % and 95 % confidence intervals. . . . .	164
6.9	2D Map of Stark density inferences relative, absolute uncertainties (68 % confidence interval) and deviations of Monte Carlo estimate with respect to set electron density for two lines of sight as function of set Stark density and signal-to-noise level. Several contour lines are shown as indicates in the colour maps. The S/N ratio $> 30$ region is shaded. . . . .	165
6.10	Comparison between the electron density set in the synthetic line-shape generated through the Rosato model and the inferred density from the Monte Carlo fit using the parametrised Stehle model for the $7 \rightarrow 2$ Balmer line. . . . .	166
6.11	Comparison between the prescribed electron density in the synthetic line-shape generated through the Rosato model and the inferred density from the Monte Carlo fit using the parametrised Stehle model as function of $T_e$ . Both the ratio between the inferred and prescribed Stark density (a) and the relative uncertainty (95%) obtained through the Monte Carlo method is shown (b). . . . .	168
6.12	Comparison between the prescribed electron density in the synthetic line-shape generated through the Rosato model and the inferred density from the Monte Carlo fit using the parametrised Stehle model as function of $B$ . Both the ratio between the inferred and prescribed Stark density (a) and the relative uncertainty (95%) obtained through the Monte Carlo method is shown (b). The TCV range of applicable magnetic fields is shielded. . . . .	169

6.13 Comparison between the prescribed electron density in the synthetic line-shape generated through the Rosato model and the inferred density from the Monte Carlo fit using the parametrised Stehle model as function of $T_i$ . Both the ratio between the inferred and prescribed Stark density (a) and the relative uncertainty (95%) obtained through the Monte Carlo method is shown (b). . . . .	170
6.14 Comparison between the probability density functions obtained for a single LoS (4) at a single time step (1.0 s) using the full Monte Carlo Stark investigation explained above and the fast 'default' fit using the parametrised Stehle model together with its assumed uncertainty and probability density shape (Gaussian) . . . . .	171
6.15 Evolution of inferred Stark density for the first five lines of sight as function of time for discharge # 57912 using the default fit analysis and a Monte Carlo fit analysis. The inferred 95 % uncertainty margins based on the Monte Carlo fit analysis is added. . . . .	172
6.16 Stark density as function of time observed for repeat discharges numbers 52126, 52128 and 52131 while using various time windows . . . . .	175
6.17 Spectra of high-n lines during a detached discharge (#52126) observed with the horizontal system from the line of sight closest to the target indicating the formation of the recombinative pseudo-continuum after the $n = 17$ Balmer line which is still observed. . . . .	176
 7.1 Schematic overview of the analysis steps (green) in the Balmer line analysis chain together with the required measured inputs (grey, white text —including the Balmer line brightness $B_{n \rightarrow 2}$ ), assumed inputs (grey, yellow text —including the neutral fraction $n_o/n_e$ , the path length $\Delta L$ ) and inferred outputs (purple —including the Stark density $n_e$ ; inferred recombination/excitation Balmer line emission fraction $F_{rec}(n)$ , $F_{exc}(n)$ ; line integrated hydrogenic excitation/recombination radiated power loss $P_{rad,L}^{exc}$ , $P_{rad,L}^{rec}$ ; line integrated ionisation/recombination rate $I_L$ , $R_L$ and line averaged charge exchange to ionisation ratio $CX_L/I_L$ ). . . . .	180
7.2 a) Schematic overview of how the path length $\Delta L$ and $r_i, z_i$ are determined. b) Example of $\Delta L$ time trace for three lines of sight for # 56567. . . . .	182
7.3 a-c) Emission profiles (recombination/excitation/total) for the n=5,6,7 Balmer line emission obtained along the line of sight during a SOLPS simulation (#106237). d-e) Plasma profiles of electron temperature, electron density and hydrogen neutral density along line of sight. f) SOLPS grid geometry (outer divertor leg) with line of sight. . . . .	183
7.4 Estimated path lengths from the $J_{sat}$ profile compared to the actual characteristic lengths of the emission region along the line of sight; both determined through a SOLPS simulation (MDS+ shot number #106273 —see section 7.7 for more details), for the n=5,6,7 Balmer lines. . . . .	185
7.5 Comparison of the neutral fraction along the (a) separatrix and (b) emission-weighted ( $n = 7$ Balmer line) along the DSS chords; both from the outer divertor leg obtained from SOLPS-ITER simulations at different upstream densities. The SOLPS results are compared to the no-transport assumption in (a) (equation 7.4). The neutral fraction range ( $n_o/n_e = [0.001 - 0.05]$ ) is shaded in yellow. . . . .	186
7.6 Modelled $\frac{B_{5 \rightarrow 2}}{B_{6 \rightarrow 2}}$ as function of $T_e$ . Both the excitation only and recombination only trends are shown at three different densities, while the green/magenta take both recombination/excitation into account and assume a fixed $n_o/n_e$ . The black solid line indicates $\frac{B_{5 \rightarrow 2}}{B_{6 \rightarrow 2}}$ as function of $T_e$ where $n_o/n_e$ is determined as function of $T_e$ using equation 7.4, as done in [73] to determine the 'TEC'. The black plusses indicate the measured $\frac{B_{5 \rightarrow 2}}{B_{6 \rightarrow 2}}$ for # 56567 for all lines of sight of the divertor spectrometer, where $T_e$ respective of the excitation emission is used as the effective $T_e$ (see section 7.3.1 and 9.1.2). . . . .	188
7.7 $F_{rec}(n = 5)$ as function of $\frac{B_{6 \rightarrow 2}}{B_{5 \rightarrow 2}}$ for a set of fixed $n_e$ and $n_o/n_e$ . Each point in this graph corresponds to a certain $T_e$ . . . . .	190
7.8 $F_{rec}(n)$ and $F_{exc}(n)$ as function of the temperature (and hence recombination to ionisation rate ratio) for an assumed $n_e = 5 \cdot 10^{19} m^{-3}$ and $n_o/n_e = 0.05$ . . . . .	191

7.9 An illustration of the technique for obtaining a unique $F_{rec}$ : a $F_{rec}(n = 5)$ as function of $B_{6 \rightarrow 2}/B_{5 \rightarrow 2}$ where two different $T_e$ windows were used, a 'full' window and a restricted window (' $F_{rec}$ restricted $T_e$ window') where only unique solutions can be obtained. b Inferred $F_{rec}(n = 5)$ from the Balmer line ratio showing two solutions for $F_{rec}$ and a visualisation of the solution provided by the highlighted correction algorithm. c) Magnification of figure a in the $F_{rec} \sim 1$ non-unique region where four points of $T_e$ are highlighted, which are represented by the numbered vertical lines in b to link figures a, b and c. . . . .	195
7.10 a Modelled $R_L$ as function of $B_{6 \rightarrow 2}^{rec}$ for a set of $n_e$ and $\Delta L$ . b Modelled $I_L$ as function of $B_{6 \rightarrow 2}^{exc}$ for a set of $n_e$ and $\Delta L \times n_o/n_e$ . . . . .	198
7.11 a Emission-weighted (recombination/excitation/total), along DSS lines of sight, $T_e$ profile from target to separatrix. b Emission-weighted (recombination/excitation/total), along DSS lines of sight, $n_e$ profile from target to separatrix. . . . .	199
7.12 a) Both the calculated $F_{rec}(n = 5)$ and the post-process calculated $F_{rec}^{consistent}(n = 5)$ using the statistical techniques of section 7.6 as function of time with 68% confidence intervals. b) Visualisation of the probability density function (PDF) of $F_{rec}(n = 5)$ and $F_{rec}^{consistent}(n = 5)$ at three different times for a given chord. . . . .	200
7.13 a Modelled $P_{rad,L}^{H,rec}$ as function of $B_{6 \rightarrow 2}^{rec}$ for a set of $n_e$ and $\Delta L$ . b Modelled $P_{rad,L}^{H,exc}$ as function of $B_{5 \rightarrow 2}^{exc}$ for a set of $n_e$ and $\Delta L \times n_o/n_e$ . . . . .	201
7.14 a) Modelled $CX_L$ as function of $B_{5 \rightarrow 2}^{exc}$ for a set of $n_e$ and $\Delta L \times n_o/n_e$ . b) Modelled $CX_L/I_L$ ratio as function of $B_{5 \rightarrow 2}^{exc}$ for a set of $n_e$ and $\Delta L \times n_o/n_e$ . . . . .	203
7.15 Example of Monte Carlo analysis chain, ion source calculation. a) Examples of input PDFs for $B_{5 \rightarrow 2}$ and $n_o/n_e \times n_e \times \Delta L$ . Points are randomly sampled from these input PDFs yielding to points in the scatter plot whose colours represent the $I_L$ corresponding to that calculation. b) Shows a PDF of $I_L$ , together with the maximum likelihood estimate (MLE) and 68% Highest Density Interval (HDI). X-axis corresponds to $I_L$ magnitude and its colour bar colours of the scatter plot in figure A. . . . .	204
7.16 Monte Carlo $T_e^E$ result for # 56567 (line of sight 3; t = 0.6 s) represented as a) Point cloud. b) Histogram. c) PDF obtained through kernel density estimation [211] together with the MLE and 68 % HDI estimates. . . . .	206
7.17 Characteristic PDFs from output parameters ( $I_i, I_r, P_{rad}^{H,exc}, P_{rad}^{H,rec}, \int CX_L/I_i, F_{rec}(n = 5)$ ) (line of sight 3), $T_e^E, T_e^R$ (both line of sight 3)) obtained from #56567 at three different time steps, together with the maximum likelihood estimate (MLE - +) and the highest density interval (HDI - 68 % —shaded). . . . .	207
7.18 Characteristic PDFs from output parameters ( $I_i, I_r, P_{rad}^{H,exc}, P_{rad}^{H,rec}, \int CX_L/I_i, F_{rec}(n = 5)$ ) (line of sight 3), $T_e^E, T_e^R$ (both line of sight 3)) obtained from #56567 at three different time steps, together with the maximum likelihood estimate (MLE - +) and the highest density interval (HDI - 68 % - shaded). . . . .	210
8.1 Overview of detachment based on a high $I_p$ density ramp discharge (#56567). a Line averaged density, $\bar{n}_e$ , upstream density $n_{e,u}$ and upstream temperature, $T_{e,u}$ as function of time. b Total ion target flux ( $I_t$ ), ion target flux density at the separatrix ( $\Gamma_t$ ), recombination rate ( $I_r$ ) and $I_t$ loss rate as function of time. . . . .	214
8.2 a) Electron density (characteristic uncertainty $\sim 1 \times 10^{19} \text{ m}^{-3}$ ) traces of chords near the target (#57912) for a density ramp experiment. b) Corresponding divertor geometry and lines of sight	215

8.3	Left hand side: Experimentally (spectroscopic inferences + bolometry) determined quantities along the outer divertor leg. Right hand side: Results obtained directly from SOLPS simulation utilizing synthetic diagnostic measurements. a) Total outer ion target flux $I_t$ , outer divertor integrated ion source and recombination rate ( $I_i, I_r$ ), together with the linear scaling of the ion target flux as function of time and vertical lines corresponding to the times at which the profiles are shown in the figures below. b) Analogous ion source/sink plot (outer divertor integrated) obtained from SOLPS where the ionisation source and recombination sinks are shown as function of upstream density. c, e) Stark density profiles (c —obtained from a synthetic diagnostic —see section 5.8). e, f) Chordal integrated recombination ( $R_L$ ) /ionisation rate ( $I_L$ ) profiles. g, h) Chordal integrated total radiation profiles through bolometry – $P_{rad,L}$ ; and radiation due to hydrogenic excitation – $P_{rad,L}^{H,exc}$ . i, j) Line integrated charge exchange to ionisation ratio profiles ( $CX_L/I_L$ ) . . . . .	215
8.4	First two columns correspond to core density ramps at two different plasma currents: Core Greenwald fraction (a,b); divertor ion sources/sinks and ion target flux (d, e) as well as the loss of ion target current, recombination sink and loss of ionisation (g, h). The last column corresponds to a $N_2$ seeding ramp at constant core density (c): divertor ion source/sink and ion target flux (f) as well as the loss of ion target current, recombination sink and loss of ionisation (i). . . . .	220
8.5	The target ion flux compared to the ion source, inferred ion flow from the upstream SOL and the recombination rate . . . . .	222
8.6	Power balance investigation for the outer divertor for pulse #56567 a): ion target flux, ionisation rate and recombination rate; b) break-down of total radiation and its contributors; c) comparison between power entering the outer divertor leg, $P_{div}$ ; the power entering the recycling region, $P_{recl}$ and the power needed for ionisation, $P_{ion}$ ; d) comparison between $P_{div}$ and the outer divertor leg radiative losses plus the measured power deposited on the target by the IR for consistency. . . . .	225
8.7	a) Target ion flux, ionisation rate and recombination rate as function of time. b) Measured (summed over all chords) $D\alpha$ signal and predicted summed $D\alpha$ signal. c) Measured and predicted $D\gamma/D\alpha$ ratio along three different locations. The expected excitation limit, or minimum ratio is shown. The predicted recombination limit is $\sim 0.1$ . . . . .	227
9.1	a) Target ion flux as function of time together with the ionisation rate and recombination rate. b) Effective radiative energy cost per ionisation/recombination. c) Radiative energy cost per ionisation along a certain chord. . . . .	232
9.2	a) Predicted ion target flux based on power balance compared with measured ion target flux as function of time. b) Ion loss as function of time for the ion target flux prediction and the measured ion target flux. c) Target temperature as function of time. . . . .	233
9.3	Break-down of the fraction of $P_{recl}$ spent on ionisation ( $f_{ion}$ ); reaching the target ( $f_{target}$ ); reaching the target in the form of potential energy ( $f_{pot}$ ) and reaching the target in the form of kinetic energy ( $f_{kin}$ ). The shown fractions are modelled/predicted, based on $T_t^*$ (equation 3.11), which are compared to direct experimental inferences from power balance. Note that the fractions visualised in figure 9.3 have not been corrected for recombination, as the ratio $I_r/I_i$ is small for the TCV discharge presented (see equations 3.11 and 3.13 for further explanation). . . . .	235
9.4	Comparison of target pressure and upstream pressure. a) reference total current to the target, total ionisation source and recombination sink; b-c) Target separatrix pressure ( $p_t$ ) and ( $p_t/T_t^{1/2}$ ) ratio based on spectroscopic measurements (Stark broadening + excitation temperature of the chord closes to the target); d) Upstream separatrix pressure from Thomson scattering. . . . .	239
9.5	Thomson upstream temperature as function of time for # 56567 together with the upstream temperature prediction from conductivity. . . . .	240
9.6	a) Measured and predicted target ion flux trend. b) Break-down of the contributors to the predicted ion flux. c) Measured $p_u/q_{recl}$ compared to the critical predicted level for $p_t/q_{recl}$ . d) Inferred momentum losses from spectroscopic estimates. e) Measured upstream pressure compared to critical target pressure level. . . . .	241
9.7	Comparison of the various detachment thresholds with the experiment. a) $f_{ion}$ . b) $T_t$ . c) $p_{up}/q_{recl}$	243
9.8	Recombination to ion target flux ratio as function of Stark density obtained from the chord near the target for the three discharges presented in figure 8.4. . . . .	248

9.9	A schematic overview of the location, size and dynamics of the impurity radiation, ionisation and recombination regions on TCV; based on the profiles shown in figure 8.3 . . . . .	250
A.1	Overview of smearing of the $6 \rightarrow 2$ Balmer line and neighbouring NIII lines at 200 Hz acquisition frequency for a $N_2$ seeded discharge. a) Profile of NIII (410.33 nm) intensity as function of ROI at $t = 1.25$ s together with highlights of the ROI of which the spectra are shown. b) Profile of the NIII (410.33 nm) intensity for LoS 30 (near x-point) as function of time, together with windows corresponding to the different acquisition phases. c-g) Spectra of $6 \rightarrow 2$ , NIII (409.73 nm) and NIII (410.33 nm) both measured (non-smearing correction) and smearing corrected for four different lines of sight. Also the deviation between the spectra and the smearing-corrected spectra (plusses) is shown, which indicates the amount of smearing contributing to the measured signal. . . . .	256
A.2	Examples of a background corrected full-frame spectra of an incandescent light source (2800 K color temperature) obtained using a 1800 l/mm grating (approximately 18 nm coverage per acquisition) at different central wavelengths. a-c) Full-frame spectra with colourmap (0 minimum, each map is normalised with respect to its maximum). d) Spectra summed in the spectral direction normalised with respect to the integral over a single ROI for the three different cases, indicating different levels of signal in between the ROIs. . . . .	257
A.3	Overview of the first step of the stray light correction algorithm applied to the measured absolute calibration spectra at 369 nm without the application of a 424 nm shortpass filter. a) Measured spectra (full-frame) masking off all regions not corresponding to the 'dark spots' in between ROIs, b) interpolated spectra over the masked regions: e.g. full-frame signal expected due to signal in the optical 'dark' regions. c) Measured spectra (full-frame) masking off all regions not corresponding to the 'brightest centra' of the ROIs, d) interpolated spectra over the masked regions: e.g. full-frame emission expected due to signal in lit regions (if no fibre edges were present). e) Ratio between the expected 'dark' signal and 'lit signal'. . . . .	259
A.4	Overview of the second step of the stray light correction algorithm applied to a measured absolute calibration spectra at 369 nm without the application of a 424 nm shortpass filter. a) + b) determined ratio between the expected extrapolated 'dark' and 'lit' signals of the 600 nm measurement (of which no smearing is assumed) and the 369 nm measurement. c) Difference between these both ratios, indicating the predicted fraction of stray light the measured spectra at 369 nm has. d) Measured spectra (with stray light) at 369 nm. f) Stray-light corrected spectra (full-frame) with e) a plot as function of horizontal pixel location (spatial direction). g) Measured spectra (normalised at a single ROI's intensity) as function of horizontal pixel position (spatial direction). h) Stray-light corrected spectra (normalised at a single ROI's intensity) as function of horizontal pixel. . . . .	260
A.5	CAD model for lens to fibre (tokamak end) coupler. Pre-made parts are highlighted in cyan, 3D printed parts according to this CAD model are highlighted in red. . . . .	261
A.6	CAD model for the 3D printed assembly at the end of the tokamak, shown in picture 5.2 a). The CAD model shows the three different DSS orientations and as such, no Ocean optics collection optics mount is shown. Pre-made parts are highlighted in cyan and 3D printed parts according to this CAD model are highlighted in red. . . . .	262
A.7	CAD model for the 3D printed assembly for mounting the fibres to the slit at the spectrometer's end. Pre-made parts are highlighted in cyan, 3D printed parts according to this CAD model are highlighted in red. . . . .	263
A.8	Measured spatial instrumental functions as function of pixel positions for a range of different wavelengths (indicated by different lines with different colours). a) Spatial instrumental function of a central fibre (512 pixel index), b) spatial instrumental function of an edge fibre (970 pixel index). . . . .	264
A.9	Illustration of the pick-up calculation. Two identical spatial instrumental functions are shown for two neighbouring fibres including the total instrumental function (addition of the two). The maximum possible ROI width and the chosen ROI width are highlighted together with the ROIs centres. This illustration is only shown for the central fibre. . . . .	265

A.10 a) Calculated "efficiency" in % (e.g. fraction of signal corresponding to a single fibre caught by the ROI) as function of ROI width in pixels. b) Calculated "efficiency" in % as function of the pick-up between neighbouring fibre channels. . . . .	266
A.11 Control window for DSS operation during experiments. . . . .	268
A.12 Printscreen of the GUI used for DSS data viewing. Comments to identify the different elements are shown in red. . . . .	269
B.1 Ionisation source, recombination rate and ion target current for # 57920 (density ramp at high current - similar to #56567) when accounting for no uncertainty in the atomic coefficients or 20 % uncertainty (in the form of a uniform distribution). PDFs for various output parameters are shown for those two cases at 0.7 and 1.1 s . . . . .	271
B.2 Ionisation source, recombination rate and ion target current for # 57920 (density ramp at high current - similar to #56567) using a uniform and log-uniform PDF for $n_o/n_e$ . PDFs for various output parameters are shown using a uniform and log-uniform PDF for $n_o/n_e$ at 0.7 and 1.1 s	272
B.3 Calculated (Kendall) correlation strength of input parameters to output parameters for # 56567 as function of time for line of sight 3. Positive values are shown with solid lines and negative values are shown with dotted lines. Statistical insignificant calculations have been removed from the figure. As a reference $F_{rec}(n = 5)$ is shown. . . . .	275

# List of Tables

4.1	Overview of TCV parameters . . . . .	102
5.1	Overview of DSS parameters. . . . .	116
6.1	Overview of Stehle parametrisation parameters by Lomanowski ([74] and internal communication) for medium and higher-n hydrogen Balmer lines. . . . .	150
7.1	Summary of the output parameters of the spectroscopic analysis as indicated in figure 7.1, where Toroidal integral = Tor. $\int$ ; line integral = Line $\int$ . . . . .	181
7.2	Overview of used input parameters in the Balmer line analysis including their uncertainties and the shape of their probability density functions. . . . .	184
7.3	$T_e$ and $R_L/I_L$ corresponding to the $F_{rec} = 0.1$ to $0.3$ limits as function of $n, n_e, n_o/n_e$ . . . . .	192
8.1	Overview of MAR reactions adopted from [109] for deuterium. $D_2(\nu)$ implies vibrationally excited deuterium molecules, whereas $D^*$ denotes electronically excited atomic neutrals . . . . .	228

# Acknowledgements

This work would not have been possible without the support of my supervisor —Bruce Lipschultz; my 'unofficial' supervisor —Basil Duval; the TCV boundary group members and collaborators from CCFE/York; the TCV operations group and of course all scientists, PhD students, Master students and PostDocs at the SPC; which I'd all like to thank gratefully.

First of all, I would like to thank Bruce for his kind support during the entire project. It must not have been easy to supervise a student who is based elsewhere, but he did a stellar job to make it work. I appreciate all the time, devotion and confidence he put in this project. Without him, surely this work would have not been possible. I would like to thank Basil for all of his anecdotal advice, which helped to put things into perspective and for his vision that a PhD is not only about the research but what you learn while doing it.

There are countless others should be acknowledged for their continuous support and I would not be able to fit all of the names on one page. Certain people should, however, be mentioned explicitly. I kindly acknowledge Claudio Marini for educating me initially on spectroscopy and for all our useful discussions on spectroscopy. Mirko Wensing, Alexandre Fil and David Moulton are kindly acknowledged for helping me to make sense of the 'jungle' of SOLPS data outputs, without their support and simulations I would not have been able to compare the experimental results against SOLPS simulations. Chris Bowman is kindly acknowledged for discussions on Bayesian and other probabilistic methods for data analysis and error quantification. James Harrison is kindly acknowledged for many helpful discussions on divertor physics. Yanis Andrebe is kindly acknowledged for all his technical support on optics and for always lending me a hand when I needed it when doing technical work. Discussions with various scientists from other labs at conferences or elsewhere were extremely helpful for pushing the direction of this research further, including Bart Lomanowski, Peter Stangeby, Felix Reimold, Jim Terry, Marco Wischmeier, Joël Rosato, Sergei Krasheninnikov, Felix Para Diaz, Nicola Vianello and many others.

The TCV boundary group (Christian Theiler, Oliveir Février, Cedric Tsui, Holger Reimerdes, Benoit Labit, Hugo de Oliveira, Roberto Maurizio, Umar Sheikh and many others) and operation groups were invaluable for their support, useful discussions, and for diagnostic support during my experiments.

I would also like to acknowledge the 'unofficial TCV divertor spectroscopy group' which has been forming recently with continuously more people getting interested in TCV divertor imaging or line of sight spectroscopy, including Daljeet Gahle, Artur Perek, Mirko Wensing, Wouter Vijvers, Bryan Linehan and Xiande Feng. Working with you, as opposed to being the 'lone wolf' working full-time on TCV edge spectroscopy as in the beginning of my thesis, made me continuously more motivated in the subject and was good fun. Also working with

the 'DDJ ninjas' (Pedro Molina, Claudio Marini, Mirko Wensing, Umar Sheikh) to improve the experience of operating TCV diagnostics by PhDs smoother was a great pleasure and learning experience.

All the support from my other PhD colleagues and PostDocs at the SPC is gratefully acknowledged. There was always a group ready to go out, go to lake to barbecue or go to SAT to try to 'slay some Golden Dragons'. It was a pleasure —and I am sure I will miss you guys.

Last but not least, I gratefully acknowledge all the support back in the Netherlands from friends and family. My friends back home have been the best and were always ready to hang out and go out when I would return. The support from my family back home has been immense and this work would not have been possible without them.

Tenslotte wil ik graag mijn vrienden en familie in Nederland bedanken voor hun motivatie en geweldige steun toen ik in Zwitserland woonde. Zonder hun steun zou dit werk niet mogelijk zijn geweest.

This work has been carried out within the framework of the EUROfusion Consortium and has received funding from the Euratom research and training programme 2014-2018 under grant agreement No 633053. The views and opinions expressed herein do not necessarily reflect those of the European Commission. This work was supported in part by the Swiss National Science Foundation. The PhD research of K. Verhaegh was supported by funding from the University of York and the Swiss National Science Foundation.

# Author's Declaration

I declare that this thesis is a presentation of original work and I am the sole author. This work has not previously been presented for an award at this, or any other, University. All sources are acknowledged as References.

Portions of this thesis are based on manuscripts which have been either published or are ready to be submitted to peer-reviewed journals. I am the first author of these manuscripts. Where appropriate, these works have been referenced. For all of these cases, the vast majority of the work has been done by the main author. Pre-prints of both manuscripts are available online on ArXiv and/or ResearchGate.

These manuscripts include:

- *Spectroscopic investigations of divertor detachment in TCV*, by K. Verhaegh, B. Lipschultz, B.P. Duval, J.R. Harrison, H. Reimerdes, C. Theiler, B. Labit, R. Maurizio, C. Marini, F. Nespoli, U. Sheikh, C.K. Tsui, N. Vianello, W.A.J. Vijvers, published in *Nuclear Materials and Energy*, Volume 12, 2017, Pages 1112-1117. DOI: <https://doi.org/10.1016/j.nme.2017.01.004>. Also cited in this work as [1]. Pre-print locations,

ArXiv: <https://arxiv.org/abs/1607.04539>;

ResearchGate: [https://www.researchgate.net/publication/305389060\\_Spectroscopic\\_investigations\\_of\\_divertor\\_detachment\\_in\\_TCV](https://www.researchgate.net/publication/305389060_Spectroscopic_investigations_of_divertor_detachment_in_TCV).

- *An improved understanding of the roles of atomic processes and power balance in target ion current loss during detachment*, by K. Verhaegh, B. Lipschultz, B.P. Duval, O. Février, A. Fil, C. Theiler, M. Wensing, C. Bowman, D.S. Gahle, J. Harrison, B. Labit, C. Marini, R. Maurizio, H. de Oliveira, H. Reimerdes, U. Sheikh, C.K. Tsui, N. Vianello, W.A.J. Vijvers, to be submitted. DOI: <https://doi.org/10.13140/RG.2.2.24292.48005/1>. Also cited in this work as [2]. Pre-print location,

ResearchGate: [https://www.researchgate.net/publication/325763657\\_An\\_improved\\_understanding\\_of\\_the\\_roles\\_of\\_atomic\\_processes\\_and\\_power\\_balance\\_in\\_divertor\\_target\\_ion\\_current\\_loss\\_during\\_detachment](https://www.researchgate.net/publication/325763657_An_improved_understanding_of_the_roles_of_atomic_processes_and_power_balance_in_divertor_target_ion_current_loss_during_detachment).

30.09.2018



Kevin Verhaegh

# Preface

In this PhD thesis the physics behind detachment observations, particularly the ion target current roll-over, has been investigated experimentally on TCV. The key results of this work are shown in **Chapter 8**, where the ion current roll-over is associated with a reduction of the ion source due to power limitation —quantitatively consistent with SOLPS simulation results. Further implications of those findings are discussed in **Chapter 9**, where quantitative agreement is found between the observed detachment onset and analytic predictions of the detachment onset, after which charge exchange to ionisation ratios are observed to increase leading to volumetric momentum losses. A reduction of the upstream pressure during detachment is observed on TCV in agreement with analytic predictions of the target pressure loss required and the volumetric momentum loss estimated from charge exchange to ionisation ratios. Those two chapters form the most important and integral parts of this thesis.

To obtain these results, however, significant methodological work was required as is described in a fairly large part of this thesis —which is of secondary importance in this work. First a new diagnostic (divertor spectrometer) for the TCV tokamak has been developed, commissioned and operated as part of this thesis in Chapter 5. From the Balmer line spectra measured using this diagnostic, first the electron density has been estimated using existing Stark models, together with several technical advances and error quantification techniques in Chapter 6 to cope with the relatively low TCV densities ( $1 \times 10^{19} \text{ m}^{-3}$  to  $1 \times 10^{20} \text{ m}^{-3}$ ) leading to a relatively narrow Stark spectral broadening (full-width-half-maximum) compared to the instrumental function and expected Doppler broadening. Using the Stark inferred density and the Balmer line spectra, new ways for quantitatively analysing the Balmer line spectra have been established in Chapter 7 enabling the quantitative inference of various atomic reactions in the TCV divertor including ionisation, recombination and hydrogenic radiation.

For comparing the measured results to analytic models, a deeper analysis on the equivalence between thinking about detachment in terms of power limitation and thinking about detachment in terms of volumetric momentum loss was required. That required digging deeper into those models as has been done before in literature and making several modifications to the interpretation of such models. This has been done in Chapter 3 and is of secondary importance to the main results.

# Executive summary

Quantitative inferences of the magnitude and location of various atomic processes in the divertor, in particular the ionisation source, has been performed in this work. This has been facilitated by the new spectroscopic measurements of the TCV outer divertor plasma by a divertor spectrometer developed as part of this thesis. Those measurements are combined with a careful approach to Stark broadened line fitting (accounting for the relatively low TCV electron densities( $1 \times 10^{19} \text{ m}^{-3}$  to  $1 \times 10^{20} \text{ m}^{-3}$ )) and a new way of analysing Balmer lines developed in this work, enabling a full characterisation of the various power and particle sources and sinks (impurity radiation, ionisation and recombination) in the TCV outer divertor plasma. These new measurements provide an experimental verification that the ion source ( $I_i$ ) matches the ion target flux ( $I_t$ ) both before and during detachment while the recombination ion sink is relatively small or negligible and only develops to significant levels at the deepest detached states after the  $I_t$  roll-over. Volumetric recombination thus seems not to be a requirement for detachment. Instead, the current roll-over is caused by a reduction of the ionisation source.

We define the detachment threshold during density-ramp discharges as the point where the divertor ion source starts to deviate from its expected attached (linear) trend. That linear trend has been confirmed using measured upstream parameters in combination with analytic models (under which a Two Point Model which includes Recycling —‘2PMR’ [3, 4, 5, 6]). This is in contrast to the often-used degree of detachment scaling ( $\Gamma_t \propto n_e^2$ ) which requires modifications to account for upstream changes. During a core density ramp,  $P_{recl}$  continually drops due to increasing (intrinsic) divertor impurity radiation while the power required for ionisation ( $P_{ion}$ ) rises, both due to a rise in ionisation rate (in the attached phase) and a rise in the energy cost of each ionisation ( $E_{ion}$ ). The deviation of the ion target current with the attached trend is corresponds experimentally to  $P_{recl}$  approaching  $P_{ion}$ : ( $P_{recl} \sim 2 \times P_{ion}$ ); while the roll-over occurs closer to  $P_{recl} \sim P_{ion}$ . This indicates that  $P_{recl}$  limits the ion source and, through this, the target ion current. The start of detachment at  $P_{recl} \sim 2 \times P_{ion}$  occurs before any significant levels of recombination. All experimental results for the discharge investigated are shown to be in fair qualitative and quantitative agreement with recent TCV SOLPS simulations [7].

The behaviour of the target ion current ( $I_t$ ) before and during detachment was compared to simple analytic models. Accounting for only power and particle balance using measurements of  $P_{recl}$ , the energy cost of each ionization ( $E_{ion}$ ), and the target temperature ( $T_t$ ) lead to an  $I_t$  prediction in quantitative agreement with the measured  $I_t$ . It also shows that the ion source can be modelled as a trade-off between the maximum possible ion source ( $P_{recl}/E_{ion}$ ) and fraction of that power spent on ionisation ( $f_{ion}$ ), which can be modelled solely as function

of  $T_t/E_{ion}$  according to analytic theory —in quantitative agreement with direct measurements of  $f_{ion}$ . The modelled dependence of the fraction of  $f_{ion}$  on  $T_t/E_{ion}$  leads to a point, or threshold, where the ion current starts to rise slower than  $T_t^{-1/2}$  for decreasing  $T_t$ . Given the sheath target relation  $p_t \propto \Gamma_t T_t^{1/2}$ , this requires a target pressure drop. The thresholds at which target pressure loss needs to start to occur corresponds to  $T_t = E_{ion}/\gamma$ ,  $f_{ion} = 0.5$  and reaching, given a value for  $E_{ion}$  and  $q_{recl}$  a critical target pressure (or  $p_u/q_{recl}$  [6, 5]); which is the maximum target pressure achievable for given those variables. Quantitative agreement between all three criteria and the experimentally-determined detachment onset has been found.

It is striking that the temperatures ( $T_t < E_{ion}/\gamma$ ) at which target pressure loss must occur, according to analytic divertor models, corresponds to the temperatures at which volumetric momentum loss starts to occur, according to atomic/molecular reaction rates. Indeed, when reaching the detachment thresholds, measured charge exchange to ionisation ratios start to become elevated near the target, eventually reaching  $> 100$ . From those ratios through spectroscopic inferences, the amount of volumetric momentum loss has been estimated, which starts near the detachment threshold and reaches up to  $\sim 70\%$  during detachment —in agreement with direct experimental comparisons of the upstream/target pressure during similar discharges [8]. After reaching the detachment thresholds, the  $D\alpha$  emission starts to increase beyond atomic predictions, which is attributed to molecular reactions in quantitative agreement with SOLPS simulation results. That result is indicative of molecular activated recombination and suggest a significant presence of  $D_2$  radicals ( $D_2^+$ ), which could augment volumetric momentum loss through ion-molecule collisions, as is suggested by SOLPS simulations. Afterwards, at the deepest detached phases where the target temperature is reduced to  $\sim 1$  eV, significant volumetric recombination (although secondary to the ion source loss for TCV) can occur. ‘Power limitation’ of the divertor ion source thus seems to be a starting point and a necessity for detachment, subsequently bringing on other processes necessary or helpful for detachment (momentum loss and later volumetric recombination). This also appears to be applicable to higher power density, higher density tokamaks; although volumetric recombination will be stronger in such devices which may enable  $I_t$  to drop faster in the deepest detached states.

Our measurements show that both the target and upstream pressure roll-over concurrent with the  $I_t$  roll-over. Given a certain  $q_{recl}$  and  $E_{ion}$ , the target pressure is limited to a certain value ( $p_{t,max}$ ), which drops as  $q_{recl}$  drops and  $E_{ion}$  increases during detachment. The drop of this upper limit is the *minimum* amount of target pressure drop required during detachment, which must be consistent with the volumetric momentum loss present and the upstream pressure. Measurements of the upstream pressure and estimates of the maximum target pressure and volumetric momentum loss indicate that the observed upstream pressure drop/saturation and the amount of estimated volumetric momentum losses were *both necessary* to obtain consistency with the analytic model: both partially facilitated the target pressure drop. Reducing the target pressure can thus be more subtle than just having volumetric momentum losses. Nevertheless, these results neither confirm nor reject the idea that the drop in the target pressure could pull down the upstream pressure (as suggested in literature [6]) since the origin of the roll-over of the upstream pressure is unknown.

# Chapter 1

## Introduction

*Nuclear fusion may provide a solution to the looming energy crisis, as it may provide a nearly inexhaustible energy source with high energy density. One of the most successful nuclear fusion concepts so far is fusion through magnetic confinement in the form of 'tokamak' devices. In order to make tokamak fusion as an energy source a reality, many challenges must be faced. One key challenge in tokamak fusion is to tackle the extreme power exhaust of a fusion reactor which is predicted to reach levels higher than the surface of the sun for large scale facilities such as ITER, DEMO and beyond. A detached divertor is essential for reducing the heat flux to the target and is obtained at low target temperatures ( $\sim 5$  eV), which provokes a collection of atomic and molecular processes, ultimately resulting in a simultaneous decrease in target temperatures, target heat fluxes and target ion fluxes; all required for power exhaust handling. This work aims at improving the understanding of detachment by investigating the role of various atomic and molecular processes in the divertor by quantifying these processes through spectroscopic analysis.*

### 1.1 Energy sources and its future

Mankind's technical progress in the last 200 years has been massive, which has lead to an increased quality of life especially in the developed countries. Much of this technological progress has been initiated by the industrial revolution, which lead to exponential economic growth; tremendously changing living standards and improving social progress. Before the industrial revolution, economic output of an entity was limited by severe constraints set by the amount of land and other resources available. The industrial revolution and its economic growth has been made possible by using fossil fuels to lift these constraints. In turn, this has transformed the world's economy from a land-based economy into an energy-based economy [9] which has remained an energy-based economy until this date. As such, the gross domestic product per capita is correlated with the amount of power used per capita [10, 11]. Gross domestic product is again correlated with the quality of life of a country, measured by several metrics, including the social development index [12, 11]. The implication is clear: energy supply is vital for economic growth and the quality of life in the current day world. Since energy is most easily available from fossil fuels, the world has become strongly dependent to them.

Fossil fuels such as oil, coal and natural gas originate from fossilised plant materials.

Therefore, releasing their energy essentially implies releasing energy which has been generated from photosynthesis stockpiles over a geological time span. Mankind is burning through these fuel stockpiles at an alarming rate; a large fraction of fossil fuel resources, generated from stockpiles of millions of years, has already been used up in a relatively short time span of  $\sim$  200 years. It is estimated that the oil and gas reserves will last for  $\sim$  60 more years, whereas the coal reserve will last for  $\sim$  100 more years. These numbers are based estimates by the world energy council [13], where the current energy reserves have been divided by its yearly production.

Additionally, the usage of fossil fuels has negative impacts on the environment [14]. These range from the exhaust of particulates in the air to the exhaust of Greenhouse gasses such as carbon dioxide and nitrogen oxides. A deterioration of air quality due to these pollutants has already led to serious public health issues, related to a wide range of conditions including respiratory and cardiovascular diseases [15] as well as impeding paediatric development [16]; especially in urban areas. The existence of Greenhouse gasses has been linked to global warming, leading to global climate change [17] and a net rise in the earth's temperature. A net rise in the earth's temperature of more than a few degrees centigrade is expected to lead to irreversible effects to the environment and the melting of polar ice caps, which leads to major changes in the climate, floods and droughts in densely populated regions [17]. This, in turn, gives rise to a whole range of health concerns, including thermal stress and infectious diseases [18]. In order to prevent reaching this critical temperature rise, immediate action must be taken to keep the increase of the world's net temperature limited [17]. As a result, even if we would exhaust the fossil fuel reserves, this is unwanted as it could potentially trigger global catastrophes through global warming.

From this information, it is clear that the world needs to rehabilitate from its addiction to fossil fuels. This implies either/both transitioning from fossil-fuel based to more renewable (or nuclear) energy sources and/or a decrease of the amount of energy used. On a global scale, less than 10 % of all energy sources are currently generated through renewable energy sources [13] (less than 14 % when adding nuclear energy sources) and it is a major challenge to increase this to more substantial levels. As highlighted earlier, the increase in social development and quality of life is strongly correlated to the energy consumption. Decreasing the energy consumption (strongly) without impeding social development and quality of life is therefore a major challenge.

To complicate matters further, currently only a small fraction of the world's population lives in developed countries with a large energy availability; a large part of the world lives in 'energy poverty' [19, 20]. Developing countries are increasing their energy consumption per capita in order to improve quality of life and social development. In addition, also the population in developing and third world countries is increasing steadily while the population in the developed countries is saturating [21].

Increasing the amount of renewable energy sources, such as solar wind and tidal, is a possible solution to at least reducing the amount of fossil fuels used. Although energy sources such as solar, wind and tidal are promising, are already used and provide potential other benefits such as an energy independence to countries [22]; they do not come without drawbacks. One drawback is that such energy sources have a relatively low power (density) production [11].

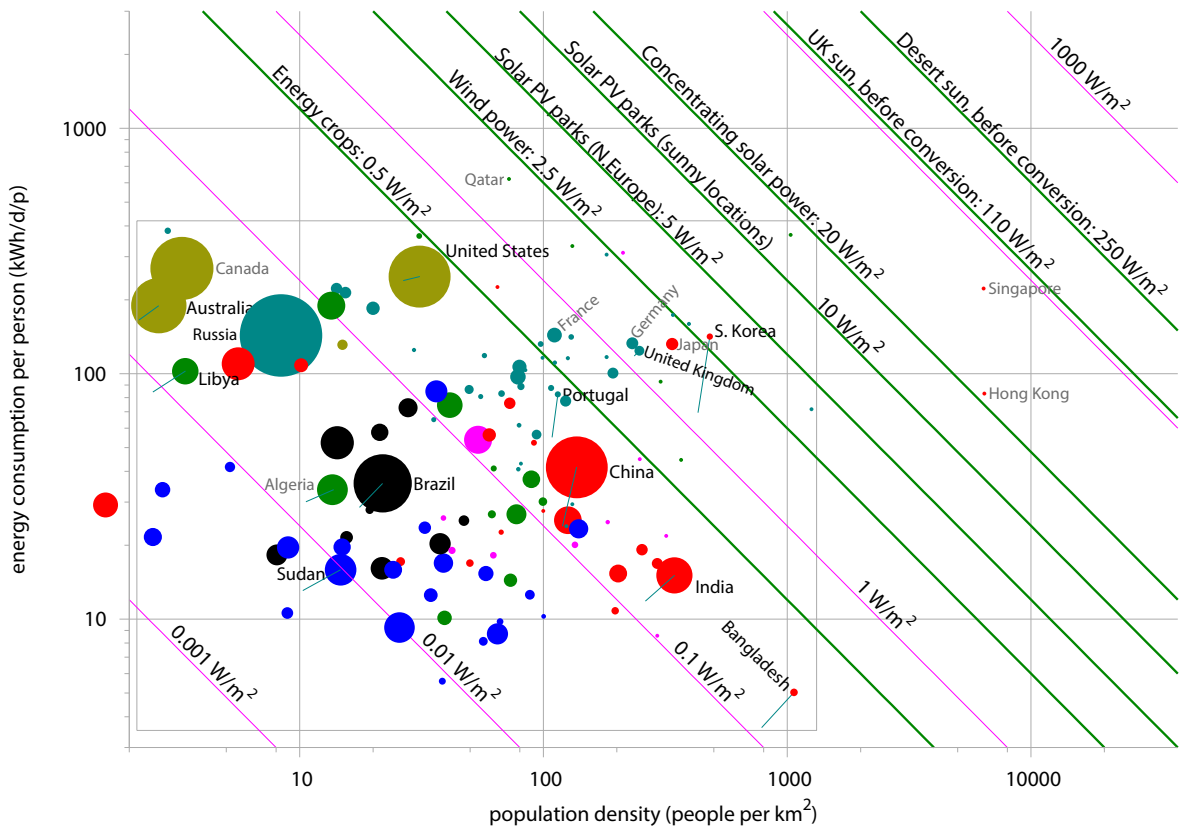


Figure 1.1: Power consumption per person versus population density, in 2005. Point size is proportional to land area. Both axes are logarithmic. The straight lines with slope -1 are contours of equal power consumption per unit area and as a reference, the energy densities generated using renewable technologies are shown. Adopted from [11, 23, 24].

As shown in figure 1.1, when considering renewables, solar panels have the highest power generation density.  $5 \text{ W m}^{-2}$  is the expected energy supply for a solar panel power park in Europe [11]. Although solar technology is still evolving, we assume this number as a reference number for energy generation through solar panels (and renewables more generally as solar panels tend to provide higher energy densities). This implies that although powering a country with renewables may be feasible, it will require country-sized energy installations [11]. For instance, as shown, most of the developed countries with high population densities, such as the United Kingdom, Germany, South Korea, require a power generation between  $1 \text{ W m}^{-2}$  to  $2.5 \text{ W m}^{-2}$ , meaning that if all of that power would need to be generated through solar photovoltaic (PV) parks with an average energy generation of  $5 \text{ W m}^{-2}$ , one would need to dedicate between 20-50 % of the country's surface to power generation; assuming these countries are fully energy dependent. A 'micro-country', such as Singapore and Hong Kong, instead requires a power generation density between  $20 \text{ W m}^{-2}$  to  $110 \text{ W m}^{-2}$ ; which is 4 to 22 times larger than the  $5 \text{ W m}^{-2}$  of power generation for a solar PV park quoted previously. Such countries thus cannot gain full energy independence through renewables and the amount of energy they can generate through renewables is severely limited by their available land.

Apart from this, other complications arise from renewable technologies. Their energy generation, for instance, can fluctuate depending on the conditions. Therefore, energy storage facilities are needed and preferably an inter-connected energy network over an entire continent is required where an excess of energy arising in one part due to an unexpected high number

of sun hours can be offset by an unexpected low number of sun hours at another position. Furthermore, renewables often require specific conditions and cannot be used anywhere, such as tidal and solar power providing more energy in sunnier areas.

Another energy source which could provide an alternative to fossil fuels is nuclear (fission-based) reactors. Although it requires uranium (ignoring thorium-based fission plants) which is supply-limited, it does provide  $CO_2$  free energy. The current total identified world's uranium resources are estimated to provide sufficient energy for over 100 years based on current requirements [13]. With thorium reactors, that number would increase greatly; however do note that thorium fission plants are still under development. Although the safety risks are small for nuclear plants [25] (e.g. it is estimated to be one of the safest energy sources when considering the 'deaths per unit of energy' metric —even lower than several renewable energy sources such as bio-fuels), when something goes wrong large-scale incidents can occur which require country-sized actions. In addition, nuclear fission power plants provide long-lived radioactive waste which must be stored for a long time (sometimes thousands of years) for it to lose its radioactivity, although some solutions to nuclear waste storage are in development [26, 27]. Due to these reasons, together with the difficulty of long-term storing long-lived nuclear waste, many European countries are moving away from fission power plants. Other disadvantages include that the capital cost/time it takes to construct nuclear power plants are relatively high, require a large amount of regulation. Nuclear proliferation is also considered a risk, especially when used in certain areas.

Nuclear fusion in theory could provide an energy source, which removes most of the disadvantages of nuclear fission: it is safe (no risk of meltdown); the energy source is abundant and easily obtained from sea water. Although fusion does produce radioactive waste, that radioactive waste is less long-lived compared to that of a nuclear fission power plant ([28, 29]). However, getting energy from nuclear fusion is technically challenging. Currently we have not been able to generate more energy from fusion than the energy we put in to sustain the reaction, where JET came the closest: 16 MW of fusion power, estimated from the measured neutron fluence, versus 25 MW of input power absorbed by the plasma [29]. Note that engineering efficiencies were not accounted for in this scientific result: the actual power input to the device is larger than 25 MW and no actual power was generated in the experiment. It should also be said that although fusion experiments have not resulted in a scientific energy gain; the problem is not that fusion does not occur —but rather that energy losses occur which are larger than the fusion energy gain such that additional heating must be injected. Going from this to a fusion power plant requires larger reactors and/or higher magnetic fields. Currently an international collaboration of Europe, the US, China, Japan, India, South-Korea and Russia is working together to build the largest fusion experiment ever conducted in France —ITER; which is planned to lead to a higher (scientific) fusion power than the injected power absorbed by the plasma. Although nuclear fusion power plants sound promising, it certainly needs more development before it will become a reality and it is not yet certain (in the sense that it is unproven) that fusion reactors which provide net energy can be built with current technology. In the case it seems infeasible to build fusion power plants, they could still be employed as a neutron source, which can for instance be used to treat nuclear waste [26, 27].

**Summary** — Evidently, the availability of energy sources is strongly linked with mankind's improvements in quality of life and social development. This is only available for a

relatively small fraction of the world's population and mostly through fossil fuels—which are both running out and which are polluting the environment, triggering global warming. At the same time, the energy demand by society increases as the world's population increases and as developing countries continue to develop.

Although there are alternative energy sources available, such as nuclear energy and renewables, each comes with a set of advantages and disadvantages. More specifically, although renewables are promising, they come with the drawbacks of having a low energy density, meaning that a solution, fully based on renewables, must be country-sized.

Fusion alleviates some drawbacks associated with fission and is sometimes in the press considered to be the 'holy grail' of energy generation. The problem, however, is that still a very significant amount of development and research is needed in order to realise fusion power plants. As quoted by Pierre-Gilles de Gennes, Nobel laureate in physics: 'We say that we will put the sun into a box. The idea is pretty. The problem is, we don't know how to make the box'.

## 1.2 Nuclear Fusion: a possible solution for the energy problem

When taking the mass of two protons and two neutrons separately; this is larger than the mass of an alpha particle which is made up of two protons and two neutrons. Using Einstein's  $E = mc^2$  relation, that means that an alpha particle has less rest mass-energy than the mass-energy of the nucleons separately. In other words; it releases energy to bind—also called binding energy, which changes as function of the nuclear structure. Nuclear energy, in general, is obtained by a transmutation reaction of one material to a different material with a higher binding energy. The difference between the two binding energies is thus released. When one plots the binding energy per nucleon, this is maximised at iron. That means that energy gain through nuclear reactions can occur two different ways: when the element is heavier than iron, one can go from a heavier element to a lighter element in a nuclear fission process. When the element is lighter than iron, one can merge two lighter elements to form a heavier element in a nuclear fusion process. Although both of these processes provide energy, as the slope for the lighter elements is steeper; a fusion process will provide more energy than a fission process. Additionally, the fusing lighter elements will not lead to radioactive products (but radioactive by-products exist due to neutron radiation), as opposed to splitting heavier elements.

The difficulty of fusion is how to make two particles fuse together in such a way that the fusion reaction provides more energy than the act of bringing the particles close enough together for fusion to occur. For fusion, two ions need to be fused together which have a strong electromagnetic force repelling them. If the particles are close enough, however, the strong nuclear force can take over, forcing the two particles to fuse together and provide net energy. The ions which can fuse together all have a fusion cross-section as function of energy. That cross-section can be transformed into a reaction rate coefficient, assuming a Maxwellian energy distribution associated with a temperature. Most of the fusion, however, occurs in the high energy tail of the Maxwellian distribution. The fuel mix which is the 'easiest' to fuse (high reaction rate at relatively low temperatures) is deuterium and tritium. This fusion reaction provides a fast neutron with 14.1 MeV of energy, whose energy can be partially collected in the form of fusion energy, and a high energy helium ion (alpha particle)

which carries 3.5 MeV of energy. Although this fuel mix is the 'easiest' to fuse, it requires high plasma temperatures of 10 keV to 100 keV which correspond to between 0.1 to 1 billion Kelvin.

However, although heating a plasma to such temperatures is sufficient for fusion to occur; it is insufficient for obtaining net energy from fusion as collisions between charged particles also lead to energy losses. As a deflection collision between two charged particles is more likely than a fusion collision, the fusion energy gain is generally insufficient for sustaining the plasma's energy losses unless the fusion fuel is 'held together' (or confined) somehow [29, 28].

When taking a very simplistic approach, a criterion for the minimum 'confinement' of the plasma for net energy generation (e.g. the 'Lawson criteria') can be established [30, 31]. To obtain a relation for the Lawson criterion, first we must provide an equation for the fusion power generated by a slab of plasma. This equals the volume of the plasma slab times the fusion reaction rate, times the density of deuterium, times the density of tritium and times the energy generated by a single fusion reaction  $E_{fusion}$ :  $P_{fusion} = V n_{DNT} \langle \sigma v \rangle E_{fusion}$ . When we investigate the reaction rate of DT for fusion, through a Taylor expansion in the region where fusion is dominant,  $\langle \sigma \rangle \sim T^2$ , resulting in the relation  $P_{fusion} \sim V n_{DNT} T^2$ . Furthermore, assuming that there is a mix of 50 % deuterium and 50 % tritium, then  $n_D = n_T = 1/2n$ , where  $n$  is the electron density (assuming a pure plasma). Accounting for this, the fusion power relation changes into  $P_{fusion} \sim V n^2 T^2$ . Apart from a relation for the fusion power, a relation for the power losses is needed —which depends on the rate at which the system loses energy to its environment —also referred to as 'confinement'. We define this energy 'confinement' through an energy confinement time  $\tau_e$ , which is defined as the ratio between the plasma energy  $W$  and the total heating power  $P_{in}$ , which is the power 'lost' when considering a fusion power plant [30]. In other words  $P_{in} = \frac{W}{\tau_e}$ . The plasma internal energy, assuming that the electron temperature equals the ion temperature (e.g.  $T_e = T_i = T$ ), equals  $W = 3VnTk_b$ , where  $k_b$  is the Boltzmann constant. The inequality  $P_{fusion} \geq P_{in}$ , thus results in  $nT\tau_e \geq C$ , where  $C$  is a constant and  $nT\tau_e$  is the triple product. Thus, for net fusion power generation the triple product  $nT\tau_e$  must exceed a certain critical value.

There are various nuclear fusion schemes which try to achieve this. Generally, these can be divided in two different roots: inertial confinement fusion and magnetic confinement fusion. Inertial confinement aims at increasing the pressure  $nT$  as much as possible while only using the target's inertia for confinement, resulting in relatively small  $\tau_e$ . This is for instance accomplished by using very powerful lasers, such as at the National Ignition Facility —NIF where laser pulses with a power of 500 TW and energy of 1.8 MJ are used to compress a small (sub-mm) pellet of fusion fuel consisting of a deuterium-tritium mix [29]. Alternative techniques utilise a magnetic field in order to confine the ionised plasma fuel in a 'magnetic cage', which leads to much larger energy confinement times and thus a more modest plasma pressure  $nT$  is required to achieve fusion conditions. Although neither of these two techniques have achieved conditions where the fusion power generated is larger than the power used, so far magnetic confinement fusion has proved to be one of the more promising routes. In this work we will only discuss magnetic confinement fusion.

### 1.3 Confining the plasma: tokamaks

In order for magnetic confinement fusion to work, a magnetic structure has to be implemented in which the fusion ions and energy is confined for a relatively long time. There are several ideas on how this can be achieved. Earlier works often focused on magnetic mirror devices: linear devices with coils at each end, which partially confines the ions. However, at the ends of magnetic mirror, one still loses particles and energy. To get rid of these end losses, both ends of the magnetic mirror have to be connected to each other, leading to a toroidal shape. Ions can be confined in such a toroidal shape using a helical magnetic field line structure.

There are roughly two ways of achieving such a helical field line structure. Stellarators aim at using unconventional coil shapes in order to generate such a helical magnetic field structure, while tokamaks use more conventional, simpler, coils to generate a toroidal magnetic field, while inducing a current in the plasma which leads to the generation of a poloidal magnetic field. Both fields added together provide the helical magnetic field structure. See figure 1.2 for a schematic overview between the two concepts. Inducing a current in the plasma has the advantage that simpler coil designs can be used while the current in the plasma also leads to plasma heating. However, its disadvantages are that such currents can lead to plasma instabilities (which can lead to performance loss or lead to an untimely end of the plasma discharge—disruptions) and that the nature of such discharges are pulsed as a transformer loop is used to generate this current. Most of the magnetic confinement research is aimed at tokamaks, which are generally easier to construct (due to their simpler coil shape) and have generally higher performance than stellarators. Recently however, a new stellarator experiment Wendelstein 7X started, which aims to provide more optimised performance levels for stellarators.

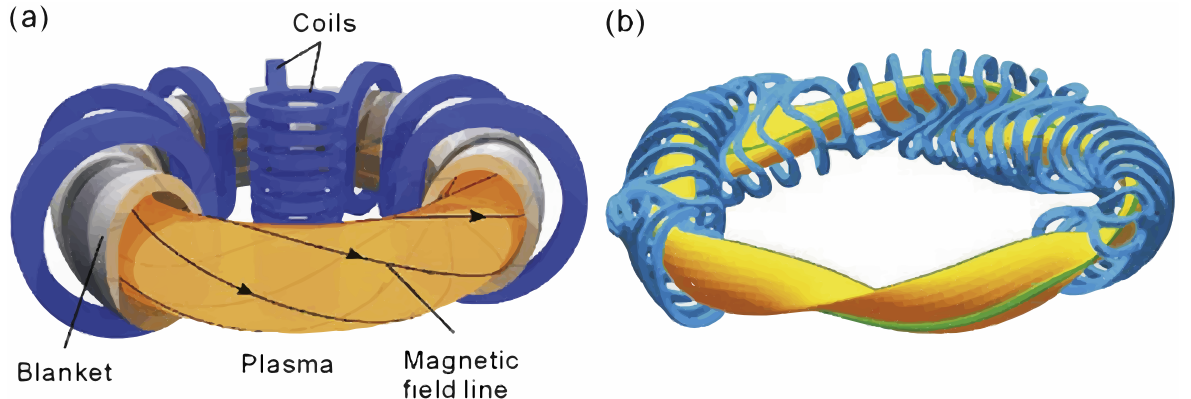


Figure 1.2: Schematic overview of a tokamak a) and a stellarator b) adopted from [32].

The rest of this work will be focussing on tokamaks. The various components of a large scale tokamak, like ITER, are highlighted in figure 1.3. Important here to note is that a tokamak contains various subsystems apart from its magnetic field. The basic tokamak components listed in figure 1.3, such as a vacuum vessel, the inner solenoid to generate a plasma current through the tokamak through a transformer action, poloidal field coils to shape the toroidal magnetic field; first wall; divertor; external heating as Ohmic heating alone is insufficient to reach reactor-relevant conditions (through neutral beams - NBI and RF heating such as ECRH, ICRH and hybrid heating) and diagnostic access. A large collection of various diagnostics is required for fusion experiments which measure various different aspects of the

fusion plasma, including basic parameters such as electron density, electron temperature and wall heat fluxes. In addition, some ITER (or fusion power plant) specific components are also shown in figure 1.3, such as the cryostat (only required for fusion devices with superconducting magnets) and tritium breeding blankets (test modules used in ITER to try and use the fusion neutrons in order to generate tritium, required for the fusion reaction, from lithium).

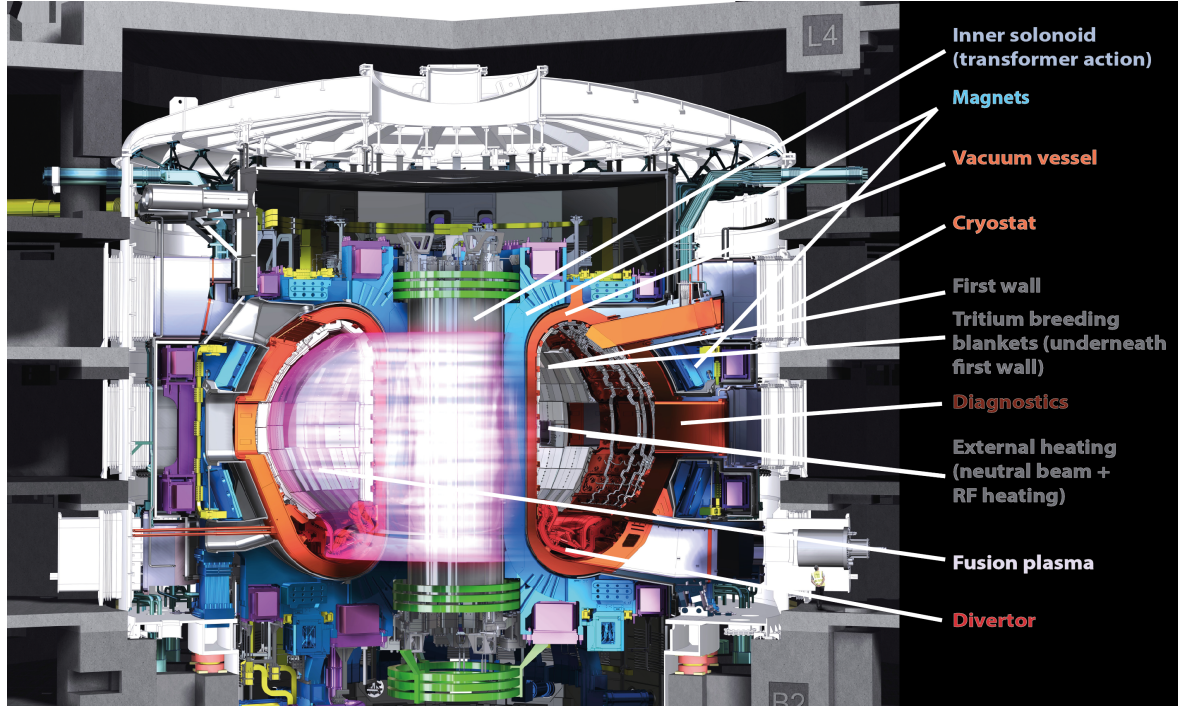


Figure 1.3: Overview of ITER and its various components. Courtesy of the ITER organisation, file obtained from <https://www.iter.org/album/Media/7%20-%20Technical>. With manually added labels.

## 1.4 The power exhaust challenge: divertors

Although the idea of a magnetic cage is to confine the plasma, this confinement is not perfect and the net power in the core of the plasma will eventually 'leak' out of the core into the edge (or Scrape-Off-Layer —SOL). Assuming a toroidal plasma, this heat will be spread over everywhere where the edge of the circular plasma gets close to the vessel walls. This will heat up the vessel wall material while the plasma temperature and particle flux to the wall gives rise to sputtering leading to impurities being injected into the core of the plasma. These impurities will radiate, leading to a loss of power in the core, lowering the core performance, and in the worst case resulting in an untimely end of the plasma ('disruption') due to a radiative collapse of the plasma. Disruptions could cause serious damage to the machine in future tokamaks such as ITER and beyond. Furthermore, although it may seem that this spreads the heat evenly over the vessel surfaces, when one considers that vessel components have an engineering tolerance on their alignment, tiles can be misaligned in such a way that they will receive much larger heat fluxes than expected for a perfectly aligned tile, causing melting.

To improve core performance through reduced impurity levels and better manage plasma-

wall interaction, the concept of the divertor was developed [33, 3]. A divertor uses the magnetic field to 'divert' the heat and plasma leaking out of the core to a separate region: 'the divertor'. Making such a divertor only requires one to create a magnetic null region in the plasma, which is referred to as the 'x-point'. Essentially, having a 'divertor' only refers to having a magnetic null in the plasma. However, different tokamaks have different style divertors and there are tokamak with so called 'closed-divertors' where neutrals are confined in the divertor region. One way of achieving this is by installing baffles which physically separate the divertor region from the tokamak's core [34]. The higher confinement of neutrals in the divertor region gives rise to a large neutral compression. The increased neutral content in the divertor is believed to be beneficial for divertor performance [35]. Furthermore, having a closed divertor is supposed to help keep the impurities in the divertor region. In that way, the impurity radiation will occur in the divertor, where one wants radiative power dissipation, rather than in the core where it leads to a deterioration of divertor performance. Divertors where such a structure is not present are 'open divertors', which have the advantage of improved diagnostic access and improved flexibility in terms of plasma shaping [34]. An overview of the limiter and divertor configurations and the various components have been shown in figure 1.4 as a reference.

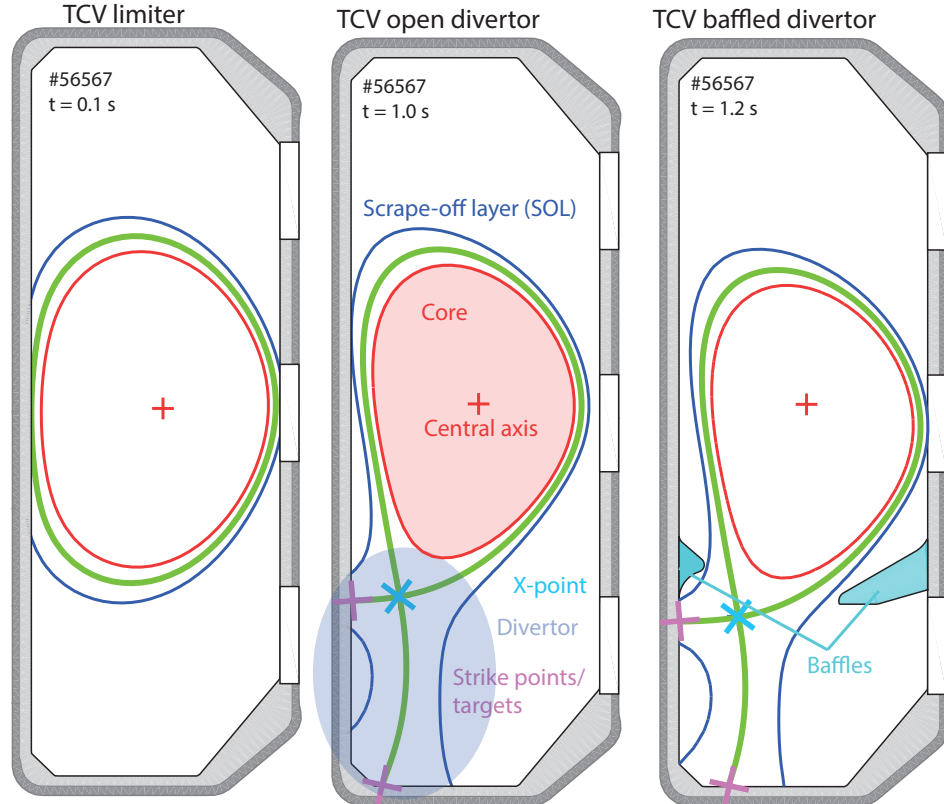


Figure 1.4: Overview of the limiter and divertor configuration on TCV, together with the planned baffle upgrade [34]. The equilibria have been taken from an experiment performed on TCV.

To consider the power exhaust challenge for future devices such as ITER and beyond, first we will evaluate the expected unmitigated heat flux for ITER. Assuming high performance operation with a burning plasma in ITER, the net power crossing the magnetic separatrix and entering the SOL is expected to be around 100 MW after accounting for radiative losses in the core [36]. Since the ratio between radial and perpendicular transport in the scrape-off-layer

(SOL) is very low, the outer layer of the plasma has a very small width compared to the tokamak major radius. The predictions of the scrape-off-layer width for ITER are  $\sim 2$  mm and at most 5 mm at the outside mid-plane [37, 38, 39, 40] while the major radius of ITER is over 6 m. This means that the power crossing the separatrix would have to be exhausted in a surface of at most  $0.4 \text{ m}^2$  at the target (when combining both strike point regions), resulting in expected unmitigated heat fluxes of  $0.5 \text{ GW m}^{-2}$  —much higher than the engineering limits of  $10 \text{ MW m}^{-2}$  for the tungsten tiles of the ITER divertor [36, 41, 3, 42, 43]. Therefore, a strong reduction of the heat flux is necessary to handle power exhaust in future fusion devices. On top of that heat flux reduction, target temperatures below 10 eV and a reduction of the ions reaching the target is required for handling the ITER power exhaust to limit sputtering of target components. The upstream temperatures on ITER are however expected to reach values of the order 160 eV according to modelling [44].

To tame this divertor power exhaust, several strategies are possible. First, by tweaking the angle of the strike point on the plasma surface, the effective wetted area can be increased. Due to engineering tolerances however, there is a maximum angle which can be used as otherwise a misalignment of a certain tile would lead to melting. Accounting for this (e.g. an angle of 2-3 degrees), the effective wetted area can be increased from the quoted  $0.4 \text{ m}^2$  to  $3.5 \text{ m}^2$  [45, 36, 42], resulting in almost a factor 10 reduction in target heat flux.

At low divertor densities and unmitigated power deposition (e.g. low impurity radiation fractions) the temperature profile along the field line in the divertor can be roughly constant and the only thing limiting the possible target temperatures (and thus upstream temperatures) in this situation is the plasma sheath —which always builds up when plasma is in contact with matter —e.g. ‘sheath-limited conditions’. When increasing the density, depending on the magnitude of the heat flux going towards the divertor, the conductivity of the heat flux is lowered, which can give rise to a temperature reduction accompanied by a density increase near the target and a decoupling between the target and upstream temperature. In such conditions, the plasma operation is limited by conduction: ‘conduction-limited’ conditions. The ITER upstream temperature of the order 160 eV ([44]) is based on conduction-limited conditions and would be larger at sheath-limited conditions. However, the temperature at the target cannot be decreased indefinitely through this action as that would require an indefinite increase in the upstream density. The upstream density is however correlated to the core density [3] and as there is an operational, plasma physics limit to how high the core density can be driven —e.g. the ‘Greenwald limit’ [46]; there is a limit to how high the upstream density can be driven and thus a limit on how much conduction alone can drive down the target temperature. That said, for a sufficiently high power crossing the separatrix, it may not be possible to reach a conduction-limited regime without volumetric power removal. In addition, it should be noted that conduction —by itself and assuming that ionisation does not require any energy cost - does not reduce the heat flux going to the target.

Further reductions of the heat flux must be performed by dissipating the power through volumetric radiation and charge power losses. For ITER, 60 to 70 % of the power arriving in the divertor must be dissipated this way to make steady-state power handling possible [36]. Intrinsic impurities in the divertor can also lead to strong power dissipation, which can be sufficient for tokamaks with carbon walls and lower power entering the divertor (for TCV conditions —for instance) but is insufficient for tokamaks such as ITER and beyond. For such

tokamaks, radiative losses need to be likely provoked by seeding impurities. The volumetric radiation spreads the divertor heat flux over a larger surface, reduces the plasma's heat flux and facilitates a further reduction of target temperatures. Considering parameters for ITER and beyond, such a power removal mechanism is also likely necessary for reducing the target temperatures significantly with respect to the upstream temperature.

## 1.5 Taming the power exhaust: detachment

Power removal and density increases are however, by themselves, generally do not reduce the ion target flux. Instead, reducing target heat flux, target temperature and target ion flux simultaneously can be achieved by operating the divertor in a *detached state: detachment*. Detachment (or partial detachment) will be paramount for operation of ITER and beyond [3, 35, 36, 47]. Detachment generally implies a simultaneous reduction of target temperatures, target heat fluxes and target ion fluxes.

The state of detachment is generally entered when the target temperature drops below a threshold value of  $\sim 5$  eV. When the target temperature reaches such low values, a relatively large amount of power entering the ionisation region is spent on the ionisation process. On top of that, various atomic processes start to become more dominant in such temperature regimes. Temperatures below 2 eV, for instance, give rise to volumetric recombination which removes ions from the plasma before they can reach the wall. At low temperatures ( $\leq 5$  eV) charge exchange also starts to dominate over ionisation, leading to a power loss mechanism as neutrals carry heat to the walls and leading to momentum losses. Such momentum losses result in a pressure drop along the field lines, which has often been associated with detachment.

One of the difficulties of detachment is that it generally lacks a precise definition. Instead, there are several features associated with detachment which are generally monitored using an array of different diagnostics. However, all detachment observations are linked to the low temperatures ( $< 5$  eV) required during detachment near the target.

Due to the various aspects of detachment, a large array of various diagnostics is used to measure parts of the detachment process. This includes Langmuir probes for measuring target ion current; heat flux measurements through infra-red cameras for measuring target power deposition; bolometry for measuring radiated power and spectroscopic measurements of the divertor for measuring emissions associated with various atomic processes in the divertor; for instance recombinative emission associated with recombination. Instead of measuring emissions associated with atomic processes in the divertor, spectroscopic measurements can also be used for estimating the electron densities and temperatures.

## 1.6 Detachment: an in-depth overview, its gaps in knowledge and the relevance of this work

Parts of this section have been adopted from: *An improved understanding of the roles of atomic processes and power balance in target ion current loss during detachment*, by K.

Verhaegh, B. Lipschultz, B.P. Duval, et al., to be submitted. DOI:

<https://doi.org/10.13140/RG.2.2.24292.48005/1>

As discussed, divertor detachment is predicted to be of paramount importance in handling the power exhaust of future fusion devices such as ITER and limits the target power by reducing the target temperature  $T_t$  and ion target flux  $\Gamma_t$  simultaneously. However, before detachment is entered, as explained, it is preceded by the heat flux along the field lines being conduction limited, which allows a temperature (density) gradient to form along the field lines while the total pressure remains roughly constant. Therefore, as the target temperature drops for such attached conditions ( $p_t$  constant), there is a strong rise in  $\Gamma_t$  (equation 1.1). This means that, even if target heat fluxes and target temperatures are reduced, a target pressure drop is required for reducing  $\Gamma_t$ . Detachment is thus inextricably linked to a reduction of target pressure  $p_t$ , according to sheath target conditions (equation 1.1):  $p_t$  must drop faster than  $T_t^{1/2}$  for  $\Gamma_t$  to drop. In addition to  $p_t$ , in most realistic conditions, also power removal is a necessary ingredient for a simultaneous drop of  $\Gamma_t$  and  $T_t$ .

$$\Gamma_t \propto p_t/T_t^{1/2} \quad (1.1)$$

Important to note is that a drop  $p_t$ , does not per se necessitate momentum losses along the field lines. In the absence of momentum losses the upstream pressure,  $p_u$ , would need to drop during the ion current roll-over. One could imagine, for instance, a case where the pressure is constant along a flux tube, but due to changes in the core plasma the pressure all along the flux tube is reduced. Such a degradation of the upstream pressure is likely to be avoided for a reactor-relevant divertor solution, which requires  $p_u > p_t$  and thus volumetric momentum loss.

Target-current roll-over is often taken to be the definition of detachment, although sometimes it is defined differently, such as  $T_t$  being less than some specified value (5-10 eV, e.g. [4, 48]). Therefore, in addition to playing a central role in the control of target heat flux,  $I_t$  is experimentally important as a marker for the occurrence of detachment; it is the most accurately and easily measured detachment indicator in most tokamaks (using Langmuir probes) compared to others like  $p_t$  and  $T_t$ . Because of the above points, experimentally studying the role of the various processes of momentum, power and particle loss leading to the drop in  $\Gamma_t$  during detachment is thus an important area of research. More detailed information from experiments will provide a better basis for (de)validation of our current models of divertor plasma characteristics.

The loss of  $\Gamma_t$  during detachment is often described from a viewpoint that emphasises pressure drop along the field lines [33, 3, 4]. Pressure drop is usually attributed to the dominance of ion-neutral reactions (e.g. charge exchange and ion-molecule [4, 49, 50]) over ionisation reactions at low temperatures ( $T_e \leq 5 - 10$  eV [3]). Such studies note that the reduction of  $\Gamma_t$  requires both parallel power loss and pressure loss.

Some researchers have also described the loss of  $\Gamma_t$  from a viewpoint that emphasises power and particle balance [51, 5, 6, 52, 53]. In such models the divertor region is assumed to be 'self-contained' in the sense that the target ion flux is dominated by the sum of ion sources in the divertor (ionisation) minus the sum of ion sinks (recombination) [51, 5, 52]. We define this as high recycling conditions [5, 6] in this work. This simplification ignores the ion flux into the divertor from upstream along a flux tube and any cross-field transport of particles (and momentum). Both the decrease in divertor ion source and increase in ion sink can play an important role. Those studies maintain that momentum loss, for instance through ion-neutral

collisions, does not directly lead to a loss of  $\Gamma_t$  [5, 52, 47] but may facilitate conditions where this occurs. This momentum loss is a consequence of a reduction in power flow to the target lowering  $T_t$  and thus creating the conditions for momentum loss.

While viewing target ion current roll-over during detachment alternatively through the viewpoints of pressure loss or as a competition between ion sources (ionisation) and sinks (recombination) may appear to describe detachment differently, they are, in fact, not mutually exclusive and all cited processes can/will occur [4, 3, 5]. In this thesis we show that both power loss (in fact power-limitation of the ion source) and target pressure loss is required for detachment —consistent with equation 1.1, while volumetric momentum loss is required to find a consistent solution between the analytical model (based on equation 1.1 combined with power/particle balance) and experimental observations of the upstream pressure.

Apart from power/particle balance playing a key role in the ionisation and thus ion target flux, often the role of volumetric recombination is predicted to play a key role in target ion flux reduction [54, 55, 56, 57, 58, 59]. The existence of recombination has been confirmed experimentally [51, 60, 61, 62, 63, 64, 65] and is often found, through quantitative analysis to be significant in the reduction of the ion target flux [51, 60, 61, 62, 63, 64, 65, 66]. However, in current work at TCV [1], the volumetric recombination rate is shown, as part of this thesis, to be only a small fraction of the reduction of ion flux, which is in agreement with recent TCV simulations [7], but in contrast with earlier TCV simulations [58]. Earlier studies of detachment in C-Mod [51, 60, 63, 66] and ASDEX-Upgrade [64] (both higher density than TCV) show a range of contributions of recombination to target ion current loss from important to small/negligible (e.g.  $N_2$ -seeded discharges in C-Mod [51]).

The ion target flux  $\Gamma_t$ , which in steady-state (and negligible recombination) equals the ionization rate  $\Gamma_i$ , must be compatible with the amount of power flowing into the ionisation (or recycling) region, here termed  $q_{recl}$ ; and the amount of power reaching the target in the form of kinetic energy  $\Gamma_t\gamma T_t$ . Important here is that ionisation 'costs' a certain amount of energy; namely  $E_{ion}$  per ionisation. This amount of energy consists out of two parts: one part depicting the amount of radiative energy losses occurring during the excitation collisions preceding detachment (which is strongly temperature dependent) and one part depicting the amount of potential energy required to transform a neutral hydrogen atom into a hydrogen ion, which is 13.6 eV not accounting for molecular effects. Under these assumptions, equation 1.2 [51, 5, 6, 52] arises from power balance (e.g.  $q_{recl} = \Gamma_i E_{ion} + \Gamma_t \gamma T_t$ ) and particle balance (e.g.  $\Gamma_t = \Gamma_i$  —where the closed box approximation was used and recombination is assumed to be negligible).

$$\Gamma_t = \frac{q_{recl}}{E_{ion} + \gamma T_t} \quad (1.2)$$

Imagining a case where  $\gamma T_t \ll E_{ion}$  (putting in realistic numbers of  $\gamma = 7$  and  $E_{ion} = 35$  eV, this leads to  $T_t \ll 5$  eV), that means that  $\Gamma_t \sim \frac{q_{recl}}{E_{ion}}$ ; in other words, the amount of ionisation is limited for such a case through the amount of power flowing into the recycling region and the energy cost per ionisation; which all in turn limit the ion target flux. Naturally, equations 1.2 and 1.1 need to be satisfied simultaneously; meaning that such a case of 'power limitation' of the ionisation source must be paired with a reduction of target pressure.

Therefore, as an alternative to reducing  $I_t$  through volumetric recombination, both simplified models as equation 1.2 (or variations thereupon), which were employed on experimental

data [51], and SOLPS simulations [52, 67, 68, 7] show the ion source in the divertor itself can be reduced through a lack of sufficient power flowing into the ionisation region: a form of ‘power limitation’. As such a reduction of  $I_t$  also requires target pressure loss, if one were to assume that  $p_u$  is constant and unaffected by the divertor, this would require volumetric momentum loss [3, 4]. Other references, however, argue that  $p_u$  can be influenced by the divertor and it is indeed in this work observed that during a density ramp  $p_u$  rolls-over when the divertor enters detachment [5, 5, 52, 53]. These references also argue that momentum losses may play a role in maintaining a high  $p_u$  during detachment.

Power limitation of the ionisation source is facilitated by both a reduction in  $q_{recl}$  and an increase in  $E_{ion}$ . Although  $E_{ion}$  is a strong function of electron temperature [3, 69], generally it is assumed to be constant [51, 5, 6, 3, 4]. A reduction in the  $q_{recl}$  could be realised through either increasing impurity radiation inside the divertor (shown in this thesis) or by reducing the power flowing into the SOL [45] —which was achieved through neon seeding on TCV. Power starving the ion source can be as important as recombination in target ion current loss, if not the primary process [51]. Although experimental indications for such a process are available (either from ‘inferred ion sources’ [51]), or from qualitative spectroscopic ‘indicators’ based on  $D\alpha$  [70]), one weakness of previous results is that this hypothesized reduction of the ion source during detachment has not been measured quantitatively. However, the work in this thesis and other recent studies are providing more information on ionisation during divertor detachment [1, 71, 72].

## 1.7 Goals and objectives of this thesis

The main objective of my thesis is to investigate the atomic and molecular physics processes, which are crucial during detachment and are the basis to detachment, experimentally and quantitatively in order to explain the observation of the various detachment quantifiers, such as a target power reduction, temperature reduction and most importantly the integrated ion current ( $I_t$ ) roll-over. For that purpose, a new divertor spectrometer for TCV (section 4) has been developed, commissioned and operated as part of this thesis (chapter 5). Using existing Stark line shape models, electron densities have been inferred from the Stark broadened Balmer lines in TCV (chapter 6). Despite Stark broadening analysis being routinely used on higher density devices (C-Mod [51, 66]; ASDEX-Upgrade [73]; JET [74], NSTX [75], MAST [76] and W7-AS [77]), this is particularly challenging for TCV conditions due to the modest electron densities on TCV ( $1 \times 10^{19} \text{ m}^{-3}$  to  $1 \times 10^{20} \text{ m}^{-3}$ ). New techniques (chapter 6) have been developed to cope with this, such as an accurate accounting of the instrumental function and its uncertainty; application of weighting functions in the fit to emphasise the Stark wings and combining Stark analysis with Monte Carlo fit techniques for including uncertainties. Novel analysis techniques for the Balmer line series have been developed, which are applied after obtaining a density estimation, based on first quantitatively separating the excitation and recombination contributions to the Balmer line’s emission, after which these contributions are used to quantitatively extract ionisation rates, recombination rates, hydrogenic radiation, charge exchange to ionisation ratios and electron temperatures (chapter 7) using a Monte Carlo approach for an accurate accounting of the uncertainties.

Using this methodology (chapters 5, 6, 7), quantitative analysis of the various atomic

physics processes in the divertor has been made possible. Those inferences are used in order to investigate the main objective of this work; namely experimentally and quantitatively investigating the role of the various atomic/molecular physics processes play during detachment and how they are related to the various detachment observations, most importantly the ion current ( $I_t$ ) roll-over. Those main results of this work are presented in chapter 8 including an in-depth comparison between spectroscopic inferences, other diagnostic and SOLPS modelling results. Main achievements and conclusions related to this objective are:

- The ion target flux measured on TCV matches the measured ionisation source in both attached and detached conditions, providing proof that the open TCV divertor is in high recycling conditions and the closed-box approximation (e.g. the ion target current equals the total ionisation source minus the total ionisation sink) can be applied.
- The roll-over of the ion target flux is due to a reduction of the ionisation source, rather than volumetric recombination which has generally (especially during seeding and low density operation) a much smaller influence. In addition to the magnitudes, the timing in this is crucial: a flattening and roll-over of the ion current occurs first related to a limitation/reduction of the ionisation source; volumetric recombination can only start to become more dominant at the strongest detached phases when the target temperature is further decreased. The divertor electron density plays a key role in the magnitude of volumetric recombination during detachment, which is largely determined by the upstream density. The maximum obtainable upstream density is determined by the plasma current through the Greenwald limit.
- The roll-over of the divertor ion source is concurrent with a movement of the peak in ionisation along the divertor leg from near the divertor target towards the x-point. The charge exchange to ionisation ratio increases in the region where the divertor ion source has decreased, likely resulting in momentum losses. In a smaller region (up to 15 cm) volumetric recombination appears while its peak remains at/near the target (within 5 cm). A roll-over of the electron density near the target in a yet smaller region (within 5 cm) is observed.
- The amount of ionisation is consistent with the amount of power entering the recycling region. This quantitative information provides (qualitative) proof that the ionisation during detachment is limited by the amount of power entering this region and by the ionisation energy cost. Both of these processes seems to lead to the ion current reduction.
- Measured  $D\alpha$  brightnesses are consistently higher than predictions of  $D\alpha$  using atomic reactions, especially during detachment where the measured  $D\alpha$  becomes up to 7 times as bright as the atomic predicted  $D\alpha$ . This is consistent with/indicative of the presence of molecular reactions, particularly Molecular Activated Recombination (MAR). As MAR involves molecular charge exchange; this also suggests the presence of molecular charge exchange reactions in the divertor, which may give rise to momentum losses [49, 4, 50].

A secondary goal of this thesis is to compare this understanding with advanced divertor modelling such as SOLPS, for validation of divertor models. Using the improved Balmer

line analysis techniques developed in this work, 1D profiles in the divertor of various atomic reactions are obtained, which have not been previously obtained in literature. This excess of information provides more information along the divertor leg which can be compared with modelling results. To perform the closest comparison possible between the SOLPS modelling and the experimental observations, a suite of various synthetic diagnostics have been developed (sections 4.3, 5.8). The main result here is that a fair quantitative and qualitative comparison between SOLPS and the experiment has been shown (section 8.1.1). In addition, a fair agreement between the SOLPS predicted total  $D\alpha$  emission and the measured  $D\alpha$  emission has been shown; together with the agreement between the SOLPS predicted atomic  $D\alpha$  emission and the experimentally inferred atomic part of the  $D\alpha$  emission; thus suggesting that the molecular emission of  $D\alpha$  has been correctly predicted by SOLPS providing confidence that the SOLPS predicted molecular reactions indeed correspond to the experimental reactions (section 8.4). Furthermore, using synthetic diagnostic approaches, the newly developed spectroscopic analysis techniques have been validated and a good agreement between the data inferred from a synthetic diagnostic and the actual rates in the divertor in the SOLPS model have been obtained (section 7.7).

Another primary goal of this work is to use these new measurements in combination with analytic models in order to both investigate how such models agree (or disagree) with the experiment and to gain a better understanding of the key points leading to detachment (chapter 9). Such analytic models (chapter 3) are based on power/particle balance as well as power/particle/momentum balance, which accounts for the influence of ionisation on the particle and power balance accurately, while the often-used standard two point model does not account for this. Furthermore, the analytic models are analysed in this work in greater detail than in literature (chapter 3), providing more information about the implication of such models and forming a bridge between thinking about detachment in terms of power limitation [5, 6] or in terms of momentum losses [3, 4].

- One striking observation from the analytical model is that, based on divertor physics, one would expect target pressure loss to start when  $T_t \approx E_{ion}/\gamma$ , which occurs around 4-6 eV. This is exactly the temperature range in which the molecular and atomic processes are such that one would expect the development of volumetric momentum loss (either from charge exchange dominating over ionisation or from molecular processes) to start to occur. In this work it is shown that these two points indeed occur simultaneously for the experiments analysed.
- Analytical model predictions of  $I_t$  (e.g. integrated ion target flux) based on power-/particle balance and power/particle/momentum balance are in agreement with the measured  $I_t$  quantitatively and qualitatively, respectively. That investigation also correctly models the TCV observation that  $I_t \propto \bar{n}_e$ , which is in contrast to the  $I_t \propto \bar{n}_e^2$  scaling expected/observed on other tokamaks. A careful analysis shows that changes in upstream conditions apart from the density (e.g. upstream temperature, likely related to a combination of a fixed  $P_{sep}$  with a widening of the SOL width), as well as changes in divertor radiation, can influence this scaling during a density ramp. This combined with ionisation source measurements also shows that the TCV  $I_t \propto \bar{n}_e$  observation does not imply that TCV is in low recycling conditions.

- An analytical model of power/particle balance predict  $I_i$  in agreement with the measurement, based on only the power entering the recycling region, the target temperature and the energy needed per ionisation event. This shows again, but more quantitatively, that the ion source is consistent with the amount of power available for ionisation. Furthermore, operationally, this shows that knowing the target temperature (or knowing that the target temperature is small) enables one to predict the divertor ion target flux using only power/particle balance (as given by equation 1.2). To include the behaviour of the target temperature, one needs to include momentum balance in the analytical model, however.
- During 'deep' detachment, where most of the power entering the recycling region being spent on ionisation, both a reduction of the power entering the recycling region and an increase in the measured energy cost per ionisation ( $E_{ion}$ ), which in literature is often assumed to be constant [51, 5, 6, 78, 4] but is observed to increase 50 % during TCV experiments, are important in the reduction of the ion source.
- Combining power/particle/momentum balance highlights three different plasma conditions, after which a reduction of the target pressure and onset of detachment is expected to occur. All of these three 'detachment thresholds' ( $p_{up}/q_{recl} \geq (p_{up}/q_{recl})_{crit}$ ,  $T_t \leq E_{ion}/\gamma$ ,  $f_{ion} \geq 0.5$ ) are measured to correspond well to the point where the ion target flux no longer follows the expected attached (linear) scaling, which highlights the onset of detachment. The onset of detachment is thus obtained when, given a certain  $q_{recl}$  and  $E_{ion}$  a critical, maximum, target pressure is achieved.
- Using charge exchange to ionisation ratio measurements, momentum losses are estimated through the Self-Ewald model. These start to develop after the detachment thresholds are reached and reach up to 70%, in agreement with previous measurements of the momentum loss [8].
- The maximum target pressure which can be obtained at any time during the discharge (given a measured  $q_{recl}$  and  $E_{ion}$ ) must be consistent with the upstream pressure obtained and any volumetric momentum loss present. The above estimates of momentum loss together with estimates of  $q_{recl}$ ,  $E_{ion}$  and upstream pressure measurements indicate that this requires a drop/saturation of the upstream pressure for the TCV case analysed. That is in quantitative agreement with the measured drop in upstream pressure.

## 1.8 Merit of this work

The merits of this work can be roughly divided in two areas: diagnostic interpretation/analysis including uncertainty analysis and the interpretation of detachment.

### 1.8.1 Diagnostic interpretation, analysis and development

In the scope of this work advances in spectroscopic analysis have been made for fusion plasmas which emphasises the importance of separating out emission components and of treating the emission quantitatively as opposed to qualitatively. This forms a paradigm shift with respect to previous diagnostic spectroscopic techniques which often work by assuming that the

emission is due to one particular process [63, 70] and which focus on line ratios [73, 79, 76, 80] and qualitative statements [80]. For instance, when investigating detachment observations in literature reference works, it is often suggested that sudden rises in Balmer line ratio imply that 'volume recombination is an essential and necessary element in divertor detachment' [3] and also [73]. This work, however, shows that such line ratio changes only imply that the *emission* of a particular Balmer line is becoming dominated by volumetric recombination. Given only the line ratio, one cannot determine whether recombination reactions are dominant over ionisation reactions —which requires a quantitative analysis. As a matter of fact, such changes in the Balmer line ratio may occur already when the volumetric recombination rate only reaches a few percent of the ionisation rate, depending on which Balmer line is chosen and depending on the electron density. Additionally, the work here specifically shows that the measured  $D\alpha$  is inconsistent with predictions based on atomic processes, consistent with the presence of molecular reactions. Its associated ratios, which are often used in literature [3, 70], thus cannot be used for investigating excitation/recombination emission based on a purely atomic collisional radiative model. However, they can be compared with modelling which includes molecular reactions in the  $D\alpha$  emission such as [76, 79]. This also shows the origin of the anti-correlation between the ion target current and  $D\alpha$  often highlighted in literature and sometimes called a detachment indicator [3]. This anti-correlation only occurs due to molecular reactions leading to additional  $D\alpha$  emission in the detached phase and does not say something about detachment (the anti-correlation does not occur during  $N_2$  seeding). All of this shows the importance of separating emission components, which is one of the basis's of this work. That development thus forms an important addition and clarification to previous spectroscopic diagnostic methods in the divertor.

Further diagnostic development in this work features a thorough development on probabilistic (Monte Carlo) approaches and a full and accurate accounting for all diagnostic uncertainties; including a full diagnostic verification check against synthetic diagnostic applied to SOLPS simulations. Such frameworks, developed for TCV, can be extended to other machines and enables fairer comparisons between different diagnostics and between the experimental data and the simulation. This enables better model validation.

### 1.8.2 Detachment interpretation

Although it is known that power removal (radiation) is important for detachment, it also occurs before detachment and the key elements to detachment are often understood to be volumetric momentum loss and volumetric recombination —as those processes are thought to be unique to detachment [3]. As such, one of the detachment ion current roll-over interpretations during detachment is, citing [3]: "'Where did the particles go?'. The best answer to that is probably: 'They didn't go anywhere. They just stayed longer. The particle confinement time simply went up because the drain got plugged'. The partial plugging is likely due to i-n (ion-neutral) friction which, since it is not a feature of the regimes preceding detachment, is therefore the 'new player' and thus might be called the 'explanation of detachment'.".

This work shows a different explanation of detachment: the ion target flux drops as fewer ions are being generated in the divertor as the ionisation source decreases through power limitation. Nevertheless, this description still has to obey equation 1.1 and thus the *target* pressure has to drop (not specifically a pressure gradient along the field lines) for the ion

current roll-over. However, reaching power limitation conditions (and thus driving down the target temperature) initiates a sequence of processes, which lead to volumetric momentum loss (e.g. movement of the ionisation peak off-target, giving rise to heightened charge exchange to ionisation ratios near the target).

The precise role of momentum loss, however, is unknown. The results in this work highlight that for the TCV conditions investigated, both the roll-over of the upstream pressure and volumetric momentum losses need to occur for the target pressure to remain below its maximum obtainable level, given the decreases in  $q_{recl}$  and increases in  $E_{ion}$  observed during density ramp detached discharges on TCV. This is consistent with the notion that one of the roles of volumetric momentum loss is to increase the maximum pressure [5, 6]. However, the nature of the upstream pressure roll-over is not understood and it is not understood whether this roll-over is coincidental due to core processes or whether it is caused by the divertor. Such an understanding is necessary for ascertaining the role of momentum losses in detachment. For instance, if the upstream pressure cannot be influenced by the divertor, then all the reduction required for  $p_t$  needs to come from momentum losses. What builds up the upstream pressure is currently unknown and may require combining core models with edge models as it is not known in what ways/magnitudes the core and plasma edge contribute to setting up the upstream pressure. This work opens up new questions in that area and illustrates the need to pursue such investigations.

## Chapter 2

# Literature and theory of detachment

*This section provides an overview of the theoretical basis from literature of divertor physics, atomic/molecular processes and detachment. Reduced analytical models from literature are highlighted for understanding and modelling divertor operation.*

One of the biggest challenges for ITER and beyond is to handle the power exhaust. Atomic physics processes can be used to reduce the heat load at the target by operating the divertor in a 'detached state'. This achieved the goal of having simultaneously low ion target fluxes (which are necessary to limit chemical sputtering giving rise to erosion [68, 81]); low electron temperatures (e.g below 5 eV) —which are necessary to limit physical sputtering giving rise to erosion [68, 81] and low target heat fluxes. However, this 'detached state' can grow unstable and result in radiative collapses [82, 83], such as MARFEs [83], or reduced core performance [84]. Robust divertor detachment with minimal impact on core performance is a requirement for ITER and beyond. In previous experiments, divertor detachment requires relatively high densities and impurity fractions; which can decrease core performance and core stability. Additionally, detachment depends critically on the plasma parameters in the SOL —which narrows the operational space in which detachment occurs and which makes the position of the detachment front sensitive to perturbations [82]. Alternative divertor concepts alter the magnetic geometry with the aim of enhancing divertor performance, certain advanced divertor concepts aim to achieve this by adding additional x-point(s) to a (conventional) single null divertor.

The physics of the divertor and the governing processes is reviewed. Crucial to the understanding of divertor physics and detachment is the underlying atomic and molecular processes and reactions, which are reviewed together with an overview of collisional radiative modelling. Detachment is, in essence, induced by a collection of atomic/molecular reactions which have a complex interplay with each other. Due to this, there are various different facets of detachment and due to that detachment tends to lack a precise definition. Instead of a definition, general detachment observations are discussed. Crucial to understanding divertor physics and detachment are diagnostic interpretation of the detachment-related observations, which are briefly discussed and more in detail in chapter 4 and for spectroscopy chapters 5, 6 and 7. A global idea of expectations between the different divertor parameters are shown by introducing and deriving the 'Two Point Model', which is often used for investigating divertor

physics [3]. Such analytic models, however, are a simplification and there is a push for going to more complete models which can take neutral transport and the underlying atomic/molecular physics accurately into account on a 2D mesh. One of these models, SOLPS-ITER, is briefly discussed.

## 2.1 Divertor physics fundamentals and its processes

Transport and losses of heat flux in the divertor are a crucial area of study for divertor power exhaust. Not only does the heat flux flowing through the divertor determine the heat flux reaching the target, it also plays a strong role in determining the temperatures of the scrape-off-layer and the divertor; including the target. The target temperature is important as it plays an important role in physical sputtering [68, 81] and thus plays a role in impurity production and wall erosion [29]. In addition, the temperature in the divertor plays a strong role in the atomic and molecular processes occurring in the divertor as discussed in section 2.4.

The transport of heat in the divertor plays an important role in the ion target flux reaching the targets. as the ion target flux in tokamak divertors is generally believed to be due to particle recycling, [5, 6, 3]. A divertor, especially one with neutral baffles, can have a cloud of neutral particles in the divertor which is (partially) ionised by the heat flux flowing through this cloud. This ionisation, in turn, makes up most of the ions reaching the target; which we refer to as high recycling conditions in this work [5, 6, 51]. More specifically, this means that there is a balance between the divertor ion source, the ion target sink and any volumetric ion sink (such as recombination) —the divertor is a ‘self-contained’ region. Through the continuity equation the formation of an ion source also plays an important role in determining the plasma flow profile in the divertor, giving rise to a complex 2D velocity profile [52] —which is strongly dependent on the location and shape of the ionisation region [5, 3, 52]. Reducing the ion flux is important as a high ion flux gives rise to strong erosion as chemical sputtering scales with the ion flux [68].

The importance of particle recycling is believed to be one of the key differences between tokamak divertors and linear machines, often thought of as ‘divertor simulators’, where the working chamber is not generally ‘self-contained’ as usually not all of the plasma is generated in the working chamber [52, 6, 5]. SOLEEDGE2D-EIRENE simulations for a particularly high density linear machine, Pilot-PSI, however indicate that ionisation just after the external ion source can be non-negligible compared to the external ion source (up to 50 %) [85], although ionisation is insignificant for the most part of the working chamber [86, 85]. Another difference is that sputtered ions can be locally re-deposited in a tokamak, which is generally not true for linear devices.

A crucial and critical insight into the workings of the divertor is that each ionisation event requires a certain amount of energy [3, 5, 51]. Ionisation is thus a power sink, occurring in the form of radiative losses and potential energy loss by converting neutrals into ions. That means that *the amount of power entering the ionisation region can limit the amount of ion source possible*. That insight is crucial for the work in this thesis and will be discussed in greater detail in chapter 3.

**Conduction-limited divertor** — Transport of heat in the divertor is generally per-

formed through convection, conduction or drifts [3]. Based on this, the divertor operational mode can generally be distinguished between two types: sheath-limited heat transport and conduction-limited heat transport. A sheath-limited SOL is generally characterised by a SOL along which the electron temperature is constant, e.g quasi-static. These conditions are generally reached at relatively low electron densities where the SOL collisionality is small, meaning that the electron collisional mean free path (for epithermals) is larger than the connection length (e.g distance a particle travels along a field line in the SOL [87]) [3]. In such a case, the electron temperature along the SOL is fully determined by the sheath developing at the target and the conservation of pressure —assuming there are no momentum and power (radiation) losses in the SOL [3]. Since the temperature at the target is the highest in this sheath-limited regime, sputtering of plasma-facing components will be the highest [81], leading to high erosion rates and strong impurity production [29]. Convective heat transport, as opposed to conductive, weakens the temperature gradient and can thus facilitate isothermal field lines [3] (see section 2.2.2).

When the electron density in the divertor is increased, the mean free path of the electrons and ions is decreased, resulting in more collisions of the plasma particles in the SOL (e.g. the epithermal collisional mean free path being smaller than the connection length), resulting in temperature gradients along the SOL [41, 88] through heat conduction. In this case heat transport along the SOL is primarily carried by electron heat conduction [3, 29, 76]. This occurs at high divertor collisionalities and hence relatively high upstream densities; low SOL heat flux and a large connection length. The temperature gradient in the conduction limited regime is accompanied by a density gradient which keeps the pressure constant along the SOL. The increase in density near the target in the conduction-limited regime implies that possibly the temperature drops while the Mach number is constant such that the velocity drops and the density can rise and/or a particle source is present near the target. This particle source is realised by neutral hydrogen recycling from the divertor target; the ionisation of which gives rise to most of the ion target flux as explained previously. This occurs as the influx of recycled neutral particles is ionised near the target leading to an additional particle influx [89, 41, 81, 3]; which is also why the conduction-limited regime and an observation of a temperature gradient/high collisionality in the divertor is expected to correspond to high recycling conditions. Although this is expected, it has not yet been experimentally confirmed in literature with direct measurements of the ionisation source.

One of the more striking observations of the conduction-limited regime is a rapid rise of the ion target current as the divertor cools (see section 2.2). A lack of this observation and/or the observation of isothermal field lines is often associated with a SOL in low recycling conditions [45]. Although there is a correlation between low collisionality and a low recycling divertor, where the *ionisation mean free path* —as opposed to the collisional mean free path—is large compared to the divertor size, a lack of trends expected from the conduction-limited trend does not necessarily imply that the ion target current is not delivered by ionisation as will be discussed in chapter 3.

**Reducing peak heat loads** —Reduction of peak heat loads on plasma facing components is essential for the success of the next generation of high fusion power tokamaks (ITER and beyond) [54, 47, 36]. There are several mechanisms for reducing peak heat loads and one of the key mechanisms is a volumetric power sink, for instance through radiative losses. One

important radiative loss mechanism is through impurity radiation, which is a key mechanism for reducing the heat flux reaching the target [54, 3]. Hydrogenic radiation, on the other hand, is a relatively smaller power sink —although it can play a crucial role during detachment as it contributes to the ionisation energy cost, as will be explained in chapter 3.

Depending on the first wall material, intrinsic impurities in the plasma can radiate a large fraction of power entering the SOL [54]. This intrinsic radiation is especially important in low-Z devices, such as carbon machines. Low-Z atoms tend to be particularly effective radiators at fairly low plasma temperatures ( $\sim 10$  eV) [54]. In this work, it is indeed shown that for TCV conditions the intrinsic carbon radiation dominates over the hydrogenic radiation and strongly increases while the divertor plasma is cooled (section 8.3). Contrastingly, assuming a metallic first wall —such as tungsten —the radiative losses are less pronounced at low temperatures, but instead are more pronounced at high temperatures —possibly resulting in core radiative losses. In high power devices, intrinsic impurity radiation and hydrogenic radiation are often insufficient to achieve an acceptable level of power removal. In such conditions, extrinsic impurity seeding is likely required [67, 90, 91, 92, 45, 93, 94, 90, 95]. As lower electron temperatures (5-40 eV —this depends on the impurity [96]) lead to stronger radiative cooling, a temperature gradient in the SOL would lead to enhanced radiative cooling in the divertor [82]. When there is significant radiative cooling in the divertor leg, the temperature in the divertor leg as a result decreases, which leads to more radiative cooling. This synergistic effect —a radiation condensation instability —can lead to a significant removal of power from the plasma in the flux tube [83, 65] and plays a crucial role in divertor physics. The disadvantage of this method is that some fraction of the impurities gets back into the core, which leads to fuel dilution and which can lead to a decrease in energy confinement due to radiation cooling in the core [84, 97]. It should also be noted that increasing radiative losses lowers the target temperature and increases the target density, which gives more easily rise to a temperature gradient (e.g conduction-limited operation). Impurity radiation is a crucial field of study for power exhaust physics and the radiative losses can strongly depend on plasma transport; where transport of charged ions and transport of metastables can greatly influence radiative losses [91, 95]. Hydrogenic and impurity (carbon) radiation will be further discussed in section 2.4, where also an illustration of the influence of transport on carbon radiation will be shown.

Apart from a radiative volumetric power sink, power can also be displaced from the plasma to the main walls by charge exchange [5, 6]. If charge exchange between a hot and colder ion occurs, a hot neutral is created. Assuming this hot neutral is not ionised, it can reach the wall —thus leading to a power transfer from the divertor plasma to the main wall (as opposed to the strike points specifically). This is potentially considered an important power loss [54], but depends on the precise details of neutral dynamics on the divertor, including how likely it is that the hot neutral are re-ionised (which depends on the ionisation rate and thus strongly on temperature). Investigations into such effects can be performed by full fledged divertor models, such as SOLPS, which can include neutral transport through a Monte Carlo code such as EIRENE. Further discussion on such models will be shown in section 3, which includes an analytical model for charge exchange related energy loss. SOLPS-ITER results for TCV indicate that volumetric power losses due to charge exchange occur, but their magnitude is smaller than power losses due to impurity and hydrogenic radiation [98].

To understand the formation of peak heat loads, understanding the shape of the heat flux

profile at the target, which is influenced by certain plasma parameters such as the upstream density [99], is important [100, 40]. Additionally, instead of altering the heat flux profile at the target also the target geometry or divertor geometry can be modified to create an effective change in the heat flux profile, for instance by increasing the major radius of the strike point (so called  $R_t$  divertor), which increases the wetted area and thus reduces peak heat loads [101].

Ultimately through conduction and power removal the divertor temperatures can be decreased to 5 eV, at which the divertor will enter a state of 'detachment'. During detachment the target temperature, target heat flux and target ion flux are simultaneously reduced through a collection of atomic and molecular physics reactions.

## 2.2 Understanding different divertor operational regimes through simplified modelling: Two Point Model

The divertor and complex 3D structure of the SOL can be more easily visualised by straightening [3] out this structure to a 1D linear slab of plasma, depicted in figure 2.1 (implemented from [81] and the JET image database). At the upstream location (denoted by ' $u$ '), the heat from the plasma core enters the scrape-off layer. This location could be taken at any position along the separatrix up until the x-point, but is generally taken at the mid-plane location of the separatrix. Heat entering upstream is eventually transported towards the target denoted by ' $t$ ' in figure 2.1. The two point model is a simplified analytical model often used in divertor research, which relates the upstream temperature, density and heat flux with the target densities and temperatures [3] and consists of three equations which combine pressure balance; parallel heat conduction and the target sheath conditions.

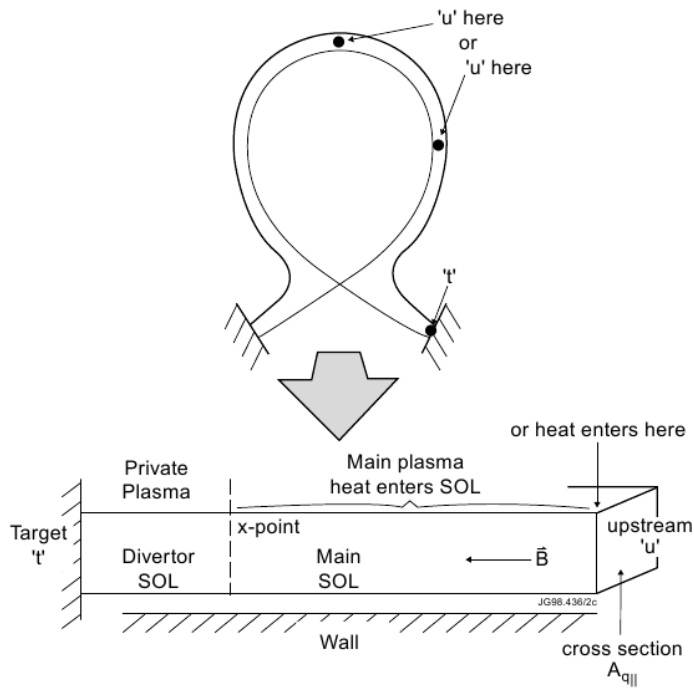


Figure 2.1: A schematic picture of straightening out the poloidal SOL geometry in a 1D model, implemented from [81] and the JET image database.

For deriving the 2 point model, we make the assumptions listed below [81, 3]. In revised versions of the two point model correction terms for some of these assumptions are introduced [3, 73, 81], which will be discussed later.

- The SOL is 1D (the complex 3D magnetic structure is straightened out).
- There are no power losses along the SOL. Radiation losses are neglected and the energy it costs for ionisation is neglected.
- The influence of ionisation on the flow profile is ignored.
- Heat is only transported by parallel heat conduction. Convective heat transport is not taken into account.
- The pressure is assumed constant across a field line. Momentum losses are not taken into account.

### 2.2.1 Derivation of the 'basic' two point model

The pressure along a field line is constant inside the plasma core of a tokamak, according to MHD theory [28]. By assuming there are no pressure losses in the SOL, a pressure balance equation —essentially a conservation of momentum equation—can be set up. Important to note is that the pressure consists out of two parts: the static pressure  $p = n_e T_e + n_i T_i$ , which is dictated by the electron/ion temperature/density and the dynamic pressure—which arises from the net movement of electrons/ions [81, 3]. For simplicity, we will assume that the ion temperature equals the electron temperature ( $T = T_e = T_i$ ). Furthermore, we assume a pure hydrogenic plasma, and this through quasi-neutrality implies that  $n = n_e = n_i$ . The static pressure can thus be written as  $p = nT$ .

When plasma in general gets close to a wall, the wall acts as a sink for the fast, mobile electrons. The electrons charge up the plasma at the wall (since the wall is usually grounded), which leads to an additional 'ambipolar' electric field [3]; generally referred to as the sheath which occurs in a thin layer ( $\sim$  mm or less) from the wall. This field accelerates the ions impacting on the surface to the sound speed (Bohm criterion) of the plasma:  $c_s = \sqrt{\frac{2T}{m_i}}$  (where  $m_i$  is the electron mass) [3], resulting in a dynamic pressure of  $m_i n c_s^2 = nT$  at the target which equals the static pressure. This leads to the first equation of the two point model (equation 2.1) by assuming balance between the upstream pressure  $p_u = n_u T_u$  ('u' denotes upstream)—assuming no dynamic pressure upstream—and the target pressure  $p_t = n_t T_t + n_t T_t = 2n_t T_t$  ('t' denotes target).

$$n_u T_u = 2n_t T_t \quad (2.1)$$

Since power losses are neglected, the heat flux entering the SOL is fully transmitted from upstream to the target. By analysing the effects of the ambipolar field at the sheath, the power density transmitted to the target can be related to the target parameters, leading to equation 2.2 [3], where  $\gamma$  is the sheath power transmission factor (which accounts for the accelerated ions bombarding the target due to the sheath effect), generally assumed to be 7.

This means that the heat flux entering the target is proportional to the pressure at the target times the square root of the target temperature ( $p_t$ ).

$$q_{\parallel} = \gamma n_t T_t c_{st} \propto n_t T_t^{3/2} (= p_t T_t^{1/2}) \quad (2.2)$$

As the electrons are more mobile than the ions, heat conduction through the electrons is the most dominant form of heat transport (assuming no drifts and no convection). Assuming that all heat transport is through parallel electron heat conduction, an equation relating target and upstream temperatures can be obtained forming the third equation of the two point model. Assuming classical diffusion of the electrons, the parallel heat conductivity can be written as  $\xi_{\parallel,e} = v_{th,e}^2 \tau_e$ , in which  $v_{th,e} \propto T_e^{1/2}$  is the thermal electron velocity and  $\tau_e \propto T_e^{3/2}$  is the electron collision time; and thus  $\xi_{\parallel,e} \propto T_e^{5/2}$ . Using this, we can set up a differential equation linking  $q_{\parallel}$  to the temperature:  $q_{\parallel} = -\kappa T^{5/2} \frac{dT}{dx}$ , in which  $\kappa$  is the electron parallel heat conductivity coefficient (generally assumed to be  $\kappa \approx 2000$ ) [3, 28, 30]. By making an assumption on the heat flow profile in the divertor, one can solve this differential equation and obtain a relation between  $T_t$  and  $T_u$ . For this we assume that all of  $q_{\parallel}$  enters the SOL upstream (e.g from the top of the 1D model) and remains constant throughout the SOL, where a connection length  $L$  later it reaches the target. By integrating the equation for the parallel conduction, a relation between the temperature upstream and the temperature at the target can be derived, which is performed at equation 2.3. Alternatively, one could assume that all heat enters not from the top of the 1D model but gradually throughout the connection length, which leads to only marginal differences in equation 2.3 [3].

$$\begin{aligned} q_{\parallel} &= -\kappa T^{5/2} \frac{dT}{dx} \\ \rightarrow T^{5/2} dT &= -\frac{q_{\parallel}}{\kappa} dx \\ \rightarrow T_u^{7/2} &= T_t^{7/2} + \frac{7q_{\parallel}L}{2\kappa} \end{aligned} \quad (2.3)$$

Equations 2.3, 2.2 and 2.1 make up the two point model, relates  $n_t, n_u, T_t, T_u$  for given  $q_{\parallel}$ ,  $L$ ,  $\gamma$ ,  $m_i$  as listed in equation 2.4. Assuming fixed values for  $q_{\parallel}$ ,  $L$ ,  $\gamma$ ,  $m_i$  and other constants, having three equations with four unknowns ( $n_t, n_u, T_t, T_u$ ) means that one of these unknowns must be supplied and then the other parameters can be modelled from equation 2.4.

$$\begin{aligned} n_u T_u &= 2n_t T_t \\ T_u^{7/2} &= T_t^{7/2} + \frac{7q_{\parallel}L}{2\kappa} \\ q_{\parallel} &= \sqrt{\frac{2}{m_i}} \gamma n_t T_t^{3/2} \end{aligned} \quad (2.4)$$

Equation 2.3 (and thus equation 2.4) has to be solved numerically, unless one assumes that fairly large temperature gradients (e.g conduction limited regime) occur  $T_u \gg T_t$ , which facilitates simplifying 2.3 (see equation 2.5), enabling an analytic solution for 2.4 as shown in equation 2.6. This formulation is written such that  $T_t, n_t, T_u$  can be directly obtained if a value from  $n_u$  is assumed.

$$T_u^{7/2} \approx \frac{7q_{\parallel}L}{2\kappa} \rightarrow T_u = \left( \frac{7q_{\parallel}L}{2\kappa} \right)^{2/7} \quad (2.5)$$

$$\begin{aligned}
T_t &= \frac{q_{||}^2}{n_u^2 T_u^2} \frac{2m_i}{\gamma^2} \propto \frac{q_{||}^2}{n_u^2 T_u^2} \\
n_t &= \frac{n_u^3 T_u^3}{q_{||}^2} \frac{\gamma^2}{4m_i} \propto \frac{n_u^3 T_u^3}{q_{||}^2} \\
T_u &= \left( \frac{7q_{||}L}{2\kappa} \right)^{2/7}
\end{aligned} \tag{2.6}$$

The main results of this version of the two point model is that an increase in  $n_u$  results in a decrease in  $T_t$  while  $T_u$  remains constant (assuming conduction-limited operation), increasing the temperature gradient. As  $T_t$  is reduced,  $n_t$  must increase when  $n_u$  is increased as the pressure must be constant along the flux tube, resulting in higher divertor densities. In reality these higher divertor densities will result, together with the decay in divertor temperatures, into more divertor radiation (which is not accounted for in this model); facilitating detachment.

The heat flux reaching the target (not accounting for the ion's potential energy, a more careful analysis in chapter 3 does account for this) essentially comprises the number of ions reaching the target (e.g  $\Gamma_t$ ) and the energy each ion carries to the target  $\gamma T_t$ : e.g  $q_{target} = \Gamma_t \gamma T_t$ . It is important to note that combining this with equation 2.2 results in equation 1.1 used to introduce detachment in the introduction.

Using the relation obtained for  $T_t$  (e.g 2.6), the scaling of the ion target flux can be derived through the two point model as shown in model (equation 2.7). In the absence of both volumetric power loss and convective heat transport,  $\Gamma_t \propto \frac{n_u^2 T_u^2}{q_{||}}$  —or using equation 2.5 and assuming conduction-limited operation,  $\Gamma_t \propto \frac{n_u^2}{q_{||}^{3/7}}$ . Therefore, under such assumptions and with a fairly fixed  $q_{||}$ ,  $\Gamma_t \propto n_u^2$  is expected. This scaling is important in literature as it forms the basis for quantifying the depth of detachment by comparing the obtained  $\Gamma_t$  to this scaling [101, 58, 45, 3, 102, 37, 73]. However, the assumptions used are violated during TCV detachment where both  $T_u$ ,  $q_{||}$  and divertor radiation change during a density ramp while the power entering the divertor is kept constant; which will be treated in detail in chapters 3 and 8.

$$\Gamma_t = \frac{n_u^2 T_u^2}{q_{||}} \frac{\gamma}{2m_i} \propto \frac{n_u^2 T_u^2}{q_{||}} \tag{2.7}$$

### 2.2.2 Including 'missing' physics by implementing correction terms

The above two point model makes strong assumptions on having no convective transport, having no divertor radiation and having no volumetric momentum losses. Especially the no divertor radiation is a strong assumption in carbon machines, where intrinsic impurity radiation is substantial. Using the methodology of [3], we can apply correction factors to the governing equations of the two point model which can partially account for missing these processes. Radiative losses essentially provide a decoupling between the heat flux entering the SOL  $q_{||}$  and the heat flux reaching the target  $q_t$ , which can be written as  $q_t = (1 - f_{power})q_{||}$  where  $f_{power}$  is the fraction of power loss both due to radiation and due to charge exchange. If hydrogenic radiation occurs, this is also included by  $f_{power}$ . However, a fixed  $f_{power}$  cannot properly include hydrogenic radiation as the amount of hydrogenic radiation will depend on the amount of ionisation, which makes up  $\Gamma_t$  almost fully in high recycling conditions assuming recombination is negligible. Thus, accounting for  $f_{power}$  does not account for power losses

due to recycling accurately. Accounting for this is crucial when 50 % of the power reaching the ionisation region is spent on the ionisation process, which is expected to be a detachment threshold and occurs at target temperatures of 4-7 eV (see chapter 3). Therefore, even this 'corrected' two point model is not applicable in such low temperature regimes. As momentum losses only occur in such low temperature regimes, we will not introduce a correction factor for momentum losses.

Impurity radiation will reduce the heat flux towards the target as well as influence the conduction equation 2.3, where a heat flux profile along the field lines has to be assumed. Generally it is assumed that all radiative loss occurs close to the strike point (e.g  $s_0 \approx 1$ ), such that  $\int q_{\parallel}(s)ds \approx q_{\parallel}(0)L$  [3], which is a reasonable assumption. Due to the dependencies in that relation, having the radiation region more upstream would only have a small influence on this relation: making a conservative assumption of radiating 90 % of the heat flux halfway of the connection length would lead to a 16 % deviation from assuming that all radiative losses occur at the target (assuming  $T_u \propto (\int q_{\parallel}(s)ds)^{2/7}$ ). As such, one can assume that impurity radiation in the two point model only reduces the target heat flux.

To account for convection,  $q_{\parallel}$  in equation 2.3 has to be replaced with the conductive part of  $q_{\parallel}$ , defined as  $f_{cond}q_{\parallel}$  [3]. Conductive and convective heat transport could differ along the flux tube, so a certain profile of conductive versus convective transport along the field lines needs to be assumed. Commonly it is assumed that conductive versus convective transport remains fixed along the connection length (e.g  $f_{cond}$  is fixed) [3]. When the heat flux entering the SOL is fully carried through convection (e.g  $f_{cond} \approx 0$ ), then according to equations 2.3 and 2.4,  $T_t \sim T_u$  and no temperature gradient along the field line would exist. Convection thus reduces temperature gradients as a fraction of the heat entering the SOL is not carried to the target through conduction but directly by convection. Assuming sufficiently strong temperature gradients do occur,  $f_{cond}$  would influence the upstream temperature through equation 2.5 by only  $f_{cond}^{2/7}$  (assuming  $T_u^{7/2} \gg T_t^{7/2}$ ), which is small especially when considering that strong convective transport would lead to quasi-static field lines where this simplification no longer holds. Likely the best way of accounting for convective transport is to use, instead of equation 2.5 for the upstream temperature, a measured value of the upstream temperature; which intrinsically accounts for  $f_{cond}$  and any influence of divertor/SOL radiation on the upstream temperature. In essence, when taking the measured  $T_u$  into account as opposed to determining  $T_u$  using  $q_{\parallel}$  and  $L$ , this is identical to only using the first and third equation in equation 2.4; e.g the conduction equation is taken out of account.

As such, we will only consider the influence of radiative losses in the two point model, which alters equation 2.6 into 2.8. Radiated losses thus reduce the target temperature; increase the target density; and increase ion target fluxes.

$$\begin{aligned} T_t &= \frac{(1 - f_{power})^2 q_{\parallel}^2}{n_u^2 T_u^2} \frac{2m_i}{\gamma^2} \propto \frac{(1 - f_{power})^2 q_{\parallel}^2}{n_u^2 T_u^2} \\ n_t &= \frac{n_u^3 T_u^3}{(1 - f_{power})^2 q_{\parallel}^2} \frac{\gamma^2}{4m_i} \propto \frac{n_u^3 T_u^3}{(1 - f_{power})^2 q_{\parallel}^2} \\ T_u &= \left(\frac{7q_{\parallel}L}{2\kappa}\right)^{2/7} \\ \Gamma_t &= \frac{n_u^2 T_u^2}{q_{\parallel}(1 - f_{power})} \frac{\gamma}{2m_i} \propto \frac{n_u^2 T_u^2}{q_{\parallel}(1 - f_{power})} \end{aligned} \quad (2.8)$$

The main parameters which can thus be used for driving the divertor into detachment for a given upstream heat flux is increasing upstream density and increasing divertor radiative losses; whereas the upstream temperature can be expected to be fairly constant (in the conduction-limited regime) as it is only weakly sensitive to  $q_{\parallel}$  and  $L$ . In section 3 we will apply the two point model, in the form of equation 2.8 while determining  $T_u$  numerically from equation 2.3 where applicable, to TCV relevant regimes to show the various scalings and to show the different expected divertor operation regimes in TCV. In addition, a two point model from literature [3, 4, 6] which explicitly takes energy loss arising from recycling and power balance into account, is introduced.

## 2.3 Detachment

As illustrated, reducing the target temperature through an increased collisionality/conduction (e.g higher  $n_u$ ) and radiative losses do reduce target heat fluxes and target temperatures simultaneously, but they do not decrease the ion target flux. Despite these two aspects (e.g increasing  $n_u$  and decreasing  $f_{power}$ ) are crucial for detachment and certainly are ingredients to providing the conditions for detachment; there must be other processes involved facilitating detachment which do drive down  $\Gamma_t$ , such that  $\Gamma_t$ ,  $q_t$  and  $T_t$  can all be driven down simultaneously. That reduction of  $\Gamma_t$  also enables a reduction of target heat flux to occur faster than in the attached case (e.g.  $q_t \Gamma_t T_t \propto p_u T_t^{1/2}$ ) as function of  $T_t$ . In any case, as discussed in the introduction through equation 1.1, any target ion flux reduction requires reducing the target pressure faster than  $T_t^{1/2}$ . This is why detachment is often classified in literature as a state where a pressure gradient develops along the field lines [3] —assuming the upstream pressure is constant/unaffected by the divertor, this would lead to a  $p_t$  reduction [3, 4]. However, the upstream pressure may not be constant/unaffected by the divertor as it may partially be built-up by divertor ionisation [5, 6] and, furthermore, reducing  $\Gamma_t$  does not specifically require volumetric momentum losses —only target momentum loss. The other ingredient to detachment is, assuming high recycling conditions, a reduction in ion source which requires power limitation during detachment for which divertor (impurity) radiation are crucial. This contrasts *during detachment* the behaviour predicted by the two point model in equation 2.8. The temperatures at which such power limitation starts to occur according to *plasma physics* is around 4-7 eV (chapter 3), which corresponds precisely to the temperatures at which volumetric momentum loss is expected to occur according to *atomic/molecular physics* (which is further discussed in section 2.4). In other words, the 'classical' understanding that detachment is characterised by a pressure gradient which is linked to an ion target flux reduction in literature [3] may have arisen from the similarity between these two temperature regimes. A further and deeper discussion on combining this power limitation aspect with the sheath target conditions which require  $p_t$  to drop is shown in chapter 3. For now we will highlight the general idea of detachment, characterised by the appearance of a pressure gradient.

A pressure gradient is thought to develop due to ion neutral interactions resulting in momentum losses. During detachment, the ionisation region moves from near the target towards the x-point, giving rise to a region below the ionisation region (with temperatures of  $\sim 5$  eV or lower) where charge exchange between hot plasma ions and recycled cold neutral

particles from the wall dominate over ionisation, as the ionisation has disappeared there. In this process, the hot plasma ions gain electrons from cold neutral particles, leading to cold plasma ions and hot neutral particles, resulting in momentum and energy losses (to the wall) [103, 3, 104], which has been observed through a pressure gradient along the divertor leg [3, 29, 81, 104, 41, 101]. Additionally, current studies suggest that the lower temperature region is suspected to give rise to an enhanced molecular density, facilitating ion-molecule interactions and associated momentum losses through molecular charge exchange [4, 49, 50]. This can be —under certain conditions —more dominant than momentum losses arising from molecular charge exchange [49]. The interaction of neutral particles with the plasma ions can strongly depend on the magnetic and physical geometry of the divertor [29, 58, 105, 33]. A closed divertor helps to confine the neutral particles and is expected to reduce the detachment threshold. However, the baffling structure puts higher strains on engineering demands and makes the divertor more difficult to diagnose. Additionally, the precise directory of the neutral particles coming from the strike point plays an important role in the plasma-neutral interaction [33, 105].

When the temperature is further reduced below 5 eV, volumetric recombination can become important [3, 6], leading to momentum, energy and particle losses [51, 66, 62]. Volumetric recombination can arise from both electron-ion recombination (EIR) [63, 51, 62] and molecular reactions —Molecular Activated Recombination (MAR) [63, 106, 57, 107, 108, 109, 110, 111]. MAR, which can play a role at temperatures below 7 eV, can be obtained through several combinations of molecular reactions [112] and which of these are dominant strongly depends on machine conditions [109]. For tokamaks with relatively high densities ( $1 \times 10^{19} \text{ m}^{-3}$  or higher) compared to linear machines [109], EIR generally dominates over MAR [108, 57, 110] and becomes important at temperatures below 2 eV. Volumetric recombination in the divertor region has been shown to be a relevant sink of ions for the detached plasma in high density conditions [63, 51, 64]. EIR is thus often considered a very important process in detachment [3, 5, 113, 6, 73]. More information on the details of the atomic and molecular physics and the underlying rates is provided in section 2.4.

Experimentally, detachment is generally either achieved through a density ramp (e.g. increasing upstream density) and/or by increasing radiative losses through an impurity seeding ramp. While such scans occur, the divertor transitions from an attached case to a detached case. It should be noted that experimentally these two aspects are often not distinguishable. For instance, during a density ramp also radiated losses will increase as the divertor becomes more dense and colder. Additionally, also the power entering the divertor can change.

The general processes and sequences during such a core density ramp or seeding ramp is illustrated in figure 2.2 a for TCV conditions. During a density or seeding ramp, first the radiation in the divertor increases overall while being peaked near the targets where the electron temperature is relatively low. Once target temperatures below the optimum radiative temperature are achieved (which depends on the impurity specie —for carbon this is around 10 eV), the radiation front starts to move from the target towards the x-point. When radiative losses and/or the electron density further increase, the target temperatures and the power reaching the ionisation region are further reduced until, eventually, the ionisation region starts to move towards the x-point, detachment starts to occur (second frame of figure

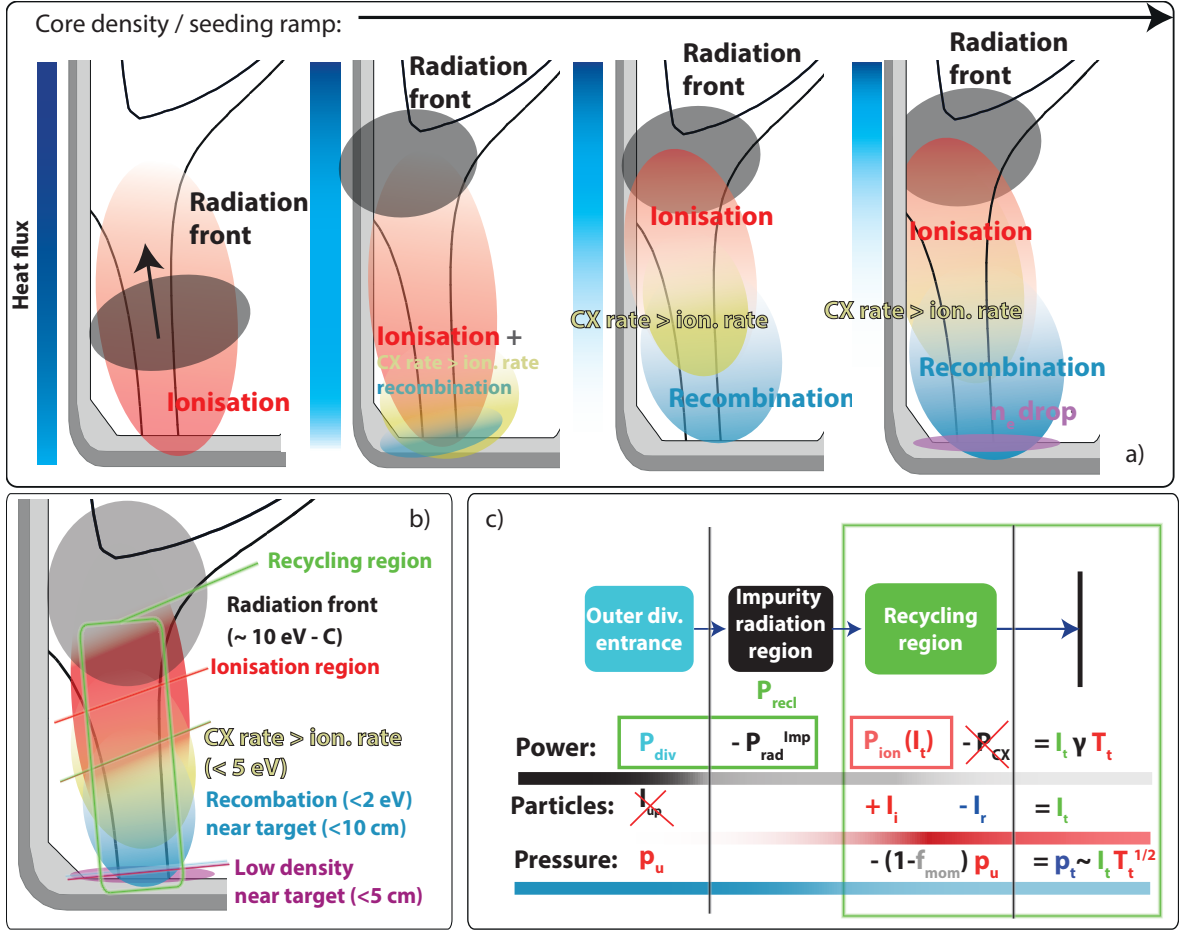


Figure 2.2: A schematic overview of the various detachment processes in the divertor adopted from [1] and [2]. a) Schematic overview of TCV detachment processes as function of increasing upstream density or seeding level. b) More detailed schematic overview of a detached TCV divertor. c) A schematic overview of the different processes in the divertor and their influences on power, particle and momentum balance.

2.2 a) and charge exchange becomes more dominant over ionisation near the target. When the radiative losses/divertor densities further increase, the ionisation region moves further up and the area where charge exchange dominates over ionisation increases while ultimately volumetric recombination starts to occur near the target. At the strongest detached phase, the target density may decay [73, 41] and thus the density front (and often corresponding recombination front as recombination scales with  $n_e^{2-3}$  [41, 63]) may start to move towards the x-point. Such a target density reduction in the strongest detached states is also observed in TCV where it occurs in a small region ( $< 5$  cm) [1, 2]. When the density/core radiation is further increased, strong radiative losses in the core may occur and the plasma could disrupt due to a radiative collapse [114, 115, 29, 3, 58, 83, 41].

As explained, all of these different processes occur in different regions of the divertor, which can overlap as shown in this work (section 8.1.1). The reason for this is that the divertor consists of several temperature zones [29] and for each temperature different atomic processes are dominant as illustrated in figure 2.2 b. A schematic and simplified overview of the result of the total detachment process in terms of power, integrated ion flux ( $I_t$ ) and pressure along the divertor leg is shown in figure 2.2 c, where the recycling region is highlighted. For visualisation

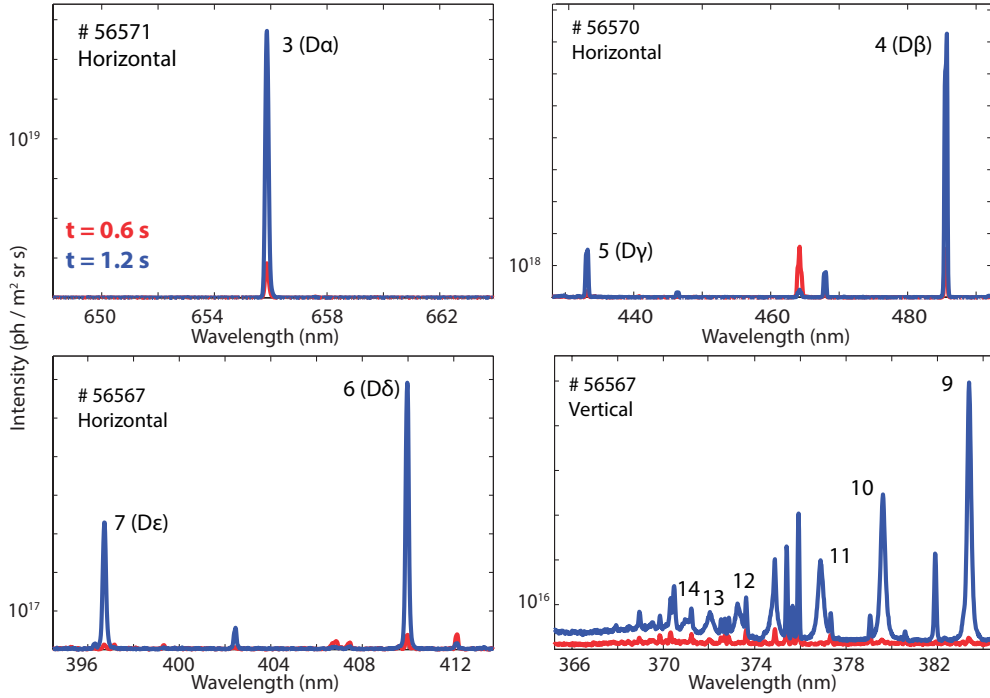


Figure 2.3: Various divertor spectra measured by the DSS on TCV obtained during repeat discharges. They are shown for both an attached (red) and detached (blue) case.

purposes we define the recycling region as the region covering the ionisation region until the target (e.g it covers the ionisation, momentum loss and recombination ion loss regions). This schematic overview and the various equations are discussed in more detail in chapter 3, but here we provide a brief overview below as a reference. The power entering the divertor  $P_{div}$  is reduced by impurity radiation ( $P_{rad}^{imp}$ ). The power which is left enters the recycling region  $P_{recl}$  and is further reduced by the power loss associated with ionisation  $P_{ion}$  (which scales linearly with the ionisation source  $I_i$ ) and other power loss mechanisms such as power losses due to charge exchange  $P_{CX}$  (which are often neglected). The remaining power reaches the target, where  $I_t T_t \gamma$  forms the kinetic power reaching the target. This ion target flux is mainly generated by ionisation, can be reduced by recombination ( $I_r$ ) and can be influenced by an ion flow from upstream in non-high recycling conditions ( $I_{up}$ ). This ion target flux, together with a target temperature, implies that there must be a certain target pressure  $p_t$ , which again has to be consistent with the upstream pressure  $p_u$  and the amount of momentum loss denoted by  $-(1 - f_{mom})p_u$ , where  $f_{mom} = 1$  means no momentum loss and  $f_{mom} = 0$  means all momentum is lost. Several models for  $f_{mom}$  are introduced in section 2.4.

### 2.3.1 Observing and characterising detachment

There are various ways and methods to define and characterise detachment [3, 37, 73, 81]. One of the difficulties of detachment is that it involves a large collection of different processes having different effects on the plasma and target parameters. This is largely why there is not a consensus on a precise detachment definition, although the characteristics and processes involved in detachment are generally well-known. When diagnosing detachment, a large range of diagnostics are used to measure the different aspects of detachment. These often measure at different locations, which is necessary as radiation losses, charge exchange reactions and

recombination in the divertor are all volumetric and the nature of the detached plasma is thus 2D (assuming axisymmetry). It is important to obtain a coherent picture between the different diagnostics while accounting for the individual short-comings of each diagnostic. To do this, measurements from the different diagnostics have to be compared with both each other and with detachment modelling. Furthermore, as the nature of the detached plasma is 2D, in order to study detachment, having 2D diagnostics measurements can be very beneficial [76] or at least having measurements along the divertor leg (1D). Such volumetric measurements enable characterising and investigating the *processes* behind detachment as opposed to the *results* of detachment at the target.

Below several ways and methods to quantify and discuss detachment are introduced together with the relevant terminology.

**Diagnosing detachment** Ultimately the main aspect to detachment is a simultaneous reduction of the ion target flux, target temperature and target heat flux. The ion target flux [3, 116, 117, 118, 119] can be routinely measured by Langmuir probes, although they likely cannot be used for measuring the target temperature in detached conditions (see section 4.2). The target heat flux is expected to decay simultaneously with a decay in the target temperature and can also be measured through IR camera measurements. Based on the reduction and shape of the heat flux profile, different 'strengths' of detachment can be defined —such as 'pronounced' detachment [91, 120].

Ideally target parameters, such as  $T_t, n_t, q_t$  are compared to upstream parameters. One of the difficult points of measuring reduction of target heat fluxes, target ion fluxes and target temperatures is that such changes can also be brought by changing parameters upstream; which makes us wonder whether it can then still be called a 'detached state'. Therefore, it is crucial when investigating detachment to monitor the temperature, density and power flow into the divertor upstream. The upstream temperature and density can be measured partially by Thomson scattering, which is a continuous measurement at a reasonable temporal resolution (generally of the order of 100 Hz) but (generally) at a relatively poor spatial resolution (5-10 mm). Otherwise, they can be monitored by measurements through a reciprocating probe which performs high spatial resolution measurements of upstream densities and temperatures; but this can only be performed a few times per discharge. Repeat discharges are thus necessary to monitor a density ramp or seeding ramp continuously using reciprocating probe plunges.

Those reciprocating probe plunges enable, perhaps, one of the most direct ways of evaluating detachment by comparing the upstream and target pressure profiles to investigate pressure balance and momentum losses. As shown in the result obtained for TCV in figure 2.4, obtained from [101], the upstream and target pressure profiles overlay well at the start of a density ramp. However, when the core density increases and the divertor is cooled, a deviation between the pressure profiles starts to occur and as detachment proceeds develops to be stronger, this deviation increases. Similar investigations have been performed on other tokamaks, indicating stronger pressure drops [41]. The overview shown in figure 2.4 also shows the evolution of the ion target current, ion target current profile and the heat flux profile during detachment.

By using the upstream parameters measured through reciprocating probes or Thomson scattering, it is possible to quantify the 'depth' of detachment by determining the ratio

between the ion target flux expected based on upstream parameters (such as equation 2.8) and the measured ion target flux —also called the ‘Degree of Detachment’ (DoD) [37, 102, 3]. For density ramps, it is then often assumed that the upstream temperature/(total) divertor radiation do not change while the upstream density scales linearly with the core density [3], leading to the prediction that  $I_t \propto <n_e>^2$ . That scaling is then fitted to the observed trend at an attached phase [73, 101, 58, 45], as shown in figure 2.4 a [101]. Suddenly deviating from this scaling is then attributed to detachment and the amount of deviation is reflected by the ratio between the expected  $I_t$  according to the trend and the measured  $I_t$ ; e.g the DoD as shown in figure 2.4 b. Having a weaker increase of the ion target flux during a density ramp in attached conditions is often attributed to not being able to apply the predicted Two point scaling and thus a lack of high recycling conditions [45]. In this work we evaluate the predicted ion target flux while accounting for changes in upstream parameters accurately, which provides a more nuanced picture than these assumptions. However, nevertheless, as shown in figure 2.4 b, the increase of the DoD is indeed well correlated with the appearance of a simultaneous reduction of target temperature, target heat flux and target ion current; as well as a reduction of target pressure and appearance of a pressure drop.

These techniques focus on measuring the results of detachment, rather than the actual processes which requires volumetric information. Bolometry provides volumetric information on the radiation map through a tomographic inversion. Using this or profile measurements, the radiation region can be tracked and can be observed to move from the target towards the x-point during a density (or seeding) ramp experiment. Other methods which provide such volumetric information are line-of-sight spectroscopy and filtered camera imaging —which provides a 2D picture of a spectral line —applicable for various purposes [76, 121, 122, 123]. For instance, the peak in CIII 465 nm emission monitored in 2D can be seen to move from the target towards the x-point when the divertor is cooled; which corresponds well (in carbon tokamaks without impurity seeding) with the observed peak in radiation measured by bolometry as  $C^{2+}$  is one of the main radiating ions in such conditions [79].

**Diagnosing detachment through line of sight spectroscopy** Line-of-sight spectroscopy (and imaging spectroscopy) can be a very effective tool for diagnosing detached divertor plasmas [41, 51, 76, 124, 125, 63, 62, 64, 74, 73, 126, 61]; electron densities [74, 73, 127]; impurity concentrations [128]; plasma flows [129]; hydrogen molecules [111, 112, 106, 110] and neutral populations [125, 130]. Although such parameters are of value when investigating detachment, detached divertors are most often investigated by measuring the deuterium Balmer lines in the spectrum [51, 62, 63, 76, 125, 73, 124, 74]. When observing the hydrogen Balmer lines, the higher-n Balmer lines are relatively more sensitive to volumetric (electron-ion recombination) compared to lower-n Balmer lines, which are relatively more sensitive to excitation (and molecular reactions [109, 110, 72, 106, 112]). In addition, the higher-n Balmer lines have less wavelength separation and thus multiple Balmer lines can be measured in a single high resolution spectra. These high resolution spectra, together with the more pronounced Stark broadening of higher-n Balmer lines, provides access to inferring the electron density from Stark broadening of the Balmer lines [74, 73, 63, 127, 131]. Therefore, detached conditions are often investigated through the high-n Balmer lines ( $n > 9$ ) or medium-n Balmer lines ( $n = 6, 7$ ), which are measured by a high resolution spectrometer [1, 74, 72, 73, 51, 63, 132, 133].

These high-n Balmer lines ( $n > 9$ ) only tend to appear when recombinative emission is present. The appearance of these Balmer lines is thus an indicator for the *presence* of volumetric recombination, which does not necessarily say anything about the *magnitude* of volumetric recombination. Furthermore, the ratio between the various high-n Balmer lines (assuming the emission only originates from recombination) obey a Boltzmann like scaling when they are in a (partial) local thermodynamic equilibrium [51, 63, 62, 66, 60, 65, 41]. By investigating this scaling, an estimate for the electron temperature, which is a 'characteristic temperature' of the recombination radiation region, can be obtained. Using that electron temperature in combination with an estimate of the electron density obtained through Stark broadening, enables estimating the 'photons to recombination reactions' conversion ratio [63, 62, 66, 80] by using collisional radiative models such as ADAS [134, 135]. Using that ratio, together with an absolutely calibrated spectrometer, where the amount of counts measured on the sensor can be converted to a number of photons emitted by the plasma, and together with the viewing geometry of the system, the volumetric recombination rate can be quantitatively estimated [63, 62, 66, 80]. Such approaches, however, rely on the assumption that all Balmer line emission is due to recombination and thus does not apply that easily to medium and lower-n Balmer lines ( $n < 9$ ), where the emission measured can be due to a mix of excitation and recombinative emission. For reference, an example Balmer line spectra in attached and detached conditions measured on TCV through the diagnostic developed in this work is shown in figure 2.3 (partially adopted from [1]).

**Detachment onset, window and sensitivity** When investigating detachment, it is important to quantify the onset of detachment and the window of detachment. As explained, detachment can be entered through a core density ramp or an impurity seeding ramp or a combination of both. The onset of detachment can be quantified in terms of a detachment threshold, given a series of control parameters (including core density; power crossing the separatrix  $P_{sep}$  and the impurity fraction) [82]. After the onset of detachment is reached and the control parameters are driven further into detachment (for instance a higher core density while keeping  $P_{sep}$  and the impurity fraction constant), at some point the low temperature region will start to expand from the target towards the x-point, evidenced with a movement of peaks of emission lines, ionisation and radiation. The upstream end of that cold region is sometimes defined as the 'detachment front' (or 'thermal front') [82, 113, 136]. The 'speed' (or 'sensitivity') at which the low temperature region expands with respect to the controlling parameter is important for robust control of the low temperature region [82]. This can be determined quantitatively as the partial derivative of the 'thermal front' location to the control variable [82] by quantifying the location of the thermal front, tracking this location and scanning one of the control parameters (preferably while keeping the other constant). During such an experiment 'the range in a control variable within which the front location can be stably held at any position from the target to the X-point' can be obtained, which is defined as the detachment window [82]. Having a low detachment location sensitivity is beneficial for controlling the front location, for instance to actively prevent it from reaching the x-point by altering the control variable or to position the front at a specific location (for instance one which happens to provide the required target parameters while maximising core performance).

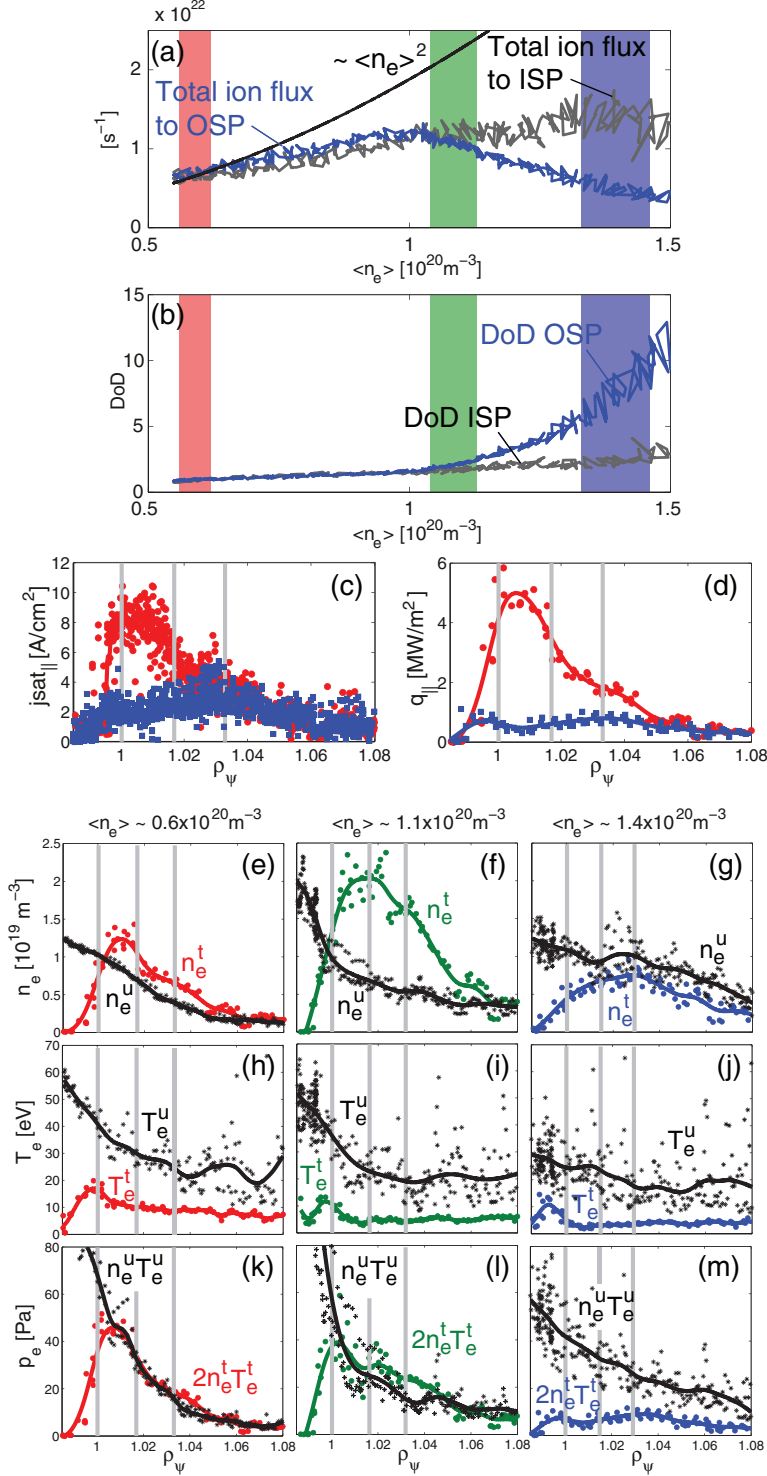


Figure 2.4: Overview of TCV detachment adopted from [101]. a) Ion target current (integrated) evolution during a core density ramp  $\langle n_e \rangle$ . b) Evolution of the degree of detachment during a core density ramp. c) Profiles of the ion target flux compared between an attached/detached phase. d) Profiles of the heat flux at the target compared between the attached/detached phase. e-g) Comparison between upstream (reciprocating probe) and target (Langmuir probe) density profiles during attached/detached conditions. h-j) Comparison between upstream (reciprocating probe) and target (Langmuir probe) temperature profiles during attached/detached conditions. k-m) Comparison between upstream (reciprocating probe) and target (Langmuir probe) pressure profiles during attached/detached conditions.

## 2.4 Atomic physics and its role in divertor physics

Crucial to divertor physics and especially detachment is the role of atomic and molecular processes. The various influences and the various reactions have already been provided in the previous sections. In this section, atomic databases and the various reaction rates of ionisation, recombination and charge exchange will be discussed together with a detailed discussion of impurity radiation and how it can be influenced by transport.

### 2.4.1 Atomic databases and collisional radiative models

Several databases and models are available for modelling reaction rates and emission rates for spectroscopic analysis and radiative power analysis, one of the most prominent being ADAS [134, 135]. ADAS is a collisional radiative model which models the population densities of the energy levels of various ions. It does so by accounting for electron collisional transitions; radiative decay; collisional ionisation and recombination (radiative, dielectronic and three-body are all included). It is thus a general model for modelling populational densities which can be applied in regions where either a coronal approximation (only radiative processes) is appropriate; regions where a (partially) local thermodynamic equilibrium is appropriate (only collisional processes) or regions in between. When modelling populational states through a collisional radiative model, the various reactions in the model acting on the populational densities eventually leads to a large system of equations representing a differential equation for the populational densities [137]. Effective ionisation and recombination rates can be obtained [137, 138] by applying certain groupings of terms in the differential equation —which take a collection of process into account to make up the effective rates [135, 134]. The various line emissivities can be modelled using Einstein coefficients by determining these population densities. By determining those emissivities for the entire spectrum (or for the most energetic lines in the spectrum), the radiated power loss by the plasma due to impurities or hydrogen can be determined.

Collisional-radiative models such as ADAS thus provide information on ionisation rates (named **SCD** in  $\text{reac m}^3 \text{s}^{-1}$ ), recombination rates (named **ACD** in  $\text{reac m}^3 \text{s}^{-1}$ ), radiative power loss rates (named **PLT** for excitation and **PRB** for recombination and Bremsstrahlung both in  $\text{W m}^3$ ) and line emission intensities (named Photon Emission Coefficient —**PEC** for excitation and recombination in  $\text{ph m}^3 \text{s}^{-1}$ ) [138]. These values, provided as tables [134], are functions of temperature and density and need to be multiplied by the respective densities of the two species involved in the reaction process to get the respective reaction/emission/radiation rates as volumetric parameters in the plasma, which can be multiplied with the volume monitored to get the total radiation/emission/reactions. For instance, recombination is an ion-electron process, thus to get a volumetric recombination rate in  $\text{reac m}^{-3} \text{s}^{-1}$ , the ion density would need to be multiplied with the electron density and the ACD coefficient and multiplying that with the volume would result in a recombination rate in  $\text{reac s}^{-1}$ .

To solve the differential system for the populational densities, the number of equations are generally reduced through various assumptions, including those on the starting conditions of the populational densities and their time derivative. It is often assumed, for instance, that only the time variation of the ground state needs to be tracked while the excited states are in quasi-equilibrium as excited states have very short time scales compared to changes in

the ground state, metastable state or plasma parameters. ADAS has some extensions upon this as it is a 'Generalised Collisional Radiative' model [138] (GCR). The advantage of a generalised collisional radiative model is that both ground and metastable populations are tracked, which is important for impurity studies. Furthermore, the influence of excited states on the ionisation balance is accounted for in GCR (like ADAS) while this is not usually done in a 'standard' CR [139]. Including the influence of excited states in the ionisation balance, which is done by ADAS [139], leads to a density dependence of the ionisation rate —which is also found experimentally [139]. ADAS accounts for the atomic level structure in detail to account for excited states in, amongst other things, the ionisation balance.

#### 2.4.2 Hydrogen Ionisation, recombination and charge exchange rates

To investigate the hydrogen ionisation, recombination and charge exchange rates predicted by ADAS, the SCD, ACD and CCD (e.g charge exchange) rate coefficients are shown in figure 2.5 as function of electron temperature. Note that these correspond to reaction rates and not the effective volume rates which requires multiplying with the respective densities. As the ADAS grids in the used ADAS datasets (`scd12_h.dat`, `acd12_h.dat`, `ccd12_h.dat`, `plt12_h.dat`, `prb12_h.dat`, `cccd12_h.dat`, `pec12_h.dat`), which are based on a fairly recent correction on the default hydrogen ADAS dataset in 2012 by Martin O'Mullane [140], are rather coarse, the values have been obtained by interpolating the ADAS datasets. As the ADAS grids correspond to a logarithmic grid and vary over multiple orders of magnitude, the logarithm of the electron density, electron temperature and of the ADAS data is taken. Linear 2D interpolation is then applied, after which the result is re-factorised in order to undo taking the logarithm (e.g  $10^{\text{result}}$ ). This interpolation mechanism has been found to provide the most stable and satisfactory results and obtains identical results to [73].

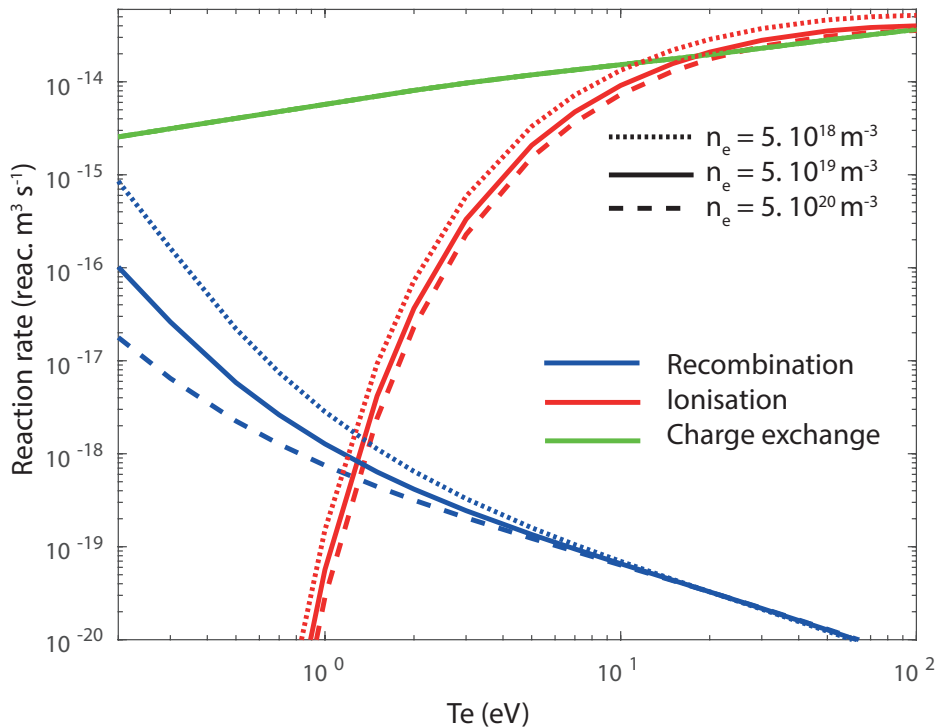


Figure 2.5: Hydrogen effective recombination, ionisation and charge exchange rates as function of electron temperature for three different electron densities.

The shown reaction rates highlight the discussion on the nature of detachment: when the temperature is reduced, first the charge exchange rate starts to become stronger than the ionisation rate (this occurs between 5-10 eV), while going to even lower temperatures results in the recombination rate becoming stronger or similar to the ionisation rate (this occurs between 1-2 eV). One of the reasons for this is a decrease in ionisation rate at lower temperatures. Even at the highest recombination levels, the recombination rate is lower than the ionisation rate at 10 eV. One should note however that these are reaction rates and not volume rates; the effective volume rate of ionisation compared to recombination is also determined by the neutral fraction (under the assumption of a pure hydrogenic plasma,  $Z = 1$ ), which for TCV is around  $1 \times 10^{-3}$  to  $1 \times 10^{-1}$  (see chapter 7). This fraction acts as a weight on the relative importance of ionisation.

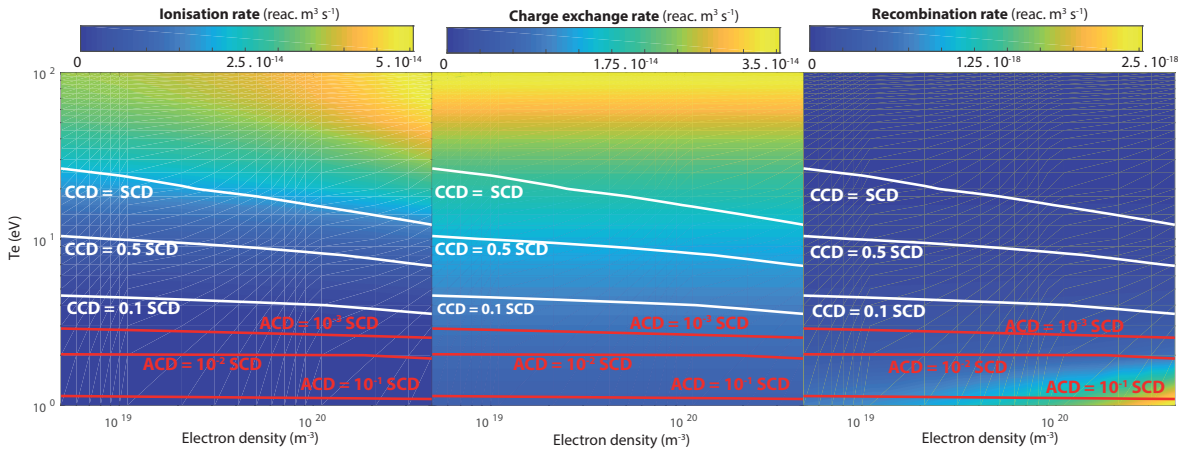


Figure 2.6: 2D maps of effective recombination, ionisation and charge exchange rates as function of electron temperature and electron density with a linear colour map. Contour lines are shown which correspond to cases where the charge exchange rate is 1, 2, 10 times the ionisation rate and where the recombination reaction rate is  $10^{-1}$ ,  $10^{-2}$ ,  $10^{-3}$  times the ionisation rate (which would correspond to a case where the recombination volume rate and ionisation volume rate equal each other assuming a neutral fraction of  $10^{-1}$ ,  $10^{-2}$ ,  $10^{-3}$ ).

All shown reaction rates in figure 2.6 are mostly affected by  $T_e$ , although the recombination and ionisation rate do have some  $n_e$  dependence, which is particularly strong for the recombination rate as shown in the 2D map of reaction rates as function of temperature and density in figure 2.6 on a colour map. Recombination has a strong  $n_e$  dependence as the effective rate is shown which accounts for three-body recombination. This becomes more dominant at high densities (e.g. the effective volume recombination rate increases with  $n_e^{2-3}$  [51, 66]). The contour lines in figure 2.6 show where the charge exchange reaction rate is 1, 2, 10 times the ionisation rate and where the recombination reaction rate is  $10^{-1}$ ,  $10^{-2}$ ,  $10^{-3}$  times the ionisation rate, corresponding to the recombination rate being equal to the ionisation rate at neutral fractions of  $10^{-1}$ ,  $10^{-2}$ ,  $10^{-3}$  respectively. Interesting to note is that in this figure the influence of the electron density on the ionisation rate is more prominent. This is also noted in the contour lines of the charge exchange rate being 1, 2, 10 times the ionisation rate; which shift to lower temperatures when the electron density is increased. This thus highlights the importance of accounting for the  $n_e$  influence on the ionisation rate as is done through the ADAS general collisional radiative model.

#### 2.4.3 Momentum losses due to atomic and molecular reactions

Having discussed the dominance of charge exchange reactions over ionisation in detached conditions, one may wonder why such a dominance would lead to momentum losses in the first place. To highlight this, we first step away from discussing the atomic physics and its databases, to which we will return later and introduce the Self-Ewald model. This is a simplistic analytic model used for highlighting the influence of the dominance of charge exchange over ionisation on momentum loss in literature [3] and is sometimes used for a quantitative comparison [141].

The Self and Ewald model [142, 6, 141, 33] assumes that an isothermal plasma flow occurs to the material surface in a divertor, where this flow travels through a stationary neutral gas. While this process occurs, charge exchange collisions are considered to act as a drag force on the momentum equation, dependent on the charge exchange cross-section, while the heat flow is generating ions, dependent on the ionisation cross-section. Here it is assumed that each charge exchange collision leads to momentum loss. It is then assumed that the Mach number of the flow reaches one near the target, while there is no flow upstream: e.g. the flow is fully determined by a competition between ionisation acting on the flow through the continuity equation and charge exchange slowing down this flow. This reasoning then leads to a relation for a density gradient (which equals the pressure gradient as isothermal field lines are assumed), which depends on the ratio between the ionisation cross-section and the charge exchange cross-section given by equation 2.9, where  $\langle \sigma v \rangle_{CX}$  and  $\langle \sigma v \rangle_{ion}$  are respectively the charge exchange and ionisation cross-sections [33].  $f_{mom}$  is defined similarly as in section 2.2; e.g.  $p_t = f_{mom} p_u$ .

$$f_{mom} = 2 \left( \frac{\alpha}{\alpha + 1} \right)^{\frac{\alpha+1}{2}} \quad (2.9)$$

$$\alpha = \frac{1}{1 + \frac{\langle \sigma v \rangle_{CX}}{\langle \sigma v \rangle_{ion}}}$$

The ratio between charge exchange and ionisation is around 1 and strongly increases above that when dropping from above 10 eV to 5 eV and lower, decreasing  $\alpha$  from approximately 0.5 towards 0; resulting in a drop of  $f_{mom}$  from almost 1 (e.g. 0.9) towards 0; as shown in figure 2.7 where ADAS rates were used to interrogate equation 2.9. More specifically, this figure shows that  $f_{mom}$  is mostly a function of temperature (weak density dependence) and results in  $f_{mom} > 0.9$  at a temperature of  $\geq 7$  eV, which transitions into  $f_{mom} < 0.1$  at a temperature of  $\leq 2$  eV.

As this model assumes isothermal field lines (which is not true under tokamak divertor conditions), measurements of target temperatures are used to interrogate the reaction rates [141], which makes the Self-Ewald model essentially a function of target temperature. This temperature is lower than temperatures higher up the divertor leg resulting in higher charge exchange to ionisation ratios and higher momentum loss estimates (likely overestimation). Although the Self-Ewald model is not an accurate physics picture of the divertor processes (as the divertor is not isothermal), its results are often in fair agreement with modelling and measured momentum loss [141, 4, 41]. That agreement may arise 'accidentally' from the temperature trend of  $f_{mom}$  predicted through the Self-Ewald model, rather than the Self-Ewald model predicting the underlying physics correctly.

Various measured and simulated momentum loss values have been collected in literature

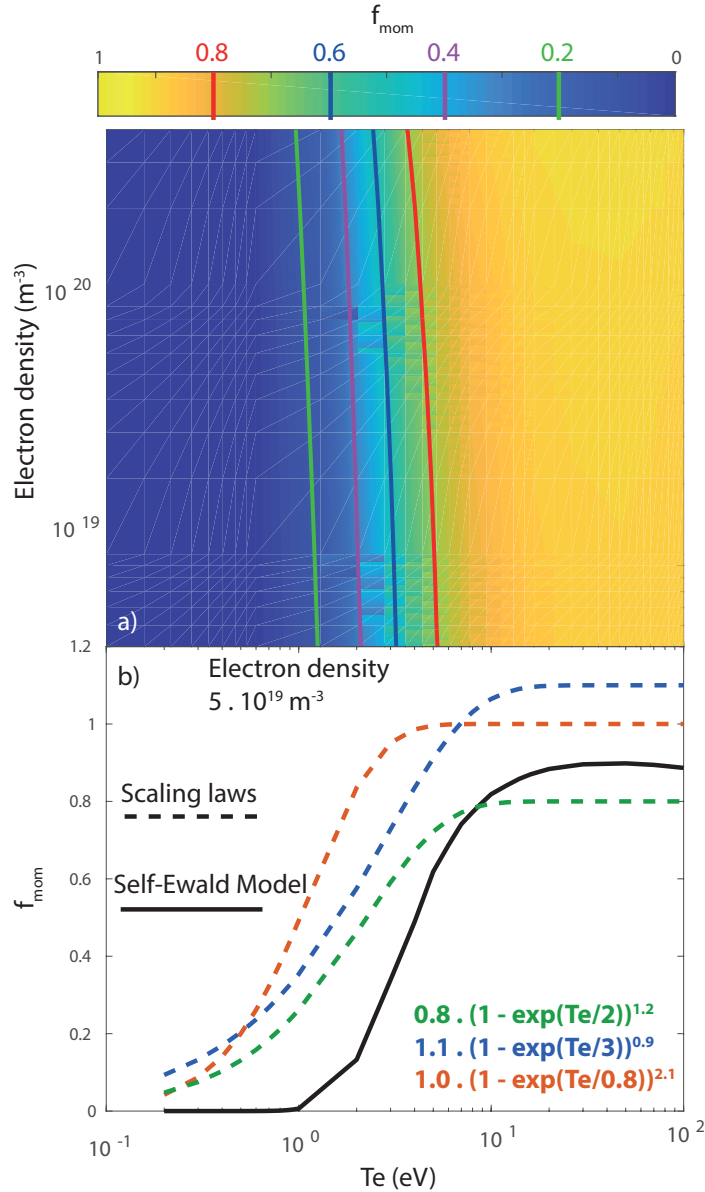


Figure 2.7: a) 2D evaluation of  $f_{mom}$  through the Self-Ewald model as function of  $n_e, T_e$  using ADAS and equation 2.9 with contour lines. b)  $f_{mom}$  as function of  $T_e$  (for  $n_e = 5 \times 10^{19} m^{-3}$ ), together with several scaling laws obtained from [4, 49].

[4, 49] and several scaling laws for momentum loss are proposed, some of which are shown in figure 2.7 b and compared to the Self-Ewald model. The behaviour of the relation is qualitatively similar to the Self-Ewald result but quantitatively different. The Self-Ewald model predicts a stronger momentum loss than the other scaling laws, which could be due to the charge exchange to ionisation ratio being higher at the target; thus overestimating the momentum loss in the Self-Ewald model.

However, the relations of  $f_{mom}$  obtained through the scaling laws are obtained by fitting SOLPS data from various sources in [4]; which take more processes into account than just charge exchange dominating over ionisation, for instance molecular processes. Instead of charge exchange dominating over ionisation, it may be some of these other processes resulting in momentum losses being a strong function of temperature. SOLPS simulations have shown a strong correlation between the molecular deuterium density in the divertor and the target

electron temperature [78]. Other SOLPS simulations have indicated that molecules play a strong role in reducing momentum in the divertor as opposed to charge exchange dominating over ionisation [50, 78]; while other SOLPS simulations suggest the influence of molecules is small on momentum losses [141]. In addition, differences in transport could contribute to the observed and simulated pressure loss during detachment —for instance, cross-field transport may ‘smear-out’ pressure across the field lines, leading to a reduction in the high pressure regions near the separatrix [141].

Volumetric recombination also leads to momentum losses [51, 54, 143]. Using a simplified model of momentum loss due to recombination as provided by [143], the relative importance between momentum loss through ion-neutral friction and momentum loss through recombination is equal to the ratio between the recombination and charge exchange rates multiplied with  $\frac{1}{1-\frac{v_H}{v}} \times \frac{1}{n_H/n}$  where  $n_H/n$  is the neutral fraction ( $10^{-3}$  to  $10^{-1}$ ) and  $\frac{v_H}{v}$  is the neutral to ion velocity ratio. When assuming kinetic velocities, for TCV parameters, the expected momentum loss through recombination is negligible. Furthermore, momentum losses start to occur in a higher temperature regime (1-10 eV) where the charge exchange cross-section is  $10^{3-4}$  higher than the recombination cross-section as shown in figure 2.5. Thus, recombinative momentum loss may be a secondary effect when deeply detached but it will be negligible at the onset of detachment.

#### 2.4.4 Hydrogen Balmer Line emissivities

The spectral emissivity of a hydrogen plasma with a certain electron density, electron temperature and neutral density can be modelled by multiplying ‘Photon Emission Coefficient’ (PEC) provided by ADAS [134, 138, 140, 135] with the respective densities of the two reacting species (e.g for excitation emission the neutral density times the electron density; for recombinative emission the electron density times the ion density) —which then forms the emissivity per volume:  $\text{ph m}^{-3} \text{s}^{-1}$ .

The PEC coefficient corresponding to the low-n and medium-n Balmer lines (e.g  $n = 3 - 8$ ) are shown in figure 2.8 for both recombination and excitation at three different electron densities. Qualitatively, a similar behaviour as between the ionisation rate and recombination rate (figure 2.5) is shown as between the PECs for every Balmer line. Despite each Balmer line having a similar behaviour of the excitation and recombination PEC, the deviation between the excitation PECs between different Balmer lines is greater than for the recombination PECs and thus the point where the recombination and excitation PECs cross each other is at higher temperatures for higher-n Balmer lines. This means the emission of a higher-n Balmer line will be more susceptible to recombination than of a lower-n Balmer line: e.g the relative influence of recombination on each Balmer line increases with increasing  $n$ . When increasing the electron density, the excitation PECs decrease slightly while the recombination PECs increase. Thus, for higher density conditions, the emission of a Balmer line will be dominated by recombination at higher temperatures. Two important points should be noted: 1) to get actual emissivities the PECs need to be multiplied by the respective densities, so the relative importance between excitation/recombination emission depends also on the neutral fraction. 2) having recombination emission dominate over excitation emission does not imply that the recombination rate dominates over the ionisation rate.

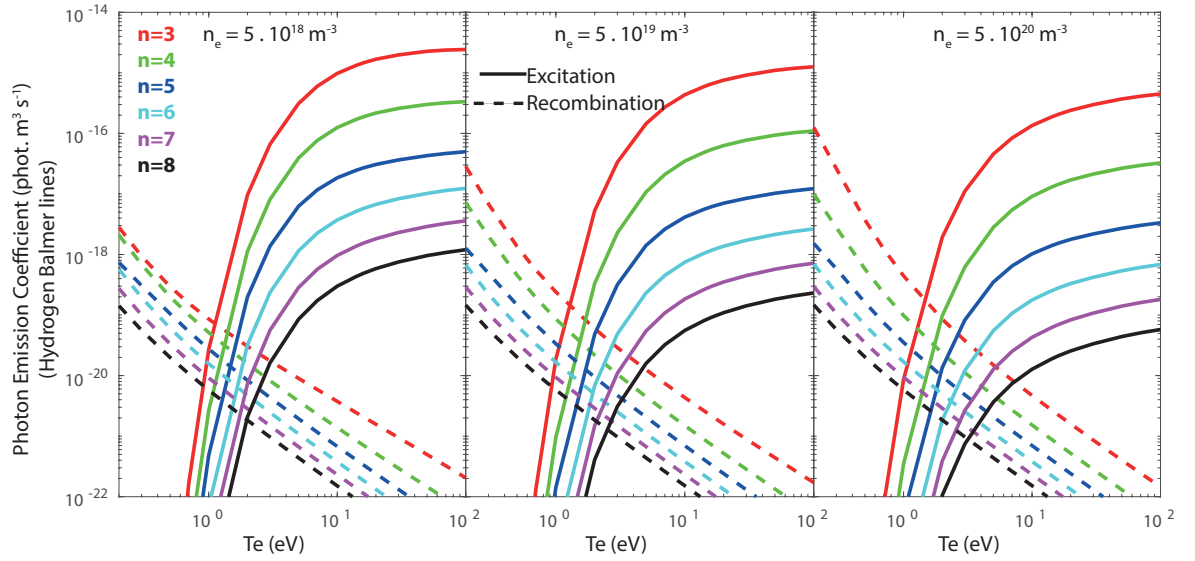


Figure 2.8: Photon emission coefficients (PEC) for the hydrogen Balmer lines of  $n = 3 - 8$  as function of  $T_e$  for three different electron densities. Both the excitation and recombination PECs are shown.

#### 2.4.5 Hydrogen radiative losses

Summing the radiation arising from line emission according to the ADAS PECs provides information on the hydrogenic radiative power loss, which are ultimately tabulated as the PLT (excitation radiation) and PRB (recombinative radiation, which also contains continuum emission arising from recombination and Bremsstrahlung) rates. We apply a correction to the PRB rate using [30] in order to subtract the Bremsstrahlung component and only get the radiation arising due to recombination (both line emission and continuum emission).

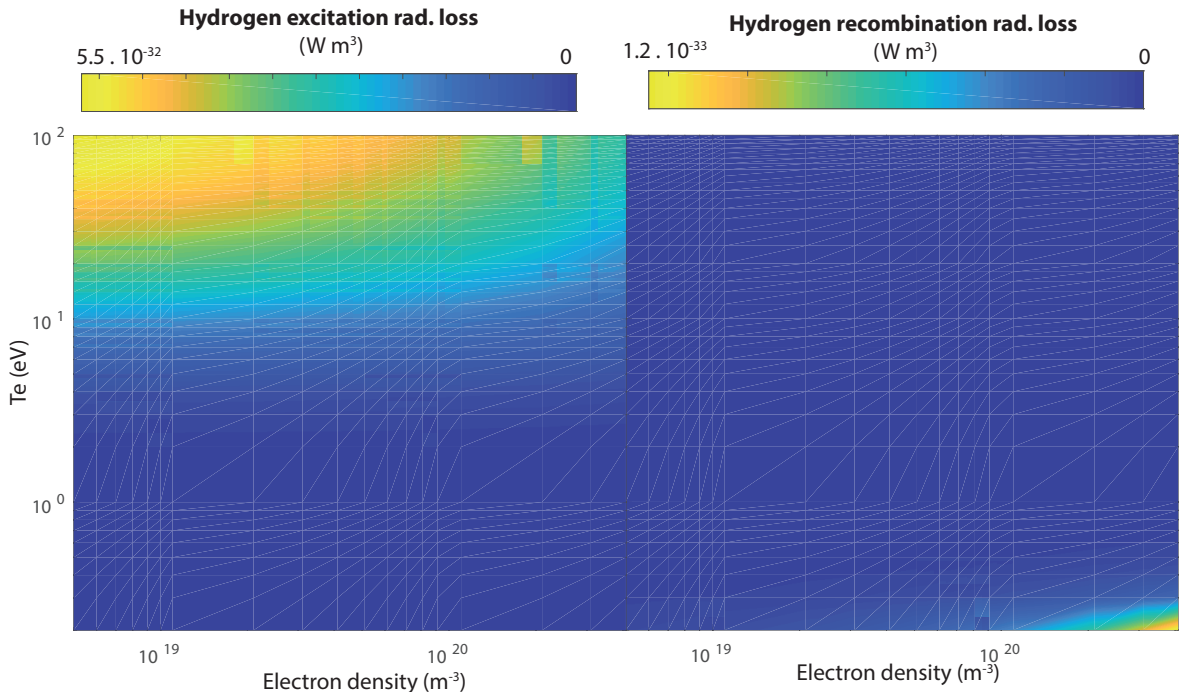


Figure 2.9: 2D maps of the PLT and (corrected) PRB coefficients as function of electron temperature and electron density with a linear colour map.

These rates are shown for hydrogen in figure 2.9 and indicate a similar behaviour as the PECs: the hydrogen excitation radiation loss strongly reduces at low temperatures while the hydrogen recombination radiation loss strongly increases at low temperatures. Furthermore, again, both have a density dependence: the hydrogen excitation radiation loss decreases at higher electron densities while the recombination radiation loss increases. Note that the maximum PRB value shown is still a factor 50 smaller than the maximum PLT value: radiative losses due to recombination thus appear minor compared to radiative losses due to excitation (however, the relation between the volumetric radiative losses of excitation and recombination depends on the neutral fraction as well).

As will be discussed later, an important parameter is the hydrogenic ionisation energy cost (chapter 3); which is partially made up by the division between the hydrogenic excitation radiative loss and the ionisation rate (e.g excitation radiative loss per ionisation event). In figure 2.6 we saw that the ionisation rate increases at higher electron densities while figure 2.9 indicates the opposite trend for the hydrogenic excitation radiative loss. In other words, the radiative energy loss due to excitation per ionisation will be higher at low densities than at high densities. As will be shown in figure 3.2, the trend of  $E_{ion}$  remains unchanged; the deviation in  $E_{ion}$  between  $n_e = 1 \times 10^{19} \text{ m}^{-3}$  to  $1 \times 10^{20} \text{ m}^{-3}$  is approximately 20 %.

#### 2.4.6 Impurity radiation —carbon

Impurity radiation (carbon) can also be analysed through the ADAS PLT, PRB and PRC (radiative power loss due to charge exchange between hydrogen and the impurity) coefficients. Of these coefficients we will only focus on the PLT coefficient, which is far dominant for carbon radiation on TCV.

When investigating the PLT coefficients for carbon, each ion charge state has its own PLT value. Metastable resolved PLT values are also available, but for simplicity unresolved values are used (e.g. it is assumed that the ground states of carbon ions are dominant). All ion-charge resolved PLT curves as function of temperature assuming an electron density of  $n_e = 5 \times 10^{19} \text{ m}^{-3}$  (although the influence of  $n_e$  is negligible) are shown in figure 2.10. These deviate significantly between the different charge states: the PLT for  $C^0$  to  $C^{3+}$  is much larger than the PLT corresponding to  $C^{4+}$  and beyond. In order to calculate the expected carbon radiation, one not only needs to know the overall carbon content but more specifically the charge-state resolved carbon content, which can be known through the 'fractional abundance' (e.g fraction of carbon which is in a certain charge state) times the total carbon density [137]. Often, no transport assumptions are used to have a rough idea of the general radiation curves; which means that the fractional abundance is set by a ratio between ionisation and recombination [96, 54]. Using such a prediction together with the charge-resolved PLT coefficients, a rough predictive 'effective' PLT can be determined assuming ionisation balance while neglecting transport, shown for carbon in figure 2.10.

However, transport effects can be extremely important in explaining / modelling the radiation expected of a particular impurity [91, 95]. Transport influences the temperature regime in which a certain charge state can be found. For instance, transport can enable  $C^{3+}$  ions to travel through a higher temperature region where they would normally not occur as they would ionise; thus increasing the effective radiation. Divertor simulation packages such as SOLPS-ITER can track the various impurity charge states (and where applicable

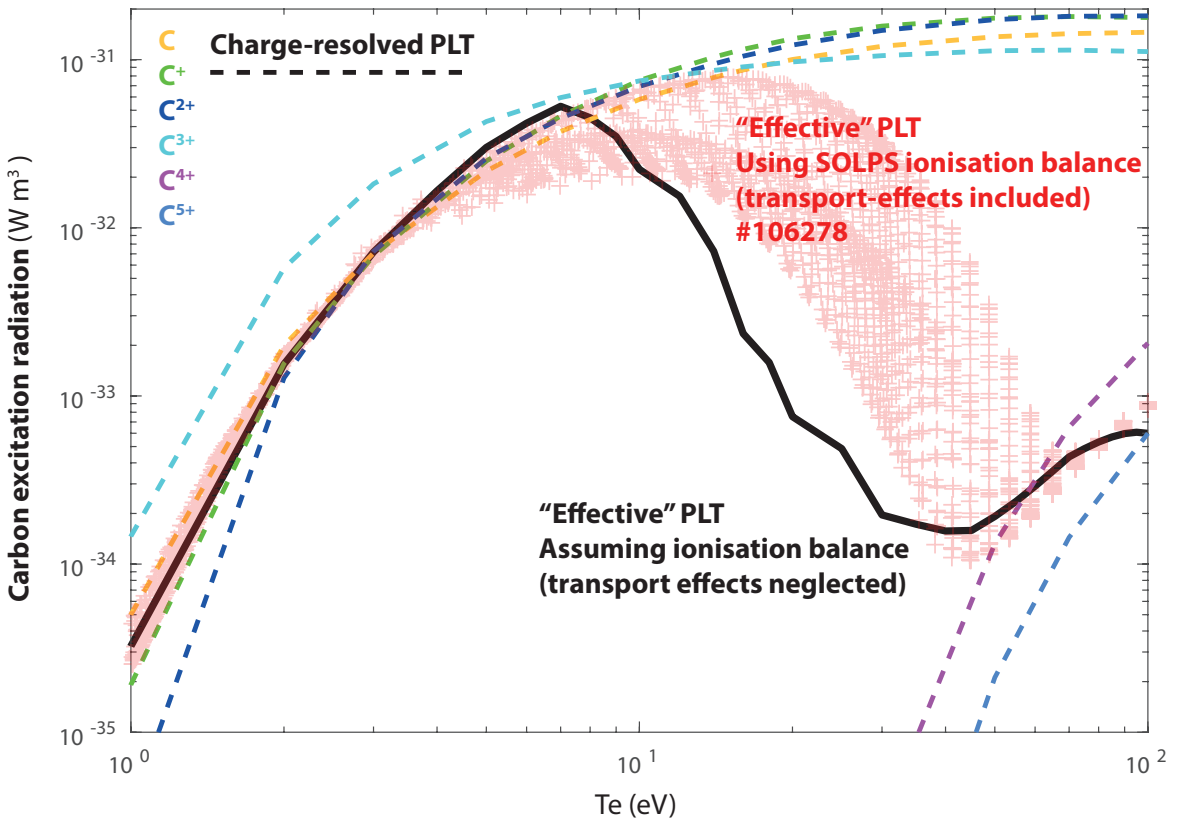


Figure 2.10: Charge resolved carbon PLT coefficients as function of temperature. An effective PLT—which is determined assuming ionisation balance determined through ionisation and recombination coefficients and assuming no transport is shown. An ‘effective’ PLT curve which includes TCV simulated transport is shown for a SOLPS modelled discharge # 106278 where the effective PLT is determined by determining the individual PLTs for each charge state in the grid cell using  $n_e$ ,  $T_e$  and multiplying those with the simulated fractional abundances obtained from the SOLPS simulation. All PLT values for all grid cell are shown where one data point represents one grid cell.

metastables) individually to account for transport. Using a SOLPS-ITER simulation of a TCV detached discharge (#106278), the ‘effective’ PLT is calculated by using the simulated fractional abundances obtained from SOLPS which are multiplied with the charge-resolved PLT tables obtained from ADAS using the SOLPS simulated  $n_e$ ,  $T_e$ . This result is shown in figure 2.10 for each SOLPS grid cell. For a fixed  $T_e$  a range of PLT values is obtained, covering one order of magnitude, as the fractional abundances from two grid cells can be different—due to transport—despite their temperatures being the same. This range in obtained PLT values for a given fixed  $T_e$  illustrates the influence ‘simulated’ transport can have on carbon radiative losses. It should be noted, however, that this result is likely different from including transport by assuming a fixed ‘residence time ( $\tau$ )’ [91], which relies on a simplified model for transport [144] and relies on assuming a single lifetime; e.g. a range of lifetimes [95] would be required to describe the non-uniqueness of the effective, SOLPS-transport included, PLT observed. The point where the PLT for carbon is maximised is around 8 eV assuming a no transport assumption, while the SOLPS simulated case has a maximum at 15-20 eV and a difference up to a factor 100 can occur between the two around 20 eV. Accurately accounting for impurity transport is thus crucial for modelling and understanding impurity radiation.

Transport is not only crucial for describing impurity radiation, but also for explaining trends in the hydrogenic line emission. As explained, to compare the excitation and recombination values to each other in terms of volumetric parameters; we needed to assume a neutral fraction. By using no transport assumptions, one can obtain such a value as function of temperature through an ionisation and recombination balance. For TCV this, however, leads to grossly different parameters and dynamics as those found from measurements, while the TCV SOLPS-ITER simulations are in agreement with the measured results. This will be further discussed in chapter 7, where the methodology for quantitative analysis of the hydrogen Balmer lines developed in this paper will be discussed.

#### 2.4.7 Molecular reactions

As discussed, molecules may lead to momentum losses in the divertor. The plasma ions can undergo charge exchange collisions with the molecular cloud in the divertor, and through this momentum can be lost. Molecular reactions can also influence particle balance through molecular activated recombination (MAR) and molecular activated ionisation (MAI), where molecules contribute to recombination and ionisation [112, 106].

Diagnosing the rich molecular physics is complicated and requires measurements of the Fulcher molecular band [106, 112] as well as collisional radiative models which account for molecular processes such as Yacora [145]. The complicated part is that molecules can undergo a large subset of different reactions, which also depend on vibrational populational states. Furthermore, diagnosing the Fulcher band is tricky as their emission is extremely small (on TCV we measure they are roughly  $10^5$  smaller than  $D\alpha$ ), and requires both a high resolution (sub-angstrom —preferably higher) and a large spectral coverage (40 nm). Due to this, the experimental investigations of the physics of molecules and their role on detachment is fairly limited experimentally, but has been done in [106, 112]. Modelling efforts have also been done to investigate the influence of molecular reactions on the divertor. These have found that MAR/MAI is relatively small for tokamak conditions [108], while the expected power loss due to molecules is expected to be limited [110]. In other conditions, however, such as in linear machines, they have found that MAR can be a very important process and the main contributor to detachment by diagnosing the Balmer series [109]. Molecules are expected to contribute to the Balmer line emission, especially  $D\alpha$  [110, 5, 130, 112, 106] and also  $D\beta$  [5]; which is not accounted for by the ADAS collisional radiative model but can be modelled through SOLPS-ITER. Likely, measuring  $D\alpha$  with respect to other Balmer lines and comparing this to SOLPS-ITER simulation results is one of the quicker and easier ways of obtaining qualitative information on molecular reactions in the plasma.

However, the precise role of molecules in divertor physics is currently unknown and more investigations would need to be performed.

### 2.5 Alternative geometries and divertor performance

By shaping the plasma equilibrium by using multiple coils around the vessel —to which TCV has access [146, 101, 147, 34] —the divertor geometry can be modified by moving the position of the x-point, strike points, adding flux flaring and adding a secondary x-point close to the primary x-point (snowflake). Such modifications are often referred to as 'advanced' divertor

geometries [101, 147] and potentially lead to reductions of the peak heat load, detachment threshold, detachment sensitivity and an increase in detachment window —overall aiding access to and robustness of detachment [148]. An overview of some different geometries obtainable in TCV is shown in figure 2.11.

In the snowflake divertor [149] a second x-point is added close to the original single null x-point, leading to two extra divertor legs. In an exact snowflake, the second x-point is positioned at the first x-point, creating a second order null where the derivative of the poloidal magnetic field is zero. However, the two X-point locations are often somewhat separated as an 'exact' snowflake would be hard to control. The shown snowflake configuration in figure 2.11 corresponds to a so-called snowflake +.

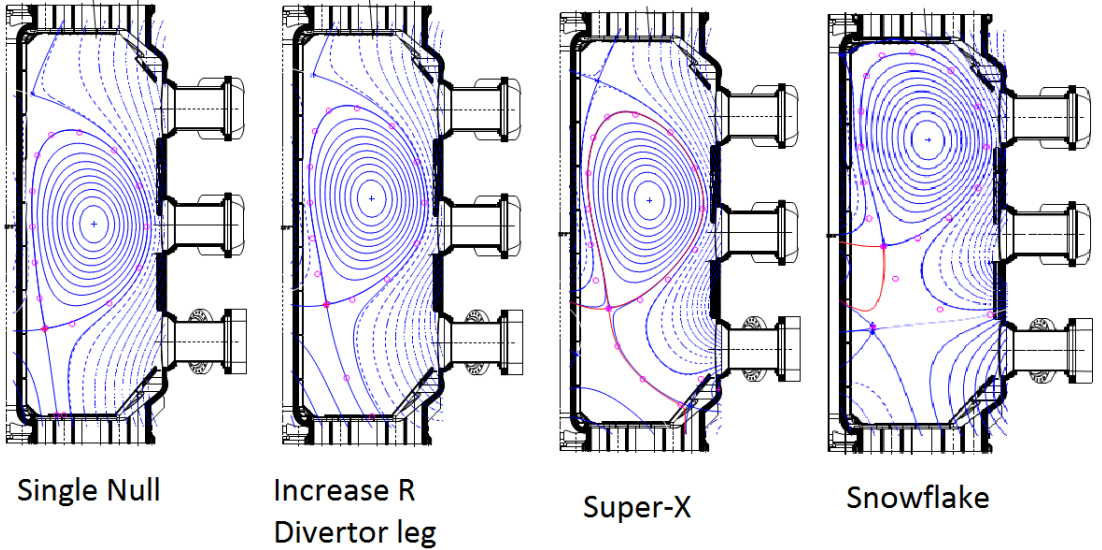


Figure 2.11: Designed TCV magnetic geometry configurations, corresponding to single-null, snowflake, super-X divertor geometries.

By moving the plasma column vertically, in the TCV tokamak it is possible to realise different type of snowflake configurations (e.g '+' and '-') [150]. Observations of the snowflake divertor indicate that the connection length and magnetic shear is increased in the snowflake configurations [150, 151]. The increase in connection length leads to a higher collisionality in the SOL and larger divertor volume, which may facilitate divertor radiation, aiding detachment access. H-mode snowflakes have been achieved in the TCV tokamak, which indicate a reduction in ELM frequency and a reduction in ELM energy losses [151, 152]. The large magnetic null region in the snowflake also is purported to have a stabilising effect on the movement of the radiation front during detached conditions [147].

The X-divertor is a magnetic geometry with an added x-point close to the target outside of the vessel, resulting in flux flaring close to the target. This differs from a snowflake divertor where the additional x-point is close to the original x-point [148, 153] and thus the x-point region is modified instead of the target region. Due to the flux flaring, the field lines are diverging to the target for the X-divertor [148], which may have a stabilising effect on detachment sensitivity [148] as the interaction region of the plasma with neutrals is reduced when going from the target towards the x-point resulting in an intrinsic feedback system for various detachment 'fronts'. Another predicted benefit of the X-divertor is an increased flux

expansion near the target which broadens the wetted area and increases the radiating volume.

A variation on the x-divertor is the super-X divertor, which is planned to be installed on MAST upgrade [154, 155, 156, 157]. In the super-X divertor, the divertor leg to which an X-point is added at the target or outside the vessel is brought out to the low field side of the tokamak, expanding the radius of the divertor leg, expanding the plasma wetted area with respect to the single null, X-divertor and snowflake divertor. Additionally, analytic and SOLPS modelling predicts [82, 50, 158] this stabilises the thermal front and hence decreases detachment front sensitivity [82, 159].

A second variation on the x-divertor and super-x divertor is the x-point target divertor. In the x-point target divertor, the secondary x-point is not positioned outside the reactor, but just in front of the target, which can also be combined with increasing the radius of the divertor leg [159]. By positioning an x-point close to the target, the poloidal field is further reduced and the flux expansion and connection length is further enhanced. It is expected that by positioning a secondary x-point near the target, an x-point radiation region will form near the target in the divertor volume, which potentially counters the detachment front moving to the x-point, allowing fully-detached operation over a large operational space.

## 2.6 Advanced modelling of divertor plasmas and detachment: SOLPS-ITER

Although simplified models such as the two point model are often used for quick experimental comparisons and for getting a rough idea of the different scalings in detachment, the actual —‘real’—detachment dynamics are far more complicated. First of all, simplified models such as the two point model lack the complex atomic and molecular physics required, which form the key to detachment (sections 2.3, 2.4). Secondly, the nature of the neutrals must be addressed and is intrinsically of a 2D nature. An accurate treatment of the neutrals thus requires a 2D simulation, which can for instance be accounted for using a Monte Carlo code.

One of the most often used suites for advanced divertor modelling is SOLPS-ITER [160, 161]. SOLPS combines a fluid code, B2.5 [162], which solves the Braginskii equations for ions and electrons together with EIRENE [69, 162], which is a Monte Carlo neutral code which also incorporates several atomic, molecular and chemical physics databases. Reactions such as volumetric recombination, molecular activated recombination, transport of metastables, chemical sputtering and more can for instance be taken into account through this code. The works in [68, 53, 7, 98, 90, 67, 50] contains several investigations performed using either SOLPS-ITER or other versions of SOLPS.

After a SOLPS solution is obtained, the result provides plasma parameters such as the electron density, temperature, neutral density, charge-resolved impurity densities and more for each simulated grid cell. Target parameters (such as the ion target current) are also provided by the model. Such parameters can be compared to measured parameters in experiments. This can also be performed by using the SOLPS output to simulate a synthetic signal of what a certain diagnostic would measure given that output. In this way a more direct comparison between the model result and the experiment can be performed. In this work, an in-depth comparison between the experiment and SOLPS results is performed (sections 8.1.1) employing synthetic diagnostics as discussed in sections 4.3, 5.8.

# Chapter 3

## Analytical divertor models

*Analytic models describing power/particle/momentum balance are introduced with a focus on high recycling divertor operation and are used to illustrate TCV divertor dynamics both before and after detachment. In this chapter several additions to works in literature by Peter Stangeby [4, 3] and Sergei Krasheninnikov [6, 5] on these models have been made highlighted specifically with boxed frames. This is combined with a more explicit derivation of such models and re-arranging the various equations to bring together 'seemingly' contrasting arguments in literature. An explicit illustration of model predictions for the TCV operational regime is shown.*

Parts of this chapter have been adopted from: *An improved understanding of the roles of atomic processes and power balance in target ion current loss during detachment*, by K.

Verhaegh, B. Lipschultz, B.P. Duval, et al., to be submitted. DOI:

<https://doi.org/10.13140/RG.2.2.24292.48005/1>

Power and particle balance of the recycling region (section 3.1) provides us with a model (ignoring recombination for the below discussion) for the ion current ( $I_t$ ) dependent on the power entering this region ( $P_{recl}$ ), the energy cost per ionisation ( $E_{ion}$ ) and the fraction of that power utilised for ionisation. That fraction depends on the ratio between the power spent on ionisation ( $E_{ion}$  per ion) and the power reaching the target in the form of kinetic energy ( $\gamma T_t$  per ion) — $\gamma T_t/E_{ion}$ . This ratio will play a crucial role throughout this chapter. To model the ion current in terms of power and particle balance, one needs a priori knowledge on  $\gamma T_t/E_{ion}$ . However, the observation that almost all of  $P_{recl}$  is spent on ionisation (ignoring recombination), would already intrinsically suggest that  $\gamma T_t/E_{ion} \rightarrow 0$  and is thus *operationally* sufficient to say that ion source can be fully described by power/particle balance alone, using  $P_{recl}$  and  $E_{ion}$ .

That, however, requires already (strongly) detached conditions ( $T_t \ll E_{ion}/\gamma$ , where  $E_{ion}/\gamma$  is generally around 4 – 7 eV). For other cases one needs to account for the behaviour of  $T_t$  —which is not provided by power/particle balance as it requires  $T_t$  as an input value. To model the behaviour of  $T_t$ , power and particle balance need to be combined with the sheath target boundary (equation 1.1), which links  $T_t$  to the ion source and the target pressure ( $p_t \propto I_t T_t^{1/2}$ ). In other words, one has to account for target pressure trends and power/particle balance simultaneously to get a full picture of divertor operation and detachment. That can be achieved by combining equations 1.2 and 1.1, resulting in a 'Two Point (like) Model' (discussed previously in section 2.2) which accounts for particle balance and Recycling power

losses (e.g. '2PMR'). The target pressure is however not considered a control parameter in the divertor, while the upstream pressure is. Including momentum balance, the upstream pressure  $p_u$ , heat flux entering the recycling region ( $q_{recl}$ ) and  $E_{ion}$  become the driving parameters of the 2PMR, which then forms a power/particle/momentum balance model (section 3.3). That model enables one to merge two paradigms of thinking about detachment in terms of momentum losses and thinking about detachment in terms of power limitation.

### 3.1 Power and particle balance

To model the target flux in terms of power and particle balance, first we must discuss and investigate in more detail the principle power loss/gain and particle loss/gain processes in the divertor, which were introduced in section 2.3 and which are visualised in figure 3.1. Although the power and particle balance described/shown in this section apply to the entire (outer or inner) divertor, these equations can also be applied to individual flux tubes, under the assumption that heat and particle transport across the flux tubes in the divertor is negligible.

The power entering the divertor,  $P_{div}$ , is lost partially due to radiation,  $P_{rad}$ , after which the remaining power ends up at the target ( $P_{target}$ ): both in the form of potential energy  $P_{target}^{pot} = I_t \epsilon$  and kinetic energy  $P_{target}^{kin}$ . Here,  $I_t$  is the (integrated) ion target flux (ion/s),  $\epsilon = 13.6\text{ eV}$  (where for simplicity the energy associated to molecular dissociation —2.2 eV—is omitted [90]) is the surface recombination term (e.g. the potential energy deposited per ion which recombines at the divertor plate) and  $\gamma$  is the sheath transmission factor used previously in chapter 2.2. Therefore, divertor power balance can be written as shown in equation 3.1.

$$P_{div} - P_{rad} = P_{target} = P_{target}^{pot} + P_{target}^{kin} = I_t(\gamma T_t + \epsilon) \quad (3.1)$$

The radiated power in equation 3.1 can be split into different portions: hydrogenic radiation and impurity radiation. Hydrogenic radiation has both an excitation ( $P_{rad}^{H,exc}$ ) and a recombination ( $P_{rad}^{H,rec}$ ) contribution as shown in equation 3.2. Any radiated power due to hydrogen molecules is ignored here, which is expected to be fairly small [110].

$$P_{rad} = P_{rad}^{H,exc} + P_{rad}^{H,rec} + P_{rad}^{imp} \quad (3.2)$$

Separating hydrogenic and impurity radiation is crucial for understanding the detachment process in high recycling divertors as the hydrogenic excitation radiation increases depending on the ionisation (as will be shown below) and thus the ion target flux. It is therefore an integral aspect of combining power/particle balance. However, separating impurity radiation and hydrogenic radiation is experimentally generally not performed as radiation is measured through bolometry, which provides the total radiative loss. However, hydrogenic or impurity radiation can be estimated through using collisional radiative modelling, combined with temperature, density, transport and concentration estimates/assumptions, which can be paired with spectroscopy (as will be shown in section 7) to reduce the number of unknowns and/or by using absolutely calibrated VUV measurements [163, 126]. If one were to infer the hydrogen radiated power from spectroscopy, one could obtain impurity radiation by combining these inferences with bolometric measurements.

After having established power balance, we will move towards particle balance. Generally speaking, the sum of the divertor ion source ( $I_i$ ) and the net ion flow towards (or away from)

the divertor ( $I_{up}$ ) minus the divertor ion sink (e.g. recombination) ( $I_r$ ) equals the ion target flux. Under high recycling conditions,  $I_i$  will strongly dominate over  $I_{up}$ . In that case  $I_{up}$  can be neglected, also referred to as the 'closed box' approximation [5, 6, 51, 52], shown in equation 3.3. This approximates particle balance in the divertor to be fully closed from upstream flows; flows from one divertor leg to the other and puffing/pumping [5] are either neglected or assumed to balance each other.

$$I_t = I_i - I_r \quad (3.3)$$

To obtain further insight into the interplay of power and particle balance in the divertor, we can combine the two through combining equations 3.1, 3.2 and 3.3, resulting in 3.4. The terms underlined in equation 3.4 show the influence of all the different processes highlighted in figure 3.1.

$$\underbrace{(P_{div} - P_{rad}^{imp})}_{P_{recl}} - \underbrace{(P_{rad}^{H,exc} + \epsilon I_i)}_{P_{ion}} - \underbrace{(P_{rad}^{H,rec} - \epsilon I_r)}_{P_{rec}} = \underbrace{I_t \gamma T_t}_{P_{target}^{kin}} \quad (3.4)$$

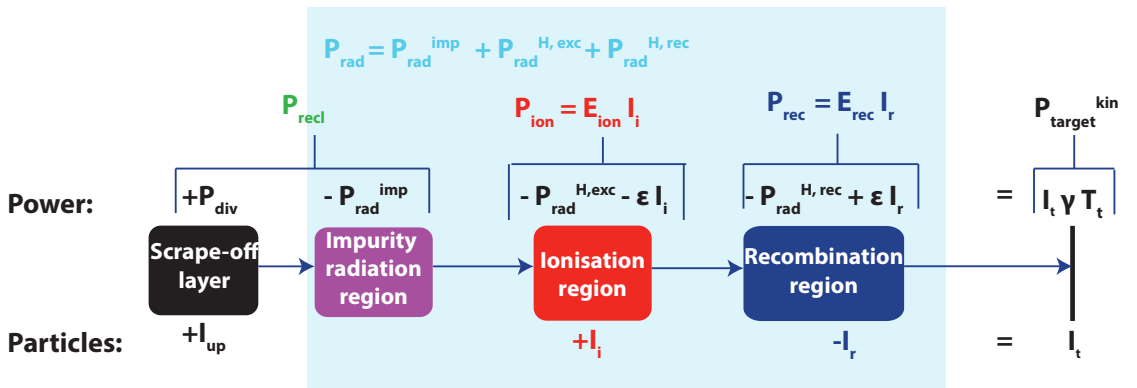


Figure 3.1: Schematic overview of power and particle balance in the outer divertor. The blue shaded region represents the divertor. The various parameters are defined in the text.

Using this separation of the different regions, we can define the power entering the recycling region ( $P_{recl}$ ) to be provided by equation 3.5. Note that the separation of these regions is a visualisation tool and the application here does not rely on this separation.

$$P_{recl} = P_{div} - P_{rad}^{imp} \quad (3.5)$$

In the recycling region, that power passes first through the ionisation region, where neutrals are converted into ions with an energy cost of at least  $\epsilon$  per ionisation event. However, before ionisation occurs, multiple excitation collisions precede, which lead to radiative losses. Such radiative losses ( $P_{rad}^{H,exc}$ ) can hence be counted as an energy 'cost' due to ionisation [51, 3, 69, 5, 6]. The total power spent on ionisation ( $P_{ion}$ ) is then provided by equation 3.6a, where the effective energy loss per ionisation event  $E_{ion}$  is obtained by dividing  $P_{ion}$  with the

ionisation source  $I_i$ .

$$P_{ion} = P_{rad}^{H,exc} + \epsilon I_i \quad (3.6a)$$

$$E_{ion} = \frac{P_{ion}}{I_i} = \frac{P_{rad}^{H,exc}}{I_i} + \epsilon \quad (3.6b)$$

An evaluation of  $E_{ion}$  is shown in figure 3.2 as function of  $T_e$ . In that graph,  $E_{ion}$  has been divided by  $\gamma$  for future reference where we will see that  $T_t = E_{ion}/\gamma$  is an important detachment threshold.  $E_{ion}$  at relatively high temperatures ( $> 15$  eV) is approximately constant while  $E_{ion}$  strongly increases when the temperature drops below 5 eV as more excitation collisions are required to have a single ionising one; resulting in relatively higher radiative losses per single ionisation event.

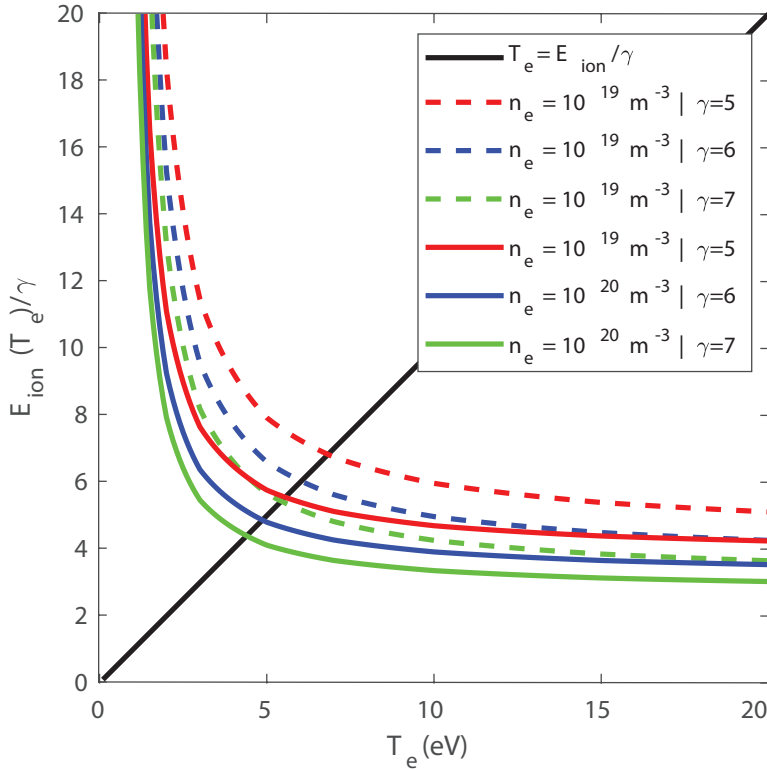


Figure 3.2:  $E_{ion}/\gamma$  as function of  $T_e$  including the  $T_e = E_{ion}/\gamma$  curve for a range of  $n_e$  and  $\gamma$ .

Apart from momentum losses in detached conditions, charge exchange can also transport hot ions away from the plasma towards the side walls if the neutrals after charge exchange can travel a sufficient distance before re-ionising, making it a power loss. Charge exchange is a neutral-ion collision while ionisation is a neutral electron collision; both thus depend on the neutral density. In other words, the 'more neutrals participate in ion-neutral energy exchange, the higher the probability for ionisation is' [6]. That implies that the power loss due to charge exchange can be expressed as an energy loss due to charge exchange per ionisation event,  $E_{CX}$ . In other words, if the power loss due to ionisation is  $P_{ion} = I_i E_{ion}$ , the power loss due to charge exchange would be  $P_{CX} = I_i E_{CX}$ . Since both  $P_{ion}$  and  $P_{CX}$  scale the same, it could be included in equation 3.4 by replacing  $P_{ion}$  with  $P_{ion} + P_{CX} = I_i(E_{ion} + E_{CX})$ . Power losses due to charge exchange then effectively increase the ionisation energy cost  $E_{ion}$  [6, 5, 52].

However,  $E_{CX}$  is not well-known and large discrepancies between the various  $E_{CX}$  estimates occur in literature: 3 eV to 5 eV [5, 52] to 1 to 3.5 times the effective temperature of the ionisation region [6, 164] (based on the ratio of heat to particle diffusivity of neutrals [6]). [165] provided an analytic model for determining  $E_{CX}$  as shown in equation 3.7, which pictures  $E_{CX}$  as losing a fraction of the energy of an ion in the recycling region  $\frac{3}{2}T_i$ , depending on how many collisions a neutral undergoes before a wall is reached (approximated as the ratio (with a maximum of 1) between the ion-neutral mean free path ( $\lambda_{in}$ ) and the characteristic divertor width ( $\Lambda$ )), and depending on how likely it is that such collisions are charge exchange collisions as opposed to ionisation collisions, (approximated by the charge exchange to ionisation ratio  $\frac{CCD}{SCD}$  —section 2.4). Naturally, this analytic estimate is oversimplified as the neutral dynamics is inherently 2D and rough approximations were made to estimate the effective fraction of energy loss per ion in the recycling region. This, including the large discrepancies between the various  $E_{CX}$  estimates in literature is why we do not include  $E_{CX}$  in our investigations and in addition the effects of  $E_{CX}$  are found secondary to  $E_{ion}$  in SOLPS modelling for TCV [98].

$$E_{CX} = \frac{3}{2}T \times \frac{CCD}{SCD} \times \frac{\lambda_{in}}{\Lambda} \quad (3.7)$$

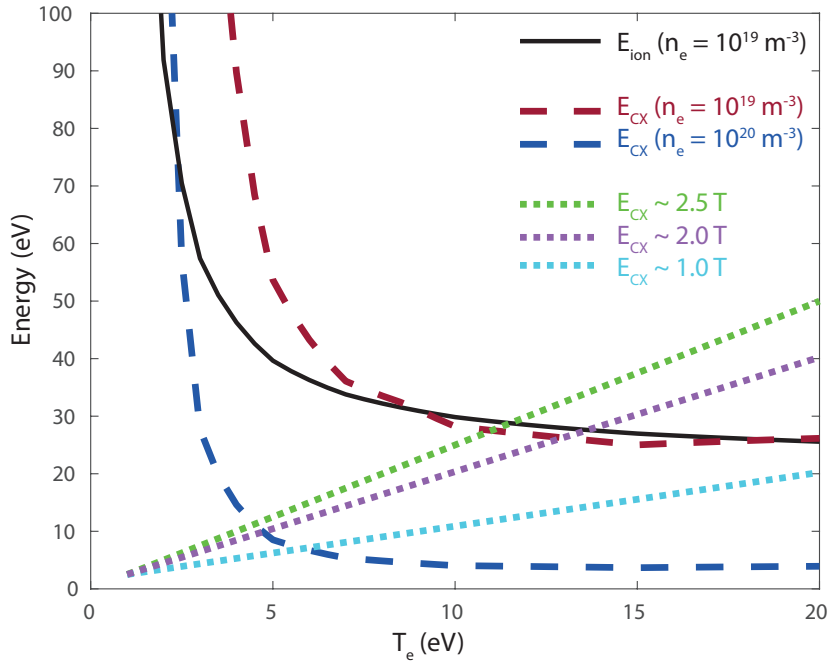


Figure 3.3: Evaluation of different models for  $E_{CX}$  compared to  $E_{ion}$  as function of temperature.

We will however, investigate how  $E_{CX}$  would depend on the plasma parameters according to the model by [165] and how this would increase the effective  $E_{ion}$ , illustrated in figure 3.3. For this we assume an effective divertor leg width of 5 cm (at the target for TCV this is between 3-10 cm (latter in detached) according to IR measurements). In this,  $T_e = T_i$  is assumed. According to the model provided by equation 3.7, a divertor more transparent to neutrals would have larger  $E_{CX}$  as the fast neutrals would escape more easily (e.g. maximising  $\frac{\lambda_{in}}{\Lambda}$ ). For TCV conditions, generally the ion-neutral interaction mean free path is of the order of 1 cm to 10 cm; which is close to  $\Lambda$  especially at low densities. Therefore, the opacity of the TCV divertor significantly changes depending on the electron density, causing a strong

density dependence of the modelled  $E_{CX}$  as shown in figure 3.3. During detachment,  $E_{CX}$  increases strongly as the divertor becomes more transparent (increased ionisation mean free path) and the ratio between charge exchange and ionisation increases, resulting in a strong rise in  $E_{CX}$  at temperatures below 5 eV (figure 3.3).

The obtained behaviour for  $E_{CX}$  using the model provided by equation 3.7 with TCV parameters leads to different predictions than elsewhere in literature (such as  $E_{CX} = 3 - 5$  eV [5] or  $E_{CX}$  being some fixed factor times the temperature of the ionisation region [6, 164]). Depending on the electron density, a very wide range of possible  $E_{CX}$  is predicted. In high density conditions, however,  $E_{CX}$  is expected to be much smaller than  $E_{ion}$  and is thus negligible.  $E_{CX}$  remains secondary to  $E_{ion}$  except for particularly low density cases ( $n_e \leq 1 \times 10^{19} \text{ m}^{-3}$ ) and particularly low electron temperatures.

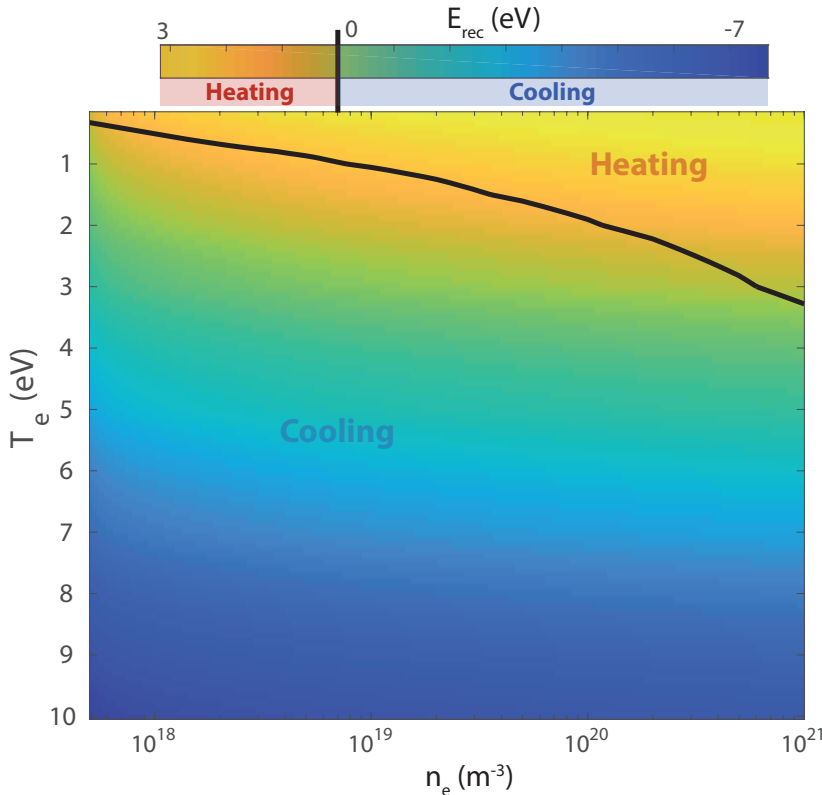


Figure 3.4:  $E_{rec}$  as function of  $T_e, n_e$  with a contour line at zero.

Going closer to the target, we can find at the lowest temperatures a recombination region during detachment acting as an ion sink losing  $I_r$  ions. From a power balance perspective, there are both energy gains and losses in the recombination process. During the recombination process, the potential energy  $\epsilon$  can be released back to the electron catalysing the three body reaction during three-body recombination or to the neutral during radiative recombination. At the same time, recombination leads to radiative losses, expressed here as  $P_{rad}^{H,rec}$  which are determined through ADAS which provides an *effective* radiative loss accounting for both radiative/two-body recombination and three-body recombination. Assuming that each recombination reaction releases  $\epsilon$  back to the plasma as done in [136], the power sink  $P_{rec}$  due to recombination can be written as equation 3.8a. Here a positive  $P_{rec}$  implies radiative losses dominate over the potential energy gain and a negative  $P_{rec}$  implies the reverse. By dividing  $P_{rec}$  with the recombination sink, the effective energy loss/gain (negative) per recombination

event can be obtained.

$$P_{rec} = P_{rad}^{H,rec} - \epsilon I_r \quad (3.8a)$$

$$E_{rec} = \frac{P_{rec}}{I_r} = \frac{P_{rad}^{H,rec}}{I_r} - \epsilon \quad (3.8b)$$

Using the tables shown in section 2.4,  $E_{rec}$  can be modelled using ADAS as function of  $n_e, T_e$ , shown in figure 3.4. It is seen that at low temperatures and high densities a net plasma heating (of up to  $E_{rec} \sim 3$  eV for TCV parameters) can occur. This is because radiative recombinative losses per recombination are smaller for three-body recombination than for two-body recombination (where a net energy loss occurs according to figure 3.4). However, such an energy gain is negligible compared to the influence of  $E_{ion}$  and  $E_{CX}$  on the power balance and it can be assumed that recombination has a negligible influence on the power balance (e.g.  $E_{rec} \sim 0$ ).

## 3.2 Modelling the ion source from power/particle balance

Equation 3.4 already shows that  $P_{rec}$  can be lowered through impurity radiation to a point where  $P_{rec}$  starts to constrain  $P_{ion}$  and consequently the generated ion source  $I_i$ : a form of 'power limitation' (or 'starvation' [5]). This reduction of the ion source leads to fewer ions entering the recombination region and thus a reduced ion target current  $I_t$ . As part of power limitation the temperature in the recycling region and at the target both drop, affecting processes such as recombination and ion-neutral collisions which are related to momentum loss processes. An equation for  $I_t$  to show power limitation can be derived quantitatively using the previous equations 3.5, 3.3, together with the assumption that  $E_{CX} \sim 0$  and  $E_{rec} \sim 0$ , leading to equation 3.9, where  $I_t$  is written as function of  $P_{rec}$ ,  $T_t$  and  $I_r$ . Variants of equation 3.9 have been derived/shown in [51, 5, 6, 53, 52]. Note that as the closed box approximation is used, any transport of ions into the divertor region or between the different divertor regions is not accounted for.

$$I_t = \frac{P_{rec} - E_{ion} I_r}{E_{ion} + \gamma T_t} \quad (3.9)$$

In this form,  $I_t$  corresponds to the integrated ion target flux at the inner or outer target and thus  $T_t$  in equation 3.9 is essentially a heat flux averaged target temperature [51], which is not necessarily representative of the peak temperature at the target. However, this model is also applicable to a single flux tube when heat/particle transport across the flux tubes is ignored.

The following description in this section (and subsection) is unique to this work and [2] and has not been done before in literature.

For further insight into the dynamics of 3.9 it can be rewritten as equation 3.10a, where the term  $f_{ion}(T_t^*)$  is introduced. In the absence of recombination (e.g.  $I_i \approx I_t$ )  $f_{ion}$  (defined in equation 3.10b) represents the fraction of power entering the recycling region being spent on ionisation. In this power and particle balance model this is fully determined by  $T_t^* = \frac{\gamma T_t}{E_{ion}}$

(equation 3.10c) which represents, again in the absence of recombination, the ratio between the kinetic power reaching the target and the power used for ionisation, e.g.  $\frac{\Gamma_t \gamma T_t}{\Gamma_t E_{ion}}$ .

$$I_t = \left( \frac{P_{recl}}{E_{ion}} - I_r \right) \times f_{ion}(T_t^*) \quad (3.10a)$$

$$f_{ion}(T_t^*) = \frac{1}{1 + T_t^*} \quad (3.10b)$$

$$T_t^* = \frac{\gamma T_t}{E_{ion}} \quad (3.10c)$$

The term  $\frac{P_{recl}}{E_{ion}}$  provides the *maximum possible ion source* one could generate when all the power entering the recycling region is spent on ionisation. In that limit, as indicated by equation 3.4 and 3.6b,  $P_{recl} = P_{ion}$  and thus  $P_{target}^{kin} \rightarrow 0$ , meaning  $T_t \rightarrow 0$ . In other words, depending on the fraction of power spent on ionisation, the fraction of power reaching the target is determined, which is directly related to the target temperature. One can express this with the term  $f_{ion}$  in equation 3.10b, for which  $f_{ion} \rightarrow 1$  for  $T_t^* \rightarrow 0$  and  $f_{ion} \rightarrow 0$  for  $T_t^* \rightarrow \infty$ . That relation is directly obtained from equation 3.4, as  $P_{recl} = I_t(\gamma T_t + E_{ion})$  (in the absence of recombination) and thus  $\frac{P_{ion}}{P_{recl}} = \frac{I_t E_{ion}}{I_t(\gamma T_t + E_{ion})} \approx \frac{1}{1+T_t^*} = f_{ion}$ . Essentially this means that *depending on the fraction of power entering the recycling region spent on ionisation a certain target temperature is achieved*. This also shows that separating impurity and hydrogenic radiation is important for the understanding of divertor power/particle balance as impurity radiation reduces  $P_{recl}$  and hydrogenic radiation is mostly determined by  $E_{ion}$  and the modelled  $I_t$ : both impurity and hydrogenic radiation thus play different roles. The  $f_{ion}(T_t)$  scaling will be crucial to the critical point (e.g. detachment thresholds) obtained from the 2PMR in section 3.3.

As a side-note, it should be mentioned that the above formalism is written for divertor 'effective' ( $T_t$ ) or 'integrated'  $P_{recl}, I_t$  parameters. This can be re-written as local, flux tube, parameters by replacing  $I_t$  with  $\Gamma_t$ ;  $P_{recl}$  with  $q_{recl}$  (e.g. heat flux entering the recycling region) and  $T_t, E_{ion}$  become local, flux tube specific, values. This is valid under the assumption that transport of heat and particles across the flux tubes is negligible.

$$f_{ion}(T_t^*) = \frac{1}{1 + T_t^*} \quad (3.11a)$$

$$f_{kin}(T_t^*) = \frac{T_t^*}{1 + T_t^*} \quad (3.11b)$$

$$f_{pot}(T_t^*) = \frac{\epsilon/E_{ion}}{1 + T_t^*} \quad (3.11c)$$

$$f_{target}(T_t^*) = \frac{\epsilon/E_{ion} + T_t^*}{1 + T_t^*} \quad (3.11d)$$

Other fractions for insight into the power dynamics of the recycling region can be determined (equation 3.11), similarly to how  $f_{ion}$  is defined. One can define  $f_{kin}$  which is the fraction of  $P_{recl}$  ending up at the target in the form of kinetic energy.  $f_{kin}$  is obtained, again assuming that recombination is not present, as  $f_{kin} = \frac{P_{target}^{kin}}{P_{recl}} = \frac{I_t \gamma T_t}{I_t(\gamma T_t + E_{ion})} = \frac{T_t^*}{1+T_t^*} = 1 - f_{ion}$ . This is not surprising as, the power in the recycling region not spent on ionisation reaches the target in the form of kinetic energy. However, since ions recombine at the target's surface

when reaching the target, the actual fraction of  $P_{recl}$  reaching the target is higher than  $f_{kin}$ . The fraction of  $P_{recl}$  reaching the target in the form of potential energy,  $f_{pot}$ , can be modelled as (again assuming recombination is not present) as  $f_{pot} = \frac{P_{target}^{pot}}{P_{recl}} = \frac{I_t \epsilon}{I_t(\gamma T_t + E_{ion})} = \frac{\epsilon/E_{ion}}{1+T_t^*}$ . It may seem surprising that  $f_{pot} + f_{kin} + f_{ion} > 1$ , however, the reason for this is that, due to the definition of  $E_{ion}$ , a portion of  $f_{ion}$  will eventually reach the target in the form of potential energy ( $\epsilon/E_{ion}$ ). In other words, the power reaching the target is the power entering the recycling region not reduced by the full ionisation power cost, but only reduced by the radiative part of the ionisation power cost (e.g.  $\frac{P_{rad}^{H,exc}}{I_i}$ ). The actual fraction of  $P_{recl}$  reaching the target is then  $f_{target} = f_{pot} + f_{kin}$ , as shown in equation 3.11d.

In the above discussion, we have made the simplification that no recombination is present, which is generally accurate for TCV as the recombination rates are generally (much) lower than the ionisation rate. When including recombination, the term  $P_{recl}/E_{ion} - I_r$  in equation 3.10a represents the maximum possible ion source minus the recombination rate, which forms the maximum possible ion target flux for a given  $I_r$ . It may seem peculiar that  $f_{ion}$  is multiplied by  $P_{recl}/E_{ion} - I_r$ , since it means that when there is recombination  $I_r$  in this model, the ion target flux is not lowered by  $I_r$  but by  $I_r f_{ion}$ . The reason for this is that when recombination is included, assuming a fixed target temperature, fewer ions arrive at the target, less power is deposited at the target and thus a larger fraction of  $P_{recl}$  is used for ionisation.

$$I_t = \beta \left( \frac{P_{recl}}{E_{ion}} \right) \times f_{ion}(\beta T_t^*) \quad (3.12a)$$

$$T_t^{**} = \frac{\beta \gamma T_t}{E_{ion}} \quad (3.12b)$$

$$\beta = \frac{I_t}{I_i} \quad (3.12c)$$

Equation 3.10a can be re-written to include this effect more intuitively in both the  $I_t$  prediction and the different fractions highlighted in equation 3.11, leading to equations 3.12a and 3.13 respectively. These results are highly similar to the no-recombination cases 3.10a, 3.11 but with the inclusion of  $\beta$  which describes the fraction of the ionisation source reaching the target ( $\beta = \frac{I_t}{I_i} = \frac{I_i - I_r}{I_i}$ ). The influence of recombination on equations 3.12a and 3.13 can be understood by thinking about recombination as *effectively* 'enhancing' the 'ionisation' energy cost. For instance, if 50 % of the ionisation source is recombined volumetrically, for each two ionisations one ion reaches the target; so the 'effective' power spent to get that ion to the target is twice as in the case without recombination. One could define such an effective ionisation energy as  $P_{ion} = I_t E_{ion}^{eff} = I_i E_{ion} \rightarrow E_{ion}^{eff} = \frac{E_{ion}}{\beta}$ . Replacing  $E_{ion}$  with  $E_{ion}^{eff}$  in equations 3.10a and 3.11 lead to identical relations as shown in equations 3.13.

$$f_{ion}(T_t^{**}) = \frac{1}{1 + T_t^{**}} \quad (3.13a)$$

$$f_{kin}(T_t^{**}) = \frac{T_t^{**}}{1 + T_t^{**}} \quad (3.13b)$$

$$f_{pot}(T_t^{**}) = \frac{\beta \epsilon / E_{ion}}{1 + T_t^{**}} \quad (3.13c)$$

$$f_{target}(T_t^{**}) = \frac{\beta \epsilon / E_{ion} + T_t^{**}}{1 + \beta T_t^{**}} \quad (3.13d)$$

### 3.2.1 Physical expectations of power/particle balance and scalings

To obtain further insight into the derived relations and their predictions, we will investigate the physical expectations of these relations and their scaling in this section. For this discussion we imagine a hypothetical case where the target temperature is varied while  $P_{recl}$  is kept constant and no recombination is assumed:  $I_r = 0$  (or  $\beta = 1$ ).

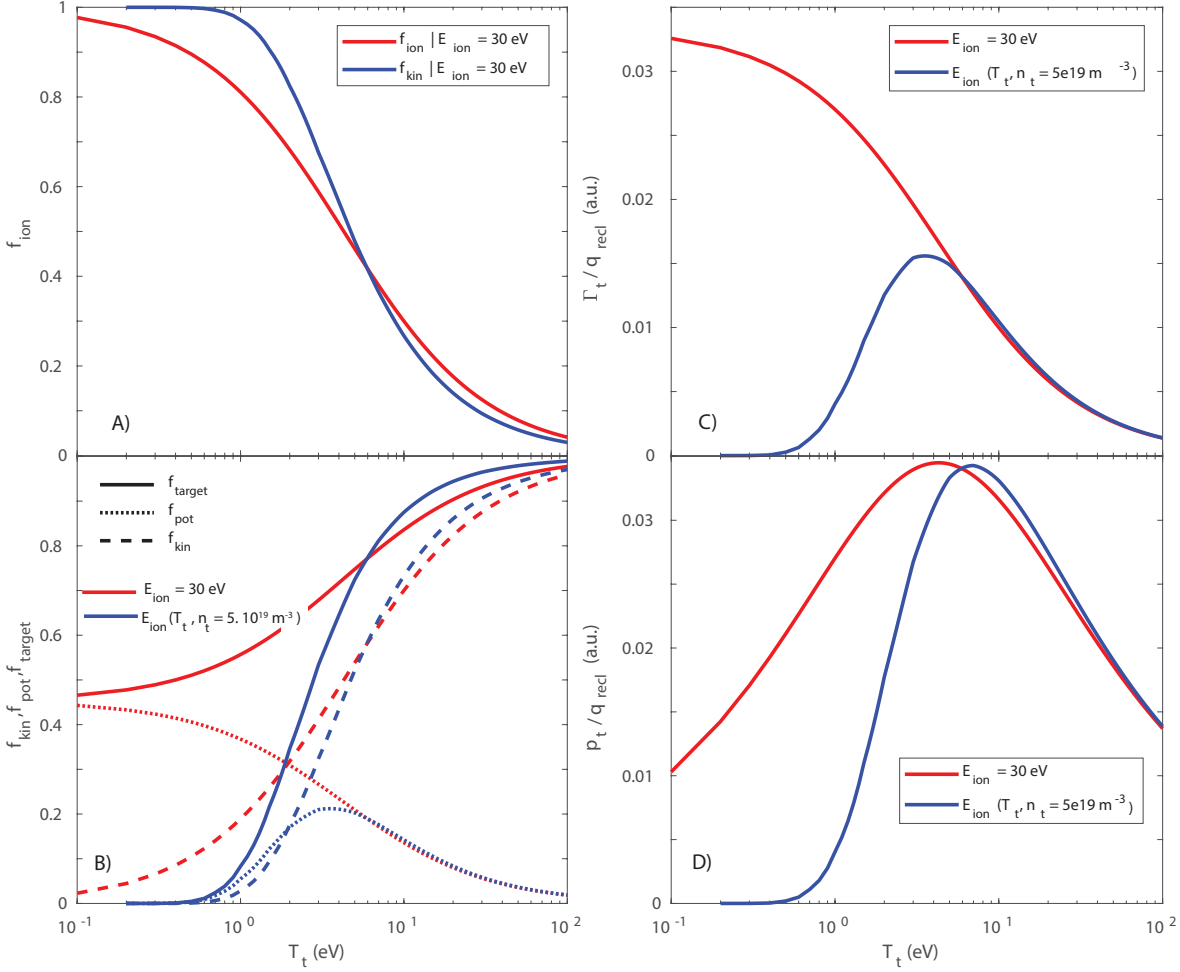


Figure 3.5: a)  $f_{ion}$  as function of  $T_t$ , b)  $f_{target}$ ,  $f_{pot}$ ,  $f_{kin}$  as function of  $T_t$  c)  $\Gamma_t / q_{recl} = \frac{f_{ion}(T_t^*)}{E_{ion}}$  as function of  $T_t$ , d)  $p_t / q_{recl}$  as function of  $T_t$ . All of this is shown for both a fixed  $E_{ion}$  and for  $E_{ion} = f(T_t, n_t)$ .

First we will discuss the trends expected when  $E_{ion}$  is fixed at 30 eV, which is often used in literature [3, 4, 5, 6, 51]. The shown  $f_{ion}$  and  $f_{kin}$  (figure 3.5 a, b) show a transitioning from using almost none of  $P_{recl}$  on ionisation at high temperatures (and thus almost all of  $P_{recl}$  reaches the target in the form of kinetic energy) to using almost all of  $P_{recl}$  on ionisation at low temperatures (and almost none of  $P_{recl}$  reaches the target in the form of kinetic energy). However, as more of  $P_{recl}$  is spent on ionisation at low temperatures, the ionisation source rises (figure 3.5 c); similarly to  $f_{ion}$ . This rise in ion source results in higher power deposition at the target in the form of potential energy  $f_{pot}$  (figure 3.5 b) when the temperature is decreased. When observing the total fraction of  $P_{recl}$  deposited at the target ( $f_{target} = f_{pot} + f_{kin}$ ), this drops from approximately 1 at high temperatures (as almost all power reaches the target in the form of kinetic energy) to  $f_{target} \approx \frac{\epsilon}{E_{ion}} \approx 0.45$  for a fixed  $E_{ion}$ . In other words, even though the divertor is cooled and ionisation is increased still almost 50 % of  $P_{recl}$  reaches the

target due to the ion source recombining at the surface. In other words, the target heat loads can only be reduced strongly through impurity radiation (e.g. reducing  $q_{recl}$ ) and/or reducing the ions reaching the target through recombination —if  $E_{ion}$  is fixed at 30 eV.

Secondly, we will compare these trends to expected trends using an  $E_{ion}$  evaluated from ADAS (at  $n_e = 5 \times 10^{19} \text{ m}^{-3}$  (equation 3.6b), where it is assumed that the ionisation region's temperature is the same as the temperature at the target. Of course, this underestimates the temperature as the ionisation region is not exactly at the target; especially in detached conditions where the ionisation region will move away from the target into hotter regions higher up the divertor leg. Therefore,  $E_{ion}$  is likely overestimated and the shown trends/results are likely in between the two trends. However, as noted previously, if one were to take recombination into account; this can be modelled as an effective 'boost' in  $E_{ion}$  and also charge exchange energy losses would further increase  $E_{ion}$ . Including  $E_{ion}(T_t)$  leads to a more abrupt transitioning of  $f_{ion}$  and  $f_{kin}$  (figure 3.5 a, b), although the general trend remains the same. Strong deviations are observed when including  $E_{ion}(T_t)$  for  $f_{pot}$  and  $\frac{I_t}{P_{recl}}$  (figure 3.5 b, c).  $E_{ion}$  increases strongly at low temperatures, due to the radiative part of  $E_{ion}$  leading to strong radiative power dissipation in the divertor reducing  $f_{target}$ . Also, at such strong  $E_{ion}$ , even if almost all power entering the recycling region is spent on ionisation, the cost for ionisation is so high that the ionisation source and thus the ion target flux is expected to strongly roll-over (figure 3.5 c), also reducing  $f_{pot}$  as fewer ions reach the target. However, these changes are not expected to be as strong in reality as  $E_{ion}$  at low temperatures is likely overestimated.

### 3.3 Including recycling energy cost in the Two Point Model: the 2PMR

As discussed in sections 1.5 and 2.3, the target pressure, target particle flux and target temperature are all connected through the sheath conditions. That connection is important as it forms the basis of the interplay between power/particle and momentum balance. That interplay will be formally derived here and essentially corresponds to including recycling energy losses into the two point model ('2PMR') as has been done in [3, 4], but also in [5, 6] through an alternative approach. Before going into the math, we will first indicate how changes in  $I_t$  and  $T_t$  are related to  $p_t$  through the sheath conditions just when combining the power/particle balance introduced previously with equation 1.1 —as this forms the basis of the 2PMR. The specific focus on this particular dynamics is unique to this work.

First, we start with the sheath target conditions (equation 1.1),  $p_t \propto \Gamma_t T_t^{1/2}$ , which has two implications: 1) reducing  $\Gamma_t$  and  $T_t^{1/2}$  simultaneously requires target pressure drop, 2) the onset of this target pressure drop must occur when  $T_t^{1/2}$  drops faster than  $\Gamma_t$  rises. However, as highlighted in the previous section, the ionisation source depends on the fraction of the power entering the recycling region used for ionisation —which is a *function of the target temperature*. We can derive what influence that temperature dependence has on  $p_t$  by combining relations 1.1 and the flux-tube specific version of equation 3.10a (e.g.  $\Gamma_t \propto \frac{q_{recl}}{E_{ion}} f_{ion}(T_t^*)$  - assuming no recombination), leading to equation 3.14 —which is plotted in figure 3.5d showing that  $p_t/q_{recl}$  (for a given  $E_{ion}$ ) has a maximum corresponding to  $T_t = \frac{E_{ion}}{\gamma}$ , which corresponds to  $f_{ion} = 0.5$ . This is essentially what gives rise to the 'detachment thresholds' derived later in

this section. To go to lower temperatures, a  $p_t$  reduction is required as  $\Gamma_t(T_t)$  increases less strongly than  $T_t^{1/2}$  decreases, causing  $\Gamma_t(T_t) \times T_t^{1/2}$  to decrease, which occurs at sufficiently low target temperatures ( $T_t = E_{ion}/\gamma$  —figure 3.5 b).

$$\begin{aligned} p_t &\propto \frac{q_{recl}}{E_{ion}} \frac{T_t^{1/2}}{1 + \frac{T_t\gamma}{E_{ion}}} \\ &\rightarrow p_t \propto E_{ion}^{-1/2} \gamma^{1/2} \frac{q_{recl}}{E_{ion}} \frac{T_t^{*1/2}}{1 + \frac{T_t\gamma}{E_{ion}}} \\ &\rightarrow \frac{p_t}{q_{recl}} \propto \frac{1}{E_{ion}^{3/2}} \frac{T_t^{*1/2}}{1 + T_t^*} \end{aligned} \quad (3.14)$$

### 3.3.1 Derivation and key points

A Two-Point (like) Model including hydrogen Recycling energy losses (an identical model as used in [3, 4, 5, 6]) is derived, starting with the two point model (section 2.2) and modifying power balance in the recycling region according to the discussion in the previous section, resulting in equation 3.15 where flux tube specific values are used and cross-field particle/heat transport is neglected (which can occur especially if one includes charge exchange reactions). It is assumed additionally that both charge exchange and recombination have no influence on the power balance in the divertor (as highlighted in section 3.1). Although including ionisation in the power balance includes some aspects of ionisation, it does not include all aspects and still relies on the principle assumptions of the two point model, which includes the assumption that the ionisation region is infinitely thin close to the target, which is necessary to derive a pressure balance equation from the original 1D fluid model equations [3]. Therefore, the influence ionisation (in experimental conditions) has on the velocity profile is not considered in the 2PMR. As such, changes in convective versus conductive transport on the velocity profile are not considered as well; they are however partially intrinsically included by the model as measured values of  $p_u$  are used for interrogating the 2PMR instead of the conductivity equation as discussed in section 2.2. Using the findings in the previous chapter we can write power balance in the recycling region as indicated in equation 3.15. We do this for the local flux tube parameters where it is assumed that cross-field transport of heat is negligible.

$$q_{recl} = E_{ion}\Gamma_i + q_t \quad (3.15a)$$

$$\rightarrow q_{recl} = \gamma\Gamma_i T_t \left(1 + \frac{E_{ion}}{\gamma T_t}\right) \quad (3.15b)$$

$$\rightarrow q_t = q_{recl} \frac{T_t^*}{1 + T_t^*} \quad (3.15c)$$

One should note that in equation 3.15c the term  $\frac{T_t^*}{1+T_t^*}$  is essentially  $f_{kin}(T_t^*)$  introduced in section 3.1 equation 3.20b where  $T_t^* = \frac{\gamma T_t}{E_{ion}}$  as explained previously.

To include equation 3.15 in the 2PMR, first the sheath conditions (equation 2.2 where  $q_{||}$  is replaced with  $q_t$  as heat flux losses occur) are used to express  $T_t$  as function of  $q_t$ , resulting in  $T_t = \frac{2m_i}{\gamma^2} \left(\frac{q_t}{p_t}\right)^2$  (note that  $p_t$  is defined here such that it equals the total target pressure; e.g. twice the kinetic pressure at the target). That equation is combined with equation 3.15 leading to equation 3.16a, which is an implicit equation for  $T_t$  as function of

$q_{recl}, p_u, E_{ion}$ , which can be re-written as a quadratic equation yielding a solution for  $T_t$  as function of  $q_{recl}, p_t, E_{ion}$ , which accounts for recycling energy losses and impurity energy losses. This shows that  $T_t$  depends on  $q_{recl}/p_t$  and  $E_{ion}$ , similarly to as illustrated in figure 3.5 and accompanying discussion.

$$T_t = \frac{2m_i}{\gamma^2} \left( \frac{q_{recl}}{p_t} \right)^2 \left( \frac{\gamma T_t}{\gamma T_t + E_{ion}} \right)^2 \quad (3.16a)$$

$$T_t^2 + \left( \frac{2E_{ion}}{\gamma} - \frac{2m_i}{\gamma^2} \left( \frac{q_{recl}}{p_t} \right)^2 \right) T_t + \left( \frac{E_{ion}}{\gamma} \right)^2 = 0 \quad (3.16b)$$

$$T_t = \left( \frac{2m_i}{\gamma^2} \left( \frac{q_{recl}}{p_t} \right)^2 - \frac{E_{ion}}{\gamma} \right) \pm \sqrt{\frac{m_i}{\gamma^2} \left( \frac{q_{recl}}{p_t} \right)^2 \sqrt{\frac{m_i}{\gamma^2} \left( \frac{q_{recl}}{p_t} \right)^2 - \frac{2E_{ion}}{\gamma}}} \quad (3.16c)$$

Of course, if one were to assume pressure balance, one can replace  $p_t$  with  $p_u$  in equation 3.16. To maintain generality, however, we will write the various equations in terms of  $p_t$ . In certain parts, where indicated, the dynamics is described in terms of  $p_u$  and pressure balance is assumed.

**2PMR  $T_t$  solutions** Figure 3.6 shows the target temperature determined through equation 3.16c for parameters respective of both a "pure"  $p_u$  linear ramp (respective of an "pure" density ramp without any other changes, which is generally different from what happens during a density ramp experiment) assuming pressure balance, with a fixed  $q_{recl} \sim 15 \times 10^6 \text{ MW m}^{-2}$  —a TCV-relevant value. Equation 3.16c implies that two solutions for the target temperature exist for a given  $(q_{recl}, p_u, E_{ion})$ , leading to a bifurcation as shown in figure 3.6, which can be described as a high temperature branch, which predicts lower temperatures for increasing  $p_u/q_{recl}$  and a low temperature branch, which predicts higher temperatures for increasing  $p_u/q_{recl}$ . Research has shown [3, 5] that only the positive branch of equation 3.16c is stable and the negative branch is unstable. This discussion will be continued later, but for now only the positive branch will be considered and we will assume that the negative branch cannot occur.

$T_t$  in equation 3.16c not only depends on  $p_t$  (or  $p_u$  —with pressure balance), but also on  $E_{ion}$ . One could argue that  $E_{ion}$  also has a target temperature dependence since the 'cost' for ionisation goes up when the ionisation region cools down as was shown in sections 2.4 and 3.1. Again, we can investigate the maximum possible influence of  $E_{ion}$  by assuming that the ionisation region is at the target; e.g. using  $E_{ion}(T_t)$ . Since that way  $E_{ion}$  becomes explicitly dependent on  $T_t$ , one can no longer use equation 3.16c in combination with  $E_{ion}$ . Instead,  $E_{ion}$  can be explicitly included in the implicit  $T_t$  relation presented in equation 3.16a, after which the  $T_t$  solution can be obtained numerically. That is an important general note, which is also related to the 2PMR stability as we will discuss later. Figure 3.6 shows the influence of  $E_{ion}(T_t)$  on the high temperature branch of the  $T_t$  solution is small for the stable band.

To further understand the trend of  $T_t$ , one can simplify equation 3.16c by doing a series expansion for  $\frac{m_i}{\gamma^2} \left( \frac{q_{recl}}{p_t} \right)^2 > \frac{2E_{ion}}{\gamma}$ , leading to equation 3.17 under the assumption  $T_t \gg \frac{2E_{ion}}{\gamma}$ , showing that the target temperature decreases when  $\frac{p_t}{q_{recl}}$  rises. The solution of this equation as function of  $p_u$  (assuming pressure balance) is also shown in figure 3.6, where a good

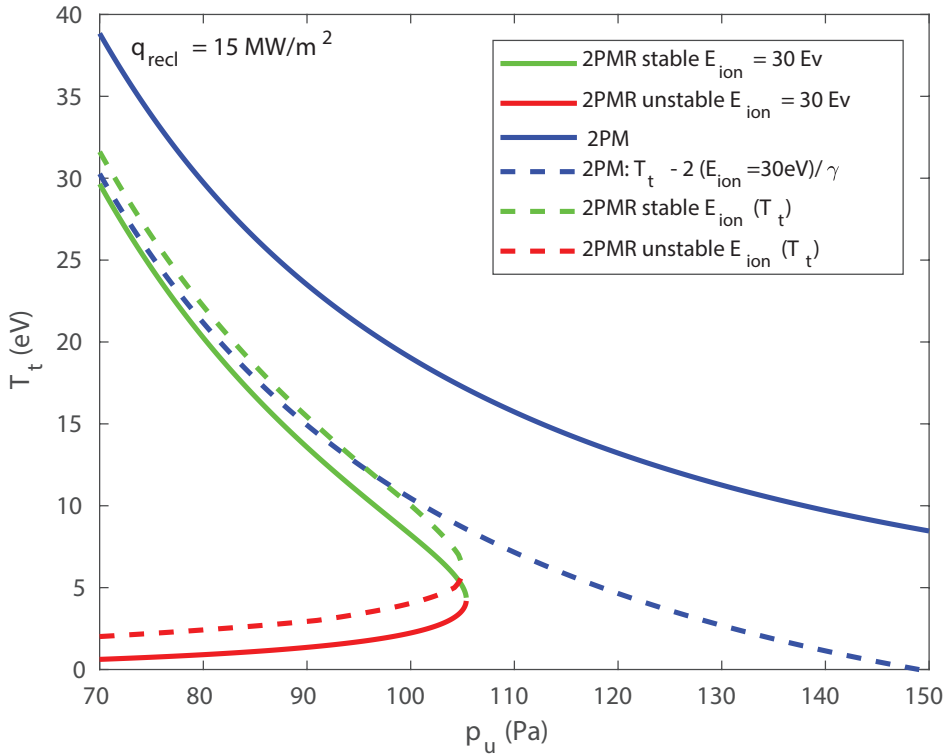


Figure 3.6: 2PMR solutions for  $T_t$  for a given  $q_{recl} = 15 \text{ MW m}^{-2}$  compared with the standard two point model solution (equation 2.4)

agreement between the high temperature branch of equation 3.16c and equation 3.17 is shown especially for high temperatures. The first term in equation 3.17 is identical to  $T_t$  provided by the basic 2PM (equation 2.4 — section 2.2 which is reduced by  $\frac{2E_{ion}}{\gamma}$  (which is  $\sim 8 \text{ eV}$  to  $10 \text{ eV}$  in attached conditions)).

$$T_t \approx \frac{m_i}{\gamma^2} \left( \frac{q_{recl}}{p_t} \right)^2 - \frac{2E_{ion}}{\gamma} \quad (3.17)$$

Instead of having a 'pure' density ramp during an experiment while keeping  $q_{recl}$  fixed, one can also cool down the divertor by impurity injection where the increase in divertor impurities leads to enhanced divertor radiation which leads to a reduction in  $q_{recl}$  while keeping  $p_u$  constant (again, experimentally, also other conditions may change during such a scan). The behaviour of  $T_t$  as function of  $p_u$  (assuming pressure balance:  $p_u = p_t$ ) and  $q_{recl}$  is compared in figures 3.7 a and 3.7 b, where figure 3.7 a is identical to figure 3.6 and in figure 3.7 b  $q_{recl}$  is reduced for a fixed  $p_u \sim 75 \text{ Pa}$  (both TCV-relevant ranges).  $E_{ion} \sim 30 \text{ eV}$  has been assumed for simplicity. This shows that the  $T_t$  behaviour (e.g. a drop in  $T_t$  when considering the high temperature branch of equation 3.16c) is very similar when  $q_{recl}$  is reduced compared to when  $p_u$  is ramped. Considering equation 3.16c this is not surprising as  $T_t$  is actually determined by the  $\frac{p_u}{q_{recl}}$  ratio. For completeness, figure 3.7c shows the behaviour of  $T_t$  with  $\frac{p_u}{q_{recl}}$  for TCV-relevant ranges.

The target temperature according to the (stable) branch of equation 3.16c will drop with increasing  $\frac{p_t}{q_{recl}}$  until a maximum critical  $(\frac{p_t}{q_{recl}})_{max}$  (which can also be expressed as a maximum  $p_{tmax}$  given a certain  $q_{recl}$ ) as indicated in equation 3.18. Again, this is the same critical point as found in figure 3.5 d and temperatures below this cannot be obtained through the stable branch unless the fundamental structure of equation 3.16a is altered

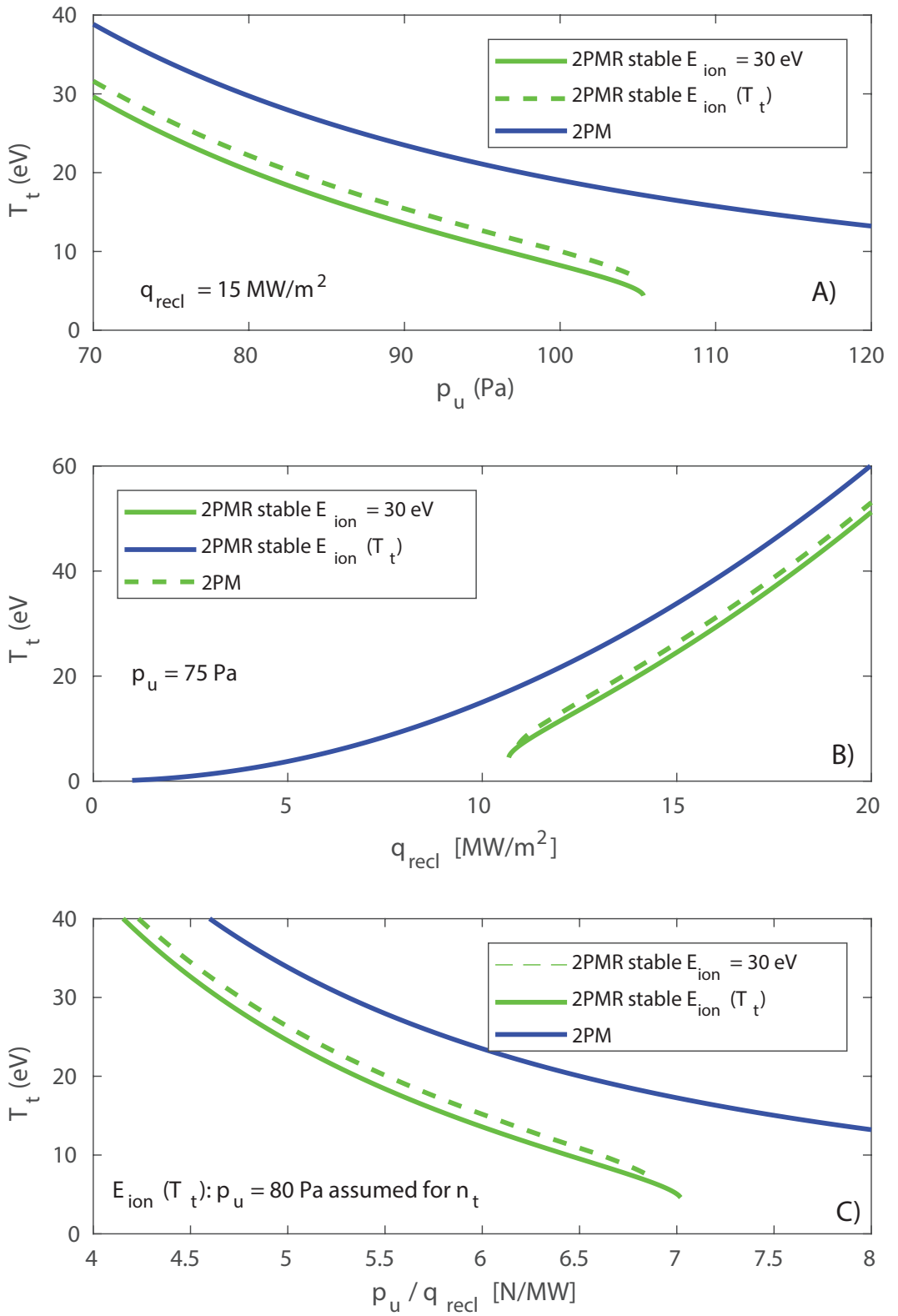


Figure 3.7: 2PMR solutions for  $T_t$  as function of  $p_u$  (same as figure 3.6),  $q_{recl}$  and  $p_u/q_{recl}$ . For the  $E_{ion}(T_t)$  function (which has a negligible  $n_t$  dependence as well),  $p_u = 80 \text{ Pa}$  is assumed in C.

by including target temperature dependencies in the terms in the equation, which we will discuss later. This critical  $(\frac{p_t}{q_{recl}})_{crit,lim}$  also corresponds to a minimum critical temperature ( $T_{t,crit} = \frac{E_{ion}}{\gamma}$ ), which can be obtained from combining equation 3.16c with equation 3.18

and is the same temperature as shown in figure 3.5 d. To investigate to which values of  $T_t$  this could correspond, we revisit figure 3.2 which shows the  $E_{ion}(T_t)/\gamma$  behaviour as function of  $T_t$  at the target. The intersections  $T_t = \frac{E_{ion}}{\gamma}$  for a range  $\gamma = 5$  to 7 and a range  $n_e = 1 \times 10^{19} \text{ m}^{-3}$  to  $1 \times 10^{20} \text{ m}^{-3}$  occur in the interval 4.5 eV to 7 eV. This range is very similar to the range in which detachment is generally expected to occur as explained in sections 2.1 and 2.3. The physical meaning of this critical point and its relevance will be discussed later.

$$\begin{aligned} \sqrt{\frac{m_i}{\gamma^2} \left(\frac{q_{recl}}{p_t}\right)_{min}^2 - \frac{2E_{ion}}{\gamma}} &= 0 \\ \left(\frac{p_t}{q_{recl}}\right)_{max} &= \sqrt{\frac{m_i}{2\gamma E_{ion}}} \\ p_{tmax} &= q_{recl} \sqrt{\frac{m_i}{2\gamma E_{ion}}} \end{aligned} \quad (3.18)$$

### $\Gamma_t$ behaviour according to the 2PMR

The expected behaviour of  $\Gamma_t$  according to the 2PMR has been discussed in literature previously [3, 4], but the following derivation indicating the equivalence between equations 3.19a and 3.19b is unique to this work and [2], as well as analysing the implication of the 2PMR on the  $I_t \propto n_e^2$  relation often used for the degree of detachment.

Using the equations obtained previously, we will investigate the 2PMR predictions for  $\Gamma_t$ . We can rewrite 3.15b into  $\Gamma_t = \frac{q_{recl}}{E_{ion}} \frac{1}{1 + \frac{\gamma T_t}{E_{ion}}}$  using the definition of  $f_{ion}$  this results in equation 3.19a. That equation is identical to the flux tube equivalent of equation 3.10a assuming no recombination losses. An alternative *and equivalent/identical* equation for  $\Gamma_t$  can be derived using equation 2.7 from the two point model and replacing  $q_{||}$  with the expression for  $q_{recl} = q_t f_{kin}(T_t^*)$  in equation 3.15c, leading to equation 3.19b. Equation 3.10a from power and particle balance seems, on first sight, to describe a different behaviour of  $I_t$  than  $I_t \propto n_e^2$  obtained from the two point model (equation 2.7) —which emphasises  $\Gamma_t$  from a momentum balance perspective. The reasoning here and the explanation indicates that both models are, however, *equivalent and identical*. That is important as it shows that the 2PMR successfully bridges power/particle/momentum balance. Furthermore, it shows that either way of reasoning provides the same answer.

$$\Gamma_t = \frac{q_{recl}}{E_{ion}} f_{ion}(T_t^*) \quad (3.19a)$$

$$\Gamma_t = \frac{\gamma p_t^2}{2m_i q_{recl} f_{kin}(T_t^*)} \quad (3.19b)$$

The expressions for  $f_{ion}(T_t^*)$  and  $f_{kin}(T_t^*)$  are obtained by using equation 3.16c in combination the expressions for  $f_{kin}$  and  $f_{ion}$ , which are provided for the sake of completeness in equations 3.20a & 3.20b.

$$f_{ion} = \frac{E_{ion}}{\frac{m_i}{\gamma} \left(\frac{q_{recl}}{p_t}\right)^2 + \sqrt{m_i} \left(\frac{q_{recl}}{p_t}\right) \sqrt{\frac{m_i}{\gamma^2} \left(\frac{q_{recl}}{p_t}\right)^2 - \frac{2E_{ion}}{\gamma}}} \quad (3.20a)$$

$$f_{kin} = 1 - \frac{E_{ion}}{\frac{m_i}{\gamma} \left(\frac{q_{recl}}{p_t}\right)^2 + \sqrt{m_i} \left(\frac{q_{recl}}{p_t}\right) \sqrt{\frac{m_i}{\gamma^2} \left(\frac{q_{recl}}{p_t}\right)^2 - \frac{2E_{ion}}{\gamma}}} \quad (3.20b)$$

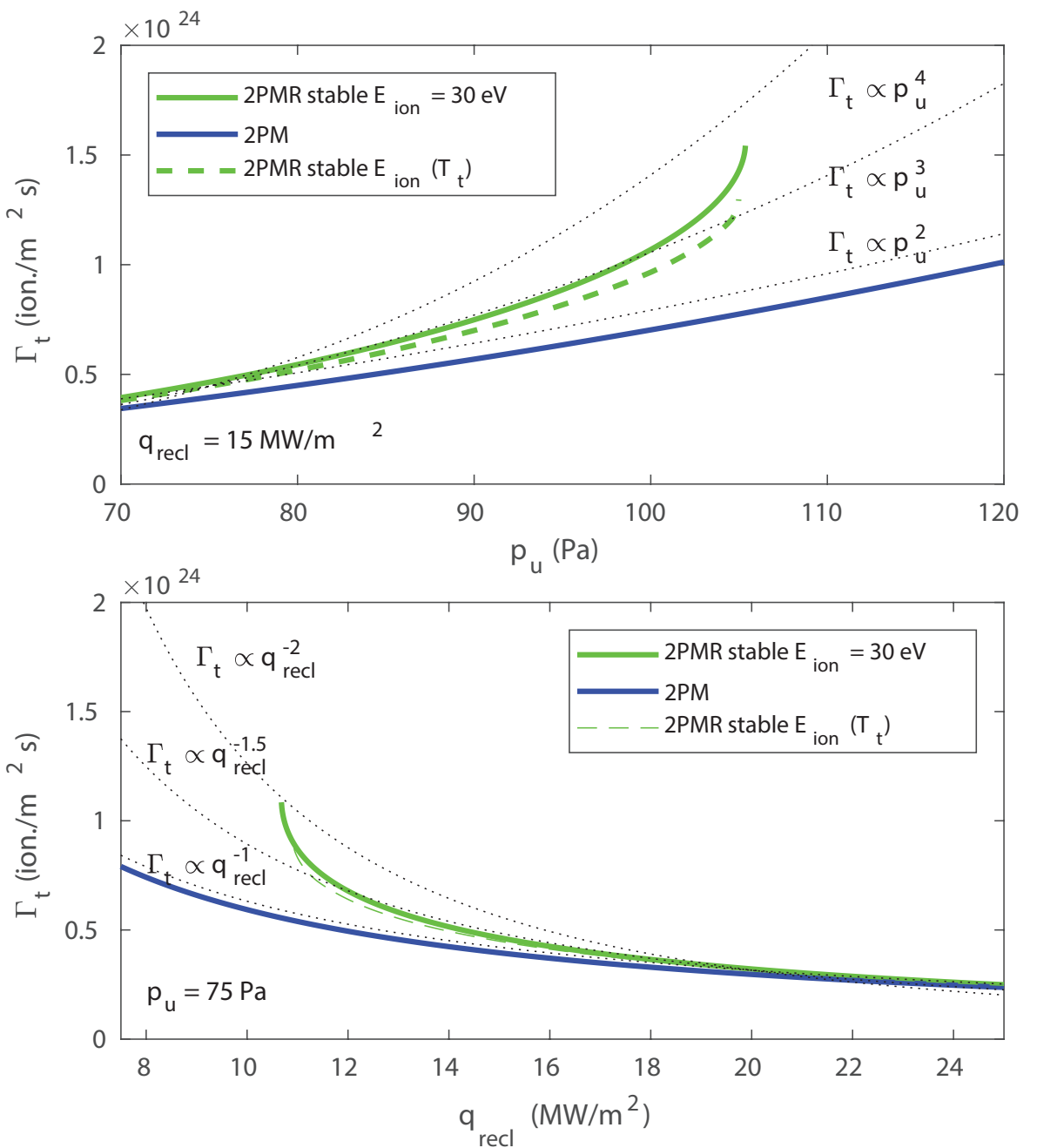


Figure 3.8: 2PMR solutions for  $\Gamma_t$  (stable branch) as function of  $p_u$  and  $q_{recl}$  compared with the standard two point model solution (equation 3.19b).

Now that a relation for  $\Gamma_t$  is obtained, we can investigate how  $\Gamma_t$  is influenced by both  $p_u$  (assuming pressure balance) and  $q_{recl}$ , which is shown in figure 3.8 where only the stable branch is shown.  $\Gamma_t$  increases with increasing  $p_u$  until the maximum achievable  $p_t/q_{recl}$  (or  $p_u/q_{recl}$  as momentum balance as assumed) is reached. In other words, the 2PMR in its current form (e.g. equation 3.16a where no specific temperature dependencies in the different terms are introduced) stops being applicable before reaching 'detached' conditions where  $\Gamma_t$  rolls over.

Through the 2PM  $\Gamma_t$  scaling,  $\Gamma_t \propto n_u^2$  is expected for a constant  $q_t = q_{recl} f_{kin}$ . However, depending on how much ionisation occurs,  $f_{kin}$  changes and thus, under a constant  $q_{recl}$ ,  $q_t$  would not be constant. Therefore, if one keeps  $q_{recl}$  constant and then scans  $p_u$ ; a stronger scaling than  $\Gamma_t \propto p_u^2$  would be expected (more along the lines of  $\Gamma_t \propto p_u^{3-4}$ ) —especially near

reaching the maximum target pressure —as shown in figure 3.8 a. The influence of  $E_{ion}$  on  $\Gamma_t$  in this modelling is rather small since the deviation of  $E_{ion}$  is rather small for the temperature regime in which a stable solution is obtained.

In figure 3.8 b, the influence of  $q_{recl}$  with a constant  $p_u$  on  $\Gamma_t$  is shown.  $\Gamma_t \propto q_t^{-1}$  is expected, which becomes  $\Gamma_t \propto q_{recl}^{-1}$  in the standard 2PM where  $E_{ion} = 0$  eV,  $\rightarrow f_{kin} = 1$  is assumed. A stronger scaling for the 2PMR is observed, which is more in line with  $\Gamma_t \propto q_{recl}^{-1}$  to  $\Gamma_t \propto q_{recl}^{-2}$ . The reason for this is, again, that while  $q_{recl}$  drops, the target temperature decreases which increase the fraction of  $q_{recl}$  spent on ionisation ( $f_{ion}$ ) such that  $q_t$  decreases faster than  $q_{recl}$ .

### 3.4 2PMR with explicit conductivity

The following description in this section is unique to this work and has not been done before in literature.

It is interesting to see if it is possible with the 2PMR to model conditions where modest or negligible temperature gradients arise as such observed behaviour is often attributed to not being in high recycling. In the 2PMR, however, by definition the ion target flux is fully built-up by ionisation: e.g. high recycling conditions.

To do this, first we need to incorporate the conductivity equation 2.3 into the 2PMR (equation 3.16a), which requires explicitly separating  $n_u$  and  $T_u$  instead of talking about trends of  $p_u$ . Ultimately, this results into the implicit equation 3.21a, which has to be solved numerically to obtain  $T_t$ , after which  $T_u$  (or  $T_t/T_u$ ) can be obtained. Including the conductivity equation into the 2PMR also means that additional parameters are required to compute  $T_t$ , including the connection length  $L$ ,  $\kappa$  conductivity and the heat flux entering the flux tube  $q_{\parallel}$ , which is coupled to  $q_{recl}$  through as shown in equation 3.21b. Here it is assumed that impurity radiation is sufficiently close to the target such that when integrating over the heat flux profile along the flux tube,  $\int q(s)ds \sim q_{\parallel}L$  is obtained as highlighted previously.

$$T_t = \frac{2m_i}{\gamma^2} \frac{q_{recl}^2}{n_u^2 (T_t^{7/2} + \frac{7q_{\parallel}L}{2\kappa})^{4/7}} \left( \frac{\gamma T_t}{E_{ion} + \gamma T_t} \right)^2 \quad (3.21a)$$

$$q_{\parallel} = (1 - f_{rad}^{imp}) q_{recl} \quad (3.21b)$$

$T_t, T_u$  are computed using equation 3.21a and are shown in figure 3.9 as function of  $n_u$  with TCV-relevant parameters of  $\kappa = 2000$ ,  $L = 10$  m,  $q_{\parallel} = 20$  MW m<sup>-2</sup> and various levels of  $f_{rad}^{imp}$  (experimental values on TCV generally range from 0.25 to 0.75). The obtained trend of  $T_t$  and  $T_u$  clearly shows that for low  $n_u$ ,  $T_t \sim T_u$  and can go up to 100 eV. While  $n_u$  is increased, both  $T_t$  and  $T_u$  decrease simultaneously until a point is reached where  $T_t$  bifurcates from  $T_u$ ; e.g. a temperature gradient along the flux tube starts to exist. Interesting to note is that the regime in which the upstream temperature is roughly constant as the density further increases in figure 3.9 is small for the 2PMR; as when these conditions are reached with a bit higher density, the applicability limit of this version of the 2PMR is reached. In other words, it implies that the often used approximation 2.5 is valid only in a very limited regime and thus care needs to be used before it is applied.

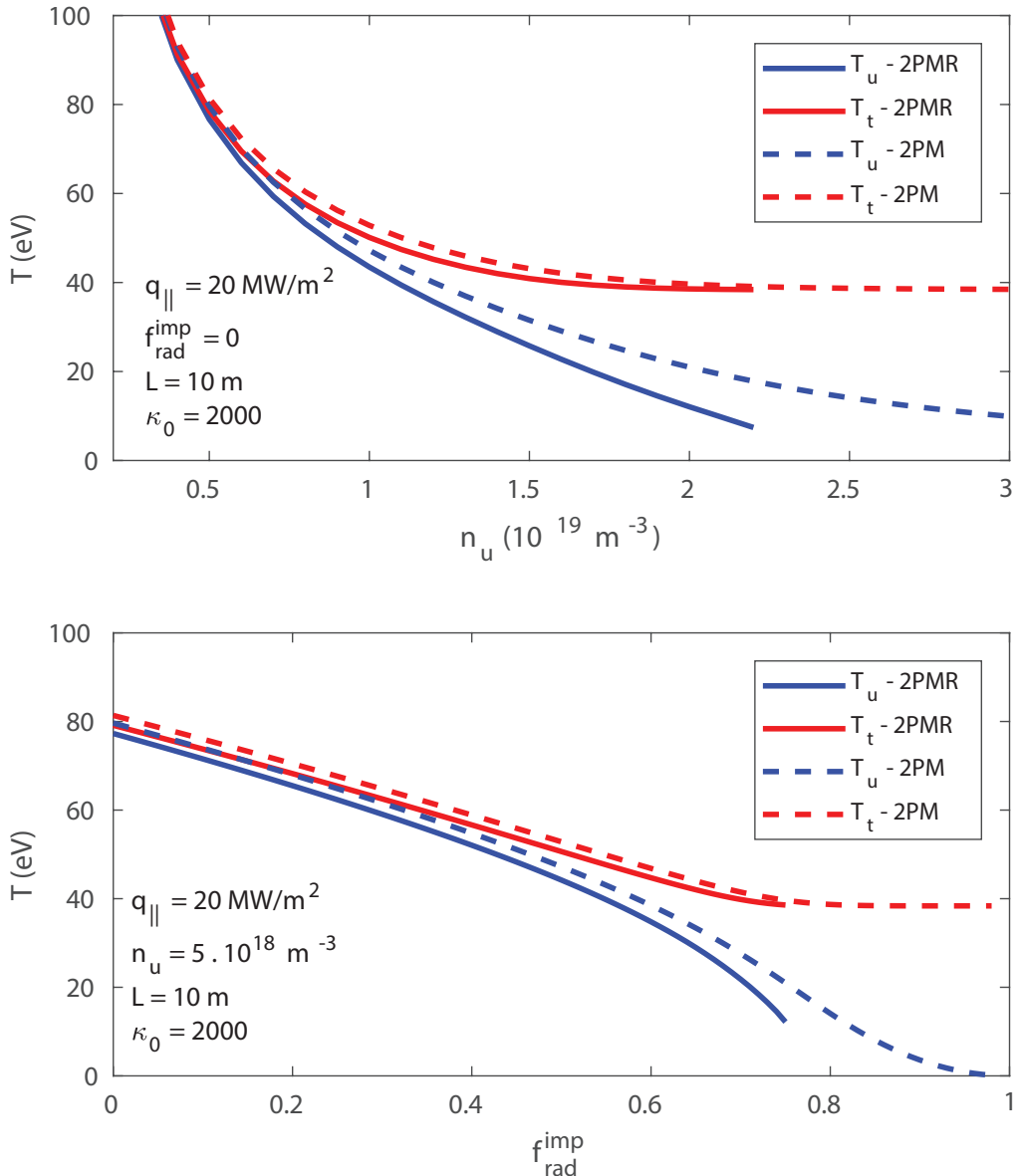


Figure 3.9: Solutions of  $T_u$  and  $T_t$  from the 2PMR, which accounts for ionisation energy losses during recycling ( $E_{ion} = 30 \text{ eV}$ ), and the 2PM, which does not account for ionisation energy losses; both while taking conductivity into account. A)  $T_t$  and  $T_u$  as function of  $n_u$  for a case with no impurity radiation. B)  $T_t$  and  $T_u$  as function of  $f_{rad}^{\text{imp}}$  (e.g. the fraction of  $q_{||}$  radiated before reaching the recycling region). The 2PMR solutions are obtained until  $T_t = E_{ion}/\gamma$  and show lower temperatures/a larger temperature gradient due to the power lost during recycling.

The fact that solutions can be obtained from the 2PMR in which  $T_t \sim T_u$  is consistent with the 'classical' notion of sheath-limited divertor operation. In other words, in the theory framework presented, situations may be possible where no significant temperature gradient along the field lines exist while the ion target flux is fully made up by ionisation. This makes it plausible that having a temperature gradient may not necessarily mean that the divertor is in high recycling conditions. One has to take into account, however, that the theory presented here is limited and does not have key physics such as drifts and convection incorporated. These findings are consistent with [3], where two forms of the 'sheath-limited' regime where

laid out: 1) cases where parallel heat conductivity is very high and weak temperature gradients are enough to carry all the power which entered the flux tube regardless of convection (which is exactly the case modelled here —convection is neglected) or 2) cases where most particles enter the flux tube upstream (e.g. not high recycling) where parallel convection carries most of the input power.

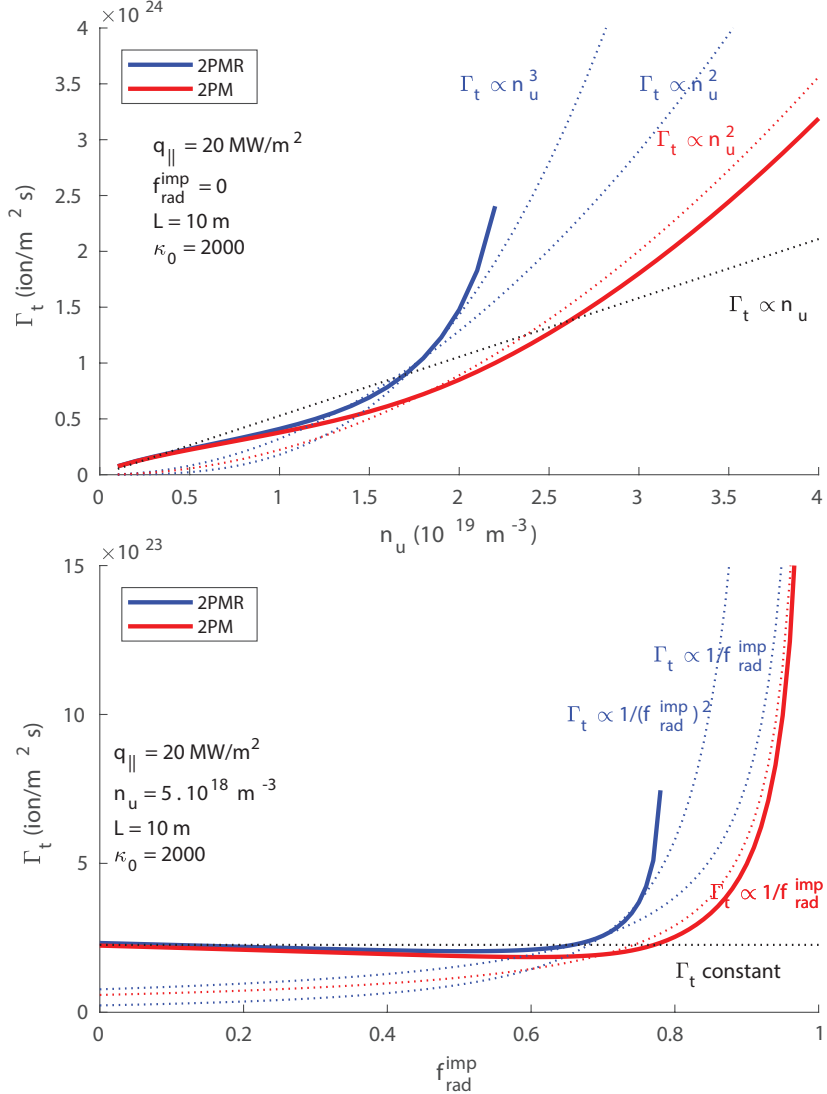


Figure 3.10: 2PMR and 2PM solutions  $\Gamma_t$  as function of  $n_u$  (A: fixed  $L, \kappa, q_{||}, f_{rad}^{imp} = 0$ ) and  $f_{rad}^{imp}$  (B: fixed  $L, \kappa, q_{||}, n_u = 5 \times 10^{18} \text{ m}^{-3}$ ) taking conductivity into account to determine  $T_u$ .  $E_{ion} = 30 \text{ eV}$  has been assumed. Dotted lines have been provided to compare the scaling of the obtained trend with power scaling dependencies.

We also model an impurity seeding ramp by keeping  $n_u = 1 \times 10^{19} \text{ m}^{-3}$ , keeping  $q_{||} = 20 \text{ MW m}^{-2}$  and by scanning  $f_{rad}^{imp}$  between 0 and 1. In other words, under these conditions the heat flux going into the recycling region is reduced while the heat flux going into the SOL is kept constant. We observe that under these conditions, a minor temperature difference between the target and upstream occurs without impurity radiation. When impurity radiation is increased, both the target and upstream temperature drop until the target/upstream temperature differences become sufficiently strong after which the upstream temperature saturates while the target temperature keeps on decreasing until the applicability limit of the

shown model is reached.

Now that we can model the behaviour of the target/upstream temperatures with the 2PMR with conduction included, we can also look at the  $\Gamma_t$  predictions. This is obtained similarly to previously (using equation 3.19b) in conjunction with the  $T_t$  obtained from solving the implicit equation 3.21a. Again, the behaviour of  $\Gamma_t$  is shown as function of  $n_u$  and  $f_{rad}^{imp}$  using the same parameters as previously in figure 3.10. This indeed shows that the increase in  $\Gamma_t$  is much slower than  $\Gamma_t \propto n_u^2$ . This occurs as the upstream temperature drops together with the target temperature, partially negating the  $n_u^2$  dependence. In certain literature sources [3, 45], the conduction-limited regime (e.g. with a significant temperature gradient) is often recognised from a  $\Gamma_t \propto n_u^2$  behaviour. This is indeed in agreement with the observation here. However, one should note that experimentally also other processes not taken into account here, such as scrape-off layer broadening, convective transport, scrape-off layer radiation can influence  $T_u$ : a decrease in  $T_u$  while the divertor target temperatures are decreased is not always an indication of sheath-limited operation.

### 3.5 Exceeding the 2PMR critical limits

Highlighting  $\frac{p_u}{q_{recl}}|_{crit,lim} = \sqrt{\frac{1}{\gamma c_{st}(T_t = \frac{E_{ion}}{\gamma})}}$  [5, 6] and  $T_t = \frac{E_{ion}}{\gamma}$  [3, 4] as critical points in the 2PMR has been done in literature, together with a discussion on the necessity of volumetric momentum loss (assuming a constant upstream pressure) to facilitate  $T_t < \frac{E_{ion}}{\gamma}$  and the ion current roll-over [3, 4]. The focus on target pressure loss, the  $f_{ion} = 0.5$  critical point and the discussion on the  $T_t$  trend in the  $T_t < \frac{E_{ion}}{\gamma}$  regime being critically dependent on the 'speed' at which target pressure drop develops (e.g.  $\partial p_t / \partial T_t$ ) is unique to this work (and partially [2]) and has not been done before in literature.

The critical point of the 2PMR discussed previously (equation 3.18), which corresponds to the maximum pressure in figure 3.5 d, can be expressed in three different forms, listed in equation 3.22.

$$\frac{p_t}{q_{recl}}|_{crit,lim} = \sqrt{\frac{1}{\gamma c_{st}(T_t = \frac{E_{ion}}{\gamma})}} \quad (3.22a)$$

$$T_t = \frac{E_{ion}}{\gamma} \quad (3.22b)$$

$$f_{ion} = f_{kin} = \frac{1}{2} \quad (3.22c)$$

In literature, this point (more specifically the  $p_u/q_{recl}$  limit —which is provided by equation 3.22a assuming pressure balance) is considered either a 'detachment criterion' [5] or a 'limit of a regime after which physics not treated in the 2PMR (which, in the version discussed, does not include volumetric momentum loss) becomes dominant in the divertor' [3]. As discussed previously, this point represents the minimum temperature the stable solution (equation 3.22) can obtain and represents the point where the unstable and stable branch meet.

We can ask ourselves the question: 'Why is this the lowest temperature one can achieve with the 2PMR?'. The reason is that the power spent on ionisation (compared to the power entering the recycling region) is so high at these target temperatures that insufficient power

reaches the target to develop the temperature at the target necessary to build-up the required target pressure [5, 6].

In other words, to obtain possible solutions at lower temperatures, the model must intrinsically support the reduction of target pressure as shown in figure 3.5 by putting a temperature dependence of the target pressure into equation 3.16a. Experimentally, such a target pressure loss can be either achieved through volumetric momentum loss as is emphasised using the 2PMR in [3, 4], or due to a reduction of the upstream pressure (as function of  $T_t$ ), which results in a reduction of  $p_t$ . To illustrate this, the implicit solution by equation 3.16a is visualised in figure 3.11 for two values of  $p_t$ . This shows that two different solutions are obtained for the lower  $p_t$  value while no solution is obtained for the higher  $p_t$  value as this is above the maximum possible target pressure (given  $E_{ion}, q_{recl}$ ) visualised in figure 3.5 d. Alternatively, another solution curve is shown for a case where  $p_t$  drops for  $T_t < E_{ion}/\gamma$  in order to match the decreasing target pressure trend in figure 3.5d, provided by equation 3.23. Note that this  $p_t$  drop can be provided by either volumetric momentum losses reducing  $p_t$  with respect to  $p_u$  (as illustrated in [4, 3]), or by a reduction of  $p_u$  as  $T_t$  drops; or by a combination of both effects. As shown, this changes the solution curve such that only one solution is still obtained and a solution is obtained for the higher  $p_{t,0}$  value. Naturally, as  $p_t$  drops with dropping  $T_t$ , the pressure at the solution (e.g. intersection) is both smaller than  $p_{t,0}$  and smaller than the maximum target pressure achievable (e.g. peak of figure 3.5 d), which is 105 Pa for these conditions, as the solution for the target temperature is below  $E_{ion}/\gamma$ .

$$p_t = \begin{cases} p_{t,0} & T_t^* \geq 1 \\ p_{t,0}T_t^{*n} & T_t^* \leq 1 \end{cases} \quad (3.23)$$

This also means that  $p_t$  needs to have a minimum 'speed' at which it reduces to enable  $T_t < E_{ion}/\gamma$ , as shown in figure 3.5. When using equation 3.14 for a constant  $E_{ion}$  in the range where  $p_t$  needs to be reduced ( $T_t^* \ll 1$ ) a series expansion can be used such that  $\frac{p_t}{q_{recl}} \sim T_t^{*1/2}$ : in other words  $p_t$  has to drop with at least the square root of the target temperature, or  $n \geq 1/2$  using equation 3.23. As explained, this target pressure drop could—in theory—either delivered by a volumetric momentum loss and/or by an upstream pressure loss. However, assuming that all target pressure loss is delivered by volumetric momentum loss, the momentum loss models illustrated in section 2.4 would all have a sufficiently strong  $T_t$  dependency (e.g. stronger than  $p_t \sim T_t^{1/2}$ )—as more explicitly illustrated in [4].

Next we will discuss different ways in which reductions of  $p_t$ , or momentum losses, can be accounted for in the 2PMR, which are also shown in figure 3.12 using a fixed  $p_{t,0}, E_{ion}$  and varying  $q_{recl}$ . First, we imagine a case with a *fixed* amount of momentum loss, meaning that  $f_{mom}$  is a term without explicit target temperature dependence, which is for instance measured through experiments. In that case,  $p_t = f_{mom}p_u$  can be introduced into the various equations. Considering that there is a maximum possible  $p_{t,max}$  means that momentum losses, in this model, would enable a higher  $p_u$  (or  $p_u/q_{recl}$ ) to obey the  $p_{t,max}$  (or  $(p_t/q_{recl})_{crit}$ ). Lower values for  $f_{mom}$  would reduce  $p_t$  if  $p_u$  is held constant ( $p_t/q_{recl} = p_u f_{mom}/q_{recl}$ ), essentially shifting the controlling parameter  $p_t/q_{recl}$ . That means for example that, if  $f_{mom}$  would be 0.5, the values modelled for  $T_t$  would correspond to those where the upstream pressure was previously twice as low (or  $q_{recl}$  was twice as high). In other words, it would delay (or shift)

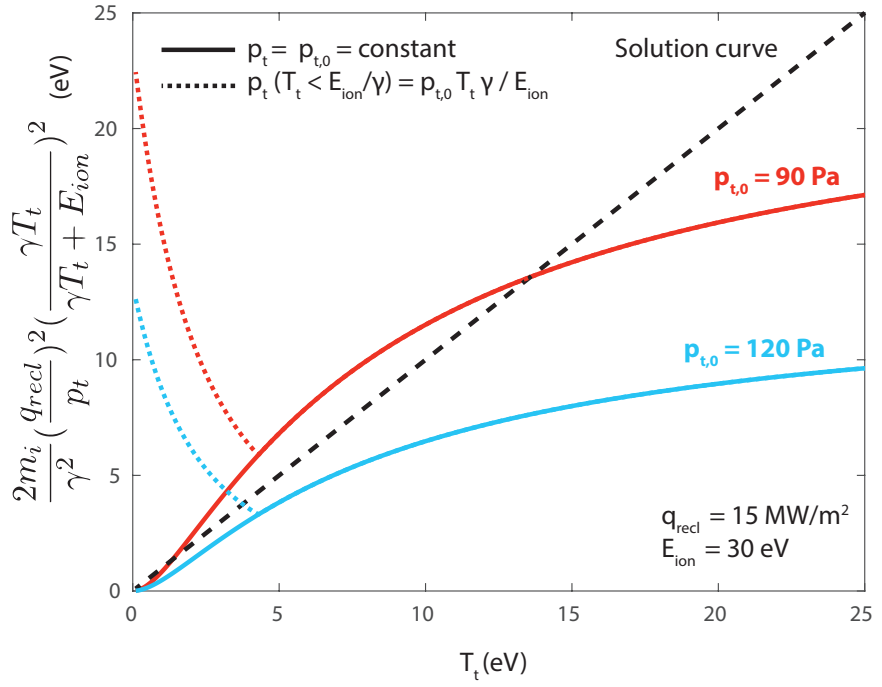


Figure 3.11: Graphical solution to the implicit equation 3.16a for the target temperature where both sides of this equation are plotted against each other. The intersection between the shown curves and the dashed line represents solution points where both sides equal. This graphical solution is shown for two values of  $p_t$  and for using a *fixed*  $p_t$  or using a *temperature dependent*  $p_t$  (equation 3.23 with  $n = 1$ ).

the decrease of  $T_t$ . The reason for this is that momentum losses partially decouple the relation between the target pressure and the target heat flux (e.g.  $q_t \propto p_t T_t^{1/2}$ ). Thus keeping  $q_t$  similar and only reducing  $p_t$  requires an increase in  $T_t$  (and thus also a strong decrease in  $n_T$  as  $p_t$  drops). However, such a shift does not introduce a target temperature dependency and thus the structure of the solution in equation 3.16a remains the same (e.g. two possible solutions as shown in figure 3.11 for a fixed  $p_t$ ); thus not supporting a  $\Gamma_t$  roll-over while scanning  $p_u$  or  $q_{recl}$  and not enabling  $T_t < E_{ion}/\gamma$ .

It is, however, possible to include a 'semi' fixed value for  $f_{mom}$  (or upstream pressure loss), which *does* enable one to have a  $\Gamma_t$  roll-over. A simple argument one could make is that since a  $p_{t,max}$  exists, some process (could be volumetric momentum losses or upstream pressure loss) always has to occur which *at least* reduces  $p_t$  to  $p_{t,max}$  (or  $p_t/q_{recl}$  to  $(p_t/q_{recl})_{crit}$ ) starting from  $p_t$  reaching  $p_{t,max}$ . In that case, once  $p_t = p_{t,max}$  is reached and  $q_{recl}$  is further reduced, a proportional decrease in  $p_t$  is required. This yields a  $T_t$  fixed at  $E_{ion}/\gamma$  and an  $f_{ion}$  fixed at 0.5, while  $\Gamma_t$  drops proportionally to  $q_{recl}$  —thus enabling the ion current to roll-over as illustrated in figure 3.12 during a  $q_{recl}$  scan. Note that all of this is neglecting volumetric recombination. That roll-over is also the strongest possible roll-over one can experience in this model as enabling a further reduction of  $T_t$  would increase  $f_{ion}$  and would imply a larger power fraction is used for ionisation, increasing the ion source. The amount of target pressure loss in this model is the *minimum* amount of target pressure possible just to obey  $p_{t,max}$ .

We can also assume that  $p_t$  will drop according to equation 3.23, which is shown for  $n = 1$  and  $n = 0.5$  in figure 3.12. For both of these cases,  $p_t$  drops more than just to  $p_{t,max}$  thus enabling higher power fractions to be used for ionisation resulting in lower target temperatures

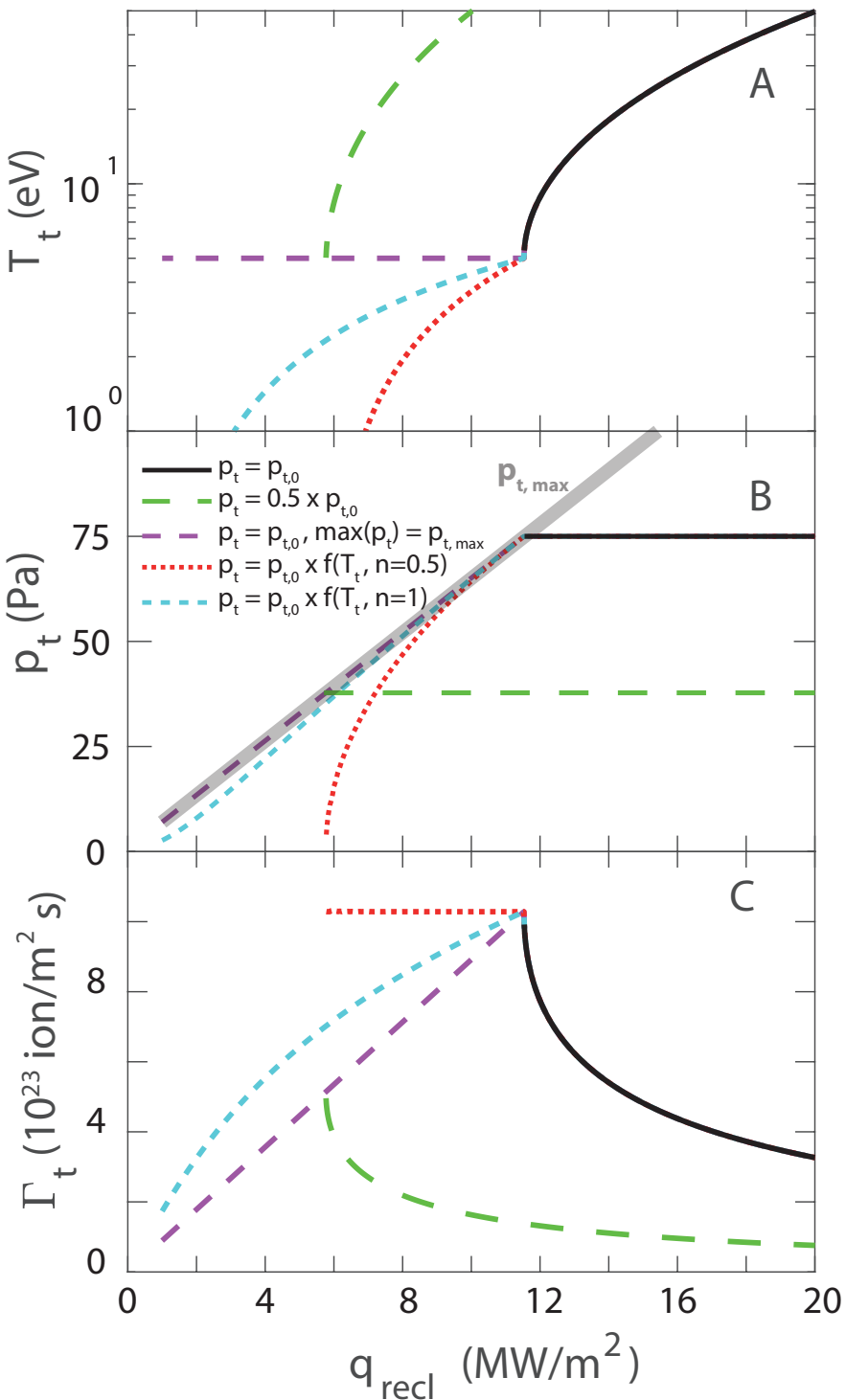


Figure 3.12: 2PMR results of  $T_t$ ,  $p_t$ ,  $\Gamma_t$  as function of  $q_{recl}$  for  $E_{ion} = 30$  eV;  $p_{t,0} = 75$  Pa. Five different relations of  $p_t$  are shown: 1)  $p_t = p_{t,0}$ ; 2)  $p_t = 1/2p_{t,0}$ , 3)  $p_t = p_{t,0}$  until  $p_t > p_{t,\max}$ , where  $p_t$  is kept at  $p_{t,\max}$ ; 4) equation 3.23 with  $n = 1/2$ ; 5) equation 3.23 with  $n = 1$ . As a reference, the  $p_{t,\max}$  trend is shown as  $q_{recl}$  varies.

( $T_t < E_{ion}/\gamma$ ). The ion current also rolls-over ( $n > 0.5$ ) while it remains flat for  $n = 0.5$ ; which means that  $f_{ion}(T_t)$  increases at the same rate  $q_{recl}$  decreases, thus leading to the same  $\Gamma_t$ . Having a stronger dependency of  $p_t$  with  $T_t$  of  $n = 1$  instead, leads to a more gradual reduction of  $T_t$ ,  $p_t$  and to a  $\Gamma_t$  roll-over when  $q_{recl}$  is scanned. That may seem as a surprising result. The  $n > 0.5$  behaviour is the minimum  $p_t(T_t)$  dependency required to alter the solution structure

of equation 3.16a. On the other hand, having momentum losses in a 2PM-like model leads to an increase in  $T_t$  or a delay in the reduction of  $T_t$ . So, having just enough  $p_t(T_t)$  dependence such that a  $T_t < E_{ion}/\gamma$  solution is obtained leads to the strongest possible  $T_t$  reduction as  $q_{recl}$  is scanned while a stronger  $p_t(T_t)$  dependency leads to a more gradual behaviour. But, that also means that the power fraction which can be spent on ionisation rapidly increases from 0.5 to 1, increasing ionisation, which is why there is no roll-over behaviour for that case —assuming that volumetric recombination is negligible.

To summarise one needs to introduce a  $T_t$  dependence in  $p_t$  (or a relation providing similar behaviour such as including volumetric momentum loss) in order to obtain solutions of the 2PMR in the  $T_t < E_{ion}/\gamma$  regime. Whether this should be done is debatable and most likely it is a sign that such simplified models stop becoming applicable in low temperature, detached regimes. It, and the accompanying discussion, does however show that in the detached regime the speed at which target pressure loss occurs is crucial for the various trends in the divertor.

### 3.5.1 Exceeding the 2PMR critical limits: upstream density loss

The following description in this section is unique to this work and has not been done before in literature.

Mathematically, as discussed, reduction in target pressure due to an  $p_u(T_t)$  dependence (e.g.  $p_u = p_t$ ) is indistinguishable from the development of momentum losses in the shown model. As we will show in section 9.2, such a loss of upstream pressure is observed in TCV and is shown in SOLPS simulation results of other devices [52, 53, 67]. That upstream pressure loss is thought to be related to an upstream density loss as opposed to an upstream temperature loss as the upstream temperature, when a large temperature gradient is present, is thought to be determined by the heat flux entering the scrape-off-layer and the connection length (equation 2.5). In other words an  $p_u(T_t)$  dependence is likely to be manifested in an  $n_u(T_t)$  dependence. All of this said, however, we must realise that this is an alternative way of describing things and a simplified investigation. The common viewpoint is that  $p_t$  drops due to volumetric momentum losses, which is likely true —in the very least to a large extent. This section here merely investigates what would happen if an  $n_u(T_t)$  dependence would exist in the 2PMR.

We evaluate how a  $n_u(T_t)$  dependence can influence  $T_t, \Gamma_t$ , similarly to how this was done in section 3.5. To do this, first we need to separate the behaviour of  $T_u$  from  $n_u$ , which is done though using the 2PMR with explicit conductivity (equation 3.21a). Similarly, such an approach requires a separation between  $q_{||}$  and  $q_{recl}$  as provided through 3.21b. For this we assume a  $n_u$  dependence in the form of equation 3.23 where  $p_t$  is replaced with  $n_u$  with  $n = 1$ . The results shown in figure 3.13 shows a very similar trend to figure 3.12 where the result for a  $p_t$  drop was visualised. The upstream temperature is indeed observed to remain constant while  $n_u(T_t)$  drops. In other words, this model and its limitations, is consistent with the notion that, in the absence of volumetric momentum losses a reduction of  $n_u$  as  $T_t$  drops during detachment could facilitate a detached solution [5, 6, 53]. Naturally, however, this does not constitute a proof in any means.

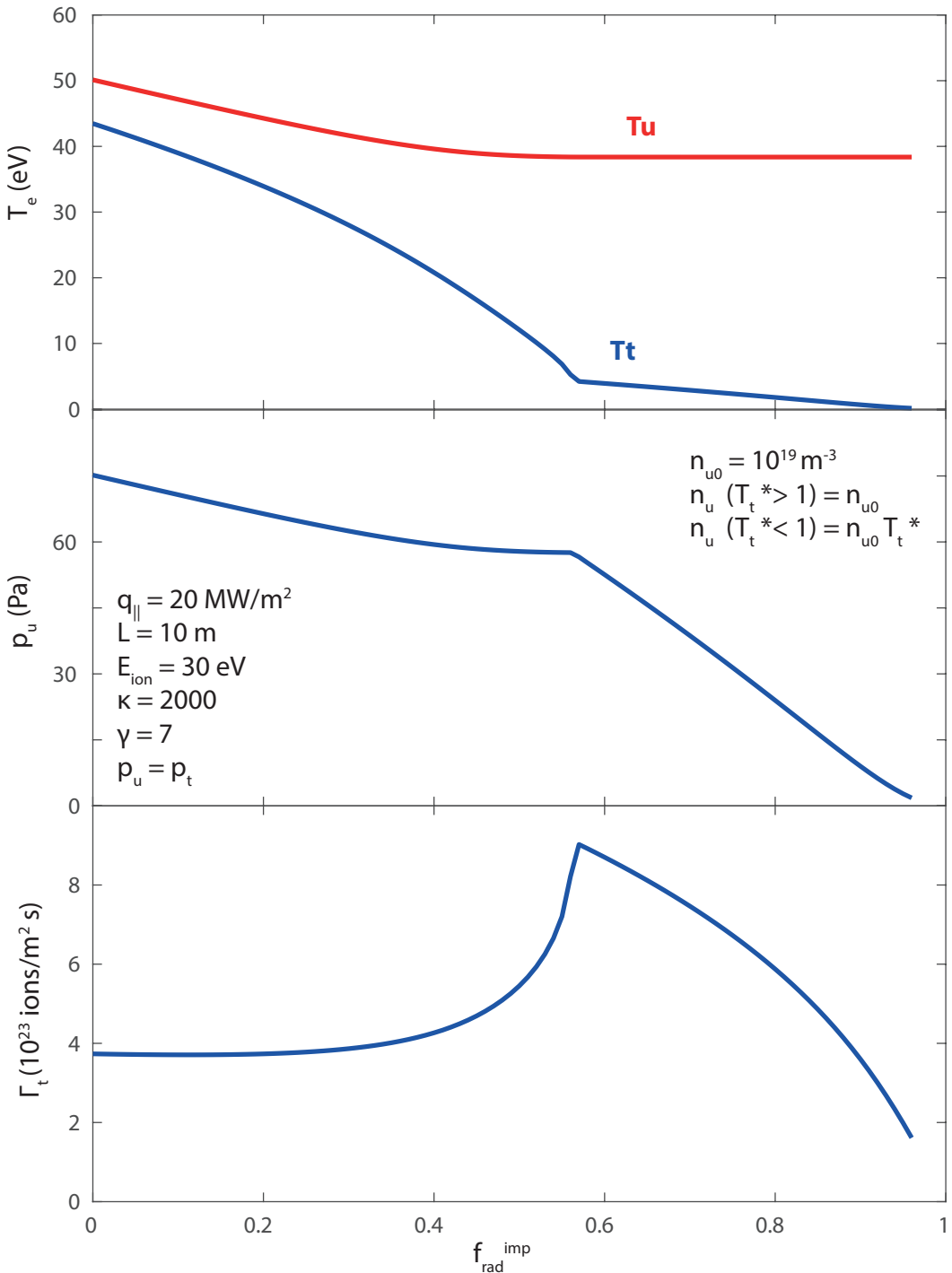


Figure 3.13: 2PMR results with explicit conductivity and  $n_u(T_t)$  dependency (similar to equation 3.23 with  $n = 1$  and  $p_t \rightarrow n_u$  of  $T_t, p_u, \Gamma_t$  as function of  $f_{rad}^{imp}$ ). The fixed parameters are:  $E_{ion} = 30 \text{ eV}$ ;  $n_{u0} = 1 \times 10^{19} \text{ m}^{-3}$ ;  $q_{||} = 20 \text{ MW m}^{-2}$ ;  $L = 10 \text{ m}$ ;  $\kappa = 2000$ .

### 3.6 Reduced analytical models in comparison with experiments

The description in this section is unique to this work and [2] and has not been done before in literature.

In this chapter we have discussed the expected relations in the divertor using reduced analytical models. Such relations can, however, deviate from the observed experimental trends since experimentally it is generally infeasible to *only* change the upstream density or *only*

change the heat flux entering the recycling region. Such parameters often have a correlation which cannot be accounted for in the reduced analytical model.

The point is that the models shown above are tools to try to understand the physics observations and global relations between divertor parameters. But the experimental observations often can only be explained through a combination of effects. To account for this, it is experimentally beneficial to include as many measured parameters as possible in the simplified models shown above. One example of this is including measurements of the upstream pressure as opposed to treating density, temperature separately through explicit conductivity. Also in all of these models there is 'physics' missing. Furthermore, there are processes missing which could describe how the divertor could influence upstream parameters, which likely requires an integrated core-edge model.

One example of how experimental data can be used to interrogate the 2PMR to predict the trend of the *integrated ion current* along the target  $I_t = \int \Gamma_t$ . The trend of  $I_t$  is important as deviations between the measured  $I_t$  and the expected  $I_t$  (e.g. the  $I_t$  roll-over) are often used to identify detachment.

In order to model  $I_t$ , first we start with the expression for the *flux specific*  $\Gamma_t$  as shown in equation 3.19b (for this calculation, we use the  $\Gamma_t$  expression featuring  $f_{kin}$ ). The value of  $\Gamma_t$  has to be obtained for every single flux surface (using the flux surface's equivalents for  $p_t$ ,  $E_{ion}$  and  $q_{recl}$ ), after which the values for  $\Gamma_t$  have to be integrated again to obtain an  $I_t$  prediction. This assumes negligible cross-field transport of power, momentum and particles. To evaluate  $\Gamma_t$ , we also assume pressure balance  $p_u = p_t$  and thus replace  $p_t$  with  $p_u$ . For the sake of simplicity we further assume that  $f_{kin}$  at the separatrix is characteristic for the entire divertor. Such a simplification can be made as we are interested in comparing ion current trends (as opposed to absolute values) and, in addition, the influence of  $f_{kin}$  on equation 3.19b is limited as  $f_{kin}$  can only vary between 0.5 and 1. Using this simplification, we can model the  $I_t$  trend as highlighted in equation 3.24, where  $s$  describes the distance of the flux tube with respect to the separatrix ( $s = 0$ ). To interrogate this equation, we require  $E_{ion}$  values —which we will see later can be obtained spectroscopically (section 9.1.1). We assume, however, that the values for effective  $E_{ion}$  of the total divertor, obtained spectroscopically are good estimates for the separatrix  $E_{ion}(s = 0)$ , as most of the ionisation occurs closer/at the separatrix (e.g. it carries the most heat flux).

$$I_t = \int \Gamma_t$$

$$I_t \propto \frac{1}{f_{kin}(T_t(E_{ion}, p_u, q_{recl}, s = 0)))} \int \frac{p_u^2(s)}{q_{recl}(s)} ds \quad (3.24)$$

To simplify the expression of the integral in equation 3.24, the upstream density, temperature and  $q_{recl}$  profiles are broken up in their respective separatrix values (e.g.  $n_u^0$  for the density) times a function describing their profile behaviour (e.g.  $f_{n_u}(r)$  for the density) as shown in equation 3.25.

$$n_u(s) = f_{n_u}(s)n_u^0$$

$$T_u(s) = f_{T_u}(s)T_u^0$$

$$q_{recl}(s) = f_{q_{recl}}q_{recl}^0 \quad (3.25)$$

By combining equation 3.24 with equation 3.25, the integral for determining  $I_t$  can be further simplified as indicated by equation 3.26.

$$I_t \propto \frac{1}{f_{kin}} \times f_p \times \frac{p_u^0}{q_{recl}^0} \quad (3.26)$$

where  $p_u^0$  is the upstream separatrix pressure,  $q_{recl}^0$  is the separatrix heat flux entering the recycling region and  $f_p$  is a parameter describing the influence of upstream profiles on  $I_t$  defined as shown in equation 3.27.

$$f_p = \int_{r_{sep}}^{\infty} \frac{f_{n_u}^2(s) f_{T_u}^2(s)}{f_{q_{recl}}} dS \quad (3.27)$$

From here onwards, we will omit the '0' when discussing the separatrix values (e.g.  $p_u$  will correspond to the separatrix values) in order to keep the expressions as clean as possible.

To evaluate equations 3.26 and 3.27, we need to estimate the spatial profile of the upstream pressure and of the heat flux entering the recycling region. We estimate  $q_{recl}(s)$  by assuming that the shape of the heat flux profile entering the recycling region is similar to the shape of the heat flux profile reaching the target ( $q_{target}$ ), which is measured through IR camera imaging. Here it is assumed that the heat flux shape at the target is similar to the heat flux shape upstream entering the recycling region and it should be noted that volumetric radiation could alter this heat flux shape. Generally, such target heat flux profiles are well characterised by the Eich profile [100]. However, during detached operation, the target profiles may deviate significantly from the Eich characterisation [99]. In this work, we thus characterise the profile with a single exponential (as opposed to an exponential convolved with a Gaussian which comprises the Eich characterisation). The advantage of such a characterisation is that the parameter  $\lambda_{q,int}$  can be used to estimate the width of the IR target heat flux profile (which was mapped upstream) from the ratio between the measured peak and total heat fluxes. The separatrix  $q_{recl}$  can then be obtained by dividing the power entering the ionisation region ( $P_{recl}$  — section 8.3) with an effective area  $A_{eff} = 2\pi R_{target} \frac{B_t}{B_p} \lambda_{q,int}$  [3], where it is assumed that the radial location of the ionisation region is the same as the target radius and where  $B_t/B_p$  represents the ratio between the toroidal and poloidal field. Uncertainties of the characterisation of  $A_{eff}$  have been neglected and could lead to systematic deviations from the portrayed trend of  $q_{recl}$ .

The upstream pressure profile and separatrix value can be obtained more straightforwardly using reciprocating probe plunges (section 4.2.4) and repeat discharges to increase the time mesh at which these probe plunges are taken (section 4.4) which provides us with upstream density/temperature profiles. In order to improve upon the time resolution of the inference (e.g. the TCV reciprocating probe can plunge at most twice a discharge — see section 4.2.4), we combine upstream (separatrix) measurements of density/temperature from Thomson scattering (section 4.2.5), providing  $n_u^0$ ,  $T_u^0$  while the reciprocating probe plunges provide  $f_{n_u}(s)$  and  $f_{T_u}(s)$ . To provide a smooth result for the profiles, the reciprocating probe upstream density/temperature profiles are fitted with a double exponential: e.g.  $f_{n_u}(s) = A_1 \exp(-\frac{s}{\lambda_1}) + A_2 \exp(-\frac{s}{\lambda_2})$ . As mentioned, a single exponential profile using  $\lambda_{q,int}$  has been used to describe the profile of  $q_{recl}(r)$  whose integral equals  $P_{recl}$ . The parameter  $f_p$  is evaluated at the time base at which reciprocating probe plunges occurred, where afterwards it is interpolated to match a higher frequency time base if required. As will be shown later,

$P_{recl}$  can be obtained experimentally (section 8.3). This provides us with all the necessary ingredients to interrogate the  $I_t$  trend according to equations 3.26 and 3.27, which will be done in section 9.2.

### 3.7 Summary and discussion

Recycling is a key process in divertor physics which leads to an intricate balance between momentum, particle and power balance. Including this in the two point model enables consolidating the 'basic' two point model (which predicts trends of the target temperature) with a 'power limitation' type of model which only includes power and particle balance (which enables modelling the ion target current roll-over *given that the target temperature is known*). Merging these two models shows that the two seemingly different scalings for the ion current by the two-point model (e.g.  $\Gamma_t \propto n_u^2 T_u^2 / q_t$ ) and by a power-limitation model (e.g.  $\Gamma_t \approx q_{recl} / E_{ion} f_{ion}(T_t^*)$ ) are *identical* when recycling energy losses are included; indicating that both ways of reasoning are equivalent and should lead to identical results. When including recycling energy losses, target pressure loss is necessary to obtain detached solutions with an ion current roll-over and temperatures below  $E_{ion}/\gamma$  (which requires the target pressure to drop with at least  $T_t^{1/2}$  as  $T_t$  decreases). Target pressure loss needs to occur when  $f_{ion} = 0.5$ ;  $T_t = E_{ion}/\gamma$ ;  $(p_t/q_{recl}) = (p_t/q_{recl})_{max}$ , providing three 'detachment onset criteria' which all correspond to reaching a maximum possible target pressure ( $p_{tmax}$ ) given the parameters  $q_{recl}, E_{ion}$ .

The actual dynamics (most notably the target pressure) after reaching this point during detached solutions ( $T_t < E_{ion}/\gamma$ ) are very sensitive to the precise speed at which the target pressure drops with respect to  $T_t$ . Solutions at  $T_t < E_{ion}/\gamma$  thus depend on a complex and intricate interplay between several processes in the divertor (atomic and molecular processes, but also 2D neutral transport and drift effects) which go far beyond what can be modelled with the 2PMR. Likely the 'safest' assumption is that once the  $p_{tmax}$  is reached; the 2PMR is no longer applicable as a specific dependency of  $p_t(T_t)$  has to be assumed. Such a relation may be dependent on a range of parameters including recycling geometry, operating density, molecular processes leading to volumetric momentum loss, etc.

Investigating the difference between including recycling in the two point model or neglecting it has shown that the behaviour of the ion current during a density ramp with fixed  $q_t$  (2PM) or fixed  $q_{recl}$  (2PMR) is radically different, leading to 2PMR predictions of the degree of detachment which are different from those obtained in literature. This point is crucial for quantifying degrees of divertor detachment as it shows that the 'classical'  $\Gamma_t \propto n_u^2$  type of behaviour can be easily violated even when 'external' parameters are controlled (e.g. the power entering the divertor; impurity radiation in the divertor). Other comparisons between the 2PMR and 2PM have shown that isothermal field lines are accessible through the 2PMR, meaning that isothermal field lines (or 'sheath limited operation') is not necessarily linked to high recycling when considering the described simplified models.

# Chapter 4

## TCV: Tokamak à Configuration Variable

*TCV is a medium-sized tokamak in Lausanne, Switzerland with an open divertor geometry and carbon walls on which the research in this work is based. The open divertor geometry enables a complete and thorough investigation of the relatively large outer divertor leg, which is exploited in this work in order to accurately measure the various processes of detachment along the outer divertor leg.*

### 4.1 TCV overview and capabilities

Table 4.1: Overview of TCV parameters

Major radius, $R$	0.89 m
Minor radius, $a$	0.25 m
Plasma elongation	0.9 - 2.8
Plasma triangularity	-0.8 - +0.9
Maximum plasma current	1.2 MA (diverted $\sim 400$ kA)
Max. discharge duration	2.6 s Ohmic (4 s ECCD)
Core peak electron density	$5 \times 10^{18} \text{ m}^{-3}$ to $5 \times 10^{20} \text{ m}^{-3}$
Max. Ohmic heating	1 MW
Max. NBI heating	1 MW
Max. EC heating	4.5 MW
Max. toroidal field $B_t$	1.54 T
Divertor densities	$3 \times 10^{18} \text{ m}^{-3}$ to $2 \times 10^{20} \text{ m}^{-3}$
Divertor temperatures	<1 eV to 50 eV
Upstream densities	$3 \times 10^{18} \text{ m}^{-3}$ to $5 \times 10^{19} \text{ m}^{-3}$
Upstream temperatures	15 eV to 50 eV

TCV, or 'tokamak à configuration variable' in French, is a Medium Sized Tokamak based in Lausanne, Switzerland. As such, it is one of the three national tokamak devices operating as European facilities within the medium-sized tokamak work package of the EUROfusion consortium. A picture of TCV is shown in figure 4.1 and the basic plasma and machine parameters of TCV are listed in table 4.1.

The TCV tokamak has a carbon wall, which is boronised after every major shutdown phase, making carbon and boron one of the main impurities on TCV. TCV has

access to one single NBI heating beam and an ECRH heating system, which is often used for advanced plasma control experiments (such as mode tracking). The discharges discussed in this paper are in L-mode without, disrupt due to MHD activity during either density or impurity seeding ramps and are in 'reversed field' (e.g.  $\nabla \vec{B}$  unfavourable for H-mode), while the current direction is also reversed to obtain the same field line helicity.

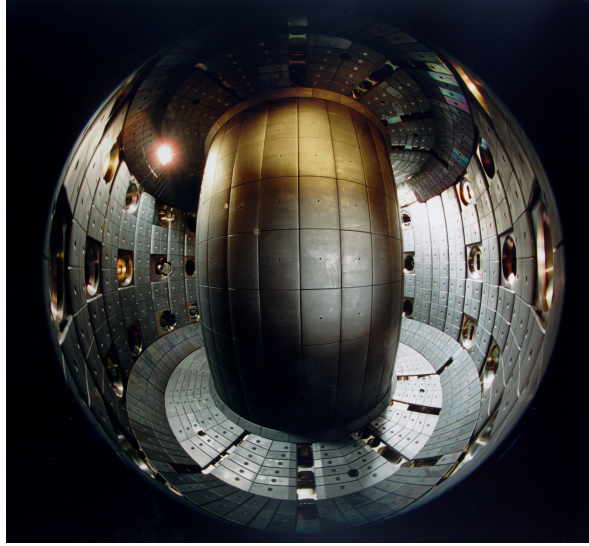


Figure 4.1: Picture of the interior of TCV with graphite tiles installed. Courtesy of SPC, EPFL, Lausanne, Switzerland

TCV is mainly known for having an open divertor geometry with 16 independently operable coils to control the plasma shape, giving rise to the unique capability of generating exotic plasma shapes, including single null ('standard' configuration), double null, snowflakes, negative triangularity, etc. Such unique shaping capability is important for scientific fusion studies focusing on the influence on plasma shape on core transport/turbulence and the influence on divertor geometry on divertor performance, detachment onset and window through accessing advanced divertor regimes (section 2.5) shown in figure 2.11.

## 4.2 TCV diagnostic capabilities

The open divertor geometry on TCV enables good diagnostic access of the divertor region of TCV, which is exploited in this work to provide a detailed characterisation of TCV detachment. A more in-depth discussion on the various diagnostics including their capabilities used in this work are shown below. As a reference, the locations and line of sight of the various diagnostics used in this work are shown in figure 4.2 adopted from [2].

### 4.2.1 Measuring radiative losses: bolometry

TCV has access to a 64 channel gold foil bolometry system, using 8 cameras with lines of sight determined through pinholes [166, 167, 168]. Radiative losses by the plasma heat up the gold foil, which is detected through measuring the resistance change of the gold foil using a balanced Wheatstone bridge, leading to a measured voltage which is calibrated to obtain the radiated power. The lateral lines of sight of the bolometry system are shown in figure 4.2b.

One disadvantage of using gold foil bolometers is that gold partially (1-35 %) reflects photons with wavelengths between 12 nm to 250 nm, while photons with wavelengths longer than 250 nm are strongly reflected (35 - 100 %). If a significant amount of radiated power is radiated in these regions, the measured radiated power can be strongly underestimated. This is thought to be problematic particularly in detached conditions, where a relatively large amount of the radiated power loss is due to line emission at such wavelengths [169]. A carbon

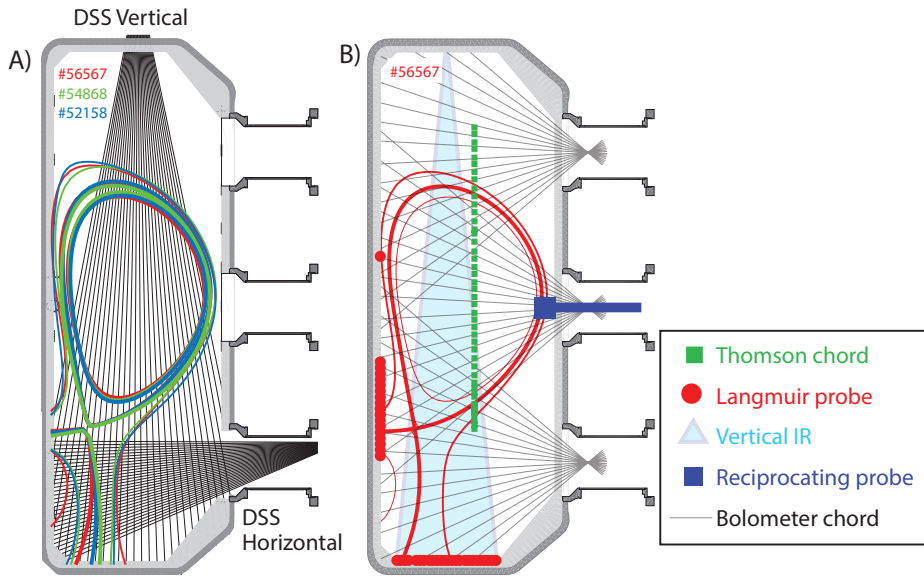


Figure 4.2: a): Lines of sight of the horizontal and vertical DSS systems. Divertor geometries for #56567 (red), #54868 (green), #52158 (blue) are shown. b) Lines of sight and locations of other diagnostics (Thomson/Langmuir probes/Vertical IR/Reciprocating probe/Bolometry together with the divertor geometry of #56567. Adopted from [2].

coated bolometer (with less reflections in those regions) has been compared with the gold foil bolometer showing  $\sim 15\%$  more radiative power in attached (limiter plasma) conditions [169], which could be larger in detached conditions. Therefore, in this work, we assume that the bolometer radiated powers are underestimated by at least 15 % while an uncertainty (68 % confidence interval) of 5 % has been assumed.

### Inversion-less analysis of bolometric data

Bolometry results are line integrated measurements which are generally inverted in order to obtain 2D maps of the radiated emissivities. By integrating over those maps (and over specific regions) the radiated power in the core, external, private flux regions and total radiated power are estimated [168]. However, given the limited bolometric coverage on TCV, such inversions can lack accuracy. Especially the difference between core radiation and SOL radiation is hard to estimate as the inversions tend to overestimate the radiation upstream, as shown in figure 4.3. Sometimes, that can be seen by calculating the required carbon concentration at that position in order to provide such radiation given estimates of the density and temperature at that location, leading to non-physically high carbon impurity fractions.

Therefore, an inversion-less technique has been established to estimate the radiated power in the divertor and core, which only uses the lateral lines of sight of the TCV bolometry system. The advantage of this technique is that it tends to provide more stable results. One large difference between this technique and the standard inversion (general TCV convention) is that the regions in which the radiation is evaluated are differently defined. As opposed to defining the regions as core, external and private flux [168], instead the plasma is divided as a divertor region (below x-point) and a core region (above x-point). As we are mainly interested in this work in the power entering the outer divertor and the radiated power in the outer divertor, the bolometric chords intersecting the inner divertor leg are omitted from the

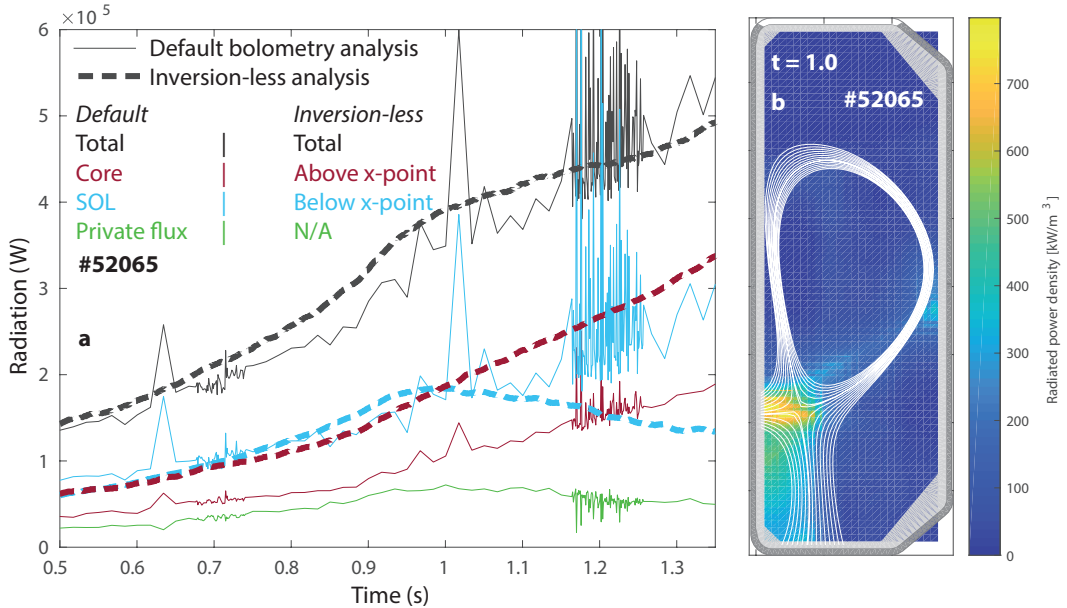


Figure 4.3: a): Radiative power as function of time for # 52065 determined through the default analysis and through the inversion-less routine. b) Example of the inversion result [2]

analysis.

The radiated power in the outer divertor leg is estimated by using the chords intersecting the outer divertor leg. This provides a profile of the outer divertor leg radiation in  $W/m^2$  as function of the  $r,z$  coordinates at which the lines of sight intersect the outer divertor leg. From this, one can estimate the radiated power in the divertor by integrating toroidally over this profile. This technique is similarly to how divertor integrated quantities obtained from the DSS are obtained, which will be explained later 7.3 and follows the analysis from [63]. Using a similar technique, the radiated power in the inner divertor leg is estimated by using chords which only intersect the inner leg/x-point region.

The radiated power in the core is estimated similarly. First, only chords are considered which integrate *only* through the core and not the divertor regions. Afterwards, the core is discretised using a vertical mesh. The intersections between the different lines of sight and the mesh are determined. It is assumed that the emission corresponding to each line of sight is equally distributed to all intersection points of that line of sight: e.g. if there are  $N$  intersections, the emission at each intersection is  $1/N$  the radiation corresponding to the chord in  $W m^{-2}$ . Alternatively, one could use the emissivities obtained through the inversion to divide the line integrated emissivity proportionally among the various intersection points (which does not lead to a noticeably different result). As such, a radiation profile is obtained on the vertical mesh which is toroidally integrated similarly to how the outer divertor leg radiation is obtained, leading to a radiative loss in W.

In order to see whether any coverage of the plasma is lacking, this technique is also used to calculate the plasma volume which is compared with the plasma volume obtained directly from the equilibrium reconstruction. The radiated powers (in the core / outer divertor / inner divertor) are multiplied with the ratio between their calculated volumes. To compensate for the lack of coverage, it is assumed that the plasma radiates similarly outside of the observed area than in the observed area: e.g. if only 90 % of the volume is covered the total radiation

is estimated to be  $1/0.9 \approx 1.11$  higher than initially estimated.

Figure 4.3 a shows an example of the radiated power of the various regions determined through the default routine and through the inversion-less routine. Although the total radiated power is of the similar order, the division of the two powers is different between the two techniques. If one would estimate the power flow into the divertor by subtracting core radiation or above x-point radiation from the power in the core, one would thus obtain radically different results and trends. Furthermore, the radiated powers estimated through this inversion-less routine are more stable; but this likely has to do with the fact that the data quality for the discharge shown is poor for the top and bottom systems which affect the inversion but does not influence the inversion-less routine as that only relies on lateral chords.

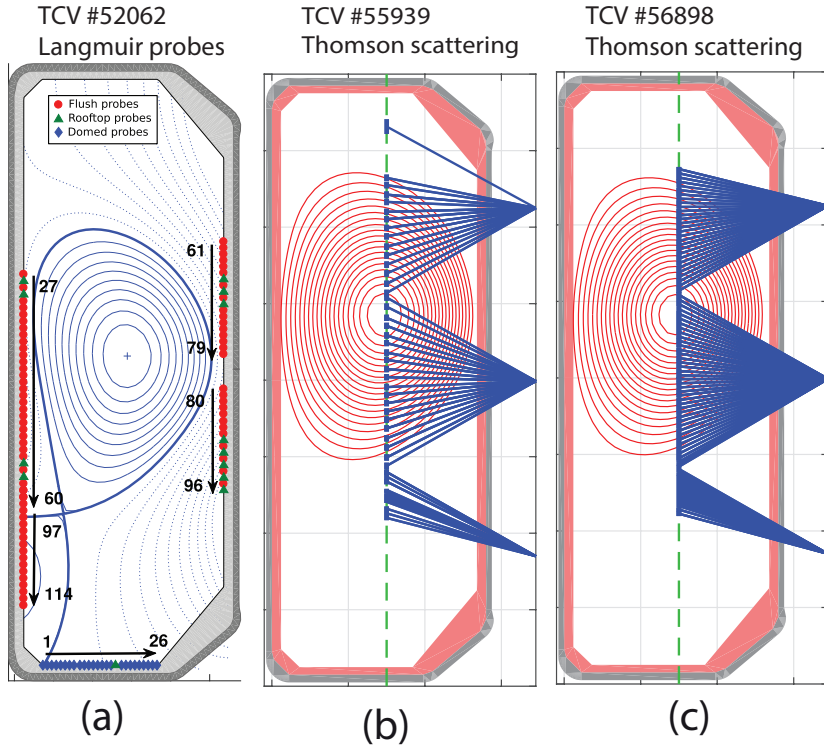


Figure 4.4: a): Langmuir probe coverage adopted from [117]. For illustration a typical plasma geometry (single null) is plotted (shot #52062). b) Thomson scattering coverage before upgrade adopted from [170]. c) Thomson scattering coverage after upgrade adopted from [170].

#### 4.2.2 Measuring target heat fluxes: infrared thermography

TCV has access to both vertical and horizontal infrared thermography cameras which provide measurements of the tile temperature due to an in-situ calibration using a heated tile which relates camera count to surface temperature [168, 99]. These estimates of the surface temperature are used in combination with the THEODOR analysis code [168, 43, 171] to provide estimates of the total power and heat flux profile reaching the strike point.

#### 4.2.3 Langmuir probes

TCV has access to an array of wall Langmuir probes (rooftop and flushed probes at the vertical surfaces, domed probes at the target) to monitor ion target current at the divertor

strike points together with electron temperature and density estimates, shown in figure 4.4a (adopted from [117]). The Langmuir probes are generally biased with a voltage which is swept, while the resulting current is measured leading to an IV measurement curve. These measurements are combined with an advanced four parameter fit in order to extract plasma parameters from the reciprocating probe measurements [117], while optimizations and cleaning to the signal are applied to remove artefacts induced due to finite resistances in the Langmuir probe circuitry.

Langmuir probes are known to overestimate  $T_e$  (and thus underestimate  $n_e$ ) in low temperature (detached  $T_e < 5$  eV) conditions [118, 119, 117]. Although the applicability of the advanced four parameter fit has found to reduce the obtained temperature in detached conditions, Langmuir probe temperatures are still likely overestimated as LP  $T_e > 3 - 4$  eV over the entire target profile are measured while volumetric recombination is observed spectroscopically. This overestimation of the temperature is attributed to the expectation that the energy distribution of the electrons reaching the target are not fully described by a Maxwellian and have a high energy component. This suprathermal electron populations will influence the  $T_e$  LP measurement and change it from the bulk  $T_e$ . Furthermore, the fact that Langmuir probes could potentially bias a flux tube due to the voltage applied, makes it not a fully passive measurement and also this may influence the  $T_e$  determination. Hence, in this work where detachment is investigated, the LP ion target current measurement is used, while the LP derived  $T_e, n_e$  are not used.

#### 4.2.4 Reciprocating probe

The TCV reciprocating probe is a reciprocating probe on loan from USCD [172, 173] which has been used on other tokamaks previously. The reciprocating probe can plunge into the scrape-off layer of the plasma (it is currently installed on the mid-plane) for a limited amount of time, to get a single (as function of time) measurement of the upstream plasma profiles (electron density and temperature) at a spatial resolution of  $\sim 1$  mm including fluctuations on those measurements [173]. Reciprocating probes are often used for investigating the shape of the upstream density/temperature and heat flux profiles [8] and for fluctuation studies [174, 175]. Their disadvantage, however, is that only two plunges per discharge can be done. Discharges thus need to be repeated in order to obtain more snapshots. One can combine the high spatial resolution RCP data with the lower spatial resolution Thomson data in order to combine the strengths of both diagnostics: high spatial resolution and high(er) temporal resolution.

#### 4.2.5 Measuring core and upstream temperatures/densities: Thomson scattering

Thomson scattering on TCV is a routine diagnostic for monitoring of both core and upstream SOL densities and temperatures. It contains three lasers which can either be interleaved or fired simultaneously for either higher temporal resolution or higher signals. Interleaving enables Thomson to operate at a maximum frequency of 180 Hz.

Recent upgrades to the Thomson system [170] have substantially improved the Thomson scattering coverage of the scrape-off layer, enabling a spatial resolution of around 1% of the

minor radius in the pedestal region, resulting in  $\sim 6$  mm spatial resolution (figure 4.4 b,c). This upgrade has proven important for monitoring the upstream conditions in this paper.

Another routine diagnostic for the electron density on TCV is a Far InfraRed (FIR) interferometer [176], through which a line integrated density estimate is obtained. Those measurements are also used for density control purposes. The default Thomson result on TCV is generally altered by a 'FIR to Thomson correction ratio', which modifies Thomson determined densities to provide the same values as the FIR line integrated density. That correction ratio is determined for every time step during a discharge. When the core density is continuously increased during a discharge; that correction ratio is observed to drift, for instance from 1.05 (low core densities) to 1.4 (high core densities and a detached divertor) for # 52065. That behaviour is not expected to be a physical correction factor for the actual density results measured by Thomson. Possibly, as the FIR densities are line-integrated, what can be is that a significant portion of the line integrated density picked up by the FIR is picked up from the divertor leg in cases where the divertor densities are high with respect to the core/upstream densities (e.g. detached cases). This is why, in contrast to standard TCV convention, we do not apply the FIR to Thomson correction ratio in this work when Thomson data is shown.

When the upstream density/temperature is determined, the values are obtained from the Thomson chord closes to the separatrix. Although this can lead to a positional error which would result in systematic deviations between the measured parameters and the actual parameters upstream; this way any calibration uncertainty between the different Thomson chords is accounted for. It is observed that this leads to less noisy (over time) trends of the Thomson upstream parameters during a density ramp.

#### 4.2.6 Measuring neutral pressures: baratrons

Two baratrons are currently installed in TCV for obtaining neutral pressure measurements at the walls. These baratrons are of a similar type of those installed on JET [177]. The baratron are magnetically shielded, vibrationally isolated and are connected to the vessel by dedicated extension tubes [101], providing a divertor and mid-plane neutral pressure measurement. Depending on the divertor geometry, the divertor neutral pressure measurement could be located in the private flux region near the strike point or in the common flux region, which can influence the neutral pressure measurement [101]. The neutral pressure measurement is thus strongly dependent on the divertor geometry.

It should be noted that the pressure gauge does not measure the neutral plasma pressure directly but indirectly as the neutral gas during a discharge enters the extension tube. The neutral pressure measured after the extension tube, thus depends on how the neutral gas flow is altered in the tube [178, 179, 68]. Thus, neutral pressure measurements may be more useful as a qualitative tool rather than a quantitative tool or one has to assume a certain physics model which determines how the neutral gas flow is altered in the extension tube.

#### 4.2.7 Spectroscopy for boundary physics studies

TCV has several spectroscopic systems which are crucial for plasma edge studies, including multi-spectral imaging through filtered cameras; charge exchange recombination spectroscopy;

overview spectroscopy; fast camera imaging and a SPRED VUV (single line of sight) system. A newly developed Divertor Spectroscopy System (DSS) which has been developed as part of this thesis (chapter 5), whose lines of sight are shown in figure 4.2.

Charge exchange recombination spectroscopy is a routine TCV diagnostic for monitoring of core and plasma edge ion temperatures/carbon content and plasma rotation using absolute intensity calibrations and an in-situ wavelength calibration which runs after every discharge [180].

Spectral imaging combines a camera image of the TCV plasma with an interference filter which transmits at particular wavelengths. By specifying interference filters such that they correspond to a certain spectral line, 2D images of spectral line emission can be established. Such images can be inverted [81, 79] and are most often used for qualitative information on the dynamics of the various emission regions in the plasma.

Multi-spectral imaging aims at using a single view and re-arranging this light in such a way that it can be imaged on multiple cameras with spectral filters. This can be either achieved using beam splitters [181] or by using an optical cavity design, just like a Thomson polychromator, which leads to less emission losses when going to a higher number of channel ( $> 4$ ) system [182, 183]. In the timespan of this thesis, three different multi-spectral imaging systems have been used on TCV, MultiCam (4 channel beam splitter design) [181]; MSI (4 channel polychromator design) [182] and MANTIS (10 channel polychromator) [184].

In figure 4.5, an application of MultiCam on #52065 is shown during attached (0.6 s) and detached (1.0 s) conditions of the CIII (465 nm) and D $\alpha$  (656 nm) emission. This data has already been inverted and is obtained from [79].

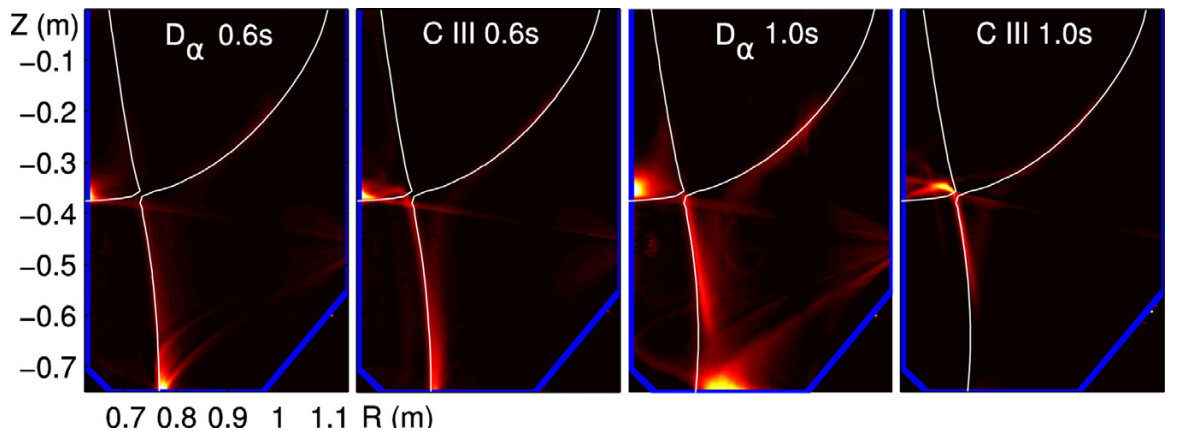


Figure 4.5: Example of inverted (non-calibrated) emissivities from the MultiCam system on #52065 in attached (0.6 s) and detached (1.0 s) conditions. Adopted from [79].

### Divertor Spectroscopy System (DSS)

The TCV Divertor Spectroscopy System (DSS) has been the principal diagnostic used in this thesis and has been developed as part of this thesis. Its lines of sight are shown in figure 4.2 a. More details are provided in chapter 5.

#### 4.2.8 TCV Diagnostic Control Systems

As part of this thesis, the general management system which controls the settings for TCV general diagnostics (also dubbed the 'Diagnostician Du Jour' (diagnostician of the day) DDJ system) and performs post-shot checks on the acquisition was improved.

Several enhancements and updates have been made to the tools which form the DDJ system in an effort to reduce repetitive tasks and further engage the DDJ in the physics behind TCV experiments and diagnostics. A new control window (through the VISTA system, a proprietary Human-Machine Interface which is the general control system for TCV actuators and diagnostics), together with data scopes, has been developed which uses MATLAB routines to perform routine checks on diagnostic data after every discharge and optimizes settings for the next discharges.

The main changes to the system can be summarised as follows:

- General oversight 'single-click' program for running routines which set diagnostic settings depending on a reference discharge ('autogain').
  - Checks for common operator errors
  - Manages possible errors and warnings output by the different setting routines
- Autogains for various diagnostics have been created or improved, including: soft-xray systems,  $D\alpha$  photodiodes, bolometry, electron cyclotron emission diagnostic and divertor spectroscopy. The new autogain implementation, for several diagnostics, has significantly reduced saturated data and significantly reduced the number of cases in which unusably low signal values were obtained.
  - Data optimization algorithms have been improved using histograms of the data obtained while excluding data taken before and the end/after the discharge.
  - Advanced data checks have been implemented which verify the reference data before using it as a data reference (this includes but is not limited to checks on erroneously low signals, checks on closed shutters, etc.).
- Automatic post-shot data verification for various diagnostics have been created or improved, including: soft-xray systems,  $D\alpha$  photodiodes, bolometry and divertor spectroscopy;
  - Checks investigate data availability, diagnostic state (e.g. whether the diagnostic is operational and follows the different states of a TCV discharge) and data quality (saturation and low signal levels).
  - Validates whether the machine's shutters for particular diagnostics during a discharge open
  - Validates if the gains set changed during the discharge cycle (which makes it such that the wrong gain values are stored, making the calibration of the data erroneous).
- Single click diagnostic start-up and shutdown routines. These routines manage the initial start-up of bolometry (including bridge balancing), divertor spectroscopy, photodiodes, soft-xray diagnostics, imaging camera diagnostics and output any warnings/errors in case something goes wrong with the initialisation of the diagnostic

## 4.3 Evaluating and using this experimental data for verification with SOLPS-ITER: synthetic diagnostics

SOLPS provides detailed simulations with a range of different output, plasma, parameters, as explained in section 2.6. Generally, such output parameters are not *directly* measured in an experiment. Instead, diagnostics measure *related* information and using numerical and physical models this information is transformed into an estimate of the plasma parameters. One way of providing a direct comparison between simulated data and the experiment is to use a *synthetic diagnostic*. Such synthetic diagnostic use models to predict what a diagnostic would see given the simulated data. This can then be compared directly with the diagnostic measurement. Additionally, it can be used to investigate whether diagnostics can actually reproduce the plasma parameters requested given their range of limitations by using the diagnostic analysis on the synthetic data and checking whether this corresponds to the data directly simulated by SOLPS.

To have the closest comparison between the experimentally measured densities and the densities obtained in the experiment, the temperature and densities simulated are interrogated at the grid cell where the intersection between the Thomson laser and the Thomson lines of sight corresponds to.

**Technical implementation** In order to establish synthetic diagnostics for TCV, a technical toolbox has to be developed which evaluates the atomic physics to get line emissivities and radiated power using ADAS (section 2.4) in combination with the SOLPS model solution. Those line emissivities and radiated power might deviate somewhat from the actual values in the simulation as different atomic physics tables have been used.

Many diagnostics make chordal integrated measurements and such synthetic diagnostics thus requires one to make a line integral though simulated parameters which are on a 2D map of grid cells where the shape of each cell deviates from one to another. When making such chordal integrals, it also has to be accounted for that a diagnostic has a certain viewing cone as opposed to a 'pencil-like' line of sight in the plasma. To account for this, each line of sight is modelled as a series of "sub lines of sight", which have a slight shift in their angle specification. The combination of those lines of sight mimics a viewing cone. A spatial profile also has to be ascribed to each viewing cone for which we use a Gaussian centred at the main angle of the line of sight. Each "sub" line of sight is discretised into many elements ( $> 1000$ ). It is checked which of these elements are inside each SOLPS-ITER grid cell and the value of the particular quantity which is line integrated is than copied to that element. This technique ensures that interpolation is not necessary.

### 4.3.1 Synthetic bolometry

As explained earlier, bolometry provides line integrated measurements which are calibrated to provide the line integrated radiated power  $W/m^2$ . For this, we have developed a synthetic diagnostic. This first calculates the radiated power in SOLPS due to carbon and deuterium using ADAS and afterwards performs line integrations given the lines of sight of TCV bolometry together with their values for the etendue, eventually yielding a measure for  $W/m^2$ , which can be fed into the bolometric inversion algorithms discussed previously.

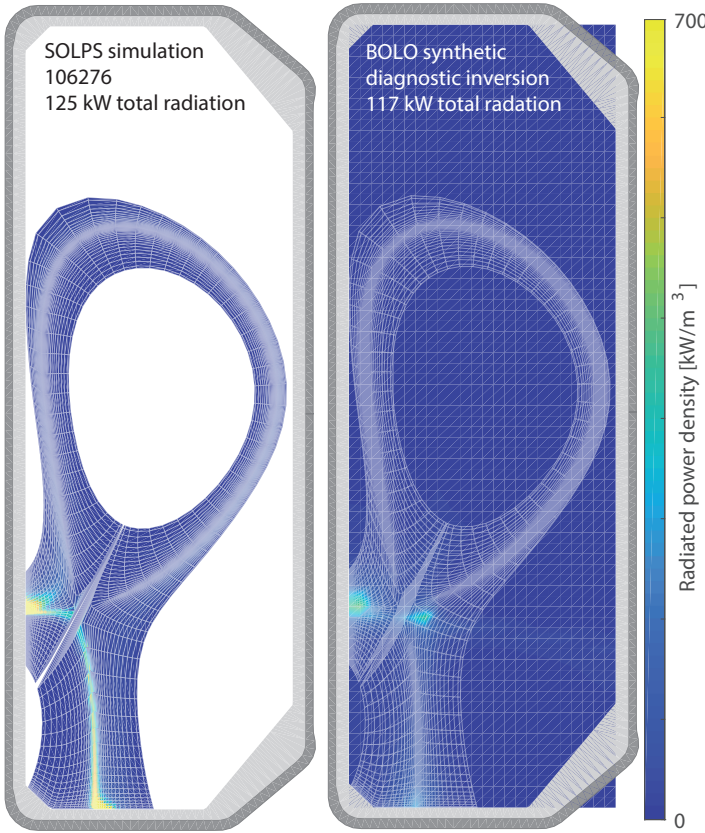


Figure 4.6: Comparison between a radiation map of a SOLPS discharge and the estimated radiation map by bolometry using a synthetic bolometer diagnostic with an inversion algorithm on the same colour axis. The SOLPS grid is over-plotted

This has been performed for SOLPS simulation # 106276 (which is attached; start of a density ramp). The actual SOLPS radiation map and the bolometry synthetic diagnostic inverted data is shown in figure 4.6. This indicates, as we expected earlier, that given the resolution of the system the detected emission is largely spread-out and can lead to artefacts, for instance the ray from the lower diagnostic port towards the x-point and the x-point emission at the low-field side of the x-point; both which are not in the simulation. Furthermore, the radiation at the target is mostly missed, which could be due to the relatively coarse resolution (figure 4.2). Despite this, the total radiation is fairly well estimated within 10 % of the simulated radiation.

#### 4.3.2 Synthetic baratrons

A synthetic neutral pressure gauge for SOLPS-ITER has been implemented based on equation 4.1, based on [68] p. 192, which can be compared with measurements by pressure gauges, installed at two different locations, during the experiment (section 4.2.6).

In this, we assume a very simplified model to translate the actual neutral pressure to the neutral pressure in the gauge [68, 179]. First, we assume that the neutrals entering the baratron are thermalised at the end of the baratron. Furthermore, we assume that the flow of the neutral gas is a non-viscous molecular flow, which is appropriate for high Knudsen numbers, meaning that the mean free path for neutral collisions (in the gas) is assumed to be larger than the dimensions of the gauge. Under such assumptions, the particle (neutral) flux

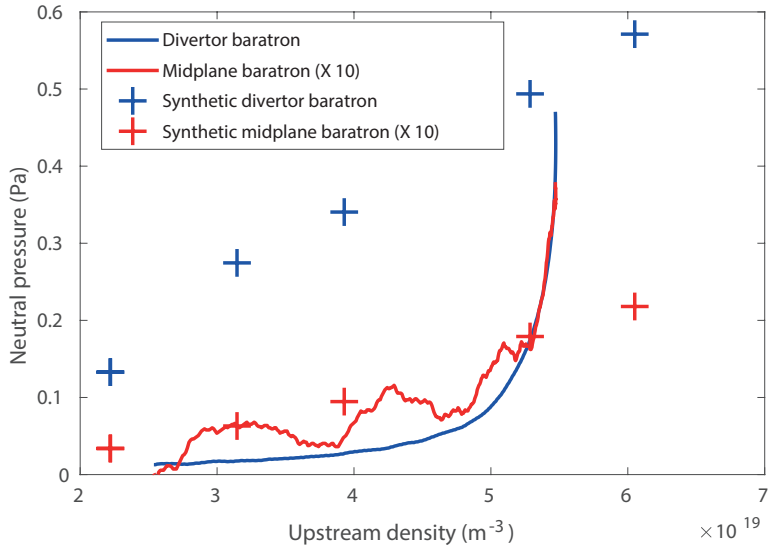


Figure 4.7: Comparison of the neutral pressure measured by baratrons (divertor and mid-plane) with the neutral pressure obtained in modelling through a synthetic baratron as function of the upstream density. The mid-plane neutral pressure has been multiplied by 10.

has to be constant, but not the pressure. Furthermore, it needs to be accounted that atoms re-associate once they reached the thermalised end of the baratron back into molecules.

Using the model above, the pressure in the neutral pressure gauge is a combination of the pressure due to neutral atoms ( $p_{atom}^{gauge} = n_{atom}^{gauge} T^{gauge}$ ) and molecules ( $p_{molecule}^{gauge} = n_{molecule}^{gauge} T^{gauge}$ ), which depends on the respective densities in the gauge  $n_{atom}$ ,  $n_{molecule}$  and the temperature of the gauge  $T^{gauge}$ . The respective densities in the gauge are determined by the respective densities outside the gauge (e.g. the plasma at the wall) ( $n_{atom}^{plasma,wall}$ ,  $n_{molecule}^{plasma,wall}$ ), which again is determined by the neutral/molecular temperature of the plasma at the wall ( $T_{atom}^{plasma,wall}$ ,  $T_{molecule}^{plasma,wall}$ ) and the wall temperature  $T_{wall}$ . It has been assumed that  $T_{wall} = T_{gauge} = 300K$ . The SOLPS-ITER simulation provides  $n_{atom}^{plasma,wall}$ ,  $n_{molecule}^{plasma,wall}$ ,  $T_{atom}^{plasma,wall}$ .

$$\begin{aligned}
 p^{gauge} &= p_{atom}^{gauge} + p_{molecule}^{gauge} = (n_{atom}^{gauge} + n_{molecule}^{gauge}) T^{gauge} \\
 n_{atom}^{gauge} &= \frac{n_{atom}^{plasma,wall}}{\sqrt{2}} \sqrt{\frac{T_{atom}^{plasma,wall}}{T_{wall}}} \\
 n_{molecule}^{gauge} &= n_{molecule}^{plasma,wall} \sqrt{\frac{T_{molecule}^{plasma,wall}}{T_{wall}}}
 \end{aligned} \tag{4.1}$$

These parameters are averaged over the surface of the pressure gauge at the tiles. Here a spherical port size for the baratrons is assumed. This is important as there can be a strong deviation in the simulated neutral pressure along the baratron's surface, depending on the discharge and plasma shape —this can be over a factor four.

Using five SOLPS simulations [7], representative of a density ramp, which will be further discussed in section 8.1.1, the synthetic baratron pressure and the measured neutral pressure are compared. Figure 4.7 shows this comparison for #52065, indicating a reasonable agreement for the mid-plane baratron. For the divertor baratron, however, the synthetic neutral pressure is a  $\sim 10$  too high at the lower upstream densities (which correspond to attached conditions). Also, as indicated in figure 4.7, the neutral pressure strongly rises at the end of the density ramp while such a sudden rise is not observed in the simulation. The neutral pressure from

the synthetic diagnostic changes across the surface of the baratron by a factor  $\sim 4$ ; indicating that the neutral pressure result can be strongly spatially dependent (in the simulation), which may explain this discrepancy.

#### 4.4 Discharge reproducibility

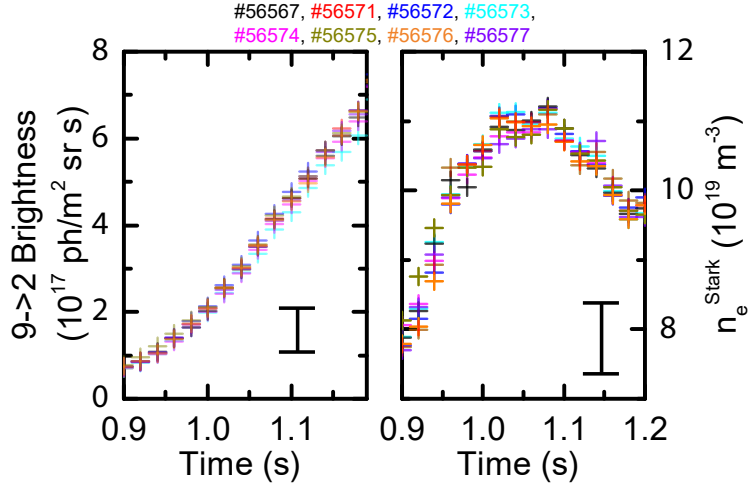


Figure 4.8: a)  $9 \rightarrow 2$  Balmer line brightness and b) inferred Stark density from the  $9 \rightarrow 2$  Balmer line obtained from the vertical system using the line of sight closest to the strike point location. Each colour indicates a different discharge. Characteristic uncertainties are shown in the figure.

As will be mentioned in chapter 7, there are cases where discharges have to be repeated in order to gain, considering the diagnostic limits, the required high resolution Balmer line measurements from two different spectral region settings on the divertor spectrometer. A case in point is TCV pulse #56567 (shown later) where lower-n Balmer lines ( $n = 5, 6$ ) are used for Balmer line ratios and ionisation/recombination calculations while the  $n=7$  Balmer line is utilized for Stark density inferences.

To demonstrate such reproducibility we show, in Figure 4.8, the variation of the brightness and Stark inferred density (see chapter 6) measurements for a set of eight identical discharges (#56567 is part of that sequence), repeated sequentially on the same day. The time dependencies of the Balmer  $n = 9$  line intensity (Figure 4.8a) and the derived chordal averaged (weighted by the  $n = 9$  (recombinative) emission profile) density (Figure 4.8b) are the same within uncertainty from discharge to discharges. In addition, results from other diagnostics (bolometry and Langmuir probes) also agree within uncertainty for the repeated discharges, indicating a sufficient reproducibility for our central measurements of the divertor plasma characteristics. However, the reproducibility of TCV discharges can deviate significantly from day to day due to altering machine conditions. In this work, only sequential diagnostic repeats are used.

# Chapter 5

## Divertor Spectroscopy System (DSS) on TCV

### 5.1 Divertor spectroscopy on TCV

*As part of this thesis, a novel divertor spectroscopy system has been developed for TCV, including the corresponding software systems for hardware control and CAD design of mechanical components. The system has been calibrated and characterised using state-of-the-art calibration techniques, including facilitating highly accurate lineshape fitting through a detailed instrumental function characterisation; smearing and stray light correction techniques.*

#### 5.1.1 Overview and capabilities of the Divertor Spectroscopy System on TCV

In scope of this thesis a novel divertor spectroscopy system has been designed, installed, commissioned and operated on TCV. The system contains of two separate spectrometers with cameras; both of which have identical hardware. Each spectrometer has a triple turret grating installed, enabling the user to change between the grating (which sets the trade-off between spectral resolution and spectral coverage) and grating angle (which sets the monitored wavelength regime) in between discharges as indicated in table 5.1. Accounting for the installed slit width, 25 µm —indicated by the dial and in agreement with measurements obtained through a microscope, laser diffraction experiment and spectrometer using the pixel size in a mirror configuration, which leads to roughly a 3 pixel FWHM instrumental function resulting in the indicative spectral resolutions of table 5.1. Using 32 lines of sight per system, which are programmed as 32 binned tracks on the CCD, the maximum acquisition frequency of the diagnostic is ∼ 200 Hz, although higher acquisition frequencies could be achieved by masking off regions of the CCD.

The horizontal lines of sight can be arranged in three different orientations, as indicated in figure 5.1. Changing between these three different orientations requires removing two screws and can be done between discharges. At the machine's side, the horizontal fibres are arranged in such a way that two linear arrays with identical coverage in the machine are present, which can be branched out to either of the two spectrometers, enabling the user to use two spectrometers simultaneously for additional spectral coverage. Alternatively, one of

Table 5.1: Overview of DSS parameters.

	Horizontal	Vertical	
Lines of sight	30-32	30-32	
Spatial resolution	1.4 cm	2 cm	
Acquisition frequency	<220 Hz		
Brightness range (discharge to discharge)	$1 \times 10^{13} \text{ ph m}^{-2} \text{ sr}^{-1} \text{ s}^{-1}$ (Fulcher band, EMCCD 50; 50 ms exp. time) - $4 \times 10^{20} \text{ ph m}^{-2} \text{ sr}^{-1} \text{ s}^{-1}$ ( $D\alpha$ , EMCCD 0; 5 ms exp. time; neutral density 2.0 filter)		
Spectrometer (grating)	1800 l/mm	600 l/mm	300 l/mm
Blaze	500 nm	500 nm	500 nm
Spectral resolution	0.06 - 1.1 nm	0.22 - 0.41 nm	0.44 - 0.87 nm
Spectral coverage	~19 nm	~63 nm	~131 nm
Operational range	350-700 nm	350 - 1000 nm	350 - 1050 nm
Grating efficiency	50-80 %	40-80 %	40-80%
Camera		Spectrometer	
Size (pixels)	1024 x 1024	Focal length	320 mm
Pixel size	13 $\mu\text{m}$ x 13 $\mu\text{m}$	Aperture ratio	f/4.6
	>85 % (410-700 nm)	Stray light	$<2 \times 10^{-4}$
Quantum efficiency	35-85 % (350 - 410 nm)	Grating	68 x 68 mm (3 x)
	5-90 % (700-1050 nm)	Spatial resolution	>8 line pairs/mm
Digitisation	16 bit @ 30 MHz	Coma correction	16.4°
Vertical shift speed	1.13 $\mu\text{s}/\text{row}$	Astigmatism	0
Temperature	- 80 °C	Mirror reflectivity	>82 %
Dynamic range	>5 $\times 10^3$	Magnification	1:1

the spectrometers can be coupled to the available vertical lines of sight.

Other features of the system include the possibility to add filters between discharges in front of the collection optics. This is a necessary feature to enable monitoring bright spectral lines without saturation, such as  $D\alpha$ .

**Hardware description** The key DSS hardware consists of an Andor iXon Ultra 888 1024 x 1024 pixels (13  $\mu\text{m}$  x 13  $\mu\text{m}$  per pixel) EMCCD camera and a Princeton Instruments SCT 320 Isoplane spectrometer. Both components have a wavelength dependent 'efficiency' —as indicated in the ranges of efficiency in table 5.1. For the spectrometer this is optimised near the grating blaze wavelength and the quantum efficiency of the EMCCD is optimised in the visible range, decaying outside the visible regime. Both components are held together using a custom designed plate, enabling the camera to rotate and be aligned to the slit. TCV port usage has been optimised by integrating other diagnostics such as  $D\alpha$  photodiodes, ECRH protection probes and collection optics for the Ocean spectrometers into the same support mount on the tokamak, which has been custom designed and 3D printed using ABS (see appendix A.3). The light emitted from the divertor region is collected by a custom designed (by Yanis Andrebe) 2" diameter  $f = 32$  mm lens with an anti-reflection coating transmitting in the near-UV range (350 nm to 700 nm), which has minimal aberrations for the edge lines of sight. That lens is coupled to a linear array of 32 440  $\mu\text{m}$  diameter fibres (400  $\mu\text{m}$  core; 40  $\mu\text{m}$

cladding (the jacketing has been removed to ensure a higher packing ratio); where each fibre corresponds to a different line of sight in the plasma as shown in figures 4.2 and 5.1. This assembly is connected to the tokamak using a custom designed 3D printed ABS assembly, and fed into a linear array of fibres, each fibre corresponding to a different line of sight in the plasma, which is connected to the spectrometer's slit using a custom 3D printed assembly in the diagnostic's cell —see picture 5.2 and further discussion in A.3.

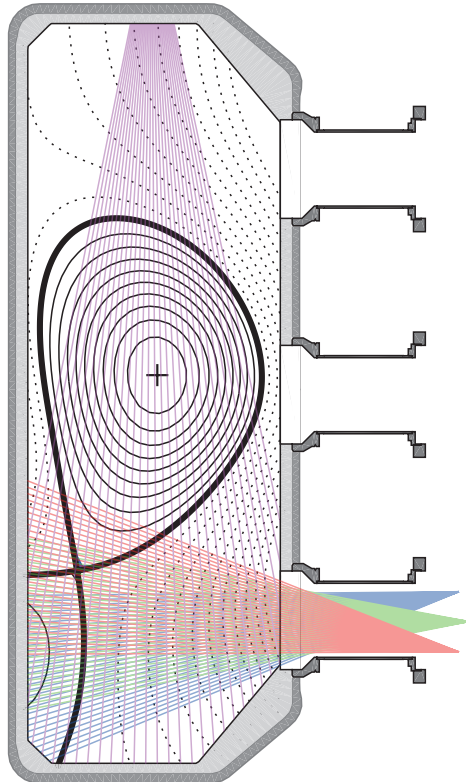


Figure 5.1: DSS lines of sight, showing the three different horizontal orientations (blue, red, green) and the vertical lines of sight (magenta) together with the equilibrium of # 56567 at 1.0 s.

nification of the system as function of object distance.

The various CAD models together with this magnification provide an estimate of the geometry of the lines of sight obtained in the tokamak. Due to mechanical tolerances and uncertainties (particularly related to mounting and re-mounting the lens-fibre coupler), a rotational uncertainty of up to 3 LoS is present, corresponding to 5 cm in the plasma. This uncertainty has been verified by back-lighting the fibres and taking images of the different light spots in the tokamak. As such an uncertainty is too large for quantitative measurements, the line of sight calibration is updated by tracking the spectral emission during the divertor formation phase of a discharge. During this phase, the strike point is formed and is swept along the inner column (and partially the floor, depending on the discharge). Spectrally, this strike point is noticeable due to a strong (spatial) peak in boron emission (BII at 412 nm).

By back-lighting the fibres, the system has been focussed. Important in this is that, as the divertor configuration can alter on TCV, the system has to be in focus for a fairly wide range (70 cm to 140 cm). This has been achieved by focussing the system somewhere in this range (more towards the low-end of the range than the upper-end of the range), while the edges of the range were tested to be of acceptable quality qualitatively, meaning that only negligible amounts of light emitted from one location will enter two neighbouring fibres due to a defocussed system as the individual fibres during back-lighting are clearly separable. By using a range of different light sources in combination with various spectral filters, ranging from < 425 nm short-pass filters to Wratten colour balancing filters emphasizing wavelengths in the red near 600 nm, the influence of chromatic aberration on the viewing optics has been tested. An acceptable focus was obtained throughout the entire regime measured and the focus has been optimised for the 400 nm to 425 nm regime. Back-lighting the system was also used to verify the magnification of the system as function of object distance.

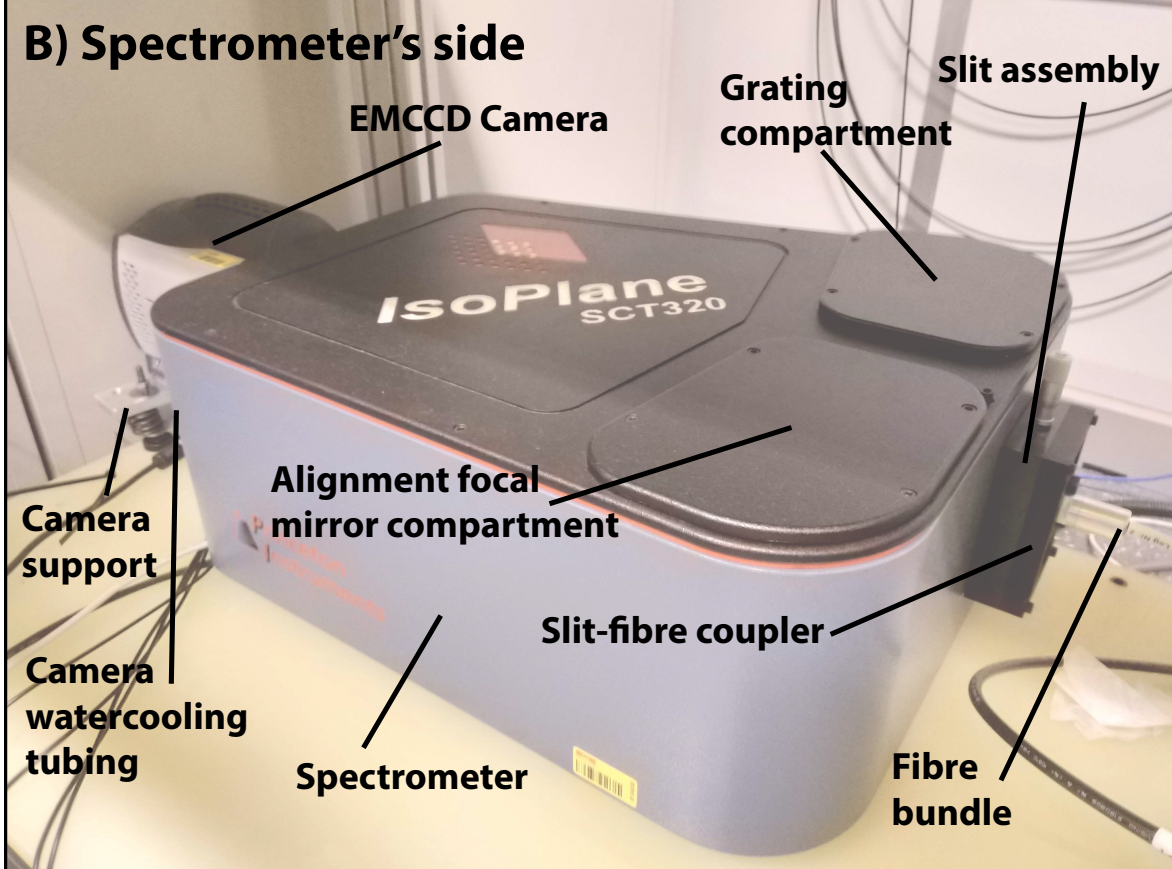
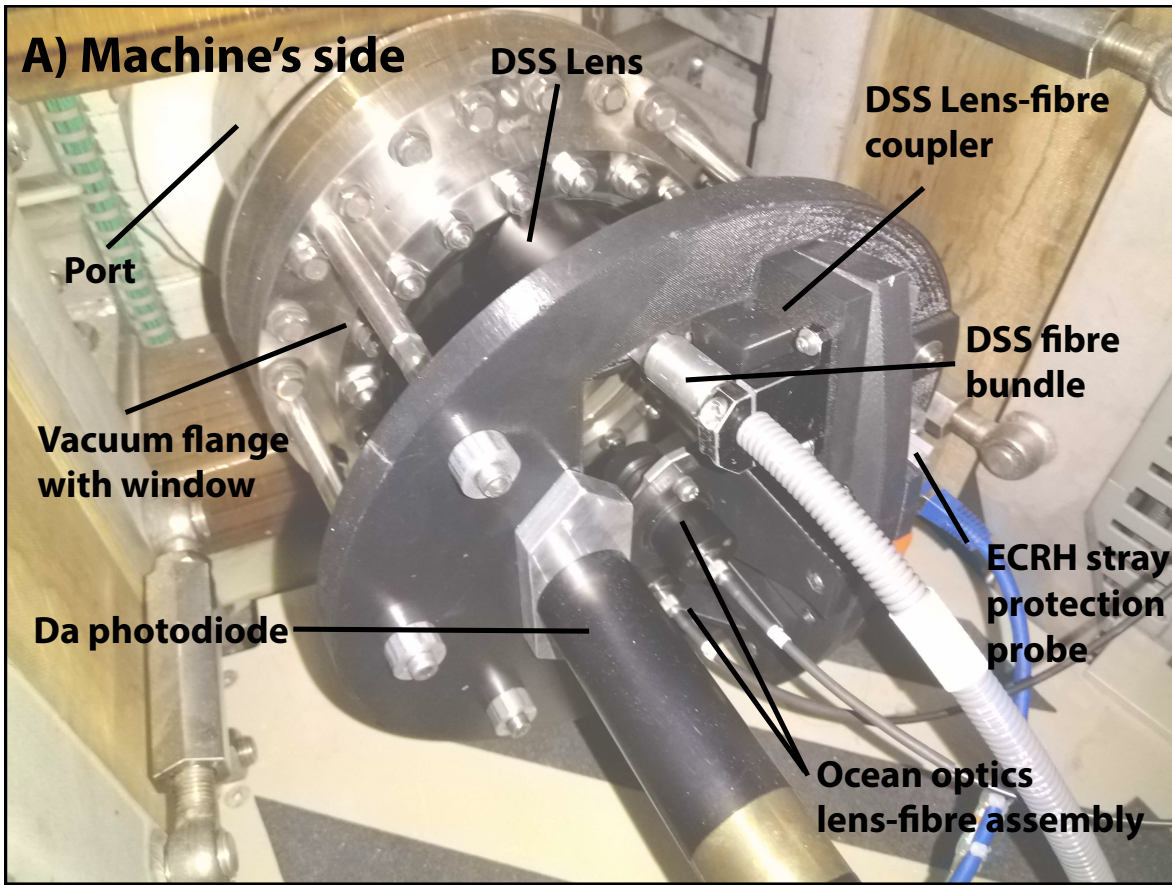


Figure 5.2: Pictures of DSS (Horizontal) system. a) Machine side. b) Tokamak side.

## 5.2 General details, alignment and track selection

Before going into the hardware details of the DSS systems, first we will highlight the alignment procedure, which also serves as an introduction for the nomenclature used. The spectrometer, camera and auxiliary systems (such as the hardware mounting, tokamak window transmission characteristics, etc.) are discussed later on, including a characterisation of these systems. Other information on the general basics on imaging spectroscopy can be found in literature [180].

To improve performance (acquisition speed, sensitivity and single to noise ratio), the camera is operated in 'tracked mode'. This means that all the emission from a set track is binned. The tracks are aligned to the different fibres, such that the emission from each fibre corresponds to individual tracks.

The camera has a spectral and spatial (fibres) dimension, which are orthogonal to each other. As only horizontal tracks can be set, the spectral dimension has to be aligned as much horizontally as possible while the spatial dimension has to be aligned as much vertically as possible. To do this, the slit is illuminated and the spectrometer is operated in its mirror configuration, such that a direct reflection is made of the light input through the slit. This should result in a vertical slit image in the CCD. The camera is rotated such that this is achieved. For that purpose, a routine has been developed which in real time outputs the slit image together with an analysis of its tilt using object recognition algorithms from MATLAB—which indicated a tilt of 1/1024 pixels at most (e.g.  $\approx 0.06^\circ$ ). For the most homogeneous results, the slit blades should be aligned as parallel as possible. The image recognition algorithm also provides an analysis of the parallelity of the slit, indicating a parallelity better than  $0.03^\circ$ .

After the camera is aligned to the spectrometer, the fibre assembly is aligned to the slit using the custom fibre-slit coupler, which provides rotational and translational freedom for the fibre bundle. The fibres are aligned in such a way that the most amount of light (given a fixed slit width) is received on the sensor, ensuring that the fibres are filling up the slit width as much as possible. This is illustrated by the image shown in figure 5.3, which shows the 2D full image observed when the system is illuminated with a spectral lamp. That image is obtained by observing a set of spectral lines, which are shifted over the sensor by modifying grating angle, which causes the periodicity observed in figure 5.3. That is done to see how the system behaves if a spectral line is positioned at a different point horizontally of the sensor. As the fibres are circular, if the fibres would be misaligned from the slit, then only the edge of the circle would be shown on the sensor. As shown, the distances between the different fibres is minimal, meaning that the centre of the fibre array is fairly well aligned to the slit.

A single spectral line generally appears curved along the length of the slit of a spectrometer, as illustrated in figure 5.3. This curve is generally observed in spectrometers (sometimes dubbed 'smile distortion') and could lead to a deterioration in spectral resolution if a significant curve occurs within a single track, corresponding to a single fibre. However, considering the fibres and the amount of smile distortion, this is negligible for this case. The smile distortion does, however, lead to a deterioration of the signal 'quality' at high framing speeds ( $> 100$  Hz) due to electronic shift smearing—which will be explained later in section 5.4.

Afterwards, the tracks have to be set-up on the sensor, also called 'regions of interest'

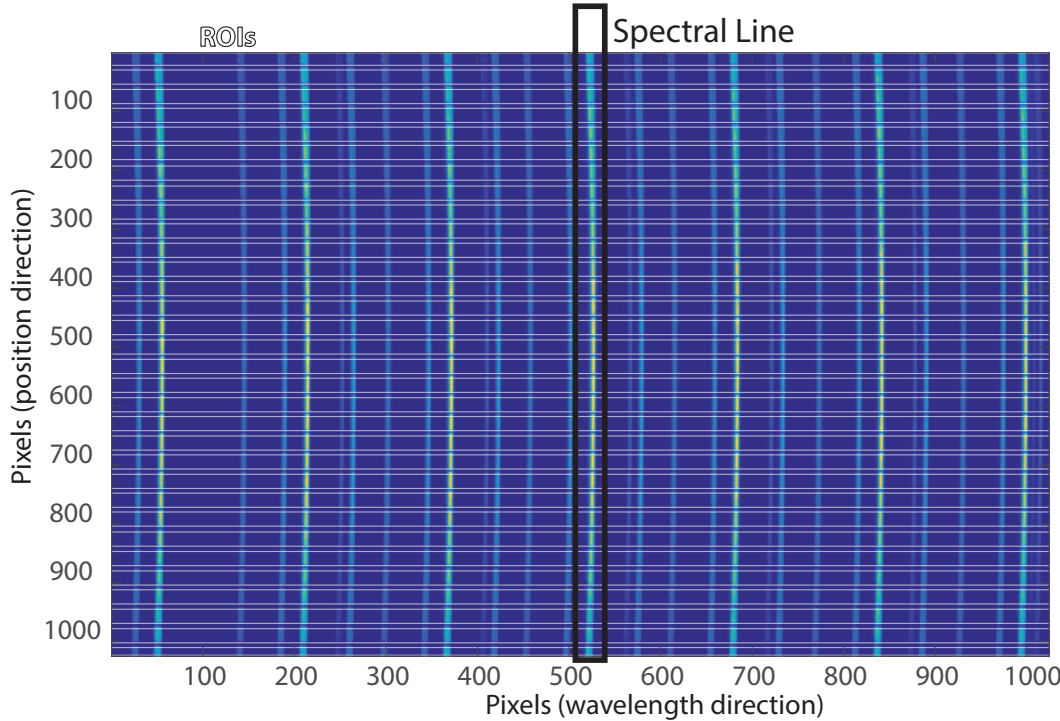


Figure 5.3: Image of the full-frame observation while monitoring a spectral lamp using the horizontal system with indicators of the spectral and spatial direction and the used ROIs. The spectral lamp used is Mercury-Cadmium at 365 nm central wavelength using a 600 l/mm grating.

(ROIs). There is a trade-off when setting regions of interest. One may think that the best way to set-up such regions is to centre them at the obtained fibres and leave no space in between the various regions of interest. Certainly, this would maximise the sensitivity of the diagnostic. However, when one would illuminate a single fibre, the light corresponding to that fibre would bleed out slightly outside of the fibre's bounds. If one would imagine that the emission obtained through one fibre is much brighter than the emission obtained through a neighbouring fibre, then this bleeding could contribute significantly to the signal of the neighbouring fibres; e.g. the signal 'pick-up' would become important. When the ROIs are narrower, pick-up decreases as an ROI would be further away from a neighbouring fibre, but the sensitivity of the diagnostic would decrease as well as some portion of the emission corresponding to the fibre monitored would be missed.

This trade-off is analysed in order to obtain the ideal spacing between the regions of interest. Such an investigation requires two separate measurements. First, the fibre illumination centres (e.g. centres of the regions of interest —ROIs) for each fibre need to be identified. This analyses/accounts for the deviations between the individual sizes of the fibre core/cladding diameters, which can deviate up to a few pixels considering the 5 % engineering tolerance. Secondly, the intensity profile of a *single* illuminated fibre vertically (in the ROI direction) on the system is required. Both of these measurements are obtained by illuminating the system with an incandescent source leading to a continuous spectrum as opposed to spectral lines. After the trade-off has been determined, the regions of interest have been chosen such that the expected pick-up remains below 30 % even if a neighbouring fibre would be ten times brighter, while 75-95 % of the signal corresponding to a single fibre is collected. An

illustration of the chosen regions of interest is shown in figure 5.4 where the grating angle is scanned such that the ROI choice can be investigated over a large wavelength range and the various measurements (e.g. images) are appended. The full analysis for obtaining the relevant ROI settings, according to the above brief description, is shown in appendix A.4.

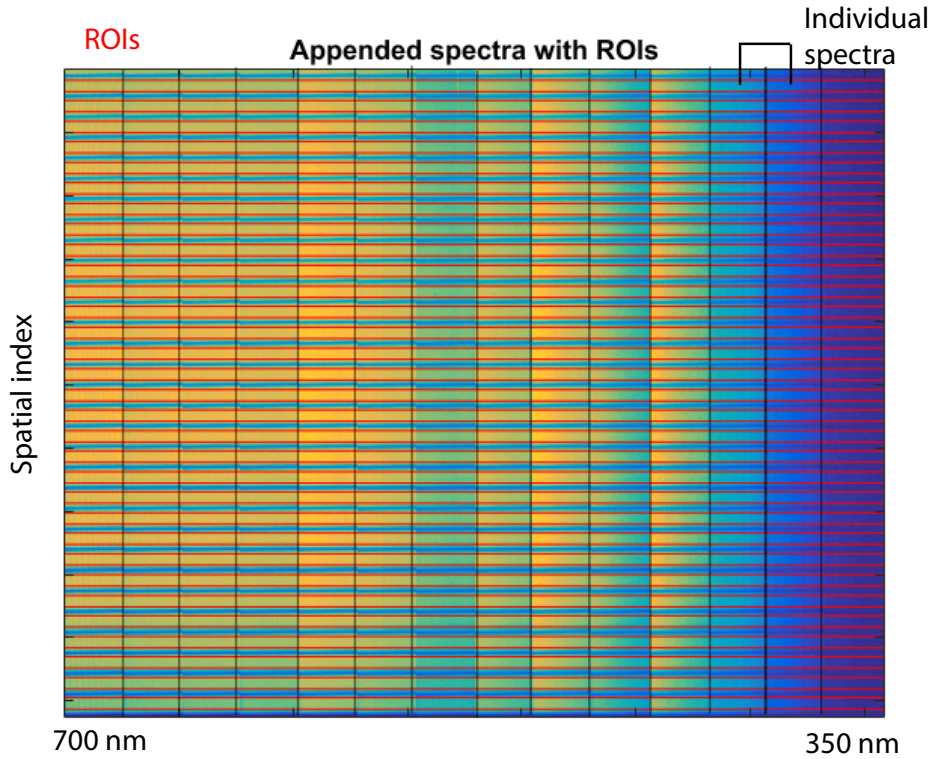


Figure 5.4: Spectra (full-framed) with tracks. Multiple spectra are appended. The colour bar corresponds to counts where yellow corresponds to the highest signal and blue corresponds to the lowest signal

**Setting the slit width** The final stage of the alignment procedure is to set-up the required slit width on the system using manually a micrometer on the slit assembly on the spectrometer. The slit width is fixed for each calibration run to maintain the calibration and due to the fact that the slit width is not reproducible, given the limitations of the mechanical design.

Considering the type of measurement the DSS has to perform, the spectral resolution of the system is close to the limit for Stark density inferences on TCV (chapter 6), considering the modest divertor electron densities on TCV ( $1 \times 10^{18} \text{ m}^{-3}$  to  $1 \times 10^{20} \text{ m}^{-3}$ ) when compared to higher density tokamaks ( $1 \times 10^{20} \text{ m}^{-3}$  to  $5 \times 10^{21} \text{ m}^{-3}$ ) such as C-Mod and ASDEX-Upgrade where Stark broadening is routinely applied [74, 73, 66]. Furthermore, especially during detachment studies, the line emission is generally not limiting and often neutral density filters need to be employed to avoid oversaturating the system. Therefore, the slit width is optimised to provide the highest possible spectral resolution as opposed to having a high system sensitivity.

Imagining an infinitely thin slit width, the obtained spectral instrumental function would be fully due to the spectrometer's intrinsic broadening. Imagining a very wide slit width, then the obtained spectral instrumental function would be almost fully dominated by the slit

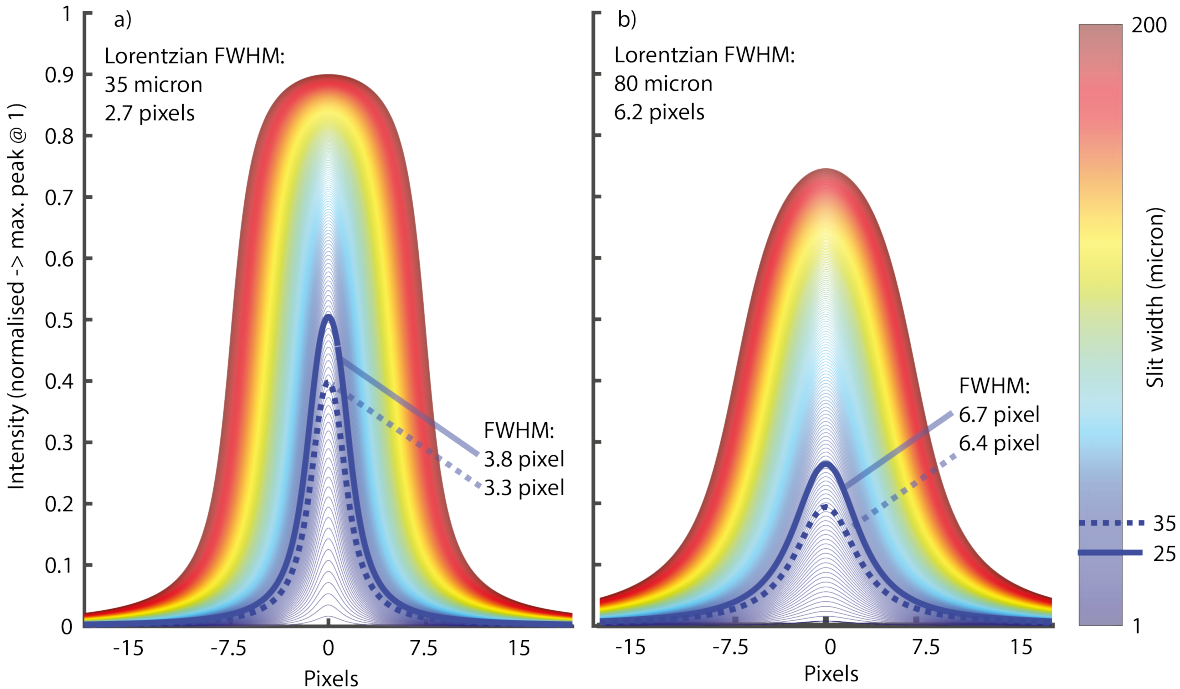


Figure 5.5: Modelled instrumental functions (convolution between a block function and a Lorentzian) as function of 'slit width', shown by the colour bar. The instrumental functions given a slit width of 25 and 35 micron are highlighted a) Lorentzian Full-Width-Half-Maximum is 35 micron (indicative of central fibres). b) Lorentzian Full-Width-Half-Maximum is 80 micron (indicative of edge fibres)

width as opposed to the intrinsic broadening of the spectrometer. The obtained instrumental function can be modelled as a convolution of the slit width (which can be modelled as a rectangular block) and the function determined by the instrument [137]. Important to note is that this is an instrumental function in micron (or pixels) on the CCD sensor and to get the spectral resolution, one has to map this with the dispersion —given by the installed grating. The obtainable dispersion of the Isoplane SCT 320 spectrometer is, however, fairly limited given the fact that the diagnostic is optimised for relatively low grating angles (see section 5.3.1). When increasing dispersion, higher grating angles are required to obtain the same wavelength range. Therefore, the aberrations in the diagnostic become significant when using a grating with higher dispersion than 1800 l/mm (the higher the lines per mm the higher the dispersion) in the visible range. That ultimately leads to a limit in spectral resolution of 0.6 Å to 1.2 Å for the DSS.

As will be discussed in section 5.3.1, the Isoplane SCT 320 spectrometer has its optics optimised for obtaining Lorentzian-like instrumental functions, as these have generally 'sharper' peaks than more common Gaussian instrumental functions. In this simplified model, the instrumental function is thus set by a convolution of a block function (describing the slit width) with a Lorentzian of a fixed width (describing the spectrometer broadening). For simplicity, we assume that the full slit is homogeneously illuminated. For instance, when the width would become larger than the fibres illuminating it; then any additional width would not increase the intensity —that is not accounted for here. That assumption can be well made as long as the slit width remains under half of the diameter of the core fibre. The obtained instrumental functions using this method are shown in figure 5.5.

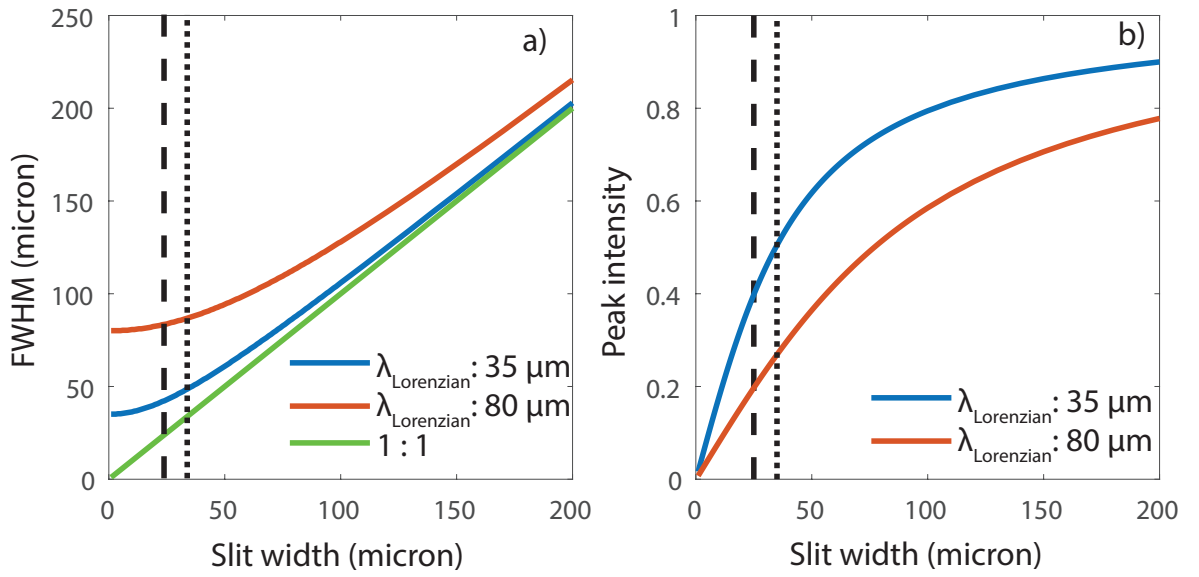


Figure 5.6: Parameters obtained from slit model highlighted in figure 5.5 as function of slit width in micron. a) Full-Width-Half-Maximum obtained for two different Lorentzian FWHMs shown together with the 1:1 trend to which the result will converge if the instrumental function is dominated by the slit function. b) Obtained peak intensity normalised such that 1 would be obtained if the slit function would no longer be smeared out.

The full-width-half-maximum and peak intensity as function of slit width using these instrumental functions is shown in figure 5.6. The obtained result shows that if one would open the slit width gradually, at first (assuming light enters the system homogeneously and no blemishes are present on the slit), the instrumental function would not change much as the convolution would be dominated by the instrument's broadening. At one point however, the instrumental function would start to widen as the slit width starts to lead to an increase in the effective instrumental function (note that this would be stronger with a conventional Gaussian instrumental broadening). As shown in figure 5.6, this roughly happens when the slit width becomes approximately half the width of the spectrometer's broadening. By qualitatively opening the slit and observing the resulting instrumental function, this point experimentally occurs around 25  $\mu\text{m}$  to 35  $\mu\text{m}$  for our spectrometer for central ROIs. From hereon we refer to this point as the 'optimisation point' (as the throughput is maximised in the region where the instrumental function is not changed much). Due to blemishes and scratches on the slit blades (estimated size of 5  $\mu\text{m}$  to 10  $\mu\text{m}$  using a microscope), slit widths below 20  $\mu\text{m}$  are not usable.

The instrumental broadening is significantly wider at the edges of the spectrometer than at the centre of the spectrometer by roughly a factor two. That means that the 'optimisation point' is first achieved at the centre of the CCD and later at the edges of the CCD. Generally, the slit width is set such that the optimisation point at the centre is just reached while it is not reached at the edges; optimising the system for sensitive line shape studies at the centre of the CCD —particularly important for Doppler broadening measurements, at the expense of throughput. However, depending on the calibration run, the slit width can also be larger up to the optimisation width for the regions at the edge of the CCD, enabling a higher throughput. When both spectrometers are available with identical lines of sight, one spectrometer is optimised for accurate fitting at the centre of the CCD and has a narrower slit

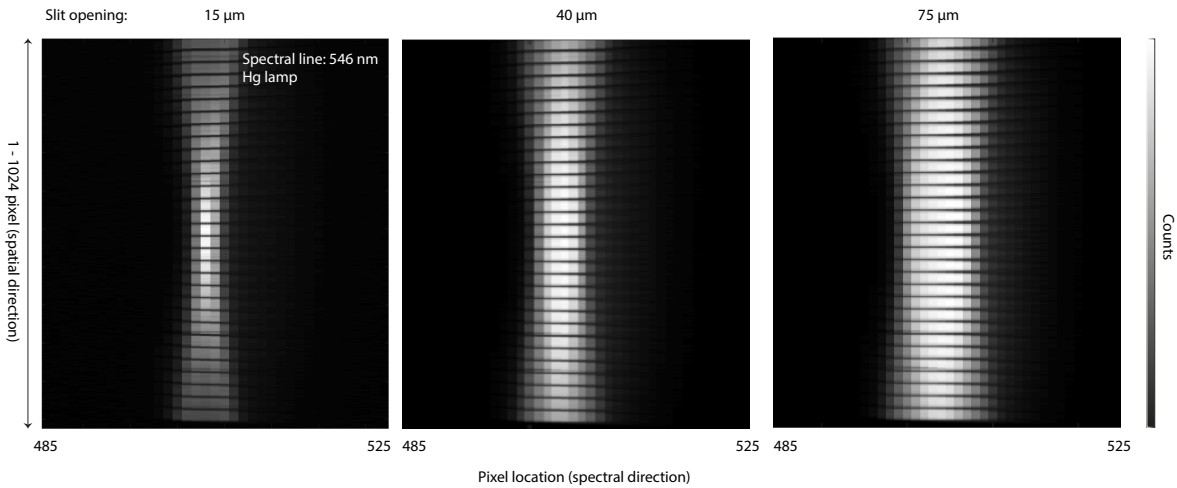


Figure 5.7: Pictures from the CCD output using a Hg spectral lamp with the spectrometer central wavelength being set at 546.1 nm (corresponding to a Hg spectral line) for three different slit widths. This shows greater deviation between central and edge pixels and lower peak intensity for the smallest slit width.

(optimisation point is reached at the centre), while the other spectrometer is more optimised for throughput and has a wider slit where the optimisation point for the edge fibres is reached.

However, as shown in figure 5.7, using such (relatively) small slit widths also leads to disadvantages. Not only does it limit throughput (the total throughput roughly scales linearly with the slit width assuming the slit width is much smaller than the fibre's diameter), it also limits the peak intensity obtained. For a fully open slit, this would theoretically be close to 1 considering figure 5.6, but that would require slit widths larger than realistic ( $>200\text{ }\mu\text{m}$ ). Limiting the slit widths to  $200\text{ }\mu\text{m}$ , the theoretical (simulated) 'peak' intensity ranges between 0.75 to 0.9 depending on the ROI location. For the slit widths currently employed (25  $\mu\text{m}$  to 35  $\mu\text{m}$ ) the 'peak' intensity ranges between 0.2 to 0.5 depending on the ROI location and precise slit width. This means that the obtained throughput (spectral line integral) and the peak line intensity could be significantly enhanced with a wider slit width.

### 5.3 Hardware and control details of the DSS

This section will provide a more in-depth overview of the used DSS hardware: spectrometer, camera and auxiliary systems (mechanical designs, details fires, back-illumination examples and window transmission). A discussion/overview of the mechanical design of the DSS is shown in appendix A.3, while further software/control details are provided in appendix A.5. A characterisation of the DSS spectrometer and camera is shown, together with an explanation of the camera's timing scheme and triggering solution. That is important as those details will explain the smearing which occurs due to the vertical shift of the CCD for which a correction algorithm is developed and shown.

#### 5.3.1 Spectrometer

The used commercial spectrometer (e.g. the Princeton Instruments Isoplane SCT 320) is a so-called Schmidt-Czerny-Turner spectrometer. In contrast to conventional mirror-based

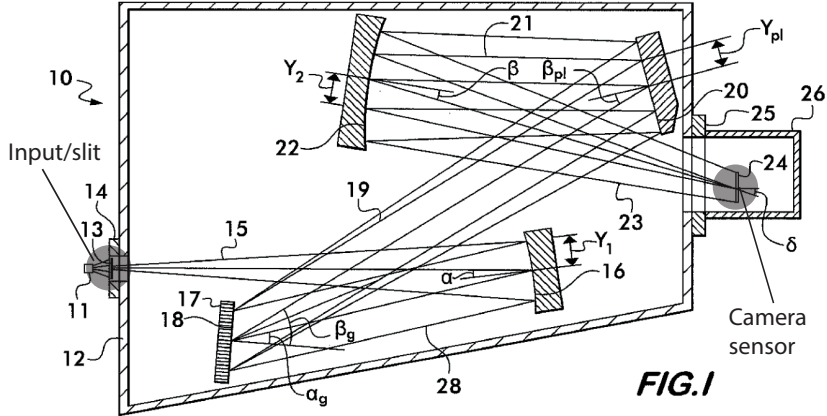


**FIG. I**

Figure 5.8: Overview of the Princeton Instruments Isoplane SCT 320 spectrometer adopted from its patent by [185]. The light input and camera sensor locations are marked.

spectrometers (Czerny-Turner), the Schmidt-Czerny-Turner adds an aspheric corrector plate which adds and/or subtracts certain aberrations. The principle idea of the design is that by choosing the right aspherical parameters, the design can be tuned (by setting the distance between the different components in certain ratios; by creating stop shifts; etc.) such that spherical, coma and astigmatic aberrations in theory cancel for a given particular grating angle [185]. To achieve this, the light does not reach the CCD's sensor perpendicularly but under a specific angle, which may lead to reflections at the CCD. This is accounted for by blackening the mount of the CCD to the spectrometer. The main specifications of the spectrometer are highlighted in table 5.1.

We will now discuss how the specification of the spectrometer agree or disagree with the investigations we have seen previously. When looking at the specifications of the system, minimal cross-talk between the channels is claimed due to the removal of astigmatic aberrations; more specifically, it is claimed that more than 100 spatial channels can be resolved with minimal cross-talk. Considering the previous discussion of the pick-up between different channels, leading to the choice of omitting  $\sim 2 - 4$  pixels in between two tracks, assuming 100 spatial channels this would mean that at least  $\sim 200-400$  pixels would be omitted from the set ROIs. It thus seems feasible to image 100 spatial channels on the CCD and possibly that is indeed related to the removal of astigmatic aberrations. Certainly the pick-up between the various positions of the CCD did not depend on the CCD position horizontally (wavelength direction); and the change in pick-up vertically is thought to be mainly due to differences in the individual fibres due to engineering tolerances. A schematic overview of the design of the spectrometer is shown in figure 5.8, which has been adopted from the patent of the spectrometer from [185].

When there is a deviation from this grating angle, spherical and astigmatic aberrations should still not exist, but coma aberration is increased, which influences the observed instrumental functions. The larger the deviation from the optimised grating angle, the stronger the coma aberration, leading to strongly asymmetric instrumental functions. The coma aberration is optimised for 465 nm using a 1200 lines/mm grating [185], which corresponds to a grating angle of  $16.4^\circ$ . Using a 1800 l/mm grating, the same grating angle would be achieved at 310 nm. Using such a high resolution grating, it is thus expected that the instrumental function

shapes deteriorates at higher wavelengths. The best performance (in terms of instrumental shape) is thus expected for the lowest operational range of the diagnostic in the near-UV ( $\sim 365$  nm). For the other installed grating (600 l/mm), this point corresponds to 930 nm, which is above the operational range of the DSS diagnostic. For those gratings it is thus expected that the performance (in terms of instrumental shape) is the highest near the upper end of the operational range. Furthermore, due to this, a better performance is expected with the 600 l/mm grating than with the 300 l/mm grating (in terms of instrumental function shape/asymmetry).

The quoted  $\#F$  number of the spectrometer is relatively large considering NA 0.22 fibres are generally used for spectrometers. That means that the acceptance cone of the spectrometer is fairly small when compared to that of the (NA 0.22) fibres. More specifically it means that the fibres will 'overfill' the acceptance cone of the spectrometer, and that excess light (75 % of the total emission of a NA 0.22 fibre, assuming the fibre is a point source at the optical access) can 'bounce around' the spectrometer, ultimately leading to stray light. On the other hand, if the fibres would 'underfill' the spectrometer; that would mean a loss of sensitivity of the system. Considering both points, the NA 0.22 fibres used previously on the DSS were replaced during this thesis with NA 0.10 fibres. Stray light is particularly an issue during absolute calibration in the near-UV range, which will be discussed in detail in appendix A.2. Furthermore, figure 5.13 shows the influence of using NA 0.22 or NA 0.10 fibres on the measured spectra in terms of stray light.

### 5.3.2 Camera

The cameras used on the spectrometer are Andor iXon Ultra 888 EMCCD cameras: back-illuminated EMCCDs with a frame transfer region, which are triggered using an external train of TTL pulses. These pulses are synchronised to the TCV clock. A vacuum seal is present on the camera together with a Peltier cooling element (with water-cooled assist), which enables the CCD to be temperature controlled and brought to below  $-80$  °C in order to minimise the dark current. The specifications and used settings of the camera are shown in table 5.1.

The photons incident on the camera's surface are transformed into photoelectrons in the light-sensitive region with a certain quantum efficiency, which for these cameras, is particularly high (up to  $> 95\%$ ) due to the back-illumination, for which the sensor was thinned. These photoelectrons are trapped in a matrix of potential wells, which make up the pixels. At each pulse, the camera starts shifting vertically the acquired (as the image is tracked 1024 x 32) image into the frame transfer region by applying voltages across the sensor. In the frame transfer region, the electrons at the bottom row travel horizontally (by applying horizontal voltages across the sensor) into the Electron Multiplication (EM) register. In the EM register, the clocking voltages used are higher, which enables electrons to acquire sufficient energy for impact ionisation, generating additional electrons. Although the probability of such an ionisation event is small, as there are many locations where such an event can occur, significant gains (up to  $\sim 1000$ ) in the electron count can be achieved through creating an avalanche. After the electron multiplication has occurred, the signal is read out and goes through an A/D converter and a pre-amplifier. As the signal multiplication takes place before the read-out phase, the low signal levels are no longer limited by the read-out noise. As such, the EM gain amplifier can be used to enhance signals above the typical noise level. EMCCD sensors

can have a much larger dynamic range than can be faithfully reproduced by the analogue to digital converter and installed electronics. To give access to the smallest and largest signals, a pre-amplifier gain can be changed, which determines the sensitivity of how many electrons lead to a count of the sensor.

The thinning of the sensor can give rise to etaloning and the appearance of fringes in the NIR wavelength region. This leads to oscillatory artefacts on the CCD, depending on the precise way the light enters the system. Such artefacts start to appear already at 600 nm: continuum illumination of the CCD would lead to an oscillatory pattern with an amplitude of <5% at this wavelength. This increases up to 15 % at 700 nm. The uncertainty of the system thus increases when measurements are performed at relatively large wavelengths ( $> 600$  nm).

The time the camera receives a TTL pulse from TCV is not exactly the time of the acquisition, but rather (near) the time the camera starts shifting the image into a buffer region and to understand how the TTL pulse train precisely correlates to the camera exposures, we have to highlight the timing scheme of the camera. When the camera receives the triggering pulse, it first waits for some time (10  $\mu$ s) after which the image is shifted vertically into the frame transfer region. As there are roughly 1024 pixels and the voltage application for each shift is clocked at 1.13  $\mu$ s per row, there is a frame shift time of roughly 1.16 ms. Important to note is that during this time, light still enters the CCD and thus falls on unintended places, leading to smearing, which will be discussed later and correction algorithms for vertical shift smearing are shown. After the vertical shift has finished, the exposure phase starts for the next TTL pulse. Assuming a perfect smearing correction and a periodic TTL pulse train with a period of  $T$ , when a TTL pulse arrives at  $t$ , the acquisition corresponds to the light sampled from  $t - T + t_{wait} + t_{shift}$  to  $t + t_{wait}$ . Using the suggested values above, this becomes  $t - T + 1.33$  ms + 10  $\mu$ s to  $t + 10$   $\mu$ s. Generally the periods used are either 10 ms or 5 ms. The latter corresponds to the fastest speed the camera can handle using the specified clock frequencies and using 32 tracks over the whole CCD. That means, for instance that for a TTL pulse at  $t$  with  $T = 5$  ms, the emission is sampled between  $t - 3.66$  ms and  $t + 0.01$  ms. The effective exposure time is thus less than the 5 millisecond period between two TTL pulses, but instead is 3.67 ms.

In order to drive the acquisition frequency as high as possible, it is beneficial to choose the fastest vertical and horizontal clock frequencies. That, however, also has disadvantages such as enhanced noise. Another difficulty is that once the clock frequencies are driven higher for shifting the electrons across the sensor, some pixels (e.g. potential wells) may start 'leaking', leading to a trail of electrons smeared over the sensor and resulting in a loss of signal integrity. To combat this, it is possible to overclock the sensor in such a way that the voltages applied are amplified, making the potential well less prone to leakage. Although this improves sensor stability when using the highest vertical shift speeds (figure 5.9a), the sensor still remains sensitive to transients. This is shown in figure 5.9b, where the sum of the integrated spectra for a single ROI is shown using a flashing LED (10 Hz) illumination source. For the first thousand frames, the stability is reasonable, but afterwards the signal starts drifting. That drifting is not present when a time-stabilised light source is used (figure 5.9b). As such, we use the second highest vertical shift speed together with the highest horizontal clock frequency; instead of the fastest settings, to ensure measurement integrity.

The cameras have various settings such as pre-amp gain, EM gain, horizontal shift speed

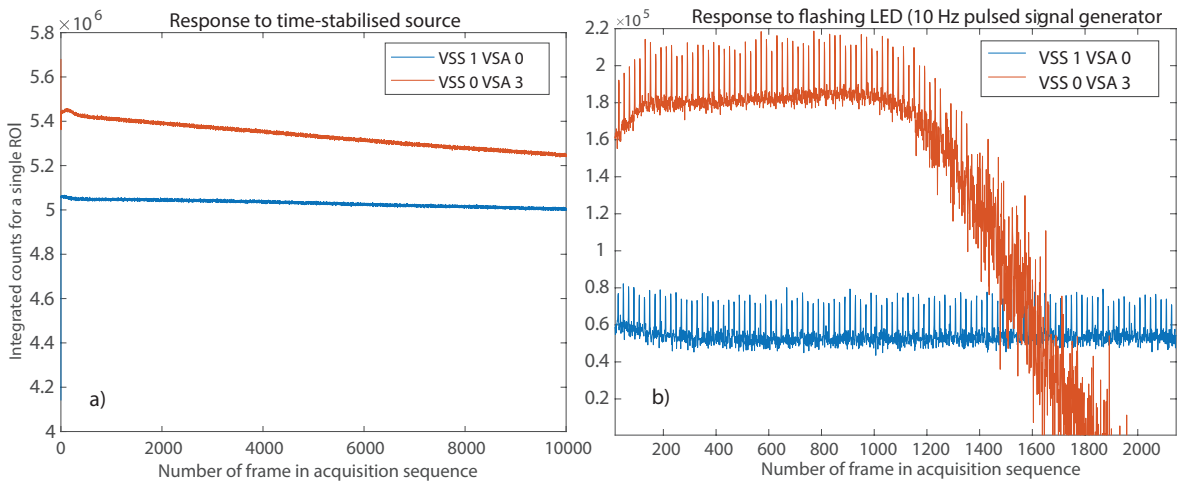


Figure 5.9: Integrated counts (not background corrected) for a single ROI as function of acquisition frame at 200 Hz acquisition for two different camera timing settings: fastest vertical shift with voltage overclock ('VSS 0 VSA 3') and second-fastest vertical shift without voltage overclock ('VSS 1 VSA 0') a) Time-stabilised source. b) LED flashing at 10 Hz.

and vertical shift speed. The sensor's sensitivity is a function of these settings; e.g. if either of these settings is changed a different calibration must be applied. The camera is therefore calibrated for a subset of these parameters, while the other parameters are held constant. This calibration is a relative calibration and is performed by using a time-stabilised source in front of the spectrometer. The calibration factor is then specified relative to the base calibration (0 EM gain and the parameters from table 5.1). When the absolute calibration is performed, these relative calibration factors are used to translate the absolute calibration to the base calibration camera setting. When an experiment is performed, the absolute calibration is used together with the relative calibration factor. The EM gain is also calibrated by scanning the EM gain and varying the exposure accordingly such that one would obtain the same counts always if the EM gain was perfectly linear. As shown in figure 5.10, this is not the case and some deviation (especially at low EM gains) between the expected linear EM gain and the measured EM gain occurs; which is accounted for in the calibration.

Furthermore, when using an EM gain it takes time (and acquisitions) to stabilise the EM gain registry. The time this takes has been measured to be  $\sim 30$  s and speeds up to  $< 10$  s after multiple acquisitions have been taken. As such, the system is programmed that some time before a discharge (e.g. in the TCV 'PrepShot' phase, which takes place 3 min to 4 min before the discharge) the required EM gain is set and a range of acquisitions (20, each with an exposure time of 1 s and a waiting time of 1 s, combined with shutter opening/closing) takes place. This is to ensure that the sensor is fully stabilised when the discharge happens. The acquisition is also programmed to occur between  $-1$  s to  $3$  s with respect to the TCV start time (the plasma break-down phase starts at 0 s).

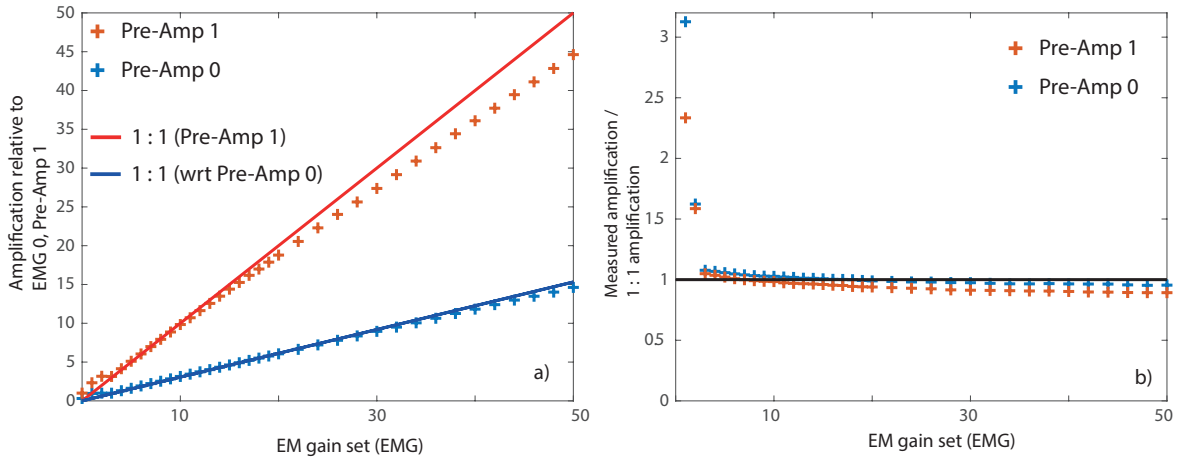


Figure 5.10: Measured EM gain calibration for Pre-Amp gain 0, 1 (1 is the default value and the highest, 0 can be used for highly sensitive studies requiring maximum dynamic range); Horizontal shift speed 30 MHz (HSS 0), Vertical shift speed  $1.33\mu\text{s}$  per row (VSS 1), no vertical shift voltage overclock (VSA 0). a) Set EM gain versus the measured EM gain shown relative to no EM gain and Pre-Amp gain 1. b) Set EM gain versus the ratio between the measured EM gain and the expected EM gain assuming a 1:1 trend between the EM gain set and the EM gain measured.

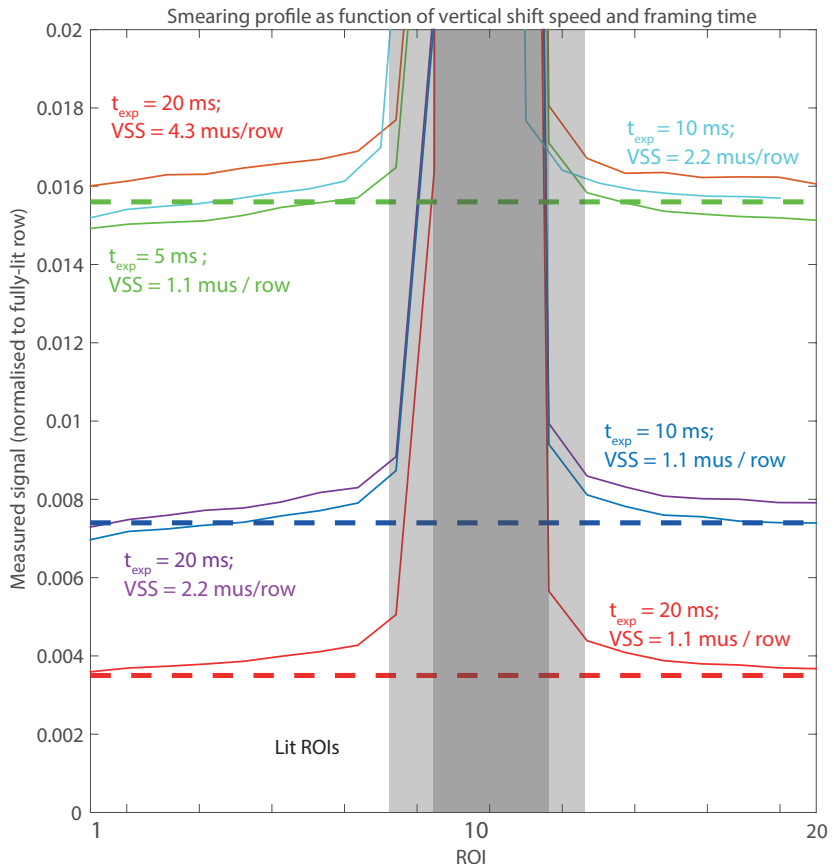


Figure 5.11: Measured signal on all ROIs when a range of ROI is illuminated for a series of exposure times ( $[t_{exp} = 5 \text{ ms to } 20 \text{ ms}]$ ) and vertical shift speeds ( $t_{VSS} = 1.1 \text{ ms to } 4.3 \text{ ms per row}$ ). The predicted smearing roughly scales as  $\frac{t_{VSS}}{t_{exp}}$ , giving rise to the horizontal dotted lines. The lit ROIs (and partially lit ROIs) are shaded. Note that this measurement was done without fibres and thus the tracks have been set-up equidistant in 20 segments.

## 5.4 Camera smearing and post-shot corrections

After spectra for a discharge have been acquired, the measured counts are corrected for the background noise by looking at the signal measured before and after the discharge. Afterwards, the signal is corrected for camera smearing and an absolute calibration is applied. The absolute calibration uses the estimated exposure time discussed previously as opposed to the period in between two TTL triggering pulses (which can deviate up to 36 % at 5 ms periods).

As explained previously, camera smearing occurs due to the fact that photons will still fall on the sensor during the vertical shift phase of the acquisition. That means that photons corresponding to a certain ROI will receive photons corresponding to other ROIs during this phase. First we will discuss the influence of this on the spectra. As discussed earlier, there is a curvature of the slit's image of a spectral line (figure 5.3). Then if the image is shifted into the frame transfer region, the tracks corresponding to the edges will get additional signal due to smearing corresponding to the location of the central ROIs while centre ROIs will get additional signal due to smearing from edge channels. In other words, due to the curvature of the slit, smearing can influence the shape of the observed instrumental function. Although the magnitude of the smearing is generally insufficient to distort the measured intensity of a line, considering that the instrumental width is often wider than Stark/Doppler broadening components, they can influence the line shape significantly to influence the spectral fitting investigations (chapter 6). Furthermore, during detached (e.g. recombinative) conditions, particular the edge chords corresponding to close to the strike points will become bright due to recombinative emission. That means that when central ROIs are shifted through these edge regions, they can receive a significant amount of smearing.

Assuming that the emission is quasi-static with respect to the inter-exposure times, the measured (smeared) signal can be related to the unsmeared signal using a matrix equation, by building on previous techniques by [186, 187, 188] as shown below. First, it is assumed that the emission is quasi-static along *two* acquisition frames, which is required as part of the smeared contribution can arise from the shift of the previous acquisition. The measured emission for a certain ROI is the actual emission of that ROI during the exposure plus the emission obtained from other ROIs during the shifting phase. For a constant light fluence  $F_i$  per second at a certain row (corresponding to track  $i$ ), the actual emission of track  $i$  is  $F_i$  times the exposure time ( $t_{exp}$ ) times the number of rows of  $i$  ( $N_i$ ):  $F_i \times t_{exp} \times N_i$ . The emission falling on that track during the vertical shifting originating from a different ROI  $j$  (smearing) is  $F_j$  times the time it takes for the other ROI to shift over the monitored ROI, which we approximate as the number of rows comprising the ROI ( $N_j$ ) times the vertical shift speed per row  $t_{VSS}$ :  $F_j \times N_j t_{VSS}$ . The signal of an ROI is thus:  $S_i = F_i \times t_{exp} \times N_i + \sum_{j,j \neq i} F_j N_j t_{VSS}$ . The real signal we are interested in is  $R_i = F_i \times t_{exp} \times N_i$ . Thus,  $S_i = R_i + \sum_{j,j \neq i} R_j \frac{N_j t_{VSS}}{t_{exp}}$ . That can be written as a matrix equation, shown in equation 5.1.

$$\begin{pmatrix} S_1 \\ S_2 \\ \vdots \\ S_n \end{pmatrix} = \begin{pmatrix} 1 & \frac{N_2 t_{VSS}}{t_{exp}} & \dots & \frac{N_n t_{VSS}}{t_{exp}} \\ \frac{N_1 t_{VSS}}{t_{exp}} & 1 & \dots & \frac{N_n t_{VSS}}{t_{exp}} \\ \vdots & \vdots & \ddots & \vdots \\ \frac{N_1 t_{VSS}}{t_{exp}} & \frac{N_2 t_{VSS}}{t_{exp}} & \dots & 1 \end{pmatrix} \times \begin{pmatrix} R_1 \\ R_2 \\ \vdots \\ R_n \end{pmatrix} \quad (5.1)$$

This matrix (for simplicity we express equation 5.1 as  $S = C \times R$ , where  $C$  is the correction

matrix) can be used as a 'simplified' smearing correction model, where  $R$  is solved from  $S = C \times R$  by inverting the correction matrix  $C$  (see equation 5.1). The correction matrix  $C$  is a square matrix with number of ROI by number of ROI elements. For each wavelength point and for each time point, there is a single vector of number of ROI elements  $\times 1$  data, which represents  $S$ . From this data,  $R$  can be determined straightforward in Matlab by looping this procedure for every wavelength point and for every time point. More advanced smearing correction algorithms which account for some time dependency are shown in appendix A.1 are more along the lines of [189] and represent original work.

When considering equation 5.1, the off-diagonal smearing elements increase with the ratio of shifting time to exposure time  $\frac{t_{VSS}}{t_{exp}}$ . This means that smearing will become a larger problem when the exposure time is at its shortest (so in practice, at 200 Hz operation). That is understandable, as one would expect a larger fraction of the measured signal to be picked-up during the shift phase if the shift phase is relatively long compared to the exposure phase. Note that the effect is actually worse than linear with the period ( $T$ ) as  $t_{exp} \approx T - 1024 \times t_{VSS}$ . An illustration of this basic smearing correction algorithm is shown in figure 5.11, where only a few fibres were illuminated by a time-stabilised source by putting a mask in front of the fibre ferrule on the collection-optics side of the assembly. At the fastest acquisition frequencies, a smearing trail can be seen below the lit regions. More than 80 % of that smearing disappeared when using the correction algorithm as shown in figure 5.11, where the predicted smearing level through equation 5.1 is shown.

The basic smearing correction can be improved, using the techniques illustrated in appendix A.1. Using those techniques is however, not straightforward in practice. They can however be partially included through a relatively simple change which accounts for the fact that there can be a difference in emission between neighbouring two frames (e.g. not for a difference in emission during a single acquisition). This technique (equation 5.2) yields similar results to the advanced smearing correction algorithms, if no strong transients (like ELMs) arise. Essentially, one needs to account for changes in the signal of a particular pixel between the time for which the correction is applied  $t_0$  and the previous acquisition  $t_{-1}$ , which can be approximated by using the ratio of the signals of both times. In the approach below, this is approximated by using the ratio of both measured (e.g. uncorrected) signals. Therefore, this approach is not entirely self-consistent, but provides fair results if one assumes that the smearing component does not change rapidly as function of time.

$$\begin{pmatrix} S_1 \\ S_2 \\ \vdots \\ S_n \end{pmatrix} = \begin{pmatrix} 1 & \frac{N_2 t_{VSS}}{t_{exp}} & \dots & \frac{N_n t_{VSS}}{t_{exp}} \\ \frac{S_1(t_{-1})}{S_1(t_0)} \times \frac{N_1 t_{VSS}}{t_{exp}} & 1 & \dots & \frac{N_n t_{VSS}}{t_{exp}} \\ \vdots & \vdots & \ddots & \vdots \\ \frac{S_1(t_{-1})}{S_1(t_0)} \times \frac{N_1 t_{VSS}}{t_{exp}} & \frac{S_2(t_{-1})}{S_2(t_0)} \times \frac{N_2 t_{VSS}}{t_{exp}} & \dots & 1 \end{pmatrix} \times \begin{pmatrix} R_1 \\ R_2 \\ \vdots \\ R_n \end{pmatrix} \quad (5.2)$$

An example of smearing correction is shown for a detached density ramp discharge where the Balmer line intensity strongly increases as function of time (figure 5.12). In the appendix, an additional example is shown for a detached  $N_2$  seeded discharge (section A.1.1, figure A.1) where the  $N$  impurity lines strongly increase when nitrogen is introduced. For all of these discharges, the fastest acquisition rate of 200 Hz was used, smearing is expected to be the strongest. For each case, three different smearing algorithms are used: the basic smearing algorithm highlighted above, the advanced smearing algorithm (section A.1) while using either

the  $D_\alpha$  intensity measured by photodiodes as a time-dependent intensity indicator ( $I(t)$ ) or by using an interpolation of the spectra as function of time to provide  $I(t)$  where low signal levels are omitted to avoid taking erroneous quick relative changes into account which occurs when noise is monitored. All corrections are done point-wise separately for every ROI and for every pixel position.

First it is important to note the following: 1) the Balmer line intensity ( $6 \rightarrow 2$ ) increases rapidly as function of time as the recombinative emission ( $6 \rightarrow 2$ ) in this discharge (#52065 see [1]) increases; 2) the Balmer line emission ( $6 \rightarrow 2$ ) is stronger near the target than further up the divertor leg, creating an asymmetry across the sensor in the emission. Both points are shown in figure 5.12 a & b.

Four different spectra are shown in figure 5.12, highlighting the ( $6 \rightarrow 2$ ) deuterium Balmer line for four different lines of sight (LoS) as shown in figure 5.12 a. From the spectra it is clear that the raw measurement of  $6 \rightarrow 2$  emission at line of sight 1 is fully made up of smearing (figure 5.12 c). All smearing algorithms indicate this and successfully remove the emission. Indeed, during the experiment, this fibre is kept dark as for this particular discharge its line of sight is vignetted at the tokamak's port.

The smearing is shown to be much smaller for the fibres corresponding to the brightest region (LoS 3) and the central region (LoS 20). As can be seen, the location of the smearing is indeed different as the location of the peak of the spectral line, which is as expected due to slit's curvature. That means that smearing, even in such cases where it is fairly low, can significantly influence the Balmer spectral line shape.

The relative influence of smearing strongly increases near the 'near x-point' region of the sensor (e.g. LoS 28-32), likely as the signal was brighter near the strike point region. One other point which plays a role in that is the sensitivity of the diagnostic. Although the measured intensity between LoS 20 and 30 is similar after calibration, the sensitivity of the diagnostic decreases near the edge and thus the same brightness corresponds to fewer counts near the edge. That is the case as, for the discharge run shown, vignetting is particularly strong as an aperture was placed in front of the collection optics to limit throughput to avoid saturation.

The deviation between the different smearing correction algorithms shown is small and is likely within the error of the smearing correction. This means the temporal change for this case is sufficiently slow to warrant the basic smearing correction. By inspecting the various smearing correction matrices manually, the advanced smearing correction shows an increase of up to 10% for the elements upper of the diagonal with respect to lower than the diagonal (which is also the difference between the advanced and simple smearing correction algorithm in this case). Those upper elements correspond to the case where lower ROI numbers shift into upper ROI numbers, whereas the lower elements correspond to the case where a new image is shifted, e.g. thus corresponding to the previous TTL pulse where the signal was lower. This change is thus not due to a change in the signal during a single acquisition, but due to the difference in the previous acquisition to the acquisition analysed: e.g. the difference between the green phase and blue phase in figure 5.12 b.

From the examples it is clear that smearing correction algorithms can be successful for removing a significant portion of the smeared signal. However, they rely on various assumptions and are not perfect. Especially cases where high S/N levels are achieved and

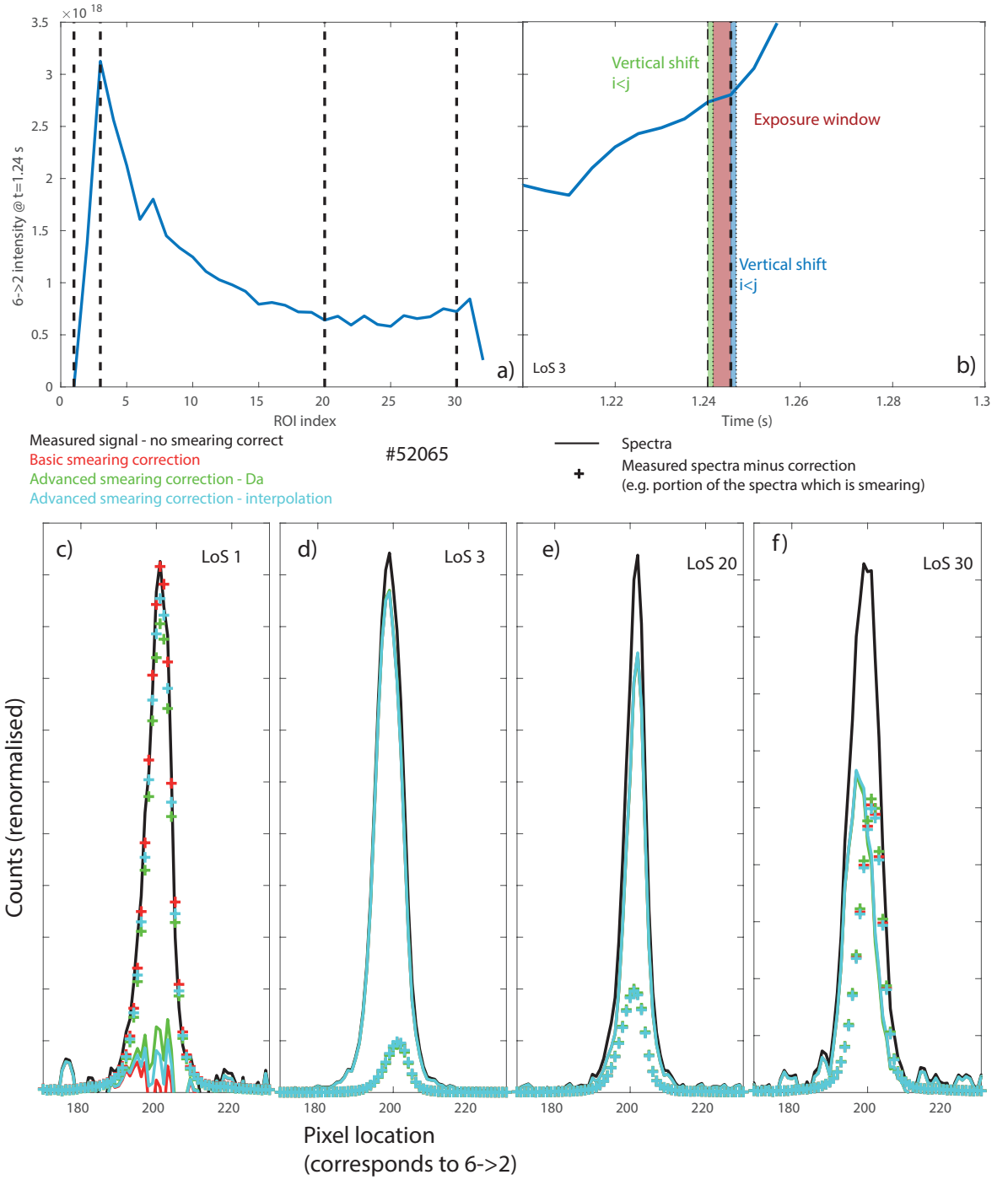


Figure 5.12: Overview of smearing correction on a measured  $6 \rightarrow 2$  Balmer line at 200 Hz acquisition frequency (# 52065). a) Profile of  $6 \rightarrow 2$  intensity as function of ROI at  $t = 1.25$  s together with highlights of the ROI of which the spectra are shown. b) Profile of  $6 \rightarrow 2$  intensity for LoS 3 (near target —brightest) as function of time, together with windows corresponding to the different acquisition phases. c-g) Spectra of  $6 \rightarrow 2$  both measured (non-smearing correction) and smearing corrected for five different lines of sight. Also the deviation between the spectra and the smearing-corrected spectra (plusesses) is shown, which indicates the amount of smearing contributing to the measured signal.

where the spectrum is relatively constant as function of time *and* across the sensor, the agreement between the different smearing techniques is adequate, providing some assurance of the smearing correction. In other cases, however, the differences between the algorithms can be up to 20 % of the smear prediction; which is a measure of uncertainty of the smearing correction algorithms. The smearing correction investigation has also shown that the edge chords are often not reliable. The reason this likely occurs is that the fibre array is slightly larger than the sensor and thus the edge chords are often only partially caught on the sensor. Their ROI width is thus smaller than for the other ROIs, making them more prone to smearing. Therefore, they are not used for quantitative investigations. The smearing correction for cases with strongly deviating signals (such as impurity seeding ramps and density ramps) —both in time and across the sensor —induces more errors and thus operation at 100 Hz or less is advised to reduce smearing. When applying the various smearing correction algorithms to ELM<sub>My</sub> discharges (not shown), they strongly deviate and show that smearing has a very strong influence on the spectra. That means that the DSS data quality during ELM<sub>My</sub> (type 1) H-mode operation with relatively fast ELM frequencies ( $> 100$  Hz) is questionable and does not enable a quantitative analysis unless hardware changes to allow for faster operation are applied.

## 5.5 Spectrometer absolute intensity calibration

The absolute intensity calibration is carried out by illuminating the DSS collection optics, by taking them off the tokamak, with a time-stabilised pre-calibrated incandescent (halogen-tungsten) lamp illuminated through an integrating sphere. Using the pre-calibration curve (which provides the radiated emission in terms of  $\text{W sr}^{-1} \text{m}^{-2} \text{nm}^{-1}$ ) together with a wavelength calibration (which provides the spectral range over each pixel), the incident  $\text{ph sr}^{-1} \text{m}^{-2} \text{s}^{-1} \text{pix}^{-1}$  can be determined through a unit conversion and integrating the reference spectra over the wavelength range of each pixel. By relating this to the number of counts per second (applying the camera calibrations as discussed previously) for a particular pixel, a calibration factor can be determined which relates the number of counts per second measured for a particular pixel (and thus wavelength) to the brightness in terms of  $\text{ph sr}^{-1} \text{m}^{-2} \text{s}^{-1} \text{pix}^{-1}$ . This is done separately for every ROI, every pixel and for every grating angle used in the experiments. The absolute intensity calibration is performed by using identical ROI tracks and camera settings as in the experiment.

The process above does not account for the transmission of the vacuum window and vignetting at the vacuum window is assumed to be negligible. That assumption is indeed supported by the mechanical design, except for the first edge chord. The vacuum window has been taken off the tokamak and its transmission has been measured by using the same technique as highlighted above both with and without vacuum window. The measured transmission in the usable range of the DSS has been measured to be smooth as function of wavelength and above 90 %. For simplicity, a 90 % transmission of the vacuum window is assumed in the calibration and presented data. The uncertainties induced due to this are negligible due to other uncertainties in the absolute calibration.

### 5.5.1 Stray light and the absolute intensity calibration

Although the calibration sequence is fairly straightforward as spectrometers are routinely calibrated, one challenge is that stray light can influence the measured signal during the calibration in the near-UV regime. The issue is that incandescent light sources, such as halogen lamps, emit a light spectrum similar to that of a black body radiator with respective colour temperatures of 2400 K to 3200 K. That means that most of the lamp's emission (spectrally) will be in the infrared or near infrared, while the emission will be much weaker in the near-UV regime. Although the influence of stray light for calibrating divertor spectroscopy systems in the near-UV regime is not treated in literature; the challenge of stray light in calibrating the near-UV regime in spectrometers has been considered critical in other spectroscopic applications, such as calibrating LED lights [190, 191, 192] and performing absorption measurements. Stray light can originate from various sources in a spectrometer, such as due to ghosts from a non-ideal grating and reflections/scatter from the walls of the spectrometer internally. These reflections can be particularly strong when the acceptance angle of the spectrometer is not well-matched. As explained, this was the case previously where the NA 0.22 fibres overfilled the Isoplane spectrometer by roughly 75 % (e.g. etendue scales with the acceptance angle squared).

There are several ways of characterising stray light. One technique uses spectral lines measured by using a spectral source, such as a laser or a spectral lamp [193, 190, 194, 195]. When high S/N measurements are performed, it can be seen that the signal between the spectral lines does not go to zero exactly, but remains at some level, as shown in figure 5.13 where the spectrum is normalised using the integral of one spectral line. Here the measured difference is shown between using NA 0.22 and NA 0.10 fibres, indeed showing a great reduction (roughly a factor three) in the signal between the spectral lines, indicative of a reduction of stray light.

As a side-note, stray light also alters the instrumental function and depends on the details of how the system is illuminated. To highlight this, the system is illuminated by a spectral Pen-Ray lamp either directly (e.g. a single angle) or through an integrating sphere which fills-up the entire cone of the acceptance angle of the fibres (Lambertian surface). If some information about these angles is conserved until the end of the slit is reached, the illumination from the fibres into the spectrometer would be at a wider distribution of angles and would thus likely lead to more stray light. This is indeed observed in figure 5.14.

To illustrate the influence of stray light during absolute calibration measurements in the near-UV range, one has to make an assumption of how the spectrometer influences the input spectrum during the measurement, also sometimes referred to as a point spread function of the spectrometer [190, 194, 195, 193]. For this we will assume that stray light is spectrally flat: meaning that if only light of one single wavelength is fed to the system, one will observe a thin peak at that wavelength while observing some fraction of its integral outside of that peak. It should be noted that this is just done for illustration purposes and does not represent an accurate model for stray light: stray light has a certain spectral shape and to fully account for it, ideally a scannable laser or a series of notch filters are used to track stray light as function of wavelength for a given grating angle [190, 194, 195, 193] —which is done in literature for advanced stray light characterisation.

Using a known spectra and using the point spread function, the spectra which would be

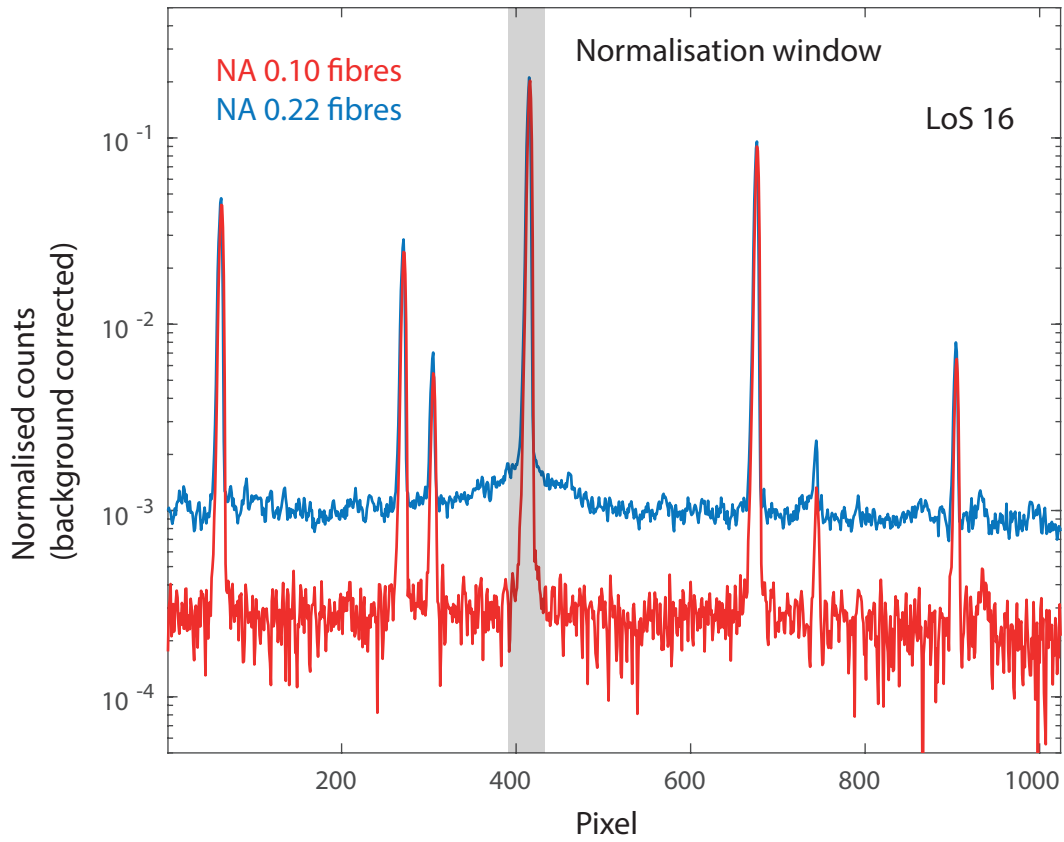


Figure 5.13: Measured spectra of a Xe spectral lamp (the input optics are illuminated through using an integrating sphere) using the horizontal spectrometer with a 1800 l/mm grating centred at 465 nm central wavelength (spectral coverage: 456 nm to 474 nm), shown both with the older (NA 0.22) fibres and the newer (NA 0.10) fibres.

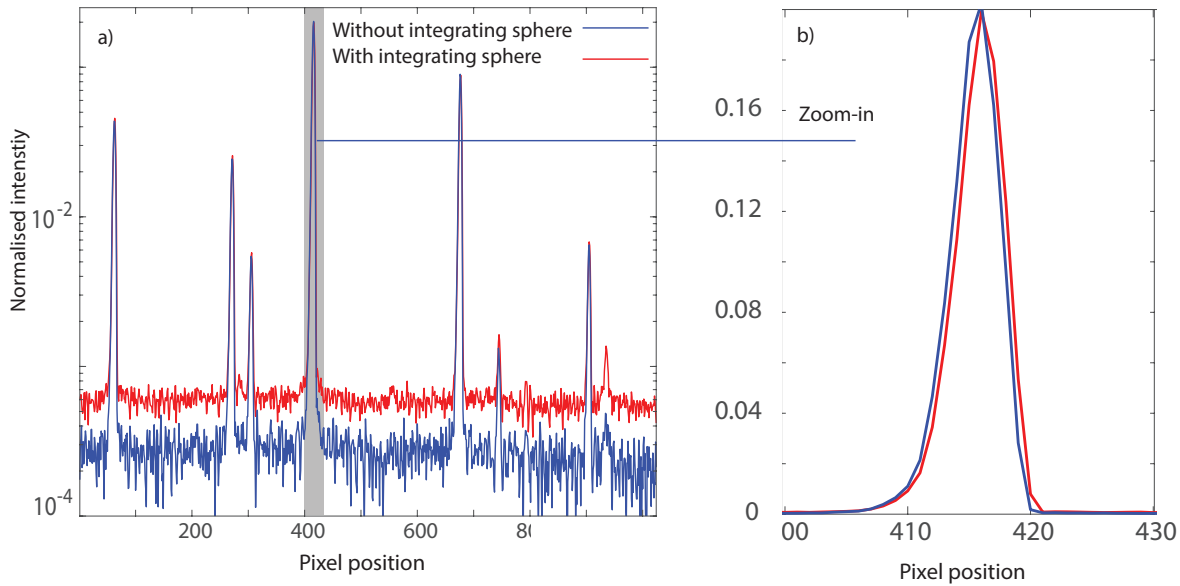


Figure 5.14: Spectra shown using a Xe lamp in the 465 nm region (central wavelength) with a 1800 l/mm grating where either the collection optics are illuminated directly by the spectral Pen-Ray lamp or illuminated through using an integrating sphere. a) Full spectra normalised such that an integral over the brightest spectral line would yield 1. b) Zoom-in on brightest spectral line.

measured by the system can be modelled through a convolution. That result is shown in figure 5.15 where the spectra of pre-calibrated incandescent light sources are used to highlight how they are influenced by stray light.

The first calibration source used in this work was a source with a lower colour temperature (2400 K). As shown in figure 5.15 a, a strong deviation between the model with/without stray light using this lamp curve occurs at low wavelengths. Significant deviations already start to occur at 500 nm, while at 400 nm most of the signal measured would be due to stray light. Note however, that the used stray light assumption ( $10^{-4}$ ) does not correspond to the stray light of the Isoplane spectrometer and here serves as an illustration (e.g. the Isoplane spectrometer specifications highlight a stray light rejection better than  $10^{-5}$ ). Stray light leads to an overestimation of the signal in the near-UV, which leads to an overestimation of the efficiency of the diagnostic and thus an underestimation of the actual measured brightnesses. Also, when taking into account how the deviation between the two spectra varies as function of wavelength (figure 5.15 b), it is clear that the deviation in the spectra can be sufficiently significant to alter determined line ratios of lines 40 nm apart by more than 20 %.

Later, a source was used with a higher colour temperature (3100 K). With a higher colour temperature, there is less deviation in the spectra between the near-UV regime and the upper visible (600-700 nm). Due to that, the influence of stray light on the calibration is reduced.

An additional technique used for reducing the influence of stray light is to use optical filters in combination to the calibration sources. In that way, the emission outside of the band monitored which leads to stray light, can be prevented from entering the system. As shown, applying a short pass filter which transmits only below 434 nm greatly reduces the amount of stray light present in the near-UV during absolute intensity calibrations. The signal with stray light is actually lower than the signal without stray light, indicating that when using this filter, a portion of the near-UV emission will end up at higher wavelengths as stray light, and as the shown spectra is normalised, the spectra would appear slightly less bright in the near-UV. It should be noted that this does not invalidate the calibration: during the experiment also some fraction of the emission corresponding to a spectral line will be 'moved' to other spectral regions in the form of stray light.

One disadvantage of this, however, is that it requires a calibrated filter. Assuming a filter calibration curve is present, there are often small oscillations (5-10 %) in the transmission of the filter as function of wavelength when using a short-pass filter. In the DSS, the way filters can be placed in the system is by attaching them to the lens. If then the lens is illuminated using an integrating sphere, the emission goes through the filter at a whole range of angles. Depending on this angle, the path length the light makes in the filter changes and as a result, the filter curve with its oscillations shifts. Using a short-pass filter in the absolute calibration thus not only increases the uncertainty in the calibration by the uncertainty in the filter calibration (5 %), but also by the amplitude of the oscillation in the transmission, as the way the light enters the filter during the calibration is not representative of how the light enters the system during the experiment.

In order to further reduce and characterise stray light we have made an analysis technique and stray light correction algorithm (appendix A.2). The easiest way to detect stray light is to check if light is observed in regions where no light is expected (for instance through a notch filter). That, however, is actually done intrinsically by imaging spectrometers with fibres. The

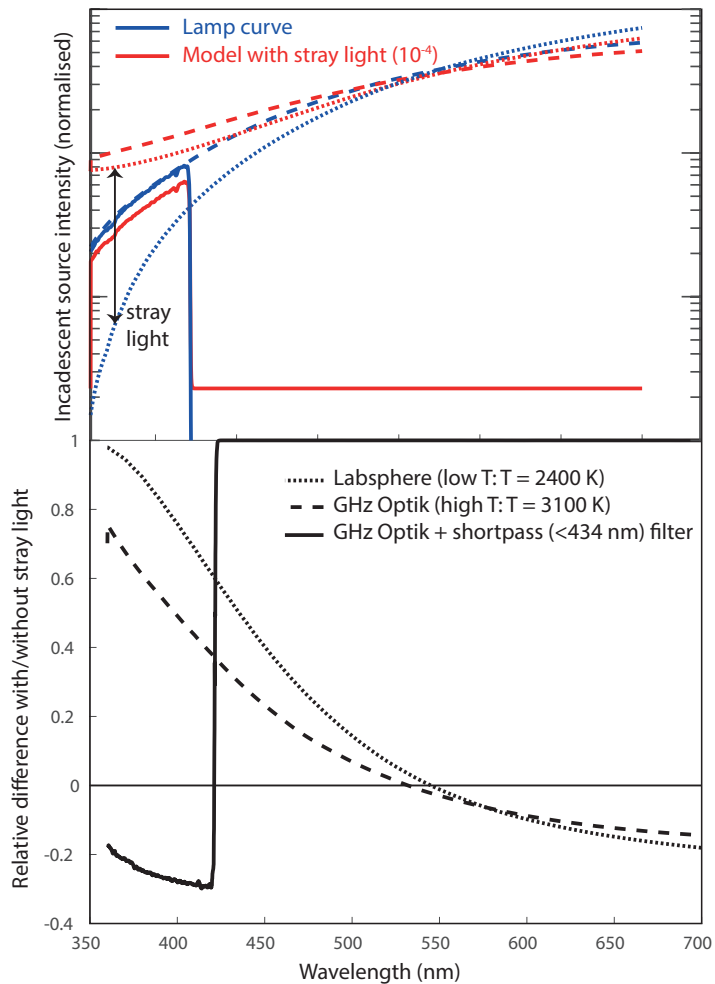


Figure 5.15: Illustration of the influence of stray light ( $1 \times 10^{-4}$  stray light (with respect to intensity) is assumed) on an absolute intensity calibration. a) Pre-calibrated lamp spectra (intensity on a log scale) where the influence of stray light has been modelled. The different lamp curves have been normalised with respect to their integral. b) Relative difference in the spectra due to stray light ((Stray light spectra — lamp spectra) / stray light spectra).

fibres provide a pattern of emission and region where no emission should occur between the fibres (e.g. fibre cladding), which is also used in [196] for stray light correction. The stray light correction algorithm shown in appendix A.2, developed as part of this thesis, aims at measuring the spectra using both tracked settings and the full-frame in order to extract the signal levels in between the fibres. These are compared between the signal levels corresponding to the fibres for a case where no stray light is expected and for the case investigated. If these values increase, this is evidence for the appearance of stray light and the amount by which they increase give an indication of the amount of stray light.

An absolute intensity calibration has been performed on a lower colour (2800 K as opposed to 3100 K) temperature lamp for illustration purposes without using the short-pass filter and with using the older fibres in figure 5.16; which all results in higher stray light levels. The stray light corrected calibration curve is indeed significantly closer to the one obtained by using a short-pass filter with respect to the uncorrected signal, which has a considerably higher (up to 2.5 times) estimated 'efficiency', meaning that the eventual calibrated signal will underestimate the brightness significantly if no calibrations or short-pass filter is used

with this particular light source at such low wavelengths. However, the stray light correction algorithm does not remove all stray light as shown and still a deviation between the estimated efficiency through using a short pass filter and by using the correction algorithm of generally less than 25 % (but can rise up until 35 %).

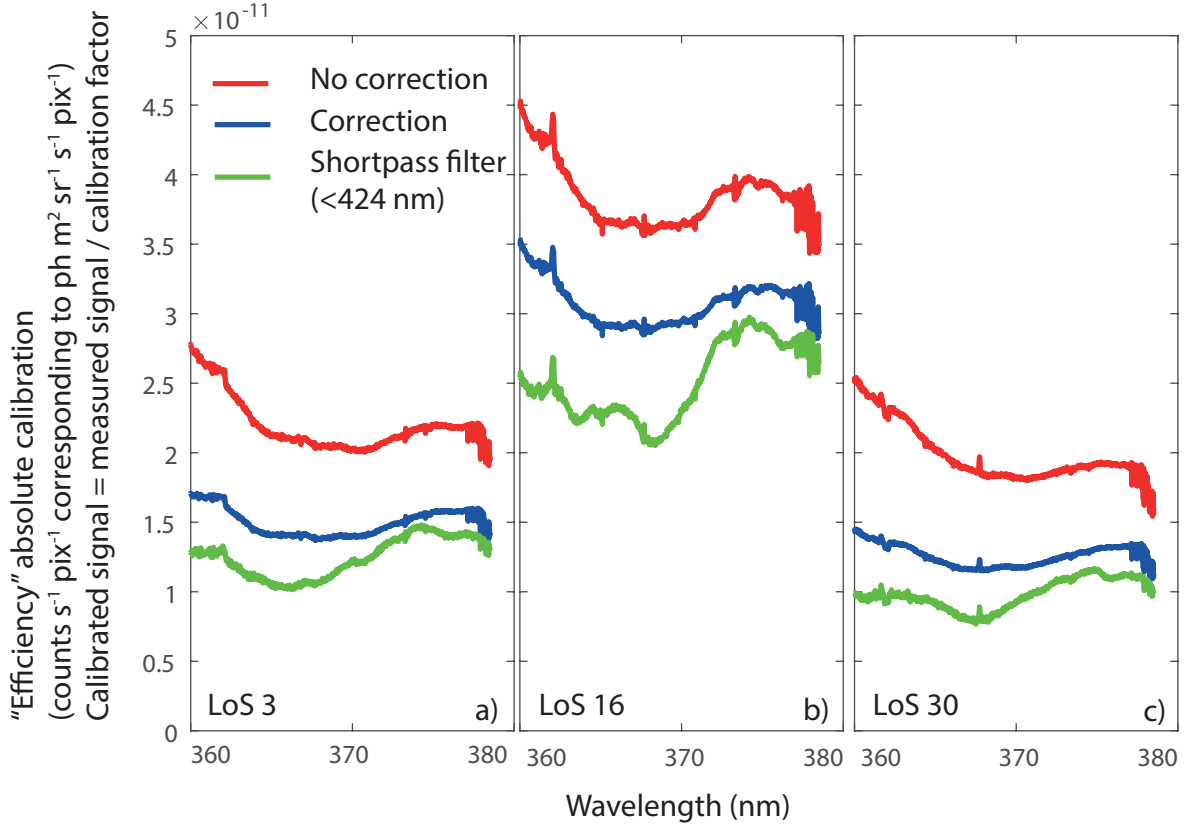


Figure 5.16: Absolute calibration curves showing the absolute calibration factors (e.g. calibrated signal = measured signal (counts / s) / calibration factor) as function of wavelength (corresponding to a single acquisition of central wavelength 369 nm —lowest calibrated wavelength) shown for three ROIs using the signal uncorrected for stray light, the stray light corrected signal and using a 424 nm short-pass filter (while taking that filter curve into account in the absolute calibration.).

By using different interpolation techniques and different smoothing parameters in the advanced stray light correction algorithm (appendix A.2), up to 10 to 20 % deviation in the obtained signals can occur. This indicates that this smearing correction itself can add up to 20 % uncertainty to the calibration. Every absolute calibration is set-up such that both the tracked and full-frame measurements are available and the contribution of stray light to the calibration is predicted. If this contribution is smaller than 20 %, stray light correction will not be applied, otherwise it will. In practice, when using the short-pass filter in combination with the higher colour temperature (3100 K) incandescent source stray light correction is only applied at 380 nm and below.

## 5.6 Spectrometer instrumental function characterisation and calibration

When performing fits for obtaining information on the measured line broadening where the measured line broadening is small or comparable to the instrumental function's broadening, it is crucial that the instrumental function's line shape is carefully monitored as function of grating used, grating angle used and ROI. The recorded instrumental function's line shapes then provide an estimate of the instrumental function's shape, which can be accounted for when performing line fits. In addition to just recording these line shapes, it is also of crucial importance that the uncertainty of this recording is quantified such that the uncertainty of the line fits can be eventually assessed.

The instrumental function shape is obtained by using a spectral lamp as a light source, which has a negligible continuum. The spectral lamps used are Mercury, Mercury-Cadmium, Xenon and Neon. Using a mix of these spectral lamps provides a good coverage of spectral lines in the visible (365 nm to 700 nm). The operational conditions in such lamps are such that most line broadening mechanisms in such lamps are negligible (Doppler broadening (low ion temperature), pressure broadening by neutral particles, Stark broadening (low electron density; low pressure) and that a negligible amount of line splitting is present (no external magnetic field) —see chapter 6 for more information about broadening mechanisms. When all of these are negligible, the emitted spectral lines can be considered to be peaks provided by delta functions. The observed spectral lines by the spectrometer from such sources provide the instrumental broadening, in that case. From hereon dubbed the instrumental function.

To account for the instrumental function's shape, first it is convenient to have a model for the shape. As mentioned previously, the spectrometer provides lineshapes which are Lorentzian rather than Gaussian. As coma aberrations are present, these aberrations can lead to asymmetrical line shapes. An example of the measured lineshape is shown in figure 5.17. Such an asymmetrical line shape can be characterised roughly through fitting it with an asymmetric Lorentzian, expressed in equation 5.3. In this equation,  $x_0$  is the peak position,  $a$  denotes the width and  $b, c$  denotes the fall-off of the Lorentzian on the left or right side of the peak. By setting a large difference between  $b$  and  $c$ , an asymmetric lineshape is obtained. Although this function can often correctly parametrise the measured instrumental function, care must be taken as its results are often not unique when fitting noisy experimental profiles. The reason for this is that a different width  $a$  can often be compensated by a change in the fall-off strength,  $b, c$ .

$$L(x) = \begin{cases} \left(\frac{1}{1+4(\frac{x-x_0}{a})^2}\right)^b & \text{if } x \geq x_0 \\ \left(\frac{1}{1+4(\frac{x-x_0}{a})^2}\right)^c & \text{if } x \leq x_0 \end{cases} \quad (5.3)$$

At first, the instrumental functions were fitted using an asymmetric Lorentzian and that fit was subsequently used as the instrumental function characterisation in the line broadening (Stark broadening —chapter 6) fits. However, more accurate Stark broadening results (reduced noise at low densities (and thus low Stark broadening)) were obtained using the measured instrumental function instead. Thus, the measured instrumental functions are recorded as function of ROI, used grating and used grating angle.

To record the measured instrumental functions, first the instrumental function's centres (or more specifically peak position) are determined by fitting the instrumental function with an asymmetric Lorentzian, provided by equation 5.3. The peak location returned by the fit is taken as the line's peak. The instrumental function is spline interpolated and split in a right-hand side and a left-hand side. Both sides are interrogated on an integer pixel mesh. That methodology is used in order to limit the influence of the pixels having finite sizes on the instrumental function (e.g. one could imagine that the recorded shape is slightly altered when an instrumental function is shifted over the space of one pixel due to discretisation). The obtained line shapes are post-processed such that a background (if present) is removed by making sure that the pixel with the lowest counts is set to zero and the instrumental function is normalised such that its integral equals one.

The obtained instrumentals (left- and right-hand side) are then recorded as function of ROI, grating used and grating angle. It is made sure that this characterisation is present for every single combination of grating and its angle used in the experiment. Important to note is that this means that the measured instrumental function can thus be at a different horizontal (spectral) position of the CCD than the observed spectral line in the plasma experiment. For simplicity, it is assumed that the instrumental function, for a given grating angle, does not change in the spectral direction of the CCD. That assumption has been investigated using a Xenon lamp at 465 nm central wavelength, where four different spectral lines (and thus instrumental functions) are measured at four different locations in the spectral direction. Alternatively, one could assume that the instrumental function depends more on the wavelength of the spectral line used to measure the instrumental function rather than the grating angle. That scenario was also investigated by scanning the spectrometer around a certain grating angle such that a given spectral line shifts horizontally along the spectral direction of the CCD as the grating angle is changed. The result is shown in figure 5.17, where it is evident that the instrumental function changes are small for either of the two cases.

As such, we will assume that the measured instrumental function at the same grating angle is the appropriate one, although the spectral line monitored during the experiment can be at a different horizontal location than the recorded spectral line during the instrumental function calibration. This method enables a simpler and faster instrumental function calibration. The deviation in the instrumental function when multiple spectral lines are simultaneously measured for a given grating angle are used to estimate the uncertainty in the instrumental function characterisation. As it is unknown how precisely the light from the tokamak enters the input optics, the instrumental function is recorded both without and with using an integrating sphere to test the influence of the illumination on the spectral shape (e.g. figure 5.14, which is accounted for in the uncertainty of the instrumental function).

### 5.6.1 Assessing the uncertainty in the instrumental function

As described previously, one can indeed use the distribution of the various instrumental functions obtained at different wavelengths for a fixed grating and grating angle as an indicator for the uncertainty of the instrumental function. The difficulty of this is that this provides a finite set of instrumental functions, for instance four, giving only a rough indication of the uncertainty. Below we describe a technique which enables us to use these multiple instrumental functions to create a large set of possible instrumentals, given the uncertainties,

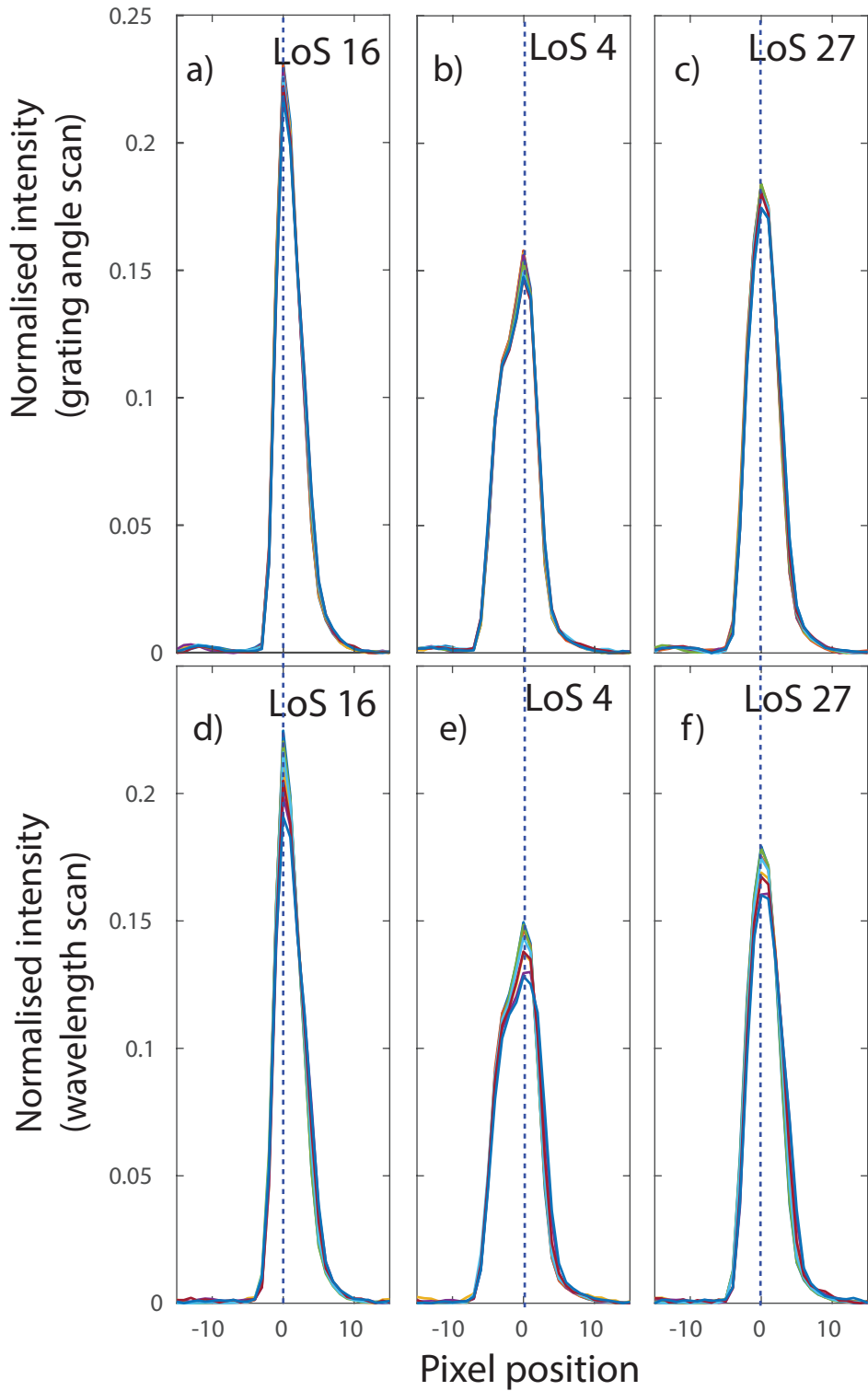


Figure 5.17: Examples of extracted instrumental functions for the horizontal DSS system using a 1800 l/mm grating around the 460 nm to 470 nm wavelength region. a-c) Different instrumental functions (different colours) shown for three different lines of sight corresponding to a 467.81 nm line from a mercury-cadmium spectral lamp, positioned between horizontal (wavelength direction) pixel number 100 and 700. d-f) Different instrumental functions (different colours) shown for three different lines of sight (16 —centre; 4 edge; 27 edge), corresponding to 458.28, 462.43, 467.12, 469.7, 473.42 nm spectral lines obtained from a Xe spectral lamp obtained during a single acquisition (single grating angle), with and without integrating sphere. Note that the situation shown in a-c is from a different calibration run than the one shown in d-f.

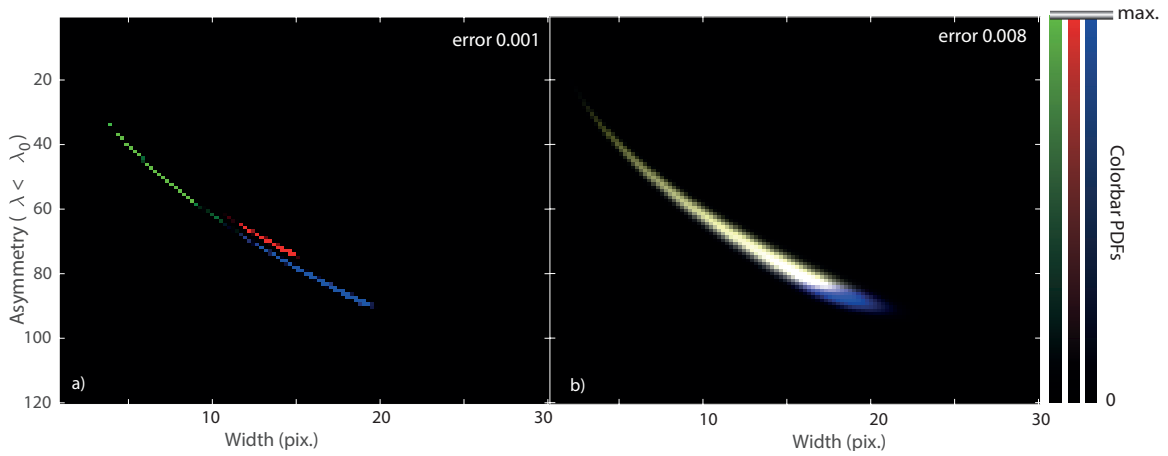


Figure 5.18: 2D PDF of the Bayesian fit (of instrumentals measured using a 1800 l/mm grating, 465 nm central wavelength and using a Xe lamp) of the  $a, c$  using equation 5.3 (the result is marginalised along the  $b$  direction), shown for two different errors. Each colour map shows the results of three separate PDFs (corresponding to three separate instrumental functions obtained during a single acquisition of the Xe lamp at different wavelengths) using red, green, blue colours. When all instrumentals overlap, a grey map would be obtained. When none of the instrumentals overlap, separate red, green, blue maps are obtained.

which can be generated in a Monte-Carlo fashion. The benefit of that technique is that instead of having for instance four separate outcomes, a smooth distribution of outcomes is generated, resulting in a probability density function. Due to that, it can also be combined with Bayesian analysis techniques, which require such a smooth evolution as otherwise strongly non-unimodal results would be obtained.

In order to generate a smooth sample of possible instrumentals, first the instrumental functions would need to be semi-characterised. For this we use the asymmetric Lorentzian function introduced previously. To provide a smooth outcome, we provide a Bayesian fit of the instrumental functions using an asymmetric Lorentzian. This is done by performing a parameter scan for all the unknowns in equation 5.3 the width  $a$  and the fall-off parameters  $b, c$  ( $x_0$  is not a free parameter as, due to the way the instrumental functions are specified, this is already set to zero). For each set of parameters, the residuals between the obtained function and the instrumental function are obtained. A certain error margin is ascribed to the measured instrumental function, meaning that the obtained residuals can be transformed to a probability (at each point of the instrumental function). All of these probabilities are multiplied, yielding a final (relative) probability for the parameter set  $a, b, c$ , yielding a probability density function (PDF). The PDF obtained for the various instrumentals of a set (which were assumed to be identical) are summed, to create one final PDF. Imagine the uncertainty specified for the instrumental function is very small, then the resulting PDFs would be narrow as only a specific set of fit parameters is most likely. When adding such narrow PDFs, the resulting PDF would be non-unimodal, which implies that multiple outcomes are feasible (as multiple instrumental functions were used for the analysis) but a solution between them is unlikely. That, however, is not true as a limited number of instrumentals has been used in the analysis (for instance four-eight). Therefore, the error of the instrumental function is tuned manually such that the various PDFs obtained responding to the various instrumental functions merge

together, leading to a single unimodal PDF (as expected). This is illustrated for two different error values in the 2D PDFs shown in figure 5.18.

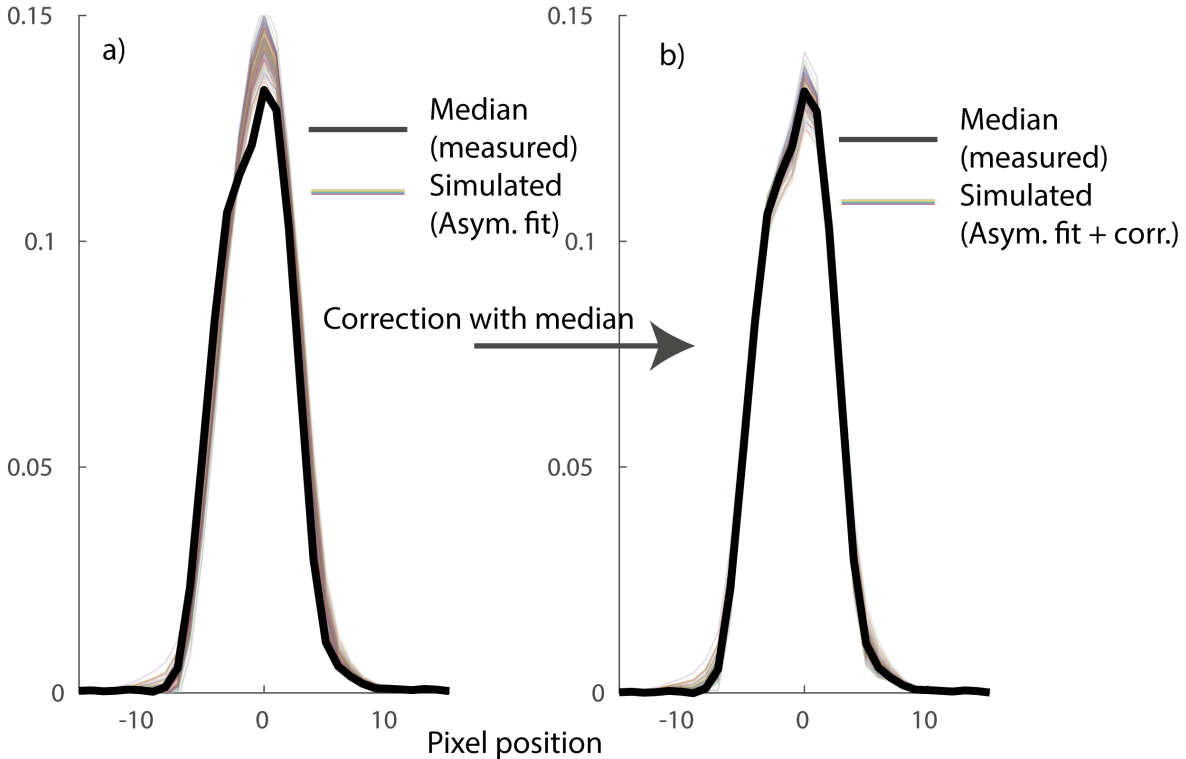


Figure 5.19: Extracted (median of distribution obtained through a Xe lamp) and a) simulated asymmetric Lorentzians obtained from the Bayesian asymmetric Lorentzian fit using the described Monte Carlo algorithm, b) simulated instrumental functions obtained by point-wise shifting the instrumental functions such that the median of the distribution of instrumental functions aligns with the input instrumental function. The data has been taken from the edge of the CCD (LoS 2) using a 1800 l/mm grating at 404 nm central wavelength, which deviates more strongly from the asymmetric Lorentzian fit than central chords, using a Mercury-Cadmium spectral lamp. Of the Monte Carlo generated instrumentals, 100 different instrumental functions are shown.

After this Bayesian fit of all the instrumental functions is completed, rejection sampling is used to generate a certain  $N$  number of different instrumental functions, which all are modelled through equation 5.3. The issue with those instrumental functions is, however, that the measured instrumental functions do not exactly fit an asymmetric Lorentzian. Especially near the edges of the sensor deviations between an asymmetric Lorentzian and the measured instrumental functions can occur. Therefore, at each point of the instrumental, the median of the obtained Monte-Carlo set of instrumentals is computed. The resulting Monte-Carlo set of instrumentals is then point-by-point shifted such that its point-wise median agrees with the median of the measured instrumentals. Afterwards, everything is re-normalised. This means that, for instance, if there is a 'bump' at the instrumental function, that bump would still be present in the Monte-Carlo set of instrumentals as the median of the Monte-Carlo set corresponds to the measured instrumental function. However, the variances between the different Monte-Carlo iterations of the simulated instrumentals is set by the Bayesian fit of the various instrumental functions. An illustration of this procedure is shown in figure 5.19.

The results of the full process are shown in figure 5.20, where the simulated instrumentals are compared with the input distribution of instrumentals and with the median obtained from the input distribution of instrumentals around which the simulated instrumentals are centred.

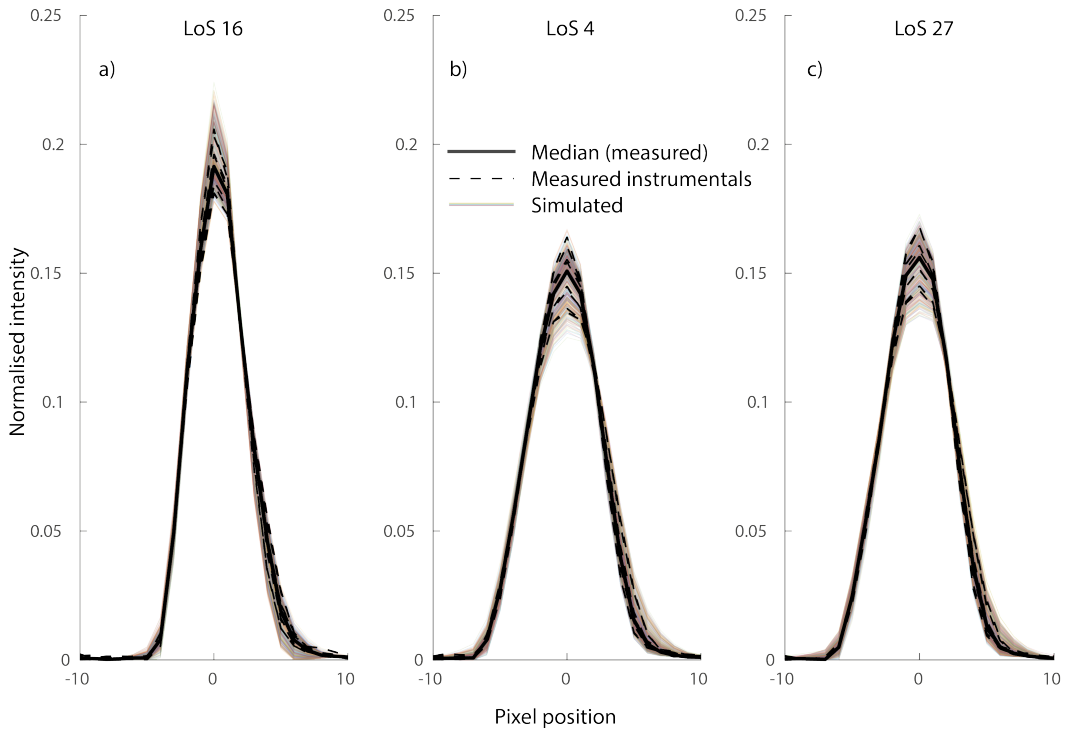


Figure 5.20: Extracted and simulated (100) instrumental functions (normalised with respect to intensity) using the described Monte Carlo algorithm for three different lines of sight. All shown correspond to spectral lines at 458.28, 462.43, 467.12, 469.7, 473.42 nm obtained from a Xe spectral lamp during a single acquisition (1800 l/mm grating), both with/without using an integrating sphere.

## 5.7 Spectrometer characterisation

After having discussed some of the more technical aspects of the spectrometer in greater detail, below we will present a characterisation of the system by presenting its sensitivity, instrumental function width and instrumental function asymmetry as function of grating, space and wavelength. The asymmetry in the instrumental function is defined by determining the deviation between the instrumental functions peak and the location where a left-hand or right hand-integral of the instrumental yield the same value; e.g. the 'centroid' of the instrumental function. This is intended to give a general idea of the system's parameters and how they vary, but these values will differ from the vertical/horizontal systems and from calibration run to calibration run.

The instrumental function characterisation is shown in figure 5.21, indicating a minimum FWHM of 3.5 pixels (at smaller slit widths, a FWHM of between 3-3.5 pixels is feasible) at the centre of the CCD (for the 15-20 most central pixels), while for the edge pixels the instrumental function width increases by roughly a factor 2. As predicted based on the optimisation angle of the spectrometer for coma correction; that optimal point for the 1800 l/mm grating occurs at lower wavelengths and thus the instrumental function's width is

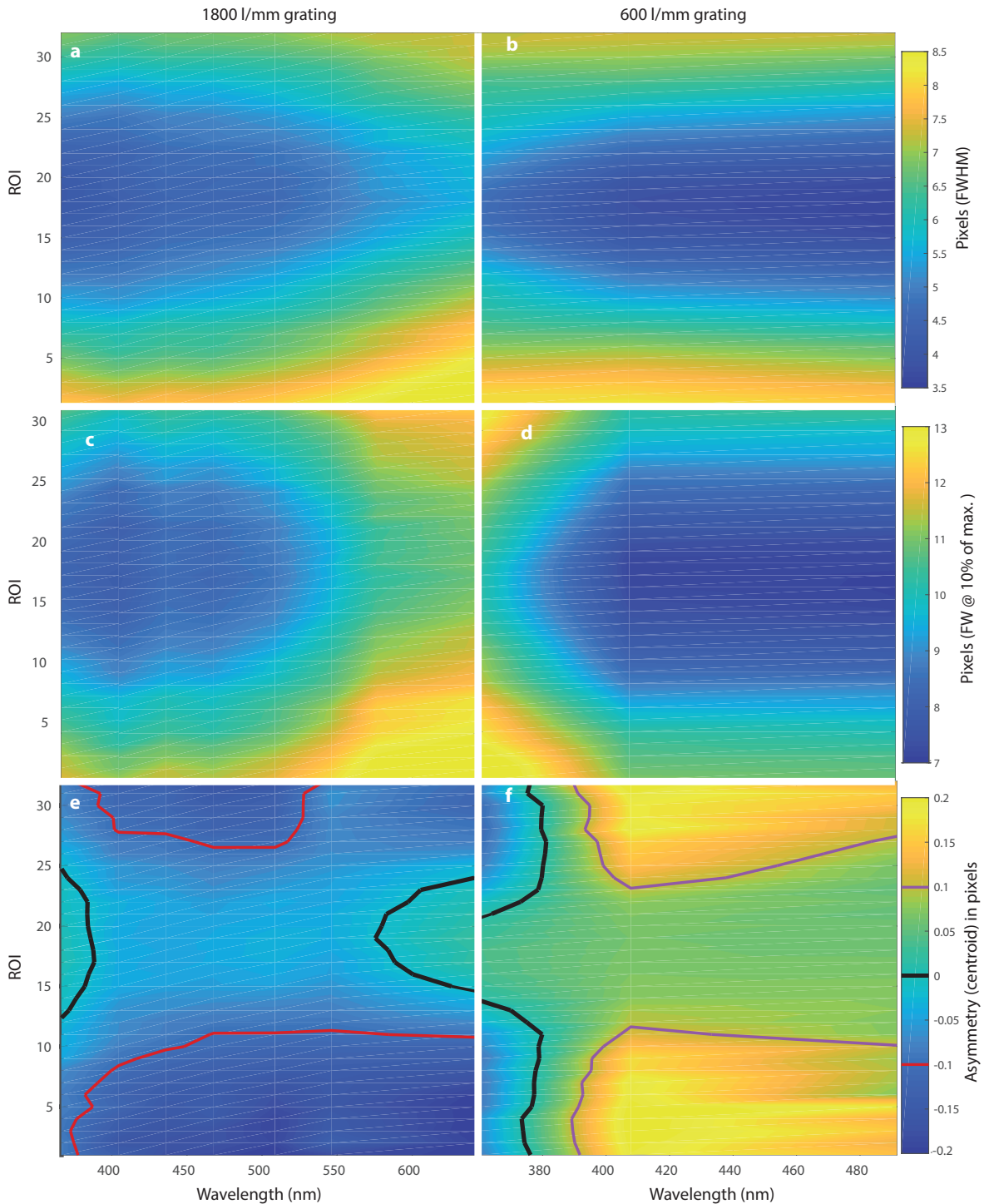


Figure 5.21: Instrumental function characterisation for the 1800 l/mm grating (a,c,e) and the 600 l/mm grating (b,d,f). Colour maps as function of ROI and wavelength are shown for the width (FWHM in pixels (a,b)) and width at 10 % of the maximum intensity (c,d)) and for the asymmetry in pixels (e,f).

expected to deteriorate with increasing wavelength. That is however the opposite for the 600 l/mm grating: thinner instrumentals are observed around 480 nm than at 380 nm; again in correspondence to our predictions based on the optimisation point (which for this grating is at 930 nm). The widening of the instrumental function at the FWHM (e.g. 50 % of maximum intensity) or at a different point (such as the full width tenth maximum —e.g. width at 10 %

of maximum intensity) shows the same picture in terms of trends.

While ROI and wavelength is scanned, the behaviour of the asymmetry of the instrumental function changes. The change in instrumental function asymmetry as function of wavelength is more 'erratic' (e.g. 'quicker') for the edge chords than for the centre chords. Starting at 380 nm for the 1800 l/mm grating, the instrumental function is relatively symmetric (particularly for the central chords). When going to higher wavelengths, the asymmetry first moves in the negative direction (e.g. centroid on the lower-wavelength side of the peak) and, close to 600 nm, again becomes positive (e.g. centroid on the higher-wavelength side of the peak). The behaviour is different for the 600 l/mm grating. First, negative asymmetries are found at lower wavelengths (with the strongest asymmetry at the edges of the CCD). At higher wavelengths, the asymmetry becomes first strongly positive (e.g. centroid more towards higher wavelengths than the peak of the instrumental), after which it goes towards zero again (symmetric case). That shift occurs most rapidly for the edge chords leading to an asymmetry range of -0.08 to +0.3, while the asymmetry remains between 0 and +0.05 for the central chords. The conclusion is that the asymmetry changes as function of wavelength and ROI, while its sensitivity is stronger at for edge chords than central chords, where also the instrumental function is more stably symmetric (in terms of their centroid not changing from 0).

Figure 5.22 highlights the obtained 'efficiency' (note that the determined correction factors are usually per pixels; to compare different gratings here the calibration coefficients have been divided by the wavelength span in nm over a single pixel), which is decreased at low wavelengths (350-425 nm) and then rises by roughly a factor 3 to 500 nm where it is roughly constant until 650 nm after which it deteriorates.

The 600 l/mm grating shows a similar behaviour but lower efficiency values. Oscillations in the efficiency curve for the 600 l/mm grating are obtained at high wavelengths (700 nm), which is due to the etaloning of the sensor as described previously. There is roughly a 33 % difference between the efficiency obtained in the centre of the CCD than at the edges of the CCD —which is not precisely symmetric as shown in figure 5.22 b). That asymmetry however deviates between the different calibration runs as shown in figure 5.22 a). Some strange artefacts are observed in the calibration maps at 388 nm; which is likely an artefact due to the stray light correction algorithms and stray light correction filter used in these regimes. Each curve in figure 5.22 is a separate calibration measurement and having multiple curves at the same wavelength is due to an overlap in wavelength map when the grating angle is slightly changed, which is not a 100 % overlap. The reason is that not only the efficiency depends on the wavelength but also on the CCD horizontal position (not just ROI). At the edges of the CCD the efficiency is reduced, leading to a sharp roll-over in the efficiency curves at high wavelengths as shown in figure 5.22 a and in the measurement of figure 5.22 b.

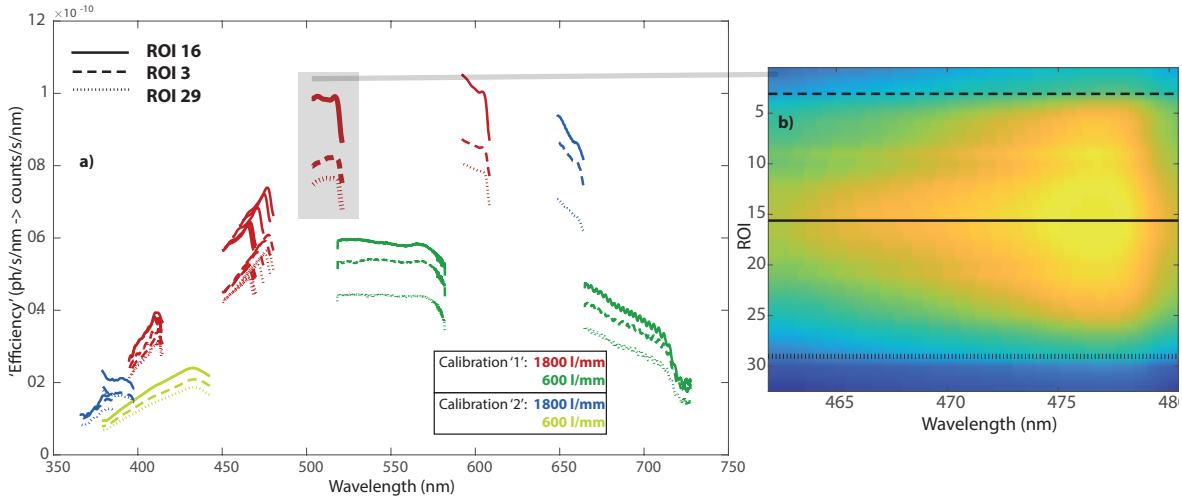


Figure 5.22: DSS 'efficiency', where the measured signal (in  $\text{counts m}^{-2} \text{s}^{-1} \text{sr}^{-1} \text{nm}^{-1}$ ) equals the calibrated signal (in  $\text{ph m}^{-2} \text{s}^{-1} \text{sr}^{-1} \text{nm}^{-1}$ ) times the shown efficiency coefficient (which is in counts per photon). The calibration coefficient is shown as function of wavelength for several calibration runs, the 1800 and 600 l/mm gratings and at several ROIs. b) Example of 2D calibration map obtained during a single acquisition corresponding to three curves highlighted in a).

## 5.8 Synthetic diagnostic implementation in SOLPS-ITER

Using the techniques described in section 4.3 a synthetic diagnostic for SOLPS-ITER simulations of the DSS has been established for deuterium Balmer and carbon impurity lines. The Balmer line emission and line shape is modelled at every grid cell of the simulation using Open-ADAS [134, 135] tables together with the simulated hydrogen ion density; hydrogen neutral density; electron density; electron temperature and ion temperature. Molecular components to the Balmer line emission are neglected. The Balmer line shape is modelled using the experimentally measured instrumental function convolved with a Doppler broadening component (using the simulated ion temperature) and a Stark line shape [74, 131] (using the simulated electron densities and temperatures)—see chapter 6. Using the techniques employed in section 4.3, the viewing cones corresponding to the synthetic DSS line of sight are discretised as multiple lines of sight whose amplitudes are governed by a Gaussian function with the full-width-half-maxima corresponding to the spot size's diameter (distance between the two chords  $\approx 12$  mm). Each line of sight is discretised into multiple points. The emissivity spectra ( $\text{ph m}^{-3} \text{s}^{-1} \text{pix}^{-1}$ ) corresponding to the grid cell in which each point houses is copied to these points. The synthetic Balmer line spectra is then obtained by integrating along the line of sight, yielding a brightness spectrum in terms of  $\text{ph m}^{-2} \text{pix}^{-1}$ . Given an experiment-relevant value for the S/N level, a noise level is simulated for the synthetic spectrum. An application of the DSS synthetic diagnostic is shown in section 7.7.

# Chapter 6

## Application of Stark broadening measurements on TCV

*Stark broadening density inferences is one of the main analysis techniques of DSS data and is required to initialise the more in-depth Balmer line analysis to provide ionisation/recombination estimates. Although Stark broadening is a fairly standard technique, utilised in various other fusion devices including C-Mod, ASDEX-Upgrade, JT60, W7-AS, JET and MAST, it is generally employed at fairly high densities ( $n_e > 1 \times 10^{20} \text{ m}^{-2}$ ) —which are generally not achieved at TCV, complicating Stark broadening analysis on TCV. The application of Stark broadening on TCV is discussed, where special techniques used are discussed in order to cope with the lower TCV densities, including a complete characterisation of the various uncertainties and comparison between different Stark models.*

### 6.1 Stark broadening introduction and fundamentals

Stark broadening is a form of line broadening due to the interaction (collisions) of the emitting particle with the background plasma (electrons and ions); therefore it is considered a form of pressure broadening. These interactions lead to a time-dependent interaction of the emitter with the background plasma, which—from a first order perspective—acts as an interruption of the emitting particle (e.g. collision), giving rise to a Lorentzian spectral line shape with increasing width the more frequent the collisions are. These collisions are mainly a function of electron density and a weak function of temperature; thus analysing Stark broadening can provide an electron density estimate.

Determining Stark broadening is rather complex due to the long-range Coulomb interaction with the many charged particles in the plasma involved. To solve this problem, the time-dependent Schrödinger equation must be solved. Although this can be, under certain assumptions, achieved through computer simulation techniques [197, 127, 198, 199], it is a complicated system to solve. Instead, two assumptions are generally made to facilitate obtaining an analytic approximative solution instead: the impact approximation and the quasi-static approximation. The impact approximation considers only the electric field produced by the electrons, which varies rapidly as they pass a neutral atom. This interaction can be treated as a collision, resulting in the Lorentzian line shape [137]. The quasi-static approximation considers only the electric field produced by the ions, which is assumed to be quasi-static

and constant at the location of the radiator; e.g. it is considered to be a 'microfield'. This eventually leads to a modified Lorentzian profile whose wings are to the power 5/2 as opposed to the power 2 of a standard Lorentzian —leading to a faster decay which is indeed generally observed in fusion plasmas hydrogen Balmer lines [74, 73]. However, larger discrepancies between the experimentally observed lineshapes and the analytically predicted line shapes can occur in the centre of the line shape when using this approximation [200, 74]. For hydrogen, both the ion and electron collisions must be accounted for and thus a combination of both approaches is required.

Table 6.1: Overview of Stehle parametrisation parameters by Lomanowski ([74] and internal communication) for medium and higher-n hydrogen Balmer lines.

$n \rightarrow 2$	$C_i$	$a_i$	$b_i$
5	$1.310 \times 10^{-15}$	0.6796	0.03
6	$3.954 \times 10^{-16}$	0.7149	0.028
7	$6.258 \times 10^{-16}$	0.712	0.029
8	$7.378 \times 10^{-16}$	0.7159	0.032
9	$8.947 \times 10^{-16}$	0.7177	0.033
10	$1.239 \times 10^{-15}$	0.7158	0.032
11	$1.632 \times 10^{-15}$	0.7146	0.028
12	$6.459 \times 10^{-16}$	0.7388	0.026
13	$9.012 \times 10^{-16}$	0.7356	0.02

[115], JET [74], MAST [76], NSTX [75], C-Mod [51, 66] and W7-AS [77]. The general uncertainties in these line shapes are expected to around 10 % [74, 73, 131], while the uncertainties in the centre of the line can be larger as MMM models due to the limitations in how the ion dynamics are included, which influence the central part of the spectral line [74, 200] and integrating the Schrödinger equation instead tend to give more consistent results for the centre [200]. Experimentally, however, this is expected not to have a strong influence on the observed line shape as also other broadening mechanisms (Doppler broadening, small Zeeman split) leads to a mixing of different mechanisms in the central part of the line, flushing out these discrepancies [73, 74].

Lomanowski [74] has analysed the Stehle databases (equation 6.1) and has provided a fit through the Stehle line shapes, which enables a fast interrogation of line shapes and provides the line shape on an arbitrarily fine grid, where  $I(\lambda, \lambda_0, n_e, T_e, I_0, i)$  is the line intensity as function of wavelength  $\lambda$ . Here  $\lambda_0$  is the central wavelength,  $n_e$  is the electron density (in  $\text{m}^{-3}$ ),  $T_e$  is the electron temperature in eV,  $I_0$  is the peak line intensity and  $i$  denotes the index of the transition.  $C_i$  denotes the general width of Stark broadening, while  $a_i$  ( $n_e$ ),  $b_i$  ( $T_e$ ) are tuning parameters determining the effective influence of  $n_e, T_e$  on the Stark width; all of these values are tabulated and partially provided in table 6.1. The uncertainty (in terms of Full-Width-Half-Maxima (FWHM)) in this parametrisation with respect to the Stehle model

There are several techniques which can combine both of these approaches. One of them, which is often used in fusion research, is the Model Microfield Method (MMM). This focusses on the quasi-static approximation, where Stark splitting is considered, and applies collisional broadening due to electron-neutral interactions to each individual Stark split [137, 73, 201], resulting in an analytic solution to the Schrödinger equation which includes both ion (through a quasi-static field) and electron (through impact theory) effects. One of the most accurate databases up to date performing such MMM calculations is developed by Stehlé [131] on a coarse spectral grid. These line shape profiles "published by Stehle [131] are widely accepted" [74] and are used to evaluate divertor densities in AUG

is < 10 %, while the uncertainties on each of the fit parameters is generally 5-10 % [74] (less than 5 % for the  $7 \rightarrow 2$  hydrogen Balmer line on which TCV stark broadening is based).

$$I(\lambda, \lambda_0, n_e, T_e, I_0, i) = \frac{I_0}{4\sqrt{2} \left| \frac{\lambda - \lambda_0}{C_i \frac{n_e b_i}{T_e b_i}} \right|^{5/2} + 1} \quad (6.1)$$

### 6.1.1 An introduction to Stark fitting on TCV

As a prelude to the following of this chapter, we will first briefly introduce the Stark broadening fit mechanism used on TCV —to get a rough idea of the spectral widths and the various dependencies. First, it is important to Stark broadening is an *additional* broadening observed to the spectral line shape: e.g. the exact Stark line shape is never *exactly* observed as the instrument itself also leads to a specific line shape even when a non-broadened (or negligibly broadened) line is observed and in addition other broadening effects (most notably Doppler broadening) also occur. If the Stark broadening is much more significant than the instrumental function or any other form of spectral broadening —it will, however, approximate the Stark function well, which is true for most devices where Stark broadening is employed (AUG [115], JET [74], MAST [76], NSTX [75], C-Mod [51, 66] and W7-AS [77]). However, due to the modest electron densities on TCV, Stark broadening only has a minor effect on the observed line shape and the fact that the observed line shape is a convolution of all line broadening effects together with the instrumental function needs to be accounted for.

The discussion on TCV’s Stark fit approach is further discussed in section 6.3. Lomanowski’s fit of the Stehle model [74, 131] is used as the default Stark fit on TCV, from hereon referred to as the ‘parametrised Stehle model’. We have checked that we obtain the same results with the tabulated version and with the full results from the Stehle tables [131]. This approach has been benchmarked with other Stark models, such as the PPP-B code [74, 202] and recently to computer simulation techniques to solve the Schrödinger equation quantum mechanical calculation of the Stark broadening [198, 199, 197] using TCV data, which has shown an agreement between both models using a manual ‘fit’ [127]. Rosato’s Stark tables [198, 199, 197, 127], where the line shape depends on  $n_e, T_e$  as well as the magnetic field and the observational angle of the diagnostic with respect to the magnetic field, have been implemented in the TCV fitting algorithms and can be used instead of the default technique —we will refer to this as the ‘Rosato model’. In section 6.6 Stark broadening results obtained through both models will be compared and discussed. By default, the  $n = 7$  deuterium Balmer line is used for Stark broadening on TCV.

In figure 6.1 various relevant line shapes (Stark, Doppler and instrumental shape) are shown for a range of TCV parameters. From these comparisons, we can conclude:

- The instrumental function is significantly *wider* than Stark broadened width (considering the Full-Width-Half-Maximum (FWHM)), except at the high(er) TCV densities  $n_e > 6 \times 10^{19} \text{ m}^{-3}$ .
- Even Doppler broadening at a modest ion temperature of  $T_i = 5 \text{ eV}$  is significantly wider than Stark broadening at modest TCV densities  $n_e < 5 \times 10^{19} \text{ m}^{-3}$ . However, the roll-off (e.g. the wings of the spectral line) are much narrower for the Gaussian Doppler profile than the Lorentzian-like Stark profiles.

- Stark broadening increases strongly with increasing electron density. The FWHM of the  $n = 7$  deuterium Balmer line scales approximately like  $\Delta\lambda_{FWHM} \propto n_e^{0.7}$  (e.g. equation 6.1 and table 6.1).
- At the lowest electron densities, Zeeman splitting can have a significant influence on the *central part* of the spectral line shape (effective widening and splitting) of even upper-n Balmer ( $n = 7$ ) lines. This mostly occurs for high magnetic fields of 2 T (inner column).
- Apart from magnetic field effects, the results obtained by the Stehle and Rosato models are similar and most of the deviation occurs in the central part of the line shape, where the Rosato model has a more blunt shape. Some discrepancy also exists in the wings where the wings predicted by the Rosato model are wider implying that lower densities with this model would be detected than with the Stehle model.

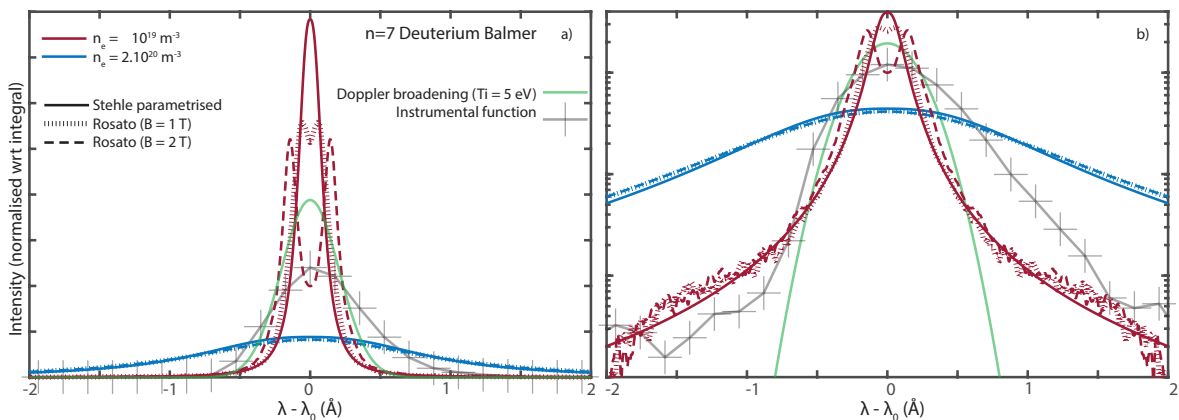


Figure 6.1: Various line shapes on a a) linear scale and b) logarithmic scale of Stark/Doppler-/Instrumental broadening for the  $n = 7$  deuterium Balmer line (397 nm). All line profiles are normalised with respect to their integral.

## 6.2 Stark broadening compared to other line broadening effects

Stark broadening is, however, not the only line-broadening mechanism for Balmer lines on TCV: other line shape effects occur, which we will summarise below. First we will discuss the line shape influences which do not influence the spectra on TCV. To illustrate how much broadening these mechanisms could lead to, we make an overestimation of the possible influence by making the following assumptions:  $\lambda_0 = 397$  nm (central wavelength corresponding to the  $7 \rightarrow 2$  transition —the calculations below are for that transition);  $n_e = 1 \times 10^{21} \text{ m}^{-3}$  (large overestimation — $n_e$  on TCV is generally in the range  $1 \times 10^{18} \text{ m}^{-3}$  to  $3 \times 10^{20} \text{ m}^{-3}$ ); neutral temperature of 12 eV (exaggerated), neutral density of  $n_o = 1 \times 10^{21} \text{ m}^{-3}$  (exaggerated by two orders of magnitude). As a reference, we note that for TCV relevant conditions, Doppler broadening of this line at  $T_n = 5$  eV would lead to a Doppler width of  $0.5 \text{ \AA}$  and Stark broadening of this line at  $n_e = 5 \times 10^{19} \text{ m}^{-3}$  would lead to a similar (FWHM) width of  $0.6 \text{ \AA}$ . Note also that these broadening levels are at the lower limit of the instrumental's FWHM of

0.6 Å to 1.2 Å (depending on the LoS used and the wavelength region used), using the highest dispersive grating of the DSS.

- Natural broadening. This arises from Heisenberg’s uncertainty principle which relates the lifetime of an excited state to an uncertainty of its energy distribution thus resulting in a spectral broadening with a Lorentzian profile [137]. For the  $7 \rightarrow 2$  Balmer line, this is expected to lead to  $3.6 \times 10^{-7}$  Å broadening. This is fully negligible. For this calculation, equation 9.15 in [137] is used in combination with NIST values [203]
- Resonance broadening. Interactions of the same kind of neutral atoms can lead to ‘resonance broadening’ —a form of spectral pressure broadening due to neutral particles. This can occur if the upper or lower level of a transition is connected to the ground state through an allowed dipole transition. Using the resonance for the  $7 \rightarrow 2$  transition to the ground state (using the  $2 \rightarrow 1$  transition), this would lead to a (FWHM) broadening of  $3 \times 10^{-5}$  Å and is thus completely negligible. For this calculation, equation 9.22 in [137] is used in combination with NIST values [203].
- Van der Waals broadening. This other form of pressure broadening due to neutral particles is due to the Van der Waals interaction between two neutral atoms of different species, resulting in a spectral line broadening. Assuming a Van der Waals interaction constant of order  $C_6 = 1 \times 10^{-40} \text{ m}^6 \text{ s}^{-1}$  [137], we expect a broadening of  $2 \times 10^{-4}$  Å using equation 9.26 in [137], assuming hydrogen to carbon collisions —which is completely negligible.
- Opacity broadening. Self-absorption of emission can occur in high density regimes. This generally plays the strongest role at a line’s centre [137]: instead of a peaked profile, the broadening leads to a more stubbed shape where the top has been cut-off. In more extreme cases, even a self-reversed double peak line profile can occur. To approximate the influence of this, we follow the simplified procedure highlighted in [204, 205] and we make the additional assumptions that the emission region is 5 cm wide and that the electron temperature is  $< 0.5$  eV (to increase the  $n = 7$  populational level, which exaggerates the opacity influence). This leads to a maximum upper limit of opacity of 1.5 % (where, as stated previously, the density and neutral density was overestimated by at least one order of magnitude) —leading to an approximate modification of the effective line width by  $\sim 0.8$  %. We can thus expect that opacity broadening (and opacity itself) is negligible for TCV plasmas; but may play a role at higher density tokamaks such as JET and C-Mod [63, 72].

There are however other line shape influences which may influence the spectra more significantly, which are Zeeman splitting; Doppler broadening and the  $T_e$  influence in Stark broadening. Below we will provide a brief overview of how such influences can influence the expected line shape. When inferring the electron density from the Stark fit, however, one has to make assumptions on these influences/parameters. In section 6.4 a more in-depth uncertainty / sensitivity analysis is performed using Monte Carlo methods which highlights how sensitive the Stark result is to such assumptions and how a mismatch between the assumed values and the actual values leads to a mismatch in Stark inferred density.

### 6.2.1 Stark broadening under the presence of a magnetic field —Zeeman splitting

Zeeman splitting arises when a magnetic field is present, which splits the energy levels of atomic systems, splitting the emission of a transition over two levels, leading to a split of the spectral line where the distance between the two components depends on the strength of the magnetic field. Each of these contributions is broadened by Stark/Doppler broadening as well as the other effects described. Depending on how strong the split is between these two different lines —the split can be such that it is not fully negligible compared to the broadening of each of the contributions and then *effectively* broadens the spectral line observed. If the split is such that it is significantly stronger than the broadening of the spectral lines, two individual curves can be observed. These Zeeman components are fully covered by the Rosato model, which we have already seen in figure 6.1.

Zeeman splitting is considered negligible for ASDEX-Upgrade-like magnetic fields (which is higher than the magnetic field on TCV) for  $n=7$  or higher Balmer lines [73, 115]. When calculating the Zeeman split using a TCV magnetic field of 1 T to 2 T (corresponding to the outer-inner column respectively with the conventional 1.4 T magnetic field at the central axis), we obtain that the Zeeman splitting expected of the  $7 \rightarrow 2$  Balmer line is  $0.1 \text{ \AA}$  to  $0.2 \text{ \AA}$ . This ignores the magnetic field generated by the plasma current.

Despite this being significantly smaller than the instrumental function, it can (especially near the inner column) play a role when inferring the Stark width in low density conditions of the order  $n_e = 1 \times 10^{19} \text{ m}^{-3}$ , where the Stark width is  $\sim 0.2 \text{ \AA}$  of the  $n = 7$  Balmer line. Likewise, lower-n Balmer lines ( $n < 7$ ) will be (relatively) effected more strongly as their Stark broadening is smaller.

Zeeman splitting is fully accounted for in Rosato's Stark model [127, 198, 199, 197]. We investigate the influence of the magnetic field on Stark broadening at several electron densities by visualising the 'width' of the obtained lineshape, expressed as the full width of some fraction of the peak intensity in figure 6.2. This confirms the above suspicions: especially at stronger magnetic fields (1.5 T to 3 T), Zeeman splitting and other magnetic field effects can influence the Stark line shape and widths significantly at low  $n_e$  ( $2 \times 10^{19} \text{ m}^{-3}$ ). At higher  $n_e$ , however, the influence is negligible. When the result is sensitive to the magnetic field, also the observational angle plays a role, which is fixed around 90 deg in the experiment (when neglecting the magnetic field generated by the plasma).

### 6.2.2 $T_e$ dependence of Stark broadening

Although Stark broadening depends mostly on the electron density, it also has some (electron) temperature dependence [131], arising from the weak temperature dependence of elastic and inelastic collision rates [137]. Using table 6.1, for the  $n = 7$  Balmer line, the Stark width is  $\sim n_e^{0.71} / T_e^{0.029}$ . The influence of a  $T_e$  range 0.6 eV to 15 eV on the inferred Stark density is  $\pm 6\%$  compared to a fixed  $T_e$  at 3 eV [1].

The  $T_e$  dependence of Stark broadening however depends on the Balmer line used. In figure 6.3 we compare the influence of  $T_e$  on the parametrised Stehle model (explained above) and the Rosato Stark model (where a magnetic field of  $B = 1.4 \text{ T}$  is assumed with an observational angle of  $\theta = 88 \text{ deg}$ ), indicating that especially at low  $T_e$  (0.5 eV to 7.5 eV) the obtained

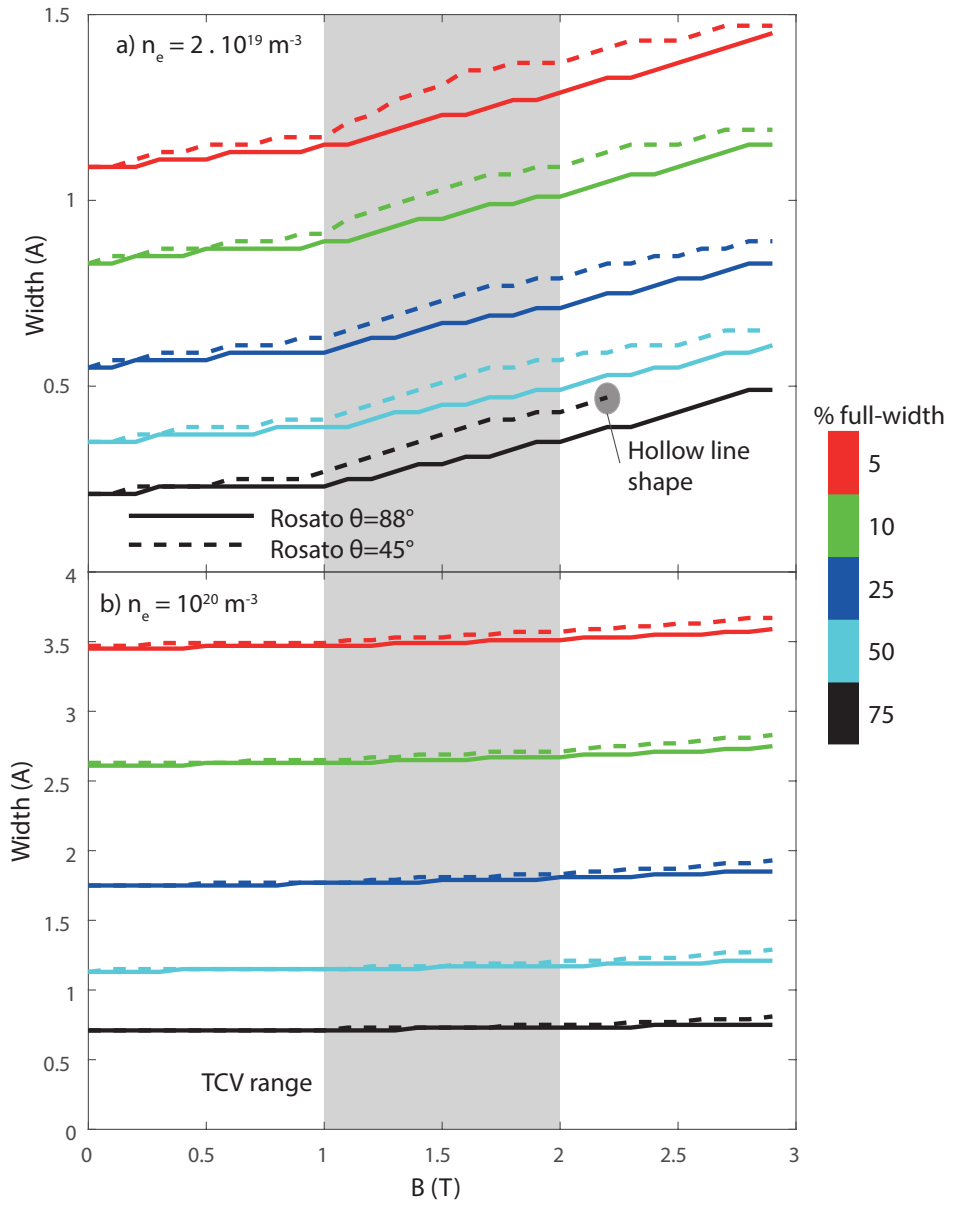


Figure 6.2: Various fractional widths of the Stark lineshape using the Rosato Stark model for two different  $n_e$  as function of  $B$  for two different observational angles.

Stark profiles can be significantly wider at 5% of its peak intensity whereas the deviation in the central part of the line shape is smaller. The influence of  $T_e$  is thus more pronounced in the Rosato model, which may imply that larger uncertainties due to  $T_e$  than  $\pm 6\%$  can be expected —especially in detached (e.g. low  $T_e$ ) conditions. That discrepancy partially arises from the parametrised Stehle model (e.g. the non-parametrised Stehle models predict a stronger  $T_e$  dependence —although not as strong as Rosato's Stark model). This could potentially influence density estimates in detached conditions, which is investigated in more detail in section 6.4.

### 6.2.3 Stark broadening and Doppler broadening

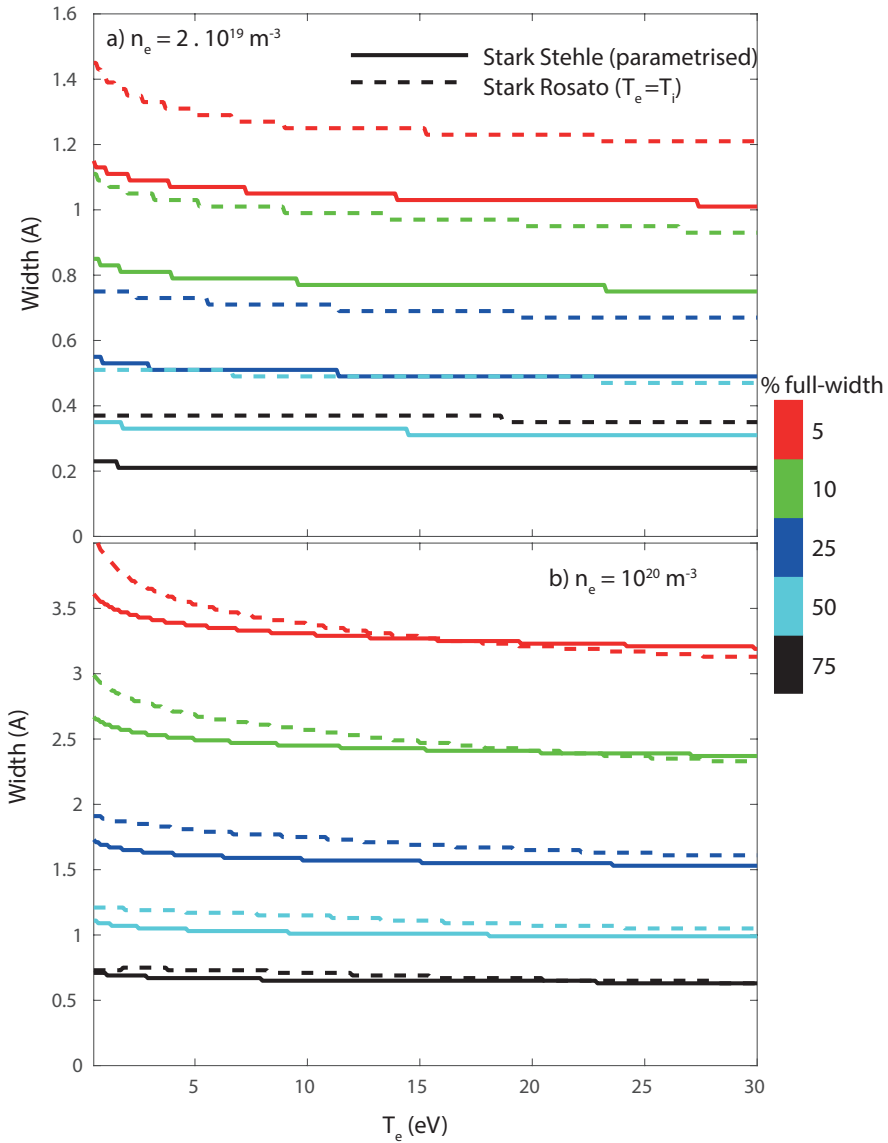


Figure 6.3: Various fraction widths of the Stark lineshape for two different  $n_e$  as function of  $T_e$  for both the parametrised Stehle model and the Rosato Stark model, which assumes  $T_e = T_i$  and accounts for ion dynamics (only the Stark shape is shown —not the Doppler shape)

Important to note is that Doppler broadening arises from the temperature of the emitting particle. For the hydrogen Balmer lines, that is, assuming excitation emission, the neutral temperature and, assuming recombinative emission, the ion temperature—which likely leads to negligible Doppler broadening as the ion temperature is likely of the order of a few eV as such low electron temperatures are required for recombination to occur. However, for legacy purposes, we refer to the Doppler-related temperature as an ion temperature.

As was already highlighted previously, the Doppler broadening of the hydrogen Balmer line can be significant compared to the Stark broadening (when the full-width-half-maxima are considered) —even at modest ion temperatures of  $\sim 5$  eV. This means that the Doppler broadening (in low density conditions) may be significant in both attached and even detached conditions.

However, as shown in figure 6.1, the wings of the Stark profile are significantly wider. That is *assuming a Maxwellian ion velocity distribution* where the Doppler line shape can

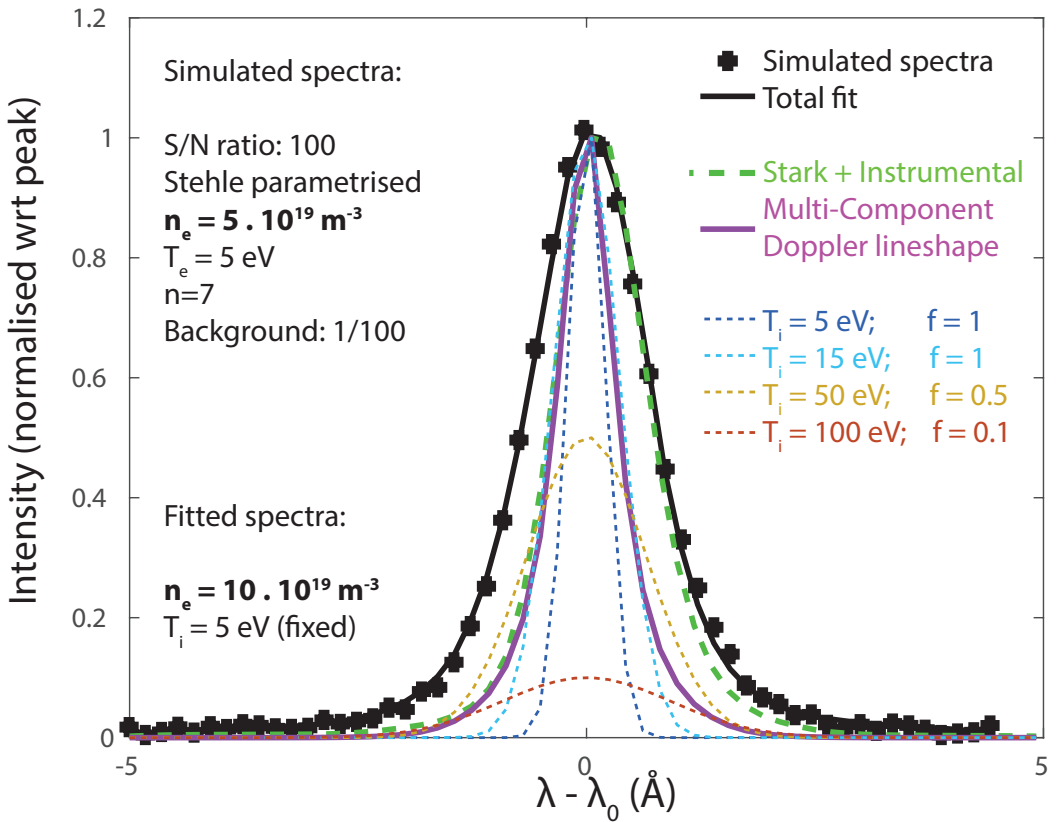


Figure 6.4: Example of a Stark fit on a synthetically simulated spectra with multiple Doppler components denoted by their ion temperature and relative strength  $f$ . The fit parameters are noted in the figure. Due to the multiple Doppler components, going to high temperatures (100 eV), wide Doppler wings are obtained (similar to Stark) and the Stark/Doppler broadening can no longer be distinguished.

be described by a Gaussian with a certain width dependent on the ion temperature [137]. Assuming such a Doppler line shape, the Stark broadening component can still be extracted from the line shape without detailed knowledge on the ion temperature by focussing on the wings of the line shape. More details on how this is done is provided in section 6.3. A quick investigation of the sensitivity of Stark fitting to the Doppler width has been employed by the author in [1]. Here, synthetic profiles with random noise have been simulated, including Stark, Instrumental and Doppler broadening with an ion temperature between 0.2 and 15 eV, the obtained Stark density differs (when fitting the synthetic line shape assuming  $T_i = 3$  eV) by less than 10% [1]. In addition, such Doppler broadening could be beneficial for the Stark analysis, to some degree, as it will smooth or 'wash' out the central part of the line shape, reducing the influence of Zeeman splitting [73, 74] and smoothing out uncertainties in the Stark line shapes which are strongest in the central part of the line shape [74, 197, 199, 198].

All of this is however assuming a Gaussian Doppler line shape, corresponding to a Maxwellian ion distribution. However, if the velocity distribution of the ions is non-Maxwellian (for instance due to the presence of a fast ion population), Doppler broadening may give rise to wider wings and a more Lorentzian-like profile, making it harder to distinguish from Stark broadening and thus effecting the Stark density inference [127]. As an illustration we will show a case where we simulate a synthetic Balmer line spectra (including the instrumental

function, Stark broadening, Doppler broadening and random noise) with a prescribed density ( $n_e = 5 \times 10^{19} \text{ m}^{-3}$ ) and a multi-component ion temperature distribution as shown in figure 6.4. That line shape is then fitted using identically to experimental line shapes (as will be explained in section 6.3) where a fixed ion temperature of 5 eV is assumed, which fits the synthetic line shape appropriately as shown visually in figure 6.4. However, the electron density inferred from this fit is  $\sim 1 \times 10^{20} \text{ m}^{-3}$ , which is *twice higher* than the prescribed electron density.

A non-Maxwellian (or multi-component) ion velocity distribution can thus be a serious issue for Stark fitting, which cannot be detected by looking at the fit residuals. One important way to detect such influences is to check the consistency of Stark fitting between different Balmer lines. The Stark width will increase with increasing  $n$  number while the Doppler width will remain constant. For the case shown for instance, the inferred Stark  $n_e$  ranges from  $2.3 \times 10^{20} \text{ m}^{-3}$  (a factor 4-5 overestimation) for a  $n = 5$  Balmer line to  $5.9 \times 10^{19} \text{ m}^{-3}$  (20 % overestimation) for a  $n = 12$  Balmer line. Consistency between different Balmer lines in the inferred Stark  $n_e$  is thus a good indicator for the validity of the Stark inference. Such a consistency is shown and investigated in section 6.6.

### 6.3 TCV's Stark fitting techniques

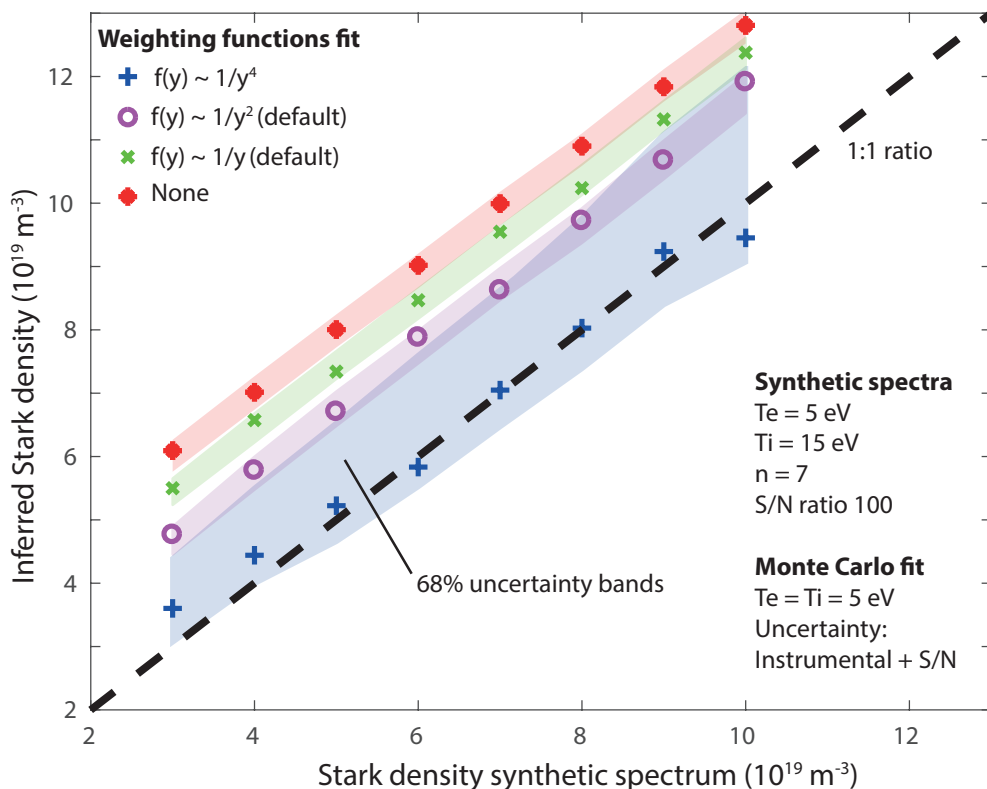


Figure 6.5: Comparison between the electron density set in the synthetic spectrum with a  $T_i = 15 \text{ eV}$  to the electron density inferred in the fit assuming a  $T_i = 5 \text{ eV}$  for different weighting functions used in the fit. Uncertainties in the instrumental function and due to the signal to noise level of the synthetic spectra are accounted for using a Monte Carlo approach.

For TCV applications, Stark fitting is performed by convolving a Stark model function

together with the measured instrumental function, which has been characterised to very high accuracy particularly for this purpose (see section 5.6), and a Gaussian function corresponding to Doppler broadening (assuming a Maxwellian ion velocity distribution with a certain ion temperature  $T_i$ ). Depending on the Stark model used, the fitting parameters (can) include electron density  $n_e$ , ion temperature  $T_i$ , peak intensity  $I_0$ , central wavelength  $\lambda_0$ , electron temperature  $T_e$ , observational angle  $\theta$  and magnetic field strength  $B$ . Some of these parameters may be fixed during the fit to reduce the number of free parameters and thus make the fitting procedure more numerically stable. Generally, only the peak intensity  $I_0$ , central wavelength  $\lambda_0$  and electron density  $n_e$  are free parameters whereas  $T_i$ ,  $T_e$  are fixed (usually at 3 or 5 eV) and if the Rosato Stark model is used,  $B$  and  $\theta$  are also fixed (at 1.4 T and 88 deg respectively). A choice has been made for using the total line shape function, obtained through convolution, as a fitting function instead of deconvolving the experimentally measured spectra, which tends to be numerically more unstable. As the plasma emission also has a background level in the experiment, a polynomial background ( $n = 1$  or  $n = 2$ ) is added to this line shape to form the full fitting function for the experimental spectrum. The actual fitting is performed through a least-squares fit through a Matlab implementation developed by Basil Duval and Alexander Karpushov of the Gradient-expansion algorithm developed by Bevington [206]. An illustration of the fit result and its various line components is shown in figure 6.6, where an experimentally observed spectra has been fitted using Rosato's Stark model (by default the parametrised Stehle model is used). For the case shown, the electron density, peak intensity, central wavelengths and polynomial background ( $n = 1$ ) were free parameters while the rest of the shown parameters ( $T_i, T_e, B, \theta$ ) were fixed as indicated. These are the free/fixed parameters generally used. The reason ( $T_i, T_e$  and  $B, \theta$  for Rosato's Stark model) are fixed is to reduce the number of free parameters in the fit, making the fit more numerically stable and faster.

As discussed, one challenge for TCV Stark fitting is that the Stark width FWHM is generally smaller than both the Doppler and instrumental FWHM and thus, somehow, the wings of the experimentally measured line shape must be emphasized in the fit to obtain a correct density inference. However, the intensity at the wings of the observed line shape is much smaller than the peak intensity of the line and measuring these wings accurately requires a significant signal-to-noise (S/N) ratio. Based on the investigation of influence of the S/N ratio and the instrumental function (shown in more detail in section 6.4 and [1]), the minimum peak signal-to-noise ratio for which a Stark fit is attempted is generally 30 (but at least 10), which is achieved by dynamically averaging the spectra over a number of frames (e.g. over a longer period of time), depending on the S/N level: less averaging is applied when the observed S/N level is larger and when the deviations in the density are faster.

$$f(y) \propto \frac{1}{y^a} \quad (6.2)$$

In addition to averaging the signal, the emphasis on the spectral wings of the fit (which carries the most and the purest information on  $n_e$  through Stark broadening) is increased by employing a weighting function which puts emphasis on the wings of the profile. These weighting functions are provided by equation 6.2, which in essence ascribes higher importance to low signal values. Here  $y$  is the measured spectrum and the power of  $a$  is set depending on the strength of the weighting required. That strength depends on the ion temperature present

and the signal-to-noise level, as making the fit more sensitive to low signal levels (larger  $a$ ), makes the fit more sensitive to noise thus requiring higher S/N levels by averaging the spectra over more frames. One main advantage of focussing on the wings of the fit is that it exploits the fact that the central part of the model fit function is not as accurate as the wings of that line shape, due to both uncertainties on the assumed Doppler/Zeeman broadening/splitting and due to the central part of the Stark line shape not being well retained by Stark models [74, 73, 131]. The inclusion of this weighting function in the fit has lead to a more robust and higher quality Stark fits —meaning:

- Deviations obtained between Stark densities of different Balmer lines have decreased
- The resultant electron density during a discharge has become less erratic (more stable) —especially at low electron densities ( $< 5 \times 10^{19} \text{ m}^{-3}$ )
- Line fitting has become less sensitive to impurity lines
- Deviations in the Stark fit due to an uncertainty in the assumed ion temperature has decreased

The ability to make the fit more insensitive to the assumed  $T_i$  by using a prescribed weighting function is shown in figure 6.5, where the inferred electron density from a synthetically simulated line shape is investigated by using different weighting functions on a case where the synthetic  $T_i = 15 \text{ eV}$  assumed  $T_i = 5 \text{ eV}$  —this deviation is particularly high and is expected to be smaller during the experiment. This analysis has been determined using the Monte Carlo approach highlighted in section 6.4.

Without applying the weighting function, a consistent overestimation of the Stark density is shown by  $3 \times 10^{19} \text{ m}^{-3}$ , which reduces when weighting is included and eventually by using stronger weighting (increasing  $a$ ), the discrepancy between the inferred Stark density and the prescribed Stark density is diminished to zero while the uncertainty increases due to a stronger dependence of the fit to the S/N ratio. Experimentally, the applied weighting can be altered to see if the fit quality (visually) improves, while the increased uncertainty (which would lead to noisier  $n_e$  inferences in an experiment) can be reduced again by increasing the S/N ratio. This visual confirmation is important as a miss-fit arising from a strong deviation between the actual and prescribed  $T_i$  can be seen by looking at the fit —which was clear from looking at synthetic line shapes obtained from SOLPS simulations near the X-point where the neutral temperature is particularly high (25 eV). Such behaviour has not been observed in the experiment.

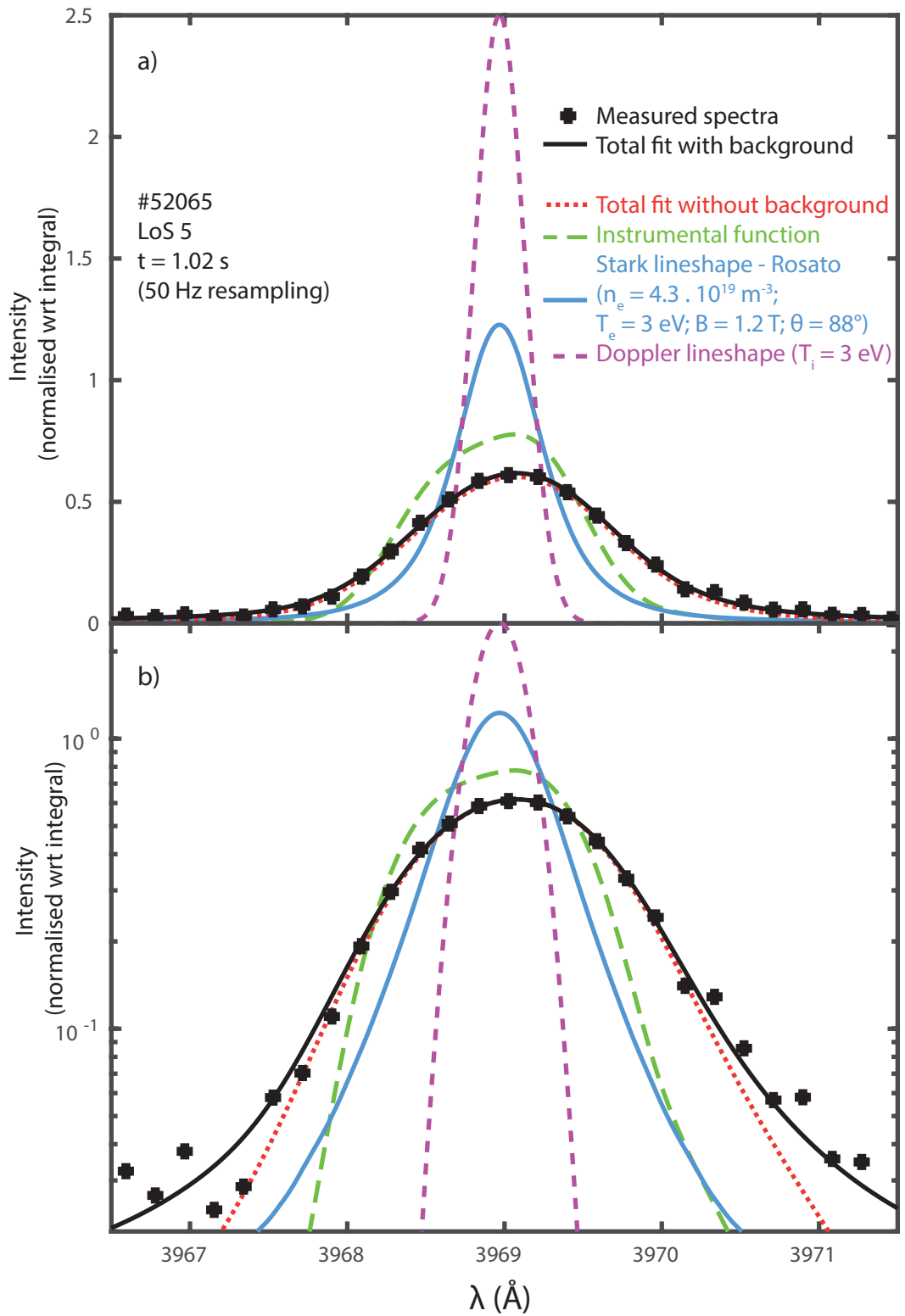


Figure 6.6: Example of a Stark fit using experimental TCV data on a linear scale (a) and a logarithmic scale (b). The shown instrumental function, Doppler line shape, Stark line shape are convolved and a polynomial background is added to form the fitting function. The shown spectral line corresponds to the  $7 \rightarrow 2$  Balmer line. All line profiles are normalised with respect to their integral.

## 6.4 TCV Stark broadening uncertainty and sensitivity analysis

A thorough and full characterisation of Stark broadening for TCV conditions has been done through a sensitivity analysis in order to investigate the applicability of Stark broadening inferences on TCV and in order to ascertain the uncertainty of such inferences. First uncertainties arising due to various effects are investigated individually, which include uncertainties due to S/N ratio and the instrumental function; uncertainties due to a mismatch in the prescribed and actual  $T_e$ ,  $T_i$ ; uncertainties induced due to Zeeman splitting and uncertainties between different Stark models (parametrised Stehle and Rosato). All of this information is eventually combined to obtain a general uncertainty. All of this analysis applies to the  $n = 7$  Balmer line.

The individual investigations have been performed by first simulating a *synthetic* spectra given a series of known parameters, which are then fitted using the basic fit routines where some parameters are free fit parameters while others are fixed. All of this is done in a Monte Carlo approach where multiple synthetic line shapes are simulated with random noise (depending on the prescribed S/N ratio) and simulated instrumentals, describing the uncertainty in the measured instrumental function in a Monte Carlo fashion as highlighted in section 5.6. Each synthetic line shape is then fitted and a value for  $n_e$  is obtained, leading to a list of values for  $n_e$ . Using statistical methods highlighted in section 7.6, that list can be mapped to a probability density function (PDF). The peak of that PDF then provides the most likely value for  $n_e$  while the width of the PDF, whose integral corresponds to a set probability, provides the confidence interval for  $n_e$ .

To address the general uncertainty, a *measured* spectrum is fitted where the fixed fit parameters are varied in a Monte-Carlo fashion ( $T_e$ ,  $T_i$ ,  $B$ , etc.), while the simulated instrumentals are used in the fit, describing the uncertainty in the measured instrumental function in a Monte Carlo fashion as highlighted in section 5.6. This again leads to a list of values for  $n_e$ , from which a PDF is extracted to obtain both the uncertainty and the expected  $n_e$  value.

### 6.4.1 Uncertainties induced due to signal-to-noise ratio and the instrumental function

The main uncertainties in TCV Stark fitting are induced by the S/N ratio and the instrumental function uncertainty. Those uncertainties/sensitivities have been analysed for a central/edge line of sight in figure 6.8 as function of S/N level. This indicates large uncertainty margins and a large deviation between the inferred electron density and the prescribed electron densities at low S/N values. When increasing the S/N level, the uncertainty converges to a fixed (much smaller) level, corresponding to the uncertainty expected due to the instrumental function uncertainty, while the electron density estimate converges towards the prescribed level. As expected, this convergence point is at a lower S/N level for higher electron densities as higher electron densities lead to brighter wings. The convergence point is also at a lower S/N level for the central chords than the edge chords, which have a narrower instrumental function. Those narrower instrumental functions, plus a smaller instrumental function uncertainty as has been determined in section 5.6, also lead to a significantly smaller uncertainty by a factor two. For all criteria, the uncertainty is fully converged at S/N ratios higher than 70.

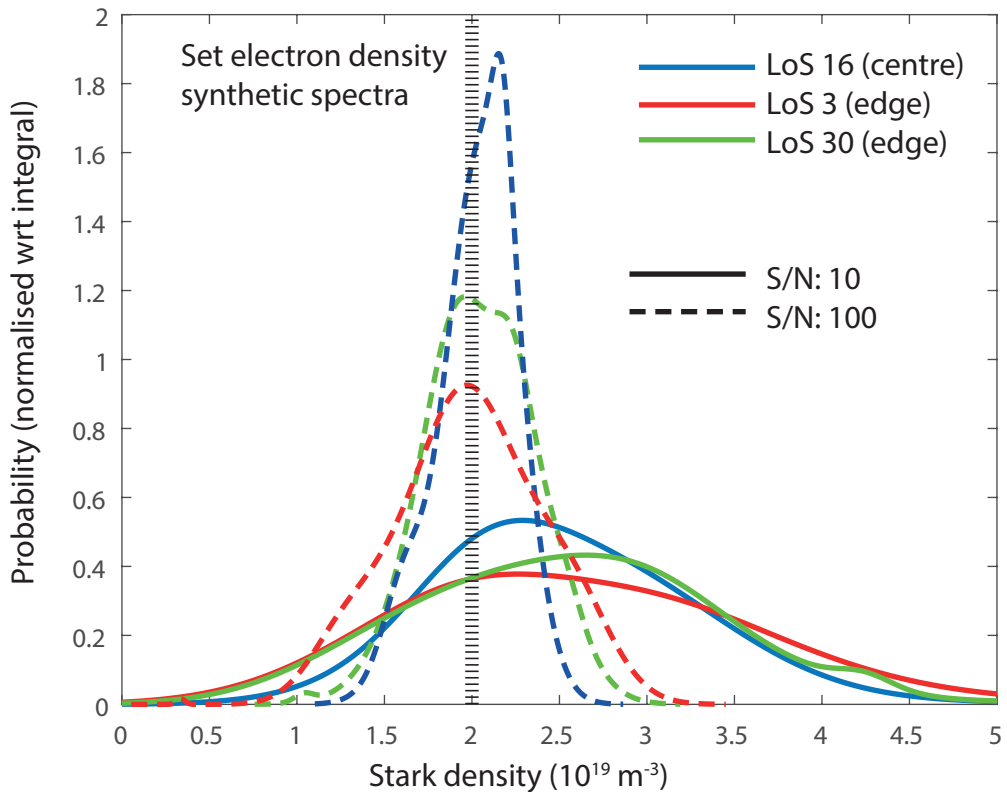


Figure 6.7: Probability density functions (PDFs) for the Monte Carlo inferred Stark density where the random noise and the instrumental function (according to its error) is varied for a case where the electron density corresponding to the synthetic spectra is fixed at  $2 \times 10^{19} \text{ m}^{-3}$ . Different PDFs are shown for different lines of sight and different signal to noise level.

The large deviation between the inferred electron density estimate and set electron density at low S/N levels implies that a minimum S/N level is required for reliable electron density inferences. For all conditions shown, this is achieved at a S/N level of 10 or higher while the influence of noise on the fit is small for signal-to-noise levels higher than 30, where 68 % confidence margins of less than  $1 \times 10^{19} \text{ m}^{-3}$  are expected ( $2 \times 10^{19} \text{ m}^{-3}$  are expected for S/N levels between 10 to 30); leading to the minimum S/N criteria of 10 to 30 for TCV Stark fitting mentioned previously (dynamic averaging is applied to reach those criteria).

Before proceeding with the characterisation of the expected uncertainties, we should note that the shown information (peak values and uncertainties) does not visualise all information from the obtained PDFs. A characteristic example of the obtained PDFs is shown in figure 6.7. It is important to note that the PDFs shown are clearly unimodal (e.g. have a single peak) and are smooth; meaning that there is a single result which is most likely with a given uncertainty given by the widths of the PDFs. Therefore, it is fair to visualise this analysis by focussing on the estimated  $n_e$  (peak of the PDF) and estimating the confidence interval by determining the bounds in which the integral of the PDF equals some prescribed uncertainty.

Given that assurance, we proceed with using the results, as shown in figure 6.8, to construct a 2D map of expected uncertainties and deviations (e.g. the difference between the estimated  $n_e$  and the prescribed  $n_e$ ) as function of prescribed electron density and signal-to-noise level, shown in figure 6.9. This indicates that the deviation between the Stark Monte Carlo inference between and the set electron density in the synthetic spectra is small for signal-to-noise ratios

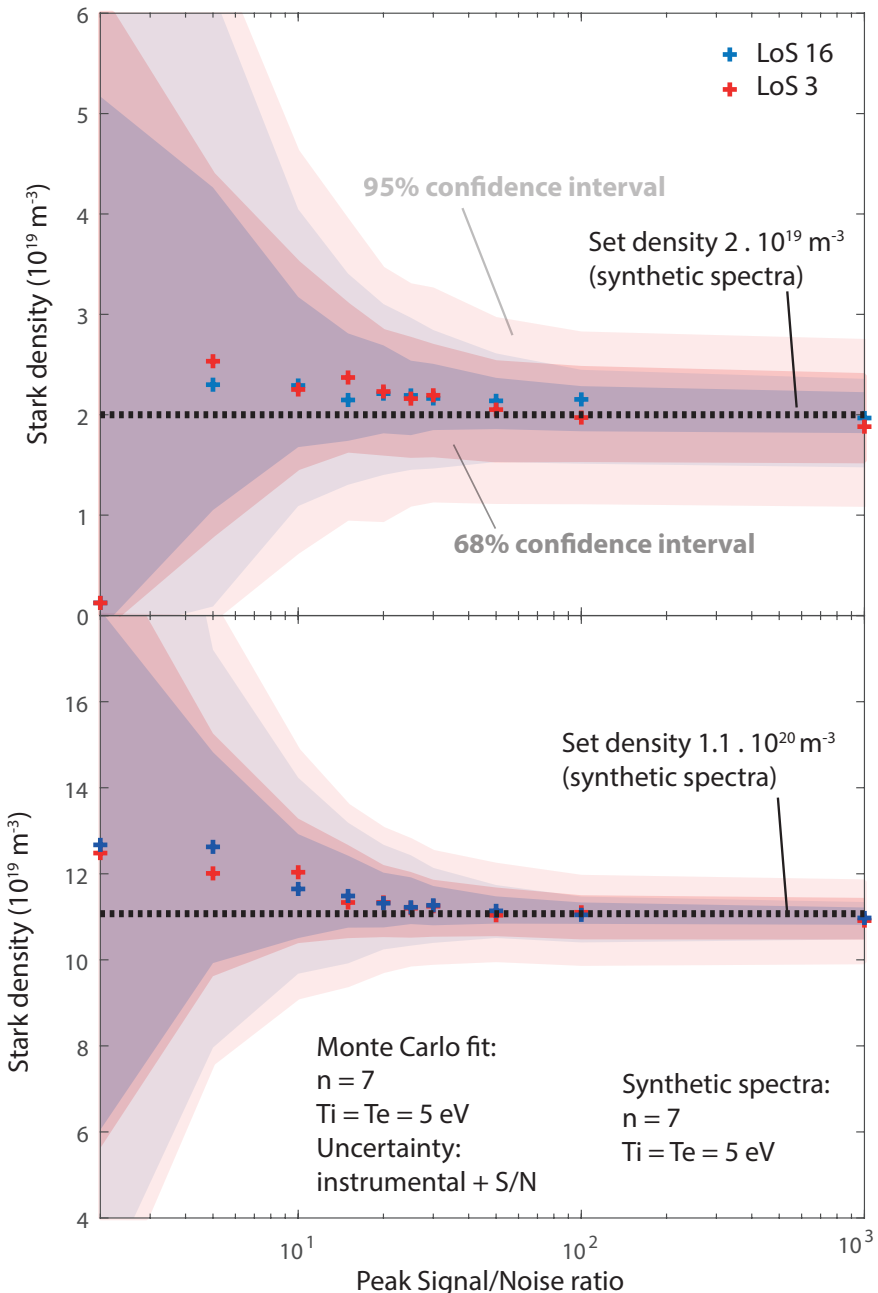


Figure 6.8: Comparison between the electron density set in the synthetic spectrum to the electron density inferred in the fit as function of S/N for two LoS at a)  $n_e = 2 \times 10^{19} \text{ m}^{-3}$  density, b)  $n_e = 1.1 \times 10^{20} \text{ m}^{-3}$  with 68 % and 95 % confidence intervals.

larger than 30 for the applicable range of electron densities and it shows that the expected uncertainty for the central line of sight is below  $1 \times 10^{19} \text{ m}^{-3}$ , while for the edge line of sight it remains within  $1 \times 10^{19} \text{ m}^{-3}$  to  $2 \times 10^{19} \text{ m}^{-3}$ . For higher densities ( $5 \times 10^{19} \text{ m}^{-3}$  and higher) a relative uncertainty below 20 % is generally noted. However, the actual uncertainties on the Stark fit are likely higher than quoted here as uncertainties in the Stark model, magnetic field, electron temperature, ion temperature are not yet accounted for. In addition, if stronger weighting is applied (for this analysis  $a = 1$  equation 6.2), a stronger sensitivity to the S/N ratio would occur.

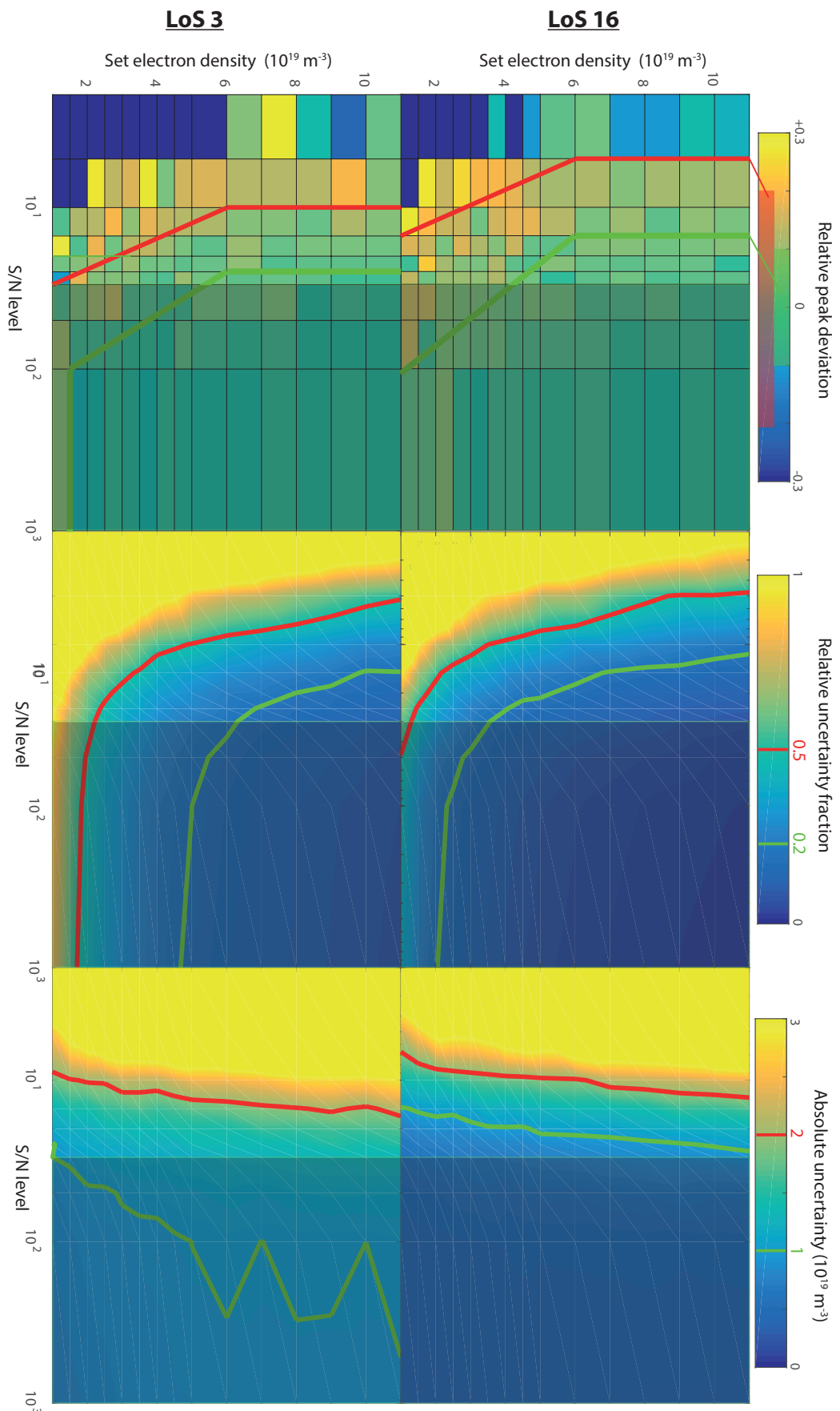


Figure 6.9: 2D Map of Stark density inferences relative, absolute uncertainties (68 % confidence interval) and deviations of Monte Carlo estimate with respect to set electron density for two lines of sight as function of set Stark density and signal-to-noise level. Several contour lines are shown as indicated in the colour maps. The S/N ratio  $> 30$  region is shaded.

#### 6.4.2 Deviations between different Stark models

Although the parametrised Stehle and Rosato model yield similar results [127], some deviations between the two can occur as shown previously. This is analysed here in detail by simulated a synthetic spectrum using the Rosato model (assuming no external magnetic field), which is subsequently fitted using the parametrised Stehle model. This choice has been made as the parametrised Stehle model is much faster than the Rosato model, which requires interpolation and file look-ups.  $T_e = T_i = 5$  eV is assumed for both the fit model and the synthetic simulated spectral line. As the influence of S/N level and the line of sight has already been investigated, this approach will only be performed for the central line of sight assuming S/N = 30.

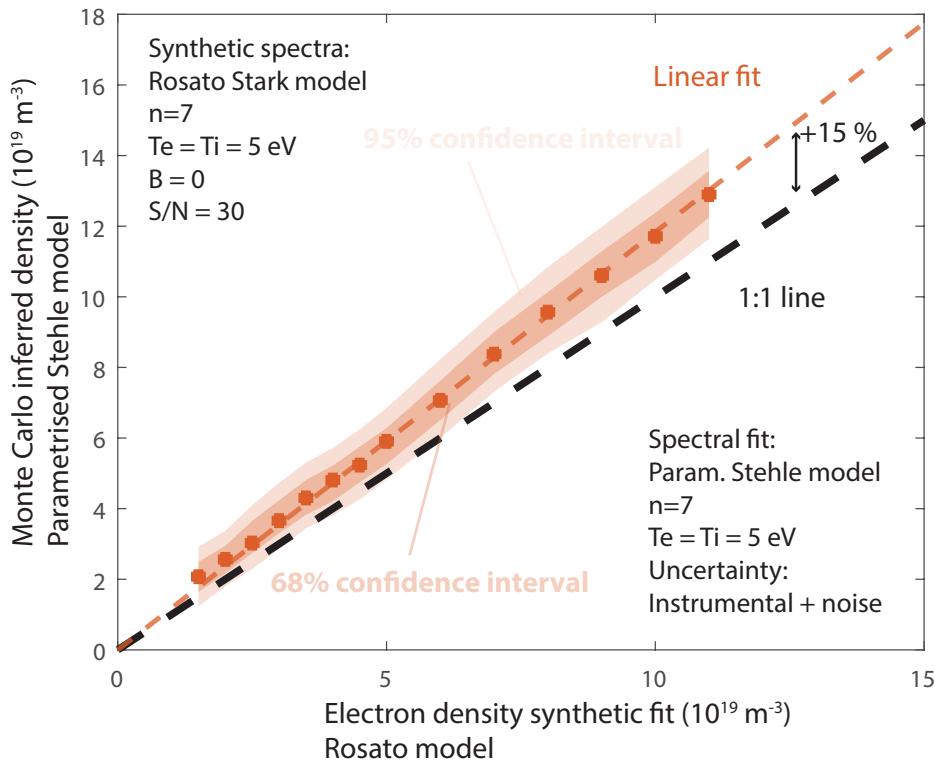


Figure 6.10: Comparison between the electron density set in the synthetic line-shape generated through the Rosato model and the inferred density from the Monte Carlo fit using the parametrised Stehle model for the  $7 \rightarrow 2$  Balmer line.

The investigation shows that the parametrised Stehle model has a slight overestimation of the electron density when compared to the prescribed electron density for the synthetic line shape using the Rosato Stark model by 15 %, as indicated by the clear linear trend between the inferred density and the prescribed density in figure 6.10. The uncertainty shown is similar to the cases studied previously (figures 6.9 and 6.8). Although Rosato's Stark model does take the various quantum mechanical processes more accurately into account; its parameters are also evaluated on a fairly coarse grid of  $n_e, T_e, B$  and thus it is unknown which of the two is closer to the actual density value. That question is beyond the scope of this work and the deviation between the two is likely more respective of the uncertainty in Stark broadening.

### 6.4.3 Uncertainties induced due to uncertainties in $T_e$ , $B$ and $T_i$ effects

The possible influences of other parameters on Stark fitting, such as the electron temperature, magnetic field and ion temperature were discussed previously briefly. Here, the influences of these parameters are discussed in a more rigorous manner by simulating synthetic line shape generated using Rosato's Stark model (which can account for  $B$ ), again with a prescribed S/N ratio (30) and while accounting for instrumental errors, with prescribed values for  $T_e$ ,  $B$  and  $T_i$ , while the basic assumed values  $T_e = T_i = 5$  eV and no external magnetic field, together with the parametrised Stehle model, were used for performing the spectral fit. All of this is based on the central line of sight and the  $n = 7$  Balmer line. These three parameters were varied individually during the investigation which indicated no different behaviour and varying the three parameters separately. Thus, the individual separation is discussed below, where the other parameters were set identically to the assumed values ( $T_e = T_i = 5$  eV and  $B = 0$  T). The results will be shown as two graphs: one graph highlighting the ratio between the result of the Stark density fit and the prescribed Stark density (e.g. 1 implies they are equal; 1.2 would imply the Stark density fit overestimates the density by 20 %); which is normalised to the default parameters ( $T_e = T_i = 5$  eV and  $B = 0$  T) in order to account for any intrinsic deviations between the parametrised Stehle and Rosato Stark model used.

#### The influence of $T_e$

We use Rosato's Stark model to generate the synthetic line shape in this case as it is more strongly influenced by  $T_e$  than the parametrised Stehle model (the influence of  $T_e$  on the inferred  $n_e$  is trivial in that case as discussed previously). The result, shown in figure 6.11, indicates that the inferred electron density, using the parametrised Stehle model with an assumed  $T_e = 5$  eV, overestimates the electron density by up to 25 % at low  $T_e < 1.5$  eV. In order to account for the default differences between Rosato's Stark model and the parametrised Stehle model, the result is normalised to the  $T_e = 5$  eV region, as  $T_e = 5$  eV is assumed in the parametrised Stehle model fitting. That overestimation of  $n_e$  is due to the fact that low  $T_e$  leads to wider Stark wings in Rosato's Stark model as shown in figure 6.3. Similarly, an underestimation by 5-10 % of the electron density can occur when the actual electron temperature is higher than 10 eV.

The overestimation of  $n_e$  by the parametrised Stehle model when using Rosato's Stark model at these low  $T_e$  may play a role during detached discharges. At this point, it is however unknown whether this stronger  $T_e$  dependence by Rosato's Stark model with respect to the parametrised Stehle model is physical or not, which requires further investigation; although it does account for the quantum mechanical processes giving rise to Stark broadening more accurately than the Stehle model. However, that discussion is outside of the scope of this thesis where we will not specifically account for a possible wider Stark wings at low  $T_e$ . That said, the uncertainty margins assumed for Stark broadening (20 % at detachment, corresponding to a 68 % confidence interval) is larger than the expected uncertainty due to the instrumental function (during detachment the S/N ratio is maximised as strong recombinative emission occurs).

As shown, the uncertainty inferred by the Monte Carlo technique is not or negligibly influenced by a mismatch between the electron temperature set and the assumed electron

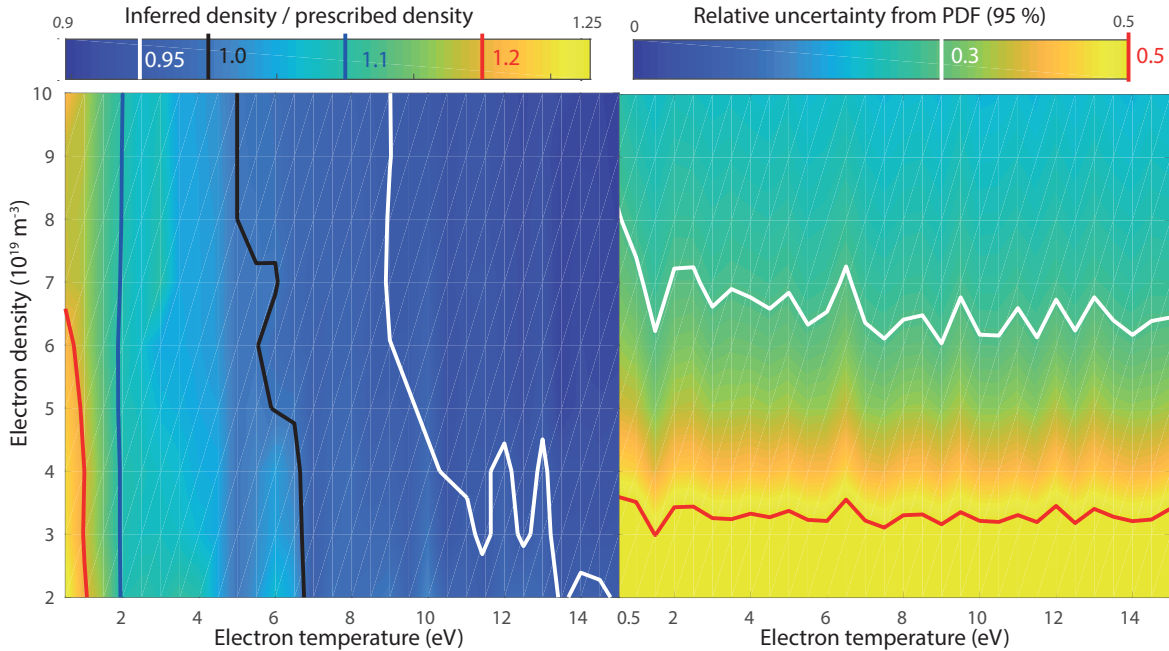


Figure 6.11: Comparison between the prescribed electron density in the synthetic line-shape generated through the Rosato model and the inferred density from the Monte Carlo fit using the parametrised Stehle model as function of  $T_e$ . Both the ratio between the inferred and prescribed Stark density (a) and the relative uncertainty (95%) obtained through the Monte Carlo method is shown (b).

temperature in the fit.

### The influence of $B$

The reason the Rosato model was used in order to investigate the influence of an external magnetic field on the Stark line shapes is that this model supports taking the magnetic field accurately into account both due to the Zeeman splitting and accounting for 'deeper' effects where the magnetic field influences the dynamics leading to Stark broadening itself. The shown result (figure 6.12) is normalised with respect to the case closest to the model assumption, namely  $B = 0$  T and indicates a mostly negligible influence of an external magnetic field on the Stark density inference: adding an external magnetic field may lead to an overestimation by the Stark density at high magnetic fields (higher than 1.5 T) of 5-7 % for moderately high Stark densities ( $5 \times 10^{19} \text{ m}^{-3}$  or higher). For such relatively high magnetic fields, an overestimation of 7-10 % is expected for lower electron densities in the range  $3 \times 10^{19} \text{ m}^{-3}$  to  $5 \times 10^{19} \text{ m}^{-3}$ , while an overestimation of 10-20 % is expected at lower electron densities. As shown, the uncertainty inferred by the Monte Carlo technique is not or negligibly influenced by a mismatch between the magnetic field set and no magnetic field assumption in the fit.

### The influence of $T_i$

The result (figure 6.13 indicates that small deviations due to the set  $T_i$  can arise at fairly low densities of up to  $5 \times 10^{19} \text{ m}^{-3}$ . This sensitivity also depends on the weighting function employed to provide emphasis on the Stark wings (section 6.3). For this investigation, equation 6.2 was used as a fit function with  $a = 1$ , while  $a > 1$  would lead to a stronger insensitivity

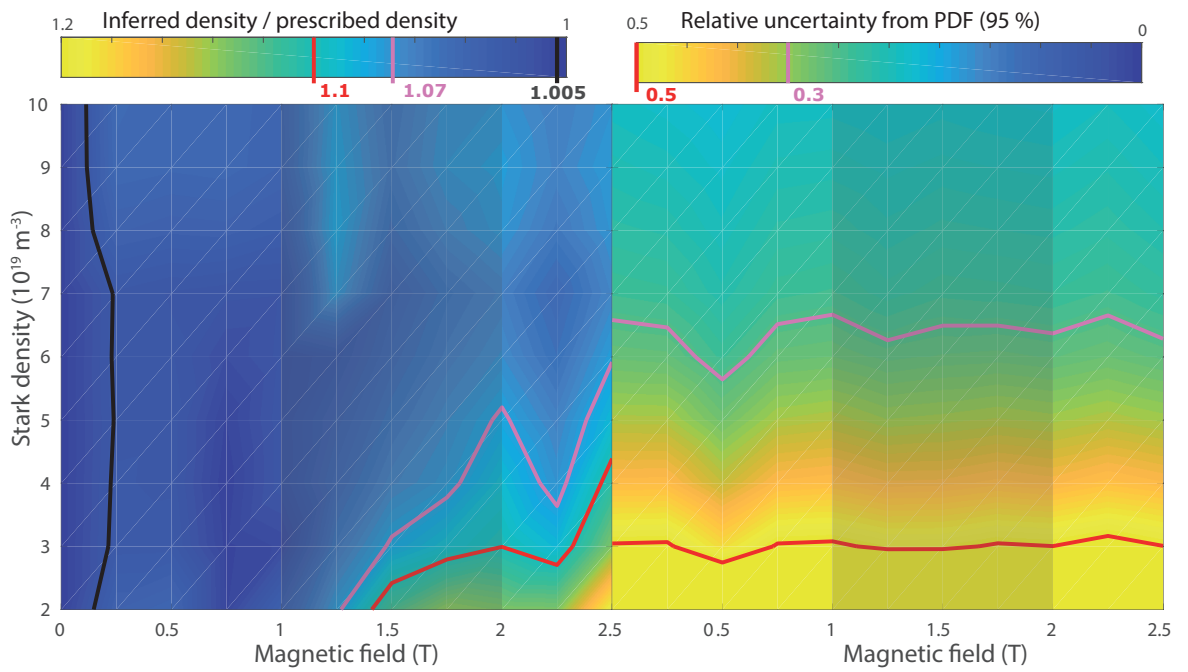


Figure 6.12: Comparison between the prescribed electron density in the synthetic line-shape generated through the Rosato model and the inferred density from the Monte Carlo fit using the parametrised Stehle model as function of  $B$ . Both the ratio between the inferred and prescribed Stark density (a) and the relative uncertainty (95%) obtained through the Monte Carlo method is shown (b). The TCV range of applicable magnetic fields is shielded.

of the Stark fit to  $T_i$ , but would require a larger S/N than 30 (likely  $\sim 100$ ). At lower ion temperatures than the 5 eV assumed in the fit model, an underestimation of the inferred electron density can occur between 5-10 % of electron densities up to  $4 \times 10^{19} \text{ m}^{-3}$ . An overestimation of the inferred electron density can occur at higher ion temperatures than the 5 eV assumed of 10-15 % for fairly low densities up to  $5 \times 10^{19} \text{ m}^{-3}$ . As shown, the uncertainty inferred by the Monte Carlo technique is not or negligibly influenced by a mismatch between the ion temperature set and the ion temperature assumption of 5 eV in the fit model.

#### 6.4.4 Putting it all together: general uncertainty

Performing a Monte-Carlo uncertainty analysis for every single spectral fit would be too time-consuming and thus instead we prescribe an uncertainty and applicability range of the default Stark fit on TCV based on the sensitivity studies above. To repeat, the default TCV Stark analysis assumes  $T_e = T_i = 5 \text{ eV}$ ,  $B = 0 \text{ T}$ , while dynamically averaging the spectra to obtain a S/N of 30 or higher (or 10 if 30 is not feasible). Based on the work in this section, we estimate the PDF of the fitted electron density with a Gaussian, peaked at the value of the fit while its 68 % confidence interval corresponds to  $1 \times 10^{19} \text{ m}^{-3}$  or 20 % of the Stark density (whichever is larger). This analysis is applicable at electron densities of  $2 \times 10^{19} \text{ m}^{-3}$  or higher. Based on the sensitivity study, the various assumption made by the simplified Stark model fit (such as no external magnetic field, electron/ion temperature of 5 eV) have an impact on the inferred result smaller than or at most the characteristic uncertainty. At lower electron densities the inferred density may have an offset with respect to the actual electron densities, unless the analysis is performed at higher signal-to-noise levels than 30.

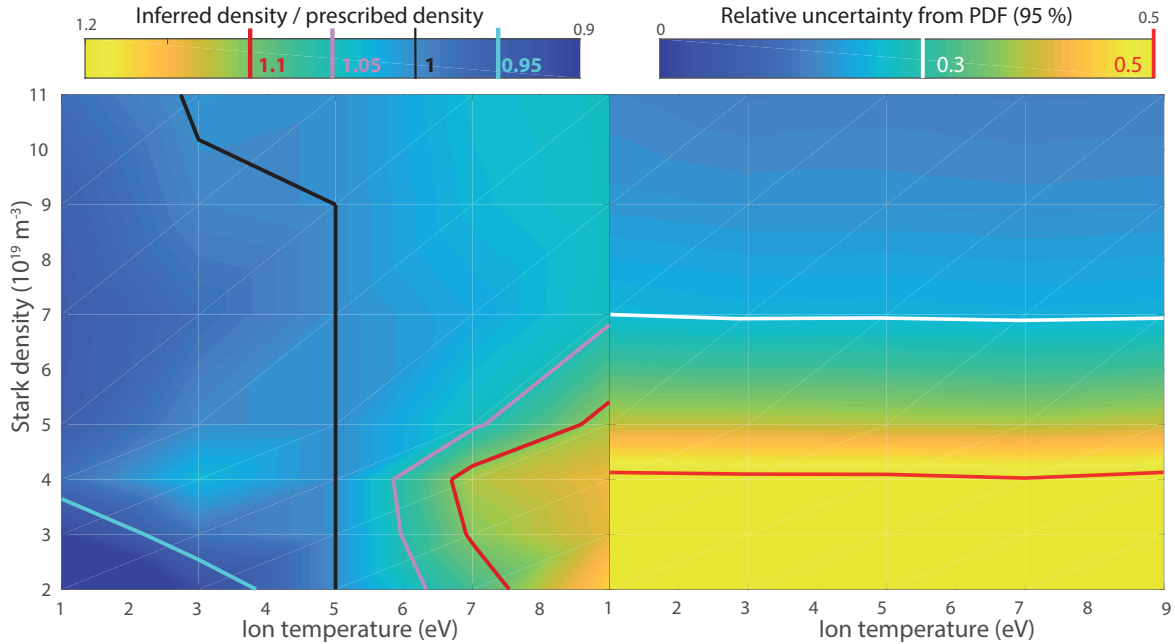


Figure 6.13: Comparison between the prescribed electron density in the synthetic line-shape generated through the Rosato model and the inferred density from the Monte Carlo fit using the parametrised Stehle model as function of  $T_i$ . Both the ratio between the inferred and prescribed Stark density (a) and the relative uncertainty (95%) obtained through the Monte Carlo method is shown (b).

There is, however, also a more formal/rigorous (although more time-consuming) way to obtain a PDF for the spectral Stark fit using Monte-Carlo techniques. For this, we fit an experimental spectrum using the Rosato Stark model in a Monte Carlo fashion where PDFs of  $T_i, T_e, B, \theta$  are assumed, together with a series of simulated instrumentals (section 5.6). This has been applied for discharge # 57912, which represents a density ramp detachment discharge, where the plasma shape has been optimised to facilitate an improved strike point coverage by the DSS. For the various ranges, a uniform distribution for  $B$  and  $\theta$  are assumed between 1-2 T and 80 – 100 deg respectively. Using the analysis techniques highlighted in chapter 7, a probability density function for the electron temperature corresponding to the excitation and recombinative emissions is eventually obtained, together with the fraction of  $n = 7$  Balmer line emission due to recombination. Using this fraction, an estimated effective weighted temperature is obtained by combining the recombinative and excitation temperatures. It should be noted, however, that a change in the inferred electron density would change these estimated temperatures. Therefore, this approach is merely indicative and not strictly self-consistent. The ion (e.g. neutral) temperature is randomly chosen to be any value between 0 eV and 150 % of the effective weighted electron temperature; as it is expected more likely that the neutral temperature is generally lower than the electron temperature —in agreement with SOLPS simulations.

We apply such an investigation here, where we first show two examples of the resulting PDF from this analysis. In figure 6.14 for a single time step and a single line of sight, compared to the PDF expected from the default analysis (parametrised Stehle model with an assumed uncertainty) and compared to the default Rosato Stark analysis (e.g. single fit assuming  $T_i = T_e = 5 \text{ eV}$ ,  $B = 0$ , with an assumed uncertainty as in the parametrised fit model).

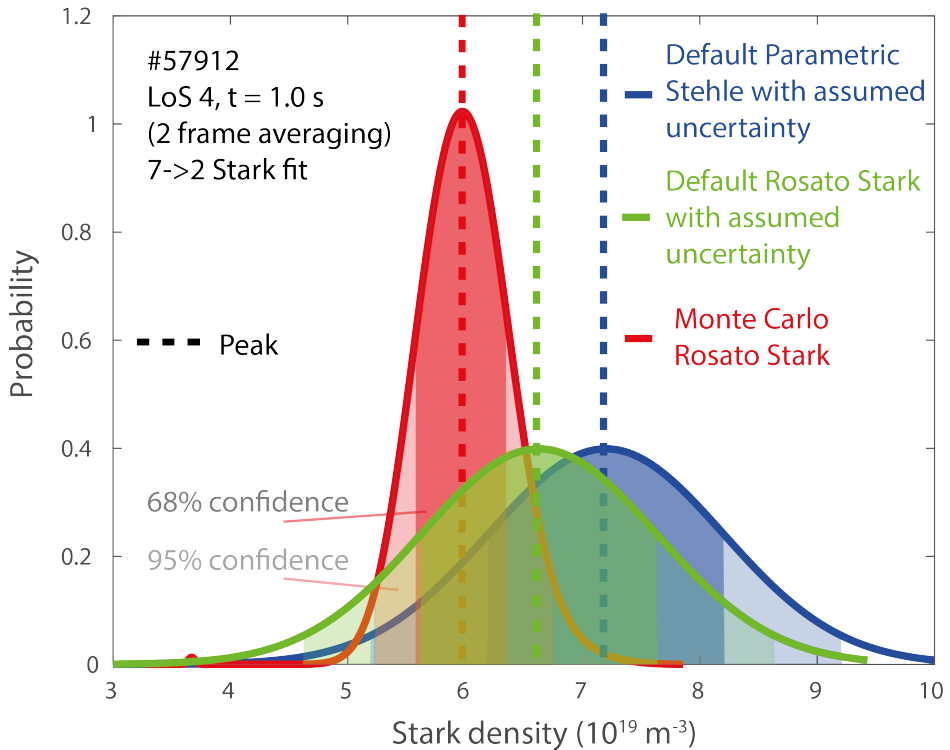


Figure 6.14: Comparison between the probability density functions obtained for a single LoS (4) at a single time step (1.0 s) using the full Monte Carlo Stark investigation explained above and the fast 'default' fit using the parametrised Stehle model together with its assumed uncertainty and probability density shape (Gaussian).

Although, there is a significant deviation between the result from the default (parametrised Stehle) fit and the Monte Carlo fit by roughly  $1.2 \times 10^{19} \text{ m}^{-3}$ ; there is still an overlap between the two PDFs, partially due to the large assumed uncertainty of the default fit. The deviation between the two functions is partially explained by differences between Rosato's Stark model and the parametrised Stehle model, but some deviation still occurs when the Rosato Stark model is used with fixed default parameters and an added assumed uncertainty. The PDF obtained from the Monte Carlo fit is clearly unimodal and is narrower by roughly a factor two, indicating that the detailed uncertainty calculation provides a factor two smaller uncertainty than the assumed uncertainty. However, this does not account for uncertainties in the Stark broadening theories and as such the uncertainty estimates are and should be larger than the Monte Carlo determined uncertainty.

After having compared the PDFs, we will compare the evolution of the electron density (and uncertainty) as function of time given by the Monte Carlo analysis and by the faster default Stark fits (both the parametrised Stehle and Rosato varieties (latter one only for LoS 1-3)). The data shown corresponds to a density ramp which will be discussed further in section 8.1.2 and the geometry and lines of sight are shown in figure 8.2 b. The trends of both the default Stark analysis and Monte Carlo analysis are similar and their main difference is that the 'full' Stark analysis, based on Rosato's Stark model, results in lower electron densities by up to  $\sim 20\%$  as already identified in figure 6.14. Again, that difference is partially due to the difference between the two Stark models, but mostly due to the mismatch in the assumed  $T_e$  and the actual  $T_e$ . As such, this difference is also largest for the LoS closest to the target

(e.g. lowest  $T_e$  conditions ( $T_e < 1$  eV)). The observed roll-over in electron density is therefore also slightly stronger in the 'full' Stark investigation (22 % drop vs 18 % drop), but this can also be explained by measurement noise. As fairly high uncertainties for the default analysis are assumed, which include these lower  $n_e$  values, the overestimation of  $n_e$  by 20 % likely does not have a strong influence on the 'deeper' analysis results which use Stark broadening as an input. Furthermore, the Rosato Stark result leads to a more erratic / noisier trend than the parametrised Stehle model, which may have to do with the technical implementation of the Rosato Stark model for TCV fitting, which depends on interpolating over a coarse  $n_e, T_e$  grid.

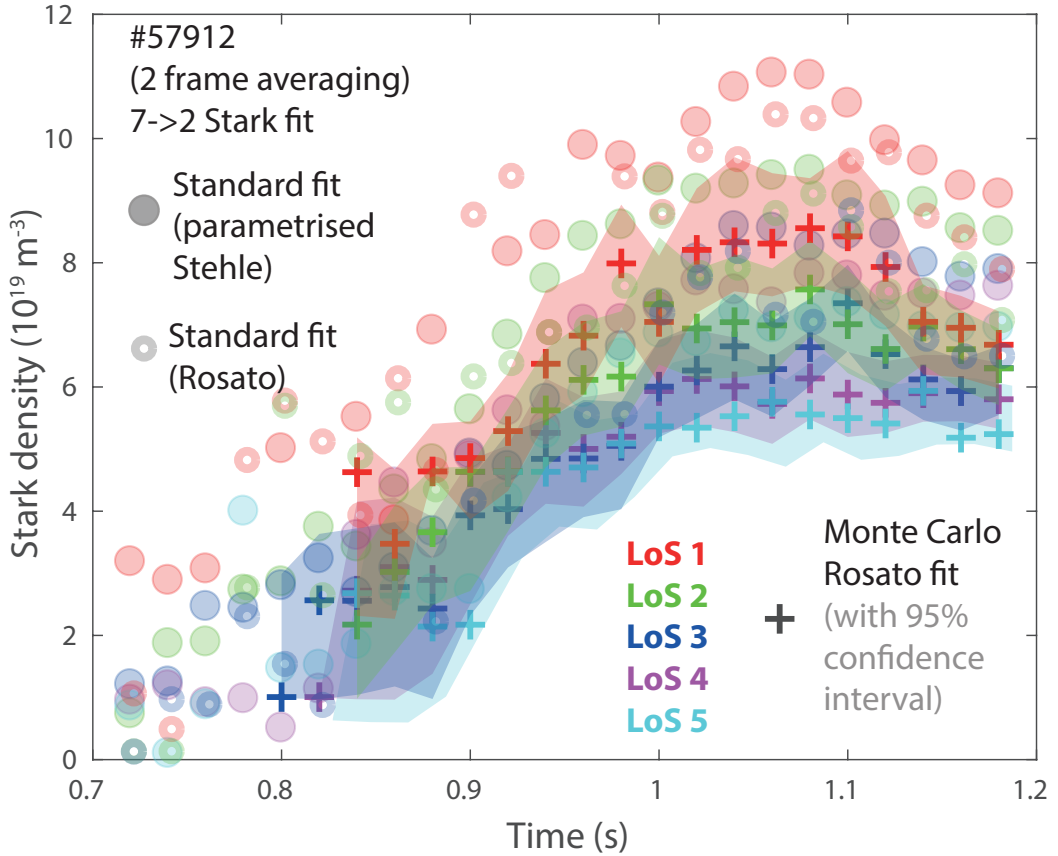


Figure 6.15: Evolution of inferred Stark density for the first five lines of sight as function of time for discharge # 57912 using the default fit analysis and a Monte Carlo fit analysis. The inferred 95 % uncertainty margins based on the Monte Carlo fit analysis is added.

## 6.5 Stark broadening and line integration effects

Spectroscopic measurements are chordal measurements where a chordal integral is performed through a plasma with varying local parameters —including the electron density. This has a certain influence on the inferred electron density and the meaning of that electron density, which is further investigated here using both a simplified analysis where a priori profiles of plasma parameters are assumed and using a synthetic diagnostic approach, which is employed to SOLPS simulations.

A preliminary investigation was performed by the author in [1] where a large range of a priori  $n_e$ ,  $T_e$  and neutral density profiles were assumed along the line of sight. At each point of the profile, the Balmer line intensity was calculated and the Stark line shape was

determined. Summing over all Stark line shapes leads to a synthetic spectrum, which is fitted using the same techniques as with which the experimental data is fitted. The obtained  $n_e$  Stark from the synthetic fit was generally 50-80% of the peak Stark density and, perhaps more importantly, corresponds well to the emission weighted electron density. That means that the Stark inferred electron density is in fact a 'characteristic' electron density of the region where most of the emission of the particular line analysed occurs. In addition, for cases where the emission profile was flat (e.g. all densities in the density profile contribute equally to the synthetic spectral line's shape), the obtained synthetic spectral line shape could not be fitted well leading to large residuals because it did no longer resemble a modified Lorentzian: the sum of a large range of modified Lorentzian deviates from the modified Lorentzian line shape. In other words, the fitting procedure will only produce an acceptable fit if the fit model has is in reasonable agreement with the experiment: meaning that most of the emission should come from a single (or narrow) electron density region. That behaviour (e.g. clear deviation from a modified-Lorentzian like Stark line shape) is not observed in the experiment.

These preliminary findings are in good agreement to a more detailed investigation which is based on determining a synthetic Stark line shape based on SOLPS simulations while accounting for the DSS geometry and the local electron temperatures/electron densities/ion temperatures/magnetic field along the DSS chordal integrals. That comparison will be shown (together with other inferred parameters from the Balmer line spectra) in section 7.7 and 8.1.1, while the synthetic diagnostic implementation is discussed in 5.8 and 4.3. The synthetic spectra could be well fitted (e.g. resulting in small residuals) and the inferred density corresponds well to the averaged electron density along the line of sight weighted by the emissivity profile of a certain Balmer line. More specifically, the synthetic diagnostic approach has shown that indeed most of the emission comes from a fairly narrow region in electron density as will be shown in section 7.7. Furthermore, this shows that the ion temperature and electron temperature are not significantly deviating the Balmer line shape from the Balmer fit model in the realistic conditions of a TCV core density ramp experiment where fairly high values for the electron density in the divertor (e.g.  $\geq 5 \times 10^{19} \text{ m}^{-3}$ ) are achieved during detached conditions. As a caveat, it should be mentioned that this investigation was performed using the parametrised Stehle Stark model, which has a lower sensitivity to  $T_e$  and does not account for the influence of  $B$ . As different Balmer lines are expected to radiate at different locations due to their different sensitivities to recombinative and excitation emission (as explained chapter 7); that means that (small) deviations between the electron density inferred between the Balmer lines can exist, where higher-n Balmer lines will lead to lower electron densities as higher-n Balmer lines; assuming that the recombinative emission corresponds from lower temperature regions where the electron density is lower. This is indeed observed in the simulations and is in agreement with the experiment —as shown in section 6.6 (although the deviations between the different Balmer lines are small and could also be described by the uncertainty).

## 6.6 TCV Stark broadening results and verifications

A general result of Stark broadening is shown in figure 8.2 a where the evolution of the electron density from the seven horizontal DSS viewing chords closest to the target (figure 8.2 b), throughout a density ramp discharge where the core electron density is continuously

increased is shown. The inferred electron density from Stark broadening near the target is in agreement with the maximum measured density measured by Langmuir probes at the target. This agreement occurs until  $\sim 0.87$  s, which coincides with the time detachment starts to occur. During detachment, the measured Stark density for the viewing chord nearest to the target continues to rise while the density measured by Langmuir probes at the target starts to drop. This is a general TCV observation and has been shown previously by the author in [1] on a different discharge. There is a concern that the Langmuir probe measurement of the target density are incorrectly low as the Langmuir probe density estimates use the Langmuir probe temperature estimate—which is overestimated in detached conditions [118, 119, 117]. As such, following a similar approach as in [1], we calculated a modified  $n_e^{LP,mod} = n_e^{LP} \sqrt{\frac{T_e^E}{T_e^{LP}}}$  using a spectroscopically inferred temperature ( $T_e^E$  (section 7.3.1)) from the excitation emission of the chord closest to the target. The target density remains significantly smaller than the observed Stark density upon detachment, even with this correction. Some combination of the width of the poloidal viewing chord (1-2 cm) and the weighting of the Stark density towards the higher densities (and thus higher emissivities) along the cone describing the target line of sight is likely driving this difference. Hence, the electron density profile must decay in a narrow region ( $< 2$  cm) close to the target. Alternatively, the electron density in the detached case may be overestimated by Stark broadening, although this effect should be much smaller (based on the sensitivity studies presented, at most  $1.5 \times 10^{19} \text{ m}^{-3}$ ) than the mismatch between the Stark inferred density and Langmuir probe inferred density during detached conditions. A more detailed discussion of these results will take place in section 8.1.2.

Apart from Langmuir probe results being in agreement with the DSS inferred Stark densities, one can also compare results from SOLPS simulations to the DSS inferred Stark densities. An adequate agreement between the Stark density obtained through a synthetic diagnostic and the values obtained experimentally is obtained in section 8.1.1.

### 6.6.1 Comparison of Stark inferred density with respect to different Balmer lines

Comparing Stark density inferences between different Balmer lines is an important cross-check for the validity of the results as the relative scaling between the Stark width and other broadening mechanisms (such as Doppler broadening) is different between the different Balmer lines. Thus, if an agreement within uncertainty of the inferred Stark density between the various Stark densities is obtained, this indicates that the Balmer lines are not significantly influenced (e.g. less than the characteristic uncertainty) by non-accounted broadening effects. This is a particular important check against the possible influence of a non-Gaussian ion velocity distribution on the Stark line shapes as those may result in pronounced wings which are interpreted by the fitting model as Stark broadening and thus enhances the inferred electron density.

This verification has been shown in figure 6.16 for the inferred Stark density of the  $n = 6, 7, 9, 10, 11, 12, 13$  Balmer lines. During the discharge shown, the core electron density was continuously increased while the power entering the divertor is kept approximately constant, driving the divertor into detachment after roughly 1.0 s and giving rise to recombinative emission, leading to the appearance of high- $n$  Balmer lines ( $n \geq 9$ ), which is further explained in chapter 7. To obtain the required spectral coverage with the highest spectral resolution

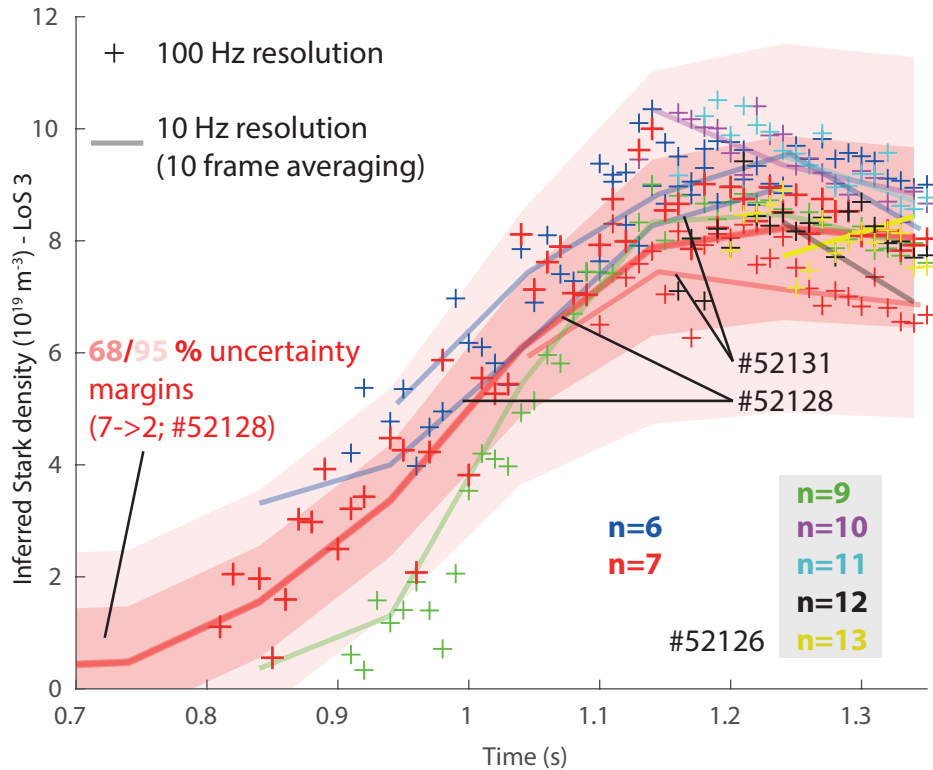


Figure 6.16: Stark density as function of time observed for repeat discharges numbers 52126, 52128 and 52131 while using various time windows

grating for both the  $n = 6, 7$  Balmer lines and the high- $n$  Balmer lines  $n \geq 9$ , repeat discharges where necessary. The reproducibility of these discharges has been found to be adequate using various diagnostic as was discussed in section 4.4. Two repeat discharges were performed with the high resolution grating aimed at the  $n = 6, 7$  Balmer lines while different gains on the camera were used in order to aid the dynamic range as the deviation in the Balmer line signal during a density ramp between attached and detached conditions can be over a factor 50 on TCV as has been shown by the author in [1]. The electron densities shown have been inferred using the default fitting analysis. This investigation has been shown for LoS 3 close to the target, although similar trends are observed for the other lines of sight.

The density inferred from the various Balmer lines are in agreement with each other within the default assumed 68 % uncertainty margin (20 % of the inference or  $1 \times 10^{19} \text{ m}^{-3}$ —whichever is larger). Furthermore, the deviation between the various Balmer lines is similar to the deviation between the inferred density from the  $n = 7$  Balmer line in high and low gain conditions. This thus indicates that likely other line broadening mechanisms (such as Zeeman splitting and Doppler broadening) are either well predicted by the assumed fit model or have a small influence. It should however be noted that the cross-validation has mainly been investigated at fairly high densities ( $\sim 8 \times 10^{19} \text{ m}^{-3}$ ) as at these the high- $n$  Balmer lines become measurable. In addition to that, other Balmer lines have different electron temperature dependencies in their line shapes. That means that if the observed electron density is consistent between the various Balmer lines, the Stark line shapes are here likely not strongly influenced by the mismatch between the assumed electron temperature (5 eV) and the actual electron temperature. A larger deviation occurs between the electron densities inferred from the  $n = 7$  and the  $n = 10, 11$  Balmer lines as the Balmer line fit for the  $n = 10, 11$

transitions is influenced by a neighbouring impurity line —which is not accounted for in the fit algorithm.

Another point where the deviation between the inferred electron densities through the  $n = 7$  and  $n = 9$  Balmer line are fairly large is around 0.9 s where recombinative emission just starts to appear, while the deviation diminishes as the core density is further increased, reaching diminishable levels at 1.05 s; likely a line-integration effect. As will be discussed later in chapter 7, the measured  $n = 7$  emission is often a mix between emission arising from excitation and emission arising from recombination (especially during the onset of detachment). On the other hand, the emission arising from the  $n = 9$  transition is purely recombinative, which —as explained previously in section 6.5 —can lead to this discrepancy. Consistent with this explanation is that 50 % of the  $n = 7$  Balmer line emission is recombinative at 0.9 s, increasing to 100 % at 1.05 s (these fractions are inferred quantitatively from Balmer line ratios —chapter 7).

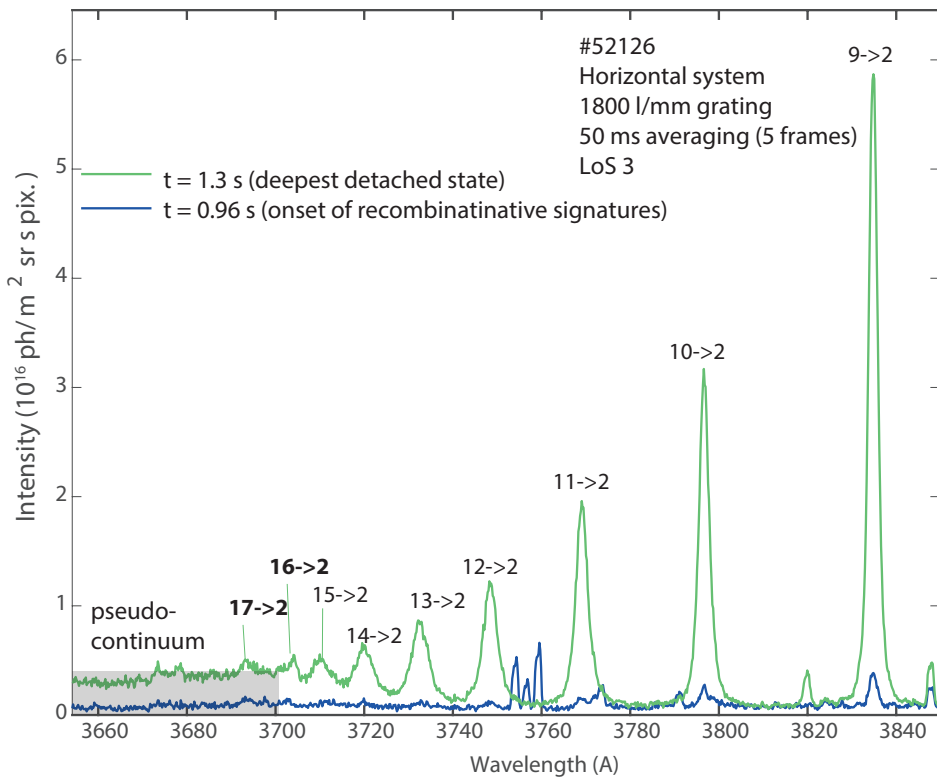


Figure 6.17: Spectra of high- $n$  lines during a detached discharge (#52126) observed with the horizontal system from the line of sight closest to the target indicating the formation of the recombinative pseudo-continuum after the  $n = 17$  Balmer line which is still observed.

The wavelength distance between Balmer lines decreases with  $n$  while the Stark width of each Balmer line increases with  $n$  —giving rise to a merging of the high- $n$  Balmer lines at some point forming a pseudo-continuum —which occurs for the hydrogen Balmer lines at some wavelength above 365 nm [125] and is density dependent as higher densities will lead to stronger Stark broadening and an earlier merging of the Balmer lines. In other words, the highest  $n$  observable Balmer line provides a rough indication of the expected electron density —referred to as the Inglis-Teller limit [137, 207]. This merging of the Balmer lines is shown for a TCV spectra in figure 6.17 at the latest phase of discharge 52126 and the highest- $n$  Balmer line observed is the  $n = 17$  transition. Using the classical equation of

the Inglis-Teller limit (which assumes a simplified Stark model) from [137], corresponds to an electron density of  $8 \times 10^{19} \text{ m}^{-3}$  with an uncertainty of  $5.0 \times 10^{19} \text{ m}^{-3}$  to  $1.2 \times 10^{20} \text{ m}^{-3}$  (when taking the neighbouring  $n = 16, 18$  transitions as the uncertainty range. These values are in good agreement with the electron density obtained at this point, which has been found to be  $8 \times 10^{19} \text{ m}^{-3}$  as shown in figure 6.16, again showing consistency of the Stark broadening results.

## 6.7 Summary and applicability of Stark broadening on TCV

Inferring a characteristic electron density of the emission corresponding to a Balmer line is routinely performed using Stark broadening on higher density tokamaks, such as C-Mod, JET and AUG and techniques have been developed to perform this analysis routinely for TCV, which operates at relatively lower densities giving rise to a whole range of challenges and important effects, which have been analysed in detail. These techniques include a highly accurate accounting for the instrumental function and its uncertainty, employing weighting functions to emphasize the Stark wings, and including dynamic averaging of the Stark broadened spectra to enhance the signal-to-noise ratio.

Sensitivity studies have shown that Stark broadening on TCV can be applied quantitatively starting from an electron density of  $2 \times 10^{19} \text{ m}^{-3}$  or higher, while it can be applied non-quantitatively between  $8 \times 10^{18} \text{ m}^{-3}$  to  $2 \times 10^{19} \text{ m}^{-3}$ . A characteristic uncertainty (68% confidence interval) of 20 % or  $1 \times 10^{19} \text{ m}^{-3}$  (whichever is higher) is found to roughly accommodate the various sensitivity studies performed.

The Stark density analysis has been verified and validated by cross-comparisons between different diagnostics, comparisons to modelling and by comparing Stark density results obtained for different spectral lines.

## Chapter 7

# Quantitative analysis of Balmer line spectra

*Inferring quantitative information from the Balmer line spectra in detachment-relevant regimes is challenging as both recombination and excitation can contribute to the Balmer line's emission and, as such, this analysis in literature is generally not performed or only the recombinative emission is analysed. In this work novel techniques for analysing Balmer line emission are developed, which quantitatively split the Balmer line's emission into recombination/excitation fractions using Balmer line ratios; enabling the analysis of ionisation/recombination rates; hydrogenic radiation; charge exchange to ionisation ratios and characteristic recombination/excitation temperatures. All of this is performed using a probabilistic approach in order to accurately account for measurement uncertainties.*

First, a brief introduction of the analysis strategy and the model used for modelling the Balmer line intensities is introduced (section 7.1) together with a description of the input parameters and their assumed uncertainties (section 7.1.2). Afterwards, each step of the analysis chain is treated in more detail in the subsequent chapters (sections 7.2, 7.3 and 7.4). One key challenge of the analysis is that certain required input parameters (for instance the neutral fraction) are generally only known within a large range, spanning multiple orders of magnitude; implying that a 'standard' Taylor-expansion based error analysis is not applicable and therefore a Monte-Carlo based probabilistic analysis has been developed to provide the range of named inferences and uncertainties from the Balmer lines (section 7.6). The assumptions made in the analysis and their robustness are verified in a statistical investigation, including an investigation into the sensitivity of the analysis on uncertainties in ADAS rates, in the appendix B. To verify and test many of these assumptions, a collection of SOLPS simulation results (representative of an electron density ramp) are used, and the results obtained directly from SOLPS and from a synthetic diagnostic analysis are compared (section 7.7).

Parts of this chapter have been adopted from: *An improved understanding of the roles of atomic processes and power balance in target ion current loss during detachment*, by K. Verhaegh, B. Lipschultz, B.P. Duval, et al., to be submitted. DOI:  
<https://doi.org/10.13140/RG.2.2.24292.48005/1>

## 7.1 Introduction of Balmer line analysis

To analyse Balmer line spectra, first a model for the Balmer line intensity has to be established. The divertor spectrometer measures the emitted spectra integrated along a line of sight through the plasma with a local emissivity map (depending on local plasma parameters -  $\text{ph m}^{-3} \text{s}^{-1}$ ), yielding a brightness in terms of  $\text{ph m}^{-2} \text{s}^{-1}$ . The brightness of the observed Balmer line ( $B_{n \rightarrow 2}$ ) models this situation as a line of sight intersecting a 0D plasma slab with spatially constant electron density ( $n_e$ ); electron temperature ( $T_e$ ); hydrogen ion density ( $n_H^+$ ); hydrogen neutral density ( $n_H^0$ ) along a path length  $\Delta L$ . For simplicity, it is assumed that  $n_H^+ = n_e$ , which follows from assuming the plasma is a pure hydrogen plasma ( $Z_{\text{eff}} = 1$ ) and invoking quasi-neutrality. *Following this assumption, we will refer to the hydrogen neutral density as  $n_0$  from this point onwards.* Furthermore, we assume that molecular reactions are not influencing the Balmer line spectra, which is valid for  $n > 4$  Balmer lines [5, 6, 108, 106, 112]. Under those assumptions, the hydrogen Balmer line emission can be modelled through equation 7.1, which has a recombination ( $B_{n \rightarrow 2}^{\text{rec}}$ ) and excitation ( $B_{n \rightarrow 2}^{\text{exc}}$ ) component, where the PEC coefficients are from ADAS [134, 135, 140] as explained in section 2.4. This line emission model forms the backbone of the entire analysis chain and the various assumptions made for this line emission model will be discussed in the various sections and in an integrated way by analysing the SOLPS synthetic spectra in section 7.7.

$$B_{n \rightarrow 2} = \underbrace{\Delta L n_e^2 \text{PEC}_{n \rightarrow 2}^{\text{rec}}(n_e, T_e)}_{B_{n \rightarrow 2}^{\text{rec}}} + \underbrace{\Delta L n_o n_e \text{PEC}_{n \rightarrow 2}^{\text{exc}}(n_e, T_e)}_{B_{n \rightarrow 2}^{\text{exc}}} \quad (7.1)$$

The first step of the Balmer line analysis is to separate  $B_{n \rightarrow 2}^{\text{rec}}$  and  $B_{n \rightarrow 2}^{\text{exc}}$  from the measured Balmer line intensity. This is done by inferring the fraction of emission due to recombination ( $F_{\text{rec}}(n)$ ) and excitation ( $F_{\text{exc}}(n)$ ) (defined in equation 7.2) quantitatively (section 7.2) using a Balmer line ratio, a density estimate (from Stark broadening —chapter 6) and a neutral fraction  $n_o/n_e$  estimate (obtained from modelling —section 7.1.2); which are applied to  $B_{n \rightarrow 2}$ .  $B_{n \rightarrow 2}^{\text{rec}}$  and  $B_{n \rightarrow 2}^{\text{exc}}$  are then used to estimate the line integrated recombination and ionisation rates (section 7.3); their respective temperatures (section 7.3.1); line integrated hydrogenic radiative power loss (section 7.4) and hydrogen charge exchange to ionisation ratios (section 7.5).

$$\begin{aligned} F_{\text{rec}}(n) &= \frac{B_{n \rightarrow 2}^{\text{rec}}}{B_{n \rightarrow 2}} \\ F_{\text{exc}}(n) &= \frac{B_{n \rightarrow 2}^{\text{exc}}}{B_{n \rightarrow 2}} = 1 - F_{\text{rec}}(n) \end{aligned} \quad (7.2)$$

### 7.1.1 Output parameters of the analysis chain

The different output parameters can be classified in two different types: chordal integrated parameters: recombination rate  $R_L$  (in  $\text{rec./m}^2 \text{s}$ ); ionisation rate  $I_L$  (in  $\text{ion./m}^2 \text{s}$ ); charge exchange rate  $CX_L$  (in  $\text{reac./m}^2 \text{s}$ ) and hydrogenic radiation rates (excitation ( $P_{\text{rad},L}^{H,\text{exc}}$ ) and recombination ( $P_{\text{rad},L}^{H,\text{rec}}$ ) in  $\text{W/m}^2$ ) —which aim to estimate the integral of a reaction rate along the line of sight; and local parameters ( $n_e$  through Stark broadening —chapter 6 and the characteristic temperatures —section 7.3.1). These parameters are discussed in summarised in table 7.1, where it is also mentioned whether the output parameter originates from the

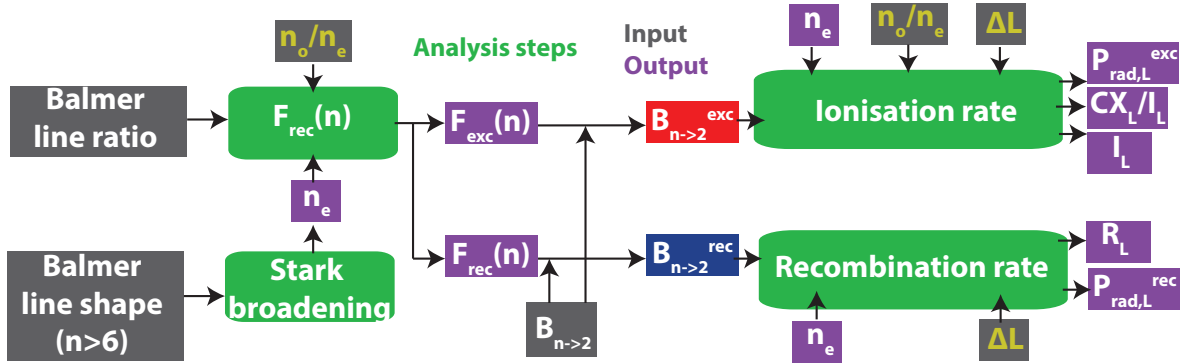


Figure 7.1: Schematic overview of the analysis steps (green) in the Balmer line analysis chain together with the required measured inputs (grey, white text —including the Balmer line brightness  $B_{n \rightarrow 2}$ ), assumed inputs (grey, yellow text —including the neutral fraction  $n_o/n_e$ , the path length  $\Delta L$ ) and inferred outputs (purple —including the Stark density  $n_e$ ; inferred recombination/excitation Balmer line emission fraction  $F_{rec}(n)$ ,  $F_{exc}(n)$ ; line integrated hydrogenic excitation/recombination radiated power loss  $P_{rad,L}^{exc}$ ,  $P_{rad,L}^{rec}$ ; line integrated ionisation/recombination rate  $I_L$ ,  $R_L$  and line averaged charge exchange to ionisation ratio  $CX_L/I_L$ ).

analysis of the excitation or recombination emission, as indicated in figure 7.1. An analysis on how these analysis inferences relate to the actual parameters of the plasma is shown in section 7.7. The conclusion of that investigation is that the integrated parameters agree within uncertainty with the actual integrated values along the chord: thus such integrated values can be obtained through passive line of sight spectroscopy and does not require 2D techniques. Passive techniques cannot however provide information on local parameters *at a specific location* of the plasma; instead a fair agreement was found between the inferred local parameters and the line averaged parameter weighted by the respective emissivity profile. That means, for instance, that a temperature derived from recombinative emission would be different from a temperature derived from excitation emission as the recombinative emission would occur at a different location along the line of sight 7.3.1.

As discussed in chapter 5, the TCV divertor spectrometer has a good coverage of the outer divertor leg for most conventional TCV divertor geometries. As such, a profile of the various inferences are obtained along the entire outer divertor leg. By integrating the profiles of line integrated estimates along the outer divertor leg ( $R_L$ ,  $I_L$ , etc.) toroidally and poloidally, the total values corresponding to the outer divertor leg of the ionisation source  $I_i$  (in ion./s); recombination sink  $I_r$  (in rec./s); hydrogenic radiation due to excitation/recombination  $P_{rad}^{H,exc}/P_{rad}^{H,rec}$  (in W) can be obtained. This integral is determined similarly to [63] through equation 7.3 (shown for  $I_i$ ), which uses the locations in figure 7.2 a where the  $r_i$ ,  $z_i$  locations are obtained from the intersection of the line of sight with the separatrix. Here it is assumed that the line integrated values can be described as if they are all originating from the separatrix, which may not be accurate if the largest part of the actual reactions are originating particularly far from the separatrix location.

$$I_i = \int 2\pi r_i I_i(r_i) dz_i \quad (7.3)$$

Table 7.1: Summary of the output parameters of the spectroscopic analysis as indicated in figure 7.1, where Toroidal integral = Tor.  $\int$ ; line integral = Line  $\int$ .

Type	Name	Parameter	Unit	(R)ecomb. / (E)xcit.
Tor. $\int$	Ion source	$I_i$	ion./s	E
Tor. $\int$	Radiated power, excitation	$P_{rad}^{H,exc}$	W	E
Tor. $\int$	CX to ionisation ratio	$I_{CX}/I_i$	-	E
Tor. $\int$	Recombination sink	$I_r$	recomb./s	R
Tor. $\int$	Radiated power, recombination	$P_{rad}^{H,rec}$	W	R
Line $\int$	Ion source	$I_L$	ion. $m^{-2}s^{-1}$	E
Line $\int$	Radiated power, excitation	$P_{rad,L}^{H,exc}$	$W m^{-2}$	E
Line $\int$	CX to ionisation ratio	$CX_L/I_L$	-	E
Line $\int$	Recombination sink	$R_L$	recomb. $m^{-2}s^{-1}$	R
Line $\int$	Radiated power, recombination	$P_{rad,L}^{H,rec}$	$W m^{-2}s^{-1}$	R
Line $\int$	Balmer emission fraction (recomb.)	$F_{rec}$	-	E & R
Line $\int$	Balmer emission fraction (excit.)	$F_{exc}$	-	E & R
Local	Excitation temperature	$T_e^E$	eV	E
Local	Recombination temperature	$T_e^R$	eV	R
Local	" $F_{rec}$ " temperature	$T_{e,F_{rec}}$	eV	E & R

### 7.1.2 Input parameters and their uncertainties

This section provides a brief overview of the used input parameters and their uncertainties in the analysis chain as listed in table 7.2 and shown in figure 7.1. Due to the nature of the probabilistic analysis (section 7.6), the input parameter has to be described as a probability density function (PDF), meaning that 1) the shape of the PDF must be defined; 2) the peak of the PDF must be defined; 3) the width of the PDF must be defined. The list provided in table 7.2 features mostly already discussed parameters with exception the path length  $\Delta L$  (section 7.1.2) and  $n_o/n_e$  (section 7.1.2) which are further discussed below. As highlighted in sections 5.5, the uncertainties in the Balmer line intensities and Balmer line ratios are driven by the uncertainties in the absolute intensity calibration, estimated to be  $\sim 17.5\%$  (68 % confidence interval); and the relative intensity calibration, estimated to be  $\sim 12.5\%$  (68 % confidence interval) —both described by a Gaussian PDF. Based on section 6.4, we assume the uncertainty in the Stark inferred density to be  $\sim 20\%$ , with a minimum uncertainty of  $10^{19}m^{-3}$ . The PDF is described by a Gaussian, considering that the inferred density and its uncertainty can be fairly close to each other, this Gaussian could lead to non-physically low densities (and even negative densities). Therefore, a minimum density cut-off is applied to its PDF using rejection sampling, where values sampled below the cut-off are omitted and re-sampled; such that a Gaussian PDF with a cut-off is obtained.

## Path length $\Delta L$

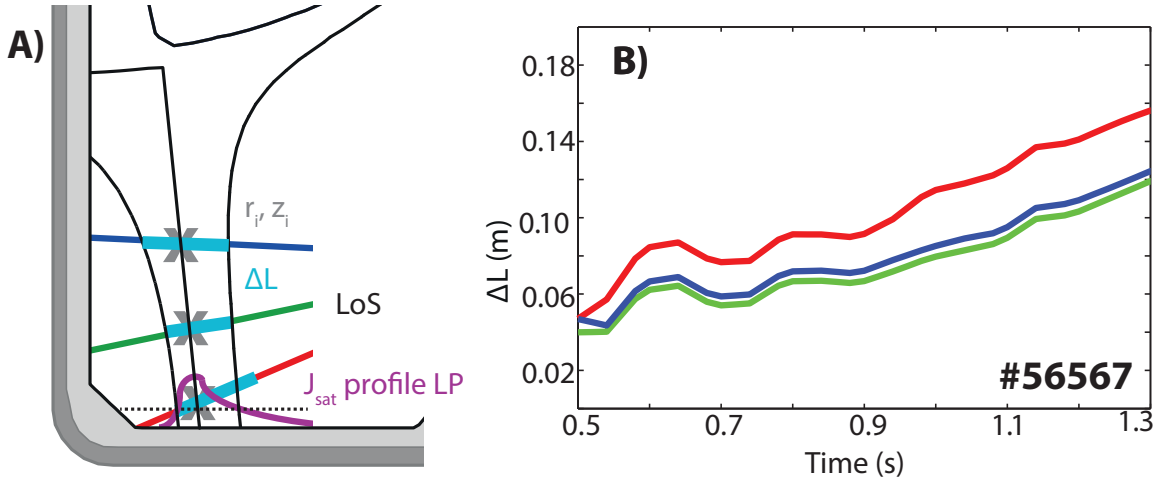


Figure 7.2: a) Schematic overview of how the path length  $\Delta L$  and  $r_i, z_i$  are determined. b) Example of  $\Delta L$  time trace for three lines of sight for # 56567.

An estimate has to be obtained for the characteristic length —or path length,  $\Delta L$ —along the lines of sight over which the plasma contributes most strongly to the measured brightness. Ideally, one would use multi-spectral imaging for this purpose. However, that is not always available and the path length is expected to differ between the different Balmer lines as they have varying sensitivity to recombination and excitation and both processes are expected to occur at different positions in the plasma. As such, one would need to use the same Balmer line in multi-spectral imaging for such an endeavour. This was attempted, but the imaging quality and spatial resolution of the multi-spectral imaging systems at the time on TCV was insufficient for this purpose. We use, therefore, an alternative approach for obtaining an estimate for the path length. The line emission for both excitation and recombination depends on the density as shown in equation 7.1. According to theory, the saturation current measured by Langmuir probes at the target  $j_{sat} \propto n_e \sqrt{T_e}$  also depends on density. Hence, we model  $\Delta L$  at the target as the FWHM of the  $j_{sat}$  profile squared to get a density squared dependence. The points corresponding to the FWHM are mapped upstream along their two corresponding flux surfaces. The intersection between each line of sight and the corresponding flux surfaces is calculated and  $\Delta L$  is determined as the distance between both intersections. An illustration visualising this approach for estimating  $\Delta L$  is shown in figure 7.1 a.

Especially during a density ramp, which are generally used for investigating detachment, the SOL profiles can broaden considerably by more than a factor three during the discharge as the SOL/divertor cools on TCV [99]. This is taken into account by determining  $\Delta L$  at each temporal measurement of the divertor spectrometer. An example of the result of  $\Delta L$  is shown in figure 7.2 b for discharge # 56567, further discussed in chapter 8 and [2], showing an increase in  $\Delta L$  throughout the discharge.

This method of obtaining  $\Delta L$  is a rough approximation. Although both the recombination and excitation part of the Balmer line emission depend on the electron density, they do so differently. In addition, the Balmer line intensity also depends on electron temperature and neutral density (equation 7.1) and the PECs scale non-linearly with the electron temperature. Around 5 eV temperatures, the recombination PECs increase with decreasing  $T_e$  and excitation

PECs increase with increasing  $T_e$ ; thus excitation and recombination would radiate at a different location as shown in figure 7.3, where the emission profile along a synthetic DSS chord of a SOLPS simulation is shown together with the temperature, electron density and neutral density distribution along the chord. From this we conclude:

- Recombinative and excitation emission occur at different positions of the chordal integral, which will influence the localisation of local inferences.
- $\Delta L$  can be different for excitation and recombination emission of the same Balmer line.
- $\Delta L$  can be different for each Balmer line. For instance if a Balmer line is chosen where both recombinative and excitation emission are of equal importance, the emission region can be wider than for other Balmer lines.

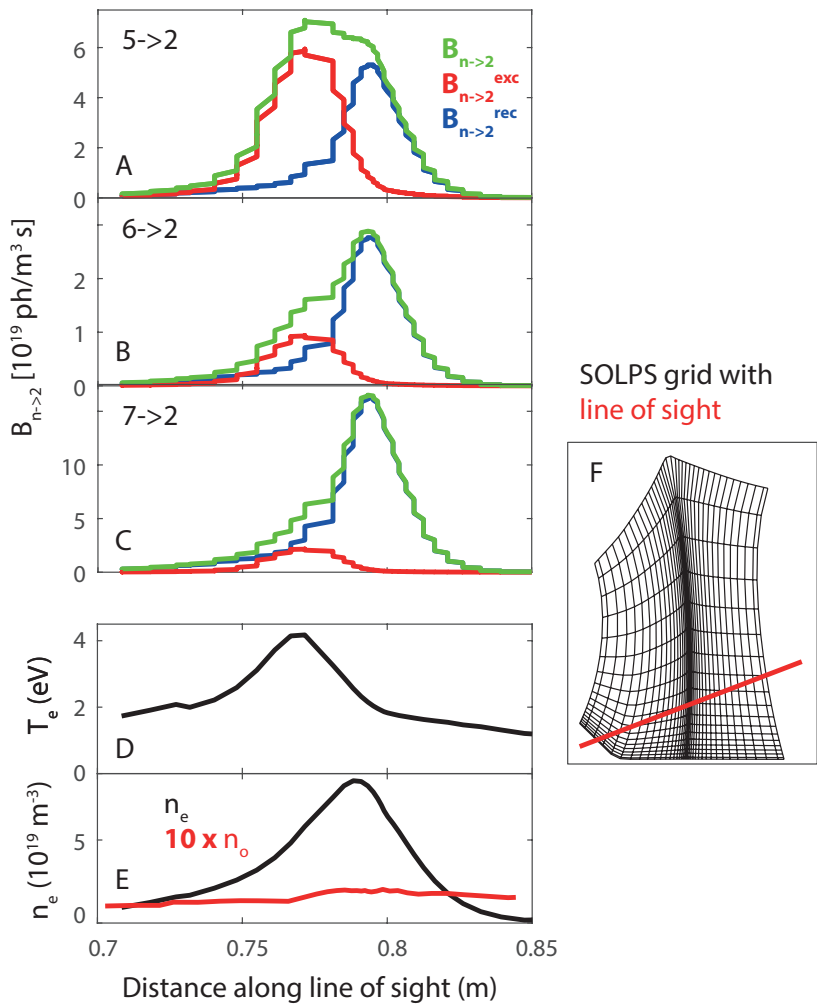


Figure 7.3: a-c) Emission profiles (recombination/excitation/total) for the  $n=5,6,7$  Balmer line emission obtained along the line of sight during a SOLPS simulation (#106237). d-e) Plasma profiles of electron temperature, electron density and hydrogen neutral density along line of sight. f) SOLPS grid geometry (outer divertor leg) with line of sight.

Since obtaining  $\Delta L$  is a rough approximation, we assume an uncertainty of  $\sim 50\%$ . As shown in [100, 99], the SOL broadening is due to two mechanisms: an upstream broadening and a diffusive broadening which occurs somewhere between upstream and the target. Hence

if the SOL width at the target is taken and mapped upstream, the  $\Delta L$  at a position of the divertor leg may be overestimated. Hence we assume that the lower uncertainty of  $\Delta L$  is -50 % and the upper uncertainty is +30 %. The PDF of  $\Delta L$  is then described as an asymmetric Gaussian where the upper half has a  $\sigma$  of +30 % and the lower half has a  $\sigma$  of +50 %; both leading to a 68 % confidence interval.

Table 7.2: Overview of used input parameters in the Balmer line analysis including their uncertainties and the shape of their probability density functions.

Input parameter	Probability density function
$B_{n \rightarrow 2}$	Gaussian Peak: Measured brightness $\sigma : 0.175 \cdot B_{n \rightarrow 2}^{peak}$
$\frac{B_{n_2 \rightarrow 2}}{B_{n_1 \rightarrow 2}}$	Gaussian Peak: Measured line ratio $\sigma : 0.125 \cdot \frac{B_{n_1 \rightarrow 2}}{B_{n_2 \rightarrow 2}}$
$n_e$ [Stark]	Gaussian Peak: Stark density from fit $\sigma : 0.2 \cdot n_e^{peak}$ . $\sigma > 10^{19} m^{-3}$ . $n_e > n_e^{min}$ . $n_e^{min} = [1 - 5] \cdot 10^{18} m^{-3}$ .
$\Delta L$	Asymmetric Gaussian Peak: Inferred $\Delta L$ $\sigma(\Delta L < \Delta L^{peak}) = 50\%$ . $\sigma(\Delta L > \Delta L^{peak}) = 30\%$ .
$n_o/n_e$	Uniform [ $10^{-3}$ –0.05]

emission and recombination emission are similar for every Balmer line. That is an important point as it means that the recombinative/excitation emission regions are the same for every Balmer line: the only difference is their respective magnitudes. That is also important for investigating line integration effects (section 7.7) as it means that once the recombinative/excitation parts are separated this should reduce the influence of line integration effects on the analysis.

### Neutral fraction $n_o/n_e$

The neutral fraction is a crucial element in the analysis chain for using  $B_{n \rightarrow 2}^{exc}$  to estimate the ionisation source. Additionally, as will be explained in section 7.2, the dynamics of  $n_o/n_e$  (as opposed to its actual value) as the divertor cools down is crucial for inferring  $F_{rec}$ . One difficulty, however, is that  $n_o/n_e$  is generally unknown and no direct measurements of the neutral density in the divertor plasma is available. Instead, one has to rely on predictions, simulations and

We can determine from the emission profiles along the line of sight determined through SOLPS (as in figure 7.3) the *minimum width* of the emission profile, where the integral is a given % of the total emission; which can be done separately for the total emission profile or the recombinative and excitation parts of the emission profile. This can be compared against the estimated  $\Delta L$  and its uncertainties from the described technique using the flux surfaces and ion target flux profile simulated by SOLPS. This is shown in figure 7.4 where the approximated  $\Delta L$  and its uncertainty roughly corresponds to 50 to 75 % of the total measured line intensity; and thus seems to give a reasonable estimate as a rough predictor. Here, the previous points made about the emission region when figure 7.3 was discussed are confirmed, showing that, although the estimated path length provides a reasonable estimate of  $\Delta L$ , the real situation is more complicated and  $\Delta L$  can deviate between different Balmer lines and between the recombination/excitation emission regions. On the other hand, the size of the emission regions for excitation

neutral pressure measurements through baratrons (section 4.2.6) which measure the neutral pressure due to both molecules and neutrals at a fixed target location. However, such baratron measurements do not provide volumetric neutral pressure measurements and require a model to convert the neutral pressure measurement into a neutral pressure in the plasma.

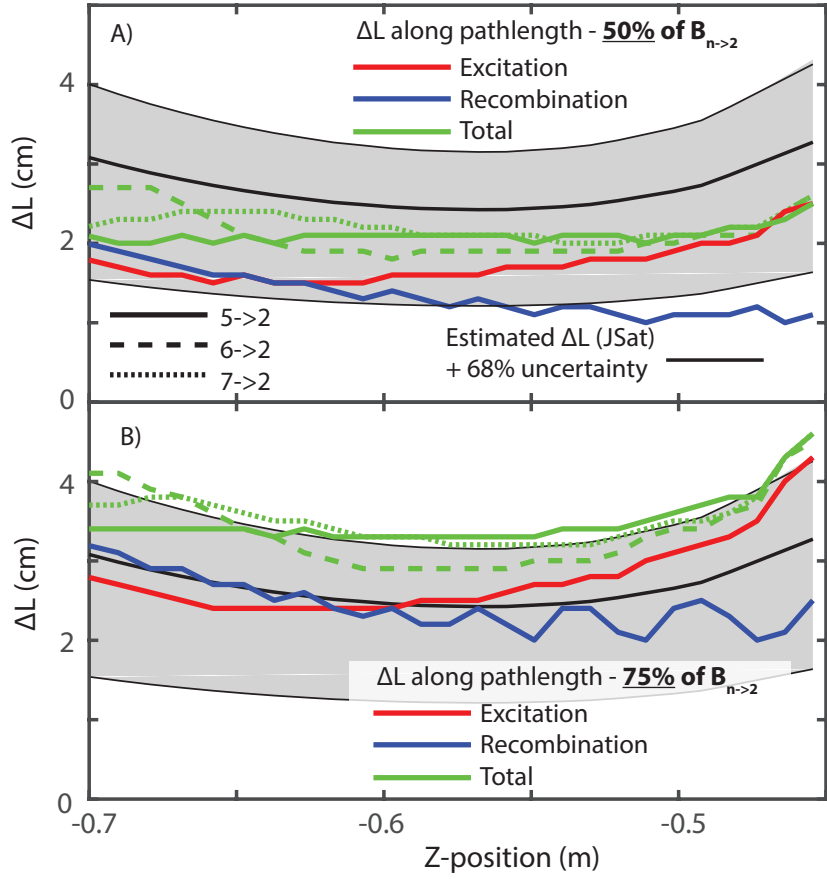


Figure 7.4: Estimated path lengths from the  $J_{sat}$  profile compared to the actual characteristic lengths of the emission region along the line of sight; both determined through a SOLPS simulation (MDS+ shot number #106273 —see section 7.7 for more details), for the  $n=5,6,7$  Balmer lines.

There are several processes influencing the neutral dynamics in the divertor. Ignoring neutral transport, one can argue that ionisation reduces the neutral density (as neutrals are being used up in the process), whereas recombination increases the neutral density (as neutrals are being created in the process). As such, in a transport-less plasma, the neutral fraction is the recombination to ionisation ratio (assuming a pure hydrogenic, quasi-neutral plasma) is provided by equation 7.4 where SCD, ACD are ADAS parameters [138, 135, 134] explained in section 2.2, which are strongly temperature dependent. Thus, in a transport-less plasma,  $n_o/n_e$  is strongly temperature dependent where, for an increasing range  $T_e = 0.2 \text{ eV}$  to  $100 \text{ eV}$ , the neutral fraction obtained from this model decreases from  $\frac{n_o}{n_e} = 1 \times 10^{25}$  to  $1 \times 10^{-7}$ . Such a model for the neutral fraction is sometimes used in literature for modelling the Balmer line emission [73, 115].

$$\frac{n_o}{n_e} = \frac{ACD(T_e, n_e)}{SCD(T_e, n_e)} \quad (7.4)$$

Apart from ionisation and recombination, neutral transport in the divertor also plays a

role in the dynamics of the neutrals. Transport generally moves neutrals from colder regions of the plasma to hotter regions, flattening the strong temperature dependence of the neutral fraction. Neutral fluxes from the plasma facing components due to recycling also must be considered as additional neutral sources at the target.

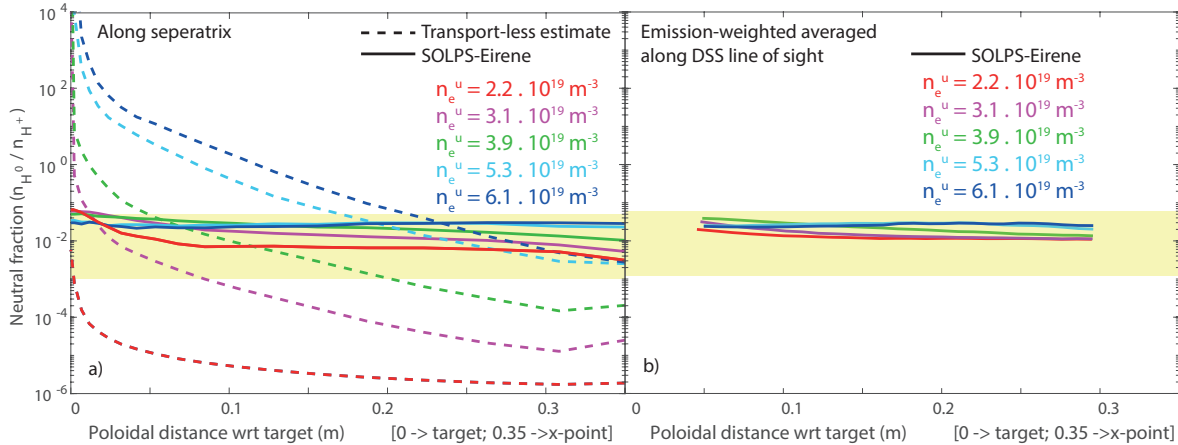


Figure 7.5: Comparison of the neutral fraction along the (a) separatrix and (b) emission-weighted ( $n = 7$  Balmer line) along the DSS chords; both from the outer divertor leg obtained from SOLPS-ITER simulations at different upstream densities. The SOLPS results are compared to the no-transport assumption in (a) (equation 7.4). The neutral fraction range ( $n_o/n_e = [0.001 - 0.05]$ ) is shaded in yellow.

SOLPS simulations also provide neutral density profiles and account for ionisation/recombination, transport and neutral influxes from the wall simultaneously. These results are compared to the no-transport model (equation 7.4 where  $n_e, T_e$  is provided by the SOLPS simulation) in figure 7.5 for a field line at the separatrix during an upstream density ramp ( $n_e^u$ ) in which the divertor goes from attached to detached conditions, respective of discharge # 52065 as has been presented in [7]. The no transport assumption clearly shows a very strongly varying neutral fraction along the divertor leg (factor  $> 100$ ) which increases as the divertor is cooled (factor  $> 10^6$ ), whereas the SOLPS simulated neutral fraction is relatively flat (deviations within a factor  $< 10$ ). This information shows that the neutral dynamics is almost fully governed by transport in the TCV divertor according to SOLPS simulations, resulting in an almost flat response in the neutral fraction: ionisation and recombination only have small effects on the neutral density. One may, however, argue that the values presented in figure 7.5 a are not respective of the effective neutral density contributing to a measured brightnesses as the emission does not precisely occur at the separatrix locations on which figure 7.5 a is based. To make up for that, the neutral fractions averaged along the line of sight, weighted by the  $n = 7$  Balmer line emission profile is shown in addition in figure 7.5 b; which shows a similar trend with an even smaller deviation during the upstream density ramp and along the outer divertor leg.

SOLPS modelling [7, 68] and OSM-Eirene modelling [79] indicates neutral fractions between  $n_o/n_e = [0.005 - 0.05]$  and here the results presented here from [7] are on the upper part of that range. However, as shown from the comparison between neutral baratron pressure measurements and a synthetic baratron diagnostic in section 4.3 has indicated that the neutral density may be overestimated in the SOLPS simulation; although there are other reasons why

a deviation between the two can occur (such as the simplifications used when translating the baratron neutral pressures to plasma neutral pressures). Given that information, we assume in the analysis that the neutral fraction is constant within a certain range ( $n_o/n_e = [0.001 - 0.05]$ ).

Not only the value or range of  $n_o/n_e$  is important for the analysis, it is also important to consider the dynamics of the neutrals in the TCV divertor and the influence this has on the dynamics of the Balmer line emission. Information on the neutral dynamics of  $n_o/n_e$  are important when the plasma is continuously cooled. As will be explained in section 7.2, one needs to assume that  $n_o/n_e$  is 'fairly' insensitive to  $T_e$ ; which agrees with the shown SOLPS results. One other indicator for this is that, assuming a constant  $n_o/n_e$ , it is expected that the ratio between two Balmer lines will be similar to the ratio expected when only excitation is present at high temperatures, which transitions to a higher line ratio, respective of only recombination present, at lower temperatures. In other words, the Balmer line ratio is expected to 'step up' at some point when the plasma is continuously cooled. If one were to assume a no transport case (equation 7.4), a different behaviour would be observed. This step-like behaviour of the Balmer line ratio is clearly observed on TCV (figure 7.6) and [1], which is thus indicative of a 'fairly' constant  $n_o/n_e$  as has been shown in the SOLPS simulations. This will be explained in further detail in section 7.2 where the methodology to determine  $F_{rec}$  is highlighted.

## 7.2 Separating recombination and excitation contributions to the Balmer line emission

Hydrogen Balmer lines become more sensitive to volumetric recombination with increasing  $n$  number. High-n Balmer lines ( $n > 9$ ), for instance, are only observed in tokamaks during detachment (when recombination is present); whereas lower-n Balmer lines are always observed. Since Balmer lines become more sensitive to volumetric recombination with increasing  $n$ , the ratio between an upper-n and lower-n Balmer increases when recombination contributes more strongly to the Balmer line emission; the ratio between two Balmer lines changes depending on how much of their emission is due to recombination. By investigating Balmer line ratios, we have found that Balmer line ratios can be employed to separate excitation and recombination contributions to a Balmer line's emission quantitatively. That is an important finding as the excitation and recombination parts of a Balmer line's emission are often both important during detached conditions; which complicates analysis strategies performed in literature where it is assumed that the Balmer line emission is either fully due to recombination [66, 51, 72] or excitation [70, 73, 72]. Thanks to the separation technique found in this work, the excitation and recombination contributions can be analysed individually, making the Balmer line analysis much less cumbersome. Furthermore, as we have seen in figure 7.3, the Balmer line emission location along the line of sight can be different for each Balmer line as the excitation and recombination parts of the Balmer line emission can occur at different locations along the line of sight. Separating excitation/recombinative emission in such cases enables a better localisation of the emission, reducing line integration effects on the analysis as shown in section 7.7.

To separate the excitation/recombination components of a Balmer line's emission we first establish relations, based on the model presented in section 7.1 equation 7.1, for a Balmer

line's ratio  $\frac{B_{n_2 \rightarrow 2}}{B_{n_1 \rightarrow 2}}$  and the fraction of Balmer line emission due to recombination, which we define as  $F_{rec}(n)$ , leading to equations 7.5 and 7.6. As shown, both the Balmer line ratio and  $F_{rec}$  in the model depend on  $n_e, T_e, \frac{n_o}{n_e}$ . Therefore, for a given  $n_e, \frac{n_o}{n_e}$ , both  $\frac{B_{n_2 \rightarrow 2}}{B_{n_1 \rightarrow 2}}$  and  $F_{rec}(n)$  become functions of only  $T_e$ .

$$\frac{B_{n_2 \rightarrow 2}}{B_{n_1 \rightarrow 2}} = \frac{PEC_{n_2 \rightarrow 2}^{rec}(n_e, T_e) + \frac{n_o}{n_e} PEC_{n_2 \rightarrow 2}^{exc}(n_e, T_e)}{PEC_{n_1 \rightarrow 2}^{rec}(n_e, T_e) + \frac{n_o}{n_e} PEC_{n_1 \rightarrow 2}^{exc}(n_e, T_e)} \quad (7.5)$$

$$F_{rec}(n) = \frac{PEC_{n \rightarrow 2}^{rec}(n_e, T_e)}{PEC_{n \rightarrow 2}^{rec}(n_e, T_e) + \frac{n_o}{n_e} PEC_{n \rightarrow 2}^{exc}(n_e, T_e)} \quad (7.6)$$

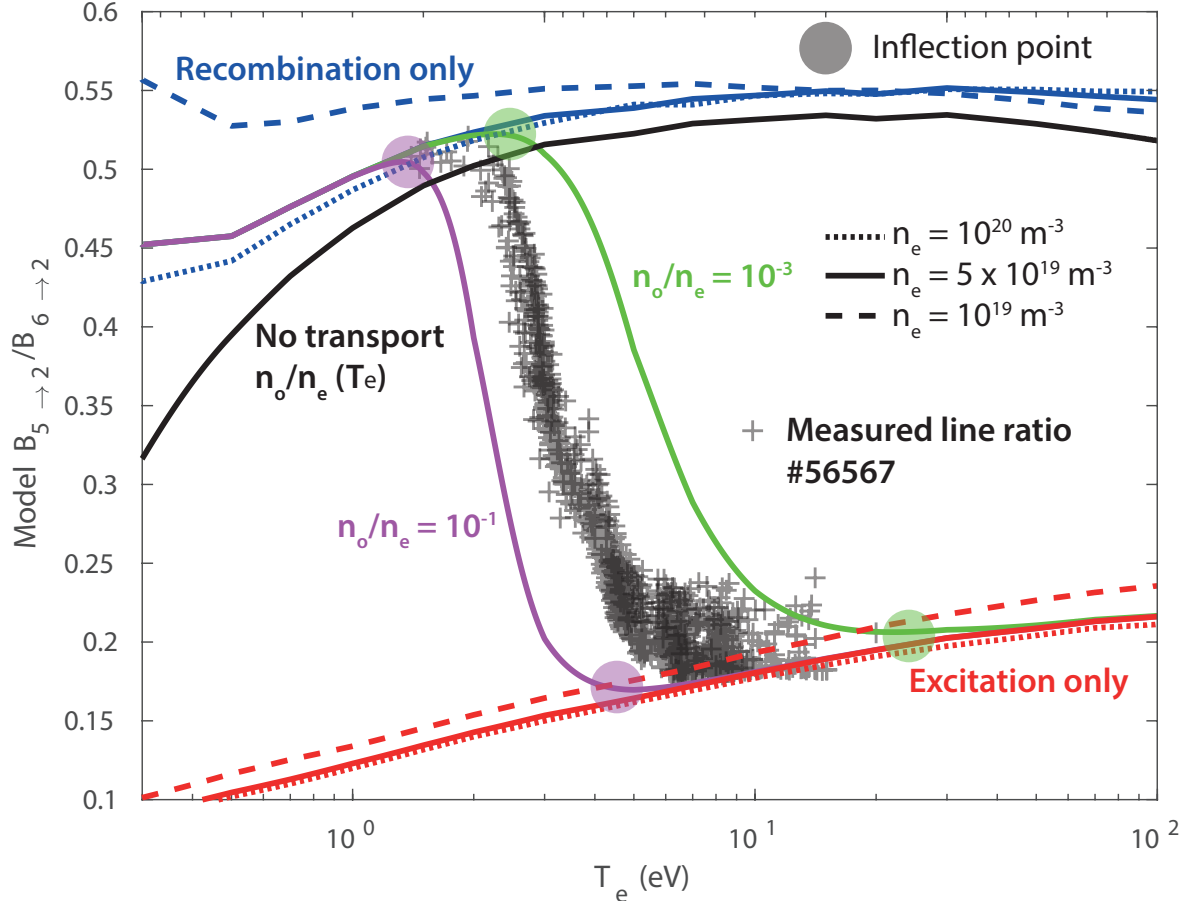


Figure 7.6: Modelled  $\frac{B_{5 \rightarrow 2}}{B_{6 \rightarrow 2}}$  as function of  $T_e$ . Both the excitation only and recombination only trends are shown at three different densities, while the green/magenta take both recombination/excitation into account and assume a fixed  $n_o/n_e$ . The black solid line indicates  $\frac{B_{5 \rightarrow 2}}{B_{6 \rightarrow 2}}$  as function of  $T_e$  where  $n_o/n_e$  is determined as function of  $T_e$  using equation 7.4, as done in [73] to determine the 'TEC'. The black plusses indicate the measured  $\frac{B_{5 \rightarrow 2}}{B_{6 \rightarrow 2}}$  for # 56567 for all lines of sight of the divertor spectrometer, where  $T_e$  respective of the excitation emission is used as the effective  $T_e$  (see section 7.3.1 and 9.1.2).

Secondly we investigate the temperature dependence of the modelled Balmer line fraction, shown in figure 7.6. As explained previously, the ratio between an upper-n Balmer line and a lower-n Balmer line is expected to rise as the recombination contribution to the spectra becomes stronger. However, there is a lower limit ( $| \frac{B_{n_2 \rightarrow 2}}{B_{n_1 \rightarrow 2}} |_{exc-limit}$  —equation 7.7) to this where both Balmer lines are dominated by excitation emission ( $F_{rec}(n_1, n_2) \sim 0$ ). There is also an upper

limit to this rise ( $|\frac{B_{n_2 \rightarrow 2}}{B_{n_1 \rightarrow 2}}|_{rec-limit}$  —equation 7.7) where both Balmer lines are dominated by recombinative emission  $F_{rec}(n_1, n_2) \sim 0$ . Both of these limits only depend on  $n_e, T_e$  and are relatively constant compared to the difference between the two limits. The modelled line ratio, assuming a fixed neutral fraction ( $n_o/n_e$ ), starts at the excitation limit at high temperatures where, at some point, it starts to rise towards the recombination limit when reducing the temperature while saturating at the recombination limit later (figure 7.6); e.g. at some point when the temperature drops, a transitioning occurs from excitation dominated emission towards recombination dominated emission. The points where this transitioning occurs are inflection points, as shown in figure 7.6 where the temperature derivative of the modelled line ratio changes direction. That behaviour is however observed for a fixed  $n_o/n_e$  while determining  $n_o/n_e$  through a no-transport model (equation 7.4), as is sometimes employed in literature [73], yields a completely different behaviour where no longer a transitioning from excitation to recombinative emission occurs (figure 7.6). Instead, a smooth trend arises which indicates recombination dominant emission at high temperatures (as the neutral fraction drops) and when transitioning to low temperatures the Balmer line emission becomes more excitation dominant (as the neutral fraction rises).

$$\begin{aligned} |\frac{B_{n_2 \rightarrow 2}}{B_{n_1 \rightarrow 2}}|_{exc-limit} &= \frac{PEC_{n_2 \rightarrow 2}^{exc}(n_e, T_e)}{PEC_{n_1 \rightarrow 2}^{exc}(n_e, T_e)} \\ |\frac{B_{n_2 \rightarrow 2}}{B_{n_1 \rightarrow 2}}|_{rec-limit} &= \frac{PEC_{n_2 \rightarrow 2}^{rec}(n_e, T_e)}{PEC_{n_1 \rightarrow 2}^{rec}(n_e, T_e)} \end{aligned} \quad (7.7)$$

This predicted transitioning behaviour of the measured  $\frac{B_{6 \rightarrow 2}}{B_{5 \rightarrow 2}}$  line ratio (or other Balmer line ratio) from low values (quantitatively consistent with the modelled  $|\frac{B_{n_2 \rightarrow 2}}{B_{n_1 \rightarrow 2}}|_{exc-limit}$ ) to high values (quantitatively consistent with the modelled  $|\frac{B_{n_2 \rightarrow 2}}{B_{n_1 \rightarrow 2}}|_{rec-limit}$ ) is observed as has been shown by the author [1], when the plasma on TCV is continuously cooled (e.g. density ramp discharge). The fact that such a clear jump in the Balmer line ratio occurs in TCV as the plasma cooled is an experimental indicator that the neutral fraction is fairly constant in the TCV divertor, which is in agreement with SOLPS simulation results for TCV as shown in figure 7.5. Furthermore, similar dynamics of Balmer line ratios have been shown in MAST [81, 208] and JET [80, 61]. It thus seems that using a no transport assumption for modelling  $n_o/n_e$  may not be (always) appropriate. To visualise the observed step-like behaviour in the Balmer line ratio, the measured  $\frac{B_{6 \rightarrow 2}}{B_{5 \rightarrow 2}}$  results of a density ramp (# 56567) have been added to figure 7.6 while using the temperature obtained through analysing the excitation emission ( $T_e^E$  as will be discussed in section 7.3.1) as a characteristic temperature. One other interesting observation is that, depending on  $n_o/n_e$ , the  $T_e$  at which this transitioning in the Balmer line ratio occurs changes. The observed trend thus suggests that  $n_o/n_e$  in the experiment is in between  $1 \times 10^{-3}$  to  $1 \times 10^{-1}$ . Furthermore, the precise temperature at which this transitioning occurs may give information on  $n_o/n_e$ ; meaning that with further analysis advances it may be possible to use Balmer line ratio trends together with temperature estimates to infer the neutral fraction, which will be future work. Please note, however, that this  $T_e^E$  deviates from the  $T_e$  obtained from the line ratio analysis as will be discussed in section 7.3.1 and figure 7.12. The transitioning of medium-n Balmer line ratios ( $n = 6, 7$ ) from excitation dominant emission to recombination dominant emission can be relatively slow and occurs at different times for different locations along the divertor leg. This means that, for a large part of a density

ramp discharge, the Balmer line intensities can have both significant excitation/recombination contributions, showing the importance and necessity of quantitatively splitting the Balmer line emission in its excitation and recombination components rather than assuming the Balmer line emission is either recombination or excitation dominant.

Now that we have established that a constant neutral fraction assumption is appropriate for describing TCV line ratio trends, we can go onwards to third step, which is to quantify  $F_{rec}$  given a measured Balmer line ratio. Since both the modelled  $F_{rec}$  and the modelled  $\frac{B_{n_2 \rightarrow 2}}{B_{n_1 \rightarrow 2}}$  are functions of only  $T_e$  for an assumed fixed  $n_e, \frac{n_o}{n_e}$  (equations 7.6, 7.5), we can visualise  $F_{rec}(n)$  as function of the Balmer line ratio (figure 7.7) where each point corresponds to a certain  $T_e$ . The relation shows that a measured line ratio leads directly to a unique  $F_{rec}$  for  $F_{rec} = [0.1 - 0.9]$  where both recombination and excitation contribute to the Balmer line emission. Although this is only presented here for the  $n = 5, 6$  Balmer lines, similar relations are found for other combinations of Balmer lines and the Balmer line for which  $F_{rec}$  is shown is not necessarily one of the Balmer lines used in the Balmer line ration, although this may lead to higher uncertainties.

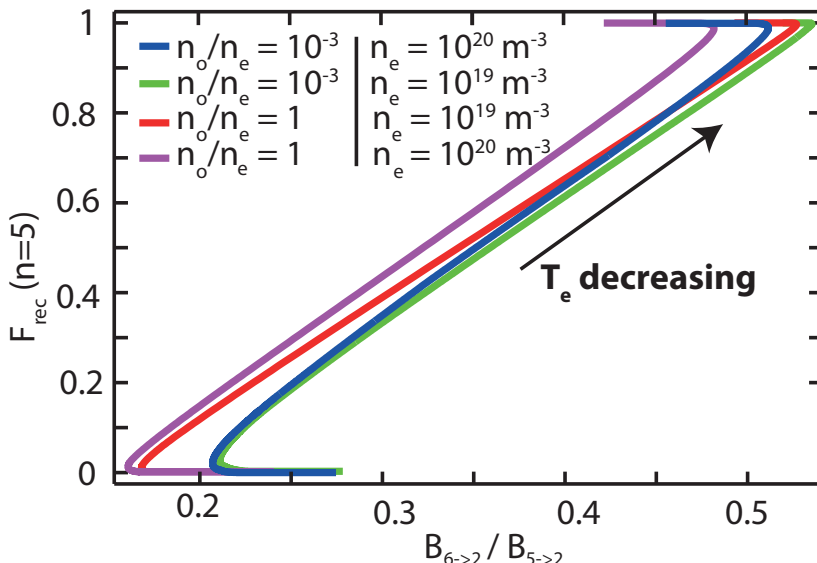


Figure 7.7:  $F_{rec}(n = 5)$  as function of  $\frac{B_{6 \rightarrow 2}}{B_{5 \rightarrow 2}}$  for a set of fixed  $n_e$  and  $n_o/n_e$ . Each point in this graph corresponds to a certain  $T_e$ .

It is clear from figure 7.7 that the  $F_{rec}(n)$  obtained is insensitive to the electron density and neutral fraction, although the deviations can lead to small shifts in the relationship between the line ratio and  $F_{rec}(n)$ . Due to this insensitivity, the obtained  $F_{rec}(n)$  is strongly insensitive to line integration effects, which will be further discussed in section 7.7. The characteristic uncertainty of  $F_{rec}(n)$  is  $\sim 0.2$ , which has been determined through the probabilistic analysis presented in section 7.6. From  $F_{rec}$  the respective recombination and excitation parts are determined using the measured line intensity:  $B_{n \rightarrow 2}^{rec} = F_{rec}(n) \times B_{n \rightarrow 2}$  and  $B_{n \rightarrow 2}^{exc} = (1 - F_{rec}(n)) \times B_{n \rightarrow 2}$ , as was shown in equation 7.2.

One important point to note is that the unique solution for  $F_{rec}(n)$  from the measured ratio of two Balmer lines is only obtained when  $F_{rec}(n)$  is in between  $\sim 0.1$  and  $\sim 0.9$ : e.g. if almost all Balmer line emission is due to recombination ( $F_{rec}(n) = 0.9$  to  $1.0$ ),  $B_{n \rightarrow 2}^{exc}$  cannot be determined (all that can be said is that it is much lower than  $B_{n \rightarrow 2}^{rec}$ ). It should be noted

also that the  $F_{rec} = 0.1$  to  $0.9$  range is an approximative range, which can vary depending on the neutral fraction, electron density and line integration effects tend to reduce this range by 0.1 (section 7.7). For simplicity, however, we refer to the validity range as  $F_{rec} = 0.1$  to  $0.9$ . Outside of this range either recombination or excitation dominates the Balmer line emission.

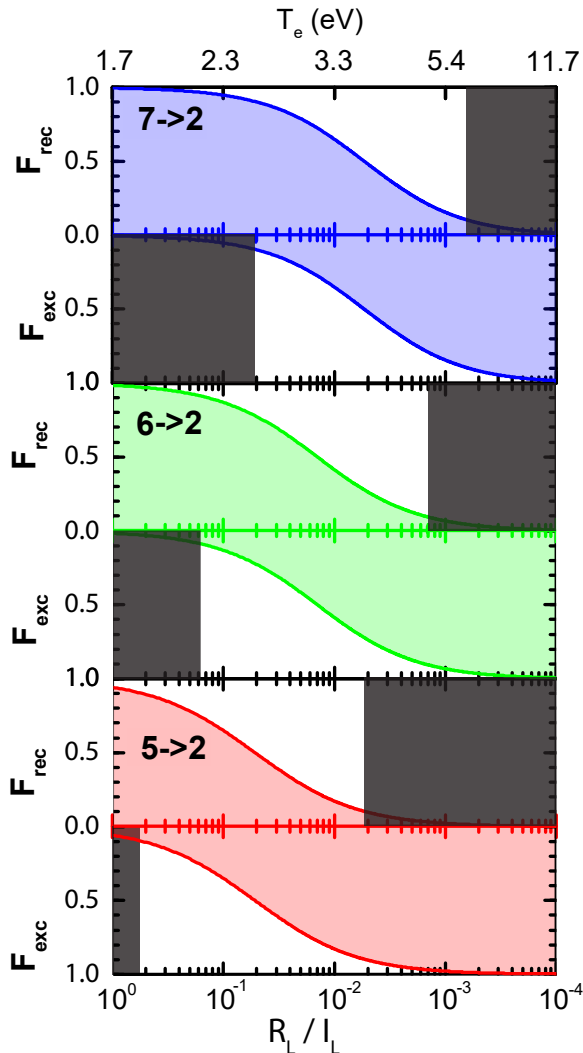


Figure 7.8:  $F_{rec}(n)$  and  $F_{exc}(n)$  as function of the temperature (and hence recombination to ionisation rate ratio) for an assumed  $n_e = 5 \cdot 10^{19} m^{-3}$  and  $n_o/n_e = 0.05$ .

(with a fixed  $n_e, n_o/n_e$ ) leads to an increasing recombination to ionisation ratio ( $R_L/I_L$ ) with decreasing temperature. Shaded regions for each Balmer line in figure 7.8 show where  $F_{rec} < 0.1$  or  $F_{exc} < 0.1$ . For the reader's convenience, these  $F_{rec}$  limits are shown in more detail in table 7.3, where these limits are presented for different Balmer line as function of  $n_e$  and  $n_o/n_e$ . Recombination emission is strongly dependent on electron density and thus, with increasing electron density, the recombination emission will dominate the Balmer line ratio at higher  $T_e$  and lower  $R_L/I_L$ , as shown in table 7.3. This means that, at high densities, the Balmer line emission of medium-n Balmer lines is easily dominated by recombination—even if the recombination rate is smaller than the ionisation rate; complicating the extraction

This, however *does not* provide (by itself) any information on whether the actual recombination rate dominates over the ionisation rate or gets close to the ionisation rate. The reason for the loss of uniqueness outside this validity range is that, as shown in figure 7.6, the excitation only and recombination only trends of the Balmer line ratio have a weak  $T_e$  dependence, which is smaller than the change in Balmer line ratio when transitioning from  $F_{rec} \sim 0 \rightarrow F_{rec} \sim 1$ . Due to that weak dependence, if only the line ratio is known, and  $F_{rec}$  is outside the validity range, there are two possible solutions for  $F_{rec}$  and  $T_e$  (figures 7.6 and 7.7), one corresponding to the step in line ratio and one corresponding to the recombination only ( $F_{rec} \sim 1$ ) or excitation only ( $F_{rec} \sim 0$ ) trend.

Depending on which Balmer lines are used in the analysis; the validity regime ( $F_{rec} = 0.1$  to  $0.9$ ) corresponds to different plasma parameters. As such, the Balmer lines for the various outputs of the analysis must be chosen appropriately based on one's goal and based on the plasma parameters. This is illustrated in figure 7.8 where, for a fixed density and neutral fraction, the evolution of  $F_{rec}(n)$  and  $F_{exc}(n) = 1 - F_{rec}(n)$  is given for three different Balmer lines as a function of temperature as indicated in the top label in figure 7.8. This change in temperature

of  $B_{n \rightarrow 2}^{exc}$  during detachment, which is necessary to infer the ionisation rate and hydrogenic radiative power loss (see overview figure 7.1). To combat this, one can use a lower-n Balmer line which is less sensitive to recombination; but that will also lower the minimum  $R_L/I_L$  at which recombination can be detected. Interesting to note is that changing  $n_o/n_e$  has only a small influence on the  $R_L/I_L$  window in which  $F_{rec}$  can be inferred, although the temperature regime in which this occurs changes strongly (as also shown in figure 7.6).

We note, however, that there is a limit to using  $F_{rec}$  for estimating  $B_{n \rightarrow 2}^{exc}$  at high electron densities and high recombination rates as the lowest-n Balmer line which can be used in this analysis is the  $n = 5$  Balmer line. Lower-n Balmer lines ( $n = 3, 4$ :  $D\alpha, D\beta$ ) cannot be used as molecular reactions may contribute significantly to their intensity [109, 5]. This is consistent with our analysis of the  $D\alpha$  emission, which indicated that the observed  $D\alpha$  during detached conditions is much higher than the expected  $D\alpha$  from atomic processes (section 8.4) most likely due to molecular reactions (mostly molecular activated recombination) contributing to the  $D\alpha$  brightness. Therefore, for cases where the recombination and ionisation rates become of comparable magnitude, assuming densities around  $n_e \sim 1 \times 10^{20} \text{ m}^{-3}$ ,  $F_{rec}(n = 5) > 0.9$  will be reached; complicating the ionisation rate analysis as  $B_{5 \rightarrow 2}^{exc}$  can no longer be accurately estimated, which is an issue especially during high density operation as shown in table 7.3.

Table 7.3:  $T_e$  and  $R_L/I_L$  corresponding to the  $F_{rec} = 0.1$  to  $0.3$  limits as function of  $n, n_e, n_o/n_e$

$F_{rec}$ limit		$n = 5$	$n = 6$	$n = 7$	$n = 8$	$n = 9$		
0.1	$n_e [\text{m}^{-3}]$	$1 \times 10^{18}$	$T_e [\text{eV}]$	5.1	6.8	8.8	11	14.5
	$n_o/n_e$	$1 \times 10^{-3}$	$R_L/I_L$	0.09	0.03	0.01	$7 \times 10^{-3}$	$4 \times 10^{-3}$
	$n_e [\text{m}^{-3}]$	$1 \times 10^{18}$	$T_e [\text{eV}]$	2.1	2.5	2.9	3.3	3.9
	$n_o/n_e$	0.1	$R_L/I_L$	0.1	0.03	0.01	$6 \times 10^{-3}$	$3 \times 10^{-3}$
	$n_e [\text{m}^{-3}]$	$5 \times 10^{20}$	$T_e [\text{eV}]$	24	40	61	91	130
	$n_o/n_e$	$1 \times 10^{-3}$	$R_L/I_L$	$9 \times 10^{-4}$	$4 \times 10^{-4}$	$2 \times 10^{-4}$	$1 \times 10^{-4}$	$8 \times 10^{-5}$
	$n_e [\text{m}^{-3}]$	$5 \times 10^{20}$	$T_e [\text{eV}]$	4.5	6.2	8.2	11	14
	$n_o/n_e$	0.1	$R_L/I_L$	$8 \times 10^{-4}$	$2 \times 10^{-4}$	$9 \times 10^{-5}$	$4 \times 10^{-5}$	$2 \times 10^{-5}$
0.9	$n_e [\text{m}^{-3}]$	$1 \times 10^{18}$	$T_e [\text{eV}]$	2.2	2.6	3	3.5	4
	$n_o/n_e$	$1 \times 10^{-3}$	$R_L/I_L$	9	3	1	0.5	0.2
	$n_e [\text{m}^{-3}]$	$1 \times 10^{18}$	$T_e [\text{eV}]$	1.3	1.5	1.6	1.8	1.9
	$n_o/n_e$	0.1	$R_L/I_L$	12	3	1	0.5	0.2
	$n_e [\text{m}^{-3}]$	$5 \times 10^{20}$	$T_e [\text{eV}]$	4.7	6.5	8.8	12	15
	$n_o/n_e$	$1 \times 10^{-3}$	$R_L/I_L$	0.07	0.02	$8 \times 10^{-3}$	$4 \times 10^{-3}$	$2 \times 10^{-3}$
	$n_e [\text{m}^{-3}]$	$5 \times 10^{20}$	$T_e [\text{eV}]$	2	2.4	2.8	3.3	3.9
	$n_o/n_e$	0.1	$R_L/I_L$	0.1	0.02	$8 \times 10^{-3}$	$3 \times 10^{-3}$	$2 \times 10^{-3}$

For TCV divertor conditions using the  $n = 6, 7$  Balmer lines generally suffices for extracting  $F_{rec}$ . The advantage of monitoring these two lines is that they can be acquired simultaneously using the highest resolution grating of the DSS, which suffices for Stark broadening measurements (chapter 6). However, for a relatively strongly recombining divertor (L-mode density ramps with  $I_p > 340 \text{ kA}$  where divertor electron densities of  $\sim 1 \times 10^{20} \text{ m}^{-3}$  are achieved during detachment), the  $F_{rec}(n = 6, 7) > 0.9$  limit is exceeded before the ion target current

roll-over. Although this indicates that the Balmer line emission of the  $n = 6, 7$  Balmer lines is fully dominated by recombination as shown in figure 7.8 and table 7.3, this only corresponds to recombination to ionisation ratios of more than a few percent. By including a lower-n Balmer line ( $n=5$ ) in the analysis, the point where  $F_{rec}(n = 5) > 0.9$  is reached only occurs at recombination to ionisation ratio of tens of percent's. Since high resolution data of the  $n = 7$  Balmer line is still required for electron density inferences through Stark broadening, obtaining both  $n = 5, 7$  Balmer lines while having a high resolution measurement of the  $n = 7$  Balmer line required a repeat of discharges to change the spectrometer's wavelength range. That is also one of the reasons why the DSS was modified later in order to enable both spectrometers to be used with (identical) horizontal lines of sight as explained in chapter 5. Using the  $n = 5$  Balmer line as opposed to higher-n Balmer lines does mean that the sensitivity to detecting recombination becomes weaker, but recombination is still detectable when it increases beyond  $\sim 1\%$  of the ionisation rate. Nonetheless, even when using the  $n = 5$  Balmer line, the  $F_{rec}(n = 5) = 0.9$  limit is reached during the strongest detached phases of high current density ramp discharges on TCV. Although the loss of uniqueness at  $F_{rec}(n) > 0.9$  is cumbersome, this is not a 'hard' limit and can be alleviated by using certain numerical algorithms (section 7.2.1), which exploit the fact that the temperature is continuously decreasing in the divertor during a core density/seeding ramp in order to estimate whether a solution corresponds to the excitation/recombination branches or the transitioning branch (figure 7.6).

### 7.2.1 Determining $F_{rec}(n)$ in the $F_{rec}(n)$ limits

As explained previously and shown more explicitly in figure 7.9, the loss of uniqueness for  $F_{rec}$  occurs as two  $T_e$  solutions are possible outside the  $F_{rec} = 0.1$  to  $0.9$  interval. Using the information that the temperature is continuously decreasing, we can determine which of these two solutions is valid. First we describe the structure of the two solutions obtained for a monotonous drop in temperature, as shown in figure 7.9 b —where we first model the Balmer line ratio obtained and from this infer the  $F_{rec}$  obtained. Starting at a high temperature, two  $F_{rec}$  solutions are obtained, where the blue trend shows the 'Correct  $F_{rec}$ ', and the red trend shows the wrong 'Secondary  $F_{rec}$ '. When dropping the temperature, at some point the bifurcation disappears and a single  $F_{rec}$  solution is obtained. When comparing this to figure 7.9 (where obtaining double valued  $F_{rec}$  for the same line ratio is highlighted with two circles and a connecting red line), the point where that bifurcation disappears corresponds to the minimum/maximum value the Balmer line ratio can obtain. During a density ramp, the Balmer line ratio is observed to exhibit an 'S'-like behaviour: where the line ratio first decreases as the temperature is reduced, afterwards increases as the contribution of recombination to the Balmer line emission becomes more significant and decreases again as the Balmer line emission is fully dominated by recombination —as indicated by the measured line ratio and modelled fixed  $n_o/n_e$  trends in figure 7.6. The two inflection points in this correspond to the minimum/maximum Balmer line ratio obtainable. Before reaching the first inflection point (e.g. at high temperatures where  $F_{rec} \sim 0$ ) we assume that  $F_{rec}$  has a random value between 0 and the  $F_{rec}$  value corresponding to the inflection point —which depends on density/temperature/neutral fraction, but is usually  $\sim 0.02$  or smaller. Between the first and second inflection point a unique value for  $F_{rec}$  is obtained through the line ratio analysis. After reaching the second inflection point (at low temperatures where  $F_{rec} \sim 1$ ) we assume

that  $F_{rec}$  has a random value between the  $F_{rec}$  value corresponding to the inflection point (which is usually  $\sim 0.98$  or higher) and 1. This leads to the inferred  $F_{rec}$  trend shown in figure 7.9 b. This procedure is performed on each Monte Carlo iteration (as discussed in section 7.6).

The difficulty in this is, however, finding the inflection points —as the precise value where this occurs changes throughout the discharge as the density changes. Furthermore, due to measurement uncertainties, one will never reach exactly the inflection point. Therefore, first we assume that a certain line ratio always corresponds to temperatures between the two inflection points as shown by the red trend in figure 7.9 a) —' $F_{rec} T_e$  restricted'. This results in a 'S-like' trend of the inferred  $F_{rec}$  as function of decreasing temperature as shown by the red curve in figure 7.9 b). The minimum and maximum  $F_{rec}$  obtained as the divertor temperature is continuously cooled then corresponds to the two inflection points (cyan —figures 7.9, 7.6). Smoothing/fitting has applied where appropriate to make sure the result is not affected by measurement noise. Then the algorithm mentioned above is used in order to 'correct'  $F_{rec}$  for regions where a double valued solution was obtained, which is our 'first' correction algorithm for dealing with situation where  $F_{rec}(F_{exc}) \sim 1$ .

As  $F_{rec}$  approaches 1, the upper uncertainty bound is reduced given the physically limit at 1. Therefore, given measurement uncertainties, it is easier to underestimate  $F_{rec}$  rather than underestimate  $F_{rec}$  when  $F_{rec} \sim 1$ . If  $F_{rec}(n) > 0.9$  even small underestimates of  $F_{rec}(n)$  can lead to a large (relative) overestimation of  $B_{n \rightarrow 2}^{exc}$ . Given that the medium-n Balmer line emission strongly increases due to the presence of recombination (factor  $\sim 50$  on TCV for the  $n = 6, 7$  Balmer lines as has been shown by the author in [1]), this can lead in practice to the non-physical result of a strongly increasing  $B_{n \rightarrow 2}^{exc}$  (and thus the ionisation rate) during detachment. To deal with this, we have devised a 'second' correction algorithm. Given the way the ionisation rate is extracted from  $B_{n \rightarrow 2}^{exc}$  (as will be explained in section 7.3), a temperature ( $T_e^E$ ) is inferred from the magnitude of  $B_{n \rightarrow 2}^{exc}$ . Higher temperatures lead to a stronger emissivity. Therefore, a non-physical rise in  $B_{n \rightarrow 2}^{exc}$  is accompanied by an increase in the inferred  $T_e^E$  from  $B_{n \rightarrow 2}^{exc}$  —which is against the expectation of a continuously decreasing temperature. Therefore, assuming that the temperature continuously drops, cases where the inferred  $T_e^E$  strongly increases during a density ramp can be filtered out numerically. Again, where appropriate smoothing/fitting is used to make sure that this approach is not affected by measurement noise. Furthermore, there is a limit on how strong the slope in  $T_e^E$  has to be for the result to be filtered. It is important to note is that only the trend of  $T_e^E$  plays a role here and not the magnitude. Furthermore, the corrections are performed for each individual Monte Carlo randomisation. Therefore, they are not influenced by the wide PDF obtained for  $T_e^E$  (as will be shown in section 7.6). Furthermore, it should be noted that the randomisation in the Monte Carlo approach (see section 7.6) is kept constant for a given iteration for all different time points. This means, for instance, that  $n_o/n_e$ , is fixed throughout time and other parameters are some fixed factor (as function of time), specified according to their respective PDFs, times the measured value, enabling the application of both correction algorithms while using the probabilistic analysis approach. Both mentioned correction algorithms are only applied to cases where  $F_{rec} > 0.9$  is achieved for a relatively long duration of the discharge and a relatively large number of chords.

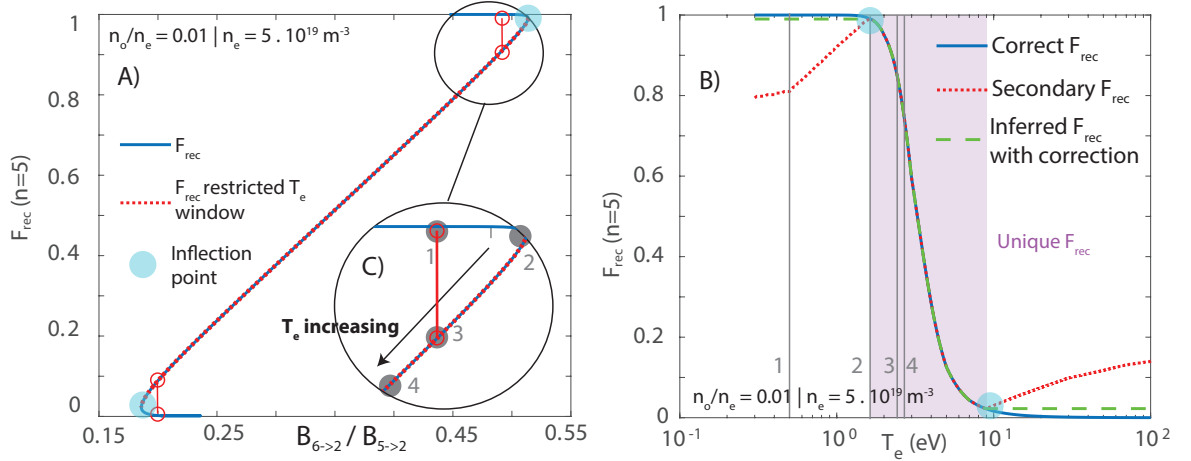


Figure 7.9: An illustration of the technique for obtaining a unique  $F_{rec}$ : a  $F_{rec}(n = 5)$  as function of  $B_{6 \rightarrow 2} / B_{5 \rightarrow 2}$  where two different  $T_e$  windows were used, a 'full' window and a restricted window (' $F_{rec}$  restricted  $T_e$  window') where only unique solutions can be obtained. b Inferred  $F_{rec}(n = 5)$  from the Balmer line ratio showing two solutions for  $F_{rec}$  and a visualisation of the solution provided by the highlighted correction algorithm. c) Magnification of figure a in the  $F_{rec} \sim 1$  non-unique region where four points of  $T_e$  are highlighted, which are represented by the numbered vertical lines in b to link figures a, b and c.

### 7.2.2 $F_{rec}(n)$ and the recombination to ionisation fraction

Apart from table 7.3 indicating rough limits to extracting excitation/recombination emissivities which can be alleviated using the techniques of the previous section; that table has another very important implication. It means that, especially at high densities, a single recombination reaction leads to much more photons than a single ionisation reaction. In various works [115, 3, 61, 79] line ratio techniques are employed to make statements on the 'dominance' of recombination. However, as shown in figure 7.8, the 'dominance' of higher-n Balmer line emission ( $F_{rec}(n = 6, 7) > 0.9$ ) can start to occur at recombination to ionisation rate ratios of  $1 \times 10^{-2}$  to  $1 \times 10^{-1}$ : even if Balmer line emission is dominated by recombination, the ionisation rate can still be much higher than the recombination rate. This is strongly dependent on electron density as indicated in table 7.3; especially in density regimes higher than typical TCV divertor electron densities ( $n_e > 1 \times 10^{20} \text{ m}^{-3}$ ) the higher-n Balmer line emission will be recombination dominated at recombination rates which are much lower than the ionisation rate. Although line ratio techniques can be employed to gauge whether recombination is present and whether the Balmer line emission of a particular transition is dominated by recombination, it does not provide direct information on the magnitude of volumetric recombination and neither information on the 'dominance' of the recombination rate over the ionisation rate. Instead, quantitative calculations are required to infer the magnitude of both the ionisation and recombination rate.

Another implication is that, as illustrated, excitation emission (which is the signature of ionisation) is increasingly more difficult to extract in the presence of some recombination level at higher densities; this requires further investigation and may imply for future devices that other techniques need to be employed to infer the ionisation source, such as using Lyman series measurements [72].

### 7.3 Inferring recombination and ionisation rates

Once  $B_{n \rightarrow 2}^{rec}$  and  $B_{n \rightarrow 2}^{exc}$  are obtained experimentally, both the recombination rate ( $R_L$  in  $\text{m}^{-2} \text{s}^{-1}$ ) and ionisation rate ( $I_L$  in  $\text{ion. m}^{-2} \text{s}^{-1}$ ) integrated along a spectroscopic line of sight can be obtained.

Using the 0D plasma model described in section 7.1, the line integrated recombination rate ( $R_L$ ) can be determined as indicated in equation 7.8 [1]. Given a certain  $\Delta L$  (as determined through the approach in section 7.1.2) and a certain  $n_e$  (as determined through Stark broadening —chapter 5), the modelled  $R_L$  becomes a function of only  $T_e$ . For this, the effective recombination coefficients  $ACD(n_e, T_e)$  from Open-ADAS [134, 138, 135] have been used, which takes both radiative and three-body recombination into account as was explained in section 2.4. Similarly, with those parameters set, the modelled  $B_{n \rightarrow 2}^{rec}$  also becomes a function of only  $T_e$  (equation 7.1). Given a measured  $B_{n \rightarrow 2}^{rec}$ , this means that  $R_L$  can be inferred from the comparison between the modelled  $B_{n \rightarrow 2}^{rec}$  and  $R_L$  as shown in figure 7.10.

$$R_L = \Delta L n_e^2 ACD(n_e, T_e) \quad (7.8)$$

The physical interpretation of this analysis approach is that an electron temperature estimate of the recombinative emission region  $T_e^R$  is obtained by matching the modelled  $B_{n \rightarrow 2}^{rec}$  (given a certain  $\Delta L$  and  $n_e$ ) to the experimental  $B_{n \rightarrow 2}^{rec}$ . As discussed in section 2.4, the hydrogen Balmer line PECs for the recombinative part of the emission are such that lower  $T_e$  lead to higher emission rates. Using  $T_e^R$  and  $n_e$ , the recombinations per Balmer line recombination photon ratio  $\frac{ACD(n_e, T_e^R)}{PEC_{n \rightarrow 2}^{rec}(n_e, T_e^R)}$  are used to 'translate' the experimentally obtained  $B_{n \rightarrow 2}^{rec}$  into the effective line integrated recombination rate  $R_L$ .

As shown in figure 7.10, for a given  $B_{n \rightarrow 2}^{rec}$  a unique solution for  $R_L$  is obtained. Although figure 7.10 shows this example for the  $n = 6$  Balmer line; other Balmer lines provide similar trends. The recombination rate, for a given  $B_{n \rightarrow 2}^{rec}$ , is only weakly dependent on changes in  $n_e$  and  $\Delta L$ , meaning that even large uncertainties in  $n_e$  and  $\Delta L$  would only have a minor influence on the recombination rate. One reason for this is that the temperature dependence of the recombination PEC and the recombination rate (ACD) are relatively similar meaning that even though a small change in temperature leads to both a large change in recombination rate (figures 2.5, 2.6) and a large change in the recombination emissivity (figure 2.8) such that the ratio between the two changes relatively less [63]. Since  $B_{n \rightarrow 2}^{rec}$  is robust to changes in  $n_e, \Delta L$ ; this method can also be expected to be robust to line-integration effects. This is indeed shown by the author in [1] where the influence of a priori density/temperatures on inferring the recombination rate through the 0D model presented in section 7.1 (equation 7.1). This will be further discussed in section 7.7 using a synthetic diagnostic approach on a SOLPS discharge.

Using an analogous approach, the ionisation rate integrated along a spectroscopic line of sight can be obtained from  $B_{n \rightarrow 2}^{exc}$  by using the Stark inferred density and the combined parameter,  $\Delta L \times n_o/n_e$ . First, the line integrated ionisation rate using the 0D model described in section 7.1, is modelled as indicated in equation 7.9 using the effective ionisation coefficient  $SCD(n_e, T_e)$  from Open-ADAS [134, 138, 135] (section 2.4). Using  $n_e$  and  $\Delta L \times n_o/n_e$ , both the modelled  $B_{n \rightarrow 2}^{exc}$  and modelled  $I_L$  becomes functions of only  $T_e$ . Therefore, again, given a measured  $B_{n \rightarrow 2}^{exc}$ , the  $I_L$  can be inferred assuming a certain  $n_e$  and  $\Delta L \times n_o/n_e$  as shown

in figure 7.10. This means, again, that an effective excitation temperature ( $T_e^E$ ) is used as a free parameter for the modelled  $B_{n \rightarrow 2}^{exc}$  to reach the experimentally obtained  $B_{n \rightarrow 2}^{exc}$ ; where higher values for  $T_e^E$  lead to higher emissivities (figure 2.8). Using this  $T_e^E$  and the assumed  $n_e$  the ionisations to Balmer line excitation photon ratio  $\frac{SCD(n_e, T_e^E)}{PEC_{n \rightarrow 2}^{rec}(n_e, T_e^E)}$  is used to 'translate' the experimentally observed  $B_{n \rightarrow 2}^{exc}$  into a line-integrated ionisation rate  $I_L$ . The effective temperatures of the excitation region and recombination region are generally not the same and considering that the spectroscopic line of sight integrates through a plasma profile one would not expect them to be the same. This is further discussed in section 7.3.1.

$$I_L = \Delta L n_o n_e SCD(n_e, T_e) \quad (7.9)$$

Although one can obtain ionisation ratios using this analogous approach, the ionisation rate has a much larger sensitivity to its input parameters than for  $R_L$ , as shown in figure 7.10 B in comparison to figure 7.10 A. From figure 7.10 b it is clear that both the ionisation rate inference is sensitive to both  $n_e$  and the assumed combined parameter  $\Delta L \times n_o$ . These large sensitivities, combined with the fact that the atomic physics coefficients used from ADAS can have strong non-linear scalings, means that a standard uncertainty analysis based on first order Taylor expansions [206, 209] is inadequate for evaluating both the uncertainty and the estimated parameters. Given these larger uncertainties we have developed a probabilistic analysis to extract a more robust measure of both the value and uncertainty of  $I_L$ ,  $R_L$  and other output parameters using a Monte Carlo approach as will be explained in section 7.6.

Line integration effects (section 7.7) lead to larger deviations between the inferred ionisation rate and the 'true' ionisation rate than deviations between the inferred/actual recombination rate due to the larger sensitivity of the ionisation rate determination to other input parameters. In both cases, however, the uncertainty induced by line integration effects remains significantly smaller than the characteristic uncertainty of the quantities itself as will be shown in section 7.7. To minimize the uncertainty in  $I_L$ , the lowest  $n$  Balmer line used in the Balmer line ratio for determining  $F_{rec}(n)$  (which yields the lower  $F_{rec}(n)$  of the two and hence the higher (and more accurate)  $F_{exc}(n)$  of the two) is used to determine  $I_L$ . The highest- $n$  Balmer line used in the Balmer line ratio for determining  $F_{rec}(n)$  (which yields the higher (and more accurate)  $F_{rec}(n)$  of the two) is used to determine  $R_L$ . The results agree within uncertainty when either Balmer line of the Balmer line pair used to determine  $F_{rec}(n)$  is used to determine either  $R_L$  or  $I_L$ . When permutations are performed of different Balmer line ratios, for cases where several Balmer lines have been monitored through diagnostic repeats, the obtained  $R_L$  and  $I_L$  agree within uncertainty. The analysis flow described above provides, in TCV, a poloidal profile of the line-integrated ionisation and recombination rate. Exploiting the full coverage of the DSS lines of sight of the outer divertor leg (figure 5.1), the total volumetric ionisation and recombination rates are obtained (ion, rec / s), by integrating this profile toroidally and poloidally, with uncertainties provided by the probabilistic analysis as was explained in section 7.1 equation 7.3.

### 7.3.1 The excitation and recombination temperatures

As explained above, the analysis of the emission due to excitation and the emission due to recombination yields two different (in the analysis independent) temperatures: the excitation

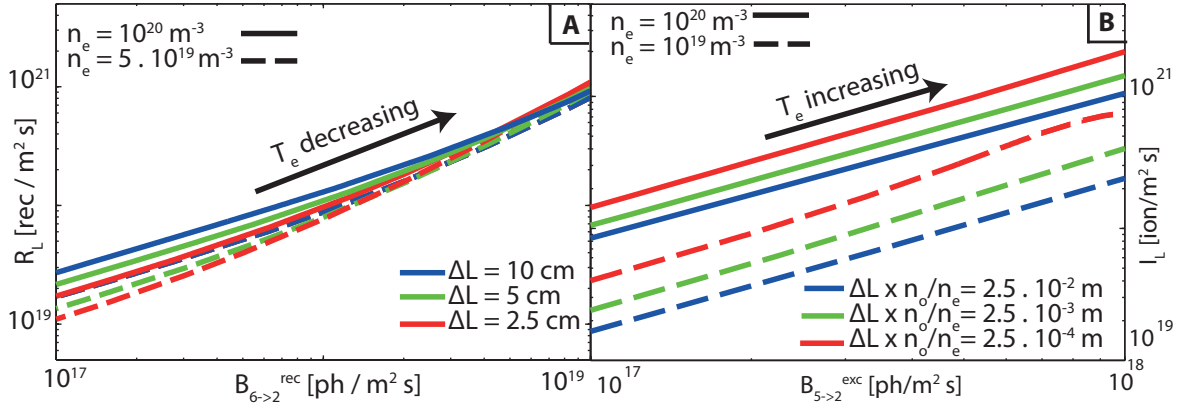


Figure 7.10: a Modelled  $R_L$  as function of  $B_{6 \rightarrow 2}^{rec}$  for a set of  $n_e$  and  $\Delta L$ . b Modelled  $I_L$  as function of  $B_{6 \rightarrow 2}^{exc}$  for a set of  $n_e$  and  $\Delta L \times n_o/n_e$

temperatures inferred from our measurements typically range from 3 eV to 20 eV, whereas the recombination temperatures inferred from our measurements range typically from 0.5 eV to 4 eV.

First we have to ask ourselves the question, is it physical to obtain two different temperatures from the same analysis? Or, more specifically, what is the physical meaning of these temperatures? To answer this question, first we will look at the emission-weighted temperatures given a certain line of sight from a series of SOLPS discharges, which are described in more detail in section 2.6 and literature [7]. The way the synthetic Balmer line emissivities are generated are discussed in 7.7.

In figure 7.3, section 7.1.2, we discussed the emission profile along a line of sight for the  $n = 5, 6, 7$  Balmer lines, and we concluded that the excitation/recombination emission can occur at different positions of the line of sight while excitation/recombination occurs at the same location for each Balmer line. Therefore, the temperature at the excitation/recombination locations is different as is shown in the same figure by the accompanying density/temperature profiles along the line of sight. Using emission profiles along the line of sight (as in figure 7.3), an emission-weighted  $T_e$  and  $n_e$  can be computed for each DSS chord, which is shown in figure 7.11. This shows that the difference between the excitation emission weighted or recombination emission weighted temperature can be up to a factor two, while the difference in the effective density is  $\sim 1 \times 10^{19} \text{ m}^{-3}$ , similar to the expected inference uncertainty (chapter 6). The investigation in figure 7.11 again shows that the temperature of the excitation/recombination region is the same for every Balmer line; but the effective temperature per Balmer line is different as the relative importance of recombination increases with  $n$  (figure 7.11 a). This is an important conclusion for passive Balmer line emission analysis, as it shows that the effective recombination/excitation temperatures are the same for all Balmer lines (neglecting molecular contributions). Therefore, by separating out the excitation and recombination parts of the emission (assuming the separation is not influenced by line integration effects), the analysis becomes more robust to chordal integral effects; this and a comparison between the emission-weighted temperatures and an inferred temperature using a synthetic spectrometer diagnostic approach on SOLPS simulations will be further discussed in section 7.7.

Now that we have established that the Balmer line emission can be written as the excitation part (with an 'excitation' temperature  $T_e^E$ ) and the recombination part (with

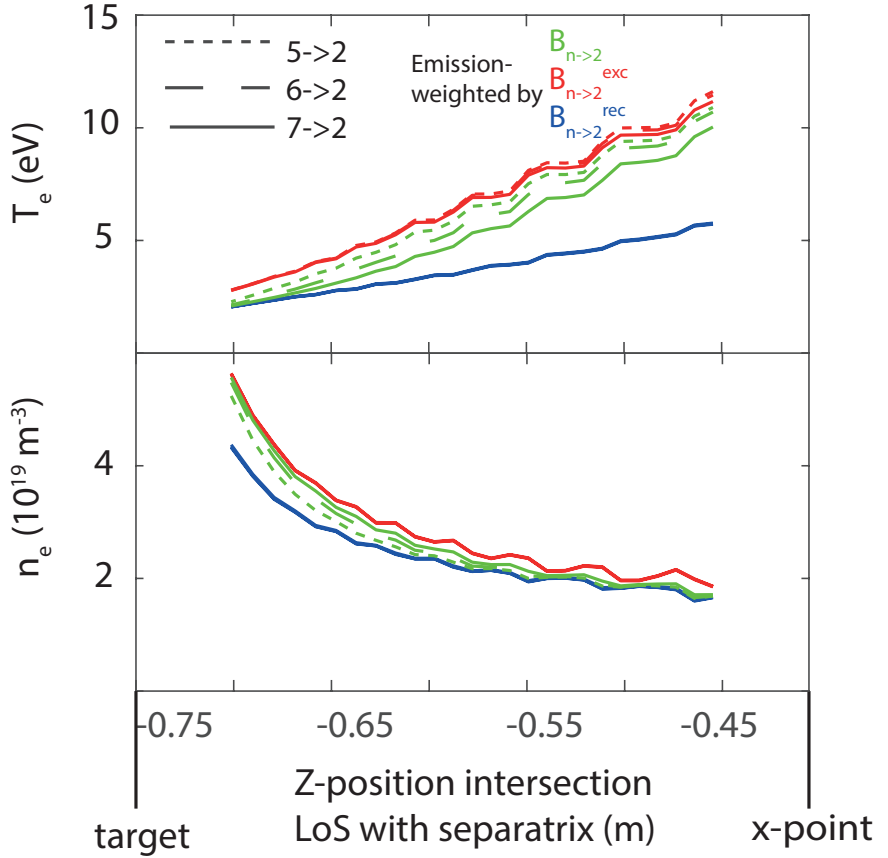


Figure 7.11: a Emission-weighted (recombination/excitation/total), along DSS lines of sight,  $T_e$  profile from target to separatrix. b Emission-weighted (recombination/excitation/total), along DSS lines of sight,  $n_e$  profile from target to separatrix.

a 'recombination' temperature  $T_e^R$ ), we have to go back to the  $F_{rec}$  calculation. Here we implicitly assumed that  $T_e = T_e^E = T_e^R$  to keep the numerical approach as simple as possible. This can be validated, however, using  $T_e^E$  and  $T_e^R$  provided by the full-analysis to compute a self-consistent, post-processed  $F_{rec}$  (equation 7.10).

$$F_{rec}^{consistent}(n) = \frac{PEC_{n \rightarrow 2}^{rec}(n_e, T_e^R)}{PEC_{n \rightarrow 2}^{rec}(n_e, T_e^R) + \frac{n_e}{n_e} PEC_{n \rightarrow 2}^{exc}(n_e, T_e^E)} \quad (7.10)$$

This is performed for discharge # 56567 in figure 7.12 where  $F_{rec}^{consistent}(n)$  was computed using a Monte Carlo approach. When inspecting  $F_{rec}$  as a function of time for a given chord (figure 7.12 a), an agreement within uncertainty is shown while the post-processed  $F_{rec}$  has slightly smaller uncertainties at low  $F_{rec}$  values. The PDF outputs of both techniques for a given chord at three different time steps are compared to provide a more detailed comparison between the two in figure 7.12 b. This shows a slightly wider PDF at  $t = 0.6$  (low  $F_{rec}$ ) for the standard calculation with a spike at 0, which is an after effect of the techniques used for dealing with the non-uniqueness of  $F_{rec}$  at  $F_{rec} \sim 0$  or  $F_{rec} \sim 1$ . Incorporating  $T_e^E$  and  $T_e^R$  into the  $F_{rec}$  determination is another way on dealing with the non-uniqueness of  $F_{rec}$  close to its limiting cases. As such, the agreement between the post-processed  $F_{rec}$  and the estimated  $F_{rec}$  also provide some assurance to the application of the correction algorithms presented in section 7.2.1. For the two later time steps shown, the shapes of the PDFs are likely within the uncertainty of the statistical mapping of Monte Carlo values into a PDF (see section 7.6);

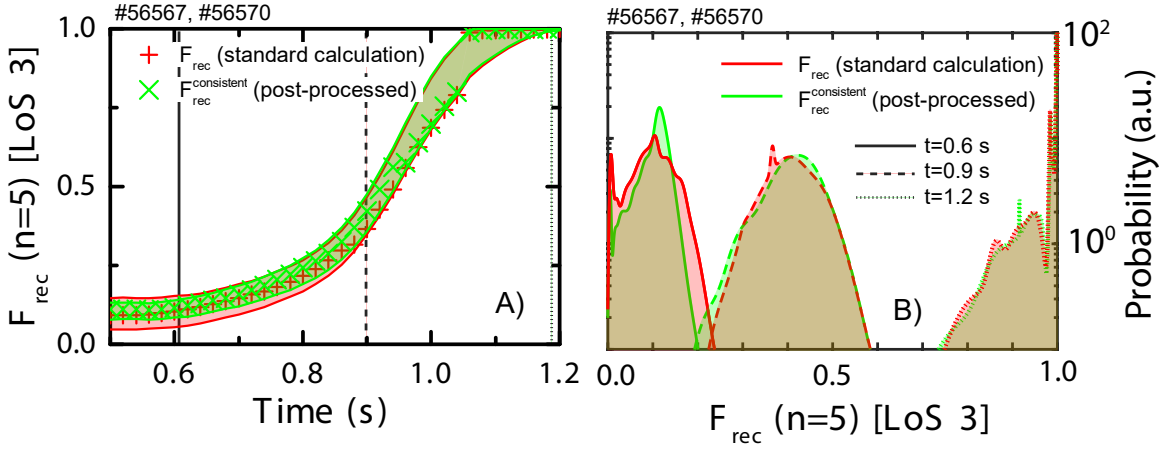


Figure 7.12: a) Both the calculated  $F_{rec}(n = 5)$  and the post-process calculated  $F_{rec}^{consistent}(n = 5)$  using the statistical techniques of section 7.6 as function of time with 68% confidence intervals. b) Visualisation of the probability density function (PDF) of  $F_{rec}(n = 5)$  and  $F_{rec}^{consistent}(n = 5)$  at three different times for a given chord.

meaning that the two are virtually indistinguishable.

## 7.4 Estimating hydrogenic radiative losses

The amount of energy expended for each ionisation is central to our analysis of the role of power balance in the ionisation process. That energy cost includes several to multiple, excitation collisions, where energy is lost due to line radiation as the atom de-excites; power losses which occur before the final ionisation collision (e.g. radiative energy loss) as well as the potential energy it requires to convert a neutral into an ion (at least  $\epsilon = 13.6 \text{ eV}$  [90, 37] —not accounting for the dissociative energy cost of  $D_2$  molecules into  $D$  neutrals).

The local radiated power density due to excitation collisions is modelled using the same 0D plasma slab model presented in section 7.1. Internally, as explained in section 2.4 this is done by modelling the full excitation hydrogen spectra using ADAS, after which it is integrated (in spectral domain) to obtain the ADAS 'PLT' parameter in  $\text{W m}^{-3}$  [134, 138, 135] as function of electron temperature and density (figure 2.9 a). The (excitation) radiated power ( $P_{rad,L}^{H,exc}$  in  $\text{W m}^{-2}$ ) due to excitation given the plasma slab model integrated over a line of sight is then given by equation 7.11. By using the Stark density and an estimate for the combined parameter  $\Delta L \times n_0/n_e$ , again both  $B_{n \rightarrow 2}^{exc}$  and  $P_{rad,L}^{H,exc}$  become only functions of  $T_e$  and thus a measured  $B_{n \rightarrow 2}^{exc}$  can be translated into a value for  $P_{rad,L}^{H,exc}$  using figure 7.13 b. This is analogous to how the ionisation rate was obtained. As such, again, the magnitude of  $B_{n \rightarrow 2}^{exc}$  is used to estimate the temperature, which is used to interrogate the PLT to PEC ratio (e.g. radiated energy per observed excitation photon), with which the measured  $B_{n \rightarrow 2}^{exc}$  is multiplied. This is identical to using equation 7.11 together with the previously obtained  $T_e^E$ .

$$P_{rad,L}^{H,exc} = \Delta L n_0 n_e PLT(n_e, T_e) \quad (7.11)$$

As mentioned, also potential energy is required to convert a neutral into an ion. As such the total power 'cost' due to ionisation along a given line of sight is ( $P_{ion,L} = P_{rad,L}^{H,exc} + \epsilon I_L$ ) as was explained in section 3.1. Note that  $P_{ion,L}$  and  $E_{ion} = \frac{P_{ion,L}}{I_L}$  are always positive and

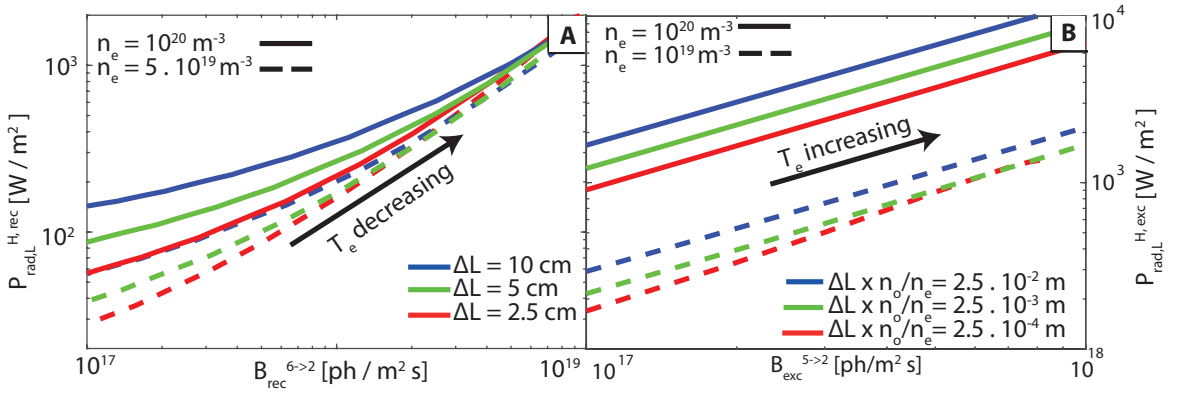


Figure 7.13: a Modelled  $P_{rad,L}^{H,rec}$  as function of  $B_{6\rightarrow 2}^{rec}$  for a set of  $n_e$  and  $\Delta L$ . b Modelled  $P_{rad,L}^{H,exc}$  as function of  $B_{5\rightarrow 2}^{exc}$  for a set of  $n_e$  and  $\Delta L \times n_o/n_e$ .

always indicate an energy loss. Examination of the ADAS cost per ionisation (figure 3.2 section 3.1) reveals that the radiated energy per single ionisation event increases strongly at low temperatures increasing the energy 'cost' per recombination as the plasma cools (figure 2.9 a and 3.2). For TCV conditions (experimental estimates of  $E_{ion}$  are shown in section 9.1.1), the effective  $E_{ion}$  for the total divertor (e.g. averaged over the entire divertor weighted by the ionisation rate) is 25 eV to 30 eV in attached conditions, rising to 40 eV to 50 eV in detached conditions while below the ionisation region in detached conditions  $E_{ion} = 80$  eV to 100 eV can be reached.

Using a similar approach, the radiated loss due to volumetric recombination can be inferred spectroscopically. As explained in section 2.4, radiative loss due to recombination can be modelled using ADAS [138, 135, 134] by first modelling the full recombination spectra and then integrate this (spectrally) to obtain the 'PRB' parameter, which combines various forms of electron-ion recombination (two-body recombination, three-body recombination) and Bremsstrahlung. To separate the hydrogenic Bremsstrahlung component (whose contribution is negligible for recombination-relevant temperatures) from the recombination component, the Bremsstrahlung is modelled using equation 4.25.5 from [30], divided by  $n_e^2$ , and subtracted from the ADAS "PRB" parameter to generate an effective 'PRB' parameter purely due to recombination, which we use when we refer to the 'PRB' parameter (shown in figure 2.9 b). Using the 0D model again introduced in section 7.1, we can model the radiative power loss due to volumetric recombination ( $P_{rad,L}^{H,rec}$  W m<sup>-3</sup>) as shown in equation 7.12. Again, by assuming a value for  $n_e$  (Stark broadening —chapter 6) and  $\Delta L$  (section 7.1.2) both  $P_{rad,L}^{H,rec}$  and  $B_{n\rightarrow 2}^{rec}$  become functions of only  $T_e$ . These are plotted as function of each other in figure 7.13 a and thus a measured value for  $B_{n\rightarrow 2}^{rec}$  can be translated into  $P_{rad,L}^{H,rec}$ ; analogously to how the recombination rate was obtained. Again, this is identical to using equation 7.12 together with the previously obtained  $T_e^R$ .

$$P_{rad,L}^{H,rec} = \Delta L n_e^2 PRB(n_e, T_e) \quad (7.12)$$

When recombination occurs, energy is lost due to radiation, but also the resulting neutrals gain energy since the potential energy of the ion,  $\epsilon$  is released [4, 136] as was highlighted in section 3.1. The total power loss due to recombination ( $P_{rec,L}$ ) can thus be either positive or negative (power loss). For the cases observed in this work (see section 2.4),  $E_{rec} = \frac{P_{rec,L}}{R_L}$  can

range from  $-2\text{ eV}$  to  $2\text{ eV}$  in recombination-relevant conditions (figure 3.4). It shows hence that radiative energy losses and the potential energy gain roughly balance (as shown during the experiment in section 9.1.1 figure 9.1), implying that volumetric recombination can be neglected as an energy source or sink.

## 7.5 Estimating charge exchange rates and charge exchange to ionisation ratios

Similarly to how the ionisation rate and hydrogenic radiation due to excitation is calculated, the charge exchange rate can be estimated using the Open-ADAS 'CCD' parameter [134, 138, 135], which is a function of density and temperature (section 2.4). Using the simplified 0D plasma slab model we have been using continuously in this section, the line integrated charge exchange rate  $CX_L$  in  $\text{reac m}^{-2} \text{ s}^{-1}$  is provided in equation 7.13. Again, analogous to how  $I_L$ ,  $P_{rad,L}^{H,exc}$  were estimated, one can estimate  $CX_L$  using the  $B_{n \rightarrow 2}^{exc}$  line intensity with an estimated  $n_e$ ,  $\Delta L \times n_o/n_e$ , which again is equivalent to using  $T_e^E$ . Implicitly, this is assuming that the region in the line integral where charge exchange reactions occur is the same as the excitation emission region; which seems reasonable considering that charge exchange is an ion-neutral collision and ionisation is an electron-neutral collision (and hydrogen ion/electron densities are identical at the same location assuming local quasi-neutrality and  $Z_{eff} \sim 1$ ). On the other hand, excitation emission drops rapidly as function of temperature while charge exchange reactions can still occur at those temperatures. Figure 7.14 a shows  $CX_L$  as function of  $B_{5 \rightarrow 2}^{exc}$ , from which it is clear that the  $CX_L$  rate is highly insensitive to  $T_e$  (and hence to  $B_{n \rightarrow 2}^{exc}$  once  $\Delta L, n_o/n_e, n_e$  have been fixed), but when  $\Delta L, n_o/n_e, n_e$  is changed,  $CX_L$  changes dramatically. This finding is not surprising since the charge exchange rate (hydrogen) is fairly relatively insensitive (e.g. compared to ionisation/recombination) to the electron temperature as shown in figure 2.5 section 2.4. Hence, the analysis shown here is not appropriate for estimating charge exchange rates and to measure the 'absolute' charge exchange rate, an improved estimate of the neutral fraction is required.

$$CX_L = \Delta L n_o n_e CCD(n_e, T_e)$$

$$\frac{CX_L}{I_L} = \frac{CCD(n_e, T_e)}{SCD(n_e, T_e)} \quad (7.13)$$

However, classically, momentum losses are not related to the absolute charge exchange rate but to the dominance of charge exchange over ionisation [3, 142, 141]. This raises the question, although our charge exchange rate estimate is strongly inaccurate, could we estimate the charge exchange to ionisation ratio? As was discussed previously in section 2.4, the charge exchange to ionisation ratio is strongly sensitive to temperature due to the temperature dependence of the ionisation ratio while the charge exchange reaction rate is relatively unchanged. See, for instance, figure 2.7 where the charge exchange to ionisation ratio was used to interrogate the expected momentum loss using the Self-Ewald model. Using the expression for  $CX_L$ , we can model the  $CX_L/I_L$  ratio (equation 7.13), which only has an explicit  $T_e, n_e$  dependence. Again, using an estimated  $n_e$ ,  $\Delta L$ , both  $B_{n \rightarrow 2}^{H,exc}$  and  $CX_L/I_L$  are only functions of  $T_e$ , which are shown as function of each other in figure 7.14 b, indicating that the  $CX_L/I_L$  ratio is indeed sensitive to changes in  $B_{n \rightarrow 2}^{exc}$  (of a roughly similar magnitude as the  $I_L$  determination). Again,

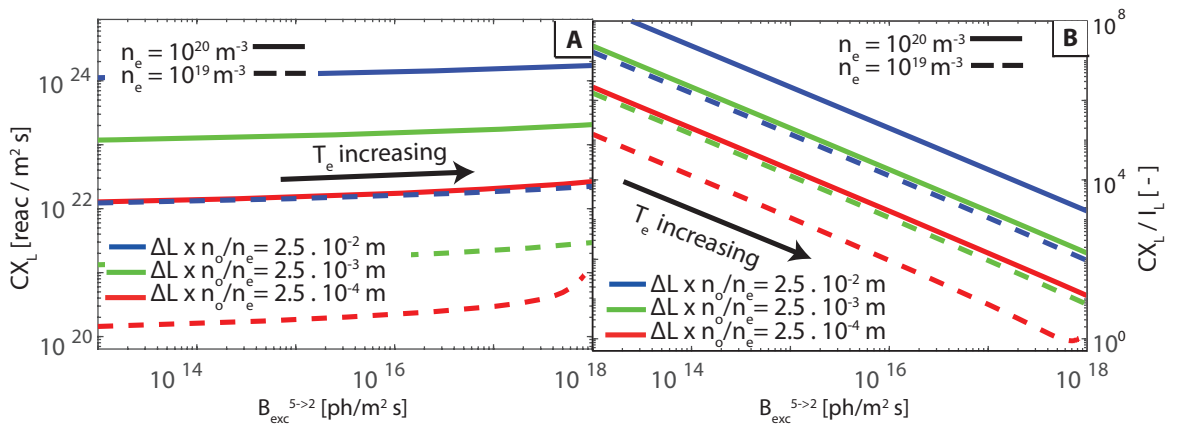


Figure 7.14: a) Modelled  $CX_L$  as function of  $B_{5 \rightarrow 2}^{exc}$  for a set of  $n_e$  and  $\Delta L \times n_o/n_e$ . b) Modelled  $CX_L/I_L$  ratio as function of  $B_{5 \rightarrow 2}^{exc}$  for a set of  $n_e$  and  $\Delta L \times n_o/n_e$

this is identical to using  $T_e^E$  to interrogate equation 7.13. The reason this inference is still sensitive to  $\Delta L \times n_o/n_e$  despite it not appearing in the  $CX_L/I_L$  expression is that  $\Delta L \times n_o/n_e$  still influences the  $T_e^E$  determination from  $B_{n \rightarrow 2}^{exc}$ . Implicitly in this determination, it is again assumed that the excitation/ionisation and charge exchange regions are all at an identical location of the chordal integral through the divertor plasma. This may not be the case for the charge exchange rate, which could also occur partially in the recombinative emission region. This, however, is not expected to be of a major influence as the charge exchange rate is not particularly sensitive to  $T_e$ . One should also note that the margin of uncertainty required on  $CX_L/I_L$  is fairly large. As illustrated when comparing figure 2.7 to figure 2.5, the momentum-loss phase takes place from 2 to 10 eV (e.g.  $f_{mom} = 0.9 \rightarrow 0.15$ ) corresponding to change in  $CX_L/I_L$  of  $\sim 1 \rightarrow 10^3$ ; one thus needs to alter  $CX_L/I_L$  by an order of magnitude to get meaningful changes in the expected momentum loss from charge exchange dominating over  $CX_L$ . How the 'actual' charge exchange to ionisation ratio compares to the inferred ratio is further discussed in section 7.7 through analysing a synthetic spectra given the strategies laid out in this chapter.

## 7.6 Monte-Carlo probabilistic analysis methodology

We have seen that the various inferences can be fairly sensitive input parameters, especially the ionisation rate and that certain input parameters (particularly  $n_o/n_e$  which is not well-known and adopted from modelling giving it an uncertainty margin of multiple orders of magnitude and  $n_e$ ) can have large absolute and/or relative uncertainties. Given this, in combination with the complicated set of analyses and the usage of atomic rate coefficients which can exhibit strongly non-linear behaviour, a 'standard' Taylor-expansion based uncertainty analysis [206, 209] is insufficient to sufficiently quantify the uncertainties in the analysis.

However, uncertainties do not play a role only in determining the uncertainty margin but can also influence the actual inferred parameter, which is not accounted for in 'standard' Taylor-expansion based uncertainty analysis. As a thought experiment we present a case where the analysis exhibits non-linear behaviour (e.g.  $y = x^2$ ) and one quantifies the uncertainty of the input parameter  $x$  through a Gaussian distribution where the peak corresponds to the measured value (e.g.  $x = 3$ ) and the width corresponds to the estimated uncertainty

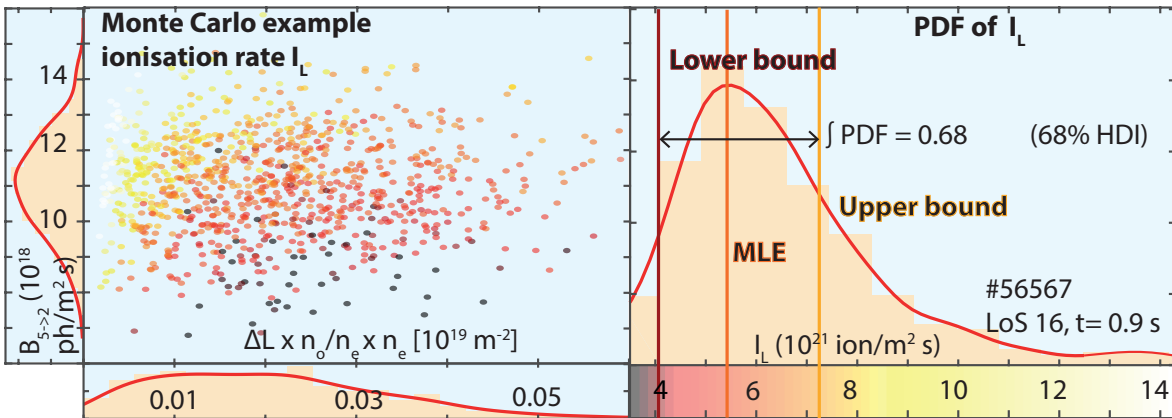


Figure 7.15: Example of Monte Carlo analysis chain, ion source calculation. a) Examples of input PDFs for  $B_{5-2}$  and  $n_o/n_e \times \Delta L$ . Points are randomly sampled from these input PDFs yielding to points in the scatter plot whose colours represent the  $I_L$  corresponding to that calculation. b) Shows a PDF of  $I_L$ , together with the maximum likelihood estimate (MLE) and 68% Highest Density Interval (HDI). X-axis corresponds to  $I_L$  magnitude and its colour bar colours of the scatter plot in figure A.

(e.g.  $\sigma = 1$  — 68 % confidence interval). Using those values, one would expect  $y = 9$  with an uncertainty of 6. Taking the full Gaussian distribution into account and determining the output values, similarly to the approach laid-out in this section for spectroscopic inferences, a probability function is obtained with a certain uncertainty range (2-13 (68 % confidence interval)) and a peak representing the highest probable estimate (6.8). In other words, the highest probable estimate, can drift significantly from the expected value if one were to use the measured value in non-linear cases [210].

We have therefore employed Monte Carlo techniques to obtain both the estimate and its uncertainty from every output parameter highlighted in section 7.1. The benefit of such an approach is that it not only leads to higher certainties on the uncertainty estimate; but it also provides an accurate estimate of the output parameters even when the uncertainties are large and the analysis is non-linear. In addition, the final result becomes less prone to errors in input parameters —as not only the estimated parameter is used for determining the outputs, but some region around this parameter (dictated by their probability functions) is used. The results from the Monte Carlo technique take the form of probability density functions (PDFs), similarly to a full Bayesian approach.

The probabilistic analysis first starts with prescribing a functional form describing the uncertainty of each input parameter in the form of a PDF. That is an important step as the shape of the assumed uncertainty (not just the magnitude) will have some influence on the inferred result. Depending on the input parameter, this ranges from Gaussian (for instance for the Balmer line intensity); to an asymmetric Gaussian (for the path length) to uniform for the neutral fraction ( $n_o/n_e$ ). Table 7.2 indicates an overview for every input parameter characterising their uncertainty in the form of a PDF, while section 7.1.2 provides motivation on the chosen shape of the input PDFs. An investigation on the sensitivity of the assumed input PDF for the neutral fraction is presented in section B.

After the input PDFs are established, random values (at least 5000) are sampled corresponding to the various input PDFs, which are randomised for every input parameter. As

opposed to changing the randomisation for every different time/profile point, the randomisation is kept the same for all lines of sight and time steps. This means that, for instance, if the randomly sampled input value indicates a brightness 10% below the measured brightness, this 10% is used for all time steps and all lines of sight. Keeping the randomisation the same as function of time and space is a necessity enabling the usage for the techniques highlighted in section 7.2.1 in cases where  $F_{rec}$  is close to 0 or 1 —which are employed to each individual randomisation. Apart from that, assuming these systematic shifts is also realistic as many of the uncertainties have a systematic nature as opposed to a random nature (for instance uncertainties in the line intensity and line ratio are dominated by uncertainties in the calibration and not random noise). For each randomisation separately, the toroidally integrated quantities (highlighted in 7.1) are obtained. For simplicity a simplified PDF for  $n_e$  (which is an input in this analysis), based on the full and complex analysis in section 6.4 is chosen instead of a Monte-Carlo result, such as presented in figure 6.7.

An example of the probabilistic analysis is shown in Figure 7.15 for the line-integrated ionisation source  $I_L$ . The main parameters driving the uncertainty in the ionisation rate ( $I_L$ ) (at a given time, for a given chord) are the uncertainties in the brightness as well as in  $\Delta L \times n_e \times n_o/n_e$  shown in figure 7.15a. Other uncertainties, such as the uncertainty in the line ratio and electron density also contribute, but to a lesser extent for this particular case. The scatter plot of figure 7.15a shows the randomly sampled values of the distributions of  $\Delta L \times n_o/n_e \times n_e$  and  $B_{5 \rightarrow 2}$  from their uncertainty PDFs which are shown as PDFs respectively below and to the left of the main figure. A ‘kernel density estimate’, a statistical non-parametric technique for providing smooth estimates for probability density functions from a distribution of values —such as obtained from the Monte Carlo output (figure 7.15 a), is employed to convert the analysis outputs into a PDF using an adaptive kernel density estimation algorithm from [211]. The colour of each point in the scatter plot (Figure 7.15a) corresponds to an ionisation rate given in the colour bar below the resultant PDF of the ionisation rate of Figure 7.15b.

An example of the adaptive kernel density estimation algorithm from [211], where the PDF is compared to a histogram and a point cloud plot is shown in figure 7.16 for  $T_e^E$ . Kernel density estimates aim to represent the histogram, but instead provide a smooth and continuous function for the histogram. This is done by assuming a certain bandwidth and applying a normalised Gaussian with a width corresponding to this bandwidth to each individual data point (whose integral is  $1/N$  where  $N$  is the number of measured points). The sum of all of these Gaussians provides the kernel density estimated PDF whose integral is one. Adaptive kernel density estimators can alter the bandwidth for each data point. This is particularly effective for reproducing asymptotic PDFs and reducing boundary bias (e.g. cutting-off the PDF after points no longer occur) [211]. However, there is still some boundary bias present as shown in figure 7.16.

We apply analysis techniques adopted from Bayesian analysis [209, 212] to extract information from the resultant output PDFs. The uncertainty of the estimate is given by the shortest interval whose integral corresponds to a requested uncertainty range; commonly referred to in literature as the ”Highest Density Interval (HDI)” [209, 212]. In this work, all confidence intervals present 68 % confidence margins (unless otherwise stated) and are presented by a lower and upper bound. For unimodal PDFs (which most of the PDFs obtained in this work

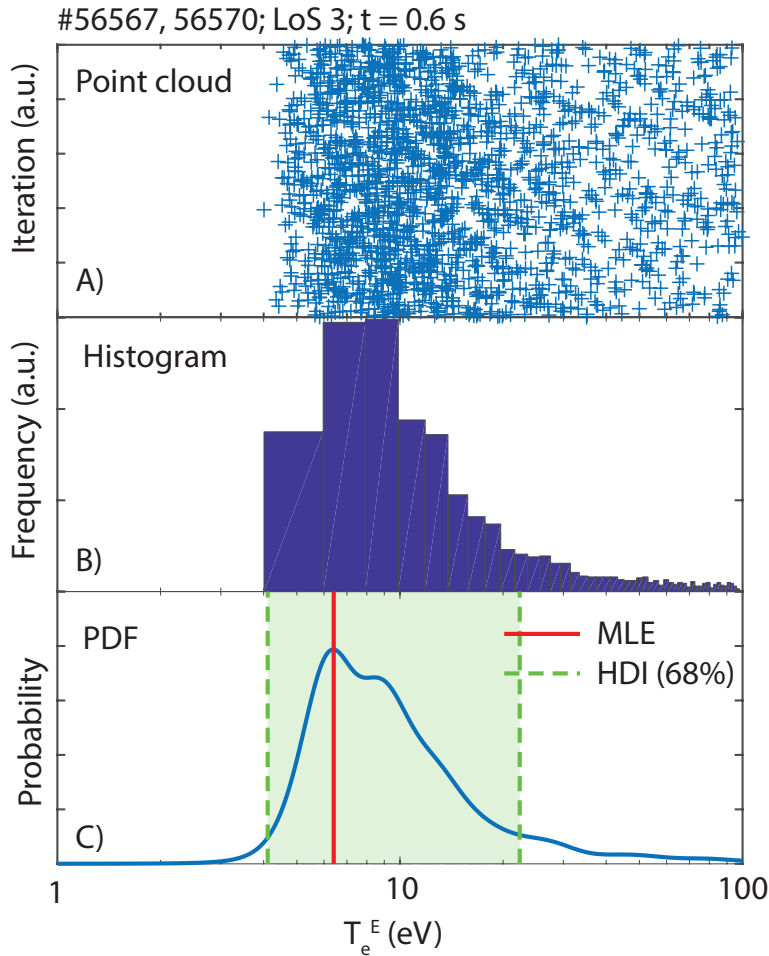


Figure 7.16: Monte Carlo  $T_e^E$  result for # 56567 (line of sight 3;  $t = 0.6$  s) represented as a) Point cloud. b) Histogram. c) PDF obtained through kernel density estimation [211] together with the MLE and 68 % HDI estimates.

are —figure 7.17) this interval also contains the maximum likelihood (MLE —peak of PDF) of the PDF [209, 212]. We use this MLE as the estimate of our result parameter, since that is the value has the highest probability to occur. It should be noted, however, that there also exist other techniques to extract information from PDFs [209], such as using an equal-tailed uncertainty margin and using the median as the estimate of the result; which would lead to (small) differences in the presented results.

Figure 7.17 presents an overview of characteristic output PDFs of the Balmer line analysis, obtained for # 56567 (a discharge which will be discussed in section 8) at three different time points —representing the attached (0.5 s), detachment onset (1.0 s) and detached phase (1.2 s). Note that this does not contain the Stark inferred  $n_e$  PDF, which was discussed in detail in section 6.4. The magnitude of the uncertainty and its asymmetry for the various analysis results can vary strongly during a single (density ramp) discharge. The PDF of output parameters, however, remains unimodal except for  $F_{rec}$ , which is most likely due to the techniques presented in 7.2.1. However, this does not influence the presented analysis results as  $F_{rec}$  is an intermediate parameter.

Deeper statistical sensitivity studies have been carried out in appendix B in order to investigate: 1) the sensitivity of the analysis to uncertainties in the atomic rate coefficients

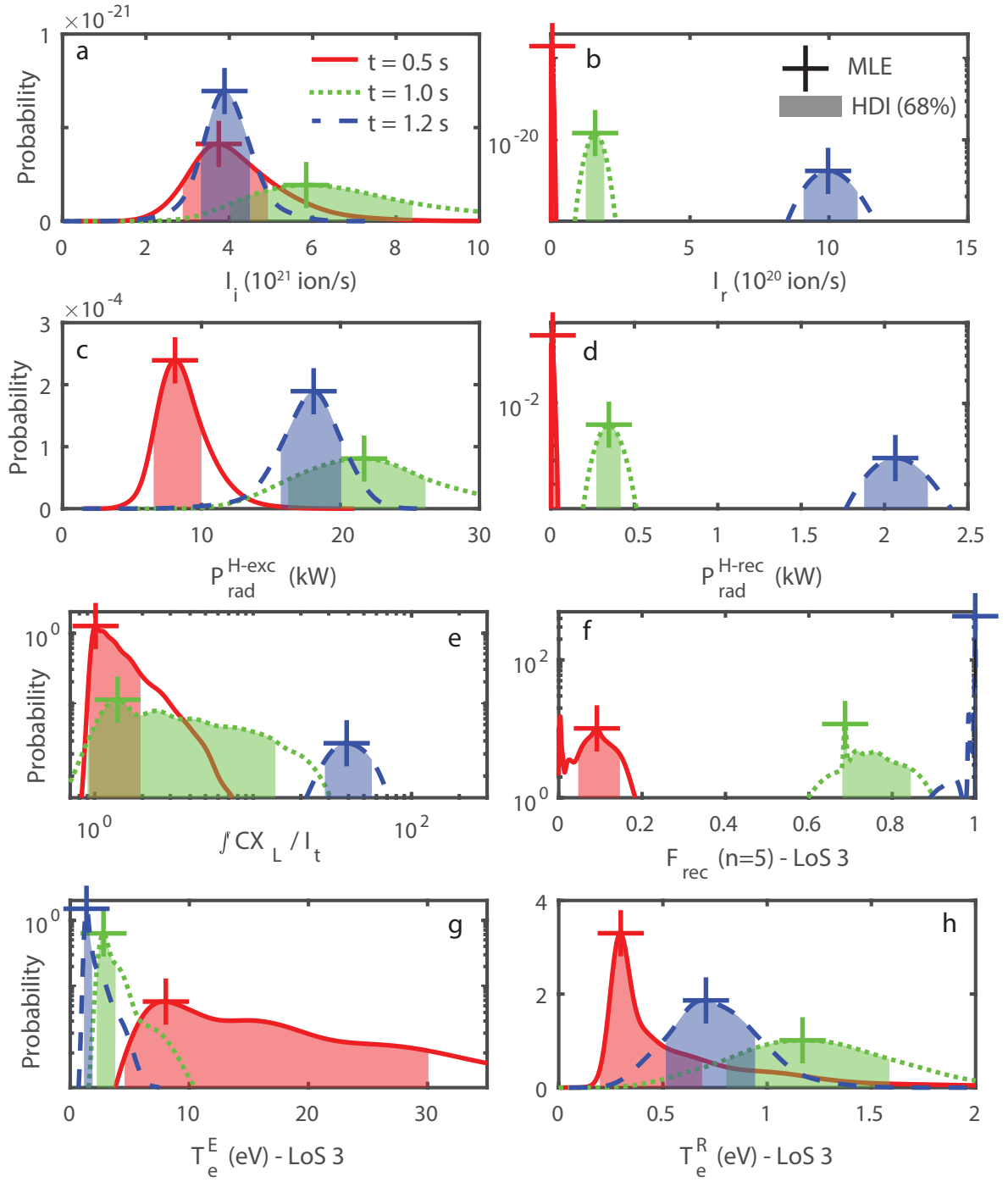


Figure 7.17: Characteristic PDFs from output parameters ( $I_i, I_r, P_{\text{rad}}^{\text{H-exc}}, P_{\text{rad}}^{\text{H-rec}}, \int CX_L / I_t, F_{\text{rec}}(n = 5)$  (line of sight 3),  $T_e^E, T_e^R$  (both line of sight 3)) obtained from #56567 at three different time steps, together with the maximum likelihood estimate (MLE - +) and the highest density interval (HDI - 68 % —shaded).

provided by ADAS; 2) the sensitivity of the analysis using a log-uniform as opposed to uniform neutral fraction input PDF; 3) a correlation study on the sensitivity of the analysis uncertainty on the uncertainties of the various input parameters.

## 7.7 Applying a synthetic diagnostic to SOLPS simulations and investigating line integration effects

As mentioned previously, various assumptions are made to obtain the local (density/temperature) and line-integrated quantities (ionisation rates/recombination rates/charge exchange rates/radiated hydrogenic power) from the analysis chain presented in this section. This section aims at verifying the analysis approach by using SOLPS simulations (see sections 2.6, 8.1.1), respective of a density ramp [7] to model the Balmer line emission obtained by a synthetic spectrometer (with the same lines of sight as the DSS —see section 5.8). The corresponding MDS+ shot numbers are shown in Figure 7.18. The synthetic spectra are then analysed identically to how the experimental data is analysed using the approach in this chapter. By comparing the inferred parameters from the synthetic spectra with the parameters directly obtained from the SOLPS model, the analysis approach has been validated. The SOLPS simulations used here include chemical carbon sputtering to reach realistic carbon concentrations in the divertor (which have been verified with the experiment using the absolute CIII (465 nm) brightness through a synthetic diagnostic approach). Puffing/pumping is performed to reach the required upstream density in the situation as opposed to using a density boundary.

Before moving on to actually comparing the inferred output parameters through the synthetic diagnostic with the direct output parameters directly from SOLPS, the reader should note that many individual parts/assumptions of the analysis were already verified previously in this chapter against SOLPS. Assumptions based on the neutral fraction have already been verified in section 7.1.2; assumptions on the validity of using a different excitation and recombination temperature have already been verified in sections 7.3.1 and 7.1.2; and the validity of the path length  $\Delta L$  has been verified in 7.1.2. The validity of assuming  $Z_{eff} = 1$  has been investigated and verified by the author in [1] using  $Z_{eff}$  estimates from the measured plasma conductivity, showing that (combined with fractional abundance modelling through ADAS using carbon and boron as the main plasma impurity species), 60 to 100 % of  $n_e$  is provided by hydrogen ions. Accounting for this leads to negligible changes in  $F_{rec}, R_L, I_L$  and to small changes in  $T_e^R$ ; which are all significantly smaller than the estimated uncertainty in those parameters. All of these assumptions are tested in this synthetic diagnostic approach.

Apart from a synthetic diagnostic approach using SOLPS simulations, also a more simplified approach has been performed where a priori Gaussian  $n_e \times T_e$  profile was chosen with a fixed width, a peak temperature of 4 eV and a peak density of  $5 \times 10^{19} \text{ m}^{-3}$  while a flat neutral density profile of  $1 \times 10^{18} \text{ m}^{-3}$  was assumed. An additional Gaussian profile of either  $n_e$  or  $T_e$  was assumed where the width was varied and the resulting profile shape of the other quantity was computed using the assumed electron pressure profile. The Balmer line emissivity and Stark line shape profile (assuming  $T_i = T_e$  for the Gaussian part —see chapter 6) was generated similarly to the synthetic diagnostic case using SOLPS below while assuming  $Z_{eff} = 1$  and  $\Delta L$  was estimated to be the FWHM of the  $n_e T_e^{1/2}$  profile as  $\Gamma_t \propto p_t T_t^{-1/2}$  (equation 1.1). That investigation, which is partially presented by the author in [1], has indicated that the local inferred parameters are in adequate agreement with the emission-weighted averaged parameters; while a significant deviation between the peak  $n_e, T_e$  and the inferred local parameters (e.g. density, temperature) can occur, depending on the situation.

The inferred integrated parameters were in agreement with the actual integrated parameters (e.g. ionisation source, recombination sink, etc.) within the expected characteristic uncertainty. The SOLPS approach highlighted below serves as a more detailed investigation, which uses a physics model to generate the various  $n_e$ ,  $T_e$ ,  $n_o$  profiles along the lines of sight instead of an assumed a priori profile and properly accounts for the influence of  $T_i$  (through Doppler broadening) and  $n_H^+$  (as  $Z_{eff} \neq 1$  in the SOLPS simulation due to the presence of carbon impurities).

**Methodology** Using the simulated hydrogen ion density; hydrogen neutral density; electron density; electron temperature and ion temperature, a synthetic Balmer line spectra in terms of  $\text{ph m}^{-2} \text{sr}^{-1} \text{s}^{-1} \text{pix}^{-1}$  (identically to the measured data) is obtained using the techniques from section 5.8 and 4.3. The synthetic line shape includes the instrumental function using the default parametrised Stehle Stark line shape model while not accounting for Zeeman splitting (chapter 6). For simplicity, the SOLPS grid cells corresponding to the inner strike point have been omitted to prevent pollution of the synthetic spectra originating from the inner strike point. Atomic tables used in the synthetic (and experimental) analysis from Open-ADAS are used to determine all atomic rates (ionisation, recombination, etc.) using the simulated parameters to avoid any discrepancy between the atomic tables used in the synthetic analysis and the simulation.

This synthetic spectrum is treated identically to the experimental data and first the various Balmer line shapes are fitted using the experimental technique (see chapter 6), yielding both the Stark broadening electron density estimate and the Balmer line intensity. The obtained  $n = 6$  to  $n = 5$  Balmer line ratio and Balmer line intensities are then fed into the experimental analysis together with the Stark density inferred for the  $n = 7$  Balmer line (analogous to the technique used for # 56567, which will be analysed in detail in chapter 8). An estimate for the path length ( $\Delta L$ ) is obtained analogous to the experiment from the simulation's ion target flux profile and flux surfaces (section 7.1.2). The same uniform range for  $n_o/n_e$  is assumed as is used for the experiments. Also the same uncertainties assumed for the experiment are applied to the synthetic data. This provides all the input information required for the analysis as illustrated in table 7.2. As the 'resolution' of the upstream density scan of the SOLPS runs is fairly limited (e.g. five separate simulations of which the last two reach higher upstream densities than the experiment), the techniques for 'correcting'  $F_{rec}$  near its applicability limit (section 7.2.1) have not been employed as they require a smooth evolution of the temperature.

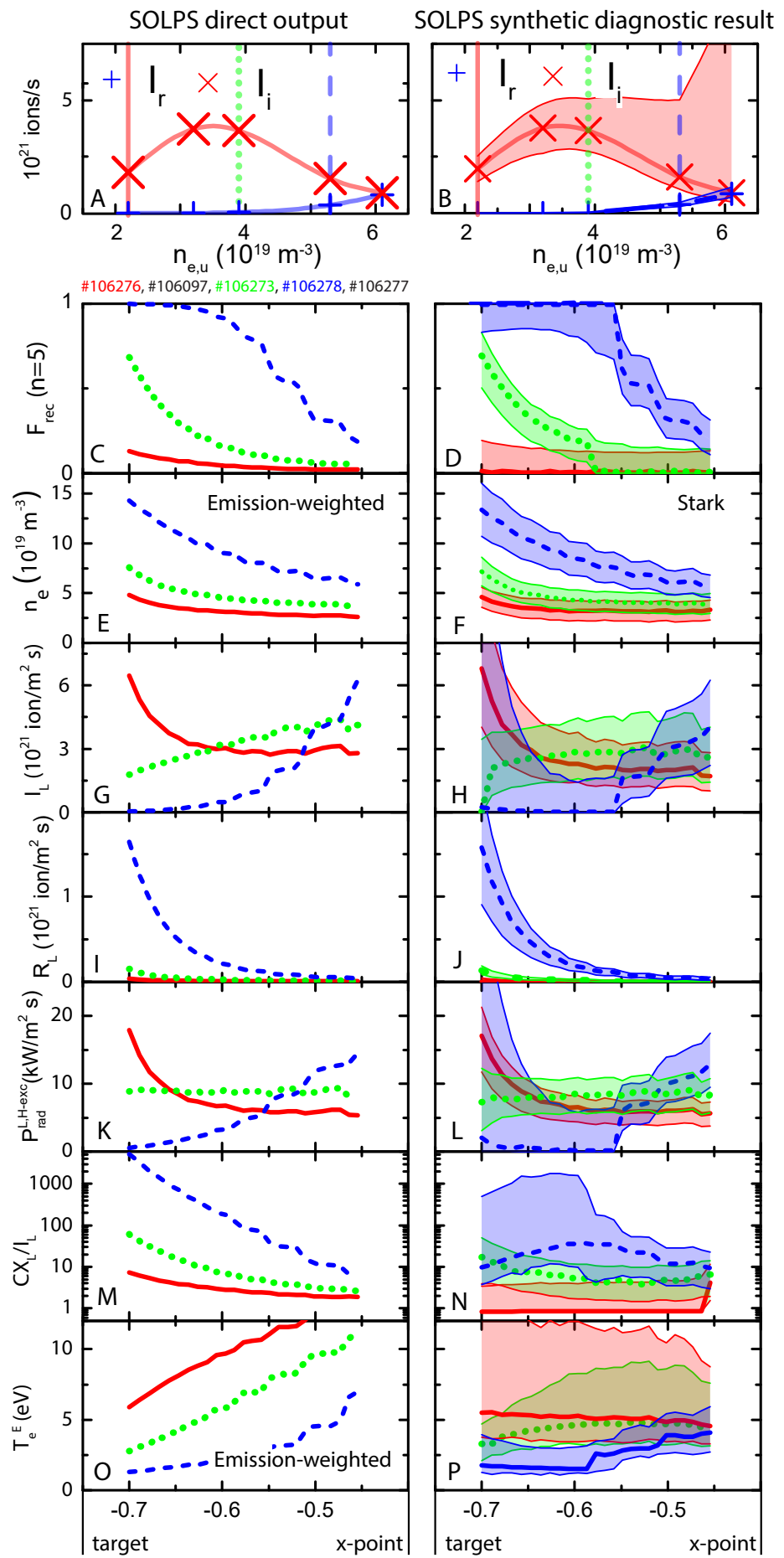
**Results** After utilising the full analysis presented in this section, including the statistical analysis, estimates of  $F_{rec}(n = 5)$ ,  $I_L$ ,  $R_L$ ,  $P_{rad,L}^{H-exc}$ ,  $CX_L/I_L$  and  $T_e^E$  with 68% uncertainty margins are obtained along the outer divertor leg as shown in Figure 7.18. The  $I_L$  and  $R_L$  profiles are then used to obtain the total ion source  $I_i$  and total ion sink (recombination)  $I_r$  in the outer divertor. These are compared with the direct SOLPS solution by summing the ionisation/recombination rates of every divertor grid cell caught in between the two outer spectroscopic lines of sight. The obtained  $I_i$  and  $I_r$  from the synthetic diagnostic are in good agreement with the direct result from SOLPS (< 5% deviation) (7.18 a,b) throughout the density ramp. Below the figure with  $I_i$  and  $I_r$  (Figure 7.18) are profiles of various analysis output parameters for three different simulations, whose upstream densities are indicated by

the vertical lines in Figure 7.18 a,b. Good agreement between the synthetic diagnostic with direct SOLPS results for is found all line integrated parameters ( $F_{rec}(n = 5)$  7.18 C,D);  $I_L$  7.18 G,H);  $R_L$  7.18 I,J);  $P_{L,rad}^{H,exc}$  7.18 K,L)) except the charge exchange to ionisation ratio ( $CX_L/I_L$  7.18 M,N)). The deviation of the  $CX_L/I_L$  ratio occurs when  $F_{rec} \sim 1$  while the corrections of  $F_{rec}$  could not be applied. This is also the reason why the ionisation source starts to be overestimated (as predicted in section 7.2.1), leading to a strong rise in the upper uncertainty boundary of  $I_L$  and  $I_i$  at the highest upstream density close to the target (figure 7.18 h). Again, it should be said that at those highest upstream densities, the SOLPS simulations are more 'detached' and has higher recombination rates/recombinative emission than the experiment, which disrupts at a lower upstream density (around  $4 \times 10^{19} \text{ m}^{-3}$  assuming a linear trend see figure 8.1 and the accompanying discussion). Due to this and to having no correction for  $F_{rec} \sim 1$ , the uncertainties shown in figure 7.18 are larger than the uncertainties obtained for the experiment (figure 8.3).

We have also used the SOLPS model of TCV plasmas to examine the interpretation of local (e.g. 'slab') quantities inferred from chordal integrated emissivities through passive spectroscopy by comparing them to the emission-weighted averaged quantities over the DSS chords along the SOLPS grid using the same techniques as in section 4.3. An adequate agreement between the Stark density (from the synthetic diagnostic) and the emission-weighted  $n_e$  is shown (Fig. 7.18 e,f), indicating that the Stark density can be interpreted as the 'respective density' of the emission region. There is qualitative agreement (variation with upstream conditions) between the inferred  $T_e^E$  from the synthetic diagnostic and the  $T_e$  respective of the excitation emission region of the  $5 \rightarrow 2$  Balmer line. The reason for poor quantitative agreement is the reduced sensitivity of  $T_e^E$  at larger  $T_e$  as the magnitude of the excitation emission (e.g. the PECs) become relatively more insensitive to the electron temperature as shown in figure 2.8. This is also apparent from the wide PDFs obtained for  $T_e^E$  at such temperatures (see figure 7.17g at 0.5 s), which also implies that the  $T_e^E$  result is not well localised (e.g. there is not really a single  $T_e^E$  likely at such temperatures—but an entire range of  $T_e^E$ ).

In summary, we find that although several assumptions are made in the analysis, the deviation of the analysis results due to these assumptions is negligible compared to the uncertainty of the inferred results given the analysis. Hence, the analysis appears to be robust against line integration effects and assumptions regarding  $Z_{eff}$ . One of the reasons why the analysis chain presented is robust against line integration effects is that the Balmer line emission due to recombination and excitation is separated and that a separate temperature is assigned to the recombination/excitation regions. By doing so, the emission coming from the locations where excitation and recombination occurs is separated, alleviating issues due to line integration effects.

Figure 7.18: Characteristic PDFs from output parameters ( $I_i, I_r, P_{rad}^{H,exc}, P_{rad}^{H,rec}, CX_L/I_i, F_{rec}(n = 5)$  (line of sight 3),  $T_e^E, T_e^R$  (both line of sight 3)) obtained from #56567 at three different time steps, together with the maximum likelihood estimate (MLE - +) and the highest density interval (HDI - 68 % - shaded).



# Chapter 8

## The physics of detachment and its dynamics on TCV

*The ion target flux on TCV is in agreement with the measured ionisation source rate: TCV is in high-recycling conditions in the sense that the ion target flux is predominately generated by divertor ionisation. The reduction of the ion source during detachment is directly responsible for the ion current roll-over while recombination is only a secondary effect on TCV. When the ion current rolls-over, the ionisation peak leaves the target and moves towards the x-point while both recombination and density remain peaked near the target, leading to elevated charge exchange to ionisation ratios near the target, giving rise to momentum losses. The ion source reduction occurs when the power entering the recycling region becomes limited for ionisation.*

*All of these observations are in quantitative agreement with both SOLPS simulations and analytic models introduced in chapter 3.*

First, the general detachment characteristics on TCV are discussed and compared to observations from other machines, including a quantitative description of the evolution of the impurity radiation, ionisation and recombination regions along the divertor leg, which is in fair quantitative agreement with SOLPS simulations (section 8.1). After discussing these dynamics based on profiles in the divertor, we integrate these profiles to obtain the total ionisation source/recombination sink which are discussed and compared to the ion current (section 8.2), together with a discussion on  $D\alpha$  emission which is indicative of the presence of molecular activated recombination (MAR). This investigation shows that the ion current roll-over is concurrent with a roll-over in ion source, which is further investigated by looking at the power balance in the divertor (section 8.3).

Parts of this chapter have been adopted from: *An improved understanding of the roles of atomic processes and power balance in target ion current loss during detachment*, by K. Verhaegh, B. Lipschultz, B.P. Duval, et al., to be submitted. DOI:  
<https://doi.org/10.13140/RG.2.2.24292.48005/1>

### 8.1 General detachment characteristics on TCV

As explained in section 2.3, detachment is often studied through a density ramp, where the core density is increased continuously, or an impurity seeding ramp; where at some point the

detached state is entered.

As a reference to the general detachment characteristics on TCV, we will discuss these dynamics during a density ramp experiment (# 56567), where feedback control of the  $D_2$  fuelling is used to obtain a linear increase of the line averaged core density  $\bar{n}_e$ , measured by a vertical FIR interferometer chord (section 4.2.5). This discharge is an L-mode discharge without external heating and is performed in reversed field (e.g.  $\nabla B$  in the unfavourable direction) to stay out of H-mode. To keep the same field line helicity, both the  $B_t$  direction and  $I_p$  direction were reversed. The equilibrium of the discharge together with the DSS viewing geometry is shown in figure 4.2 a. The line averaged density ( $\bar{n}_e$ ) is increased until the plasma disrupts at  $t = 1.25$  s, achieving a maximum Greenwald fractions of  $\sim 0.65$  (figure 8.1 a). Both the total ion target flux integrated across the divertor target,  $I_t$  in  $ion/s$ , and the target ion flux density at the separatrix ( $\Gamma_t$  in  $ion/m^2s$ ) (Figure 8.1 b) initially increase linearly with both the line-averaged and separatrix density,  $n_{e,u}$  (Figure 8.1 a). At  $\sim 0.85$  s,  $\Gamma_t$  starts to roll-over while  $I_t$  starts to deviate from its linear trend. As this linear trend is respective of attached conditions on TCV (more information is provided in section 9.2), we use that deviation to define the onset of the process of detachment. For the case presented, this point corresponds to the roll-over of the ion target flux at the separatrix (figure 8.1 b), but that observation may not be general [101]. Later, we will show that this point is in accordance with the peak in the ionisation profile along the outer leg lifting off the target and is in accordance with detachment onset predictions (section 9.2), which were derived previously in section 3.3. Note that the  $I_t$  roll-over (negative slope in  $I_t$ ) can occur after the point where  $I_t$  starts to deviate from its linear trend. This separation between the deviation and roll-over times can vary from one discharge to another as shown in figure 8.4. At the time when the total ion target flux rolls-over, the upstream temperature is observed to drop rapidly while the upstream density saturates (figure 8.1); indicative of an upstream pressure drop. The upstream pressure drop will be compared to momentum loss estimates and the minimum required target pressure drop (as explained in section 3.3) in section 9.2.

The linear scaling of  $I_t$  and  $\Gamma_t$  with the upstream/core density for attached plasmas was observed for all the density ramp studies at TCV [58, 45, 101, 1, 79]. This contrasts the  $\Gamma_t \propto n_{e,u}^2$  scaling observed in other tokamaks [115, 37, 33]. Further analysis in section 9.2, using the models presented in section 3.3 and 3.1, will show this linear increase of  $I_t$  and  $\Gamma_t$  is expected from both power/particle balance and from power/particle/momentum balance where the reduction of upstream temperature and increase in divertor radiation, observed experimentally throughout the density ramp, is considered. To quantify the loss of target ion current for this study we determine a linear, in upstream density and thus time, fit to the ion target current during the attached phase and extrapolate into the detached phase. The ‘ $I_t$  loss’ is then the difference from this to the measured ion target current,  $I_t$  (see Figure 8.1).

Although spectroscopic signatures of recombination start to appear just before the ion target flux roll-over, the  $I_t$  loss is significantly larger than the total recombination sink integrated over the entire outer leg (Figure 8.1 b), indicating that the recombination sink alone is insufficient (at least by a factor three) to fully explain the  $I_t$  roll-over. This observation is general on TCV (as shown by the author in [1] and shown in section 8.2) and has also been observed under higher density conditions in Alcator C-Mod [51] as well as under  $N_2$  seeded conditions in JET [72].

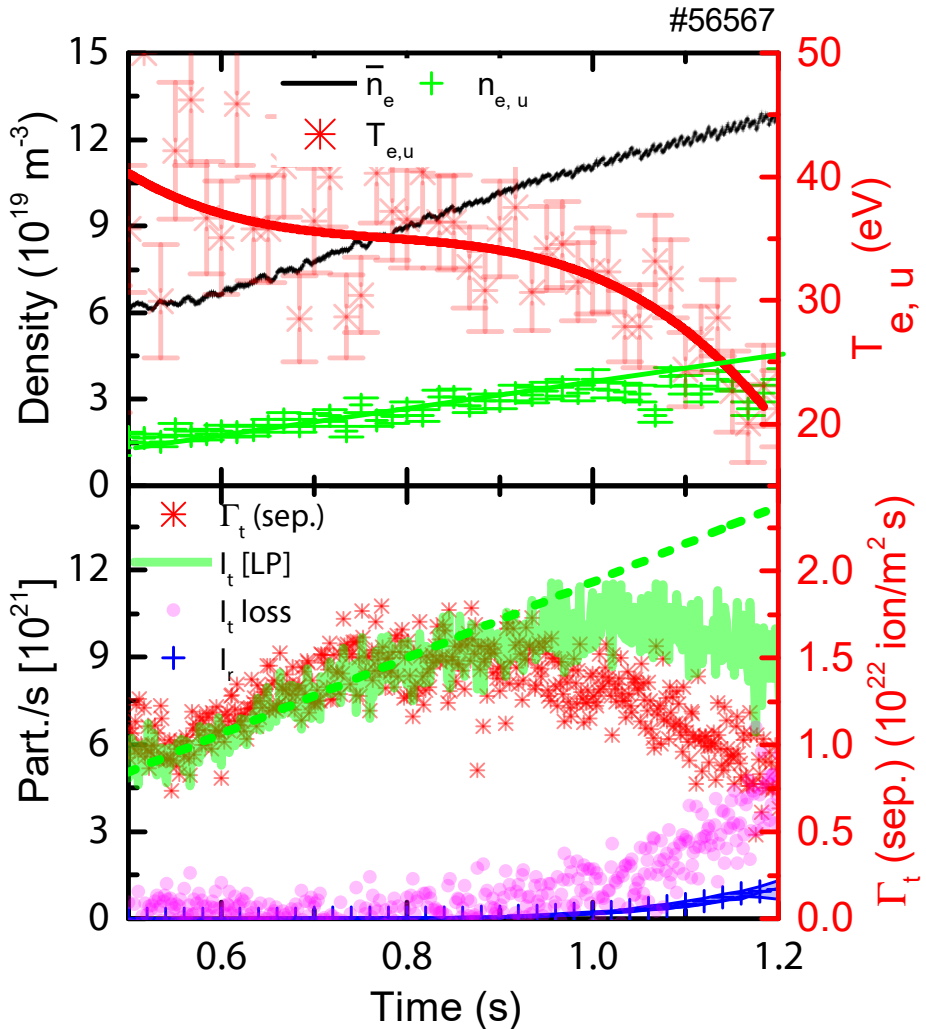


Figure 8.1: Overview of detachment based on a high  $I_p$  density ramp discharge (#56567). a Line averaged density,  $\bar{n}_e$ , upstream density  $n_{e,u}$  and upstream temperature,  $T_{e,u}$  as function of time. b Total ion target flux ( $I_t$ ), ion target flux density at the separatrix ( $\Gamma_t$ ), recombination rate ( $I_r$ ) and  $I_t$  loss rate as function of time.

### 8.1.1 Experimentally observed TCV detachment dynamics with a comparison to SOLPS results

During the periods before, during and after the target ion current roll over ( $\sim 1$  s) the poloidal profiles of several plasma parameters along the outer divertor leg vary, as was indicated by the cartoon in figure 2.2. Instead of a cartoon, various of these reaction rates / parameters are measured and shown in figure 8.3e, g, i at the times indicated by the vertical lines of Figure 8.3a. In figure 8.3d, f, h, j we display the plasma dynamics for a series of SOLPS simulations [7] that are representative of a density ramp obtained by performing multiple simulations for a range of upstream densities, which are reached by varying the gas puffing in the code for this particular run.

Before detachment, the density along the divertor leg (Figure 8.3c), the radiated power (Figure 8.3g –  $P_{rad,L}$ ) and the ionisation rate (Figure 8.3e –  $R_L$ ) are all spread-out along the entire outer divertor leg while their peak is near the target. Increasing  $\bar{n}_e$  and  $n_{e,u}$  further

generates a gradual shift in the radiated power peak towards the x-point (concurrent with the observation of the CIII front leaving the target [79, 101]), followed by a displacement of the peak in the ionisation region (Figure 8.3e –  $I_L$ ). The process of detachment starts to occur when the ionisation peak 'detaches' from the target, corresponding to a flattening of the measured ion target current ( $\sim 0.83$  s Figure 8.3a). As the ionisation moves away from the target, a region where charge exchange dominates over ionisation is left behind (Figure 8.3i), eventually extending over a region up to  $\sim 20$  cm from the target. During the entire detached phase, both the Stark density and recombination rate continue to increase along the entire divertor leg whilst their peaks remain near the target (Figure 8.3c and 8.3e) where the lowest DSS measurement chord is  $\sim 5$  cm above the target surface. At the highest core density, recombination dominates over ionisation only over a small region ( $< 10$  cm) close to the target (Figure 8.3e). The development of detachment on TCV, illustrated by the profiles in Figure 8.3, is generally observed in TCV.

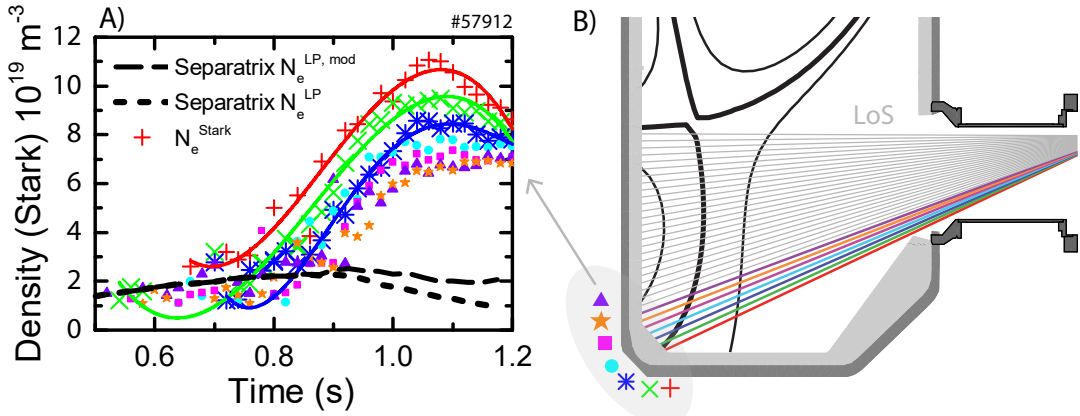


Figure 8.2: a) Electron density (characteristic uncertainty  $\sim 1 \times 10^{19} \text{ m}^{-3}$ ) traces of chords near the target (#57912) for a density ramp experiment. b) Corresponding divertor geometry and lines of sight

All the above observations are in excellent qualitative (and in most cases even quantitative) agreement with the SOLPS simulation results (Figure 8.3a vs b; Figure 8.3c vs d; Figure 8.3e vs f; Figure 8.3g vs h; Figure 8.3i vs j). The upstream density corresponding to the times indicated by the vertical lines in figure 8.3a are shown in figure 8.3b. This simulation does not reproduce the experimental result that the upstream density saturates upon detachment as is shown in the experiment. As such, a linear trend of the upstream density has been used to match the chosen times to the appropriate  $n_{e,u}$ . The three simulations used to compare the SOLPS profiles to experimental profiles are indicated by the enlarged symbols in figure 8.3b, where their colours correspond to the vertical lines at which the experimental data is taken, shown in figure 8.3a. The SOLPS results (Figure 8.3f, h, j) are obtained by integrating through the 2D SOLPS profiles of ionisation, recombination, etc. along the DSS and bolometric chords (Figure 8.3h —  $P_{rad,L}$ ), enabling a closer comparison between experiment and simulation (see section 4.3). Shown SOLPS integrated results (figure 8.3 b) are obtained by integrating the ionisation source/recombination sink over the region covered by the entire horizontal DSS viewing chord fan (figure 5.1). The SOLPS 'Stark density' result (Figure 8.3d) is obtained from the Stark fit of a synthetic DSS diagnostic (see section 5.8).

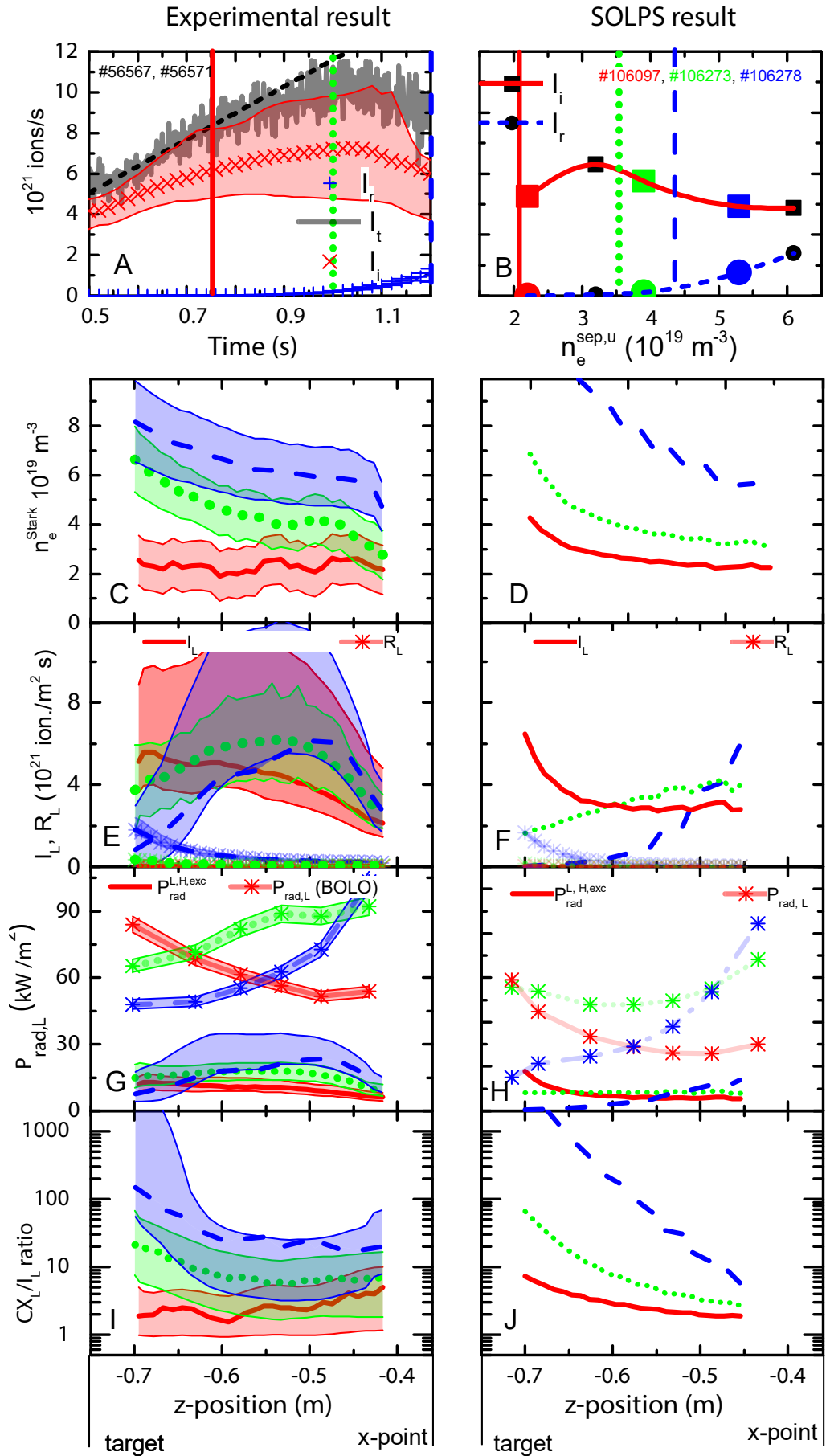


Figure 8.3: Left hand side: Experimentally (spectroscopic inferences + bolometry) determined quantities along the outer divertor leg. Right hand side: Results obtained directly from SOLPS simulation utilizing synthetic diagnostic measurements. a) Total outer ion target flux  $I_t$ , outer divertor integrated ion source and recombination rate ( $I_i, I_r$ ), together with the linear scaling of the ion target flux as function of time and vertical lines corresponding to the times at which the profiles are shown in the figures below. b) Analogous ion source/sink plot (outer divertor integrated) obtained from SOLPS where the ionisation source and recombination sinks are shown as function of upstream density. c, e) Stark density profiles (c —obtained from a synthetic diagnostic —see section 5.8). e, f) Chordal integrated recombination ( $R_L$ ) /ionisation rate ( $I_L$ ) profiles. g, h) Chordal integrated total radiation profiles through bolometry — $P_{rad,L}$ ; and radiation due to hydrogenic excitation — $P_{rad,L}^{H,exc}$ . i, j) Line integrated charge exchange to ionisation ratio profiles ( $CX_L/I_L$ ).

### 8.1.2 Evolution of electron density near the target

The three time points in the general plasma characteristic profiles along the divertor leg (Figure 8.3c, f, g, h) do not accurately convey the dynamics of the near target region, in particular the electron density which we expect, based on previous work [90, 65, 74], to drop as the low pressure, low density region expands from the target during detachment.

Stark density measurements from the 7 horizontal DSS viewing chords closest to the target are shown in Figure 8.2a together with the viewing geometry (Figure 8.2b). This discharge is similar to the one discussed in sections 8.1.1, but with a magnetic geometry optimised for DSS strike point coverage. At approximately the time of the total ion target current roll-over ( $\sim 0.87$  s), which coincides with the time when the integrated ion current deviates from its linear trend (not shown), the measured Stark density for the viewing chord nearest to the target rises above the peak density measured by Langmuir probes at the target (Figure 8.2a). Afterwards, when the core density is further increased, the Stark density (within  $\sim 5$  cm from the target) peaks after which it rolls-over, which happens after the ion target current roll-over and after the target separatrix target density measured by Langmuir probes, Figure 8.2a, starts dropping. This data is consistent with observations from the vertical DSS system indicating a reduction in line averaged ( $9 \rightarrow 2$  Balmer line, thus recombination emission weighted) density throughout the divertor leg (Figure 4.8). Since the density peak must have started at the target before detachment, the strong decreasing trend of the lowest viewing chord density would be consistent with the density peak starting to move up along the leg. The decay in Stark density could be stronger than shown, due to the reduction of the target temperature increasing the Stark width, which is not accounted for in the default Stark fit analysis; as was discussed in detail for this particular discharge (# 57912) in section 6.4, figure 6.15, where the target Stark density peaks at 1.1 s ( $n_e = 8 \times 10^{19} \text{ m}^{-3}$ ) and rolls over reaching  $6 \times 10^{19} \text{ m}^{-3}$  at the end of the discharge.

There is a concern that the Langmuir probe measurement of the target density is incorrectly low. Since the Langmuir probe density inferences uses the Langmuir probe temperature inference ( $J_{sat} \propto n_e^{LP} \sqrt{T_e^{LP}}$ ), the density would be underestimated when  $T_e^{LP}$  is overestimated —which generally occurs in cold divertor conditions [118, 119, 117]. As such, following a similar approach as developed by the author in [1], we calculated a modified  $n_e^{LP,mod} = n_e^{LP} \sqrt{\frac{T_e^E}{T_e^{LP}}}$  using a spectroscopically inferred  $T_e^E$  (section 7.3.1) from the excitation emission of the chord

closest to the target (figure 8.2 a).  $n_e^{LP,mod}$  remains significantly smaller than the observed Stark density upon detachment. Some combination of the width of the poloidal viewing chord (1-2 cm) and the weighting of the Stark density towards higher emissivities (and thus higher densities) along the cone describing the target line of sight is driving this difference. This discrepancy thus suggests that the electron density strongly decreases in a narrow region ( $< 2$  cm) close to the target. A decay of the electron density in such a narrow region during detachment is also observed in the SOLPS simulations [7]: the density, emission-weighted ( $n=7$  Balmer line) over radial cells in the divertor, drops poloidally by  $1 \times 10^{19} \text{ m}^{-3}$  in a region smaller than 1 cm near the target.

## 8.2 Characterisation of the loss of source and its effect on the ion target flux

In the survey of discharge characteristics (figure 8.1), the inferred ionisation source magnitude and time dependence appears to determine the current reaching the target. The following discussions are based on particle balance over the entire divertor and not just a particular flux tube and focus on divertor ion sources and ion sinks. During that discussion, three discharges are discussed of which two are density ramps and one is an impurity seeding ramp (nitrogen) at constant core density. All three of these discharges are in L-mode and without external heating, performed in reversed field (e.g.  $\nabla B$  in the unfavourable direction) to stay out of H-mode. To keep the same field line helicity, both the  $B_t$  direction and  $I_p$  direction were reversed. The equilibria of all three discharges together with the DSS viewing geometry are shown in figure 4.2 a.

The balance of sources and sinks within the divertor can be written as equation 8.1a, where the target ion flux (the sink for ions at the target),  $I_t$ , is the sum over the divertor target surface while both the ionisation source,  $I_i$ , and the recombination sink,  $I_r$ , are integrated over the entire outer divertor leg.  $I_{up}$  represents the net contribution of ion flows towards the ion target. Under the assumption that  $I_t \gg I_{up}$ , the divertor is a closed, self-contained system, where the total divertor ion target current is fully dominated by divertor ion sources (equation 8.1b); an approach used previously [51, 5, 52]. To investigate this assumption, an estimate of the upper bound for  $I_{up}$  based on reciprocating probe upstream profiles is presented in section 8.2.3. In this work we define the high recycling regime to be where the total divertor ion target current is dominated by divertor ion sources as opposed to sources outside the divertor; e.g. cases where equation 8.1b is valid.

$$I_t = I_i - I_r + I_{up} \quad (8.1a)$$

$$I_t = I_i - I_r \quad \text{if} \quad I_t \gg I_{up} \quad (8.1b)$$

### 8.2.1 Characterisation of ion sinks and sources in density ramp discharges

We show examples of the equivalence of the divertor ionisation source and target ion current for two density ramp discharges (which were ramped until disruption) at two different plasma currents in the first two columns of figure 8.4.

The ionisation source (figure 8.4b & e),  $I_i$ , tracks the increasing target flux,  $I_t$ , (within uncertainties) during the attached phase for both density ramp cases while recombination,  $I_r$ , is either ignorable (for the low current case —Figure 8.4b) or small (for the higher current case —Figure 8.4e). We conclude that the majority of ion target flux derives from ionisation within the divertor, in agreement with the self-contained divertor approximation (equation 8.1b), which shows that TCV is operating under ‘high recycling’ conditions. These measurements also indicate that the additional source from ion flux into the divertor from the SOL should be either relatively small or balanced by ion flows flowing from the outer divertor towards the inner target.

High recycling divertor operation has been visualised/simplified as being a narrow ionisation region in front of the target [3]. This contrasts with our TCV observations, as was highlighted previously in section 8.1.1, which may deviate from other tokamaks due to the relatively large mean free path of ionisation on TCV (5-10 cm). This indicates that having a narrow ionisation region may not be necessarily a requirement for cases where equation 8.1b applies.

The various ion losses for the density ramp cases can be compared quantitatively by assuming that both the ion target flux and  $I_i$  should increase linearly with time for the density ramp discharges (red dashed lines Figure 8.4d, e). The losses are then calculated by subtracting the measured  $I_t$  and  $I_i$  from these respective linear scalings. These linear scalings in attached conditions will be verified in section 9.2 using the two point model with recycling energy losses introduced in section 3.3. The measured target ion current loss and the ionisation source loss track well within uncertainties for both density ramp cases (Figures 8.4g, h). The recombination ion sink is only significant at the end of the high plasma current discharge; it only starts to develop to significant levels after the deviation of the measured  $I_t$  from its linear (attached) scaling and after the ion target flux roll-over. Even at the latest phases of discharge # 56567, the recombination loss remains more than a factor 4 lower than the loss of target ion current or loss of ionisation source.

There is a clear difference in the role volumetric recombination plays between the low and high current cases. This is an interesting observation, as it suggests that (for the same core Greenwald fraction) the plasma current is a ‘control knob’ for the influence of recombination on the ion target flux. The recombination rate in the high current case is 5-10 times higher at the same core Greenwald fraction, whereas the ion target flux is only  $\sim 25\%$  higher. That change is consistent with the predictions from equation 2.7 as the higher current also increases the Ohmic power (by roughly a factor two), thus increasing  $q_{||}$  (assuming similar SOL widths and core radiation fractions) for the higher current case. One explanation for the higher recombination rates is that the  $\sim 1.5$  times higher  $n_{e,u}$  leads to higher divertor densities —which are observed (Stark density) to be  $\sim 3$  times higher for the high current case. This agrees with the expected strong dependence of the divertor density on  $n_{e,u}$  (cubic [3], based on equation 2.8 assuming  $T_u^2/q_t$  is similar between the two cases). Assuming identical divertor temperatures between the two cases, this would result in  $\sim 10$  times higher recombination rates, using the tables presented in section 2.4.

### 8.2.2 Characterisation of ion sinks and sources in $N_2$ seeded discharges

$N_2$  seeded discharges develop significantly differently than the core density ramp discharges discussed previously. The line averaged density for the discharge shown (# 52158) is held

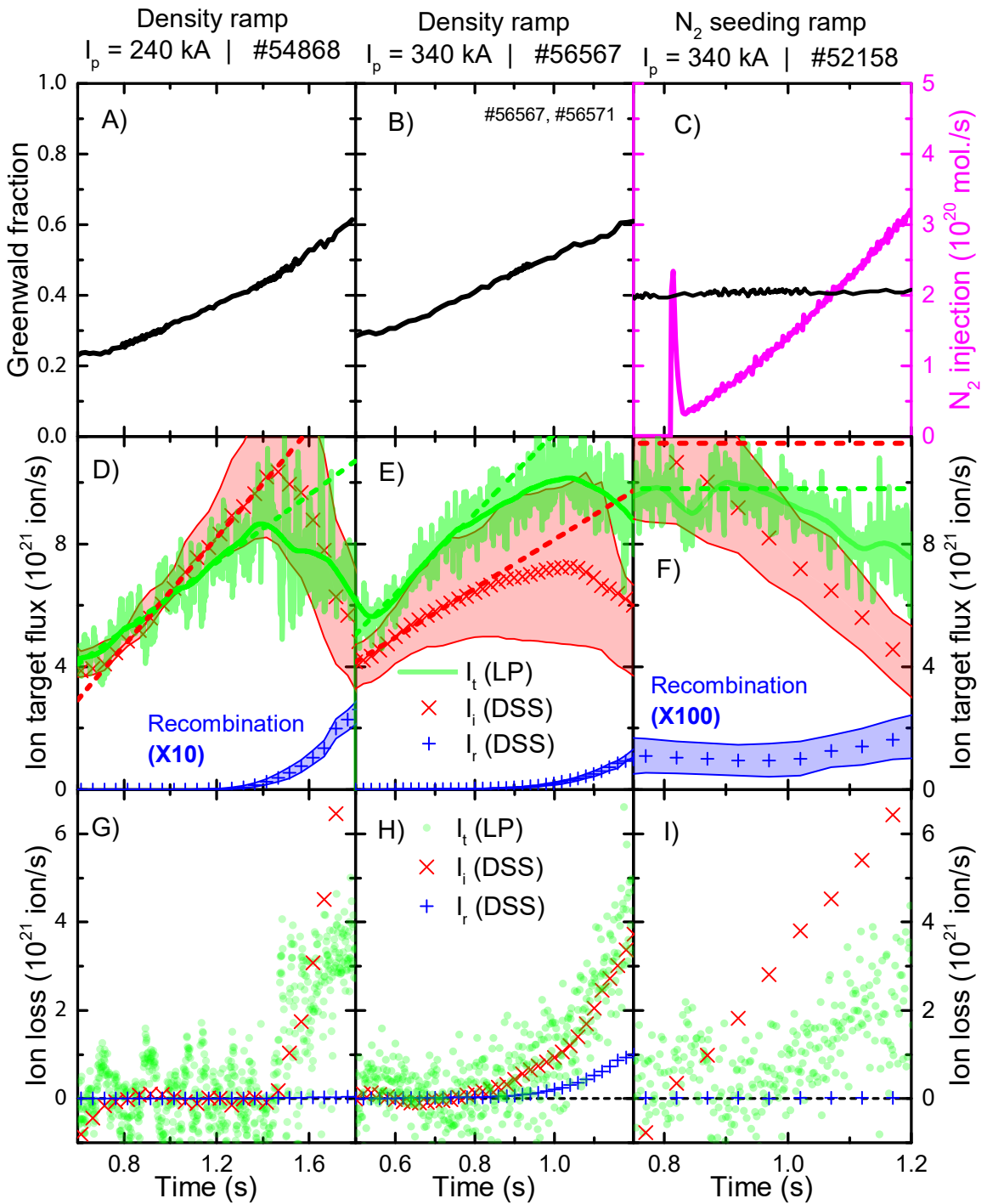


Figure 8.4: First two columns correspond to core density ramps at two different plasma currents: Core Greenwald fraction (a,b); divertor ion sources/sinks and ion target flux (d, e) as well as the loss of ion target current, recombination sink and loss of ionisation (g, h). The last column corresponds to a  $N_2$  seeding ramp at constant core density (c): divertor ion source/sink and ion target flux (f) as well as the loss of ion target current, recombination sink and loss of ionisation (i).

constant over the  $N_2$ -seeding ramp at a fixed Greenwald fraction of  $\sim 0.4$  (Figure 8.4c). This is just below the core density at which the ion target flux roll-over occurred in the equivalent high current, density ramp discharge (pulse # 56567; Figure 8.4 e). While the core density is kept constant, a ramp of  $N_2$  seeding is introduced, starting at 0.8 s as shown in figure 8.4 c. The ion target current loss is quantified as previously using the pre- $N_2$  seeding scaling as a reference. This likely underestimates the actual value of the ion target loss as in attached conditions, assuming only impurity radiation in the divertor is altered, the ion target flux is expected to increase according to the two point model (equation 2.7).

Both the ion target flux and ionisation source are observed to drop with increasing  $N_2$  gas puff rate while recombination remains fully negligible (figure 8.4 f). The magnitude of the ion source loss, including the range of uncertainty, is however larger than the ion target current loss and starts to rise earlier (figure 8.4 i). One possible explanation for this discrepancy is that a significant fraction of the target ion current was carried by nitrogen ions. To explain the mismatch between the ion target current measured by Langmuir probes and the ionisation source prediction, a nitrogen concentration of 10 to 25 % would suffice, assuming an average nitrogen ion charge of 2.

A crude analysis, using Open-ADAS photon emission coefficients together with the NII (399.6 nm) line brightnesses measured by the DSS and the statistical ( $T_e^E$ ,  $n_e^{Stark}$ ,  $\Delta L$ ) PDFs obtained from the Balmer line analysis, indicates the ratio between the  $N^+$  density and  $n_e$  to be at least 4% (e.g. 4 to 30 %). The total nitrogen concentration is likely significantly higher than the  $N^+$  concentration; assuming a transport-less plasma (which is not true —this calculation serves only as an illustration), one would expect only a small fractional abundance ( $< 0.1$ ) for  $N^+$ , considering the  $T_e^E$  and  $n_e^{Stark}$  ranges obtained from the Balmer line analysis where NII radiates. Although the  $N^+$  fractional abundance is most likely larger than this, the crude analysis shown does support the explanation of a significant fraction of target ion current being generated due to  $N$  ions, but it does not constitute a proof. One of the reasons for this is that the inferred ( $T_e^E$ ,  $n_e^{Stark}$ ) from the Balmer line series does not necessarily match the temperature/density from which the NII emission originates [213] and provide wide ranges leading to a large uncertainty margin in the expected  $N^+$  concentration. Furthermore, the  $N^+$  concentration is linearly sensitive to the assumed  $\Delta L$ ; meaning that if NII radiates in a larger region than predicted by the simplified  $\Delta L$  analysis based on the Langmuir probe  $J_{sat}$  profile (section 7.1.2), the  $N^+$  concentration would be overestimated. Additionally, to convert the  $N^+$  concentration into a total nitrogen concentration, a much more sophisticated analysis including non-equilibrium ionisation balance modelling is required.

Recombination being smaller during  $N_2$  seeding can be (partially) explained due to the lower upstream and divertor densities obtained during  $N_2$  seeding as during a density ramp at the same plasma current. The recombination rate from the density ramp experiment (# 56567) at the same upstream density as the  $N_2$  seeding experiment is in the range  $1 \times 10^{19}$  to  $4 \times 10^{19}$  ions/s (between 0.7-0.8 s), which agrees within uncertainty with the recombination rate for the  $N_2$  seeding experiment just before the  $N_2$  puff ( $5 \times 10^{18}$  to  $1.5 \times 10^{19}$  ions/s). Interestingly, the measured recombination rate during the  $N_2$  seeding ramp only increases slightly as the  $N_2$  seeding is increased. This is contrasting with the behaviour during a density ramp and also contrasts one's expectations as a higher  $N_2$  seeding rate would be expected to decrease the divertor temperature, which should increase recombination, assuming that the

local density is not strongly decreased (consistent with Stark inferences indicating a static  $n_e \approx 3 \times 10^{19} \text{ m}^{-3}$  within an uncertainty of  $1 \times 10^{19} \text{ m}^{-3}$ ) and the plasma is not detached before  $N_2$  seeding. This seems to be consistent with the measurements, which will be further discussed in section 9.3.

### 8.2.3 Estimating the flow of ions from upstream into the divertor

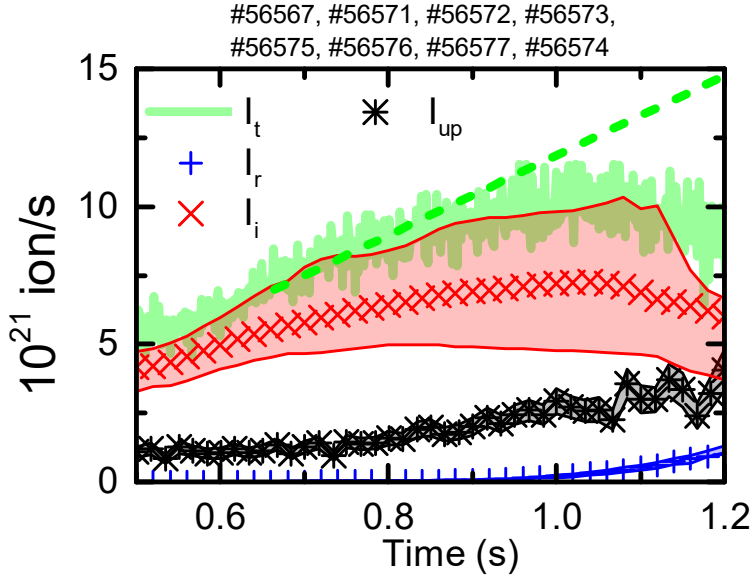


Figure 8.5: The target ion flux compared to the ion source, inferred ion flow from the upstream SOL and the recombination rate

In this section we have shown that in both attached and detached conditions, the measured ion current of the outer divertor leg during reversed field discharges, does correspond to the ionisation source estimated of the outer divertor leg, obeying the closed box approximation and therefore, the notion of a high recycling divertor. While direct measurements of  $I_{up}$  are unavailable, the ion flow from upstream can be estimated through equation 8.2, in which  $M_u$  is the upstream Mach number and  $r$  is the radial distance from the separatrix [214], which includes fluid flows along the magnetic field but ignores several types of drift flows such as  $E \times B$  flows, ignores ionisation in the SOL outside of the spectroscopic view and ignores flows from the inner target to the outer target or visa versa.

$$I_{up} \approx 2\pi M_u \frac{B_p}{B_t} \int_{separatrix}^{wall} r n_u(r) \sqrt{\frac{T_u(r)}{m_i}} dr \quad (8.2)$$

To estimate the maximum possible  $I_{up}$ , we use  $M_u \sim 0.5$ , the upper bound of a previous survey of upstream Mach number profiles across 3 tokamaks [214]. To compute this conservatively large  $I_{up}$  (equation 8.2), separatrix upstream densities and temperatures were measured using Thomson scattering, while their profiles were measured with a reciprocating probe (details are provided in section 3.6). The resulting  $I_{up}$ , shown in figure 8.5 for discharge (# 56567) previously discussed, remains small compared to the divertor source of ions and the target ion current, but can increase up to  $\sim 30\%$  of  $I_t$  during detachment.

When these values for  $I_{up}$  are included in the overall particle balance (equation 8.1a), this would be consistent with the Langmuir probe  $I_t$  measurements and the ionisation source measurements  $I_i$  within uncertainties. However, even with  $I_{up}$  included,  $I_i$  remains the largest contributor to the target ion flux and its roll-over at the detachment onset. Based on the other results in this section (figure 8.4); it is likely that this is the case also for lower current (e.g. lower density) discharges. Another possibility is that, if there would be a significant  $I_{up}$  or a significant amount of SOL ionisation, these ions flow towards the inner divertor instead of the outer divertor; thus making the outer divertor self-contained such that the influence of  $I_{up}$  is ignorable on the outer divertor.

### 8.3 Power balance in the divertor and its relationship to ionisation

Although the divertor ion source appears to be the main determinant of the ion target flux, we did not address the question as to what causes the ionisation source to decrease. It has been suggested previously, both experimentally [51] and theoretically [52, 5, 68] that the ion source can be limited by the amount of power available for ionisation in the divertor, or the power entering the recycling region, which was highlighted in the power balance structure shown in section 3.1, which provides a model for divertor power balance (figures 3.1, 2.2). To pursue this question, we aim to compare the power entering the recycling region,  $P_{recl}$  and the power required for ionisation  $P_{ion}$ . The power required for ionisation,  $P_{ion}$ , depends on hydrogenic excitation radiative losses  $P_{rad}^{H,exc}$  and the ionisation rate (equation 3.6a section 3.1); which both can be obtained spectroscopically as shown in sections 7.3, 7.4. This power balance investigation is applied to the outer divertor of # 56567 (high  $I_p$  density ramp), shown in Fig. 8.4, for #56567, while charge exchange power losses (section 3.1) are neglected.

Estimating the power entering the recycling region ( $P_{recl} = P_{div} - P_{rad}^{imp}$ ), as shown in equation 3.5, requires estimating both the power entering the divertor ( $P_{div}$ ) and the power loss due to impurity radiation ( $P_{rad}^{imp}$ ). The power entering the divertor can be estimated by first estimating the power flowing into the SOL from the core plasma ( $P_{SOL}$ ). Since the discharges included in this study are Ohmically heated the heat source of the core is Ohmic  $P_{Ohm}$ .  $P_{SOL}$  is obtained by subtracting the core radiated power ( $P_{core}^{rad}$ ), measured by foil-bolometer arrays (section 4.2.1), from  $P_{Ohm}$ . After establishing  $P_{SOL} = P_{Ohm} - P_{core}^{rad}$ , the portion of power from the core flowing to each strike point (or the asymmetry in the power flow) has to be established, described by  $\alpha$  in equation 8.3, representing the fraction of power crossing the SOL going towards the outer strike point. An in-depth study [215] has provided us with an overview of  $\alpha$  for different configurations. For the reversed field discharge discussed here (#56567), with  $I_p = -340kA$  and  $f_x \sim 8$ , the power flowing towards the inner/outer strike point are roughly equal ( $\alpha \sim 0.5$ ). To account for the uncertainty in  $P_{div}$ , no uncertainty in  $\alpha$  or  $P_{Ohm}$  is assumed. The uncertainty for  $P_{rad}^{core}$  is described in section 4.2.1.

$$P_{div} = \alpha(P_{Ohm} - P_{rad}^{core}) \quad (8.3)$$

Using the power balance discussed in section 3.1,  $P_{rad}^{imp}$  can be estimated by subtracting the spectroscopically estimated hydrogenic radiated power loss ( $P_{rad}^{H,exc} + P_{rad}^{H,rec}$ ) from the

total radiated power  $P_{rad}$  estimated from bolometric measurements, leading to equation 8.4.

$$P_{rad}^{imp} = P_{rad} - P_{rad}^{H,exc} - P_{rad}^{H,rec} \quad (8.4)$$

After having established how to obtain the various power loss channels, we can investigate how these power losses and power flows vary during a density ramp discharge, which is shown in figure 8.6 for #56567; similar qualitative trends are found for the other two discharges presented in the previous section. We include again the measurements of the target ion flux and the ionisation source (Figure 8.6a) as a reference. Figure 8.6b, which shows the various radiative loss channels in the divertor shows that throughout the density ramp, intrinsic impurity radiation is dominant (x 3) over  $P_{rad}^{H,exc}$  while recombination radiative losses are essentially ignorable. That is an important observation as it shows that TCV, being a carbon wall machine, has a very significant amount of impurity radiative losses intrinsically, which become stronger as the density ramp continues both due to an increase in divertor density and due to divertor cooling increasing carbon radiation in detachment as shown in figure 2.10.

The increase in divertor impurity radiation throughout the discharge causes  $P_{recl}$  to steadily drop (Figure 8.6c) during the ramped increase of the core and edge density while the power into the outer divertor,  $P_{div}$ , remains roughly constant. This suggests that, even in non-seeded density ramp discharges, impurity radiation due to intrinsic impurities (carbon in the case of TCV) is not just the dominant radiative loss, but plays a key role in reducing the power reaching the recycling region in TCV. Reducing  $P_{recl}$  is what causes power limitation near the time of the ion target flux roll over, ( $\sim 1.05$ s) as  $P_{recl}$  has dropped to roughly  $P_{ion}$  at that point. This quantitative information suggests that the ion source is being limited by the power reaching the recycling region. When  $P_{recl}$  has dropped to roughly  $P_{ion}$ , most of the power flow entering the recycling region is expended on ionisation and thus the kinetic power reaching the target is relatively small  $P_{target}^{kin} \ll P_{recl}$  (section 3.1). This both implies that low target temperatures are achieved, as is expected from detachment and observed (section 9.1.2); and it implies that the target temperature no longer plays a role in power/particle balance, which is a sufficient observation to state that the ion source from that point onwards is expected to be driven by the power entering the recycling region and the energy required for ionisation, as was explained in section 3.1 and will be further investigated in section 9.1.

We note that, however,  $P_{recl}$  is larger than  $P_{ion}$  when the target ion current deviates from the linear trend (in fact,  $P_{recl}$  is approximately twice  $P_{ion}$  at the start of detachment); which makes sense as some power, beyond ionisation, is required to maintain a target temperature. This empirical observation coincides with predictions of the detachment threshold ( $P_{recl} < 2P_{ion}$ ) presented in sections 3.1 and 3.3, which will be further discussed in sections 9.1.3 and 9.2.2.

Figure 8.6d includes a check of the overall divertor power balance. The sum of the total radiated power and the power reaching the target,  $P_{rad} + P_{target}^{IR}$  (the latter term from IR measurements), is compared with the power flowing to the outer divertor region,  $P_{div}$ ; which should equal each other (section 3.1). The two are shown to match within uncertainties, giving confidence in the  $P_{div}$  determination. Note that  $P_{rad} + P_{target}^{IR}$  is no longer shown after 1.05 s due to failures in the IR background subtraction algorithm.

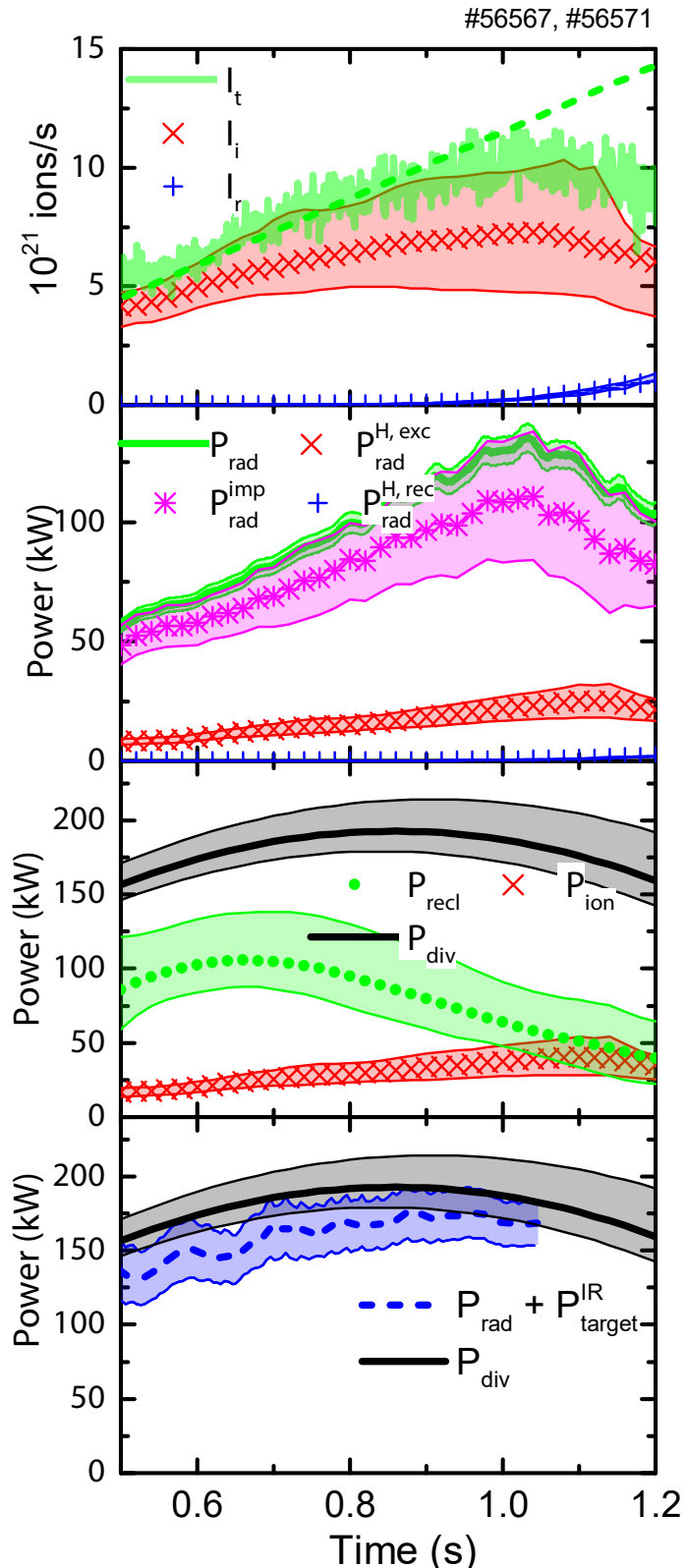


Figure 8.6: Power balance investigation for the outer divertor for pulse #56567 a): ion target flux, ionisation rate and recombination rate; b) break-down of total radiation and its contributors; c) comparison between power entering the outer divertor leg,  $P_{div}$ ; the power entering the recycling region,  $P_{recl}$  and the power needed for ionisation,  $P_{ion}$ ; d) comparison between  $P_{div}$  and the outer divertor leg radiative losses plus the measured power deposited on the target by the IR for consistency.

## 8.4 Evidence for molecular reactions during TCV detachment

A detailed analysis of the  $D\alpha$  brightness measured spectroscopically in TCV indicates that the observed  $D\alpha$  brightness is larger than expected from atomic processes, which do explain the brightness of other Balmer lines. This discrepancy is indicative of molecular reactions as other studies have shown that several molecular reactions (most notably Molecular Activated Recombination —MAR [111, 106, 110]) can enhance the  $n=3$  population level, increasing the  $D\alpha$  emissivity [109, 111, 106]. A comparison between the experimental measurements and SOLPS simulations also indicates that the observed strong rise in  $D\alpha$  emission during density ramp detachment is due to molecular reactions.

We estimate the atomic contribution to  $D\alpha$  by using medium-n Balmer line brightnesses ( $n=5,6$  Balmer line intensities) to predict the  $D\alpha$  brightness, based on atomic reactions for each view, which is compared with the measured values for  $D\alpha$  (figure 8.7b). That information is compared with the SOLPS-simulated atomic contribution to  $D\alpha$ , using ADAS, and SOLPS-simulated molecular contribution to  $D\alpha$ , using EIRENE (figure 8.7b); which are both obtained using a synthetic diagnostic approach (section 5.8). The following process of estimating additional contributions to  $D\alpha$  is based on the formalism discussed in section 7.2. First we determine  $F_{rec}$  from the  $B_{6 \rightarrow 2}/B_{5 \rightarrow 2}$  line ratio to obtain  $B_{5 \rightarrow 2}^{exc}$  and  $B_{5 \rightarrow 2}^{rec}$  (corresponding to  $D\gamma$ ). Secondly, using the Stark density and the respective excitation/recombination temperatures from the Balmer line analysis, we determine  $D\alpha$  to  $D\gamma$  ratios separately for the excitation and recombination components ( $B_{3 \rightarrow 2}^{exc}/B_{5 \rightarrow 2}^{exc}$  and  $B_{3 \rightarrow 2}^{rec}/B_{5 \rightarrow 2}^{rec}$ ). Thirdly, using these ratios we 'upscale' the measured  $B_{5 \rightarrow 2}^{exc}, B_{5 \rightarrow 2}^{rec}$  brightnesses into respective  $B_{3 \rightarrow 2}^{exc}, B_{3 \rightarrow 2}^{rec}$  brightnesses by multiplying the measured  $B_{5 \rightarrow 2}^{exc}, B_{5 \rightarrow 2}^{rec}$  with the estimated  $B_{3 \rightarrow 2}^{exc}/B_{5 \rightarrow 2}^{exc}, B_{3 \rightarrow 2}^{rec}/B_{5 \rightarrow 2}^{rec}$  ratios. Summing the  $B_{3 \rightarrow 2}^{exc}, B_{3 \rightarrow 2}^{rec}$   $D\alpha$  contributions leads to the prediction of  $D\alpha$  intensity due to atomic reactions:  $B_{3 \rightarrow 2}^{atomic} = B_{3 \rightarrow 2}^{exc} + B_{3 \rightarrow 2}^{rec}$ . The statistical approach described in section 7.6 has been used to estimate the most probable  $D\alpha$  and its (68%) uncertainty margin. In this technique, the fact that the excitation and recombination emission occur at the same location along the chordal integral for each Balmer line (section 7.3.1), is exploited to enable the assumption that the excitation/recombination temperatures from the Balmer line analysis are respective of the excitation/recombination temperatures of  $D\alpha$ . This makes the upscaling particularly insensitive to line integration effects. We note that a similar technique found consistency between the measured and predicted  $n=5-9$  Balmer line intensities.

The measured  $D\alpha$  brightness is always higher than that predicted (based on atomic processes) during a density scan. Figure 8.7 displays the measured and predicted  $D\alpha$  brightnesses, integrated over all DSS chords (Figure 8.7b). The measured  $D\alpha$  starts  $\sim 50\%$  higher than predicted. When the core density is increased, the measured and predicted  $D\alpha$  further diverge up to a factor three at the detachment onset and more than a factor six during the detached phase of the discharge.

We have also compared the measured  $D\gamma/D\alpha$  ratios with predictions based on atomic collisional radiative modelling alone. As highlighted in section 7.2, such line ratios are predicted to start at values expected for excitation emission and then, as the plasma cools, increase towards values expected for recombinative emission (which is  $\sim 0.1$  —a factor  $\sim 10$  larger than the excitation limit for the  $D\gamma/D\alpha$  ratio) as estimated from the PECs presented in section 2.4. The measured  $D\gamma/D\alpha$  along 3 DSS lines of sight (covering regions close to the target,

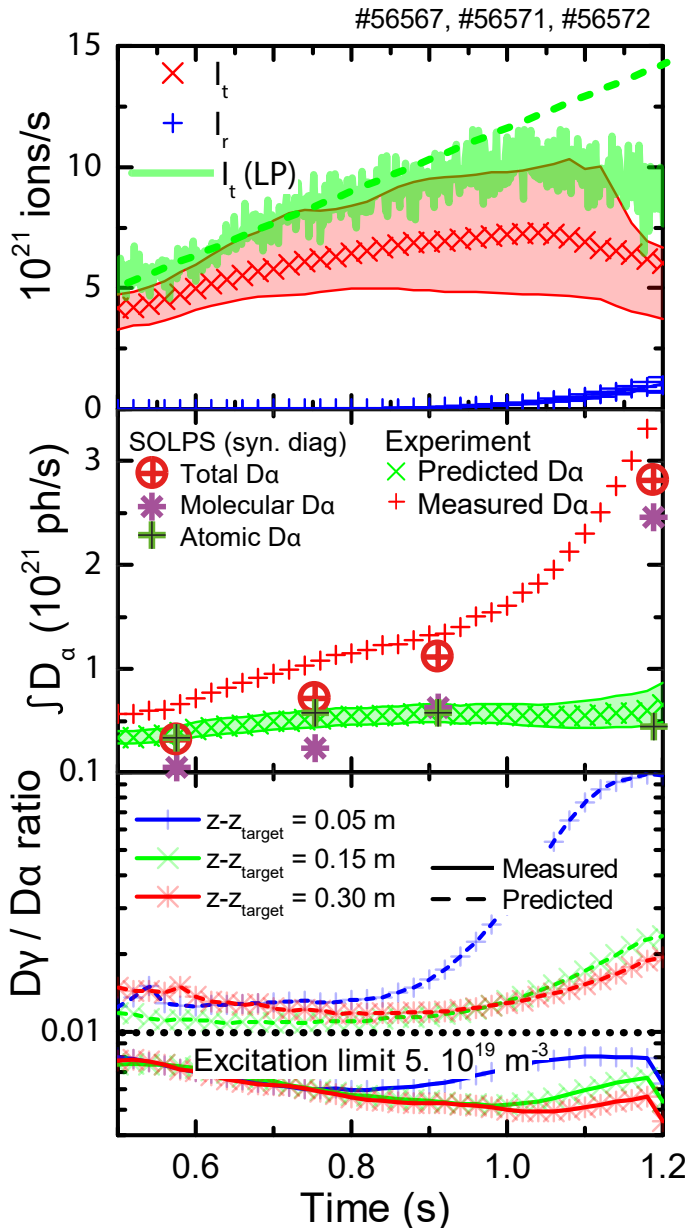


Figure 8.7: a) Target ion flux, ionisation rate and recombination rate as function of time. b) Measured (summed over all chords)  $D\alpha$  signal and predicted summed  $D\alpha$  signal. c) Measured and predicted  $D\gamma/D\alpha$  ratio along three different locations. The expected excitation limit, or minimum ratio is shown. The predicted recombination limit is  $\sim 0.1$ .

middle of the divertor leg and close to the x-point) are shown in figure 8.7c. It is striking that even before detachment all three measurements are lower than the excitation only limit (which only takes atomic excitation into account). As the plasma cools down after detachment the observed  $D\gamma/D\alpha$  actually decreases further—in contrast to the strong increase expected.

All these observations indicate that the  $D\alpha$  line intensity is elevated compared to expectations based on atomic collisional radiative modelling alone. In other words, there must be other reactions, such as molecular ones (most notably MAR), contributing to the  $D\alpha$  emission. Generally, there are three possible MAR chains [112] highlighted in table 8.1: 1) DA-MAR, which features a complex chain of reactions involving Dissociative Attachment resulting in  $D^-$ , leading to recombination [112, 108, 109], 2) IC-MAR, which features molecular Ion

Table 8.1: Overview of MAR reactions adopted from [109] for deuterium.  $D_2(\nu)$  implies vibrationally excited deuterium molecules, whereas  $D^*$  denotes electronically excited atomic neutrals

Label	Type	Reaction
<b>DA-MAR</b>	DA	$D_2(\nu) + e^- \rightarrow D^- + D$
	MN	$D^- + D^+ \rightarrow D + D^*$
<b>IC-MAR</b>	CX	$D_2(\nu) + D^+ \rightarrow D_2^+(\nu) + D$
	DR	$D_2^+(\nu) + e^- \rightarrow D + D^*$
<b>MIC-MAR</b>	CX	$D_2(\nu) + D^+ \rightarrow D_2^+(\nu) + D$
	MIC	$D_2(\nu) + D_2^+(\nu) \rightarrow D_3^+(\nu) + D$
	DR	$2D_3^+(\nu) + 2e^- \rightarrow 3D + D_2(\nu) + D^*$

Conversion (e.g. charge exchange) followed by dissociative recombination of  $D_2^+$  [112], 3) MIC-MAR, which features the generation of  $H_3^+$  through tri-atomic molecular ion conversion, eventually leading to the generation of vibrationally excited molecules [109]. On linear devices, it is believed that the presence of the MIC-MAR reaction impedes IC-MAR and generates vibrationally excited hydrogen molecules, for which the reaction rate of DA-MAR is more pronounced; which is believed to be the reason why DA-MAR is the dominant MAR chain in linear device [109]. Calculations suggest DA-MAR may also be important for tokamak plasmas [108]. In other studies, IC-MAR is considered important in elevating  $D\alpha$  in tokamaks [72, 110].

We have used SOLPS simulations [7] to further investigate the source of the  $D\alpha$  enhancement. A synthetic  $D\alpha$  brightness has been obtained and summed over all DSS chords, as shown in figure 8.7b. Here the  $D\alpha$  contributions have been distinguished into a molecular part (obtained through EIRENE [162, 69]) and an atomic part (obtained through Open-ADAS [140, 134]). It is important to note that the SOLPS simulation uses the default set of molecular reactions (see [216], in particular table 3.2), which do not include reactions with  $D^-$  and  $D_3^+$ . A good qualitative and fair quantitative agreement is found between the total measured  $D\alpha$  and simulated  $D\alpha$  and between the predicted atomic part of  $D\alpha$  and the simulated atomic part of  $D\alpha$ . This further supports the idea that the strong rise of  $D\alpha$  during the detached phase is due to molecular reactions. In addition, the quantitative agreement of the SOLPS predictions of the total and atomic part of  $D\alpha$  emission with the experiment implies that the molecular part of  $D\alpha$  predicted by SOLPS also agrees to the experiment. As this does not include any reactions with  $D^-$  or  $D_3^+$ , this suggests that the observed  $D\alpha$  emission is not due to DA-MAR, but due to IC-MAR (table 8.1) —consistent with findings in literature [72, 110].

It should be noted that the  $D_2^+$  generated during molecular charge exchange can also be involved in Molecular Assisted Dissociation (MAD)  $D_2^+(\nu) + e \rightarrow D + D^+ + e$  and Molecular Assisted Ionisation (MAI)  $D_2^+(\nu) + e \rightarrow D^+ + D^+ + 2e$  [68]. Those reactions likely play a role at high densities.

The strong enhancement of  $D\alpha$  occurs at  $\sim 0.9$  s and is correlated with the onset of detachment (figure 8.7) during a density ramp. That rise of  $D\alpha$ , is suggestive of recombination of  $D_2^+$  [110] and could indicate IC-MAR occurs, which involves molecular charge exchange in the divertor. This may also indicate a significant molecular density in the TCV divertor

—which would support the notion that the formation of  $D_2$  near the target, including the processes arising from plasma-molecule interaction (momentum losses, energy losses, MAR), are correlated with reaching sufficiently low target temperatures and the detachment onset [4, 49, 78]. However, a large content of  $D_2^+$  may have been present before the enhancement of  $D\alpha$  and may have gone into MAD and/or MAI as illustrated by the reactions above [68].

Although the amount of  $D_2$  and the momentum loss originating from it cannot be quantified through our analysis of the experimental data, the SOLPS simulations for TCV [7] do indicate that  $D_2$  continuously rises during the density ramp while momentum loss from ion-molecule interactions occur and its relative importance increases as the plasma becomes more detached, while its role (for similar upstream densities as the experiment) remains secondary to momentum loss from ion-neutral interaction. Molecule-ion collisions may also lead to an additional power sink [54] (which is thought to be minor considering the work in [110]).

The observation of  $D\alpha$  also has other implications, especially considering other literature where similar enhancements of  $D\alpha$  were observed [112, 108, 111, 106]. In literature, often ratios such as  $D\alpha/D\gamma$  have been used to indicate 'recombination dominant' emission [3, 76, 77, 80, 102, 61], which is based on the assumption that all emission is due to atomic recombination/excitation; this is however problematic as most of the  $D\alpha$  emission observed is due to molecules during detachment; which invalidates such diagnostic techniques. Instead, line ratios such as  $D\alpha/D\beta$  have to be compared with modelling which takes molecular processes into account as has been done in [79], for example.

A fuller experimental understanding of the role of molecular processes in interpreting  $D\alpha$  emission would require more sophisticated analysis with a full molecular collisional radiative model such as Yacora [145], which is out of the scope of this thesis. However, since the ion sources and sinks due to atomic ionisation and volumetric recombination match the measured target ion flux within uncertainties, it is likely that the sum of ion sources/sinks due to molecular reactions would not have a strong net effect on the particle source balance.

## 8.5 Summary

The results shown in this chapter indicate a strong particle balance correlation, in magnitude and time, between the ionisation source and the target ion current. This implies the ion current roll-over occurs due to an ion source reduction as opposed to an ion sink, such as volumetric recombination. This ion source reduction is correlated with the point where the power entering the recycling region ( $P_{recl}$ ) approaches the power used during ionisation: power limitation of the ionisation source is occurring. During a density ramp,  $P_{recl}$  is reduced through intrinsic impurity radiation in the divertor while the power entering the divertor remains roughly constant; indicating the strong role of intrinsic carbon impurities during TCV detachment. At the onset of detachment, the peak in ionisation is observed to move from the target towards the x-point, giving rise to a region near the target with enhanced charge exchange to ionisation ratios. This is correlated with the appearance of a strong mismatch between the observed and predicted (from atomic processes)  $D\alpha$  emission; which is indicative of  $D\alpha$  emission arising from molecular reactions as has also been indicated in the SOLPS simulations through a quantitative agreement.

# Chapter 9

## Discussion

Combining the results, shown in chapter 8, with the analytic models introduced in chapter 3 indicates a quantitative agreement between the modelled ion current trend and the observed (linear) ion current trend; explaining the linear rise in  $I_t$  during a TCV detachment ramp. This occurs until the predicted detachment onset criteria are reached, which agrees with the experimentally measured detachment onset and signifies the point from which target pressure loss is required. This is concurrent with a measured onset of the rise of charge exchange to ionisation ratios, from which a significant volumetric momentum loss is estimated (70 % —in agreement with experimental comparisons between the target and upstream pressure profiles [8]). Not only the target pressure is observed to roll-over, but also the upstream pressure. That is consistent with analytic model predictions as the required reduction of the target pressure, according to the analytic model, is larger than the estimated volumetric momentum loss.

Parts of this chapter have been adopted from: *An improved understanding of the roles of atomic processes and power balance in target ion current loss during detachment*, by K.

Verhaegh, B. Lipschultz, B.P. Duval, et al., to be submitted. DOI:

<https://doi.org/10.13140/RG.2.2.24292.48005/1>

The results treated in chapter 8 have quantitatively shown that the ion target current roll-over occurs when the ion source in the divertor is reduced as the power required for ionisation approaches the power entering the recycling region. The implications and the meaning of this is further investigated in sections 9.1 and 9.2 using reduced analytic models to predict the ion source behaviour and detachment thresholds based on power/particle balance (section 3.1) and power/particle/momentum balance (section 3.3). Such reduced analytical models take the minimum number of necessary physical processes into account to model the various detachment characteristics. It is observed that power/particle balance can well describe the trend in ion current —if a measured temperature is provided (section 9.1). Modelling the temperature trend, however, requires including momentum balance which leads to a prediction of a point —considered a detachment threshold —where target pressure loss needs to start to occur, as was explained in section 3.3.

These predicted detachment thresholds agree within uncertainty with the measured onset of detachment in section 9.2.2. Strikingly, the predicted detachment thresholds, which signify a point at which *target pressure loss* needs to start to occur, are in agreement with the observation of increased charge exchange to ionisation ratios indicative of volumetric

momentum loss due to ion-neutral collisions (section 9.2.3). That observation is important as it indicates consistency between the 'power limitation' and 'volumetric momentum loss' points of view (section 9.2.5). In addition, both power limitation and volumetric momentum loss is required to explain the TCV observations (section 9.2.4) —as well as a saturation/roll-over in upstream pressure, which is observed. The generality of these TCV observations is further discussed (section 9.4).

Implications and the meaning of the lack of recombinative emission during  $N_2$  seeded discharges, together with the disappearance of  $D\alpha$  emission during  $N_2$  seeding (while  $D\alpha$  greatly increases during a density ramp likely due to molecular processes —section 8.4), is further discussed (section 9.3).

## 9.1 Investigating detachment in the framework of power and particle balance

We investigate the influence of 'power limitation' on the ion source more quantitatively by predicting the target ion source through its dependence on power and target temperature using power and particle balance [51, 5], using the model highlighted in section 3.2.1.

By applying such a model,  $I_t$  is modelled through equation 3.10a using measured variables (which are assumed to be independent in the model) of the power entering the recycling region ( $P_{recl}$ ), the energy cost per ionisation ( $E_{ion}$ ) and the target temperature  $T_t$ ; showing a quantitative agreement with  $I_t$  measured by Langmuir probes. It should be clearly noted that since this model *requires* an input or measured  $T_t$ ; it does not take explicitly into account that changing the power entering the recycling region also influences the target temperature. To account for this, momentum balance has to be included in the model (section 9.2).

### 9.1.1 The variation of $E_{ion}$ during detachment

To obtain an  $I_t$  estimate through equation 3.10a we require an estimate of the energy cost per ionisation estimate — $E_{ion}$ . In simple modelling, the amount of energy spent per ionisation,  $E_{ion}$ , is often assumed to be constant [51, 5, 6, 3, 4]. An expression for  $E_{ion}$  was derived earlier in equation 3.6b:  $E_{ion} = \frac{P_{ion}}{I_i} = \frac{P_{rad}^{H,exc}}{I_i} + \epsilon$ . The excitation radiation ( $P_{rad}^{H,exc}/I_i$ ) component of  $E_{ion}$  has, however, a strong temperature dependence: as  $T_t$  is reduced, more excitations occur before ionisation happens. This leads to a strong temperature dependence of  $E_{ion}$  as shown previously in figure 3.2.

However, the expression for  $E_{ion}$  consists of parameters shown previously in the results (section 8.3) derived purely from spectroscopic inferences; thus  $E_{ion}$  can be estimated quantitatively along the divertor leg and as function of time during a discharge using the techniques highlighted in section 7.4.  $E_{ion}$  is shown as function of time in figure 9.1 b during the density ramp of the relatively high current case (# 56567), presented previously in chapter 8. This shows that during the density ramp, the effective temperature of the ionisation region drops, leading to a factor of two rise in  $(P_{rad}^{H,exc}/I_i)$ . This causes a 50 % increase in effective  $E_{ion}$  (divertor leg averaged, weighted by the ionisation rate).

When looking at the predicted scaling of  $I_t$  according to equation 3.10a, one important parameter of this is  $P_{recl}/E_{ion}$ ; which represents the maximum ion source if all the power

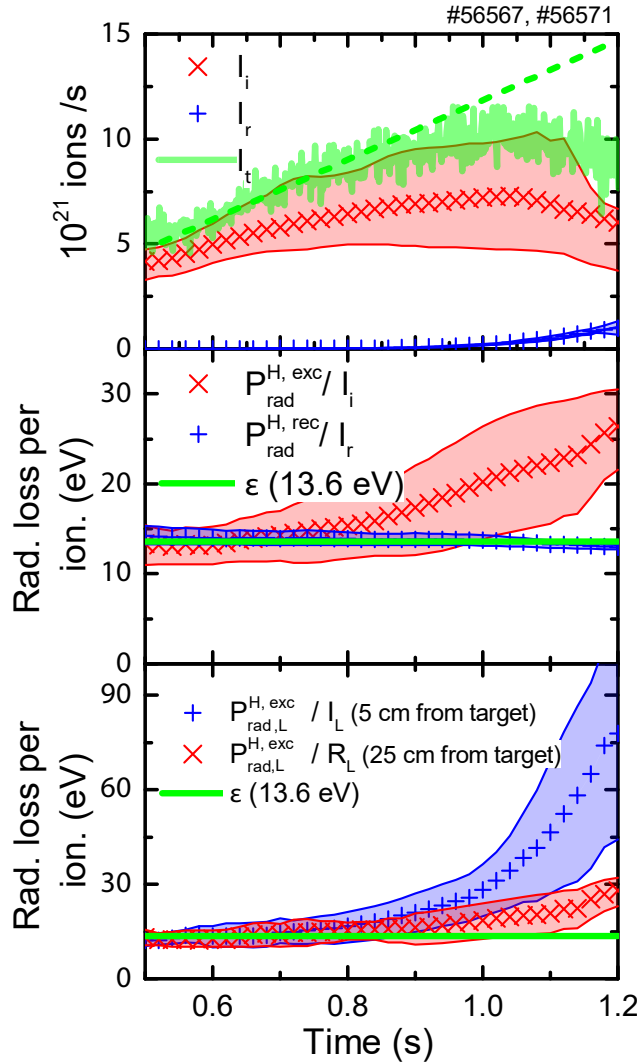


Figure 9.1: a) Target ion flux as function of time together with the ionisation rate and recombination rate. b) Effective radiative energy cost per ionisation/recombination. c) Radiative energy cost per ionisation along a certain chord.

entering the recycling region would be spent on ionisation. During the presented density ramp discharge, that value increases both before and during detachment both due to a decrease in  $P_{recl}$  due to intrinsic impurity radiation and due to an increase in  $E_{ion}$ . When investigating the detached phase where the  $P_{recl}$  starts to approach  $P_{ion}$  (e.g. a large fraction of  $P_{recl}$  is spent on ionisation - figure 8.6), the maximum ion source ( $P_{recl}/E_{ion}$ ) decreases  $\sim 30\%$  between  $t=1.0$  and  $t=1.25$  s, due to a  $\sim 10\%$  decrease in  $P_{recl}$  and a  $\sim 25\%$  increase in  $E_{ion}$ . Hence, arguably, even for the conditions where the divertor radiation is dominated by impurity radiation (figure 8.6), the increase in hydrogenic radiation through a drop in the ionisation region's temperature can play a significant role in limiting the number of ionisations (e.g. reducing  $P_{recl}/E_{ion}$ ) *during the detached phase*. However, in order to go to detachment, volumetric power removal is required, for which impurity radiation is crucial.

Since the number of excitation events required per ionisation rises strongly at low temperatures ( $\sim 2$  eV), poloidal temperature gradients lead to strong variations of the radiative cost of ionisation ( $P_{rad,L}^{H,exc}/I_L$ ) along the divertor leg as shown in (figure 9.1c), where  $P_{rad,L}^{H,exc}/I_L$  is shown for three different divertor chords. In the region close to the target  $P_{rad,L}^{H,exc}/I_L$

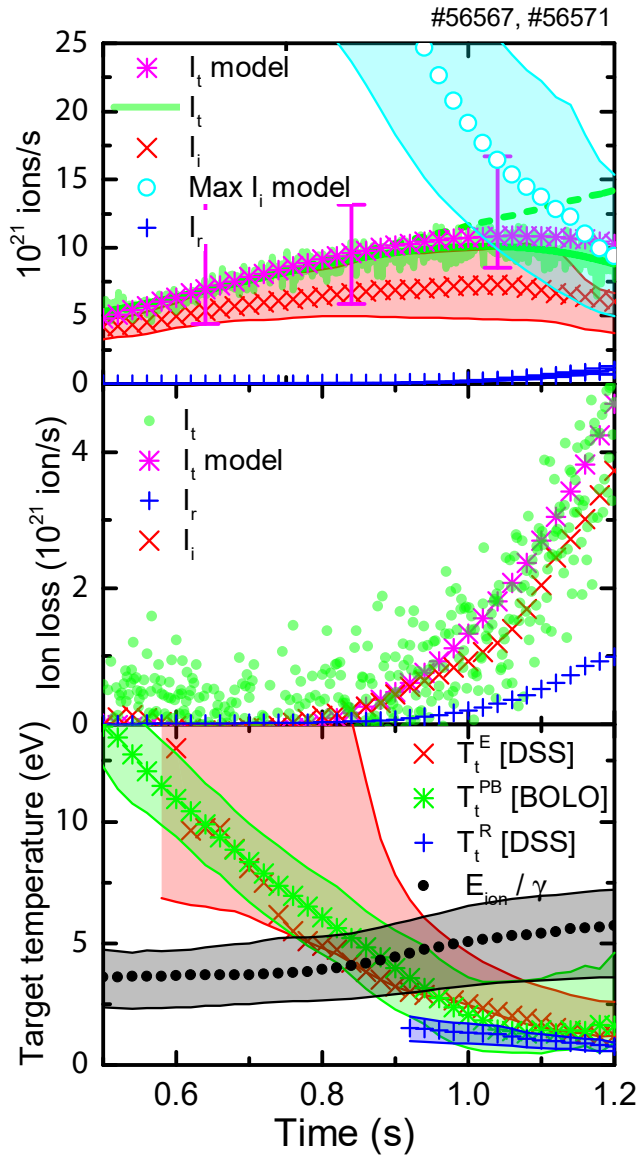


Figure 9.2: a) Predicted ion target flux based on power balance compared with measured ion target flux as function of time. b) Ion loss as function of time for the ion target flux prediction and the measured ion target flux. c) Target temperature as function of time.

increases up to 80 eV. In hotter regions of the divertor leg (chords further away from the target), where most of the ionisation takes place, the excitation radiation cost per ionisation is 15-30 eV (figure 9.1). Thus, variations in geometry (e.g. closed vs open divertor, vertical-vs horizontal-target), which lead to variations in recycling and neutral penetration, could influence the location of the ionisation region and thus could affect the dynamics of the target ion current loss through a change of  $E_{ion}$ , amongst other changes. Furthermore, the increase of  $E_{ion}$  close to the target during the detached phase may provide a second explanation (apart from the more obvious explanation of lower temperatures reducing the ionisation rate) of why the peak in ionisation has to move towards the x-point during detachment.

Whether recombination can heat the divertor plasma is determined by the competition between the energy loss due to recombinative radiation and the potential energy released back to the plasma upon recombination [4, 136], as explained in section 2.4. For the TCV conditions investigated we find that the effective radiated energy loss per recombination event

$(P_{rad,L}^{H,rec}/I_r$  —Figure 9.1b) is roughly equal to the potential energy. That is not surprising, considering the modest TCV densities and the discussion in section 2.4 and figure 3.4, where the difference between  $P_{rad,L}^{H,rec}/I_r$  and the potential energy (13.6) eV was discussed as function of density and temperature. That calculation indicates an effective heating of 0-1 eV per recombination reaction at  $T_e = 1$  eV for  $n_e$  in between  $1 \times 10^{18} \text{ m}^{-3}$  to  $1 \times 10^{20} \text{ m}^{-3}$ . Hence, volumetric recombination does not lead to significant plasma heating for the TCV conditions presented.

### 9.1.2 Target temperature predictions

In addition to  $E_{ion}$  and  $P_{recl}$  also a prediction of the target temperature ( $T_t$ ) is required for evaluating  $I_t$  based on power/particle balance. Obtaining the  $T_t$  during detached conditions on TCV is challenging as  $T_e$  measured by Langmuir probes (LP) is concluded to be often overestimated in detached low  $T_e$  conditions [118, 119, 8] —section 4.2.3.

An estimate of  $T_t$  can be obtained spectroscopically from the line of sight closest to the target, which yields two different target temperatures (section 7.3.1): one target temperature characteristic for the recombinative region ( $T_t^R$ ), which is similar to the temperature obtained by fitting the  $n \geq 9$  Balmer lines with a Saha-Boltzmann fit [51, 41], and one target temperature characteristic for the excitation region ( $T_t^E$ ). Those are both likely an upper limit with respect to the actual target temperatures as the chord views the separatrix region at  $\sim 5$  cm above the target. As a consistency check, these spectroscopically-derived target temperatures are compared with a target temperature derived from power balance ( $T_t^{PB}$  —equation 9.1), which is obtained from power balance (equation 3.4) combined with the closed box approximation (equation 8.1b). Since  $T_t^{PB}$  is obtained from the kinetic power reaching the target,  $T_t^{PB}$  can be regarded as a heat flux averaged target temperature.

$$T_t^{PB} = \frac{P_{div} - P_{rad}}{\gamma I_t} - \frac{\epsilon}{\gamma} \quad (9.1)$$

All three target temperature estimates show a decreasing trend as function of time, reaching target temperatures of 1-2 eV at the end of the discharge (figure 9.2 c).  $T_t^E$  and  $T_t^{PB}$  agree within uncertainty, whereas  $T_t^R$  (shown from 0.9 s onwards, since recombinative signatures are visible from this time) starts lower and decreases less strongly as function of time.  $T_t^R$  is likely lower since recombination-dominated emission increases strongly at low temperatures and is thus dominated by contributions from lower-temperature parts of the plasma along the line of sight (section 7.3.1). We utilize  $T_t^E$  in the following prediction of the target ion flux roll-over (equation 3.10a). This is appropriate as the excitation emission weighted temperature is likely similar to the heat flux averaged temperature, as most excitation near the target occurs at high heat fluxes.

### 9.1.3 Comparing the measured and predicted ion target current

The estimates of  $E_{ion}$  and  $T_t$  enables us, together with the estimate of  $P_{recl}$  (section 8.3) and  $I_r$  (section 8.2) to provide a quantitative model for  $I_i$  and  $I_t$  through power and particle balance (section 3.1 —equation 3.10a).

The predicted ion target flux is in good agreement (in magnitude, trend and roll-over point) with experimental measurements of  $I_t$  (Figure 9.2a). Figure 9.2b displays a comparison

of the predicted and measured target ion current loss and loss of ion source, as previously determined from the deviation of the measured/predicted values to the attached linear trend (section 8.2). This shows that the ion target flux can be described fully in terms of the maximum possible ion source,  $\frac{P_{recl}}{E_{ion}}$ , and the recombination sink,  $I_r$  once the fraction of power spent on ionisation  $f_{ion}$  is known, which requires either knowledge on  $T_t/E_{ion}$  (as explained in section 3.1), or which requires the observation that most of  $P_{recl}$  is spent on ionisation (e.g.  $P_{recl}$  approaching  $P_{ion}$ ) as this already implies that  $f_{ion} \sim 1$ .

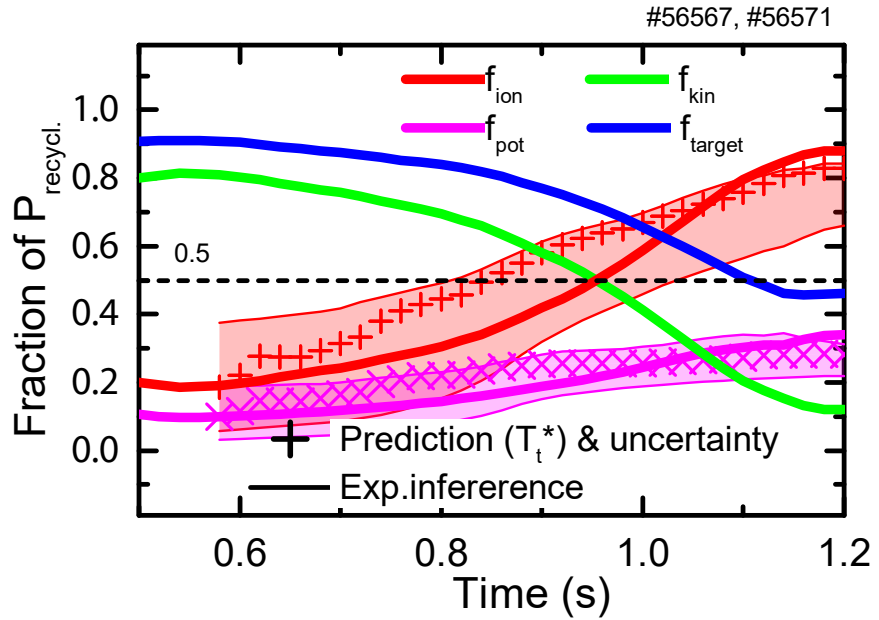


Figure 9.3: Break-down of the fraction of  $P_{recl}$  spent on ionisation ( $f_{ion}$ ); reaching the target ( $f_{target}$ ); reaching the target in the form of potential energy ( $f_{pot}$ ) and reaching the target in the form of kinetic energy ( $f_{kin}$ ). The shown fractions are modelled/predicted, based on  $T_t^*$  (equation 3.11), which are compared to direct experimental inferences from power balance. Note that the fractions visualised in figure 9.3 have not been corrected for recombination, as the ratio  $I_r/I_i$  is small for the TCV discharge presented (see equations 3.11 and 3.13 for further explanation).

The maximum ion source,  $P_{recl}/E_{ion}$ , is of order twice the ion source,  $I_i$ , at the detachment onset (where the deviation of the ion current trend from its linear reference starts), which corresponds to  $f_{ion} \sim 0.5$ . This critical point  $f_{ion} = 0.5$  can also be written in terms of the target temperature (equation 3.10b):  $T_t^* = 1 \rightarrow T_t = E_{ion}/\gamma$  (which is around 4-6 eV), which occurs when the black trend crosses the red trend in figure 9.2. As a reminder, in equation 3.10b it was derived that,  $f_{ion}(T_t^*) = \frac{1}{1+T_t^*}$ , where  $T_t^* = T_t\gamma/E_{ion}$ , where  $\gamma$  is the sheath coefficient. Both of these points are consistent with the empirical detachment threshold  $P_{recl} < 2P_{ion}$  found in section 8.3 figure 8.6. One may think that for the detachment process to start, almost all of  $P_{recl}$  should be used for ionisation, but that is not true as some finite energy must penetrate the ionisation region to sustain a  $T_t$  at the target. In fact the analytic modelling presented in sections 3.3 shows that for  $f_{ion} > 0.5$ , the expected rise of  $I_t$  with further decreases in  $T_t$  is so slow that a target pressure drop is required through the sheath conditions (equation 1.1). Due to this, this point is interpreted as either a point from which volumetric momentum loss must occur [3, 4], under the assumption that the upstream pressure

is uninfluenced by divertor processes; or as a point from which detachment is expected to occur [6, 5, 113]. For more details, see section 3.3.

Through the description of equation 3.10a we see that the dynamics of the target ion current is a competition between two terms: changes in the maximum ion source and recombination,  $(\frac{P_{recl}}{E_{ion}} - I_r)$  —figure 9.2a, which decreases during a density ramp, and changes in  $f_{ion}$  —figure 9.3, which increases during a density ramp (due to the decrease of  $T_t^*$  as both  $T_t$  decreases while  $E_{ion}$  increases). The increase in  $f_{ion}$  is stronger in the period up to  $f_{ion} \sim 0.5$ , leading to a net (linear) increase in the target ion current before detachment. After detachment starts ( $f_{ion} > 0.5$ ), the increases in  $f_{ion}$  becomes slower as function of  $T_t^*$  and becomes insufficient to fully compensate the drop of  $P_{recl}/E_{ion}$  resulting in a flattening of  $I_t$ . As  $f_{ion} \sim 1$  is approached, the drop in  $P_{recl}$ , along with any recombination and increase in  $E_{ion}$ , results in an ion current roll-over as  $I_t \sim (P_{recl}/E_{ion} - I_r)$  equation 3.10a. This observation is *operationally sufficient* to state that the ion source is becoming limited by the amount of power flowing into the recycling region. It however does not explain how one can get to this regime, which requires a detailed understanding of the precise behaviour of  $T_t$ , which requires including momentum balance (section 3.3).

In such conditions where  $f_{ion} \approx 1$ , the maximum ion source is fully set by power/particle balance and power limitation arises from a limitation (or reduction) of the maximum possible ion source ( $P_{recl}/E_{ion}$ ), which decreases during the discharge both due to a decrease in  $P_{recl}$  (section 8.3) and an increase in  $E_{ion}$  (section 9.1.1). When comparing both influences in the strongest detached phase (between  $t = 1.0\text{s}$  and  $t = 1.25\text{s}$ ), the maximum ion source ( $P_{recl}/E_{ion}$ ) decreases  $\sim 30\%$ , due to a  $\sim 10\%$  decrease in  $P_{recl}$  and a  $\sim 25\%$  increase in  $E_{ion}$ . This suggests that, once strongly detached (for which the reduction in  $P_{recl}$  throughout the discharge was crucial —section 8.3), increasing hydrogenic radiation (in the form of  $E_{ion}$ ) by cooling the ionisation region can have an important effect on the power limitation of ion source, augmenting the ion current reduction during detachment —even for the conditions shown where impurity radiation strong dominates over hydrogenic radiation (section 8.3).

#### 9.1.4 Power dynamics in the TCV recycling region

The trend in  $f_{ion}$  can be further investigated for additional physical insight into the power dynamics of the recycling region. First, as shown in equation 3.11a and highlighted previously,  $f_{ion}$  can be modelled/predicted based on  $T_t^*$ . But, considering that we directly estimate  $P_{recl}$  and  $P_{ion}$ ,  $f_{ion}$  can also be inferred *directly* from the experimental spectroscopic observations and power balance as  $f_{ion} = \frac{P_{ion}}{P_{recl}}$ . The experimental inference (solid lines) agrees with the predicted  $f_{ion}$  (symbols) within uncertainty (figure 9.3). Since  $f_{ion}$  is the fraction of  $P_{recl}$  spent on ionisation, we can also calculate the remaining fraction of  $P_{recl}$  left after passing the ionisation region in the form of kinetic energy ( $f_{kin} = 1 - f_{ion}$  —equation 3.11b), which drops from  $\sim 1$  to  $\sim 0.6$  during the attached phase, while dropping from  $\sim 0.6$  at the detachment onset towards 0, during detachment; consistent with a target temperature drop (equation 3.11b). In the absence of recombination, those ions left after the ionisation region leave the target and their associated kinetic power reaching the target is  $f_{kin}P_{recl}$ . Apart from modelling  $f_{kin}$  based on  $T_t^*$ , one can also infer  $f_{kin}$  directly experimentally:  $f_{kin} = \frac{I_t \gamma T_t}{P_{recl}}$ .

The power deposition to the target does not only depend on  $f_{kin}$  but also a part of the power spent on ionisation (e.g. a fraction of  $f_{ion}$ ) reaches the target. That part is the power

associated with the potential energy spent on neutral to ion conversion (ionisation) in the recycling region ( $\epsilon I_i$ ); which is later released as either volumetric recombination (which also leads to radiation losses, similar to  $\epsilon$  per recombination event —section 9.1.1) or surface recombination at the target. Assuming volumetric recombination is negligible, all ions would recombine at the target. The fraction of energy involved in this process of  $E_{ion}$  is  $\frac{\epsilon}{E_{ion}}$  and thus the fraction of power reaching the target in the absence of recombination in the form of potential energy is  $f_{pot} = \frac{\epsilon}{E_{ion}} f_{ion}$  (equation 3.11c). Again, this modelled  $f_{pot}$  can be compared with the directly estimate:  $f_{pot} = \frac{I_t \epsilon}{P_{recl}}$ . As shown in figure 9.3,  $f_{pot}$  throughout the discharge increases as more of  $P_{recl}$  is used for ionisation. However, as one can see, that increase has a limit at  $\frac{\epsilon}{E_{ion}}$  (which is around 0.35 assuming  $E_{ion} \sim 40$  eV) where  $f_{ion} \rightarrow 1$ .

The total power fraction of  $P_{recl}$  reaching the target is:  $f_{target} = f_{pot} + f_{kin}$  (equation 3.11d), which decreases as function of time (Figure 9.3) from 90 % to 40 %;  $f_{target}$  is never 1 due to the power lost due to radiative excitation losses associated with ionisation in the recycling region ( $P_{rad}^{H_{exc}}$ ). When  $f_{kin}$  approaches 0,  $f_{pot}$  becomes the lower limit of  $f_{target}$ , and thus the power fraction reaching the target can attain ( $E_{ion} \sim 40$  eV)  $\sim 35$  %. For a further reduction of  $f_{target}$  volumetric recombination is required. Although a deviation of the target ion flux from linear starts once  $f_{ion}$  becomes larger than 0.5, the target integrated ion current roll-over appears to start at higher  $f_{ion}$  where  $f_{pot}$  and  $f_{kin}$  are similar (Figure 9.3,  $\sim 1.05$ s); the kinetic energy of the ions reaching the target is comparable to the potential energy released at the target. That corresponds to a target temperature,  $T_t = \frac{\epsilon}{\gamma} \approx 2$  eV based on equation 3.11.

Recombination has not been accounted in this discussion as, but can be included by multiplying  $E_{ion}$  with  $1/\beta$  where  $\beta$  is the fraction of ionised ions reaching the target ( $\beta = \frac{I_t - I_r}{I_t}$ ) (see equation 3.13 and accompanying discussion). For the discharge presented,  $\frac{I_t - I_r}{I_t} > 0.85$  and thus including recombination would lead to at most a 17 % change in the 'effective'  $E_{ion}$ . Assuming a case with a fixed low divertor temperature, including recombination would 1) enhance  $f_{ion}$ , enabling it to reach 1 faster; 2) lower the limit of  $f_{pot} = \beta \epsilon / E_{ion}$  and thus enable the target power fractions to drop below the 35 % presented.

## 9.2 Investigating detachment in the framework of power, particle and momentum balance

In the previous section we have investigated the target ion flux trend in the framework of power and particle balance of the entire SOL. In this section, we add momentum (pressure) balance [3, 5] to the power/particle balance analysis of previous section, such that the target temperature is now *predicted* instead of *set* by measurements. This enables a single flux tube comparison of the observed detachment dynamics and onset with additional predictions from simplified analytical theory; the preceding work has all been for the entire outer divertor. In this discussion, only the electron pressure is considered.

Trends in target and upstream pressure are compared in figure 9.4, where  $p_u$  is obtained from Thomson scattering while  $p_t$  is obtained from spectroscopic inferences of the target density/temperature from the chord closest to the target. By assuming  $p_t \sim p_u$  before detachment,  $p_t$  appears to be significantly underestimated by approximately a factor two, which can be explained by the chordal-average nature of the spectroscopically estimated

target pressure. That factor two is consistent with the deviation between a spectroscopically inferred pressure and using the local separatrix pressure when using a synthetic spectrometer on SOLPS detached discharges.

Both the upstream and target pressure are observed to roll-over at the target ion flux roll-over (figure 9.4b, d). The upstream density saturates simultaneous with a roll-over in the upstream pressure, while the upstream temperature drops (section 8.1 —figure 8.1). As discussed in the introduction and theory section (equation 1.1), at any point during the discharge, the target ion flux scaling can be written as  $\Gamma_t \propto p_t/T_t^{1/2}$ , i.e. the target plasma pressure must drop faster than  $T_t^{1/2}$  at the target ion flux roll-over, which is indeed approximately observed (figure 9.4c). Following the discussion in section 9.1, the relation  $\Gamma_t \propto p_t/T_t^{1/2}$  links the trend in the ionisation source (equation 3.10a) to the trend in the target pressure and is thus crucial for understanding the complex interplay between momentum balance and ionisation balance (see the beginning of section 3.3).

### 9.2.1 Modelling total target ion current behaviour with both power and momentum balance

We utilise a ‘two point’ divertor model [4, 6], which accounts for hydrogen recycling energy losses, to model the total target ion current, here dubbed *the 2PMR*, which was introduced and highlighted in section 3.3 and was previously introduced in literature [78, 3, 6]. For the implementation of the 2PMR in *this subsection* we assume momentum balance. Our first goal of the application of the 2PMR is to verify the expected *integrated ion target flux trend* in attached conditions ( $I_t$ ). For this, we utilise the techniques highlighted in section 3.6 and interrogate equation 3.26. The idea behind that approach is to evaluate equation 3.19b to obtain  $\Gamma_t$  for a *single* flux tube, which is then integrated by providing a profile for the input parameters of equation 3.19b. Furthermore, pressure balance was assumed. The result for  $I_t$  is obtained by using the  $P_{recl}$  and  $E_{ion}$  inferences presented earlier (sections 9.1 and 9.1.1) together with reciprocating probe measurements to provide upstream density/temperature profiles; Thomson measurements to provide the upstream separatrix density/temperature at a higher time resolution and IR heat flux measurements to estimate the width of the recycling region (which is assumed to be the same as the width of the target heat flux).

The predicted  $I_t$  through this approach shown in figure 9.6 a is similar to the measured target flux in the attached phase, showing a clear linear increase as function of time (and thus upstream and line averaged density —figure 8.1). Hence, simply using  $I_t \propto n_u^2$ , on which the ‘Degree of Detachment’ [102] (discussed in section 2.2 and 3.3), a parameter often used to investigate the ‘depth’ of detachment [58, 101, 73], is based, is not appropriate for the TCV density ramp discharges studied and should generally be used more carefully. In fact, from a 2PMR point of view, if  $T_u, q_{recl}, E_{ion}$  are held constant and only the upstream density is increased, a different scaling than  $\Gamma_t \propto n_u^2$  is expected (see figure 3.8 a). The main term contributing to  $I_t$  (modelled through equation 3.26) is  $p_u^2/P_{recl}$  as shown in figure 9.6 b, while the influence of changes in upstream profiles on  $I_t$  (described by the term  $f_p$  equation 3.27) and the influence of  $f_{kin}$  on  $I_t$  in the attached phase are minor. This basic scaling (or  $\Gamma_t \propto p_u^2/q_{recl}$ ) not only arises from the 2PMR, but can also be obtained directly from pressure balance and the sheath target equation, resulting  $\Gamma_t \propto \frac{n_u^2 T_u^2}{q_t}$  as was derived in section 2.2 equation 2.7; providing an equivalent relation for the target ion flux as discussed here and

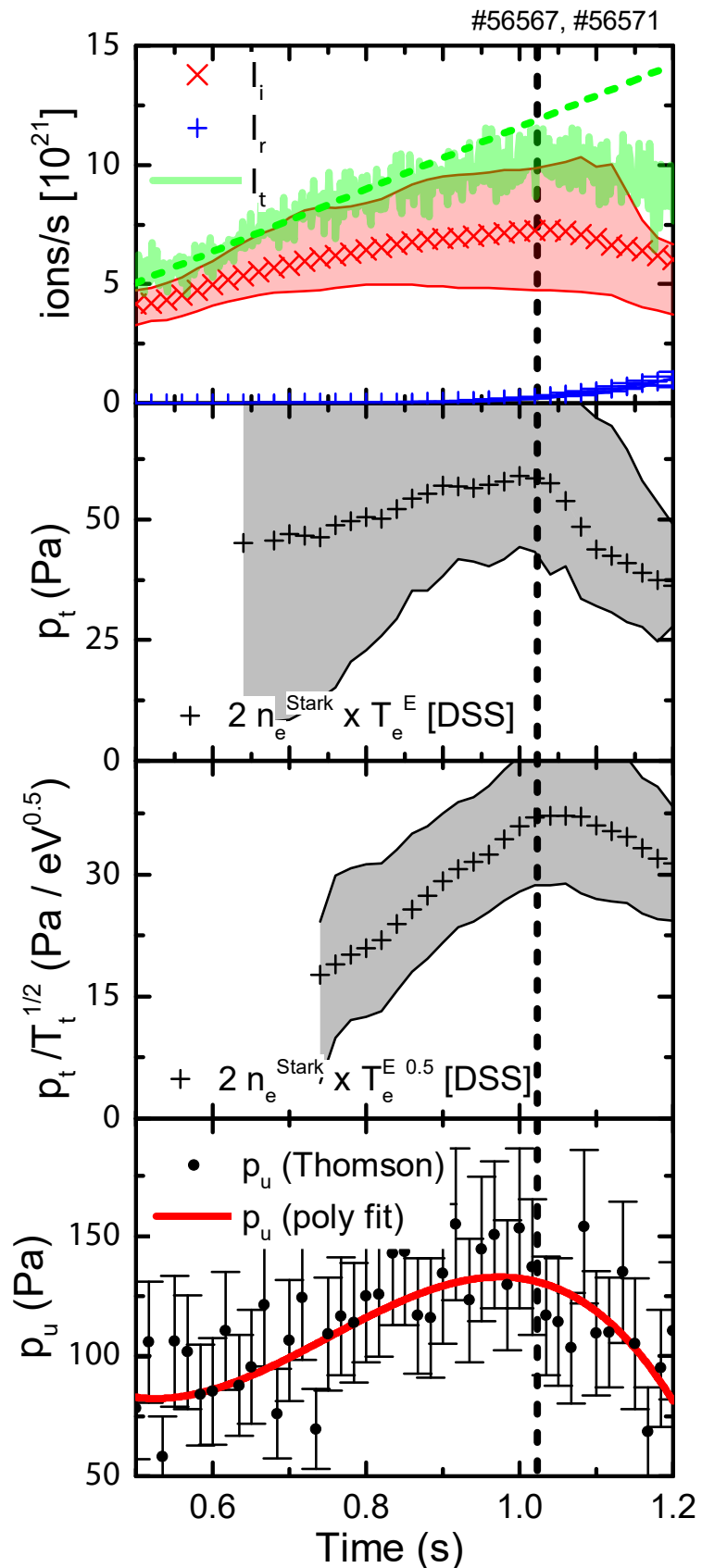


Figure 9.4: Comparison of target pressure and upstream pressure. a) reference total current to the target, total ionisation source and recombination sink; b-c) Target separatrix pressure ( $p_t$ ) and ( $p_t/T_t^{1/2}$ ) ratio based on spectroscopic measurements (Stark broadening + excitation temperature of the chord closes to the target); d) Upstream separatrix pressure from Thomson scattering.

equivalent relation to the one used in [102] for defining the degree of detachment originally (obtained by using equations 3,4,8 in [102]).

Since  $I_t \propto p_u^2/P_{rec}$  increases linearly as  $n_u$ ,  $T_u^2/P_{rec}$  must decrease roughly as  $1/n_u$ . Given that  $P_{rec}$  decreases during the density ramp (section 8.3),  $T_u$  (figure 8.1) must decrease more strongly than  $\frac{1}{n_u}$  during the attached phase to give this scaling. As  $P_{div}$  is roughly constant throughout the discharge (figure 8.6) a decrease of  $T_u$  could result from SOL broadening (which is measured by IR thermography to increase by over a factor 3 until detachment is reached for the discharge shown [99]). Alternatively, the decrease of  $T_u$  could be due to an increase in convective over conduction parallel heat transport [3] and as explained in section 2.2. The influence of the broadening of the SOL on  $T_u$  is shown in figure 9.5 where the predicted  $T_u$  based on conductivity (equation 2.5) is shown, where  $\kappa = 2000$  and  $q_{||}$  was determined using  $P_{div}$  and the measured heat flux width ( $\lambda_{q,int}$ ) and the connection length  $L$  was retrieved from the magnetic equilibrium. The  $T_u = (7q_{||}L/4\kappa)^{2/7}$  relation, respective of the heat flux entering throughout the SOL rather than from the top of the SOL ([3] equation 4.91) as this provided a more adequate agreement with the measured  $T_u$ . This indicates that the decrease in  $T_u$  during the attached phase can indeed be described through SOL broadening.

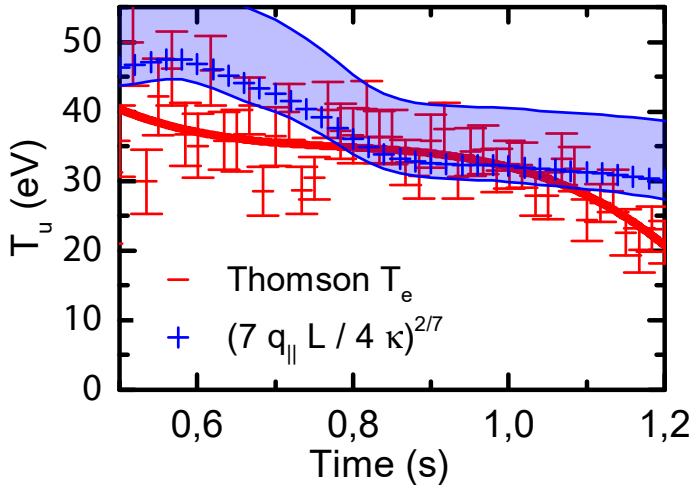


Figure 9.5: Thomson upstream temperature as function of time for # 56567 together with the upstream temperature prediction from conductivity.

A previous TCV study concluded that the observed linear trend of  $I_t$  with  $\bar{n}_e$  on TCV indicated that the divertor plasma was in a low-recycling operation [45]. However, given our measurements that the target ion current agrees with the ionisation source (section 8.2) and that  $I_t$  is properly predicted by the 2PMR (which assumes that all target ion current is due to divertor ionisation) is more consistent with characterizing the divertor as high-recycling.

### 9.2.2 Detachment thresholds and implications for momentum/pressure losses along a flux tube (separatrix)

It is evident from equation 1.1 that the ion current roll-over, together with a fixed/decreasing target temperature, must be accompanied by target pressure loss. More specifically the target pressure cannot be increased indefinitely, and a maximum exists as  $p_t \propto \Gamma_t T_t^{1/2}$  (sections 3.1 and 3.3). That critical maximum target pressure is reached at 0.8 s in figure 9.6, after which

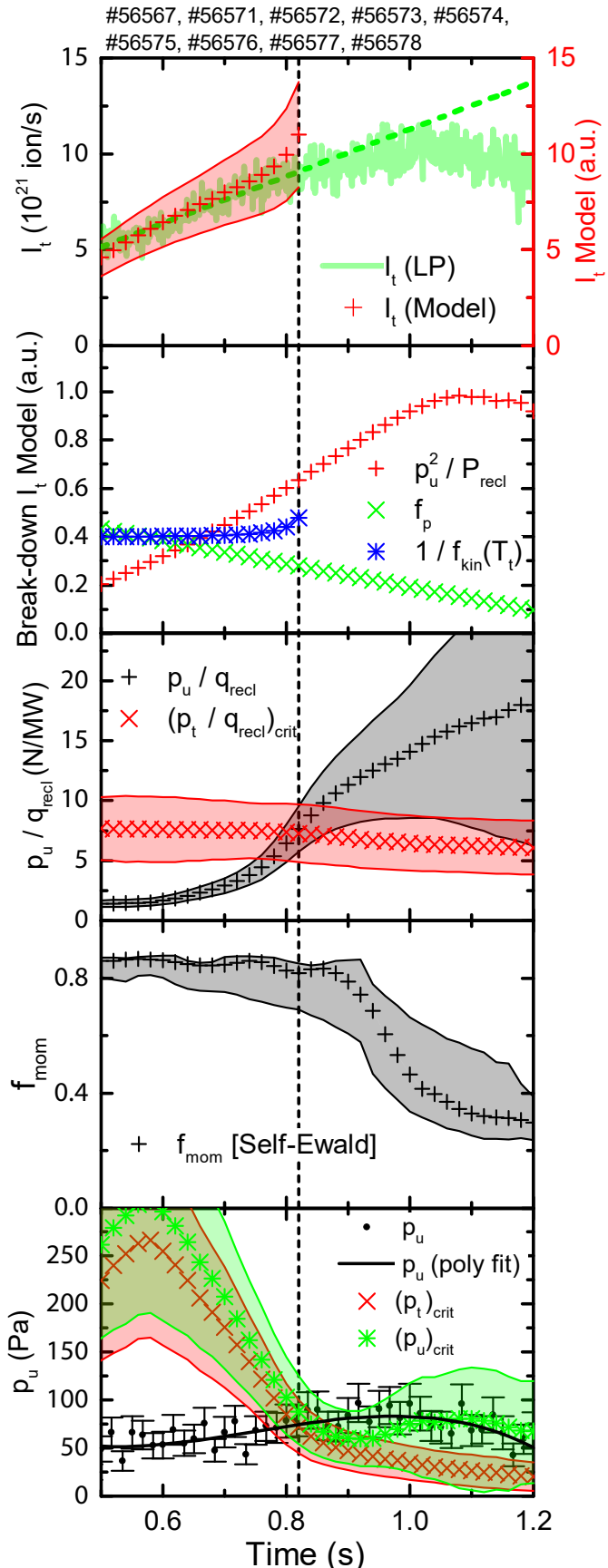


Figure 9.6: a) Measured and predicted target ion flux trend. b) Break-down of the contributors to the predicted ion flux. c) Measured  $p_u/q_{recl}$  compared to the critical predicted level for  $p_t/q_{recl}$ . d) Inferred momentum losses from spectroscopic estimates. e) Measured upstream pressure compared to critical target pressure level.

the target pressure must reduce as  $\Gamma_t$  rises slower than  $T_t^{1/2}$  drops. This is not allowed by the model assumptions of a fixed, prescribed  $p_u$  and constant pressure along the field lines; which is why the  $I_t$  result cannot be computed beyond this point (figure 9.6 a) and which is why the approach used to model  $I_t$  can only be used in attached conditions.

The point, or threshold, where the target pressure is maximised and target pressure loss is necessary has been suggested by Krasheninnikov [6, 5] to be a ‘detachment onset criterion’, which occurs at  $f_{ion} > 0.5; T_t < E_{ion}/\gamma$ . Krasheninnikov reasons that, for target temperatures below this limit insufficient power is transferred beyond the ionisation region to sustain a sufficiently high target temperature for the target pressure (which is collapsing) to match the upstream pressure. Stangeby, although not calling the above limits a detachment threshold, argues properly that to reach  $T_t < E_{ion}/\gamma$  processes such volumetric momentum loss must be accounted for, which enable the upstream pressure to remain high while the target pressure is reducing. More specifically, a prescribed function which reduces the target pressure as function of  $T_t$  (within  $T_t < E_{ion}/\gamma$ ) is required to obtain 2PMR solutions for temperatures below  $E_{ion}/\gamma$  as was also shown in section 3.5 figure 3.11. This target pressure reduction could be achieved either by  $p_u$  or  $n_u$  dropping with  $T_t$  without momentum losses (figure 3.12, 3.13); or by a fixed upstream pressure while volumetric momentum loss occurs within  $T_t < E_{ion}/\gamma$  [4, 3]; or a combination of the two. See section 3.3 for more information and for various functional forms indicating the ‘speed’ at which  $p_t$  has to drop with  $T_t$  and the effect of those forms.

The point at which target pressure loss must start to be accounted for, or ‘detachment thresholds’ are given by equation 3.22 which we have repeated for simplicity (equation 9.2) below. The  $f_{ion}$  and  $T_{t,crit}$  criteria, were found previously (figure 8.6 and 9.2) as empirical thresholds for the onset of detachment. A third (equivalent) criterion for the detachment onset has been derived from the 2PMR (equation 3.22a [5]), providing a critical maximum target pressure ( $p_{t,crit} = q_{recl}/(2\gamma c_s(T_t = E_{ion}/\gamma))$ ), more commonly written as a critical upstream limit for  $\frac{p_t}{q_{recl}}$  or —assuming pressure balance  $\frac{p_u}{q_{recl}}$  [5] where  $c_s$  is the target sound speed at  $T_t = E_{ion}/\gamma$ .  $(p_t/q_{recl})_{crit}$ , which applies to a flux tube—not the average over the divertor, is compared to the experimentally inferred  $p_u/q_{recl}$  in Figure 9.6c. The observed increase in  $p_u/q_{recl}$  is mostly ascribable to a drop in  $q_{recl}$  during the pulse. This third critical limit (equation 9.2a), evaluated at the separatrix, is also reached at  $\sim 0.8$  (figure 9.6c), similar to the other detachment criteria ( $f_{ion} = 0.5$  (Figure 9.3),  $T_t = \frac{E_{ion}}{\gamma}$  (Figure 8.6)) After this threshold is reached, the observed  $p_u/q_{recl}$  rises beyond the critical maxima for  $p_t/q_{recl}$ . All of these three points correspond to the point where the integrated target ion current starts to flatten (deviate from the linearly increasing trend); at the start of the detachment process (where, for the case presented, also the separatrix ion target current density starts to roll-over)—see figure 8.1. For the reader’s convenience and in order to better highlight the correspondence of the various detachment thresholds to the experiment, all three thresholds are shown at once in figure 9.7. Note that for figure 9.7c  $p_u = p_t$  was assumed to transform the  $(\frac{p_t}{q_{recl}})_{crit}$

threshold into  $(\frac{p_u}{q_{recl}})_{crit}$ , which is compared to the measured  $(\frac{p_u}{q_{recl}})$ .

$$(\frac{p_t}{q_{recl}})_{crit} = \frac{1}{\gamma c_s(T_t = \frac{E_{ion}}{\gamma})} \quad (9.2a)$$

$$T_{t,crit} = \frac{E_{ion}}{\gamma} \quad (9.2b)$$

$$f_{ion} = \frac{1}{2} \quad (9.2c)$$

### 9.2.3 The 2PMR and momentum losses

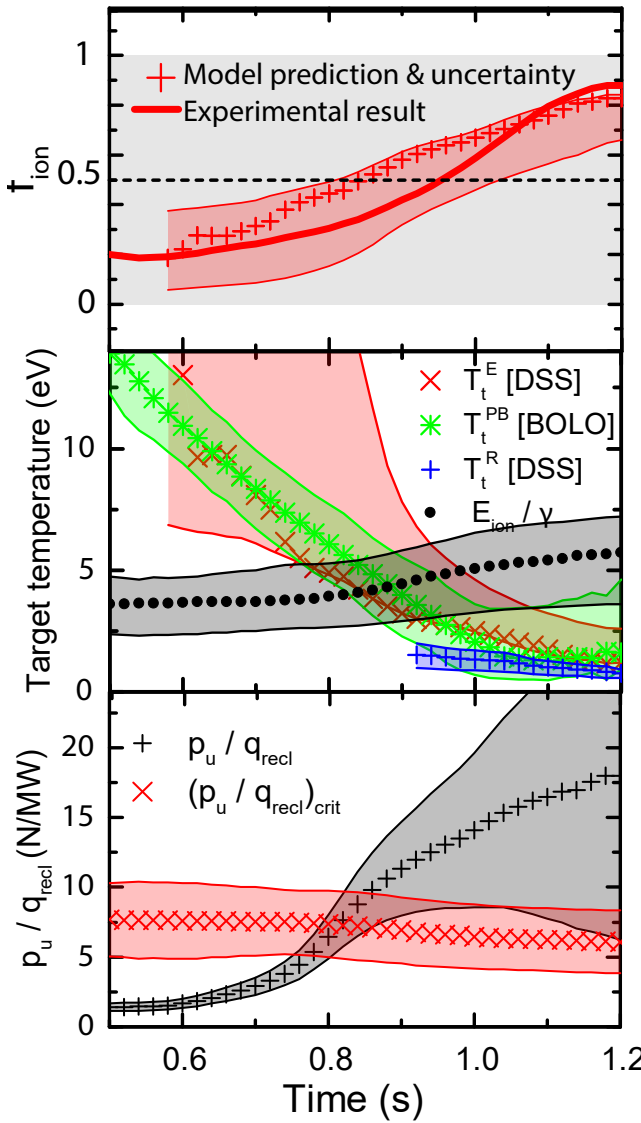


Figure 9.7: Comparison of the various detachment thresholds with the experiment. a)  $f_{ion}$ . b)  $T_t$ . c)  $p_{up}/q_{recl}$

to rise beyond  $(p_t/q_{recl})_{crit}$  and  $I_t$  to roll-over as shown in section 3.5. Momentum losses

Solutions beyond these limits (equation 9.2) require additional processes which enable  $p_t$  to drop at  $T_t < E_{ion}/\gamma$  and missing processes could also include neutral transport [5] and recombination [6]. In the following we assume that only momentum losses are “missing” from the 2PMR, defined by a factor  $f_{mom} \equiv p_t/p_u$  (note that when we refer to  $p_t$  in this work, this corresponds to  $2n_t T_t$  and already includes the dynamic pressure at the target). Since the relation between momentum loss and the target temperature is unknown for TCV, we specify  $f_{mom}$  as a function of time—which we obtain experimentally from the Self-Ewald model as explained previously (section 2.4). This contrasts to prescribing the function  $f_{mom}(T_t)$  as used in [4, 3] where various  $f_{mom}(T_t)$  relations from literature were used. Furthermore, SOLPS simulations for TCV indicate that volumetric pressure loss can occur in the volume of the divertor [7]; not just in front of the target as observed in simulations [49] for other machines on some of the  $f_{mom}(T_t)$  prescriptions in [4] are based. Assuming such a specified  $f_{mom}$  does not enable solutions for lower temperatures ( $T_t < E_{ion}/\gamma$ ) as this requires a specific  $f_{mom}(T_t)$  (section 3.3). It does, however, enable  $p_u/q_{recl}$

can therefore explain why  $p_u/q_{recl}$  rises above  $(p_t/q_{recl})_{crit}$  (e.g.  $p_u/q_{recl} = \frac{1}{f_{mom}}(p_t/q_{recl})_{crit}$ ). Using figure 9.6 c, a minimum  $f_{mom}$  drop starting at 0.8 s from 1 to 0.4 at the end of the discharge would be required to explain the increase of  $p_u/q_{recl}$  beyond the maximum  $(p_t/q_{recl})_{crit}$ , irrespective of the maximum possible target pressure. Such momentum losses in the TCV divertor during similar experiments have been determined directly from upstream and target pressure measurements [8], implying momentum losses greater than 50%.

An independent estimate of the onset and magnitude of momentum losses based solely on the dominance of charge exchange over ionisation can be made using the Self-Ewald model [33, 141] where  $f_{mom}$  is a function of the charge exchange to ionisation ratio. This model has been introduced in section 2.4 (equation 2.9) and has been used in several other studies [45, 6, 141] where some supportive evidence was shown. One key difference between such studies and the way the Self-Ewald model is used here is that in such studies often the target temperature is used to evaluate the charge exchange to ionisation ratio. This, since the target has the lowest temperature, likely leads to an overestimation of the charge exchange to ionisation ratio which is a strong function of target temperature (figure 2.7). Therefore, our approach is to utilise the spectroscopically estimated charge exchange to ionisation ratios to infer  $f_{mom}$  along the divertor leg. As momentum loss from charge exchange involves neutral-ion collisions just as ionisation, we will use the ionisation profile along the divertor leg in order to determine an averaged charge exchange to ionisation rate value of the divertor weighted by the ionisation profile. We feel such an averaged charge exchange to ionisation ratio is more respective of the situation, especially as momentum loss occurs volumetrically in TCV.

The Self-Ewald model uses an over-simplified physics model to predict  $f_{mom}$  (which assumes isothermal field lines and treats charge exchange collisions as a drag force), which is generally overestimated (figure 2.7) when compared to scaling laws introduced in [4]. Molecular-ion collisions are also not included, which provide additional momentum loss, which could be significant [50, 49, 4, 78], although other works estimate their importance to be minor [141]. Also transport may influence momentum losses, for instance transporting momentum cross-field and thus reducing it locally at the separatrix flux tube [141]. Although the level of momentum loss due to molecules is unknown for TCV, we do know that molecules are present and undergoing reactions in the volume of TCV from the investigation of  $D\alpha$  emission (section 8.4). SOLPS simulations for TCV [7] indicate momentum losses could be important in detached conditions but are secondary to charge exchange. Momentum loss can also occur due to recombination. From a simple SOL model [143] we have evaluated the reduction of  $f_{mom}$  due to recombination (section 2.4) for the case studied and found it negligible —smaller than 1.5% (in agreement with results from literature [51]).

Our estimate of  $f_{mom}$ , using the Self-Ewald model (equation 2.9), drops from  $\sim 0.9$  to  $\sim 0.3$  (0.2 to 0.4 with uncertainty) is shown in Figure 9.6d, in agreement with the momentum losses obtained experimentally [8] and with the  $f_{mom}$  required to explain the increase of  $p_u/q_{recl}$  beyond the maximum  $p_t/q_{recl}$  limit discussed above. This may be a coincidence as the Self-Ewald model provides a qualitative picture of momentum loss due to its simplifications in the physics model.

### 9.2.4 The case for divertor processes reducing the upstream pressure and density

The results of the previous section show that the rise of  $\frac{p_u}{q_{recl}}$  beyond its critical limit can be attributed, at least partially, to momentum losses. However,  $p_u$  also drops during the detached phase, which will be investigated here further together with the role it plays in matching  $\frac{p_u}{q_{recl}}$  to its critical threshold (equation 3.18). The question of what leads to the drop in upstream pressure (and density) during detachment has been discussed by several authors of analytic and modelling studies [5, 52, 53].

Recombination has been predicted to lead to saturation of the upstream density when its rate approaches the ionisation rate in a flux tube through a feedback loop [113]: as  $n_u$  increases, the divertor cools further, hence augmenting the recombination sink and moving the recombination region further towards the x-point, potentially impeding a rise in  $n_u$  [113]. This is not the case for these TCV discharges as recombination remains low (or negligible) and the recombination peak does not move far off the target (sections 8.1.1 8.2 and [1]).

Krasheninnikov [5, 6] offers another explanation for saturation of the upstream density: during detachment insufficient momentum losses along flux tubes can constrain, or pull down the upstream pressure. It is important to reiterate that, although an  $I_t$  roll-over requires a target pressure drop which increases faster than  $T_t^{1/2}$  (equation 2.2), mathematically (from the viewpoint of the 2PMR) this can be provided by either volumetric momentum loss and/or a reduction of upstream pressure (section 3.3).

In fact, the 2PMR predicts that there is a critical maximum target pressure  $((p_t)_{crit})$  allowed for a given  $q_{recl}$  and  $E_{ion}$ , which is inferred throughout the discharge in figure 9.6e. We remind the reader (see section 3.3) that this target pressure maxima occurs as there is a maximum to  $p_t \propto \Gamma_t T_t^{1/2}$  due to a maximum limit in the ionisation source (dependent on  $q_{recl}$  and  $E_{ion}$ ) and due to  $f_{ion}$ , which highlights the trade-off between the fraction of  $q_{recl}$  used for ionisation and the target temperature (e.g. ionising a larger fraction of  $q_{recl}$  leads to larger  $\Gamma_t$  but smaller  $T_t$ ). Since  $f_{mom}$  is estimated throughout the discharge using the Self-Ewald model; that also means that a maximum critical upstream pressure  $(p_u)_{crit} = \frac{1}{f_{mom}} \times (p_t)_{crit}$  can be inferred throughout the discharge as shown in figure 9.6e. Note that the target/upstream pressures do not have to be at their critical values, but below their critical values as illustrated in section 3.3. These two critical maxima pressure estimates are compared to the measured upstream pressure (Thomson scattering) in figure 9.6e. The measured upstream pressure rises during the density ramp, while both pressure limits drop due to a decrease in  $q_{recl}$  until  $p_u$  crosses the maximum  $p_t$  limit at  $\sim 0.8$  s; the detachment threshold. At the same time momentum losses start to develop, leading to a bifurcation between the upstream/target critical pressures: the  $p_t$  limit keeps decreasing while the upstream pressure initially keeps on increasing and later saturates/drops. While this occurs, the upstream pressure remains roughly at the inferred upstream pressure limit. This observation leads to several points. First, it shows that the observation is consistent with the inferred pressure limits. Secondly, since a given  $q_{recl}$  and  $E_{ion}$  leads to a maximum obtainable  $p_t$  and since  $f_{mom}$  provides the strength of the bifurcation between this maximum obtainable  $p_t$  and a maximum obtainable  $p_u$ ; more momentum loss would either support higher upstream pressures at the same level of  $q_{recl}, E_{ion}$  or would enable  $p_t$  to drop below its maximum level —which enables lower temperature solutions in the 2PMR (section 3.5). The most important point, however, is that

given the decrease in  $q_{recl}$  and increase in  $E_{ion}$  during detachment, the target pressure during the experiment must be reduced by such a large amount that the spectroscopically inferred momentum loss, by itself, would be insufficient and thus  $p_u$  would need saturate/drop for consistency —which is indeed experimentally observed.

The upstream pressure roll-over is an observation for TCV and needs to be accounted for. Although the result shown in figure 9.6e is consistent with the notion that inadequate momentum loss could lead to an upstream pressure drop as suggested by [6]; this consistency does not indicate causation. For instance, other processes (i.e. cross-field transport (particles and/or momentum)) may be reducing the upstream pressure as well. A commonly held assumption is that the upstream pressure remains constant/unaffected by detachment, resulting in the (mis)understanding that all required  $p_t$  drop must be provided by only volumetric momentum losses. These TCV results however show that both an upstream pressure drop and volumetric momentum losses contribute to the required  $p_t$  drop. Accounting for upstream pressure changes is thus crucial for understanding detachment.

### 9.2.5 The role of momentum loss and upstream pressure loss in target ion current loss

As described in the introduction researchers generally look at detachment from two different ways: power/particle balance and momentum balance, which mostly focusses on volumetric momentum losses. Both viewpoints for describing detachment must be consistent with equation 2.2. As explained earlier, the 2PMR, which combines both points of view, predicts when detachment occurs/power limitation starts ( $P_{ion} \sim 1/2P_{recl}$ ;  $T_t \sim \frac{E_{ion}}{\gamma} \sim 4 - 6\text{eV}$ ), which corresponds to the point where the ion target current increases slower than  $1/T_t^{1/2}$ , hence requiring a target pressure loss. Thus both target pressure loss and power limitation are required for detachment when the divertor is the primary source of ions.

It is striking that the temperatures ( $T_t < \frac{E_{ion}}{\gamma} \sim 4 - 6\text{eV}$ ) at which target pressure loss must occur (2PMR), according to divertor-physics, corresponds to the temperatures at which volumetric momentum loss can occur, according to atomic physics. This seeming coincidence of plasma and atomic physics implies volumetric momentum loss develops when power ‘limitation’ conditions ( $P_{recl} < 2P_{ion}$ ) are reached, implying that power ‘limitation’ is a requirement for detachment for both points of view discussed.

The results of section 9.2.4 show that the commonly held assumption that the upstream pressure remains constant/unaffected by detachment is not always true. Instead, the upstream target pressure and any volumetric momentum loss must be consistent with each other. This means the role of volumetric momentum loss can only be fully understood if all the processes influencing the upstream pressure are understood. These may be divertor, scrape-off layer and core processes. Examples could include changes in cross-field transport of energy, momentum and particles or volumetric losses within a flux tube, or both. Ionisation could also play a role in this by providing the particles in order to build up the upstream electron density, as suggested by [5]. The reality, however, is that we lack a quantitative understanding of how  $p_u$  is influenced by both the core and divertor plasma, which likely requires an integrated core-edge model. Lacking such a model prevents us from fully ascertaining the role momentum loss plays in detachment.

Nevertheless, it is unlikely that momentum losses directly reduce the ion target current

during fully power-limited ( $P_{recl} \sim P_{ion}$ ) detachment as  $I_t \sim P_{recl}/E_{ion}$  (section 9.1) for those conditions: momentum losses slow down the fluid velocity in a flux tube, but do not directly reduce the ion flux through the tube. Momentum losses may, however facilitate detachment indirectly by allowing higher upstream pressures, leading to higher divertor densities (for the same  $T_e$ ) and thus higher divertor radiation and higher recombination rates. They may play a role in providing ( $T_t < \frac{E_{ion}}{\gamma} \sim 4 - 6$  eV) solutions, which require a specific  $p_t(T_t)$  reduction in the 2PMR (section 3.5), giving access to lower temperatures. The precise dynamics of  $T_t$  during detachment, however, tends to depend very strongly on the precise speed at which  $p_t(T_t)$  is reduced (figure 3.12).

### 9.3 $N_2$ seeded detachment on TCV

One of the interesting observations during the discussed  $N_2$  seeded detachment cases (section 8.2.2) is that recombination during  $N_2$  seeding is relatively small; comparable to the pre-detached values of the density ramp experiments where the Stark/upstream densities were similar. To further investigate this, the total recombination rate relative to the ion target flux for the two density ramp discharges and the  $N_2$  seeded discharge discussed in figure 8.4 is shown in figure 9.8 as function of the inferred Stark density from the chord near the target. Here it is shown that the recombination rate is fairly stable and increases somewhat with Stark density at low Stark density values. However, when the Stark density is further increased, the observed recombination rate starts to rise more strongly during the detached phase as the temperature is reduced, leading to elevated recombination rates. This elevation point occurs at lower Stark densities for the lower current case than for the higher current case due to the differences in Ohmic power and thus power crossing the separatrix. For the  $N_2$  seeded discharge, however, the recombination rate only slightly increases with Stark density: the strong sudden rise in the recombination rate does not occur. This suggests that, although the recombination values for the  $N_2$  seeded case are similar to the recombination values for the density ramp cases when compared at the same divertor densities (which corresponds to the pre-detached values for the density ramp cases), the sudden increase in recombination due to achieving lower target temperatures does not occur for the  $N_2$  seeded case. If the target temperatures for the  $N_2$  seeded case would not be below 3-4 eV (see figure 2.5), this could explain the observation of a lack of volumetric recombination during the  $N_2$  seeded case. Other points which could explain this would be an overestimation of the Stark inferred density or a particularly high nitrogen impurity fraction such that the hydrogen ion density is significantly reduced below the electron density.

In addition to the differences in observed recombination and recombinative emission, there is also a difference in the behaviour of  $D\alpha$  between a density ramp discharge and an  $N_2$  seeded discharge at constant core density. The strong rise in  $D\alpha$  observed density ramp detachment (figure 8.7) is not observed during  $N_2$  seeded detachment. Instead, the  $D\alpha$  emission is observed to drop at a similar rate at which the excitation emission of the  $n = 6, 7$  Balmer lines drop and at a similar rate at which the ionisation drops; which is the behaviour one would expect when the  $D\alpha$  emission is dominated by atomic excitation and molecular dissociation: e.g. when MAR in particular does not contribute to the  $D\alpha$  emission. The reason for the lack of additional  $D\alpha$  emission related to MAR is currently unknown. The emission resulting from

MAR would likely be modest, again, if the temperature would be not much reduced below the temperature at the onset of detachment ( $\sim 4$  eV), which can be seen from figures 8.7 and 9.2 where the detachment onset is at  $\sim 0.85$  s. Another explanation could be that either the molecular deuterium density and/or the deuterium ion density in the divertor is reduced.

The spectroscopic Balmer line analysis for the  $N_2$  seeded discharge indicates a negligible drop in target/divertor temperatures during the detached phase; e.g. the target temperature is observed to stay fixed around 3-7 eV (close to  $E_{ion}/\gamma$ ) —which is also consistent with a power balance analysis. It should be noted, however, that these spectroscopic inferences indicate but do not prove that the temperature does not drop further during  $N_2$  seeding. Such temperatures would, however, be consistent with the observation of low and fairly constant recombination rates (e.g. for strong recombination, lower temperatures are required). In addition to that, the inferred charge exchange to ionisation ratios are such that the predicted volumetric momentum loss according to the Self-Ewald model (see sections 2.4 and 9.1) is negligible:  $f_{mom}$  remains constant around 0.8-0.9 throughout the detached phase.

During the 2PMR discussion (section 3.5), it was shown that the target temperature obtained depends critically on the precise way in which the target pressure drops as function of  $T_t$  in the range  $T_t < E_{ion}/\gamma$ . Although spending more power on ionisation reduces the target temperature, there is a limit to how much of the power entering the recycling region can be lost on ionisation which depends critically on the speed at which  $p_t$  is reduced for  $f_{ion} = [0.5 - 1]$ . More specifically, according to the model investigation in section 3.5, if  $p_t$  is reduced during detachment by the *minimum amount* to obey the  $p_t$  maximum limit, the target temperature is expected to remain fixed at  $T_t = E_{ion}/\gamma$  and any further power removal (e.g. reduction of  $q_{recl}$ ) would lead to a proportional reduction in ion source (and associated ionisation power loss) such that  $T_t$  will stay at  $E_{ion}/\gamma$ . Reducing  $p_t$  below the  $p_t$  maximum limit would enable a higher fraction of  $q_{recl}$  to be spent on ionisation, depending on how far  $p_t$  is reduced below  $(p_t)_{crit}$ , leading to lower target temperatures. If hypothetically the  $p_t$  drop during detachment as the seeding phase proceeds corresponds (or is close to) the *minimum amount* of  $p_t$  drop, this could explain why the target temperature would not drop (as) much below  $E_{ion}/\gamma$  during seeded detachment where further power removal may could lead to a proportional reduction in ion source (e.g. less power spent on ionisation) rather than a further temperature reduction. It should be noted, however, that this argument is based on an oversimplified model and reality will be different as the speed at which  $p_t$  drops will likely vary during the  $N_2$  seeding phase as  $P_{recl}$  (amongst other divertor parameters) change. On other tokamaks as C-Mod [51] and JET [72] it has also been observed that volumetric recombination is relatively small during  $N_2$  seeded detachment; and the reason for this should

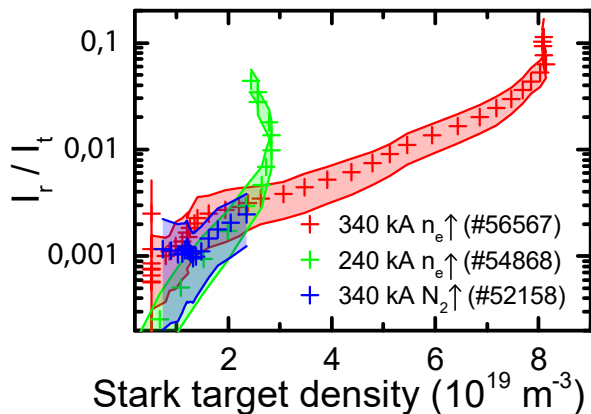


Figure 9.8: Recombination to ion target flux ratio as function of Stark density obtained from the chord near the target for the three discharges presented in figure 8.4.

be further investigated.

## 9.4 Applicability of TCV results to other existing and planned tokamaks

A central focus of this paper is on the development of target ion current loss in detachment which is set in motion when the power flowing into the recycling region drops to twice the level required for the ion source — $q_{recl}/(E_{ion}\Gamma_t) < 2$ , resulting in a ‘power limitation’ of the ion source. This appears to be the main driver of the  $I_t$  roll-over on TCV, while recombination has a much smaller effect and occurs after the roll-over of  $I_t$ . We cannot envision any situation in current or future tokamaks where power limitation is not needed for target ion current loss, assuming the ions arriving to the target are primarily ionised in the divertor; e.g. high recycling conditions. One would expect that a closed divertor would help to obtain such high recycling conditions as it would confine the neutrals in the divertor region, thus lowering ionisation rates in the SOL away from the divertor. Given that such high recycling conditions have been verified for this paper in TCV, which has an open divertor, it would likely be true that such conditions are also present in a tokamak with closed divertor baffling. Although recombination can certainly contribute to the ion current loss, it cannot be dominant until after target ion current roll-over when  $T_t$  is significantly lower than  $E_{ion}/\gamma$  and power limitation has already started. ‘Power limitation’ ( $\frac{q_{recl}}{E_{ion}\Gamma_t} < 2$ ) thus appears to be a universal requirement to reach the starting conditions for ion source reduction and significant volumetric momentum loss while recombination occurs later in the discharge.

Certainly, the much higher density (and power-density) results from Alcator C-Mod [51] appear to be consistent with power limiting the ionization source, eventually resulting in the roll-over and then rising recombination [62, 63, 66, 51]. While the recombination/ionisation ratio is much higher in C-Mod density ramp detachment than for TCV, recombination is not dominant over ionisation until past target ion current roll-over [51]. In addition, C-Mod results with  $N_2$ -seeding to reach detachment show [51], like TCV, that recombination is strongly decreased (x10-100 lower) as opposed to detaching through a density ramp. It thus seems generally true that volumetric recombination is not a requirement for (roll-over) detachment; although it (can) play a stronger role in other tokamaks, leading to larger target ion current drops relative to the peak value. Higher recombination rates at higher density machines could lead to a significant movement of the recombination and density peaks (front) at the deepest detached conditions as well, which remains small (at most a few cm) at TCV.

We do expect the characteristic gradient scale lengths of various quantities such as ionisation, recombination and charge exchange to be shorter (poloidal and along  $B$ ) in tokamaks with higher densities and parallel power densities than for TCV. Certainly the parallel heat flux would be 100x larger in ITER than TCV leading to smaller parallel-to- $B$  scale lengths in absolute value and relative to the divertor size  $\Delta L_{q\parallel}$ , e.g.  $\Delta L_{q\parallel} \sim \Delta T/q\parallel$  where  $\Delta L$  is set by the impurity cooling curve [82],  $\sim 10 - 20$  eV for carbon; this would lead to more localized impurity radiation and ionisation regions. In addition, higher densities in other tokamaks would lead to shorter charge exchange and ionisation mean free paths. The ionisation region is fairly large on TCV and covers almost the entire outer divertor leg; where the mean free path for ionisation is 5-10 cm, which is comparable to the divertor leg

width. A schematic overview of the location, size and dynamics of the impurity radiation, ionisation and recombination regions; based on the profiles shown in figure 8.3, is shown in figure 9.9 as a reminder for the TCV detachment dynamics. The ions and neutrals will be better equilibrated with shorter mean free paths, affecting the transfer of momentum and possibly affecting the power loss due to charge exchange as was predicted by the simplified charge exchange energy loss model by [54] presented in section 2.4. Such higher divertor densities, for the same upstream conditions, may be facilitated by the planned baffle upgrade [34] of TCV, which is aimed at increasing neutral compression. This would also modify the ionisation source distribution and may enhance momentum losses.

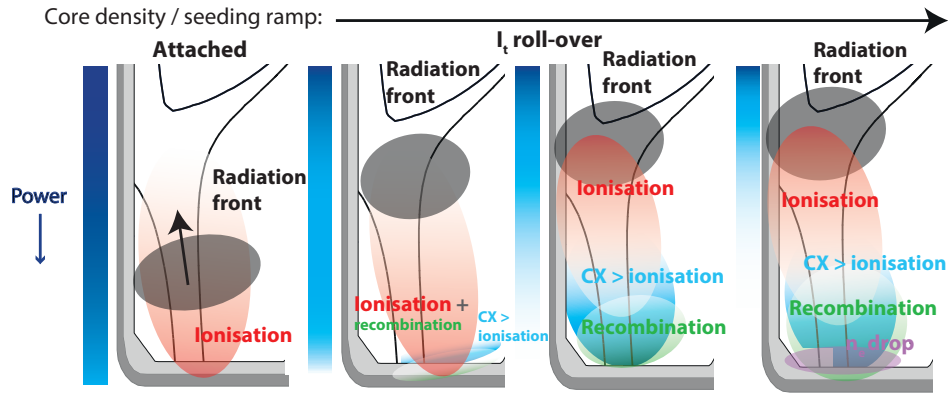


Figure 9.9: A schematic overview of the location, size and dynamics of the impurity radiation, ionisation and recombination regions on TCV; based on the profiles shown in figure 8.3

There is another likely key change in divertor characteristics engendered by larger  $P_{sep}$  and  $q_{\parallel}$ . Intrinsic carbon radiation in TCV suffices to lower  $q_{recl}$  so that it limits the ionisation source during density ramp discharges. However, as  $q_{\parallel}$  is increased, reaching  $P_{recl} \sim 2 \times P_{ion}$  without additional impurity seeding is correspondingly more difficult to accomplish during density ramps only [94]. That is particularly true for operation with high-Z metallic walls where we expect less intrinsic divertor radiation, adding impetus to needing seeded impurities to detach. However, given that impurity seeded TCV plasmas clearly show lower volumetric recombination (also true for JET [72] and C-Mod [51]) than for density ramp-driven detachment, the connection between seeding and recombination needs to be better understood.

# Chapter 10

## Conclusion

A detailed investigation of detachment on TCV has shown that TCV detachment occurs due to a reduction of the ion source generated in the divertor, rather than volumetric recombination which can be either small or negligible. We conclude that the reduction of the ion source occurs when the power entering the recycling becomes comparable to the power required for ionisation, which is in agreement with both SOLPS and analytical predictions, forming the first direct experimental proof of the concept of 'power limitation'. This conclusion is expected to be generally true, although the role of recombination may be stronger in higher density tokamaks. This is important as it provides a way of understanding detachment through a reduction in ion source, rather than ions staying longer in the divertor as increases in ion-neutral friction 'plug the drain of ions'.

The onset of power limitation is observed to occur when 50 % of the power entering the recycling region is spent on ionisation. This is in agreement with analytical predictions, which suggest that at this point target pressure ( $p_t \propto I_t T_t^{1/2}$ ) loss needs to start to occur as reducing the target temperature ( $T_t$ ) further leads to a slower increase of the ionisation source ( $I_t$ ) than  $T_t^{1/2}$  decreases. That point from analytic models can be written as three 'detachment thresholds', which are in quantitative agreement with the observed onset of detachment. Reaching this threshold implies that so much power is spent on ionisation that the near target region temperatures are severely reduced (4-7 eV for TCV), establishing a dominance of charge exchange over ionisation —enabling volumetric momentum losses; evidenced by the shift of the ionisation peak away from the target and the high charge exchange/ionisation ratio ( $CX_L/I_L$ ) region left behind. The observed target pressure loss on TCV is not only facilitated by volumetric momentum loss—but also by upstream pressure loss, consistent with analytical predictions using the estimated TCV volumetric momentum loss, heat flux entering the ionisation region and ionisation energy cost. After reaching the detachment threshold, strong rises of  $D\alpha$  emission near the target are observed beyond emission predictions based on atomic processes; indicating molecular contributions to  $D\alpha$ —quantitatively consistent with SOLPS modelling. This may be indicative of enhanced molecular densities in the divertor, which could give rise to additional momentum losses due to ion-molecule interactions. Afterwards, in dense divertor conditions, volumetric recombination may become significant—although it remain a secondary effect on TCV. 'Power limitation' is required to enable all above processes of detachment and thus forms the starting point of the detachment mechanism.

# Appendices

## Appendix A

# Technical details DSS: *Correction algorithms, Hardware and Software*

In this chapter further technical details of the DSS and the corresponding investigations are discussed.

### A.1 Advanced smearing correction algorithms

In section 5.4 smearing correction was simplified in various ways. First of all, we have to account for the fact that the spectra can change within a single (or two) acquisition phases. This means that the diagonal elements in equation 5.1 are in fact time-dependent. The technique shown here below builds upon previous techniques by [189, 188]. Such time dependency can be accounted for using an 'indicator' for the changes in the spectra. More specifically, the off-diagonal elements should correspond to the signal one row obtains at that position obtained *during* the shifting. Thus, if the time-dependency would be known (here denoted as  $I(t)$  which could be ROI dependent);  $I(t)$  should be integrated over the time in which the shifting takes place. However, for a time-dependent problem also the physical timing of the shifting has to be taken account, which was previously simplified as no time-dependency was included. For a time-dependent problem the shifting of both ROIs should be represented as a discrete convolution of two blocks, providing a weighting function for the integral over  $I(t)$ . This, for instance, reproduces correctly that most smearing of ROI  $j$  into ROI  $i$  corresponds when both rows align exactly. The convolution of two block functions leads to a trapezoidal function.  $W(t, a, b, c, d) = \max(\min(\frac{t-a}{b-a}, 1, \frac{d-t}{d-c}), 0)$ . Assuming that the shift starts at  $t_0$ , the vertical shift speed is  $t_{VSS}$  and the ROI pixel start locations are assigned with  $PS$  while the end location are assigned as  $PE$ , the different variables of this trapezoidal function become  $a = t_0 + t_{VSS}(PS(j) - PE(i))$  (the time when end of row  $i$  reaches the start of row  $j$ );  $b = t_0 + t_{VSS}(PE(j) - PE(i))$  (the time when the end of row  $i$  reaches the end of row  $j$ );  $c = t_0 + t_{VSS}(PS(j) - PS(i))$  (the time when the start of row  $j$  reaches the start of row  $i$ );  $d = t_0 + t_{VSS}(PE(j) - PS(i))$  (the time when the start of row  $i$  reaches the end of row  $j$ ). Under the assumption of quasi-constant emission during two frames, this methodology leads identical results to the smearing correction highlighted above.

In a time-dependent scenario however, the ratio between the picked-up signal and the signal obtained during the exposure time has to be computed. When the signal is acquired during the exposure time, corresponding to row  $i$  and then shifts into row  $j$  then becomes  $\frac{\int_a^d W(t,a,b,c) \times I(t,j) dt}{\int_{t_0-t_{exp}}^{t_0+1e-5} I(t,i) dt}$  (where  $t_{exp}$  is as calculated previously (e.g. period between two TTL pulses minus the shifting time) and 10  $\mu$ s is the time it takes for the camera to respond to the TTL trigger). Important to note is that for the lower diagonal elements smearing works differently. Smearing here arises from the previous shift into the registry - so from (assuming the period is  $T$ ) the shift corresponding to  $t_0 - T$ . When considering the shifting of the ROIs, the smearing on ROI  $i$  is now due to a shift of the previous ROI  $j$  into  $i$ , as opposed of the ROI  $i$  shifting. Again, this leads to a trapezoidal function, but now with parameters  $a = t_0 - T + t_{VSS}(PS(i) - PE(j))$  (the time when end of row  $j$  reaches the start of row  $i$ );  $b = t_0 - T + t_{VSS}(PE(i) - PE(j))$  (the time when the end of row  $j$  reaches the end of row  $i$ );  $c = t_0 + t_{VSS}(PS(i) - PS(j))$  (the time when the start of row  $i$  reaches the start of row  $j$ );  $d = t_0 + t_{VSS}(PE(i) - PS(j))$  (the time when the start of row  $j$  reaches the end of row  $i$ ). These elements replace the term  $N_j \frac{t_{VSS}}{t_{exp}}$  in equation 5.1.

$$\begin{pmatrix} S_1 \\ S_2 \\ \vdots \\ S_n \end{pmatrix} = \begin{pmatrix} 1 & \frac{\int W(t,t_0,2,1) \times I(t) dt}{\int_{t_0-t_{exp}}^{t_0+1e-5} I(t) dt} & \dots & -\frac{W(t,t_0,N,1) \times I(t) dt}{\int_{t_0-t_{exp}}^{t_0+1e-5} I(t) dt} \\ \frac{\int W(t,t_0-T,2,1) \times I(t) dt}{\int_{t_0-t_{exp}}^{t_0+1e-5} I(t) dt} & 1 & \dots & -\frac{W(t,t_0,N,2) \times I(t) dt}{\int_{t_0-t_{exp}}^{t_0+1e-5} I(t) dt} \\ \vdots & \vdots & \ddots & \vdots \\ \frac{\int W(t,t_0-T,N,1) \times I(t) dt}{\int_{t_0-t_{exp}}^{t_0+1e-5} I(t) dt} & \frac{\int W(t,t_0-T,N,2) \times I(t) dt}{\int_{t_0-t_{exp}}^{t_0+1e-5} I(t) dt} & \dots & 1 \end{pmatrix} \times \begin{pmatrix} R_1 \\ R_2 \\ \vdots \\ R_n \end{pmatrix} \quad (\text{A.1})$$

The simplified smearing correction matrix can then be re-written as equation A.1 which includes time-dependency, where  $W(t, x, i, j)$  corresponds to a trapezoid function  $W(t, a, b, c, d) = \max(\min(\frac{t-a}{b-a}, 1, \frac{d-t}{d-c}), 0)$  introduced earlier where  $a(x, i, j) = x + t_{VSS}(PS(i) - PE(j))$ ,  $b(x, i, j) = x + t_{VSS}(PE(i) - PE(j))$ ,  $c(x, i, j) = x + t_{VSS}(PS(i) - PS(j))$ ,  $d(x, i, j) = x + t_{VSS}(PE(j) - PS(i))$ .

We can simplify this solution under the assumption that the emission during the shifting does not change but an emission difference between two frames does occur. In that simplification, the upper diagonal elements  $\frac{\int W(t,t_0,j,i) \times I(t) dt}{\int_{t_0-t_{exp}}^{t_0+1e-5} I(t,i) dt} \approx N_j \frac{t_{VSS}}{t_{exp}}$  (e.g.  $j > i$ ), whereas the lower diagonal elements are replaced  $\frac{\int W(t,t_0-T,j,i) \times I(t) dt}{\int_{t_0-t_{exp}}^{t_0+1e-5} I(t,i) dt} \approx N_j \frac{t_{VSS}}{t_{exp}} \frac{I(t_0-T)}{I(t_0)}$ . That leads to equation 5.2 shown in section 5.4.

To apply these techniques, however, one needs an indicator for changes in the spectra - for instance by interpolating the spectra between frames, although that is not a self-consistent solution as the smeared signal is used for these indications (essentially assuming that the smeared signal to non-smeared signal ratio is quasi-static). Another alternative is to monitor  $D\alpha$  and assuming (this is a very rough assumption only valid in certain cases) that  $D\alpha$  trends measured by photodiodes provides an indicator for changes in the spectra (e.g. assuming that the ratio between  $D\alpha$  and each spectral line measured is quasi-constant during a single acquisition frames).

### A.1.1 Application of advanced smearing correction - example $N_2$ seeded discharge

Below an example of the smearing correction algorithm application on an  $N_2$  seeded discharge (#61144) with 200 hz acquisition frequency is shown. The application of the smearing correction is shown at the time a  $N_2$  puff is introduced to the system, leading to a rapid increase in the emission of the various nitrogen lines. We have applied two different implementations of the advanced smearing correction algorithm based on interpolating between different spectra: one case where the interpolated signal has been smoothed before determining the interpolant in order to obtain smoother results and one where such a smoothing was not applied. An overview of the evolution of the line intensity (the A.1 b) line) as function of time, together with the sampling window, and the spatial profile of the line intensity is shown in figure A.1 a). As the  $N_2$  seeding has just started at the time when the spectra are shown (near 0.8 s), there is a strong (local - e.g. only for those pixels where a nitrogen impurity spectral line is present) difference between the nitrogen line emission occurring during the previous vertical shift (green region in figure A.1 b), giving rise to smearing. This is not expected to occur for the Balmer lines as they do not change that rapidly/abruptly when the nitrogen impurity gas is introduced.

The differences shown in figure A.1 indicates the basic smearing correction algorithm overestimates smearing due to the lower diagonal elements while it underestimates smearing from the upper diagonal elements. This can lead to erroneous behaviour of the basic smearing correction algorithm, shown in figure A.1 for LoS 31, where the smearing correction is so strong that the obtained (background corrected) signal becomes negative. his behaviour is not shown for the Balmer lines, where differences between the different smearing techniques are smaller. A more viable result is obtained from the advanced algorithms as these partially account for the sudden introduction of  $N_2$  through the asymmetry between the upper diagonal elements and the lower diagonal elements in the correction matrix.

The obtained differences between the advanced smearing correction technique where smoothing was or was not applied is small and likely, considering the uncertainties in the smearing correction, this is likely similar or smaller to the error introduced during the smearing correction. Although this error is generally small for most spectral lines, it can increase up to 50 % (relative difference between two different smearing levels) for the nitrogen line emission at the weaker channels. This significantly alters the spectral line shape and can influence the line intensity up to 20 %.

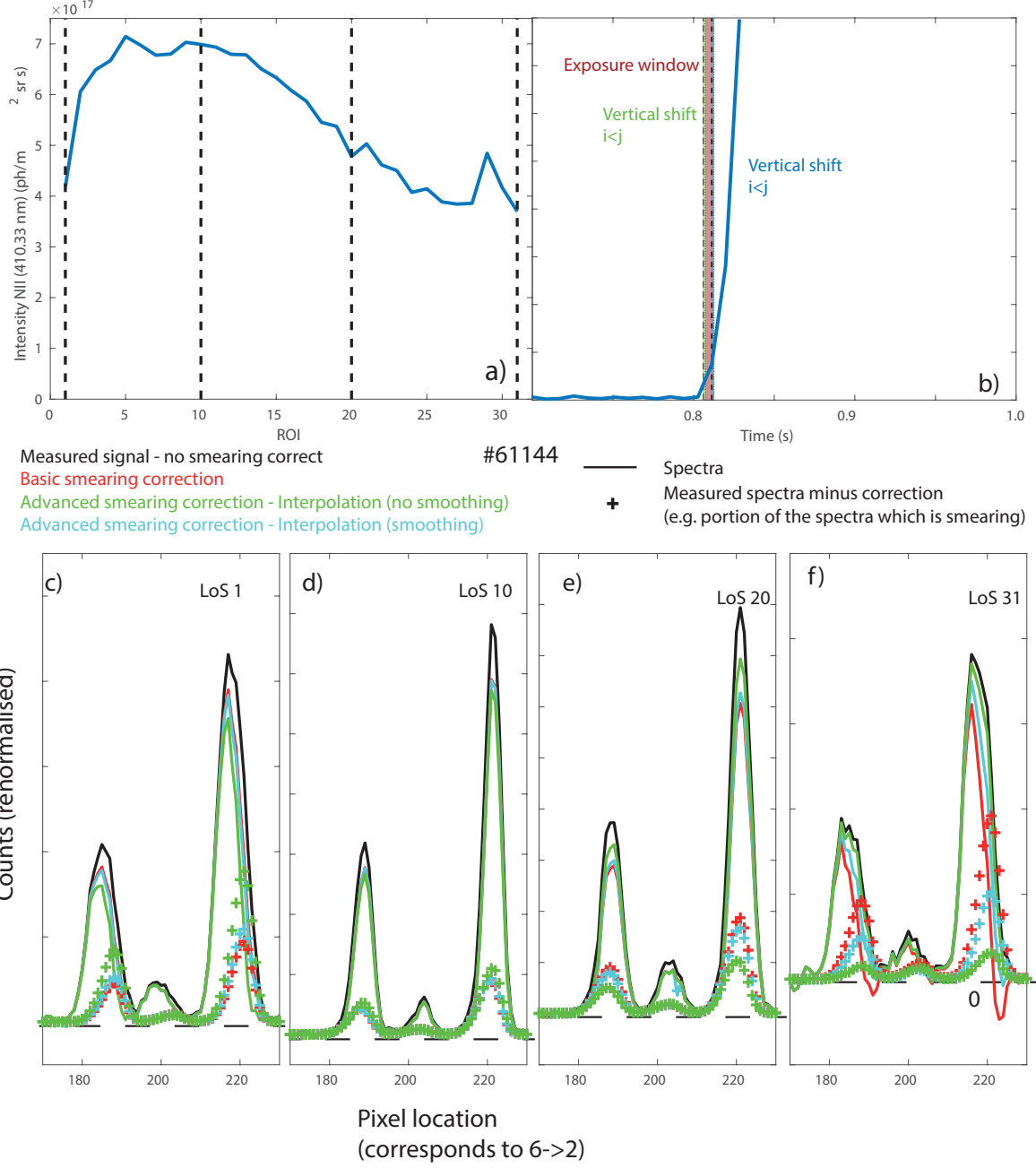


Figure A.1: Overview of smearing of the  $6 \rightarrow 2$  Balmer line and neighbouring NIII lines at 200 Hz acquisition frequency for a  $N_2$  seeded discharge. a) Profile of NIII (410.33 nm) intensity as function of ROI at  $t = 1.25$  s together with highlights of the ROI of which the spectra are shown. b) Profile of the NIII (410.33 nm) intensity for LoS 30 (near x-point) as function of time, together with windows corresponding to the different acquisition phases. c-g) Spectra of  $6 \rightarrow 2$ , NIII (409.73 nm) and NIII (410.33 nm) both measured (non-smearing correction) and smearing corrected for four different lines of sight. Also the deviation between the spectra and the smearing-corrected spectra (plusses) is shown, which indicates the amount of smearing contributing to the measured signal.

## A.2 Stray light detection and correction during absolute calibration

A technique has been developed to detect stray light during the absolute intensity calibration and to correct for this stray light. First, we investigate two different full-frame images obtained during an absolute intensity calibration, one corresponding to a central wavelength of 600 nm (where the influence of stray light is negligible) and one corresponding to a central wavelength of 360 nm (where the influence of stray light is not negligible). By comparing the full-frame images in figure A.2, it is clear that the relative signal in between the various tracks is much higher for the 360 nm case than for the 600 nm case, which is indicative of stray light. By looking at the relative increase of the signal in between the tracks, it is thus possible to detect the appearance of stray light. In spirit, this correction technique is similar to the technique used in [196]; where a periodic ruling is used to mask off regions with a fixed frequency, after which Fourier-aided analysis can be applied for stray light correction/detection.

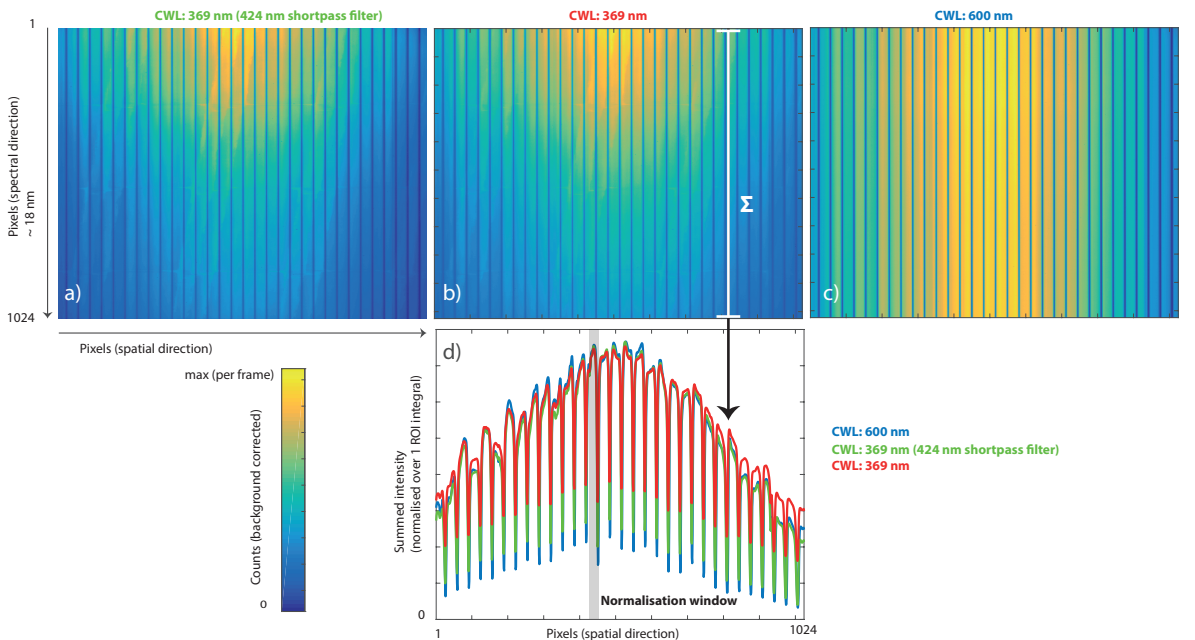


Figure A.2: Examples of a background corrected full-frame spectra of an incandescent light source (2800 K color temperature) obtained using a 1800 l/mm grating (approximately 18 nm coverage per acquisition) at different central wavelengths. a-c) Full-frame spectra with colourmap (0 minimum, each map is normalised with respect to its maximum). d) Spectra summed in the spectral direction normalised with respect to the integral over a single ROI for the three different cases, indicating different levels of signal in between the ROIs.

As the signal is generally small in between the two tracks, looking at such changes quantitatively requires averaging over many frames (100 - 1000) to improve the S/N level. By blocking out the set ROIs (with some margin) an image of the signal in between the various tracks remains with unknown (masked) regions. A signal level at those regions can be obtained using 2D interpolation techniques in order to extrapolate the signal in between the tracks to a 2D image. Care has to be taken that an algorithm is used for this which is robust. The used algorithm is based on John D'Errico's `inpaint_nans.m` Matlab function (available at [https://uk.mathworks.com/matlabcentral/fileexchange/4551-inpaint\\_nans](https://uk.mathworks.com/matlabcentral/fileexchange/4551-inpaint_nans)), which treats the

known values as boundary points between which a partial differential equation, representative of a spring model, is used to interrogate the points in the unknown region. This result is very similar to Laplacian interpolation, but instead has a constant extrapolation as opposed to a linear extrapolation of Laplacian techniques. An application is shown in figure A.3, where the ROI regions have been masked and the signal in between has been estimated using the described algorithm. To ensure a smooth result, sometimes the obtained images are smoothed manually afterwards, in order to ensure that erratic behaviour due to noise will not influence the stray light correction. Afterwards, the same technique is applied but now instead of masking the lit ROIs, the spacing in between the ROIs is masked (with some margin). The result is shown in figure A.3.

Using this information, one can obtain a 2D map of the ratio between the expected signal in between ROIs, which is assumed to span over the entire CCD, to the signal of the ROIs. This ratio increases when more stray light is present. By assuming that no stray light occurs around 600 nm, the differences of this ratio with respect to 600 nm can be determined. This forms the fraction of stray light expected. Using that matrix, the observed stray light can be corrected.

This technique is illustrated in figure A.4, where also the eventual obtained stray light corrected spectra and its differences to the non-stray light corrected spectra is shown. The stray light correction estimates that a larger contamination (20-25 % more) of stray light occurs near the edges of the CCD, which is as expected as the emission there is smaller. Thus, the stray light corrected spectra has a more peaked intensity profile in the spatial profile (as is also observed when a shortpass filter is used to reduce stray light), as shown in figure A.4 g) compared to h) and e). The amount of stray light increases from 5 - 25 % towards 15 - 40 % when reducing the wavelength from 376.5 nm to 362.5 nm (figure A.4 e), which is as expected due to the lower signals expected from the incandescent source at lower wavelengths.

By invoking the ROIs on the stray-light corrected spectra and measured spectra, both the expected measured signal for a tracked setting and the expected signal for a tricked setting with stray light correction can be determined. The ratio between the two is mapped to the 'actual' absolute calibration spectra recorded using tracked settings.

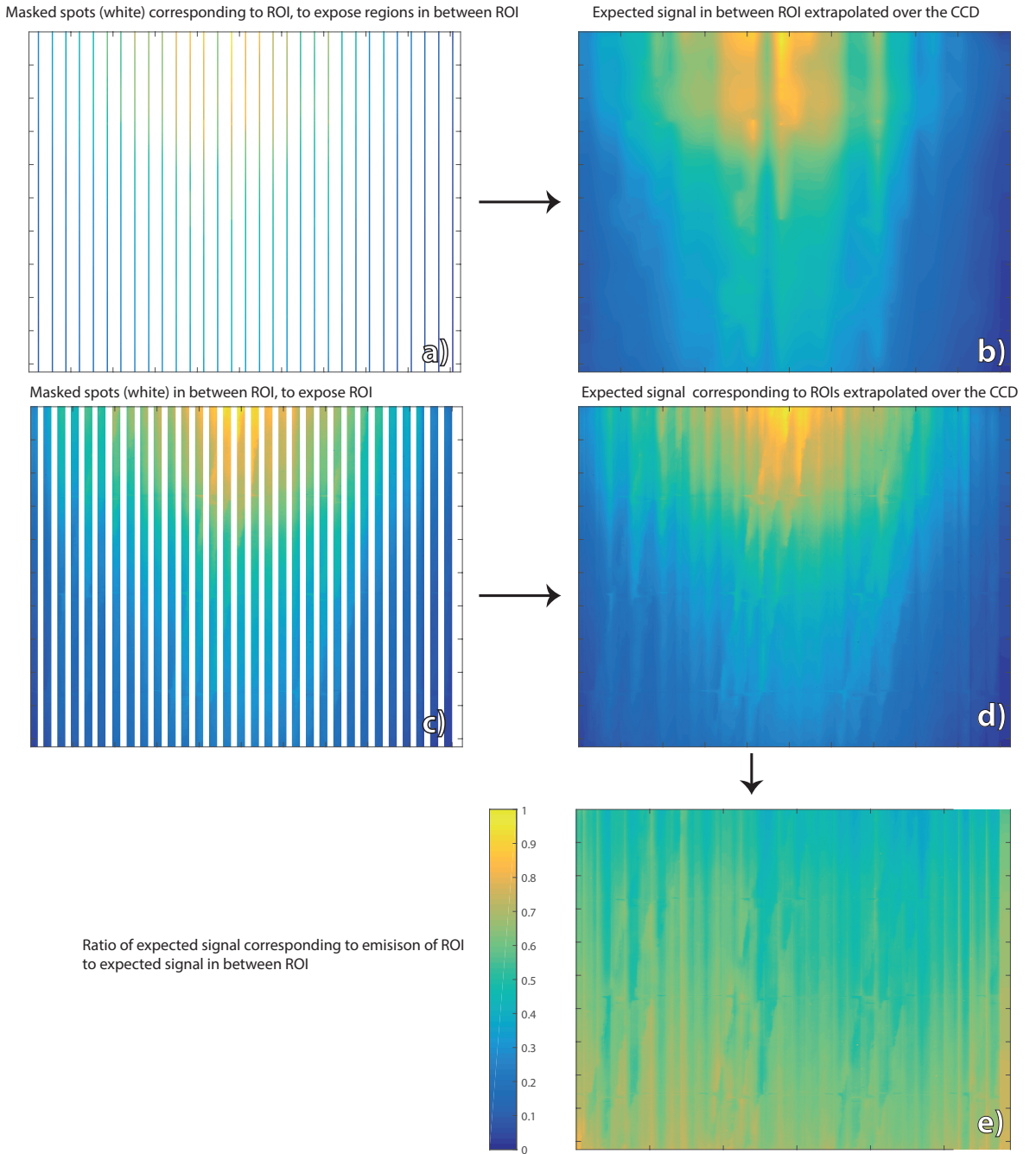


Figure A.3: Overview of the first step of the stray light correction algorithm applied to the measured absolute calibration spectra at 369 nm without the application of a 424 nm shortpass filter. a) Measured spectra (full-frame) masking off all regions not corresponding to the 'dark spots' in between ROIs, b) interpolated spectra over the masked regions: e.g. full-frame signal expected due to signal in the optical 'dark' regions. c) Measured spectra (full-frame) masking off all regions not corresponding to the 'brightest centra' of the ROIs, d) interpolated spectra over the masked regions: e.g. full-frame emission expected due to signal in lit regions (if no fibre edges were present). e) Ratio between the expected 'dark' signal and 'lit signal'.

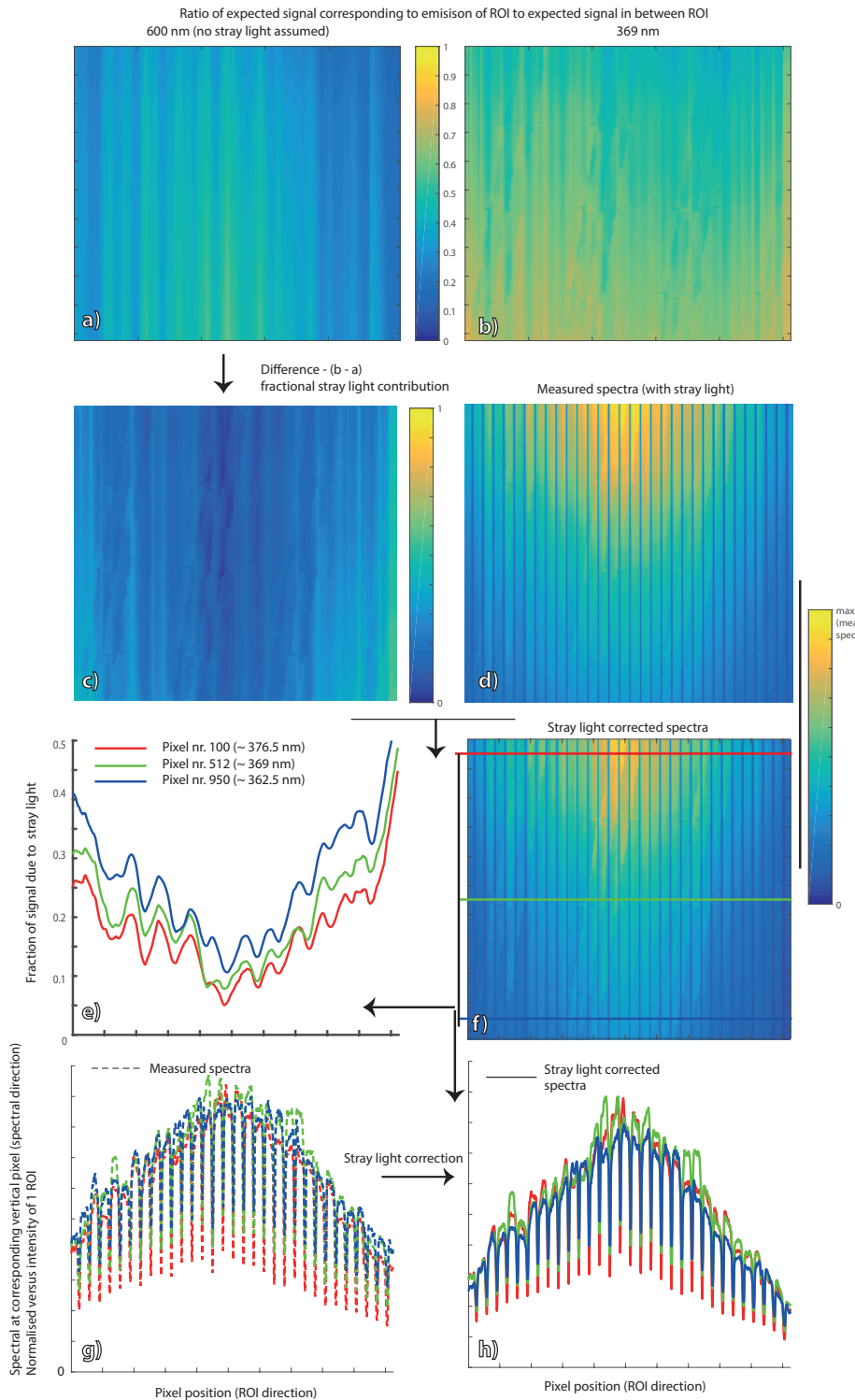


Figure A.4: Overview of the second step of the stray light correction algorithm applied to a measured absolute calibration spectra at 369 nm without the application of a 424 nm shortpass filter. a) + b) determined ratio between the expected extrapolated 'dark' and 'lit' signals of the 600 nm measurement (of which no smearing is assumed) and the 369 nm measurement. c) Difference between these both ratios, indicating the predicted fraction of stray light the measured spectra at 369 nm has. d) Measured spectra (with stray light) at 369 nm. f) Stray-light corrected spectra (full-frame) with e) a plot as function of horizontal pixel location (spatial direction). g) Measured spectra (normalised at a single ROI's intensity) as function of horizontal pixel position (spatial direction). h) Stray-light corrected spectra (normalised at a single ROI's intensity) as function of horizontal pixel.

### A.3 Mechanical and 3D printed assemblies

As part of the development of the DSS, various mounts were developed and 3D printed to ensure an integration between the different components, which are discussed here.

The CAD model of the fibre-lens coupler is presented in figure A.5, which has been largely 3D printed. The assembly mounts the lens to the fibres and allows for a linear displacement of the fibre assembly, supported by an inner guidance bar to ensure an on-axis displacement. The fibre support consists of two elements, one which is directly mounted to the fibres and which is kinematic, meaning that it can be disassembled and re-assembled with sufficient precision to maintain the various calibrations. In order to enable saving different lens position (if, for instance, different lenses would be used for an experiment), two elements are present which can be mounted to align a pin into a slot on the fibre assembly in order to 'store' two lens-ferrule positions. The ferrule mount also has two pins with two holes, enabling the installation of masks (which have been 3D printed from a rubber-like material) in front of the fibres to limit the number of fibres sending light into the DSS which could potentially be used for high speed DSS application.

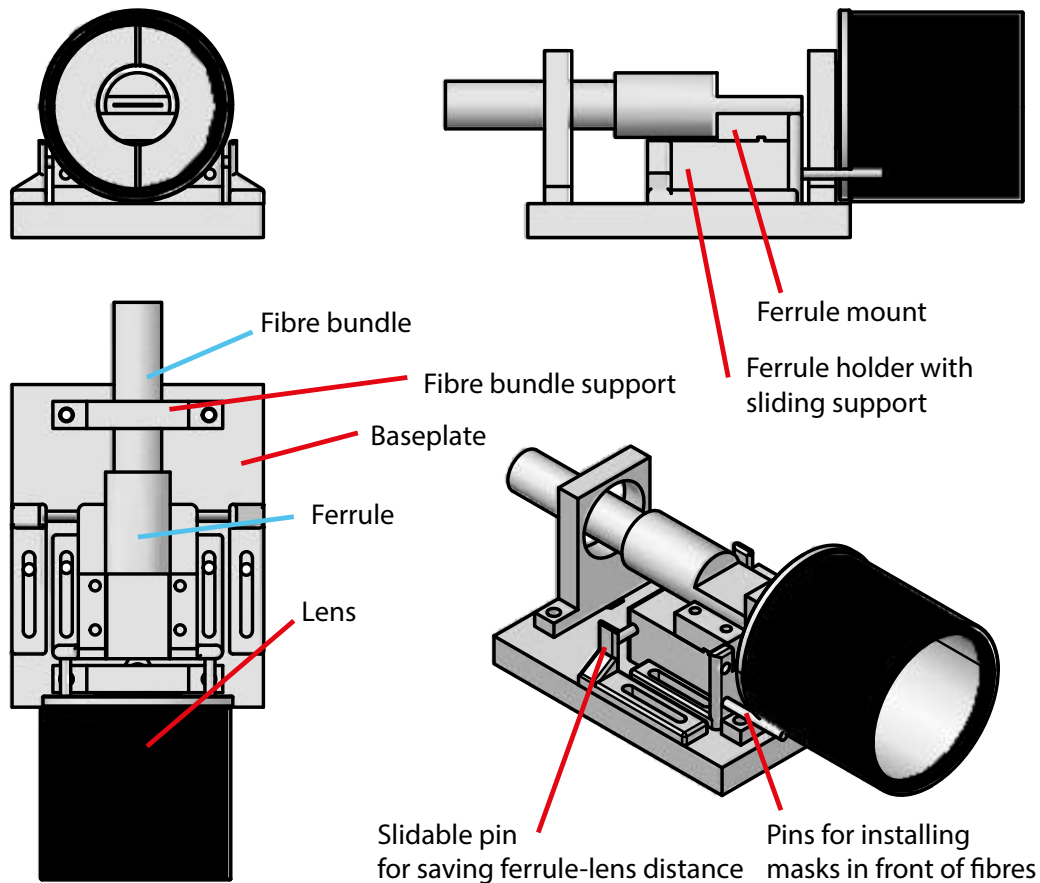


Figure A.5: CAD model for lens to fibre (tokamak end) coupler. Pre-made parts are highlighted in cyan, 3D printed parts according to this CAD model are highlighted in red.

The CAD model to mount the fibre-lens coupler to the tokamak for the horizontal port is presented in figure A.6, which has been largely 3D printed and is previously shown in figure 5.2 which also shows the other diagnostics integrated into this assembly. The assembly supports three different viewing orientations for the DSS collection optics, which can be

changed between discharges by moving the fibre-lens mount to a different orientation, which has been mounted using a location pin (inference fit) and two screws.

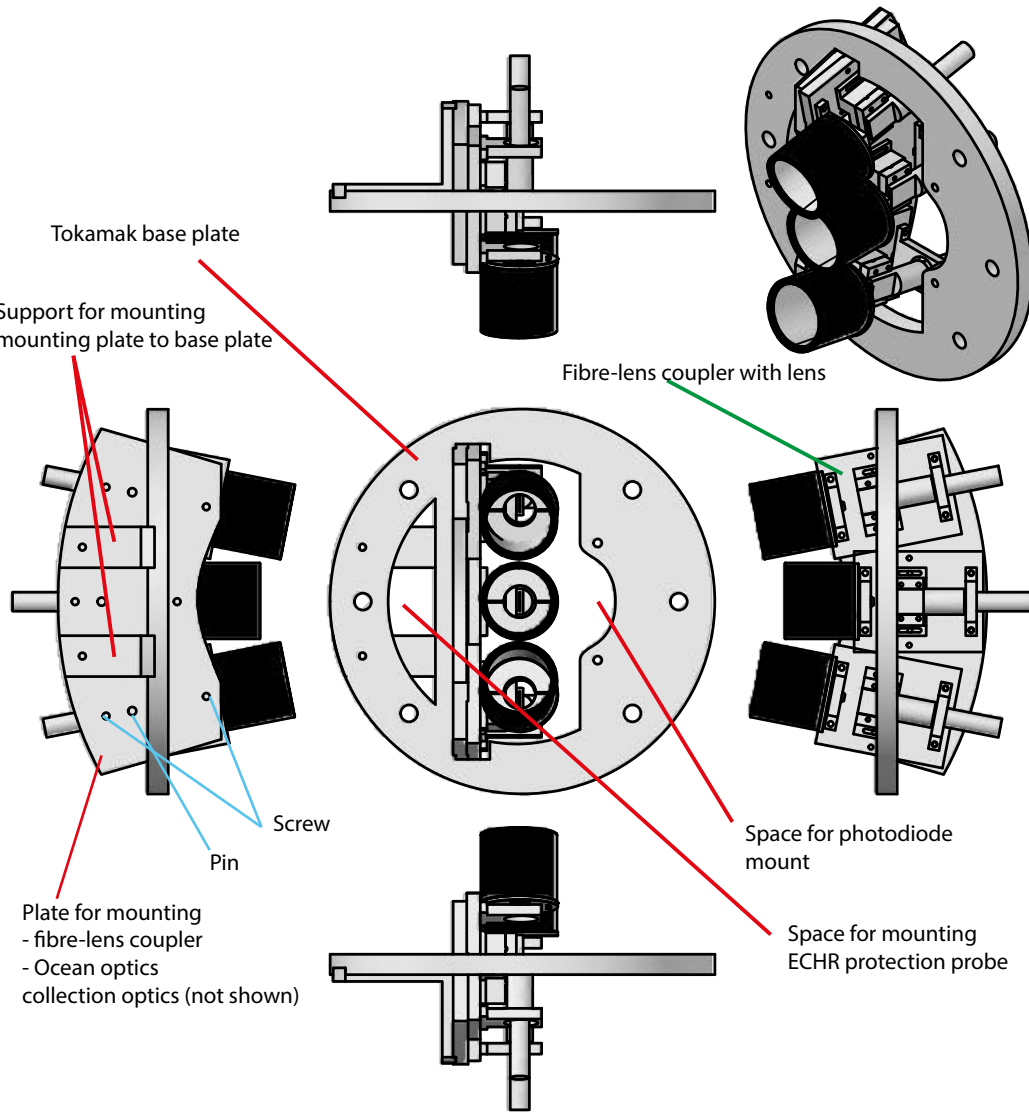


Figure A.6: CAD model for the 3D printed assembly at the end of the tokamak, shown in picture 5.2 a). The CAD model shows the three different DSS orientations and as such, no Ocean optics collection optics mount is shown. Pre-made parts are highlighted in cyan and 3D printed parts according to this CAD model are highlighted in red.

The CAD model of mounting the ferrule to the spectrometer's slit is shown in figure A.7, which has been largely 3D printed and a picture is shown in figure 5.2 b. The assembly replaces the spectrometer's baffle plate by making a thicker 3D printed baffle with an opening which fits the rectangular part of the ferrule tightly. This baffle plate has some rotational and translational freedom, enabling the fibres to be aligned to the slit, after which it is fastened with four screws. The support holder of the lens-slit coupler fits on the spectrometer's slit while leaving access to the screws required to demount the slit assembly. Using the 3D printed support for the ferrule, two long locational pins can be mounted to as a guidance for positioning the ferrule in a linear motion to the slit. An additional clamp can be mounted over the fibres in order to hold the fit of the fibres to the slit more firmly, ensuring a firm fit of the ferrule to the slit which does not change over time. To ensure the best performance,

the fibres are attached to the slit blades without leaving any space.

The fibre assembly used has been manufactured and designed by CeramOptec according to the requested design and specifications, which features two threads for mounting accessories to the fibres, which are used to mount the fibres to the various assemblies.

#### A.4 Analysing pick-up and choice of ROI

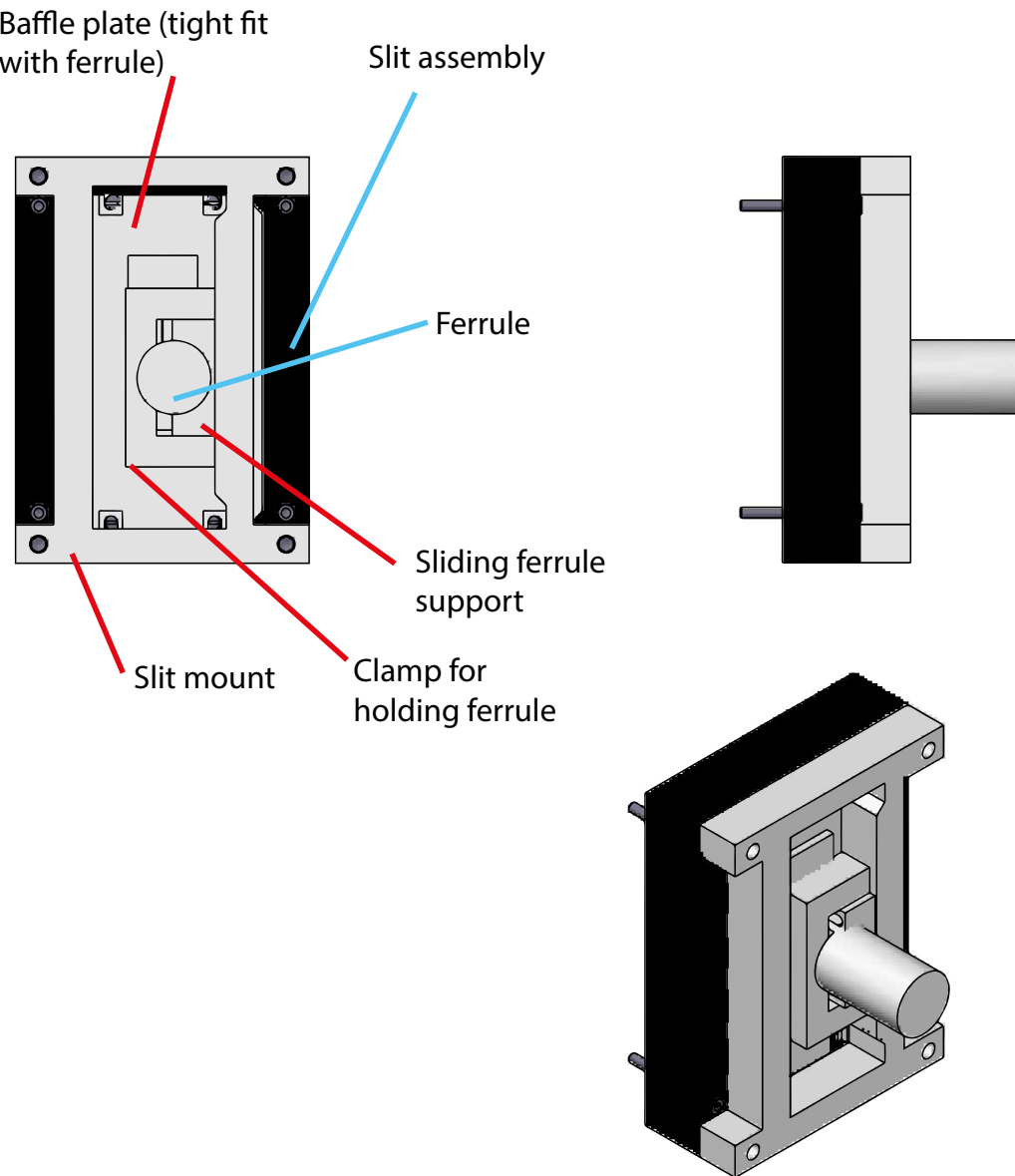


Figure A.7: CAD model for the 3D printed assembly for mounting the fibres to the slit at the spectrometer's end. Pre-made parts are highlighted in cyan, 3D printed parts according to this CAD model are highlighted in red.

As discussed in chapter 5, the ROIs need to be chosen appropriately for the diagnostic and to make that choice one needs to investigate the trade-off between capturing the most of the emission corresponding to a single fibre and picking up signal from neighbouring ROIs. That is analysed below in detail in a quantitative way using both measurements of the spreading of a single illuminated track and measurements of the position of all the different tracks and

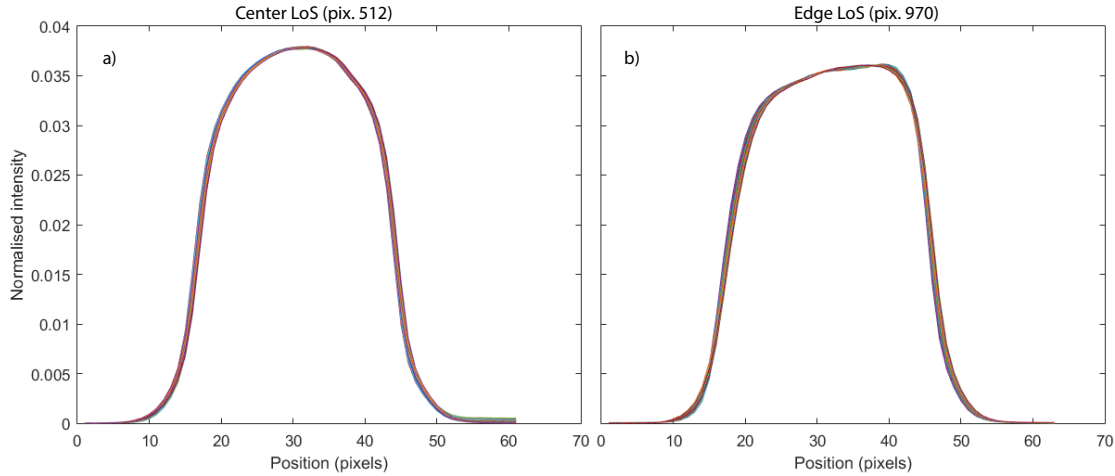


Figure A.8: Measured spatial instrumental functions as function of pixel positions for a range of different wavelengths (indicated by different lines with different colours). a) Spatial instrumental function of a central fibre (512 pixel index), b) spatial instrumental function of an edge fibre (970 pixel index).

their spacing on the CCD.

Using MATLAB's built-in image recognition algorithms, the various regions of interest are recognised and their centres/sizes analysed. This is achieved by making the image as homogeneous as possible which, considering the emission of our incandescent source (halogen bulb) is achieved by using a high resolution grating in the 500 nm to 700 nm region. To get an idea of this scan, the full-frame spectra shown in figure 5.4 of a grating angle scan with ROI regions overplot can be used. At lower wavelengths, the emission gradient along the spectral direction (e.g. the brightness of the source is higher at higher wavelengths) becomes too large for the image recognition algorithms to detect the ROIs. The drift in the ROIs has been investigated by scanning the spectrometer's grating angle in this wavelength region and the ROIs (size and position) were shown to be constant (a shift of less than half a pixel) along the 500 nm to 700 nm range. The sizes of the ROIs were found to be mostly in between 30.5 - 34 pixels (corresponding to 406  $\mu\text{m}$  to 442  $\mu\text{m}$ ), with three fibres/ROIs as small as 28.5 pixels (corresponding to 380  $\mu\text{m}$ ). The distances between the ROI centra was at least 32.2 pixels and varied between 32.2 - 34 pixels (corresponding to 418  $\mu\text{m}$  to 442  $\mu\text{m}$ ).

In order to obtain the spatial instrumental function, only a single fibre is illuminated by using a spring-loaded pinhole (smaller than 400  $\mu\text{m}$  diameter) on the machine side of the set-up ensuring that a single fibre can be illuminated despite the fibres not being separable on the machine side at the cost of having a very low throughput. By performing full-frame camera measurements, a profile is constructed of the spatial instrumental function of the fibre. This is performed as function of wavelength but, as shown in figure A.8, the wavelength dependence of the spatial instrumental function is negligible. It does, however, have a dependence on the vertical position of the CCD (e.g. ROI). As no trend in the spatial dependence was found, that dependence is not likely due to a different spatial broadening of the spectrometer at different vertical locations but instead due to differences in illumination of the fibre and the spatial illumination pattern of the fibre coming into the slit (such as engineering tolerances on the fibre sizes).

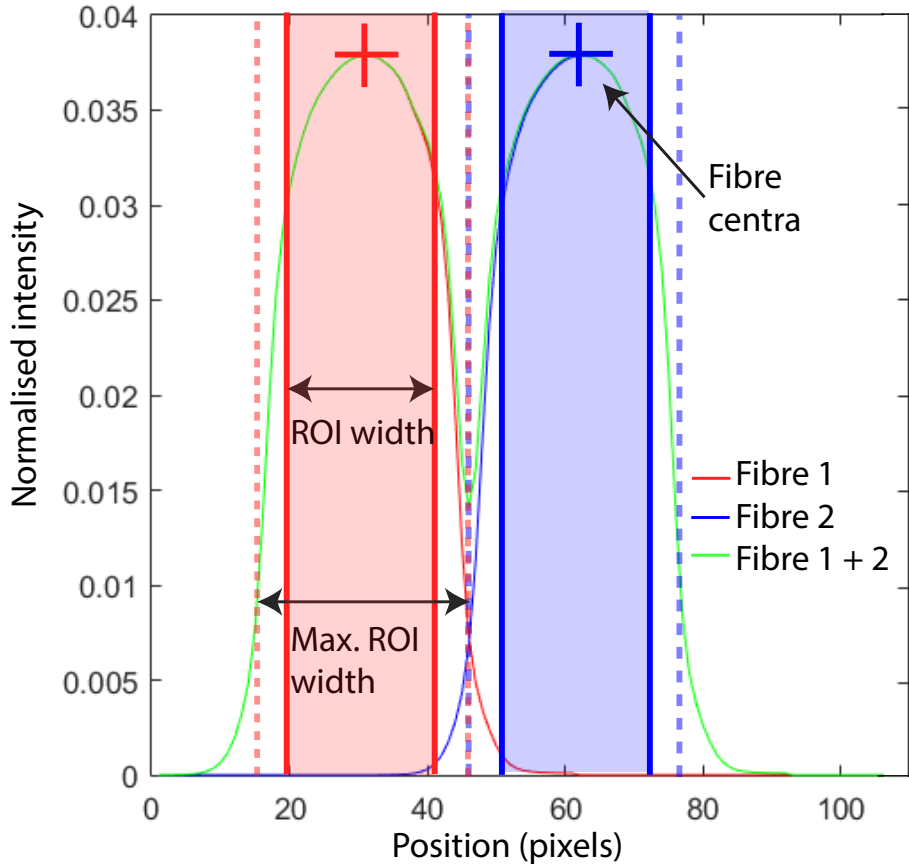


Figure A.9: Illustration of the pick-up calculation. Two identical spatial instrumental functions are shown for two neighbouring fibres including the total instrumental function (addition of the two). The maximum possible ROI width and the chosen ROI width are highlighted together with the ROIs centres. This illustration is only shown for the central fibre.

Using the full-frame measurements of all illuminated fibres, the minimum separation between two fibre centres is determined, corresponding to a worst-case scenario. Hence we will assume that two fibres have this separation, which for the case shown is  $418\text{ }\mu\text{m}$ . Furthermore, it is assumed that each fibre has an identical spatial instrumental function (which they have not). Using those assumptions, and assuming a certain intensity ratio between two neighbouring channels, a total measured intensity profile can be modelled, as shown in figure A.9. By putting different track separations between the two fibres (while centring each track at each fibre's centre), it can be investigated how much of the actual intensity is picked-up by the track and how much pick-up is picked up. Although only one neighbour is shown in figure A.9, this calculation is done by adding two neighbours. Second-order effects (non-neighbouring fibres) are assumed to be negligible, which is valid considering figure A.8.

That investigation first leads to a relation between the fraction of the signal picked up (here defined as "efficiency" and expressed as a percentage) as function of ROI (figure A.10 a) and a relation between the fraction of pick-up achieved (in % of the total measured signal) and as function of ROI (figure A.10 b); highlighting the trade-off between pick-up and efficiency. The result indicates that a negligible pick-up ( $< 5\%$ ) is present assuming the similar intensities between the central fibre and its neighbour when fairly large regions of interest ( $\sim 75\%$  of the centre to centre distance between two ROIs) are chosen which covers more than 95% of the

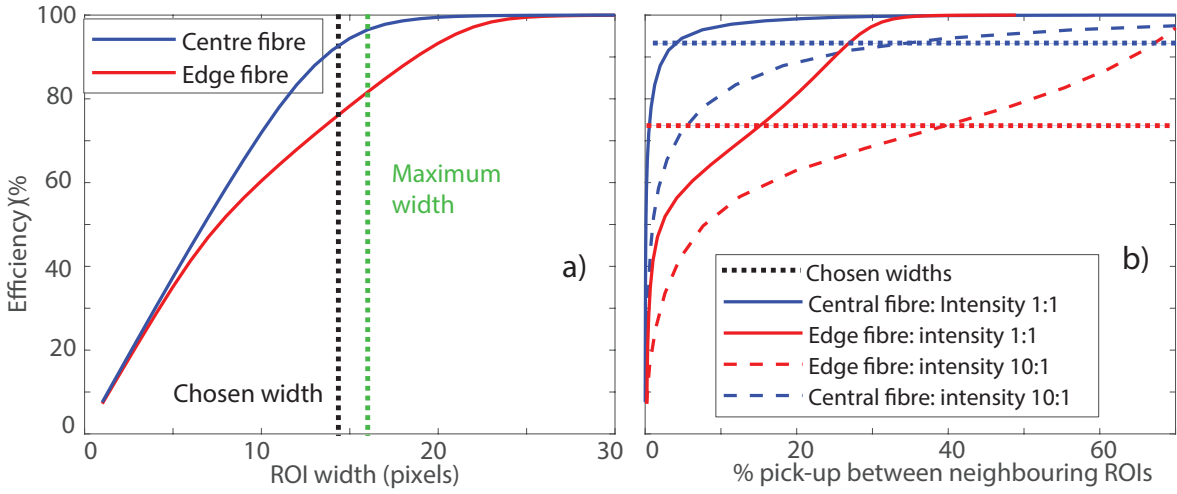


Figure A.10: a) Calculated "efficiency" in % (e.g. fraction of signal corresponding to a single fibre caught by the ROI) as function of ROI width in pixels. b) Calculated "efficiency" in % as function of the pick-up between neighbouring fibre channels.

emission corresponding to the monitored fibre. However, when using the spatial instrumental function observed for the edge fibre, the obtained efficiency for the same ROI width choice is significantly smaller (< 70%) while the obtained pick-up is larger ( $\sim 10\%$  - assuming 1:1 intensity ratios). After a qualitative inspection of the different fibres/spatial instrumental functions, this large difference is not applicable to the other edge fibres and in this case is mostly created by the wider and asymmetric emission pattern of the edge fibre chosen. That difference could be due to differences between the various fibres (figure A.8), which could be explained through engineering tolerances. Due to the asymmetric emission pattern the pick-up is likely overestimated. This, combined with the chosen worst-case scenario smallest ROI-to-ROI distance, creates a worst-case upper limit estimate of the pick-up which is likely not characteristic for the system as the ROI-to-ROI distance would increase when the core diameter of one of the fibres monitored is larger. The vertical line in figure A.10 a) / horizontal line in figure A.10 b) indicates the ROI width chosen for the calibration run presented. Given those values and assuming the neighbouring fibres are ten times as bright, a pick-up of  $\sim 25\%$  is expected for the centre spatial instrumental function while a pick-up of  $\sim 40\%$  is expected for the edge spatial instrumental function. Realistically, the intensity ratios obtained experimentally during detached discharges (smaller ratios exist during attached discharges) are generally at most 3 : 1 < 1. The 10:1 ratio estimate shown (figure A.10) is thus indicative of a worst-case event.

## A.5 Software systems and hardware control

In order to operate and monitor DSS data, a number of software programs have been developed in light of this thesis, highlighted below.

The DSS is set-up in such a way that acquisition is fully automated: at the start of the day the diagnostic is initialised and at the end of the day it is switched off. The diagnostic communicates with the TCV databases (e.g. Vista Database - VDB) in order to monitor any changes in the TCV state (e.g. whether a shot is pending) and to retrieve the required DSS

settings. When any DSS setting is changed, the diagnostic is automatically updated. When the TCV state changes and enters a shot cycle, the diagnostic is triggered and enters the shot phase. The first part of the shot phase consists of turning on the EM gain and stabilising the EM gain by doing a series of acquisitions/pauses (3-4 minutes before a discharge) and initialising the timer cards for the TTL trigger train pulses depending on the values set. In the second phase of the TCV cycle the camera is armed (30 seconds before a discharge) and prepared for the TTL triggers. When the discharge is performed, the camera acquires a set number of frames at every TTL trigger pulse and the acquisition PC saves the data locally and uploads it to MDS+, after which it can be loaded in.

The DSS control interface is shown in figure A.11 and enables changing the following: grating used, grating angle used (e.g. central wavelength must be set), EMCCD cooling temperature, EMCCD gain, timing values (start/end of TTL train, period of the TTL train and the number of TTL pulses), viewing orientation (must be changed manually on the machine side), filter installation (must be installed manually on the machine side) and CCD acquisition mode). The CCD acquisition modes are pre-programmed combinations of various CCD settings, containing information on the CCD clock speeds used (vertical/horizontal shift), triggering used (e.g. external trigger (TTL train) or internal triggering (TTL start - rest is done by the camera itself)), etc.). When a grating is changed, the corresponding track settings needed are automatically loaded and updated. Spectrometer changes (e.g. grating changes) are sent to the spectrometer using serial commands, are verified and log files are written by obtaining diagnostic data from the spectrometer. Camera changes are sent to the camera using MATLAB MEX files developed by Basil Duval, which interface directly with the camera's SDK C++ software, over a USB connection. All these settings are logged and saved for each appropriate discharge. The data loading routines load in all of these settings and apply the appropriate calibrations - e.g. if for instance a neutral density filter is installed, it will load the calibration curves for the neutral density filter and apply it to the standard calibrations.

Apart from settings, the DSS VDB also contains diagnostic information on the system. For instance, for most set values a read-back is in place to ensure that the set values were properly set. In case of errors, a message string is available displaying the relevant error. Also issues arising after the diagnostic's checks on the input parameter (for instance, when wrong timing values are set or when a TTL period smaller than the smallest possible are requested), lead to warnings in the message string. Again, all of this information is saved for each discharge.

A routine has been developed which loads all available DSS data from the MDS+ tree, applies the appropriate corrections (such as basic smearing correction, background subtraction, etc.), loads in the appropriate calibrations (camera calibrations, absolute intensity calibrations, filter curves if any filters were used, wavelength calibration and reading out the calibrated instrumental function) and loads in processed data if available (such as fit results). The processed information is stored using a dynamic allocation under several 'dummy' names in the DSS MDS+ trees which are automatically recognised by the reading program using a string attached to each field written in MDS+ in order to maintain maximum flexibility. That means that all types of results (even inferred data) can be stored under these trees and the information of the type of data/name of the data is also written to the same node, such that

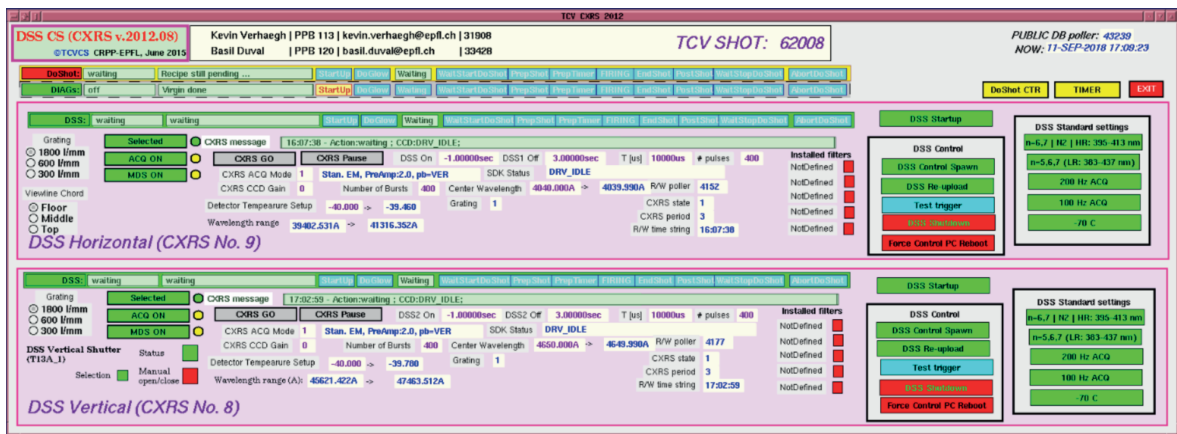


Figure A.11: Control window for DSS operation during experiments.

the reading routine can read out these instructions in order to understand how to handle the data.

These data loading routines are used automatically by two GUIs, one which can be used for looking at the DSS spectra and making simple spectral calculations (such as determining line integrals) and another one which is used for inspecting fitted data. A screenshot of the general data viewing GUI is shown in figure A.12. A shot number can be entered and the required system (e.g. horizontal or vertical) can be selected. After loading, the calibrated spectra is shown in the primary window and can be shown at different times/ROIs by using the various slider buttons. Several spectra (at different times or different ROI) can be overlaid. Using the GUI a window can be defined, which can be zoomed-in upon and integrated. This can be used for a quick inter-shot analysis by integrating various spectral lines and determining ratios between those lines. The secondary window is used for displaying processed data as function of either time or ROI. Processed data here can mean data inferred from fits or from other analysis. By default, the maximum intensity in the spectra is shown in order to detect more easily oversaturation. Using the various menu options, various actions can be done: 1) shot information (both general shot info (density, power injected, power radiated, etc.) and information on the DSS settings (EM gain, timing settings, track settings, etc.) used) can be shown; 2) the plasma equilibrium can be shown at different times with the DSS lines of sight overplotted; 3) the DSS signal can be resampled at a different time base to enhance S/N level by averaging the signal over various frames; 4) known spectral lines can be overlaid on the spectra for spectral line identification; 5) a copy of the primary or secondary window can be quickly saved; 6) a spectral fit can be initiated; 7) known spectral lines in the spectra can be used to update the wavelength calibration. Initiated spectral fits are sent as a job order to the internal MATLAB cluster, enabling parallelisation of the various fits.

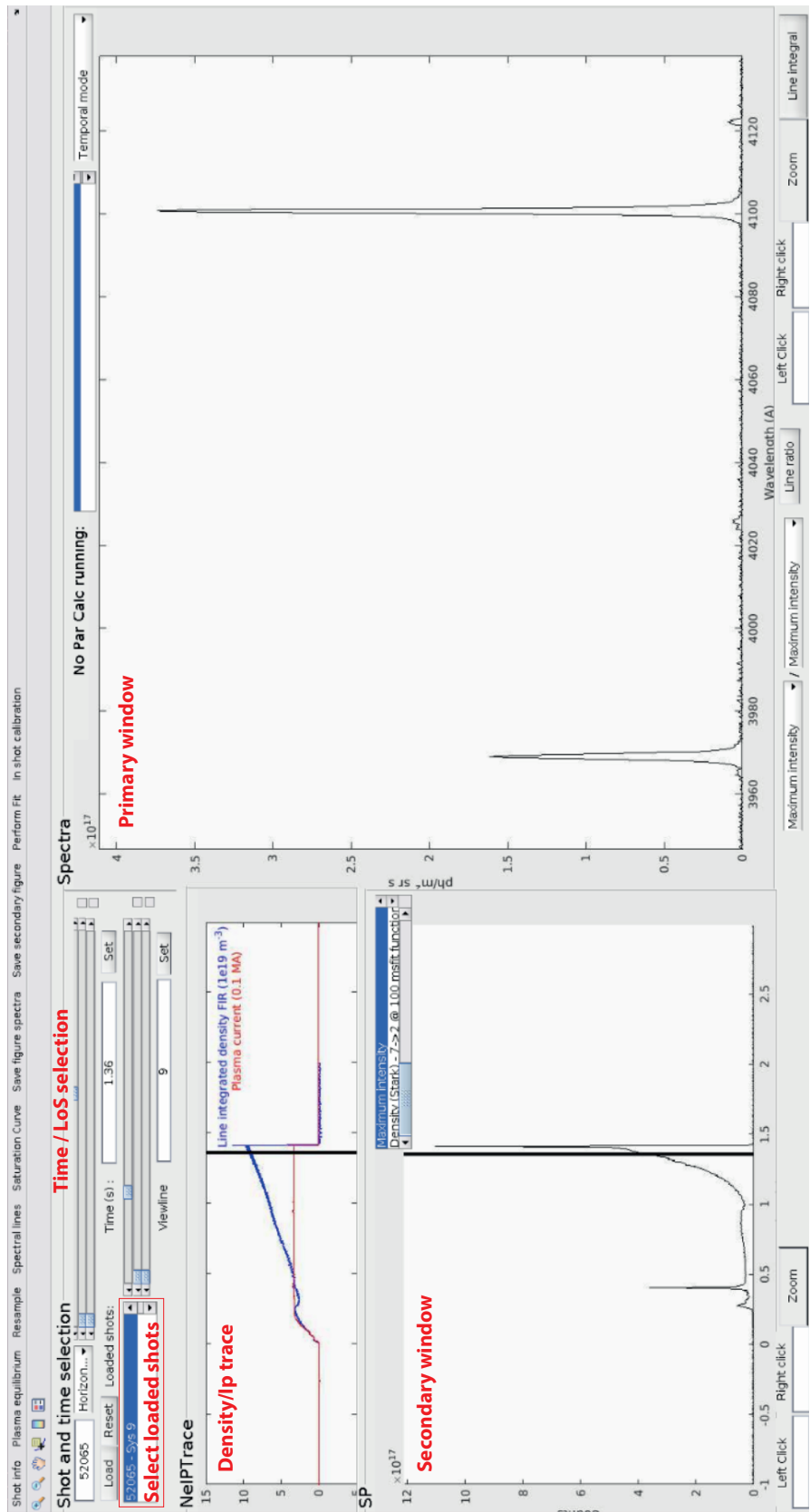


Figure A.12: Printscreen of the GUI used for DSS data viewing. Comments to identify the different elements are shown in red.

## Appendix B

# Statistical investigation of Balmer line analysis sensitivities

This section provides an in-depth study of the various analysis sensitivities.

- The sensitivity of the analysis to uncertainties in the atomic rate coefficients provided by ADAS, by assuming a uniform range of uncertainty for ADAS coefficients.
- The sensitivity of the analysis on a different (e.g. log-uniform as opposed to uniform) neutral fraction input PDF.
- The sensitivity of the analysis output uncertainty on the uncertainty of the various input parameters using a rank correlation technique.

### B.1 Investigating the influence of uncertainties in atomic rate coefficient

Atomic physics rates (e.g. the Photon Emission Coefficients (PECs), effective recombination/ionisation rates (ACD/SCD), radiated power rates (PLT/PRB) and charge exchange rates (CCD) of ADAS [134, 138, 135, 140] are not perfectly well known and can have a certain uncertainty. Such uncertainties are not well documented at this time, but based on differences between the 96 ADAS data set and the newly revised 12 ADAS dataset for hydrogen [140] which are expected to be at most 20 %. To investigate how uncertainties in the rate coefficients could influence the analysis strategy, a random (uncorrelated), uniform uncertainty of  $\pm 20\%$  is assumed for all atomic rate coefficients for one particular analysis run as shown in figure B.1. Since the number of parameters having an uncertainty is greatly increased by adding uncertainties to the rate coefficients, a higher number of Monte Carlo iterations is required to minimise the influence of Monte Carlo noise on the analysis. As such, we utilise ten times the number of iterations normally used (e.g. 50000 iterations). Note that these uncertainties are not normally included in the presented results.

Figure B.1 indicates no significant change in the parameter estimates in either the time trace of the ion source/sink or in the various PDFs which have their peak in a similar location. There is also no significant difference in the shape of the PDFs, although for some parameters, the PDFs and 68 % highest density intervals (HDI) are slightly wider when uncertainties

in the atomic coefficients are included (most notably  $P_{rad,L}^{H,exc}$ ,  $T_e^E$ ,  $T_e^R$  and  $CX_L/I_L$ ). That change in the uncertainty margin is however small when compared to the uncertainty margin as shown in figure B.1. The conclusion is thus that a random, uncorrelated uncertainty in the ADAS tables have a negligible influence on the analysis result.

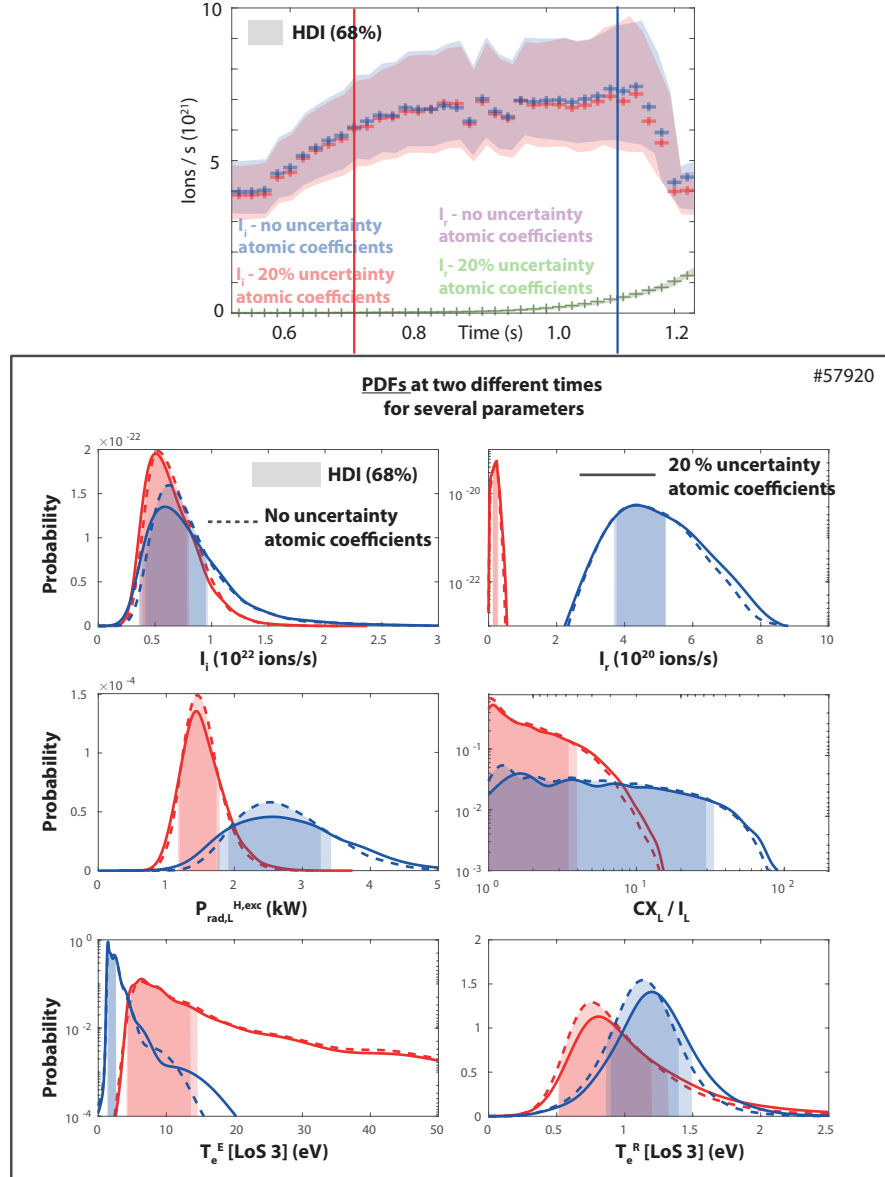


Figure B.1: Ionisation source, recombination rate and ion target current for # 57920 (density ramp at high current - similar to #56567) when accounting for no uncertainty in the atomic coefficients or 20 % uncertainty (in the form of a uniform distribution). PDFs for various output parameters are shown for those two cases at 0.7 and 1.1 s

## B.2 Investigating the robustness against various neutral fraction PDFs

To account for not knowing the neutral fraction, we assumed a uniform distribution for the neutral fraction, which ranges  $1 \times 10^{-3}$  to 0.05 exceeding several orders of magnitude. Although it is true that each value in that range has equal probability of occurring in a

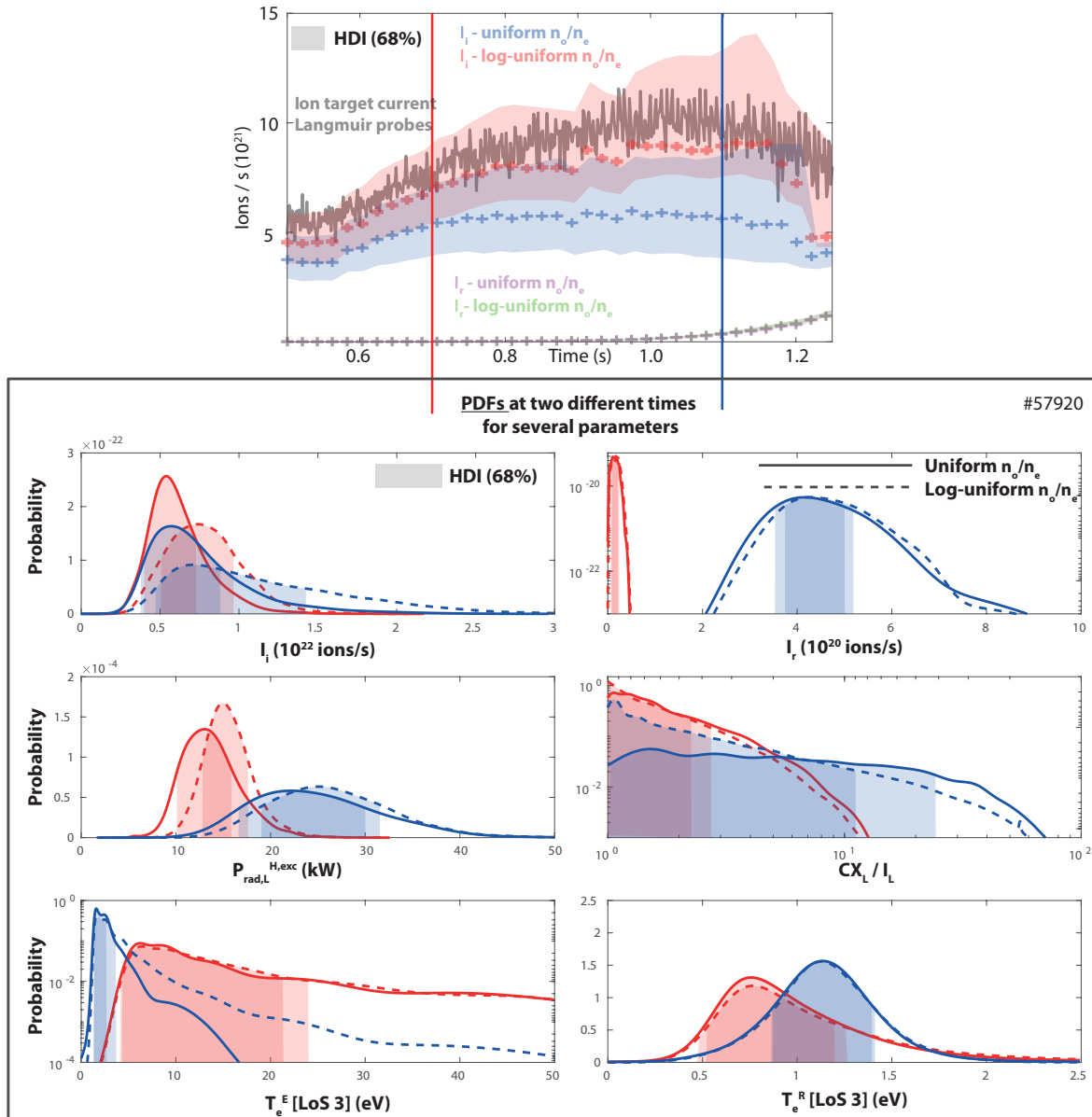


Figure B.2: Ionisation source, recombination rate and ion target current for # 57920 (density ramp at high current - similar to #56567) using a uniform and log-uniform PDF for  $n_o/n_e$ . PDFs for various output parameters are shown using a uniform and log-uniform PDF for  $n_o/n_e$  at 0.7 and 1.1 s

uniform PDF, it is ten times more likely to get a number between  $1 \times 10^{-2}$  to  $1 \times 10^{-1}$  than a number between  $1 \times 10^{-3}$  to  $1 \times 10^{-2}$ . Thus, for ranges exceeding several orders of magnitude, choosing a log-normal input PDF for a parameter which is not well known may be more appropriate. In the log-normal range, the  $\log_{10}$  is taken of the neutral fraction range, yielding  $-3$  to  $-1.3$  for a  $n_o/n_e$  range of  $1 \times 10^{-3}$  to  $0.05$  and a random value in this range is chosen  $x$ , which is transformed back to  $n_o/n_e$  through  $10^x$ . As this leads to stronger deviations in  $n_o/n_e$ , a larger number of Monte Carlo iterations is used (e.g. 20000 iterations).

A comparison between using a uniform and log-uniform neutral fraction distribution (between  $1 \times 10^{-3}$  to  $0.05$ ) is shown for discharge # 57920 (a density ramp discharge with similar parameters as #56567) in figure B.2. The log-uniform neutral fraction distribution leads to 35 % higher ionisation rate estimates as shown in figure B.2 while the trend of the

ionisation source as function of time is similar. The inferred recombination rate is practically unaltered between the two neutral fraction distribution, which is to be expected as the recombination inference only depends on the neutral fraction during the  $F_{rec}$  computation step. The shape of the ionisation source, recombination sink and radiated power (excitation) PDFs is similar between the two neutral fraction distributions, although the radiated power due to excitation is somewhat higher for the log-uniform neutral fraction. The reason for this is that higher  $T_e^E$  values are achieved for the log-uniform neutral fraction distribution as it is more likely to obtain low values for the neutral fraction, which (for a fixed  $B_{n \rightarrow 2}^{exc}$ ) has to be compensated with a higher  $T_e^E$  (or more specifically a wider  $T_e^E$  PDF which has a stronger asymptotic tail to high values), which leads to higher a higher 'ionisations per emitted excitation photon ratio' and a higher 'radiated power per emitted excitation photon ratio', explaining the rise in  $P_{rad,L}^{H,exc}$  and  $I_i$ . These higher  $T_e^E$  values also reduce the expected  $CX_L/I_L$ , especially during detached (1.1 s) conditions.

### B.3 Investigating the different sensitivities of output parameters to input uncertainties

An investigation was performed on the sensitivity of the analysis to input uncertainties using the output Monte Carlo results. For a given chord, for each time, there is a list of input and output values determined through Monte Carlo techniques. The correlation between the two is determined by using the Kendall-tau correlation technique [217], which is often used for exploratory data analysis aimed at investigating the basic relations between parameters as opposed to scatter plots such as shown in figure 7.16 a; which become cumbersome for high dimensional cases. The goal of this is to provide an exploratory overview on which uncertainties likely dominate the output variables. Kendall correlation has been chosen for, as it is a non-parametric technique (the often used Pearson correlation, for instance, is parametric and investigates a linear correlation). That said, Spearman and Pearson correlation techniques yield qualitatively similar results. The main conclusion of this exploratory investigation is that there is not a single uncertainty parameter which dominates all output parameters: the uncertainties contributing most to the output variables are different for each output variable and change as function of time as relative uncertainties change and the Balmer line emission becomes more dominated by recombination.

Kendall correlation is a non-parametric method which investigates the ordering of values (e.g. rank correlation) and for instance answers the question, if I order the dataset such that the values for  $B_{n \rightarrow 2}$  are always increasing, is the ionisation rate then also likely to increase? The result of this technique lies between -1 (means the order between the input and output variable is identically reversed), 0 (means there is no correlation) and 1 (means the order between the input and output variable is identical). Since this computation is all done for an individual time step and an individual line of sight over all the Monte Carlo values, the only deviation in all of the matrices is due to the given uncertainty - and not dynamic changes in parameters. As such, the correlation shown here only investigated the *uncertainty*: e.g. *which input uncertainties contribute most to the output uncertainties* and not which input parameters contribute most to the actual result. This also accounts for the fact that uncertainties of certain parameters (e.g.  $n_o/n_e$ ) are larger than of other parameters (e.g.  $B_{n \rightarrow 2}$ ). For instance,

in the sorted list of  $n_o/n_e$  inputs, there is a far larger deviation between the two most outer points than in the sorted list for  $B_{n \rightarrow 2}$  - and thus the average step between each value in the list is larger for  $n_o/n_e$  than for  $B_{n \rightarrow 2}$ . The correlation investigates how the influence of these deviations changes the rank (or ordering) of the result output.

Figure B.3 shows the correlation between various output parameters and various input parameters as function of time for # 56567 where a uniform distribution for  $n_o/n_e$  was used. Changing to a log-uniform distribution for  $n_o/n_e$  increases the relative importance of the  $n_o/n_e$  uncertainty for all cases, making it dominant for  $CX_L/I_L$  and  $T_e^E$ . Cases of statistical insignificance have been removed from the analysis and can occur at very low correlation strengths of 0.05 or smaller. The main conclusion from this figure is that there is not a single uncertainty parameter which dominates all output parameters: the uncertainties contributing most to the output variables are different for each output variable and change as function of time when the plasma becomes more strongly recombining and the density changes.

Below is an explanation of figure B.3 for every output parameter shown.

- $I_L$  At small  $F_{rec}$ , uncertainties in the  $B_{5 \rightarrow 2}$ ,  $n_o/n_e$ ,  $n_e$  and  $\Delta L$  contribute most to the ionisation source uncertainty. Later, the importance of  $n_o/n_e$  uncertainties increases and at higher  $F_{rec}$  the correlation of  $I_L$  with  $B_{6 \rightarrow 2}/B_{5 \rightarrow 2}$  becomes by far dominant (while other correlations decrease); which is to be expected given that at high  $F_{rec}$ , small changes in  $F_{rec}$  lead to large changes in  $B_{5 \rightarrow 2}^{exc}$ .
- $R_L$  Most important uncertainties which play a role in the  $R_L$  uncertainty are uncertainties in  $B_{5 \rightarrow 2}$ ,  $n_e$  and  $B_{6 \rightarrow 2}/B_{5 \rightarrow 2}$ . At small  $F_{rec}$  uncertainties in  $B_{6 \rightarrow 2}/B_{5 \rightarrow 2}$  (which have a strong influence on setting  $B_{6 \rightarrow 2}^{rec}$  as  $F_{rec}$  is small) and  $n_e$  (which has a large relative uncertainty due to having a low Stark inferred  $n_e$ ) dominate. At high  $F_{rec}$  uncertainties in the  $B_{5 \rightarrow 2}$  become more important.
- $CX_L/I_L$  The dominant uncertainties are similar for the  $T_e^E$  inference, but the ranking is opposite (e.g. since as  $T_e^E$  increases  $CX_L/I_L$  decreases). At low  $F_{rec}$ , the most important uncertainties are in  $n_e$ ,  $n_o/n_e$ . Later in time, first the influence of the  $n_e$  uncertainty decreases (likely again due to having higher Stark inferred  $n_e$  and lower relative uncertainties) while the influence of  $n_o/n_e$  and  $\Delta L$  uncertainties increase. At the highest  $F_{rec}$ , the correlation of  $CX_L/I_L$  with  $B_{6 \rightarrow 2}/B_{5 \rightarrow 2}$  becomes by far dominant while other correlations decrease. Again, this is due to the strong influence of  $F_{rec}$  on changes in  $B_{5 \rightarrow 2}^{exc}$  at high  $F_{rec}$ .
- $P_{ion,L}$  Somewhat similar to the correlations of  $I_L$  but  $n_o/n_e$  and  $\Delta L$  play much smaller roles. As such, the uncertainties mostly contributing to the  $P_{ion,L}$  uncertainty are  $B_{5 \rightarrow 2}$  and  $n_e$  at low  $F_{rec}$ . At high  $F_{rec}$ , again with  $B_{6 \rightarrow 2}/B_{5 \rightarrow 2}$  becomes by far dominant while other correlations decrease.
- $T_e^E$  The correlations are similar as to  $CX_L/I_L$  but in the opposite direction.
- $T_e^R$  The correlation to  $n_e$  is by far dominant at low  $F_{rec}$  while at high  $F_{rec}$ , the influence of the uncertainty in  $n_e$  increases and the influence of the  $\Delta L$  uncertainty increases.

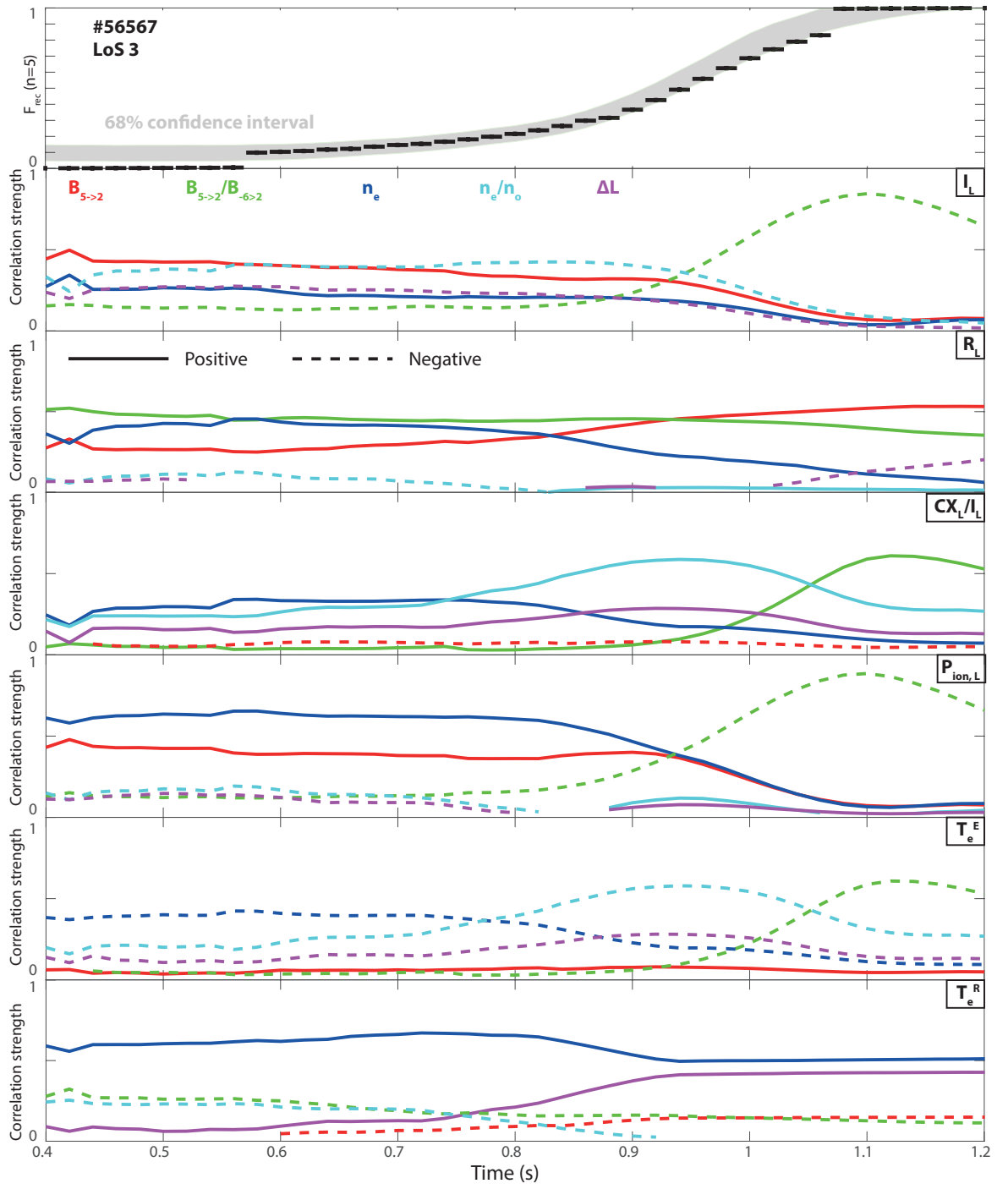


Figure B.3: Calculated (Kendall) correlation strength of input parameters to output parameters for # 56567 as function of time for line of sight 3. Positive values are shown with solid lines and negative values are shown with dotted lines. Statistical insignificant calculations have been removed from the figure. As a reference  $F_{rec}(n = 5)$  is shown.

# Bibliography

- [1] K Verhaegh, B Lipschultz, BP Duval, J.R. Harrison, H. Reimerdes, C. Theiler, B. Labit, R. Maurizio, C. Marini, F. Nespoli, U. Sheikh, C.K. Tsui, N. Vianello, and W.A.J. Vijvers. Spectroscopic investigations of divertor detachment in tcv. *Nuclear Materials and Energy*, 12:1112 – 1117, 2017. Proceedings of the 22nd International Conference on Plasma Surface Interactions 2016, 22nd PSI. doi:10.1016/j.nme.2017.01.004.
- [2] K Verhaegh, B Lipschultz, BP Duval, et al. An improved understanding of the roles of atomic processes and power balance in divertor target ion current loss during detachment. *Nuclear Fusion*, 2018 to be submitted. doi:10.13140/RG.2.2.24292.48005/1.
- [3] Peter Stangeby. The plasma boundary of magnetic fusion devices. *The Plasma Boundary of Magnetic Fusion Devices. Series: Series in Plasma Physics, ISBN: 978-0-7503-0559-4. Taylor & Francis, Edited by Peter Stangeby, vol. 7, 7, 2000.* URL: <https://www.crcpress.com/The-Plasma-Boundary-of-Magnetic-Fusion-Devices/Stangeby/p/book/9780750305594>.
- [4] Peter Stangeby. Basic physical processes and reduced models for plasma detachment. *Plasma Physics and Controlled Fusion*, 60(4):044022, 2018. URL: <http://stacks.iop.org/0741-3335/60/i=4/a=044022>.
- [5] S. I. Krasheninnikov, A. S. Kukushkin, and A. A. Pshenov. Divertor plasma detachment. *Phys. Plasmas*, 23(5):055602, 2016. doi:10.1063/1.4948273.
- [6] SI Krasheninnikov and AS Kukushkin. Physics of ultimate detachment of a tokamak divertor plasma. *Journal of Plasma Physics*, 83(5), 2017. doi:10.1017/S0022377817000654.
- [7] AMD Fil, BD Dudson, B Lipschultz, D Moulton, K Verhaegh, O Fevrier, and M Wensing. Identification of the primary processes that lead to the drop in divertor target ion current at detachment in tcv. *Contributions to plasma physics*, 12 2017. doi:10.1002/ctpp.201700171.
- [8] O Février, C Theiler, C Tsui, K Verhaegh, R Maurizio, B Labit, B Duval, JA Boedo, and B Lipschultz. Evolution of pressure drop during detachment in the tcv tokamak. *APS Conference Plasma Physics, Milwaukee, US*, 2017. URL: <http://meetings.aps.org/link/BAPS.2017.DPP.PP11.75>.
- [9] EA Wrigley. *The path to sustained growth: England's transition from an organic economy to an industrial revolution*. Cambridge University Press, 2016. doi:10.1111/ehr.12502.
- [10] J Campo and V Sarmiento. The relationship between energy consumption and gdp: evidence from a panel of 10 latin american countries. *Latin american journal of economics*, 50(2):233–255, 2013. URL: <http://www.jstor.org/stable/90003515>.
- [11] David MacKay. *Sustainable Energy-without the hot air*. UIT Cambridge, 2008.
- [12] BA. Bridge, D Adhikari, and Ma Fontenla. Electricity, income, and quality of life. *The Social Science Journal*, 53(1):33–39, 2016. doi:10.1016/j.soscij.2014.12.009.
- [13] World Energy Council. World energy resources. Unpublished work, United Nations, 2016. URL: <https://www.worldenergy.org/publications/2016/world-energy-resources-2016/>.
- [14] Jim Krane. Climate change and fossil fuel: An examination of risks for the energy industry and producer states. *MRS Energy Sustainability*, 4:E2, 2017. doi:10.1557/mre.2017.3.
- [15] B Brunekreef and ST Holgate. Air pollution and health. *The lancet*, 360(9341):1233–1242, 2002. doi:10.1016/S0140-6736(02)11274-8.
- [16] Frederica Perera. Pollution from fossil-fuel combustion is the leading environmental threat to global pediatric health and equity: Solutions exist. *International journal of environmental research and public health*, 15(1):16, 2017. doi:10.3390/ijerph15010016.

- [17] RK Pachauri, MR Allen, VR Barros, J Broome, W Cramer, R Christ, JA Church, L Clarke, Q Dahe, P Dasgupta, et al. *Climate change 2014: synthesis report. Contribution of Working Groups I, II and III to the fifth assessment report of the Intergovernmental Panel on Climate Change*. IPCC, 2014. doi:10.3390/ijerph15010016.
- [18] AJ McMichael, RE Woodruff, and S Hales. Climate change and human health: present and future risks. *The Lancet*, 367(9513):859–869, 2006. doi:10.1016/S0140-6736(06)68079-3.
- [19] Kamil Kaygusuz. Energy for sustainable development: A case of developing countries. *Renewable and Sustainable Energy Reviews*, 16(2):1116–1126, 2012. doi:10.1016/j.rser.2011.11.013.
- [20] DF Barnes and WM Floor. Rural energy in developing countries: a challenge for economic development. *Annual review of energy and the environment*, 21, 1996. doi:10.1146/annurev.energy.21.1.497.
- [21] John Bongaarts. Human population growth and the demographic transition. *Philosophical Transactions of the Royal Society of London B: Biological Sciences*, 364(1532):2985–2990, 2009. doi:10.1098/rstb.2009.0137.
- [22] Stanley R Bull. Renewable energy today and tomorrow. *Proceedings of the IEEE*, 89(8):1216–1226, 2001. doi:10.1109/5.940290.
- [23] David JC MacKay. Solar energy in the context of energy use, energy transportation and energy storage. *Phil. Trans. R. Soc. A*, 371(1996):20110431, 2013. doi:10.1098/rsta.2011.0431.
- [24] David JC MacKay. Could energy-intensive industries be powered by carbon-free electricity? *Phil. Trans. R. Soc. A*, 371(1986):20110560, 2013. doi:10.1098/rsta.2011.0560.
- [25] A Markandya and P Wilkinson. Electricity generation and health. *The Lancet*, 370(9591):979–990, 2007. doi:10.1016/S0140-6736(07)61253-7.
- [26] M Kotschenreuther, PM Valanju, SM Mahajan, and EA Schneider. Fusion–fission transmutation scheme—efficient destruction of nuclear waste. *Fusion Engineering and Design*, 84(1):83–88, 2009. doi:10.1016/j.fusengdes.2008.11.019.
- [27] CD Bowman, ED Arthur, PW Lisowski, GP Lawrence, RJ Jensen, JL Anderson, B Blind, M Cappiello, JW Davidson, TR England, et al. Nuclear energy generation and waste transmutation using an accelerator-driven intense thermal neutron source. *Nuclear Instruments and Methods in Physics Research Section A: Accelerators, Spectrometers, Detectors and Associated Equipment*, 320(1-2):336–367, 1992. doi:10.1016/0168-9002(92)90795-6.
- [28] Jeffrey P. Freidberg. *Plasma physics and fusion energy*. Cambridge university press, 2007. doi:10.1017/CBO9780511755705.
- [29] M Kikuchi, K Lackner, and MQ Tran. *Fusion physics*. International Atomic Energy Agency, 2012. URL: <http://www-pub.iaea.org/books/IAEABooks/8879/Fusion-Physics>.
- [30] John Wesson. *Tokamaks*, volume 149. Oxford University Press, 2011. doi:10.1080/00107514.2012.720285.
- [31] John D Lawson. Some criteria for a power producing thermonuclear reactor. *Proceedings of the Physical Society. Section B*, 70(1):6, 1957. URL: <http://stacks.iop.org/0370-1301/70/i=1/a=303>.
- [32] Yuhong Xu. A general comparison between tokamak and stellarator plasmas. *Matter and Radiation at Extremes*, 1(4):192 – 200, 2016. doi:10.1016/j.mre.2016.07.001.
- [33] C. S. Pitcher and P. C. Stangeby. Experimental divertor physics. *Plasma Phys. Controlled Fusion*, 39(6):779–930, 1997. doi:10.1088/0741-3335/39/6/001.
- [34] H. Reimerdes, S. Alberti, P. Blanchard, et al. Tcv divertor upgrade for alternative magnetic configurations. *Nuclear Materials and Energy*, 12:1106 – 1111, 2017. doi:10.1016/j.nme.2017.02.013.
- [35] B. Lipschultz, X. Bonnin, G. Counsell, et al. Plasma-surface interaction, scrape-off layer and divertor physics: implications for iter. *Nucl. Fusion*, 47(9):1189–1205, 2007. doi:10.1088/0029-5515/47/9/016.
- [36] R. A. Pitts, A. Kukushkin, A. Loarte, A. Martin, M. Merola, C. E. Kessel, V. Komarov, and M. Shimada. Status and physics basis of the iter divertor. *Phys. Scr.*, T138(T138):014001, 2009. doi:10.1088/0031-8949/2009/T138/014001.
- [37] A. Loarte, B. Lipschultz, A. S. Kukushkin, et al. Chapter 4: Power and particle control. *Nucl. Fusion*, 47(6):S203–S263, 2007. doi:10.1088/0029-5515/47/6/S04.

- [38] M. A. Makowski, D. Elder, T. K. Gray, B. LaBombard, C. J. Lasnier, A. W. Leonard, R. Maingi, T. H. Osborne, P. C. Stangeby, J. L. Terry, and J. Watkins. Analysis of a multi-machine database on divertor heat fluxes. *Phys. Plasmas*, 19(5):056122, 2012. doi:10.1063/1.4710517.
- [39] D. G. Whyte, B. LaBombard, J. W. Hughes, B. Lipschultz, J. Terry, D. Brunner, P. C. Stangeby, D. Elder, A. W. Leonard, and J. Watkins. Constraining the divertor heat width in iter. *J. Nucl. Mater.*, 438:S435–S439, 2013. doi:10.1016/j.jnucmat.2013.01.088.
- [40] A. J. Thornton, A. Kirk, and MAST Team. Scaling of the scrape-off layer width during inter-elm h modes on mast as measured by infrared thermography. *Plasma Phys. Controlled Fusion*, 56(5):055008, 2014. doi:10.1088/0741-3335/56/5/055008.
- [41] B. Lipschultz, B. LaBombard, J. L. Terry, C. Boswell, and I. H. Hutchinson. Divertor physics research on alcator c-mod. *Fusion Sci. Technol.*, 51(3):369–389, 2007. doi:10.13182/FST07-A1428.
- [42] R. A. Pitts, S. Carpentier, F. Escourbiac, T. Hirai, V. Komarov, S. Lisgo, A. S. Kukushkin, A. Loarte, M. Merola, A. S. Naik, R. Mitteau, M. Sugihara, B. Bazylev, and P. C. Stangeby. A full tungsten divertor for iter: Physics issues and design status. *J. Nucl. Mater.*, 438:S48–S56, 2013. doi:10.1016/j.jnucmat.2013.01.008.
- [43] A. Herrmann. Overview on stationary and transient divertor heat loads. *Plasma Phys. Controlled Fusion*, 44(6):883–903, 2002. doi:10.1088/0741-3335/44/6/318.
- [44] H.D. Pacher, A.S. Kukushkin, G.W. Pacher, V. Kotov, and D. Reiter. Modelling of the iter reference divertor plasma. *Journal of Nuclear Materials*, 415(1, Supplement):S492 – S496, 2011. Proceedings of the 19th International Conference on Plasma-Surface Interactions in Controlled Fusion. doi:10.1016/j.jnucmat.2010.10.083.
- [45] R. A. Pitts, A. Refke, B. P. Duval, I. Furno, B. Joye, J. B. Lister, Y. Martin, J. M. Moret, J. Rommers, and H. Weisen. Experimental investigation of the effects of neon injection in tcv. *J. Nucl. Mater.*, 266:648–653, 1999. doi:10.1016/S0022-3115(98)00599-6.
- [46] M Greenwald, JL Terry, SM Wolfe, S Ejima, MG Bell, SM Kaye, and GH Neilson. A new look at density limits in tokamaks. *Nuclear Fusion*, 28(12):2199, 1988. URL: <http://stacks.iop.org/0029-5515/28/i=12/a=009>.
- [47] A. S. Kukushkin, H. D. Pacher, G. W. Pacher, V. Kotov, R. A. Pitts, and D. Reiter. Consequences of a reduction of the upstream power sol width in iter. *J. Nucl. Mater.*, 438:S203–S207, 2013. doi:10.1016/j.jnucmat.2013.01.027.
- [48] RJ Goldston, ML Reinke, and JA Schwartz. A new scaling for divertor detachment. *Plasma Physics and Controlled Fusion*, 59(5):055015, 2017. URL: <http://stacks.iop.org/0741-3335/59/i=5/a=055015>.
- [49] V Kotov and D Reiter. Two-point analysis of the numerical modelling of detached divertor plasmas. *Plasma physics and controlled fusion*, 51(11):115002, 2009. URL: <http://stacks.iop.org/0741-3335/51/i=11/a=115002>.
- [50] D Moulton, J Harrison, B Lipschultz, and D Coster. Using solps to confirm the importance of total flux expansion in super-x divertors. *Plasma Physics and Controlled Fusion*, 59(6):065011, 2017. URL: <http://stacks.iop.org/0741-3335/59/i=6/a=065011>.
- [51] B. Lipschultz, J. L. Terry, C. Boswell, J. A. Goetz, A. E. Hubbard, S. I. Krasheninnikov, B. LaBombard, D. A. Pappas, C. S. Pitcher, F. Wising, and S. Wukitch. The role of particle sinks and sources in alcator c-mod detached divertor discharges. *Phys. Plasmas*, 6(5):1907–1916, 1999. doi:10.1063/1.873448.
- [52] A. A. Pshenov, A. S. Kukushkin, and S. I. Krasheninnikov. Energy balance in plasma detachment. *Nucl. Mater. Energy*, 2017. doi:10.1016/j.nme.2017.03.019.
- [53] AS Kukushkin, HD Pacher, and RA Pitts. Characteristics of divertor detachment for iter conditions. *Journal of Nuclear Materials*, 463:586–590, 2015. doi:10.1016/j.jnucmat.2014.10.042.
- [54] D. E. Post. A review of recent developments in atomic processes for divertors and edge plasmas. *J. Nucl. Mater.*, 220:143–157, 1995. URL: <GotoISI>://WOS:A1995QY75400014, doi:Doi10.1016/0022-3115(94)00453-6.
- [55] F Wising, SI Krasheninnikov, DJ Sigmar, DA Knoll, TD Rognlien, B LaBombard, B Lipschultz, and G McCracken. Simulation of plasma flux detachment in alcator c-mod and iter. *Journal of nuclear materials*, 241:273–277, 1997. doi:10.1016/S0022-3115(97)80048-7.
- [56] A Loarte. Understanding the edge physics of divertor experiments by comparison of 2d edge code calculations and experimental measurements. *Journal of nuclear materials*, 241:118–134, 1997. doi:10.1016/S0022-3115(97)80035-9.

- [57] SI Krasheninnikov, A Yu Pigarov, DA Knoll, B LaBombard, B Lipschultz, DJ Sigmar, TK Soboleva, JL Terry, and F Wising. Plasma recombination and molecular effects in tokamak divertors and divertor simulators. *Physics of Plasmas*, 4(5):1638–1646, 1997. doi:10.1063/1.872268.
- [58] R. A. Pitts, B. P. Duval, A. Loarte, J. M. Moret, J. A. Boedo, D. Coster, I. Furno, J. Horacek, A. S. Kukushkin, D. Reiter, J. Rommers, and TCV Team. Divertor geometry effects on detachment in tcv. *J. Nucl. Mater.*, 290:940–946, 2001. doi:10.1016/S0022-3115(00)00461-X.
- [59] K Borrass, R Schneider, and R Farengo. A scrape-off layer based model for hugill-greenwald type density limits. *Nuclear fusion*, 37(4):523, 1997. URL: <http://stacks.iop.org/0029-5515/37/i=4/a=I10>.
- [60] B Lipschultz, JL Terry, C Boswell, SI Krasheninnikov, B LaBombard, and DA Pappas. Recombination and ion loss in c-mod detached divertor discharges. *Journal of nuclear materials*, 266:370–375, 1999. doi:10.1016/S0022-3115(98)00534-0.
- [61] G. M. McCracken, M. F. Stamp, R. D. Monk, A. G. Meigs, J. Lingertat, R. Prentice, A. Starling, R. J. Smith, and A. Tabasso. Evidence for volume recombination in jet detached divertor plasmas. *Nucl. Fusion*, 38(4):619–629, 1998. doi:10.1088/0029-5515/38/4/311.
- [62] D. Lumma, J. L. Terry, and B. Lipschultz. Radiative and three-body recombination in the alcator c-mod divertor. *Phys. Plasmas*, 4(7):2555–2566, 1997. doi:10.1063/1.872234.
- [63] J. L. Terry, B. Lipschultz, A. Y. Pigarov, S. I. Krasheninnikov, B. LaBombard, D. Lumma, H. Ohkawa, D. Pappas, and M. Umansky. Volume recombination and opacity in alcator c-mod divertor plasmas. *Phys. Plasmas*, 5(5):1759–1766, 1998. doi:10.1063/1.872845.
- [64] U Wenzel, K Behringer, A Carlson, J Gafert, B Napiontek, and A Thoma. Volume recombination in divertor i of asdex upgrade. *Nuclear Fusion*, 39(7):873, 1999. URL: <http://stacks.iop.org/0029-5515/39/i=7/a=304>.
- [65] B. Lipschultz, J. L. Terry, C. Boswell, A. Hubbard, B. LaBombard, and D. A. Pappas. Ultrahigh densities and volume recombination inside the separatrix of the alcator c-mod tokamak. *Phys. Rev. Lett.*, 81(5):1007–1010, 1998. doi:10.1103/PhysRevLett.81.1007.
- [66] JL Terry, B Lipschultz, X Bonnin, C Boswell, SI Krasheninnikov, A Yu Pigarov, B LaBombard, DA Pappas, and HA Scott. The experimental determination of the volume recombination rate in tokamak divertors. *Journal of nuclear materials*, 266:30–36, 1999. doi:10.1016/S0022-3115(98)00812-5.
- [67] F. Reimold, M. Wischmeier, S. Potzel, L. Guimarais, D. Reiter, M. Bernert, M. Dunne, and T. Lunt. The high field side high density region in solps-modeling of nitrogen-seeded h-modes in asdex upgrade. *Nucl. Mater. Energy*, 2017. doi:10.1016/j.nme.2017.01.010.
- [68] Marco Wischmeier. *Simulating divertor detachment in the TCV and JET tokamaks*. Phd thesis, Ecole Polytechnique Fédérale de Lausanne, 2005. doi:10.5075/epfl-thesis-3176.
- [69] D Reiter et al. The eirene code user manual. Technical report, Forschungszentrum Jülich GmbH, 2008. URL: <http://www.eirene.de/manuals/eirene.pdf>.
- [70] RD Monk, A Loarte, A Chankin, S Clement, SJ Davies, JK Ehrenberg, HY Guo, J Lingertat, GF Matthews, MF Stamp, et al. Interpretation of ion flux and electron temperature profiles at the jet divertor target during high recycling and detached discharges. *Journal of nuclear materials*, 241:396–401, 1997. doi:10.1016/S0022-3115(97)80071-2.
- [71] K Verhaegh, B Lipschultz, BP Duval, O Février, R Maurizio, C Theiler, JR Harrison, B Labit, B Lomanowski, C Marini, H Reimerdes, UA Sheikh, C Tsui, and WAJ Vijvers. Spectroscopic investigations of ion sources/sinks during tcv detachment. *44th EPS Conference on Plasma Physics, Belfast, United Kingdom*, 2017. doi:10.13140/RG.2.2.29588.50568/3.
- [72] B Lomanowski, M Carr, A Field, et al. Spectroscopic investigation of n2 and ne seeded induced detachment in jet iter-like wall. *Nuclear Materials and Energy*, 2018, submitted.
- [73] Steffen Potzel. *Experimental classification of divertor detachment*. Phd thesis, Bayreuth Universität, 2012. URL: <https://epub.uni-bayreuth.de/id/eprint/210>.
- [74] B. A. Lomanowski, A. G. Meigs, R. M. Sharples, M. Stamp, C. Guillemaut, and JET Contributors. Inferring divertor plasma properties from hydrogen balmer and paschen series spectroscopy in jet-ilw. *Nucl. Fusion*, 55(12):123028, 2015. doi:10.1088/0029-5515/55/12/123028.

- [75] VA Soukhanovskii, DW Johnson, R Kaita, and AL Roquemore. Electron density measurements in the national spherical torus experiment detached divertor region using stark broadening of deuterium infrared paschen emission lines. *Review of scientific instruments*, 77(10):10F127, 2006. doi:10.1063/1.2336456.
- [76] J. R. Harrison, S. W. Lisgo, K. J. Gibson, P. Tamain, J. Dowling, and MAST Team. Characterisation of detached plasmas on the mast tokamak. *J. Nucl. Mater.*, 415(1):S379–S382, 2011. doi:10.1016/j.jnucmat.2010.12.226.
- [77] N Ramasubramanian, R König, Y Feng, L Giannone, P Grigull, T Klinger, K McCormick, H Thomsen, U Wenzel, et al. Characterization of the island divertor plasma of w7-as stellarator in the deeply detached state with volume recombination. *Nuclear fusion*, 44(9):992, 2004. URL: <http://stacks.iop.org/0029-5515/44/i=9/a=008>.
- [78] PC Stangeby and Chaofeng Sang. Strong correlation between d 2 density and electron temperature at the target of divertors found in solps analysis. *Nuclear Fusion*, 57(5):056007, 2017. URL: <http://stacks.iop.org/0029-5515/57/i=5/a=056007>.
- [79] J. R. Harrison, W. A. J. Vijvers, C. Theiler, B. P. Duval, S. Elmore, B. Labit, B. Lipschultz, S. H. M. van Limpt, S. W. Lisgo, C. K. Tsui, H. Reimerdes, U. Sheikh, K. Verhaegh, and M. Wischmeier. Detachment evolution on the tcv tokamak. *Nucl. Mater. Energy*, 2016. doi:10.1016/j.nme.2016.10.020.
- [80] J L Terry and M L Reinke. Diagnostic tools for studying divertor detachment: bolometry, spectroscopy, and thermography for surface heat-flux. *Plasma Physics and Controlled Fusion*, 59(4):044004, 2017. URL: <http://stacks.iop.org/0741-3335/59/i=4/a=044004>.
- [81] J. R. Harrison. *Characterisation of detached plasmas on the MAST tokamak*. Phd thesis, University of York, 2010. URL: <http://etheses.whiterose.ac.uk/id/eprint/1524>.
- [82] B Lipschultz, FI Parra, and IH Hutchinson. Sensitivity of detachment extent to magnetic configuration and external parameters. *Nucl. Fusion*, 56(5):056007, apr 2016. doi:10.1088/0029-5515/56/5/056007.
- [83] B. Lipschultz. Review of marfe phenomena in tokamaks. *J. Nucl. Mater.*, 145:15–25, 1987. doi:10.1016/0022-3115(87)90306-0.
- [84] J. A. Goetz, C. Kurz, B. LaBombard, et al. Comparison of detached and radiative divertor operation in alcator c-mod. *Phys. Plasmas*, 3(5):1908–1915, 1996. doi:10.1063/1.871986.
- [85] K. Jesko, Y. Marandet, H. Bufferand, J.P. Gunn, H.J. van der Meiden, and G. Ciraolo. Soledge2d-eirene simulations of the pilot-psi linear plasma device compared to experimental data. *Contributions to Plasma Physics*, 58(6-8):798–804, 2017. doi:10.1002/ctpp.201700186.
- [86] Y. Hayashi, K. Ješko, H.J. van der Meiden, J.W.M. Vernimmen, T.W. Morgan, N. Ohno, S. Kajita, M. Yoshikawa, and S. Masuzaki. Plasma detachment study of high density helium plasmas in the pilot-psi device. *Nuclear Fusion*, 56(12):126006, 2016. doi:10.1088/0029-5515/56/12/126006.
- [87] Y. Shimomura, M. Keilhacker, K. Lackner, and H. Murrmann. Characteristics of the divertor plasma in neutral-beam-heated asdex discharges. *Nucl. Fusion*, 23(7):869–879, 1983. doi:10.1088/0029-5515/23/7/002.
- [88] B. Labombard, J. Goetz, C. Kurz, et al. Scaling and transport analysis of divertor conditions on the alcator c-mod tokamak. *Phys. Plasmas*, 2(6):2242–2248, 1995. doi:10.1063/1.871248.
- [89] B. LaBombard, J. A. Goetz, I. Hutchinson, et al. Experimental investigation of transport phenomena in the scrape-off layer and divertor. *J. Nucl. Mater.*, 241:149–166, 1997. doi:10.1016/S0022-3115(96)00502-8.
- [90] F. Reimold, M. Wischmeier, M. Bernert, S. Potzel, A. Kallenbach, H. W. Muller, B. Sieglin, U. Stroth, and ASDEX Upgrade Team. Divertor studies in nitrogen induced completely detached h-modes in full tungsten asdex upgrade. *Nucl. Fusion*, 55(3):033004, 2015. doi:10.1088/0029-5515/55/3/033004.
- [91] A Kallenbach, M Bernert, R Dux, L Casali, Th Eich, L Giannone, A Herrmann, R McDermott, A Mlynek, HW Müller, et al. Impurity seeding for tokamak power exhaust: from present devices via iter to demo. *Plasma Physics and Controlled Fusion*, 55(12):124041, 2013. URL: <http://stacks.iop.org/0741-3335/55/i=12/a=124041>.
- [92] G. P. Maddison, C. Giroud, G. K. McCormick, et al. Moderation of divertor heat loads by fuelling and impurity seeding in well-confined elmy h-mode plasmas on jet. *Nucl. Fusion*, 51(4):042001, 2011. doi:10.1088/0029-5515/51/4/042001.
- [93] H. Reimerdes, G. P. Canal, B. P. Duval, B. Labit, T. Lunt, F. Nespoli, W. A. J. Vijvers, G. De Temmerman, C. Lowry, T. W. Morgan, et al. Experimental investigation of neon seeding in the snowflake configuration in tcv. *J. Nucl. Mater.*, 2014. doi:10.1016/j.jnucmat.2014.10.076.

- [94] M Bernert, M Wischmeier, A Huber, F Reimold, B Lipschultz, C Lowry, S Brezinsek, R Dux, T Eich, A Kallenbach, et al. Power exhaust by sol and pedestal radiation at asdex upgrade and jet. *Nuclear Materials and Energy*, 12:111–118, 2017. doi:10.1016/j.nme.2016.12.029.
- [95] A Kallenbach, M Bernert, R Dux, F Reimold, M Wischmeier, and ASDEX Upgrade Team. Analytical calculations for impurity seeded partially detached divertor conditions. *Plasma Physics and Controlled Fusion*, 58(4):045013, 2016. doi:10.1088/0741-3335/58/4/045013.
- [96] D. E. Post, R. V. Jensen, C. B. Tarter, W. H. Grasberger, and W. A. Lokke. Steady-state radiative cooling rates for low-density high-temperature plasmas. *Bulletin of the American Physical Society*, 22(9):1178–1178, 1977. doi:10.1016/0092-640X(77)90026-2.
- [97] W. Fundamenski. Power and particle exhaust in tokamaks: Integration of plasma scenarios with plasma facing materials and components. *J. Nucl. Mater.*, 390-91:10–19, 2009. doi:10.1016/j.jnucmat.2009.01.038.
- [98] A Fil, B Dudson, B Lipschultz, D Moulton, O Myatra, K Verhaegh, M Wensing, and O Février. On the effect of total flux expansion on tcv detachment modeling. *PSI Conference, Princeton, US*, 2018. URL: [https://www.researchgate.net/publication/325780160\\_On\\_the\\_effect\\_of\\_total\\_flux\\_expansion\\_on\\_TCV\\_detachment\\_modeling\\_with\\_SOLPS-ITER](https://www.researchgate.net/publication/325780160_On_the_effect_of_total_flux_expansion_on_TCV_detachment_modeling_with_SOLPS-ITER).
- [99] R. Maurizio, B.P. Duval, O. Février, J. Harrison, B Labit, B Lipschultz, H Reimerdes, C. Theiler, "K. Verhaegh, and W.A.J. Vijvers". Divertor heat flux characterisation during detachment experiments in tcv. In *44th EPS Conference on Plasma Physics*, 2017. URL: <http://ocs.ciemat.es/EPS2017PAP/pdf/P5.116.pdf>.
- [100] T. Eich, B. Siegl, A. Scarabosio, A. Herrmann, A. Kallenbach, G. F. Matthews, S. Jachmich, S. Brezinsek, M. Rack, R. J. Goldston, ASDEX Upgrade Team, and JET-EFDA Contributors. Empirical scaling of inter-elm power widths in asdex upgrade and jet. *J. Nucl. Mater.*, 438:S72–S77, 2013. doi:10.1016/j.jnucmat.2013.01.011.
- [101] C. Theiler, B. Lipschultz, J. Harrison, et al. Results from recent detachment experiments in alternative divertor configurations on tcv. *Nucl. Fusion*, 57(7):072008, 2017. doi:10.1088/1741-4326/aa5fb7.
- [102] A. Loarte, R. D. Monk, J. R. Martin-Solis, et al. Plasma detachment in jet mark i divertor experiments. *Nucl. Fusion*, 38(3):331–371, 1998. doi:10.1088/0029-5515/38/3/303.
- [103] Peter Stangeby. Can detached divertor plasmas be explained as self-sustained gas targets? *Nucl. Fusion*, 33(11):1695, 1993. doi:10.1088/0029-5515/33/11/I10.
- [104] G. F. Matthews. Plasma detachment from divertor targets and limiters. *J. Nucl. Mater.*, 220:104–116, 1995. doi:10.1016/0022-3115(94)00450-1.
- [105] A. Loarte. Effects of divertor geometry on tokamak plasmas. *Plasma Phys. Controlled Fusion*, 43(6):R183–R224, 2001. doi:10.1088/0741-3335/43/6/201.
- [106] E. M. Hollmann, S. Brezinsek, N. H. Brooks, M. Groth, A. G. McLean, A. Yu Pigarov, and D. L. Rudakov. Spectroscopic measurement of atomic and molecular deuterium fluxes in the diii-d plasma edge. *Plasma Phys. Controlled Fusion*, 48(8):1165, 2006. URL: <http://stacks.iop.org/0741-3335/48/i=8/a=009>.
- [107] M. Wischmeier, R. A. Pitts, A. Alfier, Y. Andrebe, R. Behn, D. Coster, J. Horacek, P. Nielsen, R. Pasqualotto, D. Reiter, and A. Zabolotsky. The influence of molecular dynamics on divertor detachment in tcv. *Contrib. Plasma Phys.*, 44(1-3):268–273, 2004. doi:10.1002/ctpp.200.
- [108] AS Kukushkin, SI Krasheninnikov, AA Pshenov, and D Reiter. Role of molecular effects in divertor plasma recombination. *Nuclear Materials and Energy*, 12:984–988, 2017. doi:10.1016/j.nme.2016.12.030.
- [109] M. Sakamoto, A. Terakado, K. Nojiri, N. Ezumi, Y. Nakashima, K. Sawada, K. Ichimura, M. Fukumoto, K. Oki, K. Shimizu, et al. Molecular activated recombination in divertor simulation plasma on gamma 10/pdx. *Nucl. Mater. Energy*, 2017. doi:10.1016/j.nme.2017.05.001.
- [110] Groth M, Hollmann E, Jaervinen A, et al. Edge2d-eirene predictions of molecular emission in diii-d high-recycling divertor plasmas. *Nuclear Materials and Energy*, 2018, submitted.
- [111] H. Kubo, H. Takenaga, K. Sawada, T. Nakano, S. Kobayashi, S. Higashijima, N. Asakura, and K. Shimizu. Spectroscopic study of hydrogen particle behavior in attached and detached divertor plasmas of jt-60u. *J. Nucl. Mater.*, 337(1-3):161–165, 2005. doi:10.1016/j.jnucmat.2004.09.039.
- [112] U. Fantz. Emission spectroscopy of hydrogen molecules in technical and divertor plasmas. *Contrib. Plasma Phys.*, 42(6-7):675–684, 2002. doi:10.1002/1521-3986(200211)42:6/7<675::AID-CTPP675>3.0.CO;2-6.

- [113] S. I. Krasheninnikov, M. Rensink, T. D. Rognlien, A. S. Kukushkin, J. A. Goetz, B. LaBombard, B. Lipschultz, J. L. Terry, and M. Umansky. Stability of the detachment front in a tokamak divertor. *J. Nucl. Mater.*, 266-269(Supplement C):251–257, 1999. doi:10.1016/S0022-3115(98)00577-7.
- [114] S. I. Krasheninnikov. Physical mechanisms in divertors and their impact on the core. *Czech. J. Phys.*, 48(2):97–112, 1998. doi:10.1007/s10582-998-0027-7.
- [115] S. Potzel, M. Wischmeier, M. Bernert, R. Dux, H. W. Muller, A. Scarabosio, and ASDEX Upgrade Team. A new experimental classification of divertor detachment in asdex upgrade. *Nucl. Fusion*, 54(1):013001, 2014. doi:10.1088/0029-5515/54/1/013001.
- [116] I. H. Hutchinson. *Principles of Plasma Diagnostics*. Cambridge University Press, 2 edition, 2002. doi:10.1017/CBO9780511613630.
- [117] O Février, C Theiler, H De Oliveira, B Labit, N Fedorczak, and A Baillod. Analysis of wall-embedded langmuir probe signals in different conditions on the tokamak à configuration variable. *Review of Scientific Instruments*, 89(5):053502, 2018. doi:10.1063/1.5022459.
- [118] OV Batishchev, XQ Xu, JA Byers, RH Cohen, SI Krasheninnikov, TD Rognlien, and DJ Sigmar. Kinetic effects on particle and heat fluxes in detached plasmas. *Phys. Plasmas*, 3(9):3386–3396, 1996. doi:10.1063/1.871615.
- [119] OV Batishchev, SI Krasheninnikov, Peter J Catto, AA Batishcheva, DJ Sigmar, XQ Xu, JA Byers, TD Rognlien, RH Cohen, and MM Shoucri. Kinetic effects in tokamak scrape-off layer plasmas. *Phys. Plasmas*, 4(5):1672–1680, 1997. doi:10.1063/1.872280.
- [120] A Kallenbach, M Bernert, M Beurskens, L Casali, M Dunne, T Eich, L Giannone, A Herrmann, M Maraschek, S Potzel, et al. Partial detachment of high power discharges in asdex upgrade. *Nuclear Fusion*, 55(5):053026, 2015. doi:10.1088/0029-5515/55/5/053026.
- [121] S. Lisgo, P. Borner, G. F. Counsell, J. Dowling, A. Kirk, R. Scannell, M. O'Mullane, D. Reiter, and MAST Team. Interpretation of spatially resolved helium line ratios on mast. *J. Nucl. Mater.*, 390-91:1078–1080, 2009. doi:10.1016/j.jnucmat.2009.01.292.
- [122] C. J. Boswell, J. L. Terry, B. Lipschultz, and J. Stillerman. Applications of visible ccd cameras on the alcator c-mod tokamak. *Rev. Sci. Instrum.*, 72(1):935–939, 2001. doi:10.1063/1.1321010.
- [123] M. E. Fenstermacher, W. H. Meyer, R. D. Wood, D. G. Nilson, R. Ellis, and N. H. Brooks. A tangentially viewing visible tv system for the diii-d divertor. *Rev. Sci. Instrum.*, 68(1):974–977, 1997. doi:10.1063/1.1147729.
- [124] A. G. Meigs, S. Brezinsek, M. Clever, A. Huber, S. Marsen, C. Nicholas, M. Stamp, K. D. Zastrow, and JET EFDA Contributors. Deuterium balmer/stark spectroscopy and impurity profiles: First results from mirror-link divertor spectroscopy system on the jet iter-like wall. *J. Nucl. Mater.*, 438:S607–S611, 2013. doi:10.1016/j.jnucmat.2013.01.127.
- [125] M. Koubiti, Y. Marandet, A. Escarguel, H. Capes, L. Godbert-Mouret, R. Stamm, C. De Michelis, R. Guirlet, and M. Mattioli. Analysis of asymmetric da spectra emitted in front of a neutralizer plate of the tore-supra ergodic divertor. *Plasma Phys. Controlled Fusion*, 44(2):261, 2002. doi:10.1088/0741-3335/44/2/309.
- [126] R. C. Isler, R. W. Wood, C. C. Klepper, N. H. Brooks, M. E. Fenstermacher, and A. W. Leonard. Spectroscopic characterization of the diii-d divertor. *Phys. Plasmas*, 4(2):355–368, 1997. doi:10.1063/1.872095.
- [127] J Rosato, N. Kieu, M. Meireni, R. Sheeba, M Koubiti, Y Marandet, R Stamm, K. Verhaegh, and B. Duval. Stark broadening of balmer lines with low and moderate quantum number in dense divertor plasmas. *Contrib. Plasma Phys.*, 2017. doi:10.1002/ctpp.201700100.
- [128] R. Neu, R. Dux, A. Geier, et al. Impurity behaviour in the asdex upgrade divertor tokamak with large area tungsten walls. *Plasma Phys. Controlled Fusion*, 44(6):811–826, 2002. doi:10.1088/0741-3335/44/6/313.
- [129] R. C. Isler, N. H. Brooks, W. P. West, A. W. Leonard, G. R. McKee, and G. D. Porter. Spectroscopic measurements of impurity temperatures and parallel ion flows in the diii-d divertor. *J. Nucl. Mater.*, 266:376–379, 1999. doi:10.1016/S0022-3115(98)00824-1.
- [130] H. Kubo, H. Takenaga, T. Sugie, S. Higashijima, S. Suzuki, A. Sakasai, and N. Hosogane. The spectral profile of the d-alpha line emitted from the divertor region of jt-60u. *Plasma Phys. Controlled Fusion*, 40(6):1115–1126, 1998. doi:10.1088/0741-3335/40/6/017.
- [131] C. Stehlé and R. Hutcheon. Extensive tabulations of stark broadened hydrogen line profiles. *Astronomy and Astrophysics Supplement Series*, 140(1):93–97, 1999. doi:10.1051/aas:1999118.

- [132] VA Soukhanovskii, AL Roquemore, CH Skinner, J Menard, HW Kugel, D Johnson, R Maingi, S Sabbagh, and F Paoletti. High-resolution spectroscopic diagnostic for divertor and scrape-off layer neutral and impurity emission measurements in the national spherical torus experiment. *Review of scientific instruments*, 74(3):2094–2097, 2003. doi:10.1063/1.1537042.
- [133] Hongmin Mao, Fang Ding, Guang-Nan Luo, Zhenhua Hu, Xiahua Chen, Feng Xu, Zhongshi Yang, Jingbo Chen, Liang Wang, Rui Ding, et al. A multichannel visible spectroscopy system for the iter-like w divertor on east. *Review of Scientific Instruments*, 88(4):043502, 2017. doi:10.1063/1.4979406.
- [134] University of Strathclyde ADAS project. Open-adas, 2018. URL: <http://open.adas.ac.uk/>.
- [135] HP Summers, MG O’Mullane, AD Whiteford, NR Badnell, and SD Loch. Adas: Atomic data, modelling and analysis for fusion. In *AIP Conference Proceedings*, volume 901, pages 239–248, 2007. doi:10.1063/1.2727374.
- [136] S Togo, M Nakamura, Yuichi Ogawa, K Shimizu, T Takizuka, and K Hoshino. Effects of neutral particles on the stability of the detachment fronts in divertor plasmas. *Plasma and Fusion Research*, 8:2403096–2403096, 2013. doi:10.1585/pfr.8.2403096.
- [137] Hans-Joachim Kunze. *Introduction to plasma spectroscopy*, volume 56. Springer, 2009. doi:10.1007/978-3-642-02233-3.
- [138] HP Summers, WJ Dickson, MG O’mullane, Nigel R Badnell, AD Whiteford, DH Brooks, J Lang, SD Loch, and DC Griffin. Ionization state, excited populations and emission of impurities in dynamic finite density plasmas: I. the generalized collisional–radiative model for light elements. *Plasma Physics and Controlled Fusion*, 48(2):263, 2006. doi:10.1088/0741-3335/48/2/007.
- [139] SD Loch, CP Ballance, MS Pindzola, and DP Stotler. The role of excited state ionization data on h and he generalized collisional–radiative coefficients. *Plasma Physics and Controlled Fusion*, 51(10):105006, 2009. doi:10.1088/0741-3335/51/10/105006.
- [140] Martin O’ Mullane. Generalised collisional radiative data for hydrogen. Report, ADAS, 2013. URL: [http://www.adas.ac.uk/notes/adas\\_c13-01.pdf](http://www.adas.ac.uk/notes/adas_c13-01.pdf).
- [141] I Paradela Pérez, A Scarabosio, M Groth, M Wischmeier, F Reimold, and ASDEX Upgrade Team. Sol parallel momentum loss in asdex upgrade and comparison with solps. *Nuclear Materials and Energy*, 12:181–186, 2017. doi:10.1016/j.nme.2017.01.026.
- [142] SA Self and HN Ewald. Static theory of a discharge column at intermediate pressures. *The Physics of Fluids*, 9(12):2486–2492, 1966. doi:10.1063/1.1761642.
- [143] CS Pitcher, JA Goetz, B LaBombard, B Lipschultz, JL Weaver, and BL Welch. The role of friction in sol pressure balance in alcator c-mod. *Journal of nuclear materials*, 266:1009–1014, 1999. doi:10.1016/S0022-3115(98)00850-2.
- [144] P G Carolan and V A Piotrowicz. The behaviour of impurities out of coronal equilibrium. *Plasma Physics*, 25(10):1065, 1983. URL: <http://stacks.iop.org/0032-1028/25/i=10/a=001>.
- [145] Dirk Wunderlich and Ursel Fantz. Evaluation of state-resolved reaction probabilities and their application in population models for he, h, and h2. *Atoms*, 4(4), 2016. doi:10.3390/atoms4040026.
- [146] S. Coda and TCV Team. The science program of the tcv tokamak: exploring fusion reactor and power plant concepts. *Nucl. Fusion*, 55(10):104004, 2015. doi:10.1088/0029-5515/55/10/104004.
- [147] H. Reimerdes, B. P. Duval, J. R. Harrison, et al. Tcv experiments towards the development of a plasma exhaust solution. *Nucl. Fusion*, 57(12):126007, 2017. doi:10.1088/1741-4326/aa82c2.
- [148] M. Kotschenreuther, P. Valanju, B. Covele, and S. Mahajan. Magnetic geometry and physics of advanced divertors: The x-divertor and the snowflake. *Phys. Plasmas*, 20(10):102507, 2013. doi:10.1063/1.4824735.
- [149] D. D. Ryutov. Geometrical properties of a ”snowflake” divertor. *Phys. Plasmas*, 14(6):064502, 2007. doi:10.1063/1.2738399.
- [150] F. Piras, S. Coda, I. Furno, J. M. Moret, R. A. Pitts, O. Sauter, B. Tal, G. Turri, A. Bencze, B. P. Duval, F. Felici, A. Pochelon, and C. Zucca. Snowflake divertor plasmas on tcv. *Plasma Phys. Controlled Fusion*, 51(5):055009, 2009. doi:10.1088/0741-3335/51/5/055009.

- [151] F. Piras, S. Coda, B. P. Duval, B. Labit, J. Marki, S. Y. Medvedev, J. M. Moret, A. Pitzschke, O. Sauter, and T. C. V. Team. "snowflake" h mode in a tokamak plasma. *Phys. Rev. Lett.*, 105(15):155003, 2010. doi:10.1103/PhysRevLett.105.155003.
- [152] W. A. J. Vijvers, G. P. Canal, B. Labit, H. Reimerdes, B. Tal, S. Coda, G. C. De Temmerman, B. P. Duval, T. W. Morgan, J. J. Zielinski, and TCV Team. Power exhaust in the snowflake divertor for l- and h-mode tcv tokamak plasmas. *Nucl. Fusion*, 54(2):023009, 2014. doi:10.1088/0029-5515/54/2/023009.
- [153] B. Covele, P. Valanju, M. Kotschenreuther, and S. Mahajan. An exploration of advanced x-divertor scenarios on iter. *Nucl. Fusion*, 54(7):072006, 2014. doi:10.1088/0029-5515/54/7/072006.
- [154] P. M. Valanju, M. Kotschenreuther, S. M. Mahajan, and John Canik. Super-x divertors and high power density fusion devices. *Physics of Plasmas (1994-present)*, 16(5):056110, 2009. doi:10.1063/1.3110984.
- [155] S. Lisgo, M. Istenic, J. M. Canik, R. Buttery, I. Katramados, M. Kotschenreuther, M. Kovari, S. M. Mahajan, M. Shannon, D. Taylor, et al. Super-x advanced divertor design for mast upgrade. In *36th European Physical Society (EPS) Plasma Physics Conf., Sofia, Bulgaria*, 2009. URL: [http://epsppd.epfl.ch/Sofia/pdf/04\\_046.pdf](http://epsppd.epfl.ch/Sofia/pdf/04_046.pdf).
- [156] M. Kotschenreuther, P. Valanju, S. Mahajan, L. J. Zheng, L. D. Pearlstein, R. H. Bulmer, J. Canik, and R. Maingi. The super x divertor (sxd) and a compact fusion neutron source (cfns). *Nucl. Fusion*, 50(3):035003, 2010. doi:10.1088/0029-5515/50/3/035003.
- [157] V. Rozhansky, P. Molchanov, I. Veselova, S. Voskoboinikov, A. Kirk, G. Fishpool, P. Boerner, D. Reiter, and D. Coster. Modeling of the edge plasma of mast upgrade with a super-x divertor including drifts and an edge transport barrier. *Plasma Phys. Controlled Fusion*, 55(3):035005, 2013. doi:10.1088/0741-3335/55/3/035005.
- [158] E. Havlickova, J. Harrison, B. Lipschultz, G. Fishpool, A. Kirk, A. Thornton, M. Wischmeier, S. Elmore, and S. Allan. Solps analysis of the mast-u divertor with the effect of heating power and pumping on the access to detachment in the super-x configuration. *Plasma Phys. Controlled Fusion*, 57(11):115001, 2015. doi:10.1088/0741-3335/57/11/115001.
- [159] B. LaBombard, E. Marmar, J. Irby, et al. Adx: a high field, high power density, advanced divertor and rf tokamak. *Nucl. Fusion*, 55(5):053020, 2015. doi:10.1088/0029-5515/55/5/053020.
- [160] S Wiesen, D Reiter, V Kotov, M Baelmans, W Dekeyser, AS Kukushkin, SW Lisgo, RA Pitts, V Rozhansky, G Saibene, et al. The new solps-iter code package. *Journal of nuclear materials*, 463:480–484, 2015. doi:10.1016/j.jnucmat.2014.10.012.
- [161] X Bonnin, W Dekeyser, R Pitts, D Coster, S Voskoboinikov, and S Wiesen. Presentation of the new solps-iter code package for tokamak plasma edge modelling. *Plasma and Fusion Research*, 11:1403102–1403102, 2016. doi:doi.org/10.1585/pfr.11.1403102.
- [162] D Reiter, M Baelmans, and P Boerner. The eirene and b2-eirene codes. *Fusion Science and Technology*, 47(2):172–186, 2005. doi:10.13182/FST47-172.
- [163] CF Maggi, JD Elder, W Fundamenski, R Giannella, LD Horton, KD Lawson, A Loarte, A Maas, R Reichle, M Stamp, et al. Measurement and analysis of radiated power components in the jet mki divertor using vuv spectroscopy. *Journal of nuclear materials*, 241:414–419, 1997. doi:10.1016/S0022-3115(97)80074-8.
- [164] Per Helander, SI Krasheninnikov, and PJ Catto. Fluid equations for a partially ionized plasma. *Physics of plasmas*, 1(10):3174–3180, 1994. doi:10.1063/1.870470.
- [165] D.E. Post, N. Putvinskaya, F. W. Perkins, and W. Nevins. Analytic criteria for power exhaust in divertors due to impurity radiation. *J. Nucl. Mater.*, 220:1014–1018, 1995. doi:10.1016/0022-3115(94)00464-1.
- [166] H Weisen, R Behn, Y Camenen, S Coda, A Degeling, BP Duval, E Fable, I Furno, B Joye, X Llobet, et al. Multi-chord diagnostics on the tcv tokamak. In *The 2nd German-Polish Conference on Plasma Diagnostics for Fusion and Applications (GPPD-2004)*. Cracow, Poland, 2004. URL: [https://www.researchgate.net/publication/237558398\\_Multi-chord\\_diagnostics\\_on\\_the\\_TCV\\_tokamak](https://www.researchgate.net/publication/237558398_Multi-chord_diagnostics_on_the_TCV_tokamak).
- [167] Balazs Tal. *Measurement of transient events in hot magnetized plasmas*. PhD thesis, Wigner Research Centre for Physics, Department of Plasma Physics, 2015. URL: <http://hdl.handle.net/10890/1448>.
- [168] Federico Nespoli. *Scrape-Off Layer physics in limited plasmas in TCV*. PhD thesis, Ecole Polytechnique Fédérale de Lausanne, 2017. doi:10.5075/epfl-thesis-7475.

- [169] U. A. Sheikh, B. P. Duval, B. Labit, and F. Nespoli. A novel carbon coating technique for foil bolometers. *Rev. Sci. Instrum.*, 87(11):11D431, 2016. doi:10.1063/1.4961271.
- [170] J Hawke, Y Andrebe, R Bertizzolo, P Blanchard, R Chavan, J Decker, B Duval, P Lavanchy, X Llobet, B Marlétaz, et al. Improving spatial and spectral resolution of tcv thomson scattering. *Journal of Instrumentation*, 12(12):C12005, 2017. doi:10.1088/1748-0221/12/12/C12005.
- [171] A Herrmann. Limitations for divertor heat flux calculations of fast events in tokamaks. In *28th EPS Conference on Controlled Fusion and Plasma Physics. Contributed Paper*, volume 25, 01 2001. URL: <http://hdl.handle.net/11858/00-001M-0000-0027-49DD-7>.
- [172] J Boedo, D Gray, L Chousal, R Conn, B Hiller, and KH Finken. Fast scanning probe for tokamak plasmas. *Review of scientific instruments*, 69(7):2663–2670, 1998. doi:10.1063/1.1148995.
- [173] J. A. Boedo, N. Crocker, L. Chousal, R. Hernandez, J. Chalfant, H. Kugel, P. Roney, J. Wertenbaker, and Nstx Team. Fast scanning probe for the nstx spherical tokamak. *Rev. Sci. Instrum.*, 80(12):123506, 2009. doi:10.1063/1.3266065.
- [174] CK Tsui, JA Boedo, JR Myra, B Duval, B Labit, C Theiler, N Vianello, WAJ Vijvers, H Reimerdes, S Coda, et al. Filamentary velocity scaling validation in the tcv tokamak. *Physics of Plasmas*, 25(7):072506, 2018. doi:10.1063/1.5038019.
- [175] N Vianello, C Tsui, C Theiler, S Allan, J Boedo, B Labit, H Reimerdes, K Verhaegh, WAJ Vijvers, N Walkden, et al. Modification of sol profiles and fluctuations with line-average density and divertor flux expansion in tcv. *Nuclear Fusion*, 57(11):116014, 2017.
- [176] Siobhán M.. Barry. *The extension of the FIR interferometer of TCV to a polarimeter and measurements of the Faraday rotation caused by the poloidal magnetic field*. PhD thesis, University of York, 1999. URL: <https://infoscience.epfl.ch/record/121172>.
- [177] Uron Kruezi, G Sergienko, PD Morgan, GF Matthews, S Brezinsek, S Vartanian, and JET-EFDA Contributors. Jet divertor diagnostic upgrade for neutral gas analysis. *Review of Scientific Instruments*, 83(10):10D728, 2012. doi:10.1063/1.4732175.
- [178] S Varoutis, C Gleason-González, D Moulton, U Kruezi, M Groth, Chr Day, S Wiesen, D Harting, and JET Contributors. Simulation of neutral gas flow in the jet sub divertor and comparison with experimental results. In *Proc. 25th IAEA Fusion Energy Conf.*, pages 1–15, 2014. doi:10.1016/j.fusengdes.2017.05.108.
- [179] Artur Niemczewski, IH Hutchinson, B LaBombard, B Lipschultz, and GM McCracken. Neutral particle dynamics in the alcator c-mod tokamak. *Nuclear fusion*, 37(2):151, 1997. doi:10.1088/0029-5515/37/2/I04.
- [180] Claudio Marini. *Poloidal CX visible light plasma rotation diagnostics in TCV*. PhD thesis, Ecole Polytechnique Fédérale de Lausanne, Lausanne, 2017. doi:10.5075/epfl-thesis-8031.
- [181] D Wagner, A Bencze, BP Duval, Y Andrebe, and F Piras. Visible video diagnostic systems on tcv. *International Conference on Plasma Diagnostics*, 2010. URL: [https://inis.iaea.org/search/search.aspx?orig\\_q=RN:43043530](https://inis.iaea.org/search/search.aspx?orig_q=RN:43043530).
- [182] BL Linehan, RT Mumgaard, M Wensing, K Verhaegh, Y Andrebe, JR Harrison, BP Duval, and C Theiler. The multi-spectral imaging diagnostic. *Review of Scientific Instruments*, 2018 in press.
- [183] RT Mumgaard, SD Scott, and M Khouri. The multi-spectral line-polarization mse system on alcator c-mod. *Review of Scientific Instruments*, 87(11):11E527, 2016. doi:10.1063/1.4959793.
- [184] WAJ Vijvers, RT Mumgaard, Y Andrebe, IGJ Classen, BP Duval, and B Lipschultz. Conceptual design and proof-of-principle testing of the real-time multispectral imaging system mantis. *Journal of Instrumentation*, 12(12):C12058, 2017. doi:10.1088/1748-0221/12/12/C12058.
- [185] J McClure. Anastigmatic imaging spectrograph. Technical Report US20130182250A1, Roper Scientific Inc, 2012. Patent US 20130182250A1. January 2012. URL: <https://patents.google.com/patent/US20130182250A1/en?inventor=Jason+McClure>.
- [186] Adrian A. Dorrrington, Michael J. Cree, and Dale A. Carnegie. The importance of ccd readout smear in heterodyne imaging phase detection applications. In *Proc. Image and Vision Computing New Zealand*, pages 73–8, 2005. URL: [https://www.researchgate.net/publication/228861523\\_The\\_Importance\\_of\\_CCD\\_Readout\\_Smear\\_in\\_Heterodyne\\_Imaging\\_Phase\\_Detection\\_Applications](https://www.researchgate.net/publication/228861523_The_Importance_of_CCD_Readout_Smear_in_Heterodyne_Imaging_Phase_Detection_Applications).

- [187] Wim Ruyten. Smear correction for frame transfer charge-coupled-device cameras. *Opt. Lett.*, 24(13):878–880, Jul 1999. doi:[10.1364/OL.24.000878](https://doi.org/10.1364/OL.24.000878).
- [188] S Tabel and W Stechele. Fast computation of readout smear correction for framestore ccd based images. In *Proceedings of the 2017 International Conference on Computer Graphics and Digital Image Processing*, CGDIP ’17, pages 18:1–18:6, New York, NY, USA, 2017. ACM. doi:[10.1145/3110224.3110233](https://doi.org/10.1145/3110224.3110233).
- [189] FA Iglesias, A Feller, and K Nagaraju. Smear correction of highly variable, frame-transfer ccd images with application to polarimetry. *Appl. Opt.*, 54(19):5970–5975, Jul 2015. doi:[10.1364/AO.54.005970](https://doi.org/10.1364/AO.54.005970).
- [190] Y Zong, SW Brown, BC Johnson, KR Lykke, and Y Ohno. Simple spectral stray light correction method for array spectroradiometers. *Appl. Opt.*, 45(6):1111–1119, Feb 2006. doi:[10.1364/AO.45.001111](https://doi.org/10.1364/AO.45.001111).
- [191] A Barlier-Salsi. Stray light correction on array spectroradiometers for optical radiation risk assessment in the workplace. *Journal of Radiological Protection*, 34(4):915, 2014. doi:[10.1088/0952-4746/34/4/915](https://doi.org/10.1088/0952-4746/34/4/915).
- [192] J Jablonski, A Arecchi, J Jacobs, and T Annicchiarco. Stray light rejection techniques for led measurements using ccd based spectrometers. In *Proceedings of SPIE - The International Society for Optical Engineering*, 02 2009. doi:[10.1117/12.809241](https://doi.org/10.1117/12.809241).
- [193] SW Brown, BC Johnson, ME Feinholz, MA Yarbrough, SJ Flora, KR Lykke, and DK Clark. Stray-light correction algorithm for spectrographs. *Metrologia*, 40(1):S81, 2003. URL: <http://stacks.iop.org/0026-1394/40/i=1/a=318>.
- [194] Yuqin Zong, Steven W Brown, Gerhard Meister, Robert A Barnes, and Keith R Lykke. Characterization and correction of stray light in optical instruments. In *Sensors, Systems, and Next-Generation Satellites XI*, volume 6744, page 67441L. International Society for Optics and Photonics, 2007. URL: <https://www.nist.gov/publications/characterization-and-correction-stray-light-optical-instruments>.
- [195] M. E. Feinholz, S. J. Flora, S. W. Brown, Y. Zong, K. R. Lykke, M. A. Yarbrough, B. C. Johnson, and D. K. Clark. Stray light correction algorithm for multichannel hyperspectral spectrographs. *Appl. Opt.*, 51(16):3631–3641, Jun 2012. doi:[10.1364/AO.51.003631](https://doi.org/10.1364/AO.51.003631).
- [196] E Kristensson, J Bood, M Alden, E Nordström, J Zhu, S Huldt, PE Bengtsson, H Nilsson, E Berrocal, and A Ehn. Stray light suppression in spectroscopy using periodic shadowing. *Optics Express*, 22(7):7711–7721, 2014. doi:[10.1364/OE.22.007711](https://doi.org/10.1364/OE.22.007711).
- [197] J Rosato, H Bufferand, M Koubiti, Y Marandet, and R Stamm. A table of balmer  $\gamma$  line shapes for the diagnostic of magnetic fusion plasmas. *Journal of Quantitative Spectroscopy and Radiative Transfer*, 165:102–107, 2015. doi:[10.1016/j.jqsrt.2015.06.018](https://doi.org/10.1016/j.jqsrt.2015.06.018).
- [198] J Rosato, I Hannachi, Y Marandet, and R Stamm. Line shape models for magnetized hydrogen plasmas. In *Journal of Physics: Conference Series*, volume 810, page 012011. IOP Publishing, 2017. doi:[10.1088/1742-6596/810/1/012011](https://doi.org/10.1088/1742-6596/810/1/012011).
- [199] J. Rosato, Y. Marandet, and R. Stamm. A new table of balmer line shapes for the diagnostic of magnetic fusion plasmas. *Journal of Quantitative Spectroscopy and Radiative Transfer*, 187:333 – 337, 2017. doi:[10.1016/j.jqsrt.2016.10.005](https://doi.org/10.1016/j.jqsrt.2016.10.005).
- [200] S Ferri, A Calisti, C Mossé, J Rosato, B Talin, S Alexiou, MA Gigosos, MA González, D González-Herrero, N Lara, et al. Ion dynamics effect on stark-broadened line shapes: A cross-comparison of various models. *Atoms*, 2(3):299–318, 2014. doi:[10.3390/atoms2030299](https://doi.org/10.3390/atoms2030299).
- [201] A Brissaud, C Goldbach, J Leorat, A Mazure, and G Nollez. On the validity of the model microfield method as applied to stark broadening of neutral lines. *Journal of Physics B: Atomic and Molecular Physics*, 9(7):1129, 1976. doi:[10.1088/0022-3700/9/7/014](https://doi.org/10.1088/0022-3700/9/7/014).
- [202] S Ferri, A Calisti, C Mossé, L Mouret, B Talin, MA Gigosos, MA Gonzalez, and V Lisitsa. Frequency-fluctuation model applied to stark-zeeman spectral line shapes in plasmas. *Physical Review E*, 84(2):026407, 2011. doi:[10.1103/PhysRevE.84.026407](https://doi.org/10.1103/PhysRevE.84.026407).
- [203] A. Kramida, Y.Ralchenko, J. Reader, and the NIST ASD Team. NIST Atomic Spectra Database (ver. 5.5.6), Available online [2017, April 9]. National Institute of Standards and Technology, Gaithersburg, MD., 2018. URL: <https://physics.nist.gov/asd>.

- [204] AM El Sherbini, TM El Sherbini, H Hegazy, G Cristoforetti, S Legnaioli, V Palleschi, L Pardini, A Salvetti, and E Tognoni. Evaluation of self-absorption coefficients of aluminum emission lines in laser-induced breakdown spectroscopy measurements. *Spectrochimica Acta Part B: Atomic Spectroscopy*, 60(12):1573–1579, 2005. doi: 10.1016/j.sab.2005.10.011.
- [205] F Rezaei and SH Tavassoli. Utilizing the ratio and the summation of two spectral lines for estimation of optical depth: Focus on thick plasmas. *Spectrochimica Acta Part B: Atomic Spectroscopy*, 125:25 – 30, 2016. doi: 10.1016/j.sab.2016.09.010.
- [206] PR. Bevington and DK Robinson. *Data reduction and error analysis*. McGraw-Hill, 2003. URL: [https://books.google.com/books/about/Data\\_Reduction\\_and\\_Error\\_Analysis\\_for\\_th.html?id=0poQAQAAIAAJ&source=kp\\_cover&redir\\_esc=y](https://books.google.com/books/about/Data_Reduction_and_Error_Analysis_for_th.html?id=0poQAQAAIAAJ&source=kp_cover&redir_esc=y).
- [207] Hans R. Griem. *Plasma spectroscopy*, volume 1. McGraw-Hill, New York, 1964. URL: [https://books.google.com/books/about/Principles\\_of\\_Plasma\\_Spectroscopy.html?id=ed2w1I5F7zMC&source=kp\\_cover&redir\\_esc=y](https://books.google.com/books/about/Principles_of_Plasma_Spectroscopy.html?id=ed2w1I5F7zMC&source=kp_cover&redir_esc=y).
- [208] B Lomanowski et al. *Visible and near-infrared divertor spectroscopy on the MAST and JET-ILW tokamaks*. PhD thesis, Durham University, 2015. URL: <http://etheses.dur.ac.uk/11437/>.
- [209] Mary Kathryn Cowles. *Applied Bayesian statistics: with R and OpenBUGS examples*, volume 98. Springer Science & Business Media, 2013. doi:10.1007/978-1-4614-5696-4.
- [210] CE Papadopoulos and H Yeung. Uncertainty estimation and monte carlo simulation method. *Flow Measurement and Instrumentation*, 12(4):291 – 298, 2001. doi:10.1016/S0955-5986(01)00015-2.
- [211] ZI Botev, JF Grotowski, and DP Kroese. Kernel density estimation via diffusion. *The Annals of Statistics*, 38(5):2916–2957, 2010. Matlab routine available: <https://uk.mathworks.com/matlabcentral/fileexchange/58309-adaptive-kernel-density-estimation-in-one-dimension>. doi:10.1214/10-AOS799.
- [212] Christopher Bowman. *Applications of Bayesian probability theory in fusion data analysis*. PhD thesis, University of York, 2016. URL: <http://etheses.whiterose.ac.uk/16978/>.
- [213] S.S. Henderson, M. Bernert, S. Brezinsek, M. Carr, M. Cavedon, R. Dux, B. Lipschultz, M.G. O'Mullane, F. Reinold, M.L. Reinke, The ASDEX Upgrade Team, and The MST1 Team. Determination of volumetric plasma parameters from spectroscopic n ii and n iii line ratio measurements in the asdex upgrade divertor. *Nuclear Fusion*, 58(1):016047, 2018. URL: <http://stacks.iop.org/0029-5515/58/i=1/a=016047>.
- [214] B. Lipschultz, D. Whyte, and B. LaBombard. Comparison of particle transport in the scrape-off layer plasmas of alcator c-mod and diii-d. *Plasma Phys. Controlled Fusion*, 47(10):1559–1578, 2005. doi:10.1088/0741-3335/47/10/001.
- [215] R Maurizio, S Elmore, N Fedorczak, A Gallo, H Reimerdes, B Labit, C Theiler, CK Tsui, WAJ Vijvers, TCV Team, et al. Divertor power load studies for attached l-mode single-null plasmas in tcv. *Nuclear Fusion*, 58(1):016052, 2017. doi:10.1088/1741-4326/aa986b.
- [216] V Kotov, D Reiter, and AS Kukushkin. Numerical study of the iter divertor plasma with the b2-eirene code package. Technical report, Forschungszentrums Jülich, 2007. Report nr. Jül-4257. URL: [https://inis.iaea.org/search/search.aspx?orig\\_q=RN:39025830](https://inis.iaea.org/search/search.aspx?orig_q=RN:39025830).
- [217] M.G. Kendall and J.D. Gibbons. *Rank correlation methods*. A Charles Griffin Book. E. Arnold, 1990. URL: <https://books.google.com/books?id=ly4nAQAAIAAJ>.